Series in BioEngineering

Eddie Y.K. Ng
Mahnaz Etehadtavakol *Editors*

Application of Infrared to Biomedical Sciences

Springer

Series in BioEngineering

More information about this series at http://www.springer.com/series/10358

Eddie Y.K. Ng · Mahnaz Etehadtavakol
Editors

Application of Infrared to Biomedical Sciences

Springer

Editors
Eddie Y.K. Ng
College of Engineering
Nanyang Technological University
Singapore
Singapore

Mahnaz Etehadtavakol
Medical Image and Signal Processing
Research Center
Isfahan University of Medical Sciences
Isfahan
Iran

ISSN 2196-8861 ISSN 2196-887X (electronic)
Series in BioEngineering
ISBN 978-981-10-3146-5 ISBN 978-981-10-3147-2 (eBook)
DOI 10.1007/978-981-10-3147-2

Library of Congress Control Number: 2016963736

Printed on acid-free paper

This Springer imprint is published by Springer Nature
The registered company is Springer Nature Singapore Pte Ltd.
The registered company address is: 152 Beach Road, #21-01/04 Gateway East, Singapore 189721, Singapore

Preface

Thermography or infrared (IR) imaging system is dependent on an accurate analysis of skin and tissue temperatures. Its diagnostic procedure allows practitioners to identify the locations of abnormal chemical and blood vessel activity such as angiogenesis in body tissue. It is a noninvasive approach by applying the technology of the infrared camera and state-of-the-art software. Nowadays available high-resolution digital infrared imaging technology benefits highly from enhanced image production, standardized image interpretation protocols, computerized comparison and storage, and sophisticated image enhancement and analysis.

We are interested here to provide latest update on chapters in recent application of infrared to biomedical sciences. More examples will be analyzed comprehensively and deeply in this book. This book certainly includes color images and tables. Since infrared imaging is a nonintrusive, contactless, safe and easy approach, it is very beneficial to medical field. Nowadays with new generation and advancement of sensor technology, image processing algorithms and sophisticated computers, infrared imaging is being paid more attention. For better and healthier society we need to look at a safe and noninvasive modality with early detection potential as an adjunctive method to detect health problem. The book covers wide-ranging topics as follows:

The book with 28 chapters has two parts. First part of the book covers six different chapters by us. Various methods and applications of IR as contributed by many IR experts are then discussed in second part of the book.

Thermography is a simple, noninvasive and reproducible test that can accurately reflect the inflammatory activity, and can be used safely and repeatedly, during biological course of inflammatory bowel disease. Chapter "Potential of Infrared Imaging in Assessing Digestive Disorders" presents the possibility of infrared imaging in assessing digestive disorders such as irritable bowel syndrome, diverticulitis, and Crohn's disease.

Pain has been a problem to be differentially diagnosed for years since it has been diagnosed subjectively. There is no test that can provide data indicating the accurate information regarding the location and amount of the pain. Hence clinicians count on the patient's own explanation of the location, form, and timing of the pain. Chapter

"Potential of Thermography in Pain Diagnosing and Treatment Monitoring" introduces pain and application of thermography for diagnosis of different pain categories as well as monitoring the treatments. Thermography can provide data of pain quantitatively as it reports detail and deep thermal variations. Indeed this method can be useful to diagnose pain objectively.

Nowadays there is a considerable appreciation of thermal physiology and the connection between superficial hotness and blood perfusion. Furthermore, the advantages of computer-aided digital imaging and the examination modality has considerably enhanced the trustworthiness of this technique in medical fields. The advantage of this new possibility and its applicability to medical determination of peripheral perfusion and liveliness of cells are shown by studies in diabetology. Researches demonstrate that routine checking up on foot temperature could terminate the occurrence of impairment conditions including foot ulcers and lower limb amputations. Thermography is identified as one of the potential techniques for temperature checking up on the feet and it can be employed as an adjunctive method for modern foot examinations in diabetes and systematically discussed in Chapter "Assessment of Foot Complications in Diabetic Patients Using Thermography: A Review". Researches indicate that routine checking up on foot temperature may terminate the occurrence of impairment conditions including foot ulcers and lower limb amputations.

In more than 30 years of IR breast cancer investigation, 800 peer-reviewed researches including more than 300,000 women contributors have exhibited thermography's potential for diagnosing breast cancer in very early stages. Identifying relationships between neo-angiogenesis, chemical mediators, and the neoplastic developments are the aim of current studies to investigate thermal feature of breast anatomy. Chapter "An Overview of Medical Infrared Imaging in Breast Abnormalities Detection" presents an overview of medical infrared imaging in breast abnormalities detection.

Chapter "Registration of Contralateral Breasts Thermograms by Shape Contexts Technique" reports that comparison of breast temperature in the contralateral breast is very helpful in breast cancer detection diagnosis. Asymmetrical temperature thermal diffusion might be a sign of early irregularity. Practically, most of the real breast thermograms do not possess symmetric borders. Consequently, a suitable registration is required for comparing temperature distribution of two breasts by investigating in contrast the extracted features. In this chapter, the proposed registration algorithm includes two steps. First, shape context, the technique as introduced by Belongie et al was used to register two breast borders. Second, a mapping function of boundary points was obtained and applied for mapping two breast interior points. Results are very encouraging. Boundary registration was accomplished perfectly for 28 out of the 32 cases.

Although it is controversial that with pseudocolored gray images more data can be allowed to the observer, but precisely produced pseudocolor image indeed is capable of tumor identification that is equivalent to the grayscale and upgrades accomplishment of other jobs like perception and judgment of a tumor. In Chapter "Color Segmentation of Breast Thermograms: A Comparative Study", three

techniques for breast thermograms color segmentation (K-means, mean shift (MS), and fuzzy c-means (FCM)) were used with 60 breast thermograms. The FCM technique allows the two first hottest areas for each subject where convenient features are obtainable. There are some conveniences of breast thermograms color segmentation by FCM such as: identification of irregular subjects by contrasting the analogous clusters from the contralateral breasts (over the symmetrical line); determination of level of malignity with identifying the two first hottest areas and extracting them some useful features.

The use of artificial sources for cooling the skin has revealed new functional information that complements steady-state thermography findings. This autonomic cold challenge has also been used to identify a tumor's blood vessels. Recent numerical methods have investigated the effectiveness of dynamic breast thermography and revealed new parameters that are strongly correlated with tumor's depth. Chapter "Potentialities of Dynamic Breast Thermography" reviews the state of the art in dynamic thermography as it is applied to breast diagnosis and identify some of the potential information that could be provided about breast diseases.

Chapter "In Vivo Thermography-Based Image for Early Detection of Breast Cancer Using Two-Tier Segmentation Algorithm and Artificial Neural Network" proposes a technical framework for automatic segmentation and classification of abnormality on multiple in vivo thermography based images. A new two-tier automatic segmentation algorithm is developed using a series of thermography screening conducted on both pathological and healthy Sprague-Dawley rats. Features extracted shows that the mean values for temperature standard deviation and pixel intensity of the abnormal thermal images are distinctively higher when compared to normal thermal images and for classification, Artificial Neural Network system was developed and has produced a validation accuracy performance of 92.5% for thermal image abnormality detection. A large data set from both healthy and cancer patients is required as future clinical study in both thermal visual and data temperature point formats to confirm the efficacy of this method.

Detection of elevation in local surface temperature due to an underlying pathology (hot spots) from conventional breast thermograms is quite challenging, mainly due to incomplete image acquisition. Chapter "Detection of Breast Abnormality Using Rotational Thermography" explores a framework in developing a breast cancer screening system using thermograms acquired with rotational thermography in multiple views to locate the position of the tumor in correlation with ultrasound and biopsy findings, its ability for localization of abnormality has also been discussed. Image features are extracted from rotational thermograms in spatial, bispectral, and multi-resolution domains. Optimal features are identified using Genetic algorithm and automatic classification is performed using Support Vector Machine. In addition to screening, attempt has been made to characterize a detected abnormality as benign or malignant.

Chapter "Application of Infrared Images to Diagnosis and Modeling of Breast" reveals several approaches that have been implemented related to the use of IR images to breast modeling and diseases diagnosis; the authors consider many aspects of the process of diagnostic tool implementation: capture thermal matrix of

patient body, storage and retrieval of images from a database, segmentation, 3D reconstruction, feature extraction and classification. The experiments and implementations were done by the Visual Lab group of the Fluminense Federal University in Niteroi, Rio de Janeiro, Brazil. The results support the statement that IR analysis is able to detect breast anomalies and to include the thermography in clinical routines for breast diseases examination and screening. When considering the dynamic protocol versus the static one, tools for diagnosis implemented using the dynamic protocol data always achieve better results even when very simple approaches are used like only the temporal series of data.

Chapter "A Semi-Analytical Heterogeneous Model for Thermal Analysis of Cancerous Breasts" studies a semi-analytical method for breast thermography through coupled stationary bioheat transfer equations. The theoretical and numerical modeling results indicate that the data parameter will influence the thermal distribution of the tumorous breast. The work provides a helpful framework for studying the thermal profile of breast cancerous tissues. It facilitates the understanding of the complex behavior of its surface temperature. In brief, thermography together with mathematical and computational modeling bring an appropriate methodology in order to allow the assessment of rapidly growing neoplasm.

Chapter "Dynamic Angiothermography (DATG)" develops Dynamic Angiothermography (DATG) for the noninvasive diagnosis of breast cancer. DATG consists of a thin plate with liquid crystals that changes color due to a change in temperature, consequently offering an image of breast vasculature. DATG is based on the angiogenesis (bioheat) theory on tumor initiation, development, and growth. A tumor needs new vessels. Therefore, by studying the changes in the pattern of vascular blood supply, it is also possible to diagnose neoplasms very early. In particular, it is shown that every human being has his or her own vascular pattern which, in the absence of disease, does not vary throughout the life time. By repeating DATG periodically, an efficient control of the onset of disease is possible, even in its early stages. This is not new, however, still only little-known technique which is a component of the overall diagnostic techniques for the study and prevention of breast cancer that serves to offer a complete clinical picture of the patient. The great advantages of DATG are: it does not use radiation; it is not invasive or painful; it is low-cost and can be repeated periodically and successfully with no drawbacks. The angiothermographic examination therefore makes it possible to visualize the breast vascularity pattern without using contrast medium. On the other hand, while highlighting changes in mammary vascularization, DATG is not able to indicate the size or depth of the tumor; even if recent researches (based on the approximated solution of the inverse Fourier heat equation) show the possibility to evaluate the depth of the tumor. In brief, DATG is affordable from the economic standpoint as it can play a very important role especially for young women and for those applicants who need frequent checks (follow-ups).

Considering the substantial increase in diabetics cases worldwide, a dedicated effort for early detection of diabetes is essential. Various studies reveal that infrared thermography is capable of the early detection of diabetic peripheral neuropathy and vascular disorders. Chapter "Infrared Thermography for Detection of Diabetic

Neuropathy and Vascular Disorder" highlights the studies on diabetic neuropathy and vascular disorder using IR thermography technique. The basics of IR thermography, classification of medical thermography techniques, details of various IR cameras available, ideal experimental conditions, data analysis, etc., along with typical case studies on the subjects are discussed. To recommend IRT as routine techniques for diagnosis of diabetic neuropathy and vascular disorder, more systematic case studies in large number of subjects from various continents and correlating the IRT results with clinical findings are a prerequisite. Further, refinement in the experimental protocols, automation, rapid and reliable data analysis approaches are to be developed. For example, diabetes mellitus (DM), lower extremity diseases (LED) include both diabetic peripheral neuropathy (DPN) and peripheral vascular disease (PVD). Other than focusing on the effect of autonomic neuropathy on the microcirculation causing atrial–venous shunting one should also look at the fundamentals that PVD itself, i.e., macroangiopathy manifesting as atherosclerosis is a separate disease progression among people with DM.

Chapter "Exploratory Thermal Imaging Assessments of the Feet in Patients with Lower Limb Peripheral Arterial Disease" introduces pilot study to explore the potential use of thermal imaging in identifying Peripheral arterial disease (PAD). Absolute, gradient, spatial, and bilateral skin temperature differences of the feet have been quantified in PAD and non-PAD legs and have found no significant differences overall. The pilot study indicates that thermal imaging from resting measurements is unlikely to be of diagnostic value in detecting significant PAD. Furthermore, the study also raises questions about the apparent misconception that in PAD the foot temperatures are always significantly reduced. Thus, reliable fast, noninvasive devices (in contrast to the ankle brachial pressure index tool) for the detection of PAD are still required to aid the diagnosis of this underdiagnosed but significant cardiovascular disease.

The feet of healthy individuals can be very variable in absolute temperature on different days but thermal symmetry is generally maintained. Characteristic thermal patterns seem to be consistent so there may be some diagnostic value in a change in pattern or symmetry. Thermal asymmetry due to transient changes during the study period need to be ruled out with repeated images. Chapter "Reproducibility of Thermal Images: Some Healthy Examples" permits a baseline understanding of thermal symmetry in the feet of healthy participants which can be used when interpreting the images of the feet of patients with diabetes and neuropathy. It concludes that when looking for significant thermal asymmetry it is important to rule out transient changes by repeated imaging and to refer to baseline images.

Chapter "Thermal Imaging for Increasing the Diagnostic Accuracy in Fetal Hypoxia: Concept and Practice Suggestions" develops a method for diagnosing fetal cerebral hypoxia with a thermal imaging camera. The method is based on the following detected principle: hypoxia and ischemia reduce the intensity of thermal radiation from tissues. Monitoring the dynamics of temperature in the central suture allows doctor to evaluate the oxygen supply to fetal brain cortex during delivery. In this context, if the temperature drop areas are not observed in fetal head skin during his passing through the birth canals, it indicates the possibility of giving birth to a

healthy child. In its turn, the occurrence of local hypothermia over the central suture of the skull indicates the hypoxic and ischemic damage to the fetal brain cortex and requires immediate hyperoxygenation of the fetus blood.

Chapter "Active Dynamic Thermography in Medical Diagnostics" shows importance of still new in medicine visualization modality called ADT—Active Dynamic Thermography. Assuming that classical thermal imaging (TI) is already broadly accepted, what in fact is only partly true as some clinicians still remember that this technology in breast cancer diagnostics failed in early stage of development, the ADT increases the role of thermal imaging in medicine. To register static TI and dynamic ADT images the same IR camera is applied. Both modalities are supplementing each other as TI shows metabolic functional thermal images and ADT allows reconstruction of structural thermal properties adding to functional also structural diagnostic data. Therefore analysis and comparison of temperature distribution and images of ADT descriptors provide better understanding of diagnostic content and support multimodality concept of advanced diagnostics in medicine.

Respiratory rate is very important vital sign that should be measured and documented in many medical situations. Chapter "Evaluation of Respiration Rate Using Thermal Imaging in Mobile Conditions" analyzes respiration rate estimators that can be used to processed sequences of thermal images captured from small thermal camera modules embedded or connected to smart glasses for respiration waveforms derived from the regions of the nostrils or mouth in thermal video sequences. After calibration of thermal camera modules and using the algorithms to estimate pulse rate from video (recorded in visible light), additional vital signs can be estimated. This could allow obtaining three the most important vital signs: body temperature, pulse rate, and respiration rate. Using the intelligent patient identification such data can be automatically stored in the Hospital Information System or other system for the management of Electronic Health Records or Personal Health Records.

Infrared thermography (IRT), one of the most valuable tools, is used for non-contact, noninvasive, and rapid monitoring of body temperature; it has been used for mass screening of febrile travelers at places such as airport quarantine stations for over 10 years after the 2003 severe acute respiratory syndrome (SARS) outbreak. The usefulness of IRT for mass screening has been evaluated in many recent studies; its sensitivity varies from 40% to 89.4% under various circumstances. Chapter "Applications of Infrared Thermography for Noncontact and Noninvasive Mass Screening of Febrile International Travelers at Airport Quarantine Stations" performs IRT evaluations in detecting febrile international travelers entering Japan at Nagoya Airport, immediately after the SARS epidemic, from June 2003 to February 2004, and at Naha International Airport from April 2005 to March 2009. The correlation of body surface temperature measured via IRT with the axillary temperature was significant. Febrile individuals were detected with good accuracy and the detection accuracy was improved by corroborating surveillance with self-reporting questionnaires. However, there are several limitations associated with the use of IRT for fever screening. To solve the unreliability and obtain higher accuracy in mass screening, the authors have developed a novel

infection screening system using multi-sensor data, i.e., heart and respiration rates are determined by microwave radar in non-contact manner and facial skin temperature is monitored through IRT. The detection accuracy of the system improved, which is notably higher compared to the conventional screening method using only IRT. In future work, one of the most promising approaches is to connect multiple infection screening systems, which enables information sharing between different systems. This will allow application of big data analysis techniques, which can be used to predict outbreaks of infectious diseases much earlier than the existing methods.

It is clinically important to detect tear instability in Dry Eye (DE) as the treatment may involve specific measures such as chronic eyelid warming therapy. To achieve this, a practical and rapid method to analyze the relevant features from different regions of the ocular surface in DE will be useful. In Chapter "Evaluation of Evaporative Dry Eye Disease Using Thermal Images of Ocular Surface Regions with DWT and Gabor Transform", efficiency of using the upper half and lower half regions of the ocular surface (cornea + conjunctiva) in the detection of evaporative dry eye is assessed using IRT images where the significance of limited ocular surface regions for the identification of DE is suggested by extracting Gabor transform features from DWT coefficients. The study shows that the lower half of the eye is superior to the upper half for the purpose of DE detection. The proposed algorithm is efficient, simple and may be employed in polyclinics or hospitals for faster DE assessment time without analyzing the entire ocular surface.

Skin, the largest organ of the human body, is essentially a temperature *mosaic* determined by the rate of blood flow through arterioles and capillaries adjacent to the skin. IR imaging has the potential to provide a robust method of surface temperature mapping in disease states where pathology disturbs the 'normal' distribution of blood flow to skin. Hierarchical clustering-based segmentation (HCS) has been used in Chapter "Infrared Thermal Mapping, Analysis and Interpretation in Biomedicine" to aid the interpretation of wound images and to identify variations in temperature clusters around and along the surgical wound for their clinical relevance in wound infection at levels not discernible by human visual processing.

Among the known and routinely used tomography methods, there is the thermal tomography, which seems to be still unappreciated. Certainly, it has some constrains, especially due to the limited depth of the body penetration by the heat waves, but on the other hand, it can be recommended for daily screening of skin tissues pathologies, burns during healing and superficial tumors. For medical thermal tomography, one proposes the cold provocation applied to the skin tissue and the measurements of body temperature recovery by IRT. Then, by applying the inverse thermal modeling of the tissue, the internal structure can be reconstructed. Inverse thermal modeling, however, requires the forward thermal models and the optimization. Both of these elements can be implemented today in a software to perform the screening since IR cameras are cheaper and widely available today. It makes possible to establish a new medical protocol for IRT screening. Chapter "Medical Thermal Tomography—Different Approaches" describes the different original approaches in medical thermal tomography developed by the authors

recently and the presented protocols can be easily and fast adapted to the practical use in the medical diagnosis.

Water transformation process operated by evaporation can be considered as one of the most important causes of thermal disequilibrium in both living and nonliving objects (i.e., porous materials). Vapotranspiration fluxes taking place on surfaces of many kind of materials has been proved to be quantitatively defined measuring surface temperature of the object being studied. This value, at the equilibrium conditions among all terms of heat exchange occurring through the surface, shows to be strongly dependent on the vapor flux rate. Correlations between temperature and evaporation rate have been confirmed in Chapter "Vapotranspiration in Biological System by Thermal Imaging" on different type of materials such as leaves, plaster, brick and human skin, proving the strong correlation between temperature and evaporation rate, both in a thin system such as leaf, porous building, materials and human skin.

Chapter "Change in Local Temperature of Venous Blood and Venous Vessel Walls as a Basis for Imaging Superficial Veins During Infrared Phlebography Using Temperature-Induced Tissue Contrasting" demonstrates a possibility of fast, safe, and efficient imaging of superficial veins with an IR imager in experiments with pigs, in studies with healthy adult volunteers, and in clinical observations of adult patients when providing vital medical care in emergency situations. This chapter describes the original techniques for infrared veins imaging enabling the authors to lay the basis for infrared venography. In order to image superficial veins, it is recommended that infrared monitoring of local temperature dynamics in the selected part of the body surface under the conditions of artificial multidirectional changes in temperature of veins and/or surrounding tissues. The chapter also shows advantages of infrared phlebography over other radiology methods to address urgent and repeated imaging of superficial veins in critical situations to optimize intravascular access for sampling venous blood, its subsequent laboratory testing and intravenous injections of medications.

Anastomotic failure is the most serious complication following colorectal resection that can lead to reoperation, permanent stoma, and even death. The current practice of assessing blood perfusion at the anastomosis bowel ends by direct inspection of bowel pulsatility, bleeding, and tissue coloration has been demonstrated to lack predictive accuracy. In Chapter "Intraoperative Thermal and Laser Speckle Contrast Imaging Assessment of Bowel Perfusion in Two Cases of Colorectal Resection Surgery," two case studies which show the feasibility of performing thermal and laser speckle contrast imaging measurements intraoperatively for assessing bowel perfusion during colorectal resection surgery are reported. This experience could pave the way to a number of other applications for these technologies in the surgical arena.

Chapter "An Approach for Thyroid Nodule Analysis Using Thermographic Images" presents a small scale preliminary study conducted in order to evaluate the feasibility in time, cost, and effect of the use of an IR camera as a tool in detections of thyroid nodules in the ambulatory service of our university hospital. The authors perform an overall analysis of thermographic images, focusing on thyroid

thermographic acquisition, processing and analysis, which is a new field of study. An autonomous region of interest (ROI) identification for the thyroid images is proposed, which is based on very simple fundamentals of computer vision. Future works will involve improving the described methodologies and analyzing the reported evidences in regard to a large scale of data.

Chapter "Modeling Thermal Infrared Imaging Data for Differential Diagnosis" introduces the two commonly used approaches for modeling thermal infrared data for differential diagnosis purposes: (i) Qualitative modeling approach based on using statistical and machine learning techniques, (ii) Quantitative modeling approach based on performing mathematical/analytical modeling of the thermoregulatory processes with three main techniques: (a) empirically using automatic control theory, (b) nonempirically using bioheat equations and (c) semi-empirically using both bioheat equations and automatic control theory. The authors summarize the advantages and disadvantages of each modeling approach. Such summarized information could serve as a guide for the IR researcher in selecting the appropriate modeling approach regarding his/her research scope and interest. However, it should be point out that it is important to take care when considering the assumptions and approximations in order to choose the suitable modeling method. Hence implementing such modeling approaches highly increase the potential ability of IR imaging to be a fascinating and promising complementary imaging tool to the gold standard medical imaging methods for differential diagnosis.

Three-dimensional thermography systems that combine 3D geometric data and 2D thermography data enable users to have a more accurate representation of the surface temperature distribution and aid in its interpretation. A system for 3D dynamic infrared thermography comprising two units is presented in Chapter "3D Dynamic Thermography System for Biomedical Applications"; each unit consists of an off-the-shelf depth camera rigidly mounted to an IR camera. The units are fixed on the arms of the device that allow their placement in desired positions near the subject. The developed 3D system provides a number of advantages in research for biomedical applications, such as the correct temperature measurements on curved surfaces, the possibility to select regions of interest by taking into account the shape of the subject and the possibility to use the 3D data to easily eliminate the background from 2D thermograms. As a future work, due to hardware limitations with the fact that a mannequin that used in the test is static, one should use a different 3D scanning technique and registration methods to improve this accuracy for implementing algorithm in living human beings, particularly when selecting ROIs of smaller parts of the body, such as the breast or the feet.

In summary, IRT is identified as one of the leading technologies in use today. It has potential for temperature monitoring of the skin and it can be used as an adjunctive method to current practices for surface temperature examinations in diabetes. Many esteemed authors have contributed generously and made this book possible by their diligent hard work and valuable time. We thank them wholeheartedly for their significant contributions. The book represents the latest infrared technologies and helps the potential readers to better appreciate their relevant mechanism and physics of the application and case studies are explored and

investigated from different aspects with illustration in detail particularly from computer aided diagnosis with classifiers.

In this book, we have made an honest effort to present information and applied methodologies of Infrared technologies to help researchers, doctors, teachers, and students particularly in biomedical science and engineering.

Singapore, Singapore — Eddie Y.K. Ng
Isfahan, Iran — Mahnaz Etehadtavakol

Review for the Book

This book packs a big punch for its size. Each chapter is written concisely and ends with a list of sources of additional information for those who are interested where appropriate. The book is understandable and useful to the Infrared community.

Prof. Waldemar Minkina, Ph.D., D.Sc.
Czestochowa University of Technology
Częstochowa, Poland

Infrared Imaging is a potent tool that has not received it due attention. It is a safe, noninvasive and noncontact tool that can well be used as a tool for detecting abnormality as well as study the recovery from illness, disease, and physiological response to an underlying pathological response. While there are quite a few sources in this imaging modality, there is no one book that addresses all the possibilities in the biomedical arena.

This is heartening to note that this book "Application of Infrared to Biomedical Sciences" covers all aspects of IR imaging as a tool to study the various disorders, symptoms and disease. Each chapter is written concisely and ends with a list of sources of additional information for those who are interested where appropriate. This, in my opinion is a "one size fits for all" in thermal imaging. This is a very useful book for the scientific community to understand and appreciate the all encompassing advantages of IR imaging. The practising community will be able to appreciate the usefulness of this tool and encourage them to consider this safe imaging modality by practising a well laid out protocol in data acquisition.

Natteri M. Sudharsan, Ph.D.
Professor and ASME Fellow, Rajalakshmi Engineering College, Chennai, India

This book fills a critical void of information and should be viewed as a required reference for any professional working in the area of biomedical sciences. It provides a comprehensive technical review of the latest cutting-edge techniques

involving infrared technology and their application to medicine. There is no other work that brings together all of this knowledge in one convenient location.

Mukul V. Shirvaikar, Ph.D.
Professor and ABET Program Evaluator
The University of Texas at Tyler, USA

Congratulation! Each chapter of this book is precisely written and can be easily understood for all researcher and students. This book will accelerate and stimulate the motivation and conductor of IR research.

Shuichi Torii, Ph.D.
Professor,
Graduate School of Science and Technology Kumamoto University, Japan

This book provides a lot of information about medical infrared imaging. Very interesting to read by everyone who likes to learn more about this technique.

Irma Wensink
Thermografie Centrum, The Netherlands

Infrared Imaging is now a mature technology. With excellent cameras and less expensive equipment, the biomedical field of applications has rapidly grown worldwide. This book presents a detailed account of many different areas of research, primarily in the medical field. It therefore provides a valuable source of information to all who are involved in this still growing area of research and application.

Francis Ring, D.Sc., FIPEM, FRPS, FRAS
Professor,
University of South Wales, UK

Currently, diagnostic infrared imaging is experiencing a renaissance that seems likely to propel it into wide acceptance. During the 1960's and 70's, novelty may have sparked the initial interest in this mode of physiologic imaging but the lack of basic science and analog equipment enabled only an empirical level of evaluation that proved unreliable outside the hands of a few genuine experts. In the past forty years, computer-linked digital thermographs have permitted a quantitative analysis by various forms of artificial intelligence that, when applied around specific pathophysiologic features, have led to new power and reliability for diagnostic infrared imaging in clinical medicine. Professor Ng has had a leading role in the development of artificial intelligence systems in this respect and this book presents new levels of objective analysis that will enable expert systems to further the progress of diagnostic thermology.

Phil Hoekstra, Ph.D., DABT
Therma-Scan Reference Laboratory, South-East Michigan,
USA

This text contributes significantly to the understanding and acceptance of the many biomedical attributes of thermal imaging technology. It provides a concise and relatively complete review of recent research literature such as the important uses for pain medicine, breast exams, diabetes and fever evaluation etc. are just some of the topics discussed in detail. There is considerable attention paid to novel diagnostic algorithms, of value to those seeking to use telethermography in a more rigorous and scientific manner. In combination with other diagnostic tests, this work shows how much more is added to the understanding of the patient condition through the use of thermographic imaging. It is a 'must have' for the clinician and scientist.

G.J. Rockley, Director and M.G. Rockley, Ph.D.
R&D for Teletherm Infrared,
USA

This book provides a truly comprehensive coverage of a wide spectrum of application examples of infrared imaging in biomedical sciences. It would serve as an excellent resource for researchers and practitioners to learn the great potential of infrared imaging, to exploit new application domains, and to further advance the science of applied infrared imaging.

Hairong Qi, Ph.D.
Gonzalez Family Professor
University of Tennessee
Knoxville, USA

Biomedical applications have always been an interesting field of infrared thermography. The authors explore an important field using high resolution thermographic cameras enabling them to find smallest thermal abnormalities.

Guido Mahler, Ph.D., ISO 9712 Level III Thermographer
Research & Development, Infrared Measurement Division
InfraTec GmbH, Infrarotsensorik und Messtechnik
Dresden, Germany

Contents

About the Editors

Eddie Y.K. Ng, Ph.D. received his Ph.D. from Cambridge University, UK and is Associate Professor at Nanyang Technological University, Singapore. He serves as an editor for 10 international journals and as Editor-in-Chief for two SCIE indexed Journals. His research interests are in thermal imaging, biomedical engineering, breast cancer detection, and computational fluid dynamics and heat transfer. He is an invited keynotes speaker for more than 18 international scientific confs./workshops. 15 of his papers have been adopted as references in Singapore Standard (SS 582: 2013) and ISO/IEC 80601-2-59: 2008. He is also presently serving as panel member for the Biomedical Standards Committee, Singapore. The coinventor of three USA patents on multiple analytical software classifier programs to identify the different stages of breast cancer development using thermal data with Lifeline's First WarningTM (Cyrcadia Health, Inc.) system, he further explores the use of IR in the field of ophthalmology for early detection of health abnormality. He has co-edited 12 and coauthored one text books.

Ng has had more than 265 ISI journal articles, 99 book chapters and 80 conference papers. He has supervised more than six researchers as well as over 25 Master and Ph.D. students. He has amassed over SGD $5M worth of research funding from various organizations in the capacity of the principal investigator.

Mahnaz Etehadtavakol, Ph.D. is a Research Scientist at the Center of Medical Image and Signal Processing at Isfahan University of Medical Sciences, Iran. Her research interests include the application of IR imaging in medicine, biosignal processing, and system biology. She has instructed numerous courses in Biomedical Engineering, Electrical Engineering and Mathematics over the past 20 years. Prior to joining Isfahan University of Medical Sciences, she served as a lecturer at Mathematics Department, Isfahan University of Technology. She has been involved in eight projects in the field of medical IR imaging applications. She is an Associate Editor of the journal of Medical Imaging and Health Informatics. Dr. Etehadtavakol received a B.S. degree in Electrical Engineering and an M.S. degree in Applied Mathematics, both from Purdue University, Indiana, United States. She received her Ph.D. degree in Electrical Engineering from Isfahan University of Technology, Iran, in 2011.

Potential of Infrared Imaging in Assessing Digestive Disorders

Mahnaz Etehadtavakol, Eddie Y.K. Ng and Mohammad Hassan Emami

Abstract Thermography or infrared imaging is determined by detailed investigation of skin and cells' temperatures. It helps clinicians to detect the regions of irregular chemical and blood vessel action in body tissue. The drive of biomedical industry with consequent rapid development in other areas of biomedical imaging has also strongly influenced the destiny of thermography in biomedical practice. During past few decades, the joint efforts of biomedical engineering and medical professionals have resulted in evolution of technological progress in infrared sensor technology, image processing, organized repository of knowledge, and their overall integration into a system. All these enabled the new tools of research and use in medical thermography. Thermography is a simple, noninvasive and reproducible test that can accurately reflect the inflammatory activities, and can be used safely and repeatedly, during biological course of inflammatory bowel disease. Objective of this study is presenting the possibility of infrared imaging in assessing digestive disorders such as irritable bowel syndrome, diverticulitis and Crohn's disease.

Keywords Thermography · Digestive disorders

M. Etehadtavakol · M.H. Emami
Isfahan University of Medical Sciences, Isfahan, Iran

M. Etehadtavakol · M.H. Emami
Gastrointestinal Disease Research Center,
Poursina Hakim Research Institute, Isfahan, Iran

E.Y.K. Ng (✉)
School of Mechanical and Aerospace Engineering,
College of Engineering, Nanyang Technological University,
50 Nanyang Avenue, Singapore 639798, Singapore
e-mail: mykng@ntu.edu.sg

E.Y.K. Ng and M. Etehadtavakol (eds.), *Application of Infrared to Biomedical Sciences*, Series in BioEngineering,
DOI 10.1007/978-981-10-3147-2_1

1 Introduction

Inflammatory bowel disease (IBD) influences chronic inflammation of all or part of the digestive section (Fig. 1). Ulcerative colitis and Crohn's disease are mainly related to IBD. Pain, severe diarrhea, weight loss, and fatigue are often prevalent in these diseases. IBD can be harmful and occasionally influences life-threatening problems. Enduring inflammation and ulcers in the innermost lining of the large intestine and rectum are caused by ulcerative colitis, which is an inflammatory bowel disease. Inflammation of the lining of the digestive section appears in Crohn's disease. However, inflammation usually influences thoroughly on involved tissues in Crohn's disease. The large intestine and the small intestine, two different parts of digestive section, or both may be affected by inflammation. Colorectal cancer is the third most typical tumor in the United States. Several factors that increase the risk of developing colorectal include eating foods rich in fat, drinking alcohol, having a low fiber, being chemical solvent exposure, and having first-degree family history. Some studies show that tumors develop from polyps in most cases. For Stage I tumor growth through the mucosa and invasion to the muscular layer of the colon or rectum, 85–95% rates and for Stage II tumor growth through the colon wall, 30–70% rates, for 5-year survival, are reported [1]. While during Stage III tumors have already spread to lymph nodes or Stage IV tumors have spread to more than one part of the body, improvement is difficult. However, by early detection of polyps and precancerous cells, we are able to increase chance of improvement. Therefore, a safe, noninvasive, reproducible, and standard adjunctively method that has potential for colon cancer early detection is appreciable. Common standard diagnostic tests to evaluate IBD involve clinical examination, laboratory tests, activity evidence as well as several imaging techniques.

The first documented practice of thermobiological signs happens to be the written works of Hippocrates at about 480 BC. Wet mud spread all over a patient to investigate the regions would dry first in order to achieve the hidden pathology of organs. Thereupon, by advanced studies and researches it has been confirmed that particular temperatures interrelated to organs of body were definitely indicative of healthy and

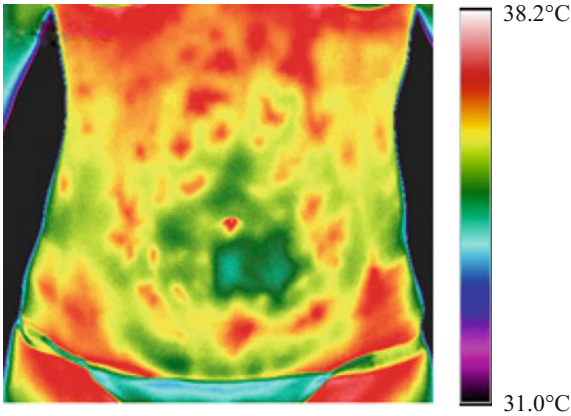

Fig. 1 Thermogram of an irritable bowel syndrome patient

unhealthy pathological mechanism [2]. The first documented use of infrared (IR) imaging in medicine was in 1956, when asymmetric hyperthermia regions and vascularity in breast thermograms were examined for breast cancer detection. Since then many discoveries have been documented [3–5]. However, thermography is not known internationally in medicine even today, mainly as a result of the inexperienced application of the method, the inadequate deep understanding of thermograms. Advances in infrared (IR) camera technologies, appropriate patient protocols, and properly calibrated thermography have led to an increased interest in the application of IR systems in the medical imaging [6]. In addition, using 3D thermal imaging to promote medical diagnosis has been considered in past two decades. In 1996, Chan et al. [7] introduced generation of 3D medical thermograms. Souza et al. [8] also used 3D thermal imaging to integrate MRI and thermographic images. In 2015, a 3D medical thermography device was introduced by Moghadam [9]. Furthermore, a patent was filed by C. Herman in Johan Hopkins University in 2015 for 3D thermal imaging for the detection of skin lesions and other natural and abnormal conditions (US 20130116573 A1). In future work, 3D thermal imaging would be useful to visualize internal organs for promoting digestive disorders diagnosis. This paper is organized as follows: Methodology is explained in "Methodology" section, eighteen case reports are presented in "Case Reports" section, results are discussed in "Results" section, and "Conclusion" section concludes the findings.

2 Methodology

In this paper, presented case reports were patients with different indications of IBD and colorectal cancer. Various diagnostic tests including physical examinations, different laboratory tests, and different imaging tests were performed for each case. Different tests include the microbiology testing of stool samples, C-reactive protein, calprotectin, esophagogastroduodenoscopy, multidetector computed tomography, total colonoscopy, magnetic resonance (MR) imaging of the abdomen or MR enterocolography, upper gastrointestinal (GI) endoscopy, histopathology testing, MR enterography, and terminal ileoscopy. However, thermal imaging was performed for all the cases. Details of different tests will be explained in "Case Reports" section for each case separately.

2.1 Thermal Imaging Protocol Guidelines

We briefly explain some guidelines to provide thermal images to detect probably some digestive disorders [10]:

- Imaging should be done before planning for endoscopy, to eliminate any potential influence of bowel cleansing and endoscopic mechanism.

- Imaging can be done in two interval times: before beginning the therapy and after the patient had attained the remission, as reported by clinical, laboratory and endoscopic evaluation [11].
- The imaging itself can be progressed in this way;

  i. Patients position in front of the camera, approximately at 1 m; so that the whole abdomen was captured by the camera lens.
  ii. Patients are undressed and requested to stand in front of the camera not touching there abdomen for the sake of attaining thermal equilibrium.
  iii. The process takes about 5–10 min.
  iv. Consequently to attain equilibrium the patient's abdomen is cooled with alcohol and then interval thermal image can be taken after equilibrium is attained again.
  v. Differences in thermal patterns and peak temperatures are captured.
  vi. Taken thermal images can be divided into four quadrants representing colonic segments: rectosigmoid, descending colon, transverse colon, and descending colon.
  vii. The same process of thermal imaging can be performed before beginning of therapy and consequently to achieve clinical remission of the disease.
  viii. Differences in observed thermal patterns and peak temperatures can be compared.

3 Case Reports

Case report I: In this report, a 43-year-old male patient presented to the emergency room with severe abdominal pain. Before admittance to the hospital, an esophagogastroduodenoscopy was performed that showed carcinoma on the back wall of the gastric corpus. The diagnosis of adenocarcinoma was confirmed by the pathohistological analysis. After admittance, the preoperative workup including

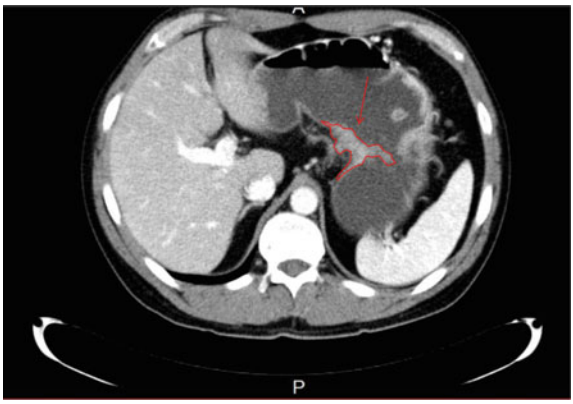

Fig. 2 MDCT showing gastric carcinoma indicated by *red part* prior operation of a 43 years male [12]

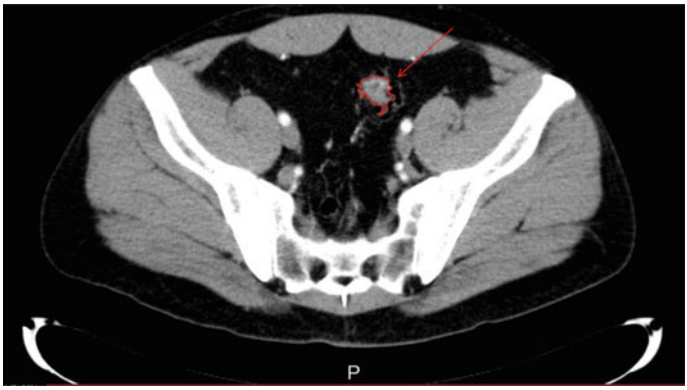

Fig. 3 Colon diverticula and opacification of the colon wall as revealed with *red part* by MDCT prior operation [12]

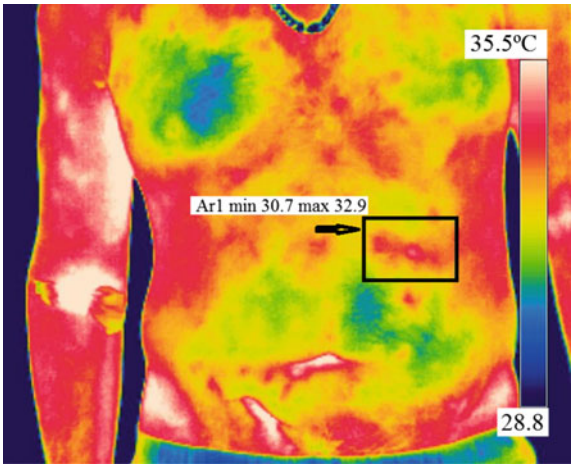

Fig. 4 Hot spot indicating inflammation as shown in thermal image of 43 years male with left UC [12]

laboratory testing and imaging methods for staging the carcinoma was performed. Laboratory testing indicated no abnormalities; however, the preformed Multidetector Computed Tomography (MDCT) indicated thickening of the gastric small curve 4 cm in diameter and a couple of affected perigastric lymph nodes. It is shown in Fig. 2.

Besides the observations in the stomach, the MDCT also revealed nonspecific opacification of the colon wall that could show an inflammatory process as it is demonstrated in Fig. 3.

There were no radiological signs of diverticulitis, besides the diverticula. However, the patient also underwent the thermal imaging as it is shown in Fig. 4. The thermal image demonstrated signs of inflammation in spots that could reflect the position of the diverticula that revealed by the MDCT.

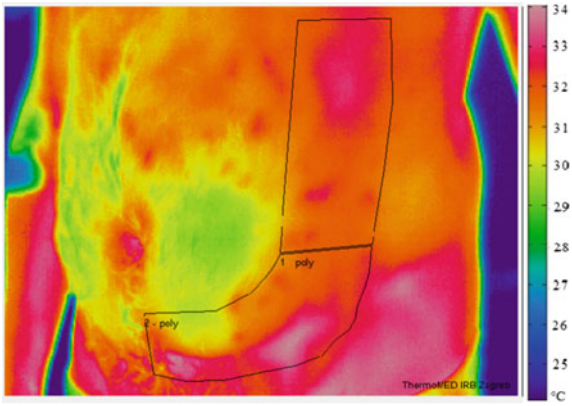

Fig. 5 Marked areas of severe inflammatory activity of 47-year male with left UC

A colonoscopy was performed to confirm and verify the diagnosis of diverticulitis (repeated). The patient was operated 5 days later. The procedure was proven. Surgical team conducted total gastrectomy with splenectomy. However, the newly diagnosed diverticulitis caused the planed adjuvant chemo-radiotherapy to be postponed. Considering that chemo-radiotherapy could provoke perforation of the inflamed diverticula and potentially be fatal for the patient [12].

Case report II: In 2013, a 47-year-old male diagnosed with left-sided ulcerative colitis (UC). He was admitted in a hospital whereas aggravation of the disease happened in September 2014. Before admittance to the hospital, the patient presented with fever, fatigue, loss of appetite, and loss of body weight, in duration of 2 weeks. The disease was characterized with abdominal cramps located in the lower left quadrant of the abdomen, and diarrhea (7–10 stools/day, mixed with mucus and blood). The laboratory tests indicated elevated leucocyte levels. Total colonoscopy suggested severe left-sided colitis with Mayo endoscopic subscore of 2 (in range 0–3). However, the patient also underwent for the thermal imaging. His abdominal thermal image is shown in Fig. 5.

Detected temperatures in quadrants were 2 °C higher than in the unaffected parts of the abdomen representing the left colon (the rectosigmoid and the descending colon). The patient was discharged clinically in better shape after 12 days of hospitalization. The plan was to take another thermogram of the patient's abdomen, upon achieving whole remission. There were no obvious signs of disease activity seven months later. Although stool frequency and consistency were normal, the patient did complain about discomfort in the lower left quadrant of the abdomen. A control thermogram was taken and surprisingly some disease activity was detected. Detected temperatures in quadrant representing the left colon were almost the same as the one taken 7 months earlier. The thermogram is shown in Fig. 6.

Two days later the patient was readmitted to the hospital with full worsening conditions. Active disease along the left part of the colon, Mayo endoscopic subscore 2 as indicated by the preformed colonoscopy [10].

Case report III: In this report, a 42-year-old female, diagnosed with UC in 2005. She consulted her gastroenterologist because of frequent bloody stools

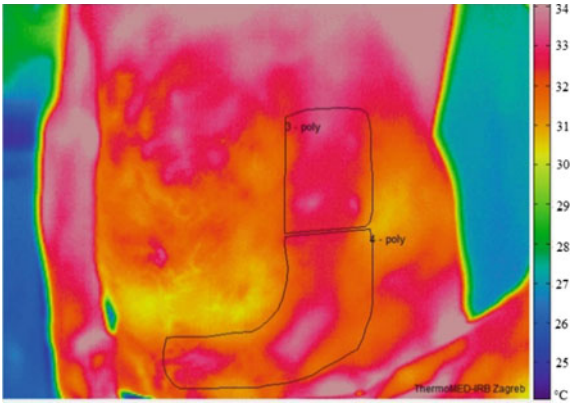

Fig. 6 Control thermogram showing some remaining disease activity after 7 months discharged from hospitalization

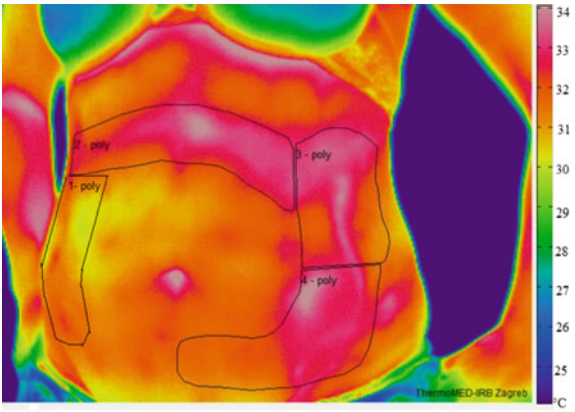

Fig. 7 Disease activity shown by the 42-year-old female patient abdomen thermogram

(7–8/day) and abdominal pain in February 2015. Active disease extending to the hepatic flexure was indicated by colonoscopy. Elevated inflammatory markers (high leukocytosis and elevated C-reactive protein) were revealed by the laboratory tests. Any infective causes were however excluded by microbiological stool analysis. A thermogram of the patient's abdomen was taken and a distinctive infrared pattern corresponding to colonoscopy findings was indicated as shown in Fig. 7.

Hot spots were observed in quadrants representing the left and the transverse colon. Intensive treatment with anti-inflammatory drugs (methylprednisolone and azathioprine, in combination with mesalamine) and after four weeks, the patient entered the remission of the disease. Clinical, laboratory, and imaging examination indicated significant improvement in disease activity. Only mild abnormalities with the significant normalization in abdominal surface temperature pattern were observed when compared to the initial thermographic examination. It indicated the remission of active colitis, [10]. His remitted thermal image was presented in Fig. 8.

Temperatures in the affected quadrant were significantly lower as can be seen in Chart 1.

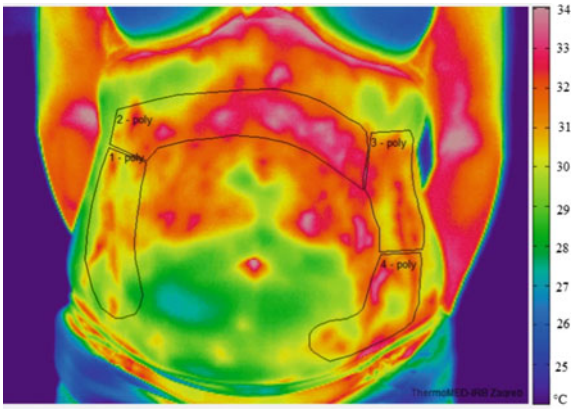

Fig. 8 Thermogram of the same patient, after 4 weeks of treatment with improvement in disease activity

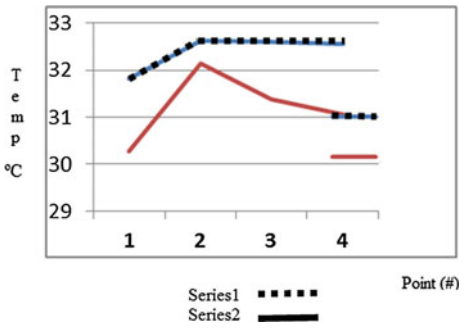

Chart 1 Temperatures before treatment (*Series1*) and after treatment (*Series2*) of case report III

Case report IV: Banic et al. [13] presented findings belonging to a 53-year-old female patient diagnosed with severe ulcerative pancolitis. The patient had been presented with fever, fatigue, loss of appetite and loss of body weight for 6 weeks before her admittance to the University Hospital of Dubrava, Croatia. The disease was characterized with abdominal cramps and diarrhea (5–10 stools/day, mixed with mucus and blood). The laboratory tests revealed anemia with elevated erythrocyte sedimentation rate and c-reactive protein (CRP) levels above normal values. The upper gastrointestinal (GI) endoscopy documented mild chronic gastritis and histopathology testing did not document the presence of *Helicobacter pylori* (*H. pylori*) infection in the stomach. The MR enterography documented no signs of Crohn's disease in the small intestines and no signs of fistulas [13].

The terminal ileoscopy indicated no signs of inflammatory involvement of the mucosa in terminal ileum. However, total colonoscopy revealed acute severe pancolitis with Mayo endoscopic subscore of 3 (in range 0–3), in each colonic segments. The initial findings of pancolitis and severe inflammatory activity of the disease were discovered through the heat patterns of thermal images taken before any treatment. Abdominal skin temperature of the patient is shown in Fig. 9 which indicates temperature abnormalities.

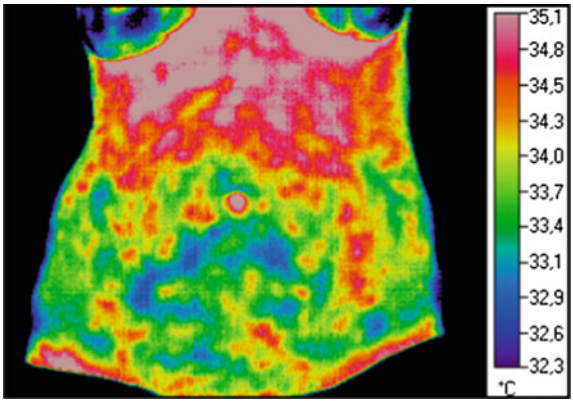

Fig. 9 A 53-year-old female patient with areas of enhanced thermal abnormalities

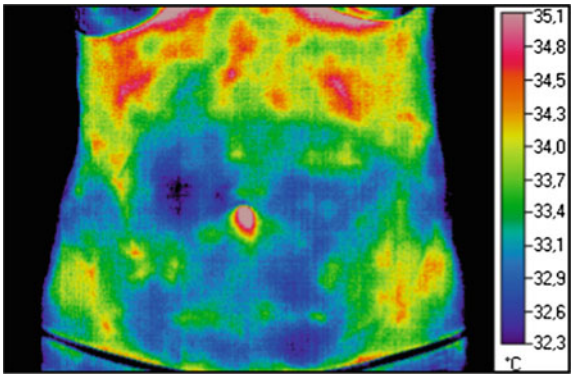

Fig. 10 Patient in Fig. 9 after 4 weeks of intensive treatment

After four weeks of intensive treatment with anti-inflammatory drugs (methylprednisolone and azathioprine, in combination with mesalamine), the patient entered the remission of the disease, documented with significant clinical, laboratory and imaging improvement in disease activity [14, 15]. The laboratory tests detected no anemia with normal values of CRP. Control examination by the means of total colonoscopy, performed 4 weeks after initial examination documented healing in each segments of colonic mucosa, expressed with Mayo endoscopic subscore of 1. This finding indicated the remission of active colitis according to the non-contact thermal image (Fig. 10) shows only mild abnormalities with the significant decrease in abdominal skin temperature compared to the first taken thermal image (Fig. 9).

Ulcerative colitis represents a chronic inflammatory and ulcerative disease of colonic mucosa. Clinically, ulcerative colitis is characterized by bloody diarrhea, and the diagnosis most often relies on invasive colonoscopy and macroscopically scoring of visualized inflammatory and ulcerative mucosal pattern [16–18]. Diagnostic methods currently in use, clinical (endoscopy), imaging (CT, MR) or laboratory (C-reactive protein, calprotectin) provide an insight into disease activity,

but are possibly associated with significant discomfort for the patient and/or increased risk of irradiation and potential allergic reactions on contrast agents.

Case report V: A typical irritable bowel thermogram is shown in Fig. 11. It shows diffuse (scattered throughout) hyperthermia (too much heat) in upper abdomen. The patient was having symptoms of gas, bloating, pain in abdomen [19].

Case report VI: A thermal image of a patient with parasite infection in gastrointestinal tract is demonstrated in Fig. 12. Localized areas of heat with "focal points" of hyperthermia are indicated. *H. pylori* bacteria was diagnosed on her blood test [19].

Case report VII: A sequence of thermograms for one treated irritable bowel syndrome (IBS) patient are presented in Fig. 13a–c [19]. In the first thermogram, we observe too much heat that is diffused throughout in the upper abdomen. Before the treatment the patient was complaining about gas, bloating, and pain in the abdomen. We observe that the thermograms are softer and cooler after taking alovera juice.

Case report VIII: An abdominal thermal image and its corresponding temperature histogram of a healthy female individual are presented in Fig. 14a, b. The temperature histogram has a normal distribution pattern with a peak temperature around 32 °C [1].

Case report IX: A thermal image of a female patient with active Crohn's colitis is included in Fig. 15a, b. A clear thermal pattern change is observable in the abdominal part. In addition, the histogram of the heat pattern has different distribution comparing to normal case (Fig. 14). The peak temperature is around 35 °C [1].

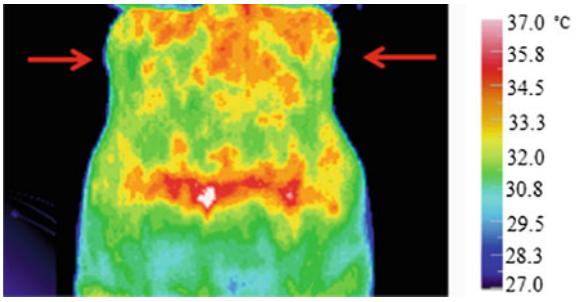

Fig. 11 An irritable bowel thermogram

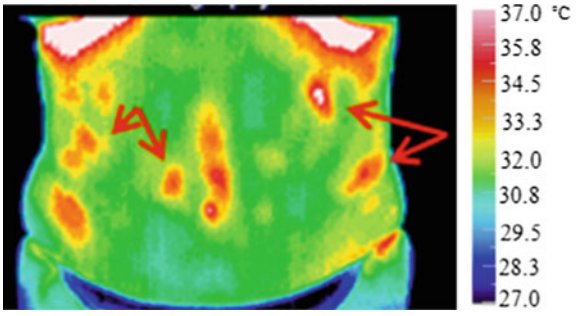

Fig. 12 A patient with parasite infection in gastrointestinal tract

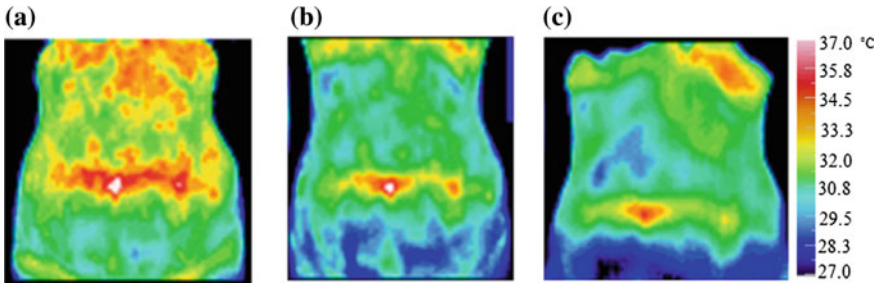

Fig. 13 IBS patient treatment with aloe vera juice. **a** Initial thermogram. **b** 5 days of taking alovera juice. **c** 13 days of taking aloe vera juice

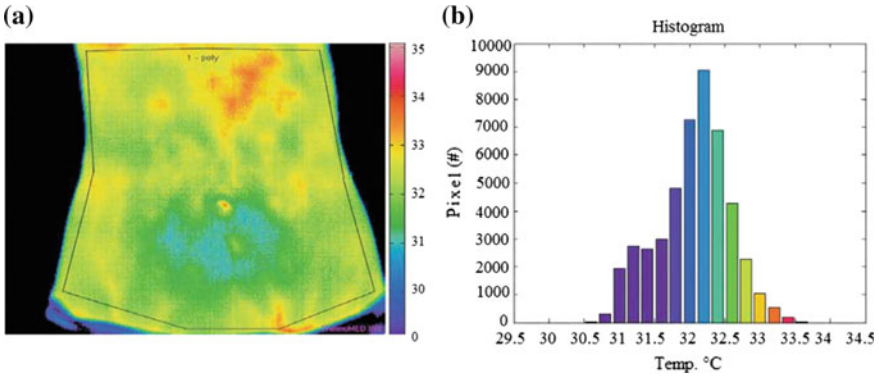

Fig. 14 A healthy female individual. **a** An abdominal thermal image. **b** Corresponding temperature histogram

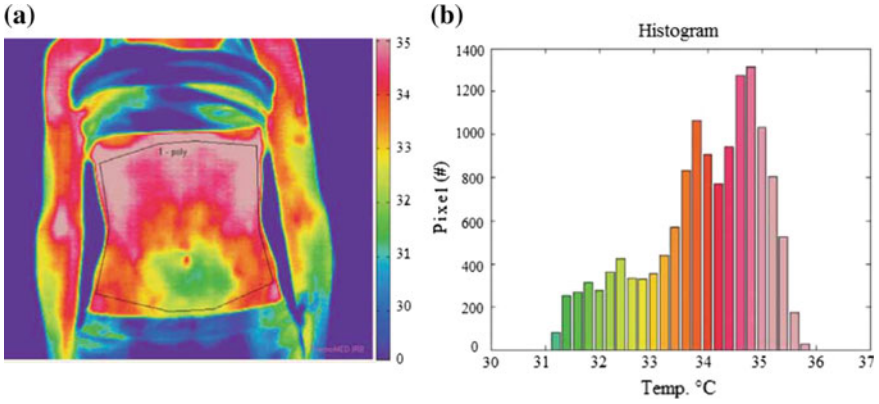

Fig. 15 A female patient with active Crohn's colitis. **a** An abdominal thermal image. **b** Corresponding temperature histogram

A thermal image of the above-mentioned female patient with active Crohn's colitis after induction of remission is demonstrated in Fig. 16. A clear thermal pattern change is evident in the abdominal part. The main peak temperature after induction of remission was 31.5 °C. However, a second less expressed peak at 32.5 °C is observed.

Case report X: A thermogram of a male patient with high-grade dysplastic polypoid lesion in left-sided ulcerative colitis is shown in Fig. 17a. A hot spot above a polypoid lesion with high-grade dysplasia is observable. Also the 3D analysis of that hot spot is demonstrated in Fig. 17b [1].

Case report XI: An abdominal thermogram of a person with hepatitis is shown in Fig. 18. After birth, the hepatic blood vessel was blocked which is shown by hot area in the abdominal thermogram. Further action was treated and the blood vessel was opened from the liver to the umbilicus [20].

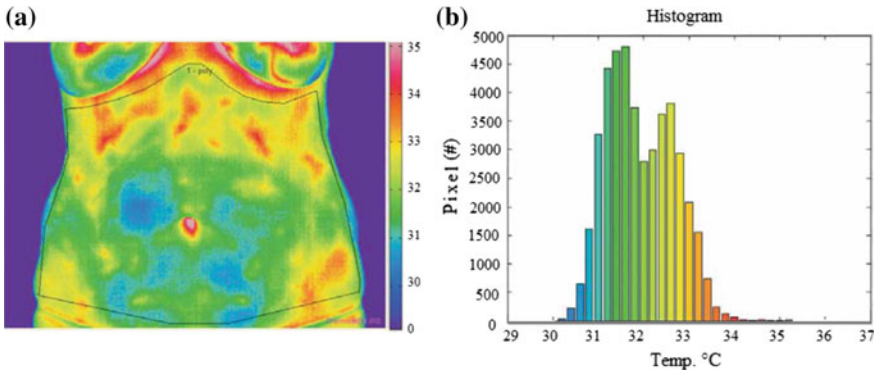

Fig. 16 **a** A thermal image of a female patient with active Crohn's colitis after induction of remission. **b** A histogram

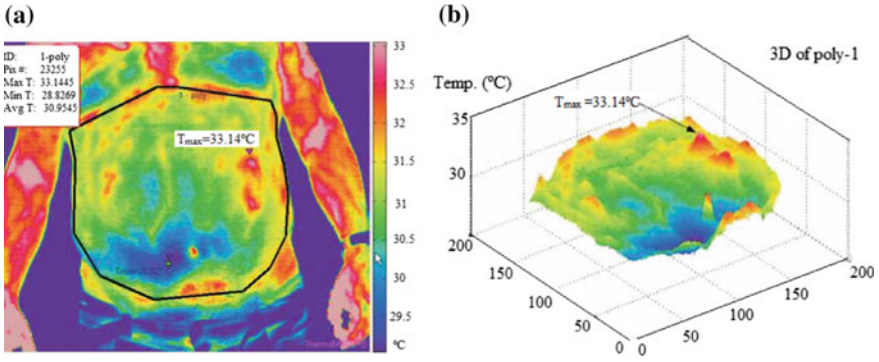

Fig. 17 **a** A thermogram of a male patient with high-grade dysplastic polypoid lesion in left-sided ulcerative colitis. **b** 3D plot of hot spots

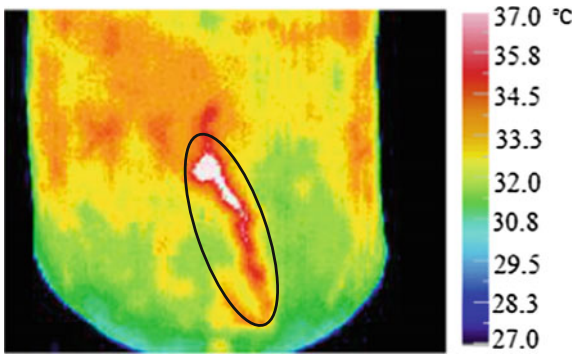

Fig. 18 A patient with hepatic blood vessel blockage [20]

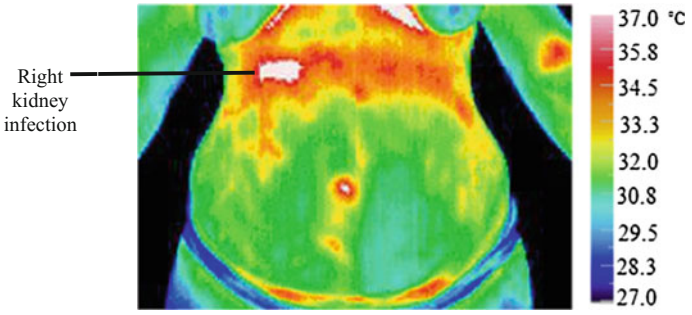

Fig. 19 Thermogram of a patient with right kidney infection confirmed with other examination

Case report XII: A thermogram of a patient complaining back pain is presented in Fig. 19. No thermal evidence was discovered in her back; however, some hyperthermia areas were observed over the right kidney through her abdomen thermogram which could address pain to the back. Besides further tests showed kidney infection as well [20].

Case report XIII: An abdomen thermogram of a female patient, depicted in Fig. 20, indicates a hyperthermia area over the hepatic flexure of the colon. Further examinations confirm diverticulitis and then suitable treatment was recommended [20].

Case report XIV: Thermography is a very useful technique for treatment monitoring of a patient. An initial abdomen thermogram of an IBS (irritable bowel syndrome) female patient is shown in Fig. 21a where the circular hyperthermia spots were indicating IBS. The patient was treated with acupuncture and Chinese herbs for 45 days. The thermogram shown in Fig. 21b was taken after the treatment. Increasing cooler and green thermal area in Fig. 21b was indicating progress in the treatment and the patient returned to a better and helthier condition [21].

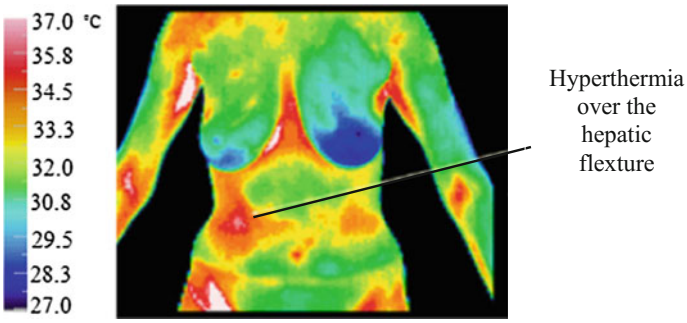

Fig. 20 Thermogram of a patient with diverticulitis [20]

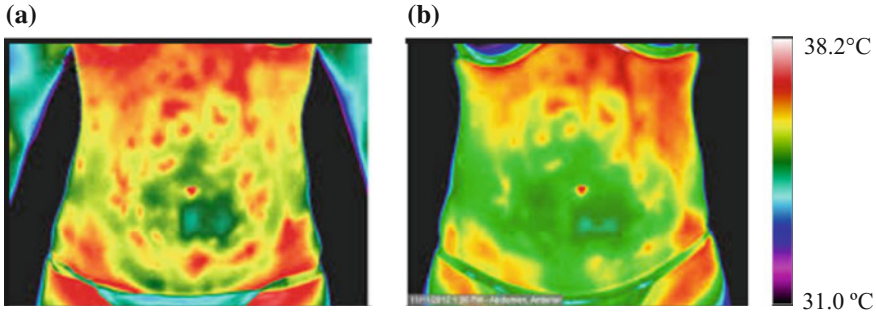

Fig. 21 Progress of an IBS patient treatment with acupuncture and Chinese herbs. **a** Before treatment. **b** After treatment

Case report XV: Fig. 22 suggests a patient with abdominal distension that happens when substances, for example gas or fluid, gather in the abdomen and generate the outward enlargement on the far side of the normal girth of the stomach and waist. Consequently, elevated abdominal pressure and volume are sensed [22].

Case report XVI: Ileocecal valve is a sphincter muscle valve that allows digested material to pass from the small intestine to the large one by opening and closing. Figure 23 demonstrates a thermogram of a patient with ileocecal valve blockage [22].

Case report XVII: One of the possible side effects of colonoscopy in rare cases is making a puncture in colon. Figure 24 shows a thermogram of a case with a punctured colon during a colonoscopy. Hot spots or hyperthermia areas are indicating inflammation or possible infection due to colon perforation [22].

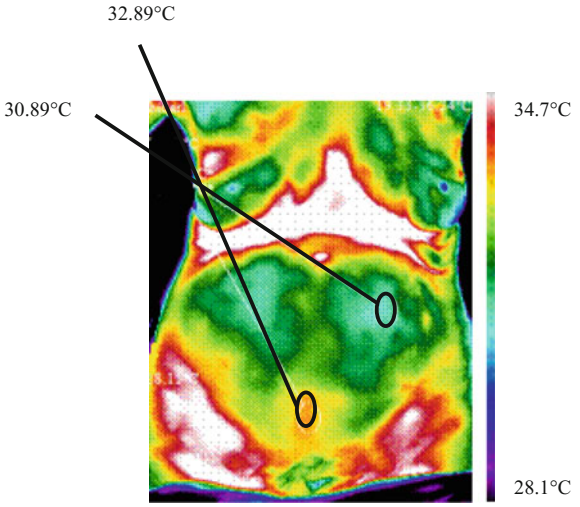

Fig. 22 A patient with abdominal distension

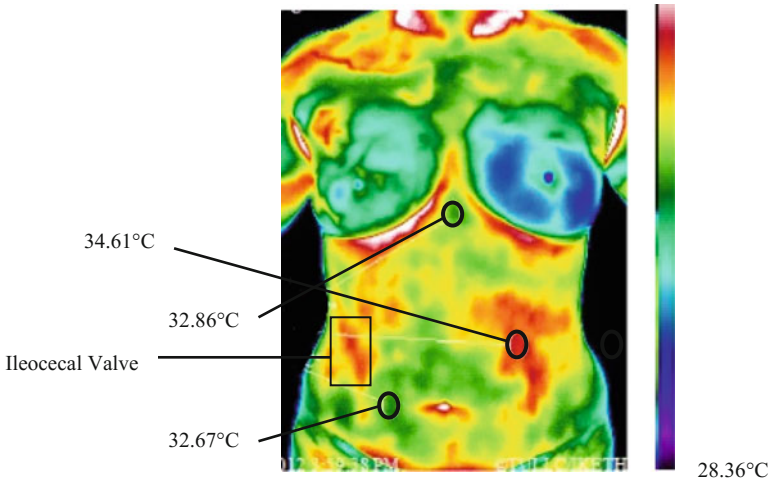

Fig. 23 Ileocecal valve blockage

Case report XVIII: In order to absorb most of the nutrients from what we eat, the intestinal track must be cleaned the dirt out. Otherwise the needed proteins, vitamins, etc., can not be absorbed by the coated intestinal walls. Figure 25 reveals an individual with belly fat and poor gut health which caused the stomach distention [22].

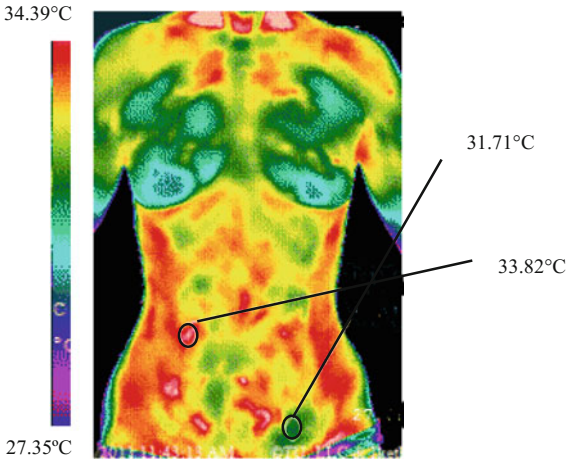

Fig. 24 Punctured colon during a colonoscopy

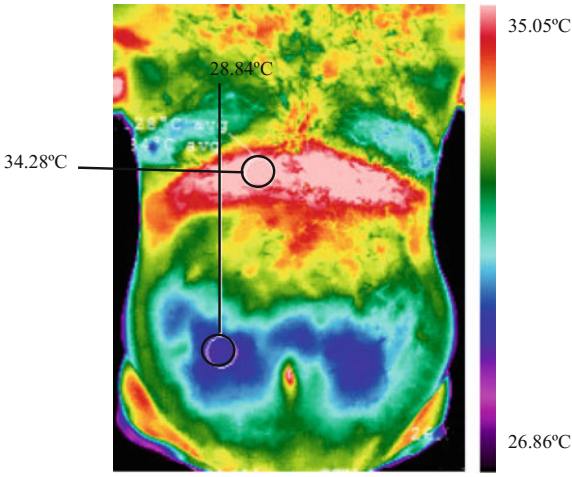

Fig. 25 An individual with extreme distension from poor intestinal health in conjunction with belly fat

4 Results

Thermography is capable of providing non-contact, in vivo diagnostic information in regard to body temperature. Also it has the possibility to map small variations in the body surface temperature and identify thermal abnormalities that accompany various physiological conditions. Being a passive technique, without external sources of radiation this technique is non-invasive and therefore intrinsically harmless.

Clear changes in thermal pattern of the abdomen of the 18 patients examined here with inflammatory bowel problems are evident. In addition, their corresponding temperature histograms have different distributions comparing to the normal cases.

5 Conclusion

Thermal imaging measures the radiation of infrared heat from human body. It presents a very early detecting system, often able to identify an abnormality process before it is distinguishable by standard diagnostic imaging techniques. On the other hand, a best application at the interface of environment and genetics is chronic inflammation which is famous to lead the development of many categories of precancerous lesions and specific diseases themselves, together with oesophageal, liver and colon inflammation.

This review has presented the potential of infrared thermography as a feasible and safe technique to be used adjunctively to evaluate patients with various manifestations of inflammatory bowel diseases. There is a need for further basic and clinical studies in order to evaluate and validate this to assess the activity and extent of intestinal inflammation and other intraabdominal inflammatory conditions.

References

1. Banic, M., Kolari, D., Borojevi, N., Ferencic, E., Plesko, S., Petncusic, L., Antonini, S.: Thermography in patients with inflammatory bowel disease and colorectal cancer: evidence and review of the method. Periodicum Biologorum **113**(4), 439–444 (2011)
2. Etehadtavakol, M., Ng, E.Y.K.: Breast thermography as a potential non-contact method in the early detection of cancer: a review. J. Mech. Med. Biol. **13**(2), 20 (2013)
3. Handley, R.S.: The temperature of breast tumors as a possible guide to prognosis. Acta Unio Int. Contra Cancrum **18**, 822 (1982)
4. Moskowitz, M., Milbrath, J., Gartside, P., Zermeno, A., Mandel, D.: Lack of efficacy of thermography as a screening tool for minimal and stage I breast cancer. N. Engl. J. Med. **295** (249), 252 (1976)
5. Threatt, B., Norbeck, J.M., Ullman, N.S., Kummer, R., Roselle, P.F.: Thermography and breast cancer: an analysis of a blind reading. Ann. N. Y. Acad. Sci. **335**, 501–527 (1980)
6. Etehadtavakol, M., Chandran, V., Ng, E.Y.K., Kafieh, R.: Breast cancer detection from thermal images using bispectral invariant features. Int. J. Therm. Sci. **6**, 21–36 (2013)
7. Chan, F.H., So, A.T., Lam, F.K.: Generation of three-dimensional medical thermograms. Biomed. Mater. Eng. **6**(6), 415–428 (1996)
8. Abreu de Souza, M., Chagas Paz, A.A., Sanches, I.J., Nohama, P., Gamba, H.R.: 3D thermal medical image visualization tool: integration between MRI and thermographic images. In: Proceedings of the Conference on IEEE Engineering in Medicine and Biological Society, pp. 5583–5586 (2014). doi:10.1109/EMBC.2014.6944892
9. Moghadam, P.: 3D medical thermography device. In: Proceedings on Thermosense: Thermal Infrared Applications XXXVII, SPIE 9485, vol. 9485, 12 May 2015. doi:10.1117/12.2177880
10. Božin, T., Kolarić, D., Ferenčić, Ž., Kuliš, T., Banić, M.: Thermography in surveillance of ulcerative colitis—a case report. In: 57th Proceedings on IEEE Catalog CFP15825-PRT, ELMAR-2015, pp. 21–24 (2015)
11. Merla, A., Romani, G.L.: Biomedical applications of functional infrared imaging. In: Diakides, N.A., Bronzino, J.D. (eds.) Medical Infrared Imaging, pp. 15-1–15-20. Boca Raton, CRC Press Taylor and Francis Group (2008)

12. Banić, M., Kolarić, D., Kuliš, T., Vukelić, M., Herceg, Ž., Petričušić, L., Antonini, S.: Thermography in abdominal comorbidity in gastric carcinoma: case report. In: 57th Proceedings on IEEE catalog CFP15825-PRT, ELMAR-2015, pp. 25–28 (2015)
13. Banic, M., Kolanc, D., Antonini, S., Ferencic, Z., Plesko, S., Petncusic, L.: Browse "potential role of thermography in evaluation of disease activity in inflammatory bowel disease—a case report". In: IEEE, 53rd International Symposium ELMAR-2011, pp. 289–291 (2011)
14. Preiss, J.C., Zeitz, M.: Use of methotrexate in patients with inflammatory bowel diseases. Clin. Exp. Rheumatol. **28**(5 Suppl 61), S151–S155 (2010)
15. Talley, N.J., Abreu, M.T., Achkar, J.P., et al.: American College of Gastroenterology IBD Task Force: An evidence-based systematic review on medical therapies for inflammatory bowel disease. Am. J. Gastroenterol. **6**(Suppl 1), S2–S25 (2011)
16. Valentini, L., Schulzke, J.D.: Mundane yet challenging: the assessment of malnutrition in inflammatory bowel disease. Eur. J. Intern. Med. **22**(1), 13–15 (2011)
17. Dinesen, L.C., Walsh, A.J., Protic, M.N., et al.: The pattern and outcome of acute severe colitis. J. Crohn's Colitis. **4**(4), 431–437 (2010)
18. Brakenhoff, L.K., van der Heijde, D.M., Hommes, D.W., Huizinga, T.W., Fidder, H.H.: The joint-gut axis in inflammatory bowel diseases. J. Crohn's Colitis. **4**(3), 257–268 (2010)
19. http://www.integratedhealthsolutions.com/medical-thermography/abdominal/. Date of last access: 10 May 2016
20. http://www.atlanta-breast-thermography.com/#!__applications-and-information/abdomen. Date of last access: 10 May 2016
21. http://cimwellness.com/screening-inflammation-to-better-monitor-womens-health/. Date of last access: 10 May 2016
22. http://www.tiofsw.com/thermal-imaging/thermography-gallery. Date of last access: 10 May 2016

Potential of Thermography in Pain Diagnosing and Treatment Monitoring

Mahnaz Etehadtavakol and Eddie Y.K. Ng

Abstract Pain has been a problem to be differentially diagnosed for years since it has been diagnosed subjectively. Thermography can provide data of pain quantitatively as it reports detail and deep thermal variations. Hence, this method can be useful to diagnose pain objectively. It is a noninvasive complementary diagnostic approach that allows the practitioners to see and quantify alterations on skin temperature. Since in a healthy human individual, there is a high degree thermal symmetry in terms of both magnitude and pattern in the same regions in contralateral parts of the body, subtle skin temperature changes can be easily detected. According to thermography pain is classified based on which part of the body is involved. It is mostly classified in diseases as neural, inflammatory, musculoskeletal, and vascular. Nowadays with the new generation of infrared cameras and very advanced sensitive sensors, thermography has been applied in many medical applications. Pain diagnosis is one of the many uses of thermography in medicine. This chapter introduces pain and application of thermography for diagnosis of different pain categories as well as monitoring the treatments.

Keywords Thermography · Pain diagnosing · Treatment monitoring

1 Introduction

In very old practice of medicine, practitioners measure temperature by hands. Hippocrates, approximately four decades B.C., applied wet sludge to patient's body to identify superficial body temperature. The areas that had disease dried more quickly. It is obvious that a number of pathological factors are involved in

M. Etehadtavakol
Isfahan University of Medical Sciences, Isfahan, Iran

E.Y.K. Ng (✉)
School of Mechanical and Aerospace Engineering, College of Engineering, Nanyang Technological University, 50 Nanyang Avenue, Singapore 639798 Singapore
e-mail: mykng@ntu.edu.sg

E.Y.K. Ng and M. Etehadtavakol (eds.), *Application of Infrared to Biomedical Sciences*, Series in BioEngineering,
DOI 10.1007/978-981-10-3147-2_2

thermoregulation of human body. Hence, extracting thermal patterns of human body can help to access valuable information regarding the underlying physiological process causing diseases. Dissipation of heat through the skin generates infrared radiation that can be captured by sensitive infrared detectors. Pain is a complicated experience and the most familiar explanation for patient–clinician discussion in most developed countries. It is a major symptom in many medical conditions. We briefly introduce different pain categories in Sect. 2. Physiology of human skin is discussed in Sect. 3. Section 4 is about interpretation guidelines. Application of thermal imaging to diagnose different pain categories and treatment monitoring are presented in Sect. 5. Conclusion is provided in Sect. 6.

2 Classifications of Pain

There are many ways to classify pain and classifications may overlap. The International Association for the Study of Pain (IASP), in 1994, categorized pain in accordance with particular aspects: (1) area of the body complication such as lower limbs and abdomen, (2) system whose abnormalities may produce the pain such as gastrointestinal and nervous system, (3) continuation and form of happening, (4) strength and duration, and (5) etiology [1]. Although this introduced system was disapproved by Woolf et al. [2] as insufficient for leading study and therapy, three categories of pain were proposed by them as nociceptive pain, inflammatory pain that is related to tissue undesirable event as well as the immune cells incursion, and pathological pain which is a disease condition caused by nervous system corruption or by its irregular behavior such as irritable bowel syndrome, fibromyalgia, tension type headache, etc. [3]. However, classification of pain is a complicated issue and still many physicians are uncertain about it. Consequently, many clinicians often practice several different classification systems and clear separation of them is not always achievable.

a. **Nociceptive pain**:

Nociceptive pain is a chronic pain generated by injury to body tissue and often characterized as a sharpened, aching, or pulsating pain. This type of pain can be a result of benign pathology or by tumors or cancerous cells that are expanding and spreading to the tumor region neighborhood. Nociceptive pain may also be due to cancer growing to the muscles, joints, or bones or that brings about the closure of an organ or blood vessels [4, 5].

b. **Neuropathic pain**:

Neuropathic pain happens when there is a real nerve injury. Nerves accompany the spinal cord to the remnant of the body and permit the brain to interact with the skin, within organs and muscles. Nutritional disparity, alcohol addiction, toxicant substances, infections, or auto-immunity can all harm this network and generate pain. In addition neuropathic pain can be generated by a cancer tumor pressuring on a nerve or

a group of nerves. Patients usually characterize this pain as a flashing or severe sensation, or numbness toward the damaged nerve direction [6–8]. Thermal (vasomotor) variations which are reactions to the afferent noxious impulses of the unmyelinated sensory (thermoreceptors) nerves in the wall of microvasculature produce the neuropathic pain, while the ordinary somatic (somesthetic) pain is not often associated with circulatory dysfunction. The somesthetic pain involves afferent somatic (spinothalamic) nerves normally with no circulatory disturbance. Hooshmand et al. [9] found a case in which dermatomal pattern is developed in the extending of nerve roots and nerve trunks with somatic pain. However, the thermatomal distribution of neuropathic pain 'matches' to an arterial distribution including femoral, carotid, or brachial arteries. Hypothermic and hyperthermic variations in pathologic stages reflected in thermal imaging can be very valuable to choose a suitable treatment protocol. Magnetic resonance imaging, computed tomography, and physiological tests including electromyography and nerve conduction velocity tests are anatomical tests that are used as major identification techniques in the somesthetic (somatic) pain management, while they are not generally descriptive techniques in neuropathic pain recognition. However infrared imaging has potential to record neurovascular connection in neuropathic pain. Hooshmand et al. [9] found that thermogram produces information regarding diagnosis and treatment information restricted to complications connecting to neurovascular, autonomic, and neuro-inflammatory changes. Contrarily, it cannot assist diagnosing nerve damages with no microvascular connection including somesthetic nerve damages.

c. **Inflammatory pain**:

Inflammation is a reaction caused by injury of living tissues. The inflammatory reaction is a defense process that expanded into higher organisms to take care of them from infection and harm. The reaction incorporates changes in blood flow, a rise in blood vessels permeability, and transferring of fluid, proteins, and white blood cells (leukocytes) from the spread to the tissue corruption spot. If an inflammatory reaction ends only in a few days, it is named acute inflammation; however, a reaction of greater lasting is termed to as chronic inflammation. Despite the fact that acute inflammation is normally advantageous, it usually motivates displeasing sensations. Unpleasantness is generally lasting only a short while and ends when the inflammatory reaction has finished its task. However, in some occasions inflammation can cause harm. Tissue damage can happen when the managing processes of the inflammatory reaction are abnormal or the capability to improve harmed tissue and irrelevant individuals is damaged. The four important signs of inflammation, introduced by Aulus Cornelius Celsus in the first century, are as follows: redness (Latin rubor), heat (calor), swelling (tumor), and pain (dolor). Redness is generated by the expansion of small blood vessels in the region of damage. By increasing blood flow direct to the region, heat is generated and is accomplished solely in peripheral parts of the body such as skin. Fever boosts the temperature at the destroyed region by chemical attributors of inflammation. Basically fluid outside the blood vessels is built up and develops swelling or edema

[10]. When tissue is first damaged, the small blood vessels in the injured region are prohibited temporarily through a mechanism called vasoconstriction. Subsequent to this transient phenomenon, the process of vasodilation occurs or the blood vessels enlarge, rising blood flow into the region. Vasodilation period varies from 15 min to a few hours. Subsequently, the walls of the blood vessels, which typically admit simply only water and salts to pass through, eventually be more penetrable. Exudate or protein-rich fluid is instantly capable to leave and arrive at the tissues. Materials in the exudate involve clotting factors, which aid the expansion of infectious agents all over the body to be limited. Other proteins involve antibodies that enhance to demolish the attack of microorganisms. If a generated inflammation cannot be removed, or if the healing mechanism occurs, then an acute inflammatory reaction may develop to the chronic phase. If acute inflammation events happen again, a chronic inflammation is generated. The physical extent, duration, and impacts of chronic inflammation change with the originator of the injury and the body's strength to becoming better. However in some situations, chronic inflammation is not ended to acute inflammation. Some of the most typical and impairing human diseases, including tuberculosis, rheumatoid arthritis, and chronic lung diseases, are described by this kind of inflammation. Chronic inflammation can be achieved by infectious organisms that are capable of opposing host defenses and remain in tissues for a lengthened time.

d. **Musculoskeletal Pain**:

Impairment of muscles, joints, ligaments, bones, tendons, or a combination can cause musculoskeletal pain. The most typical cause of pain is injuries. Fibromyalgia may produce pain in the muscles, ligaments or tendons. The pain is normally involved with tenderness in multiple sites and sometimes is hard to express it accurately. However it is commonly not originating from the joints. Patients often complain other symptoms, such as poor sleep and fatigue. Compressing nerves may generate pain in some musculoskeletal impairment. These situations are introduced in the tunnel syndromes (for instance cubital tunnel, carpal tunnel, and tarsal tunnel syndromes). The pain spread diffusely along the path provided by the nerve and may be burning [11]. It is often associated with numbness, tingling, or both. When muscle strain occurs, heat elevation is observed due to the discharged chemicals. Consequently a strong hyperthermia pattern can be observed in the affected area or provoked site as an example of fibromyalgia.

3 Physiology of Human Skin

The skin is the largest organ of the body. Body temperature regulation is obtained by skin assistance that the human body has allowances to maintain its core internal temperature. Homeostasis is a condition that the internal temperature distributed evenly and all thermoregulation processes attempt the body back to the homeostasis

condition. Healthy body has a very limited temperature range of 37 °C (98 °F)–37.8 °C (100 °F). Body temperature can be affected by various factors. Diseases are the most familiar factors. Thermoregulation may lead to either cooling down or warming up. Thermoregulation for cooling down occurs in two major steps. In the first step, signals are sent to the hypothalamus by the sensors in central nervous system (CNS) to indicate the rise of internal temperature and in the second step, the hypothalamus in controlling thermoregulation mechanism stimulates one of several processes for temperature reduction. The mechanism can be considered as a negative feedback as shown in Fig. 1.

Conversely, the thermoregulation mechanism of body warming can be summarized as shown in Fig. 2.

Thermoregulation is a very complex and striking mechanism that we are not able to consider the details in this chapter. Spectrum of human skin blood circulation is very wide. It can be extended from almost zero when the whole body or a part of it is in cooling situation to up to 8 l/min (or equal to $\sim$60% of cardiac output) in extreme heat situations [12, 13]. Hence, the skin blood perfusion is a complicated process that the blood is capable to flow from very high to very low levels and able to control all within levels in order to satisfy the combined conditions of human physiology. There are two systems for reflex sympathetic innervation of the cutaneous circulation in human bodies. These two systems are non-noradrenergic active vasodilator system and sympathetic noradrenergic vasoconstrictor system. In normothermic environments, noradrenergic vasoconstrictor nerves are typically active and their activities are improved with cold stimulation, then norepinephrine as well

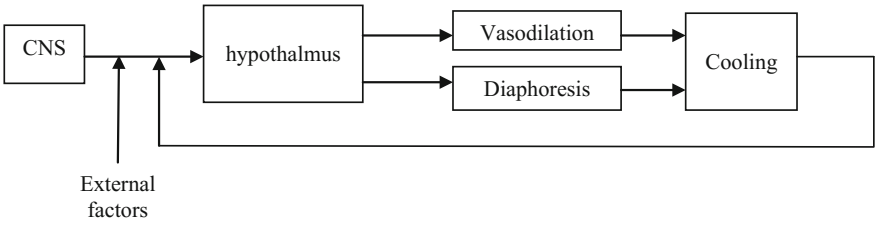

Fig. 1 Thermoregulation for cooling down

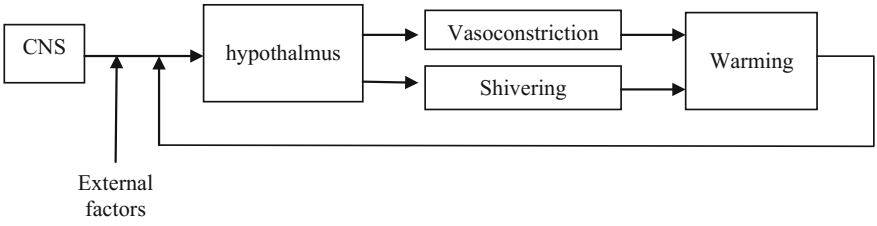

Fig. 2 Thermoregulation for warming up

as cotransmitters are released and consequently skin blood flow is decreased. However, the active vasodilator system is activated only when the body temperature is increased by heat stimulation. By cholinergic nerve cotransmission, active cutaneous vasodilation is developed. Long-term factors, such as illness, aging, and reproductive hormones as well as short-term factors such as hydration and exercise affect the processes of reflex cutaneous vasoconstriction and vasodilation [14, 15].

Skin temperatures in healthy individuals are symmetric since skin temperatures are controlled by one central controller which produces a uniform and simultaneous control system [16, 17]. Consequently, asymmetric thermal patterns of contralateral sides of the body (more than a certain level) can be a remarkable indicator of abnormality. Infrared radiation is one of different ways of human body heat loss. Planck's law considers the dry human skin nearly an ideal black body with an emissivity factor of 0.98. Hence it can be studied as a long wave infrared with a wavelength emissivity of 9.3 μm at most. The highest temperatures of human body are in the head and neck area, next trunk, and then declines over the limbs approaching the acral regions. One of the most crucial aspects of skin temperature pattern of the human body is bilateral symmetry [18–20].

4 Interpretation Guidelines

The following guidelines can be helpful to diagnose pain in using thermography method:

(1) Providing contralateral skin temperature differences in normal individuals: mean temperature difference for each part of the body. Different parts have different difference values
(2) Providing normal thermal pattern of the skin. For examples, hyperthermia is observed on the muscles (brachioradialis, trapezius, anterior tibia) [21], overlapped skin areas (under the breast, ham, axilla, groin (inguen)). While hypothermia is observed on the joint area (knee, elbow), distal area (finger tips (palm side), toe tips, cheek, heel, nose), fat area (breast, buttock, brachial region)
(3) Engaging patient's complain
(4) Identifying region of interest
(5) Testing the contralateral heat pattern to check the symmetries
(6) Testing the mean temperature difference for each part of patient's body
(7) Exploring different colors in patients' thermogram. In thermography certain colors have different interpretations. For example inflammatory disease, muscle activity related disorders and acute stage are indicated by bright red color, while neural disease and chronic stage by dark blue
(8) Discovering shape of heat from patient's thermal pattern. Shape of heat also has different implication in thermography. For instance, local muscle activity is mostly indicated by localized form (spot type), somatic or visceral induced

disorders by regional form (referred type) and thermatome, neuropathic pain by patterned form.

Many studies have been done to establish some of the guidelines. In a study, Niu et al. [22] provided normative data of the skin temperature in different areas to investigate contralateral thermal symmetry in young and old as well as male and female normal individuals in Taiwan. They tested 57 healthy subjects. They found that the neck had the highest skin temperature average of 31.9 °C with standard deviation of 0.6, while the toes had the lowest ones with average of 27.5 °C and standard deviation of 0.2. They also found slight contralateral thermal differences no more than 0.5 °C. In addition, they understood that old people had lower skin temperature particularly in the distal parts of extremities. Lower temperatures are found in different truncal regions in elderly females [22]. Gatt et al. investigated thermal patterns of the upper and lower limbs of 67 subjects. They discovered thermal symmetry in terms of both magnitude and pattern in the same regions in contralateral limbs. The warmest finger was thumb and the temperature declined gently for the second and the fifth digits. The big toe and the fifth toe were the warmest digits while the second to the fourth toes the coolest ones [23].

5 Application of Thermal Imaging

(a) **Diagnosing Different Pain Categories**

According to thermography pain is classified based on which part of the body is involved. It is mostly classified in neural disease, musculoskeletal disease, inflammatory disease and vascular disease. Pain has been a problem to be differentially diagnosed for years since it has been diagnosed subjectively. On the other hand, thermography can provide data of pain quantitatively. Hence, it can diagnose pain objectively. Thermography presents crucial data concerning neuropathic pain as a result of perivascular microcirculatory sympathetic dysfunction. It can help the physician to select a suitable and safe treatment protocol, particularly preventing needless surgery. Brusselmans et al. [24] did a test in healthy and fibromyalgia groups. They measured the autonomic response of individuals during a cold-water test. They concluded that the central body temperature, forearm temperature and peripheral (forearm)-central (ear) temperature ratio are significantly different in the two groups. In addition, fibromyalgia subjects had less tolerance to cold water than healthy subjects. They also studied the cool down rate, thermal recovery, and total temperature reduction in the two groups. In a project, Goto et al. [25] aimed to detect differentiating aspects in thermal images of venous leg ulcer (VLU), to evaluate VLU-related nociceptive pain. They concluded thermal patterns may catch nociceptive pain of VLU received by inflammation and has potential to evaluate pain as a simple and fast method. Hooshmand et al. [26] in a study investigated the role of thermal imaging for identification and management of pain. Herry et al. [27] introduced an algorithm that thermographic image of pain was computerized

automatically for pain evaluation in order to assist specialists to diagnose the diseases. A considerable betterment in circulation and indicative response to decreased pain with Electron Transfer Technology sleep system after applying it for only 4 nights was obtained by the thermal images in a case with chronic neck and upper back pain, reported by Dr. William Amalu [28]. A common cause of pain in situations of varicose veins is thrombophlebitis which results painful legs. Inflammation is generated by increasing the venous diameter that results in increase in volume, and consequently by a decrease in serous velocity [29]. Thermography helps us to visualize superficial vascular patterns of legs. Thermogram of a patient experiencing phlebitis, the inflammation of a vein, is shown in Fig. 3.

Figure 4 shows a patient with a Complex Regional Pain Syndrome in right foot with an asymmetry of 3.7 °C of contralateral feet. The patient went through the cold stress test indicating no sympathetic change. The disease spread in the right foot following the fracturing of the calcaneum 18 months earlier. At first, the disease was not recognized by nuclear imaging and failed. However, thermography could show the alterations.

Very few methods are available to indicate pain located in the metal implants sites. Glehr et al. [30] concluded that thermography had potential to identify and assess pain more accurately. They showed that the skin temperature on the painful regions of individuals complaining of anterior knee pain after implantation of

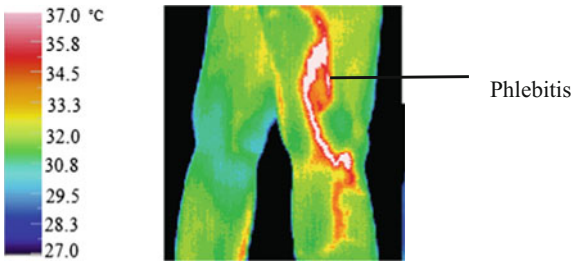

Fig. 3 Thermogram of a patient experiencing phlebitis [29]

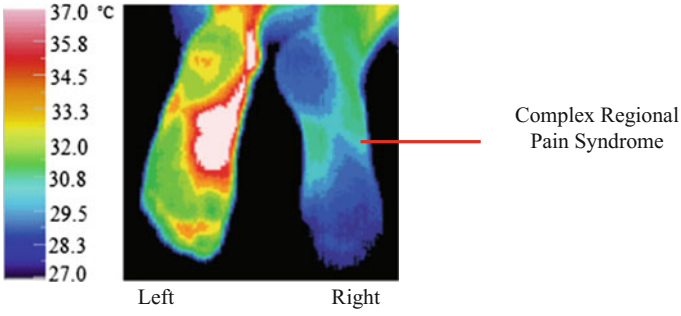

Fig. 4 Thermogram of a patient with a complex regional pain syndrome in right foot [29]

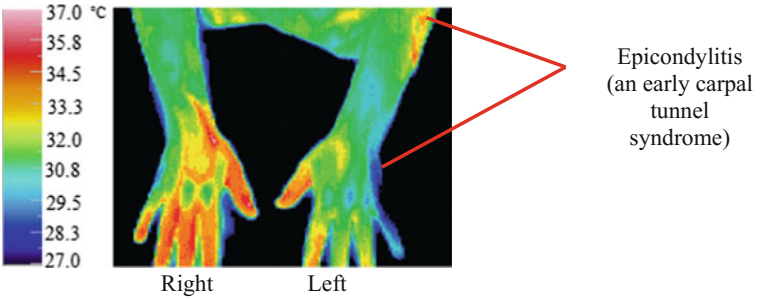

Fig. 5 Thermogram of a patient with golfer left elbow [31]

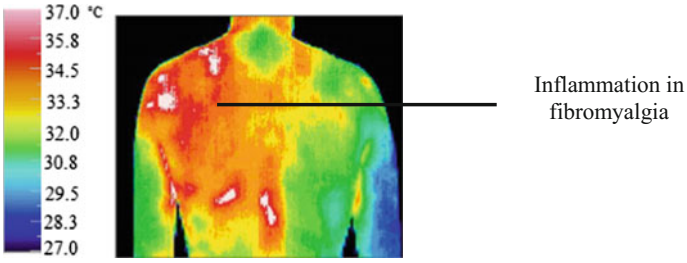

Fig. 6 Thermogram of a fibromyalgia patient [32]

artificial knee joints was significantly higher. Thermography can be helpful for patients that suffering pain that other tests cannot diagnose. Patients with golfer elbow are complaining of pain due to the condition that causes pain where the tendons of the forearm muscles attach to the bony bump on the inside of the elbow. Golfer elbow and, in some cases carpal tunnel syndrome, are all problems associated with the inflammation of the soft tissues in the wrist and elbow. Repetitive physical motion in sports or work, producing repeated impacts to the arm that finally pain can be induced from the wrist to the elbow. Thermogram of a 28-year-old male carpet layer with golfer left elbow who has pain that radiates distally through the ulna into the smallest finger is shown in Fig. 5. By doing thermography cold stress test, an early carpal tunnel syndrome was indicated [31].

A multiple symptoms such as ache, muscle tenderness, headaches, anxiety, depression, sleep pattern disruptions, fatigue as well as pain and ache throughout the body can be observed with fibromyalgia patients. Thermography is very useful to identify the muscular and myofascial inflammation accurately and objectively thus allowing the physician to monitor a comprehensive action plan of treatment. Thermogram of a fibromyalgia patient is presented in Fig. 6. Areas of pain and inflammation associated with fibromyalgia are demonstrated with different colors [32].

(b) **Treatment monitoring**

Blood circulation improvement is a powerful sign of physiological recovery. By comparing thermal images of pre- and post-therapy, treatment progress can be assessed. Consequently, if the image of post-therapy is not indicating major thermal recovery, then additional therapies could be considered. As shown in Fig. 7a, around the lower patella there is an extensive hyperthermia that indicates the inflammation development associated with swelling and pain. However, as shown in Fig. 7b, the same knee after 6 months of treatment by a comprehensive rehabilitation program [33].

Another example is a case with severe alpine skiing accident with a serious injury as a fracture. The thermogram shown in Fig. 8a was provided 3 months after a combined fracture of the tibia and fibula with intramedullary nailing [33]. However, no clear differences of the thermal pattern of two sides were observed and complete recovery was approved and confirmed with physical examination as it is evident in Fig. 8b.

In an encyclopedic study, Hooshmand et al. [34] indicated that the most sensitive tool to detect Reflex Sympathetic Dystrophy is thermography method and no other

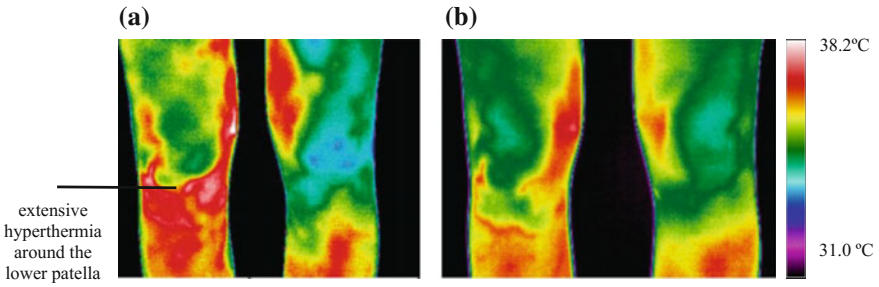

Fig. 7 Inflammation monitoring [33]. **a** Pre-therapy **b** post-therapy

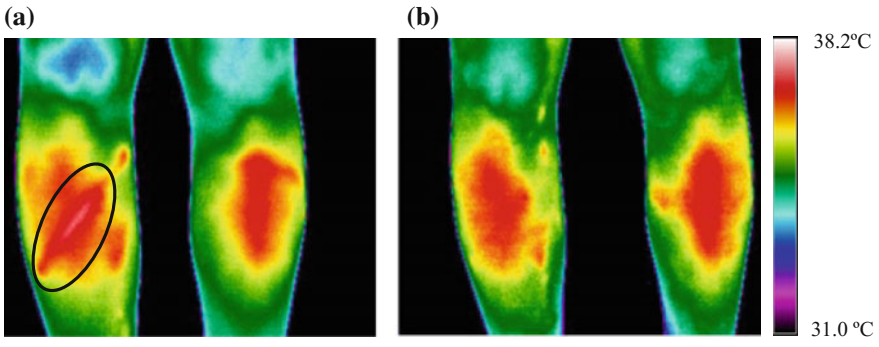

Fig. 8 Treatment monitoring of a case with severe alpine skiing accident [33]. **a** Pre-therapy **b** post-therapy

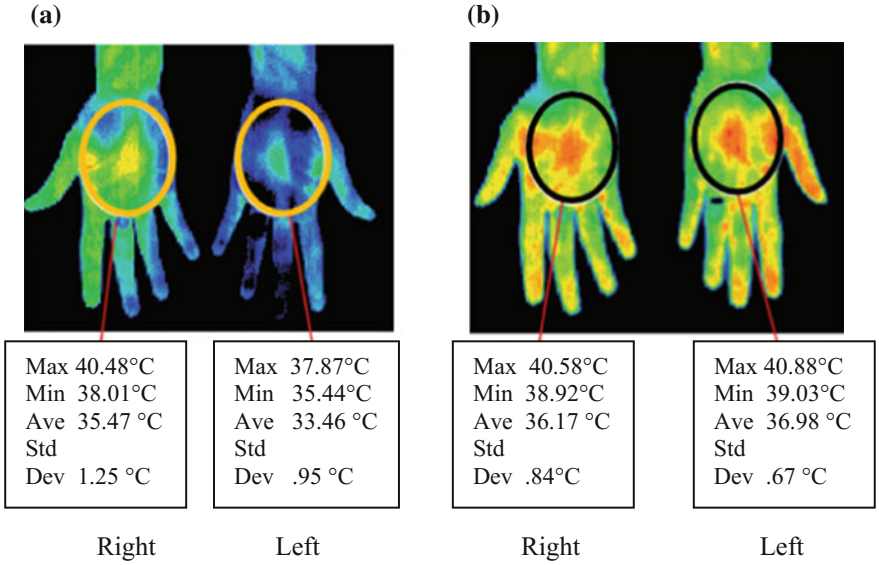

Fig. 9 A patient with reflex sympathetic dystrophy (complex regional pain) [29]. **a** Pre-therapy **b** post-therapy

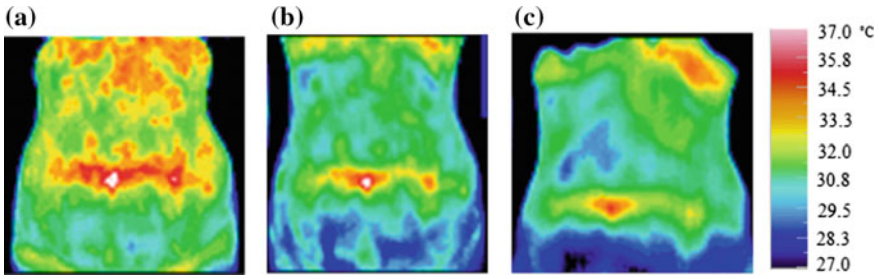

Fig. 10 Treatment monitoring of one irritable bowel syndrome (IBS) patient by taking aloe vera juice [35]. **a** Pre-treatment **b** after 5 days **c** after 13 days

test can compete with it [34]. There was a patient with Reflex Sympathetic Dystrophy (Complex Regional Pain) that had a "glove-like" hypothermia zone in the left hand as shown in Fig. 9a. The temperature differential was 1.5 °C and asymmetry was 5 °C. These numbers were notable. The patient went through the cold stress test showed the right hand had sympathetic function while the left had nothing. Provided thermal patterns of post-therapy indicated thermal symmetry as shown in Fig. 9b. In addition, cold stress test also indicated sympathetic function in both hands [29].

Figure 10a–c, are thermal images of one irritable bowel syndrome (IBS) patient who is treated with aloe vera juice. Figure 10b, c show the treatment by taking aloe vera juice 5 days and 13 days, respectively [35].

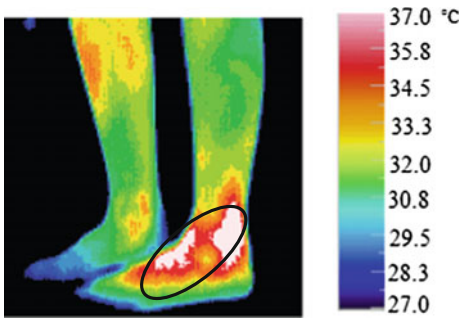

Fig. 11 A thermogram after removing the cast of a patient who had a fracture and still needs further treatment [36]

Figure 11 shows an individual who had a fracture in the left ankle. The cast was removed and unfortunately healing response was poor. Left ankle was monitoring for further treatment [36].

6 Conclusion

Pain diagnosis has been a problem for many years since the diagnosis is a very subjective and an individual experience. There is no test can provide data indicating the accurate information regarding the location and amount of the pain. Hence, clinicians count on the patient's own explanation of the location, form and timing the pain. However, thermography can provide data of pain quantitatively and be useful to diagnose pain objectively. It is a noninvasive complementary diagnostic method that can help the clinicians to discover any alterations on the skin temperature. With the new generation of infrared cameras, many specialists have considered thermography as a method to diagnose the type and location of pain precisely. It has been recognized that thermography is the most sensitive test to detect pain in some diseases for example Reflex Sympathetic Dystrophy and no other is able to compete with it. Hopefully, specialists are getting familiar with this powerful technique to use it for accurate detection of different pain categories and monitoring of different pain treatments in the near future.

References

1. Merskey, H., Bogduk, N.: Classification of Chronic Pain, 2nd edn., pp. 3–4. International Association for the Study of Pain, Seattle (1994). ISBN 0-931092-05-1
2. Woolf, C.J., Bennett, G.J., Doherty, M., Dubner, R., Kidd, B., Koltzenburg, M., Lipton, R., Loeser, J.D., Payne, R., Torebjork, E.: Towards a mechanism-based classification of pain? Pain. **77**(3), 227–229 (1998). doi:10.1016/S0304-3959(98)00099-2. PMID 9808347
3. Woolf, C.J.: What is this thing called pain? J. Clin. Invest. **120**(11), 3742–3744 (2010). doi:10.1172/JCI45178. PMID 21041955

4. Keay, K.A., Clement, C.I., Bandler, R.: The neuroanatomy of cardiac nociceptive pathways. In: Horst, G.J.T. (ed.) The Nervous System and the Heart, p. 304. Humana Press, Totowa, New Jersey (2000). ISBN 978-0-89603-693-2
5. Coda, B.A., Bonica, J.J.: General considerations of acute pain. In: Loeser, D., Bonica, J. J. (eds.) Bonica's Management of Pain, 3rd edn. Lippincott Williams & Wilkins, Philadelphia (2001). ISBN 0-443-05683-8
6. Diagnostic Methods for Neuropathic Pain: A Review of Diagnostic Accuracy Rapid Response Report: Summary with Critical Appraisal. Canadian Agency for Drugs and Technologies in Health (2015). PMID 26180859
7. Bogduk, N., Merskey, H.: Classification of Chronic Pain: Descriptions of Chronic Pain Syndromes and Definitions of Pain Terms, 2nd edn., p. 212. IASP Press, Seattle (1994). ISBN 0-931092-05-1
8. Paice, J.A.: Mechanisms and management of neuropathic pain in cancer (PDF). J. Supp. Oncol. **1**(2), 107–120 (2003). PMID 15352654
9. Hooshmand, H., Hashmi, M., Phillips, E.M.: Infrared thermal imaging as a tool in pain management—an 11 year study. Part I of II. Thermol. Int. **11**, 53–65 (2001)
10. http://www.britannica.com/science/inflammation. Last access May 2016
11. https://my.clevelandclinic.org. Last access May 2016
12. Johnson, J.M., Proppe, D.W.: Cardiovascular adjustments to heat stress. In: Handbook of Physiology Environmental Physiology (Chapter 11, Section 4), vol. II, pp. 215–244. American Physiological Society, Bethesda, MD (1996)
13. Rowell, L.B.: Cardiovascular adjustments to thermal stress. In: Handbook of Physiology. The Cardiovascular System. Peripheral Circulation and Organ Blood Flow (Chapter 27, Section 2, Point 2), vol. III, pp. 967–1023. American Physiological Society, Bethesda (1983)
14. Charkoudian, N.: Mechanisms and modifiers of reflex induced cutaneous vasodilation and vasoconstriction in humans. J. Appl. Physiol. **109**(4), 1221–1228 (1985). Published online 6 May 2010. doi:10.1152/japplphysiol.00298.2010 (Oct 2010)
15. Ong, M.L., Ng, E.Y.K.: A global bioheat model with self-tuning optimal regulation of body temperature using Hebbian feedback covariance learning. Med. Phys. **32**(12), 3819–3831 (2005)
16. Vardasca, R.: Symmetry of temperature distribution in the upper and lower extremities. Thermol. Int. **18**, 154–155 (2008)
17. Selfe, J., Whitaker, J., Hardakerh, N.: A narrative literature review identifying the minimum clinically important difference for skin temperature asymmetry at the knee. Thermol. Int. **18**, 41–44 (2008)
18. Ng, E.Y.K.: A review of thermography as promising non-invasive detection modality for breast tumor. Int. J. Therm. Sci. **48**(5), 849–859 (2009)
19. Ng, E.Y.K., Kaw, G.J.L., Chang, W.M.: Analysis of IR thermal imager for mass blind fever screening. Microvasc. Res. **68**(2), 104–109 (2004)
20. Etehadtavakol, M., Sadri, S., Ng, E.Y.K.: Application of K- and fuzzy c-means for color segmentation of thermal infrared breast images. J. Med. Syst. **34**(1), 35–42 (2010)
21. Garagiola, U., Giani, E.: The use of telethermography in the management of sport injuries. Sport Med. **10**, 267–272 (1990)
22. Niu, H.H., Lui, P.W., Hu, J.S., Ting, C.K., Yin, Y.C., Lo, Y.L., Liu, L., Lee, T.Y.: Thermal symmetry of skin temperature: normative data of normal subjects in Taiwan. Zhonghua Yi Xue Za Zhi (Taipei). **64**(8), 459–468 (2001)
23. Gatt, S.A., Formosa, C., Cassar, K., Camilleri, K.P., Raffaele, C.D., Mizzi, A., Azzopardi, C., Mizzi, S., Falzon, O., Cristina, S., Chockalingam, N.: Thermographic patterns of the upper and lower limbs: baseline data. Int. J. Vasc. Med. **2015**, 9 pp. Article ID 831369 (2015)
24. Brusselmans, G., Nogueira Carvalho, H., De Schamphelaere, E., Devulder, J., Crombez, G.: Skin temperature during cold pressor test in fibromyalgia: an evaluation of the autonomic nervous system?. Acta Anaesth. Belg. **66**, 19–27 (2015)

25. Goto, T., Naito, A., Tamai, N., Nakagami, G., Mo, M., Sanada, H.: Objective evaluation for venous leg ulcer-related nociceptive pain using thermography. Chronic Wound Care Manag. Res. **2014**(1), 23–30 (2014)
26. Hooshmand, H., Hashmi, M., Phillips, E.M.: Infrared thermal imaging as a tool in pain management—an 11 year study. Part II: clinical applications. Thermol. Int. **11**, 117–129 (2001)
27. Herry, C.L., Frize, M.: Quantitative assessment of pain-related thermal dysfunction through clinical digital infrared thermal imaging. Biomed. Eng. Online. **3**, 19 (2004)
28. http://www.earthinginstitute.net/wpcontent/uploads/2013/06/Amalu_thermographic_case_studies_2004.pdf. Last access May 2016
29. http://www.thermographyofmontana.com/patient/PractitionerInfo.pdf. Last access May 2016
30. Glehr, M., Stibor, A., Sadoghi, P., Schuster, C., Quehenberger, F., Gruber, G., Leithner, A., Windhager, R.: Thermal imaging as a noninvasive diagnostic tool for anterior knee pain following implantation of artificial knee joints. Int. J. Thermodyn. **14**(2), 71–78 (2011)
31. http://yourthermalimaging.com/node/48. Last access May 2016
32. http://www.invisionthermography.com/fibromyalgia_fatigue.html (last access May 2016)
33. Hildebrandt, C., Raschner, C., Ammer, K.: An overview of recent application of medical infrared thermography in sports medicine in Austria. Sensors (Basel). **10**(5), 4700–4715 (2010)
34. Hooshmand, H.: Chronic Pain: Reflex Sympathetic Dystrophy, Prevention, and Management, CRC Press, Reference—224 pp, 26 Mar 1993, ISBN 9780849386671—CAT# 8667
35. http://www.integratedhealthsolutions.com/medical-thermography/abdominal/. Last access May 2016
36. http://www.thermographyofmontana.com/patient/PractitionerInfo.pdf. Last access May 2016

Assessment of Foot Complications in Diabetic Patients Using Thermography: A Review

Mahnaz Etehadtavakol and Eddie Y.K. Ng

Abstract Nowadays, there is a considerable appreciation of thermal physiology and the connection between superficial hotness and blood perfusion. Moreover, the advantages of computer-aided digital imaging and the examination modality have considerably enhanced the trustworthiness of this technique in medical fields. The advantage of this new possibility and its applicability to medical determination of peripheral perfusion and liveliness of cells are shown by studies in diabetology. Researches demonstrate that routine checking up on foot temperature could terminate the occurrence of impairment conditions including foot ulcers and lower limb amputations. Thermography is identified as one of the popular techniques in practice today. It has potential for temperature checking up on the feet and it can be employed as an adjunctive method for modern foot examinations in diabetes.

Keywords Thermography · Diabetes · Foot complications

1 Introduction

The previous infrared cameras were not as accurate or reliable as those accessible recently. However, today's modern infrared cameras support high speed and high resolution. Consequently, researches reconsidered this method. Some of the most important factors accommodated pathogenesis of the diabetic foot are represented by peripheral vascular changes, such as macroangiopathy, microangiopathy, and neuropathy-induced capillary circulation changes. These factors produce superficial temperature variations which can be identified by applying thermography. Patients' difficulties cause significant costs and life quality deprivation. Abnormal areas can

M. Etehadtavakol
Isfahan University of Medical Sciences, Isfahan, Iran

E.Y.K. Ng (✉)
School of Mechanical and Aerospace Engineering, College of Engineering, Nanyang Technological University, 50 Nanyang Avenue, Singapore 639798, Singapore
e-mail: mykng@ntu.edu.sg

E.Y.K. Ng and M. Etehadtavakol (eds.), *Application of Infrared to Biomedical Sciences*, Series in BioEngineering,
DOI 10.1007/978-981-10-3147-2_3

be easily detected by thermography since temperature can be measured. Investigations indicate that routine checking up on foot hotness may terminate the occurrence of impairment conditions including foot ulcers and lower limb amputations. Many researchers comply that the thermography of the diabetic foot can be much informational to evaluate in the specified four issues: (1) the arterial circulation disorder, determination of microangiopathy and additional vascular alterations produced by diabetic neuropathy; (2) recognition of regions with great chance of ulceration or re-ulceration, determination of tissue liveliness, amputation stage, and the intra-operative skin flap activity; (3) osteomyelitis examination; (4) checking up on the reaction to medical therapy [1]. Diabetic foot wounds are in charge of more hospitalizations than any other problems of diabetes. U.S. Department of Health and Human Services stated that individuals with diabetes with some form of neuropathy are between 60 and 70% [2]. One estimate shows 16 million Americans are diabetic. Approximately 15% result a foot ulcer and for every 1000 individuals, 6–8 need amputation, correspondingly the long-term complications [1]. Indeed, in the United States, diabetes is the major producer of nontraumatic lower extremity amputations. Test of ulcer as well as the general condition of the extremity, determination of the chance of vascular inability, and determination of the chance of peripheral neuropathy are possible by different levels of physical checkup of the extremity having a diabetic ulcer. Soft tissue depth and osseous connection can identify the stage of diabetic foot wounds [3–5].

2 Considerations for Applying Thermography in Examination of the Diabetic Foot

Macroangiopathic vascular changes in the foot can be assessed using eco-Doppler and angiography. However, thermography is particularly helpful to characterize the ischemic foot and the neuropathic foot. Ischemic foot is cold while the neuropathic foot is warm. In addition, thermography has also been described to be useful in detecting areas of critical ischemia. Ischemic foot is a condition of decreased arterial perfusion. Following considerations should be reviewed for applying thermography in examination of the diabetic foot: (1) the macro-circulation pathology concentrating more often at, or below the popliteal fossa, than at the level of the aorta or iliac vessels. (2) atheromatous plaques are mono-segmental, exist in the tibial and peroneal arteries, and are generally nonexistent in the more proximal or distal (pedal) arteries. (3) changes are usually asymmetric, the tibial—peroneal triangle being the most commonly affected. (4) room temperature must be constant. (5) subject must remove their shoes, socks and seated or lay down relax up to 15–20 min.

3 Application of Thermography in Diabetic Foot Monitoring

Thermography is very useful in the detection of following cases:

3.1 Critical Ischemia Involving Small Arterial Territories

Since it involves small arterial territories it cannot be identified easily. Thermogram of a critical ischemia—hypothermic area situated above the right medial malleolus is shown in Fig. 1.

Another example is the infrared image of an ischemic foot in a patient with diabetes shown in Fig. 2. It demonstrates asymmetric heat pattern, classic for atherosclerotic lesions, caused by hypothermia on the right posterior tibialis trajectory [1].

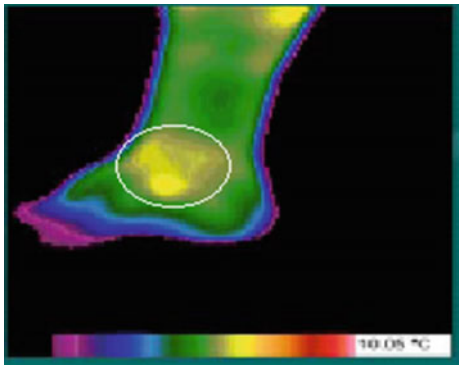

Fig. 1 Thermogram of a critical ischemia—hypothermic area situated above the right medial malleolus (hypothermic area indicated by the *white circle*) [1]

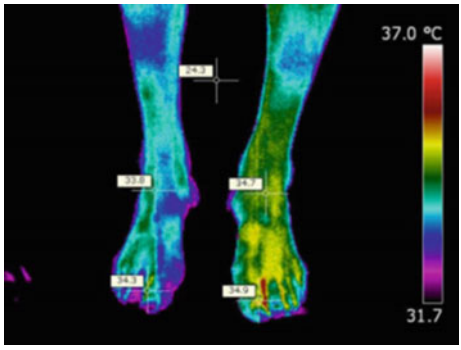

Fig. 2 An ischemic foot in a patient with diabetes (asymmetric contralateral feet and toes thermal patterns) [1]

3.2 Changes in the Cutaneous Circulation Induced by Diabetic Microangiophathy, Which Leads to Ulceration

Thermogram of a patient with symmetric decrease in infrared radiation in the distal regions of the feet is presented in Fig. 3.

3.3 Neuropathy Evaluation, Specifically Small Fiber Sensory Neuropathy

Diabetic neuropathy is a kind of nerve injury that may be developed if one individual has diabetes. High blood sugar may damage nerve fibers all over the body, however diabetic neuropathy usually harms nerves in the legs and feet. Symptoms of diabetic neuropathy may extend from pain and numbness in the extremities to complications with the blood vessels, heart, urinary tract and digestive system, based on the damaged nerves. These symptoms for some individuals are weak; for others, they can be painful, becoming physically handicapped and even death. Symptoms are varied in patients; sometimes are painful, and other times are mild or no symptoms at all. Hence careful foot examination should be mandatory to diagnose neuropathy. Two typical thermograms of patients with foot neuropathy are illustrated in Figs. 4 and 5.

Gheorghe Serbu found that average temperature of the neuropathy patients was 32.8 °C, (hyperthermia) compared to 27.9 °C in diabetic patients without neuropathy [1]. In a study, Bagavathiappan et al. [7] further confirmed that foot temperatures in subjects with diabetic neuropathy (32–35 °C) were greater than subjects without neuropathy (27–30 °C).

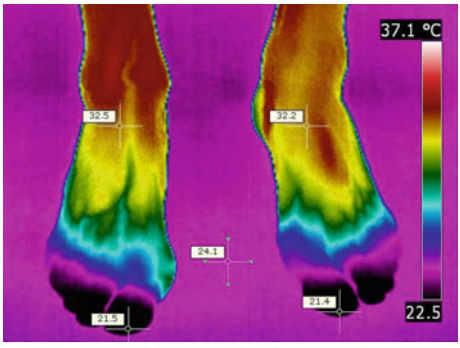

Fig. 3 Symmetric decrease in infrared radiation in the distal regions of the feet (Microangiopathy) [1]

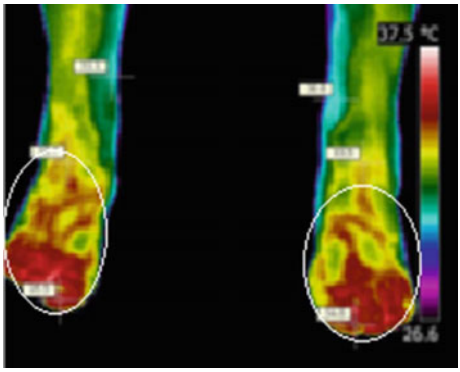

Fig. 4 A patient with neuropathy, hyperthermia of the 1/3 distal aspect of the foot and the toes (hyperthermia areas indicated by *white circles*) [1]

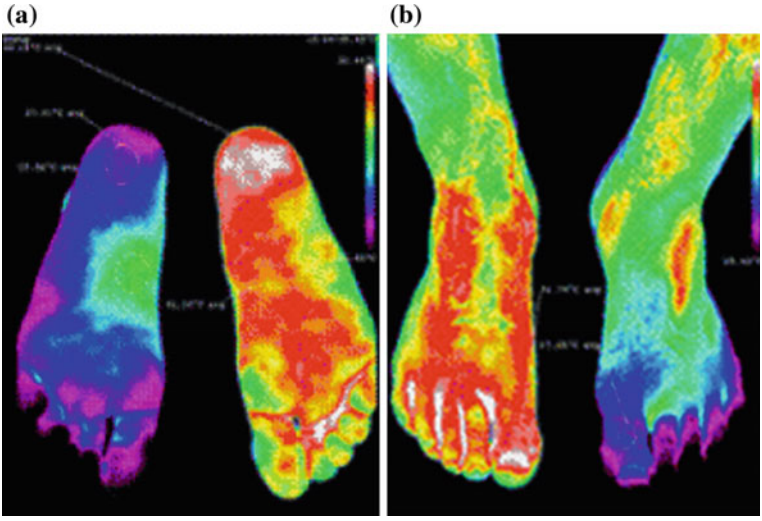

Fig. 5 A patient with foot neuropathy **a** Asymmetric contralateral feet and toes thermal patterns. **b** Asymmetric contralateral plantar thermal patterns [6]

3.4 Plantar Patterns

Skin temperature distribution of plantar in diabetic patients has been one of the valuable factors for determining feet complications in diabetic patients. Takashi Nagase et al. through a project indicated that particularized plantar thermal patterns were demonstrating larger changes in the diabetic subjects than in the healthy individuals. A new scheme of theoretical categorization of 20 contrasting classes of plantar thermal patterns in accordance with the angiosome concept of foot was

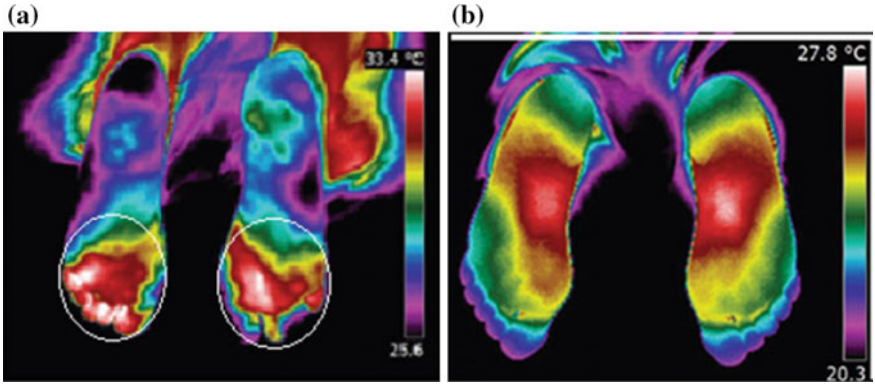

Fig. 6 **a** Plantar thermographic image in a diabetic patient (interdigital anisothermal areas indicated by *white circles*). **b** A control subject (ΔT less than 0.4 °C) [9]

introduced. In their work for the healthy category, greater than 65% of thermal patterns of feet were assigned to the two usual classes, containing the "butterfly pattern" in the whole 20 classes, considering 225 ft (87.2%) of the diabetic groups were differently assigned to 18 out of the 20 classes [8].

An image segmentation method was employed by Mori et al. to propose a novel plantar forepart thermal patterns classification system. They observed larger changes of the plantar forepart thermal patterns in the subjects with diabetes mellitus comparing with those in the control subjects [9]. In addition, Balbinot et al. employed cardiac tests (heart rate variability) as a reference standard since autonomic small fibers are damaged first by this disease for evaluating plantar thermography sensitivity and specificity to diagnose diabetic polyneuropathy. In Fig. 6, a plantar thermal image in a diabetic patient, interdigital anisothermal (ΔT less than 0.4 °C) as well as a control subject (ΔT less than 0.4 °C) are presented with Fig. 6b. They observed that plantar thermography is helpful in early diagnosing diabetic neuropathy and also, the interdigital anisothermal method alone did better performance in diabetic patients comparing the thermal recovery index alone, accompanying an improved sensitivity (81.3%) and specificity (46.2%) [10].

3.5 Detecting area at High Risk for Ulceration or Pre-ulceration and Monitoring Ulcer Healing

In diabetic patient, the ulcer is the most detecting problem and their early detection is crucial. Weak circulation, high blood sugar or hyperglycemia, nerve injury, and irritated or injured feet are mostly responsible for diabetic ulcers. Poor blood circulation can be described as a model of vascular disease in which blood cannot flow to the feet adequately [11]. In addition, poor circulation makes healing of ulcers

more difficult. A long-term effect of diabetes is nerve damage which can lead to a failure of feeling in the feet which named neuropathy. In onset of harmed nerves conditions individuals may feel stimulated and hurtful. In the long term, sensitivity to foot pain is reduced and painless wounds which have ability to cause ulcers are formed [12]. All individuals with diabetic foot ulcers must be evaluated so as to investigate the urgency for revisional surgery, debridement, vascular reconstruction, bony construction, or soft tissue coverage.

Liu et al. [13] in a study, discussed different imaging techniques applied to identify presigns of ulceration. Four different imaging techniques are as follows: photographic imaging, foot sole scanning, thermal imaging, and hyperspectral imaging. However foot sole scanning demands individuals to squeeze the foot against the scanner, which will generate some undesired force on the foot sole. Consequently, they deduced that a noninteractive foot scanner is preferable to acquire a superior view of the foot skin [13]. Some of presigns of ulceration are local skin temperature increasing, redness, callus formation, blisters and fissures that let a therapist to identify the location of risk sites. By early identification, the first appearance of diabetic foot ulcers may be halted and following treatment can be started. Nonetheless, early identification depends on repeated risk evaluation, which is not consistently manageable. Self-examination is almost not possible and regular examination by specialists is also priceless and not achievable. Liu et al. [13] focused on the basic analysis on the collected thermal images with their setup to show the ability of employing thermal imaging to identify the local temperature rising [13]. The final goal of their research was to establish an intelligent telemedicine monitoring system that can be utilized at the patients' home surroundings for repeated test of the patients' feet, to identify presigns of ulceration in an appropriate approach.

In a study, Lavery et al. [14] discovered that Infrared temperature home monitoring has potential to defeat these restrictions, to identify the early warning signs automatically, and it is non-invasive, non-contact and effortless using. It should be supported and put into action in diabetic foot care [14]. Researches indicate that there is a connection between rising temperature and foot problems in diabetes [15–17]. A week before a foot ulcer is developed; a raised temperature may be happened [15, 18]. Patients hardly experience pain in this initial stage of the disease as a consequence of neuropathic sensory loss. It shows that raised temperature can be a helpful indicative sign of foot ulceration and subclinical inflammation of the feet.

Besides, 3D surface reconstruction is also important to identify the presigns. It has potential to acknowledge the local 3D deformity of the skin superficial and present proper information about the surface textures. Geometrical changes of the surface such as fissures, papillary lines, and heavy callus as well as radiometric changes can cause these textures. Colantonio et al. [19] presented a model to reconstruct, visualize, and manage data of three-dimensional infrared volumes especially for diabetic foot disease. One example of their work is shown in Fig. 7.

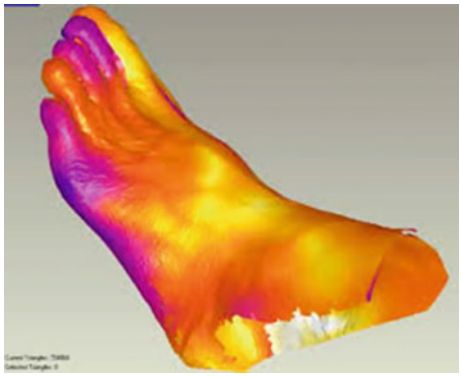

Fig. 7 3D image of the diabetic foot [19]

4 Asymmetry Analysis

Since symmetry generally shows healthy subjects [20], the rise of asymmetry development of paired structures could be a sign of abnormality. Many studies have been accomplished by applying asymmetry analysis in order to investigate breast abnormalities [21–28]. Temperature variations between corresponding areas on contralateral feet indicate inflammatory development. Investigations indicate that elevated temperatures may be identified at a level where a capable diabetic foot problem is still reversible. Temperatures of corresponding areas on contralateral feet do not generally alter of greater than 1 °C and a temperature alteration of greater than 2.2 °C (4 °F) is treated abnormal [29–31]. In a study, Liu et al. [32] showed that thermography is a hopeful technique for early identification of diabetic foot complications. The temperature differences between corresponding sites of the right and left foot are the clinically important features. Their outcome was 97.8% ± 1.1% sensitivity and 98.4% ± 0.5% specificity over 76 high-risk diabetic subjects with manual comments as a Ref. [32].

van Netten et al. [33] found that mean temperatures >1.5 °C between the ipsilateral and the contralateral foot in subjects without complications were not differentiated. In subjects with local complications, mean temperatures of the ipsilateral and the contralateral foot were identical, while temperature at the ROI was >2 °C greater contrasting with the matching area in the contralateral foot and to the mean of the whole ipsilateral foot. In addition, Netten et al. observed the mean temperature differences of >3 °C between ipsilateral and contralateral foot in patients with diffuse complications.

A methodology was presented by Peregrina-Barreto et al. [34] to provide assessable information about atypical temperature variations in symmetric sites between feet and inside of the same foot [34]. The methodology took into account the temperature differences, their distribution, and their area. Differences between symmetric areas in both feet were studied in their first analysis while studying temperatures inside the angiosomes in order to detect the existence of small abnormal areas (hot spots) was performed in their second project. In order to

accomplish asymmetry analysis, 140 thermal images were collected by Rathod et al. [35]. They concluded that the overlapping technique works well only when the feet projections sizes and shapes are the same, the scalable scanning technique works well for all types of feet projections.

Mendes et al. [36] in a work showed that thermography is able to quantify small temperature asymmetries in order to monitor some physiological conditions for recognition of subjects at risk for diabetic foot [36]. Although diabetic foot clinical examination involves a 10-g Semmes–Weinstein monofilament test, palpation of peripheral arterial pulses, subjective evaluation of skin temperature, besides the observation of structural and dermatological characteristics of the feet. Kaabouch et al. [37] established an asymmetry investigation to observe the thermal pattern of the feet for the sake of identifying inflammation that leads to foot ulceration. Extraction of higher order statistical parameters helps them to raise the performance of their introduced method. The experimental findings indicate that their method is trustworthy and have potential detecting foot inflammation.

5 Conclusion

This review article gives the reliability and availability of thermography for foot temperature monitoring as a method of early identification of foot complications in diabetes. The objective here is describing and summarizing experiences from experimental use. Researches indicate that routine checking up on foot temperature may terminate the occurrence of impairment conditions including foot ulcers and lower limb amputations.

References

1. Serbu, G.: Infrared imaging of the diabetic foot. In: Proceedings on InfraMation 2009, Romanian Society of Thermography, vol. 86, pp. 5–20 (2009)
2. http://www.healthline.com/health-slideshow/diabetic-peripheral-neuropathy-symptoms. Last accessed Oct 2015
3. Beckert, S., Witte, M., Wicke, C., Konigsrainer, A., Coerper, S.: A new wound-based severity score for diabetic foot ulcers: a prospective analysis of 1,000 patients. Diabetes Care **29** (5):988–992 (2006) [Medline]
4. Oyibo, S.O., Jude, E.B., Tarawneh, I., Nguyen, H.C., Harkless, L.B., Boulton, A.J.: A comparison of two diabetic foot ulcer classification systems: the Wagner and the University of Texas wound classification systems. Diabetes Care **24**(1):84–88 (2001) [Medline]
5. Robson, M.C., Hill, D.P., Woodske, M.E., Steed, D.L.: Wound healing trajectories as predictors of effectiveness of therapeutic agents. Arch. Surg. **135**(7):773–777 (2000) [Medline]
6. . http://www.tiofsw.com/thermal-imaging/thermography-gallery/. Last accessed Oct 2015
7. Bagavathiappan, S., Philip, J., Jayakumar, T., Raj, B., Rao, P.N.S.R., Varalakshmi, M., Mohan, V.: Correlation between plantar foot temperature and diabetic neuropathy: a case study by using an infrared thermal imaging technique. J. Diabetes Sci. Technol. **4**(6), 1386–1392 (2010)

8. Nagase, T., Sanada, H., Takehara, K., Oe, M., Iizaka, S., Ohashi, Y., Oba, M., Kadowaki, T., Nakagami, G.: Variations of plantar thermographic patterns in normal controls and non-ulcer diabetic patients: novel classification using angiosome concept. J. Plast. Reconstr. Aesthet. Surg. **64**(7), 860–866 (2011). doi:10.1016/j.bjps.2010.12.003
9. Mori, T., Nagase, T., Takehara, K., Ohashi, M.Y., Amemiya, A., Noguchi, H., Ueki, K., Kadowaki, T., Sanada, H.: Morphological pattern classification system for plantar thermography of patients with diabetes. J. Diabetes Sci. Technol. **7**(5), 1102–1112 (2013)
10. Balbinot, L.F., Canani, L.H., Robinson, C.C., Achaval, M., Zaro, M.A.: Plantar thermography is useful in the early diagnosis of diabetic neuropathy. Clinics (Sao Paulo) **67**:1419–1425 (2012)
11. Mercer, J.B., Nielsen, S.P., Hoffmann, G.: Improvement of wound healing by water-filtered infrared-A (wIRA) in patients with chronic venous stasis ulcers of the lower legs including evaluation using infrared thermography. Ger. Med. Sci. GMS e-J. **6**:Doc11 (2007)
12. http://emedicine.medscape.com/article/460282-overview. Last accessed Oct 2015
13. Liu, C., Heijden, F.V.D., Klein, M.E., Baal, J.G.V., Bus, S.A., Netten, J.J.V.: Infrared dermal thermography on diabetic feet soles to predict ulcerations: a case study. In: Proceedings of SPIE, Advanced Biomedical and Clinical Diagnostic Systems XI, vol. 8572, p. 85720N-1 (2013)
14. Lavery, L.A., Higgins, K.R., Lanctot, D.R., Constantinides, G.P., Zamorano, R.G., Athanasiou, K.A., Armstrong, D.G., Agrawal, C.M.: Preventing diabetic foot ulcer recurrence in high-risk patients: use of temperature monitoring as a self-assessment tool. Diabetes Care **30**:14–20 (2007)
15. Stess, R.M., Sisney, P.C., Moss, K.M.: Use of liquid crystal thermography in the evaluation of the diabetic foot. Diabetes Care **9**(3), 267–272 (1986)
16. Boyko, E.J., Ahroni, J.H., Stensel, V., Forsberg, R.C., Davignon, D.R., Smith, D.G.: A prospective study of risk factors for diabetic foot ulcer. The Seattle diabetic foot study. Diabetes Care **22**, 1036–1042 (1999)
17. Sun, P.C., Lin, H.D., Jao, S.H., Ku, Y.C., Chan, R.C., Cheng, C.K.: Relationship of skin temperature to sympathetic dysfunction in diabetic at-risk feet. Diabetes Res. Clin. Pract. **73**(1):41–46 (2006)
18. Armstrong, D.G., Holtz-Neiderer, K., Wendel, C., Mohler, M.J., Kimbriel, H.R., Lavery, L. A.: Skin temperature monitoring reduces the risk for diabetic foot ulceration in high-risk patients. Am. J. Med. **120**(12):1042–1046 (2007)
19. Colantonio, S., Pieri, G., Salvetti, O., Benvenuti, M., Barone, S., Carassale, L.: A method to integrate thermographic data and 3D shapes for Diabetic Foot Disease. In: Proceedings of 8th International Conference on Quantitative Infrared Thermography (QIRT), Padova, Italy (2006)
20. Uematsu, S.: Symmetry of skin temperature comparing one side of the body to the other. Int. J. Thermol. **1**(1), 4–7 (1985)
21. Golestani, N., Etehadtavakol, M., Ng, E.Y.K.: Level set method for segmentation of infrared breast thermograms. Exp. Clin. Sci. **13**, 241–251 (2014)
22. Qi, H., Kuruganti, P.T., Snyder, W.E.: Detecting breast cancer from thermal infrared images by asymmetry analysis. In: Biomedical Engineering Handbook, pp. 1–14. CRC (2006)
23. Tan, T.Z., Quek, C., Ng, G.S., Ng, E.Y.K.: A novel cognitive interpretation of breast cancer thermography with complementary learning fuzzy neural memory structure. Expert Syst. Appl. Int. J. **33**(3), 652–666 (2007)
24. Frize, M., Herry, C.H., Roberge, R.: Processing of thermal images to detect breast cancer: comparison with previous work. In: Proceedings of the Second Joint 24th Annual Conference and the Annual Fall Meeting of the Biomedical Engineering Society, IEEE EMBS/BMES Conference, vol. 2, pp. 1159–1160 (2002)
25. Ng, E.Y.K.: Is thermal scanner losing its bite in mass screening of fever due to SARS? Med. Phys. **32**(1):93–97 (2005)
26. Schaefer, G., Zavisek, M., Nakashima, T.: Thermography based breast cancer analysis using statistical features and fuzzy classification. Pattern Recogn. **42**(6), 1133–1137 (2009)

27. Etehadtavakol, M., Ng, E.Y.K., Lucas, C., Sadri, S., Gheissari, N.: Estimating the mutual information between bilateral breast in thermograms using nonparametric windows. J. Med. Syst. **35**(5):959–967 (2011)
28. Etehadtavakol, M., Ng, E.Y.K., Chandran, V., Rabbani, H.: Separable and non-separable discrete wavelet transform based texture features and image classification of breast thermograms. Infrared Phys. Technol. **61**, 274–286 (2013)
29. Armstrong, D.G., Lavery, L.A.: Monitoring neuropathic ulcer healing with infrared dermal thermometry. J. Foot Ankle Surg. **35**(4), 335–338 (1996)
30. Armstrong, D.G., Lavery, L.A., Wunderlich, R.P., Boulton, A.J.: Skin temperatures as a one-time screening tool do not predict future diabetic foot complications. J. Am. Podiatr. Med. Assoc. **93**(6):443–447 (2003)
31. Armstrong, D.G., Lipsky, B.A., Polis, A.B., Abramson, M.A.: Does dermal thermometry predict clinical outcome in diabetic foot infection? Analysis of data from the SIDESTEP* trial. Int. Wound J. **3**(4), 302–307 (2006)
32. Liu, C., van Netten, J.J., van Baal, J.G., Bus, S.A., van der Heijden, F.: Automatic detection of diabetic foot complications with infrared thermography by asymmetric analysis. J. Biomed. Optics **20**(2), 026003 (2015)
33. van Netten, J.J., van Baal, J.G., Liu, C., van der Heijden, F., Bus, S.A.: Infrared thermal imaging for automated detection of diabetic foot complications. J Diabetes Sci. Technol. **7**(5), 1122–1129 (2013)
34. Peregrina-Barreto, H., Morales-Hernandez, L.A., Rangel-Magdaleno, J.J., Avina-Cervantes, J.G., Ramirez-Cortes, J.M., Morales-Caporal, R.: Quantitative estimation of temperature variations in plantar angiosomes: a study case for diabetic foot. Comput. Math. Methods Med. 2014:10 pp (2014) (Article ID 585306)
35. Rathod, M.D., Manza, R., Rathod, D.: Early detection of peripheral neuropathy using thermography: a review. In: IJCA Proceedings on National Conference on Digital Image and Signal Processing; DISP, vol. 1, pp. 11–14 (2015)
36. Mendes, R., Sousa, N., Almeida, A., Vilaça-Alves, J., Reis, V.M., Neves, E.B.: Thermography: a technique for assessing the risk of developing diabetic foot disorders. Postgrad. Med. J. **91**(1079), 538 (2015)
37. Kaabouch, N., Chen, Y., Hu, W.C., Anderson, J.J., Ames, F., Paulson, R.: Early detection of foot ulcers through asymmetry analysis. In: Proceedings of SPIE 7262, Medical Imaging: Biomedical Applications in Molecular, Structural, and Functional Imaging, vol. 7262 (2009). doi:10.1117/12.811676

An Overview of Medical Infrared Imaging in Breast Abnormalities Detection

Mahnaz Etehadtavakol and Eddie Y.K. Ng

Abstract Thermography or infrared (IR) imaging is based on a detailed investigation of skin and tissue temperatures. Its examination scheme allocates specialists to determine the regions of irregular action of carrying blood through the tissues such as angiogenesis in the body. Infrared imaging is totally safe and uses no radiation that engages the technology of the infrared camera and advanced softwares. Nowadays this technique is getting popular on medical fields because of accessible ultra-sensitive infrared cameras, advanced image processing techniques, approved protocols for interpretation of thermograms, and matured sensing devices. In more than 30 years of investigation, 800 peer-reviewed researches including more than 300,000 women contributors have exhibited thermography's potential for diagnosing breast cancer in very early stages. Identifying relationships between neo-angiogenesis, chemical mediators, and the neoplastic developments are the aim of current studies to investigate thermal features of breast anatomy.

Keywords Infrared imaging · Breast · Cancer

1 Introduction

The writing of Hippocrates at around 480 BC is the first recorded application of thermo-biological diagnosis [1]. He applied mud slurry all over a patient and monitored area that would dry first and treated the hidden organ pathology is demonstrated. By pursuing research and clinical study since then, scientists have defined that particular hotness of some degrees related to parts of an individual were

M. Etehadtavakol (✉) · E.Y.K. Ng
Isfahan University of Medical Sciences, Isfahan, Iran
e-mail: mahetehad@gmail.com

E.Y.K. Ng
e-mail: mykng@ntu.edu.sg

E.Y.K. Ng
College of Engineering, Nanyang Technological University, Singapore, Singapore

E.Y.K. Ng and M. Etehadtavakol (eds.), *Application of Infrared to Biomedical Sciences*, Series in BioEngineering,
DOI 10.1007/978-981-10-3147-2_4

surely indicative of regular and irregular physiologic developments. Lawson [2] diagnosed that the surface temperature over a cancerous breast tumor was greater than that of healthy cells in 1956. Since the 1970s, IR technology has been applied and as early as 1975 medical books recorded thermography as one of the techniques to identify breast cancer [3]. In 1979, Maurice Bales, the originator of the first digital infrared camera at the University of California, Berkeley completed the details, and then advanced the apparatus for the thermal image processor [4, 5]. It was applied to diagnose musculoskeletal complications, for instance stress fractures. The quality of the breast thermography process is established with the quality of the imaging machinery as is true with essentially all other imaging modalities, Thomas Tierney, conveyed one statement in 1972, that exhibited, "The medical specialists expressed that thermography, at this time, is in advance of the exploratory state as a diagnostic method in the coming fields: (1) Female breast pathology, (2) Extracranial vessel disorder, (3) Peripheral vascular disorder, (4) Musculoskeletal damage".

Thermography as an adjuvant prognostic imaging technique for identifying breast cancer was confirmed and published by the Food and Drug Administration (FDA). It is documented in the Federal Register; 147(20), pp. 4419–4420, 1982 [6, 7]. Nowadays many clinics and health services all over the world have used thermography for different prognostic objectives [8].

This paper is put in order as follows: metabolism of tumors and tumor growth are explained in Sect. 2. Principals of IR imaging are presented in Sect. 3. Relationship between pathology and IR imaging and the performance of IR imaging in diagnosis of cancer are discussed in Sects. 4 and 5. Section 6 describes the limitations and advantages of IR imaging. Finally, Sect. 7 presents the concluding remarks.

2 Metabolism of Tumors and Tumor Growth

Action of carrying blood through the pre-cancerous tissues and metabolic activity in the neighborhood of a growing breast tumor is relatively ever greater than in healthy tissue. It is the principle that the digital IR imaging application is based on.

Angiogenesis, the process of prompting capillaries in the body, is a crucial natural mechanism adopted for healing and reproduction. The body disciplines angiogenesis by generating a proper balance of growth and inhibitory factors in normal tissues. Cancerous tumors deliver angiogenic growth factor proteins that prompt blood vessels to expand into the tumor, affording it by oxygen and nutrients. This mechanism generally concludes rise in sectional outer heat of the breast. Tumor expanding fluctuated greatly between individuals. For example, 5% of tumors acquire less than 1.2 months to expand in diameter from 10 to 20 mm, while another 5% acquire more than 6.3 years. The average time required for expansion of a tumor in diameter from 10 to 20 mm was anticipated about 1.7 years, rising with lifetime [9]. Angiogenesis can be absolutely invisible to the

human eye and X-rays. However it can be seen with IR eyes. IR imaging is the key to the problem of detecting angiogenesis in the earliest stage particularly for dense breast tissue which offers a harmless and painless opportunity to recognize angiogenesis as a warning sign. Breast thermography has potential to identify the foremost marks that cancer cells may be developing about 7–10 years sooner than other methods.

3 Principals of IR Imaging

3.1 Physics

IR waves are electromagnetic radiation of a special wavelength or color that is first discovered by William Herschel around 1800. Their range is from 700 nm (nanometers) to 1 mm. They are just beyond what human eyes can distinguish on the red side of the rainbow. We constantly are impacted by IR. Warm items, like human body, generate great extent of IR. Moreover, half of the energy generated by the sun is infrared, so we are being bombardment by it every moment. Temperature measurements governed by thermal cameras calculate on the electromagnetic radiation, or energy, constantly radiated from subjects and just as to their outer temperature: thermal cameras capture the IR emission radiated by subjects. The energy movements also relay on the surface emissivity and the wavelength range of the radiations emitted. Shortly, some laws restricting this event are presented. As stated in Kirchhoff's law, a black body or an ideal emitter is a body that can absorb radiations of any wavelength and re-emit them [10]. If Plank's law (spectral radiant existence) employs to this, then the intensity of the emitted radiation is described by Eq. 1.

$$W_\lambda = \frac{c_1}{\lambda^5\left\{\exp\left(\frac{c_2}{\lambda T}\right) - 1\right\}} \left(\mathrm{W\ sr^{-1}\ m^{-3}}\right), \tag{1}$$

where W_λ is the spectral radiant emittance within the spectral range at wavelength (λ) of 1 μm. c_1 and c_2 are the first and second radiation parameters correspondingly. T is the absolute temperature in Kelvin.

For the whole field of wavelengths of the electromagnetic spectrum, the Stefan–Boltzmann law can be attained by integrating this term. The total radiating energy of the black body is illustrated by this law.

$$W_\mathrm{b} = \sigma T^4, \tag{2}$$

where σ is 5.6704×10^{-8} $\mathrm{Wm^{-2}\ K^{-4}}$ (the Stefan–Boltzmann constant). Although in reality no black bodies exist, but only gray bodies exist that more or less extremely vary from the ideal behavior. By suggesting emissivity, ε, in the

Stefan–Boltzmann formula, checking the difference between the real body and the ideal behavior can be considered. Hence, the law becomes the following

$$W = \sigma \varepsilon T^4 \tag{3}$$

At the greatest, emissivity can reach 1 since it is the ratio of the radiating power of an object to the produced energy by a black body at the identical temperature and wavelength. It has a great importance to have an object's emissivity for the sake of obtaining the surface temperature of it.

3.2 Equipment Considerations

In the 2–20 μm wavelength spectrums, generally human body emits IR, with an average peak at 9–10 μm [11]. Contemporary IR observation systems utilize ultra-sensitive IR cameras and advanced computers to identify, analyze, and provide high-resolution diagnostic images.

The importance of IR cameras is depended on two aspects: resolution and sensitivity. Resolution is the detail that a camera is able to acquire and sensitivity determines how precise the camera is capable to discern levels of infrared radiation (heat) and is measured in degrees C per level. It is preferable to choose a camera with the highest resolution and sensitivity. Advanced IR cameras achieve a resolution of 480 optical lines while some cameras gain 600 optical lines. The higher is advantageous. These cameras have sensitivities at least 0.05 °C per level while some is obtaining 0.025 °C per level. The less is preferable. A resolution of 240 optical lines and a sensitivity of 0.05 °C per level is the minimum requirement for approved breast thermography. For other areas of the body imaging, cameras with requirements lower than these numbers may be applied, however, for breast thermography are not satisfactory to catch the detailed temperature variations.

First-generation IR camera systems experienced some complications, for example, inappropriate detector resolution, thermal accumulation, analog interface, and calibration that have been approximately cleared up for two decades.

3.3 Laboratory Considerations

Imaging is required to be conducted in a controlled environment considering thermography as a test of physiology. Non-clinical unrestricted room environment generate thermal artifacts that are not desirable [12]. It is crucial to provide a thermal image free from error.

4 Relationship Between Pathology and IR Imaging

Lawson conducted an early quantitative experiment which demonstrated that the rise in local superficial temperature inherent in breast cancer was associated to convection of the venous [13]. These IR data had correlation with both elevated blood flow and elevated metabolism. Since thermography of the breast may have correlation with a type of pathologic predictive aspects for example size of tumor, grade of tumor, status of lymph node and factors of tumor development then it may have an explanatory predictive significance. One prospect of the pathologic basis for these IR information can be elevated vascular flow as a result of vascular proliferation accordingly tumor related angiogenesis.

Head et al. recorded that upgraded thermograms from second generation IR cameras have potential to perform more objective and quantitative analysis in 1993 [14]. They demonstrated that the IR image interpretation greatly affiliated to the growth-rate related prognostic indicators.

In 1994 Anbar observed, using a sophisticated biochemical and immunological cascade, that small tumors had potential to generate remarkable IR changes as a result of upgraded circulation over a considerable region of the breast exterior by local tumor prompted nitric oxide vasodilatation [15]. Nitric oxide is a molecule with effective vasodilation effects that is synthesized by nitric oxide synthase (NOS). It is discovered in different forms: in form of nitric oxide synthase (c-NOS) in endothelial, and as an active form of nitric oxide synthase (i-NOS) in macrophages [16]. Using tissue immunohistochemistry, NOS has been observed in breast carcinoma [17]. It is related to an advanced tumor development. There is possibility that IR data may connect tumor NOS content. Forthcoming investigations can be done in order to investigate these possible associations.

Guidi and Schnitt called the theory of angiogenesis, as an essential part of early breast cancer, in 1996. They indicated that it is an early phenomenon in the progress of breast cancer and could be developed earlier than tumor tissues gain power to occupy the neighboring tissue and even earlier than when morphologic information of an in situ carcinoma observed [18]. In 1996, Gamagami worked angiogenesis by thermography and recorded in Atlas of Mammography (his greatly analyzed book). He recognized that 86% of non-palpable breast cancers have indication of hypervascularity and hyperthermia and for 15% of them, thermography is able to detect cancers that were not recognizable on mammography [19].

5 The Role of IR Imaging in the Detection of Cancer

Great numbers of studies have been accomplished on the utilization of thermography in breast cancer detection since the late 1950s. In more than 30 years of investigation, 800 peer-reviewed researches including more than 300,000 female contributors have exhibited potential of IR imaging for breast cancer early

detection. The prominent numbers of contributors are ranging from 10,000 to 85,000 in these particular studies. Concerning the unique capability of this technique as a risk indicator, in some of these studies, cases have been known for up to 12 years.

For more than 15 years, IR breast screening has obtained sensitivity and specificity of 90% in average with disciplinarian approved established protocols of interpretation.

A persistent abnormal thermogram is 10-fold more considerable than a first-order ancestry of breast cancer and imports a risk 22-fold greater than its normal correspondent as a future indicator for breast cancer. Investigations have shown that an abnormal thermogram is apparently the single most important risk indicator for the existence of incoming breast cancer development [20]. Gershon-Cohen in 1965, found the potential of IR imaging to medical arena [21]. Four thousands cases examined by him and a sensitivity rate of 94% and a false-positive rate of 6% were obtained. In 1968 in California, this data was reported in "A Cancer Journal for Physicians". In another research, Hoffman [22] detected 23 carcinomas in 1924 cases and obtained 8.4 and 7.4% of false-negative and false-positive rates respectively. Also, Stark and Way [23] studied on 4621 cases and diagnosed 24 cancers with a sensitivity of 98.3% and specificity of 93.5%. Amalric et al. studied thermography with 25,000 cases, attained 1878 medically recognized breast cancers. For this study, false-negative rate of 9% and false-positive rate of 9% were discovered [24]. In a study, in Hobbins [25, 26] reported 12 and 14% of false-negative and false-positive rates correspondingly for 37,506 subjects. For a period of more than 10 years, Spitalier et al. [27] tested 61,000 subjects applying IR imaging. They recorded the false-negative and false-positive rates of 11%. In addition, they also may detect 91% of Grade T_0 or tumors lesser than 1 cm of non-palpable tumors. They declared that IR imaging alone in 60% of the cancer subjects had the ability to detect the first signs of tumor growth. Isard et al. [28] discovered the exceptional thermal and vascular strength of the IR image from year to year in a normal case and the significance of identifying any considerable variation with 10,000 IR image performed subsequently with mammography for a duration of three years. They identified 4393 irregular subjects, although a mammographic examination would have been narrowed to only 1028 irregular subjects. Hence a cancer detection rate of 24.1 per 1000 was obtained by utilizing both modalities in comparison with the seven per 1000 expectedly by mammography alone. He suggested that since thermography is a non-invasive examination, it could be utilized for females with unhealthy breasts who should be checked more often. In addition, they observed thermography does not identify cancer, but only demonstrates the presence of an abnormality. Two small sets of 150 and 515 cases are studied by Moskowitz et al. [29] and Threatt et al. [30] respectively, to explore the sensitivity and accuracy of thermography. Both studies did not generate any invaluable discoveries; however the inadequacy of approved screening approaches and protocols could lead to those results. Haberman et al. [31] used thermography as well as a physical test, over a three-year term, in a singular

project involving 39,802 cases. For thermography they obtained 85% sensitivity and 70% specificity.

In 1988, Useki [32] investigated importance of IR imaging discoveries in breast cancer detection. He observed sensitivity of 88% for IR imaging to identify breast cancers. Gautherie et al. [33, 34] showed sensitivity of 90% and specificity of 88% using thermography with 85,000 subjects imaged. Jones [35] utilized approximately 70,000 cases, and obtained false-negative of 13% and false-positive of 15% for thermography in a large-scale multicenter study. To determine mammographically questionable cases, Parisky et al. [36] accomplished a project with IR imaging. They investigated 875 cases with 187 malignant and 688 benign results. In a project, a contrasting between three approaches for breast cancer detection including; physical examination, mammography, and thermography is accomplished by Nyirjesy and Ayme [37]. Three groups are involved in their project; 4716 individuals with carcinoma, 3305 individuals with benign breast disease, and 8757 healthy individuals. They additionally examined their work with other well-known works in conjunction with the National Cancer Institute (NCI)-sponsored Breast Cancer Detection and Demonstration Projects (BCDDPs). For example, they found that to identify all kind of tumors, physical examination obtained sensitivity of 75% in average and cancers lesser than 2 cm in size obtained 50%. Considering other studies with sensitivity between 35 and 66% that looks satisfactory. Mammography was recorded to obtain sensitivity and specificity of 80 and 73% respectively. IR imaging achieved sensitivity of 88% for tumors lesser than 1 cm as well as specificity of 85%. An abnormal IR image obtained a predictive value of 94%. They found that no technique alone is accurate enough to be utilized to access imaging of breast carcinoma and also cases with breast diseases. Hence the best outcomes is applying a multimodal approach. Thomassin and Giraud [38] conducted a project with 4000 subjects with breast cancer. He found 130 carcinoma subjects with tumors vary from 3 to 5 mm in diameters. Mammography as well as thermography applied alone with 130 cancer cases that 10% of individuals by mammography alone and 50% by thermography alone were detected, and 40% by both techniques. From 1967 to 1998, breast thermography has demonstrated sensitivity and specificity of 90% in average in the 15 large-scale projects. In the past decade with the state of the art thermography technology, some studies are indicating even greater sensitivity and specificity rates.

6 Restrictions and Conveniences of IR Imaging

IR imaging is not a recent technique in medicine. The adaptability, safety, and inexpensive of this technique cause it an adjuvant mechanism in medical imaging and prognostic [39–73]. It can be utilized without any restrictions since this safe method accumulates without any harmful radiation. In vivo investigations on cells without extraction of sample is achievable by this method, consequently, it is a passive examination [66].

In addition, the derived real time data can be applied as a quick observation for the patient. Despite the fact that the ability of this method has been positively identified and confirmed since 1959, however some reasons made some early studies to be eliminated. Reasons were as follows: (1) absolutely inexpert technicians took the images, (2) Inexperienced radiologists who obtained no knowledge interpreting IR images were worked, (3) Appropriate laboratory environmental controls were thoroughly neglected, (4) Standard reading protocol for IR imaging had not yet been approved, (5) Behind technology of the IR camera was insufficient, (6) Coverage/complication of medical insurance and implication upon any early suspected or indication of diagnosis.

Nevertheless, IR imaging becomes even more beneficial when its restrictions are acknowledged. It is also essential to consider that IR can generate physiological data but is not able to represent aetiologies and local anatomy. The subject irregularities in addition to the complex aspects of thermoregulation restrict the interpretation. Depletion of specificity feels necessity for incorporating these examinations with other more structural techniques (X-ray, computed tomography), alternately applying it as a complementary modality [74, 75]. Computer simulation applying bioheat transfer theory besides medical thermography as a complementary technique for breast cancer early detection has also been suggested in work by [76–78].

Two sets of images using typical thermography, mammography and ultrasound are shown in Figs. 1 and 2 respectively.

The considerable demand is to incorporate the anatomical and physiological data extracted from thermal pattern of the skin surface.

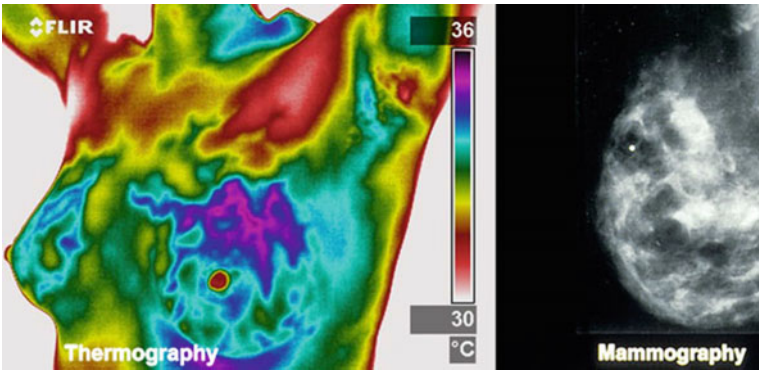

Fig. 1 Breast cancer detection using thermography and mammography (http://medscans.co.uk/thermography-and-mammography)

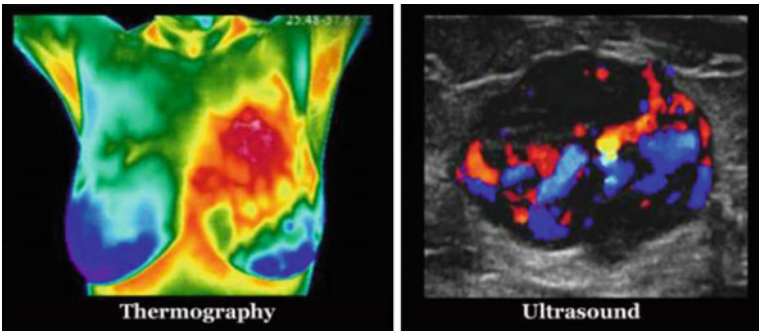

Fig. 2 Breast cancer detection using thermography and ultrasound (http://www.universalmedicalimaging.com/)

7 Conclusion

IR imaging in medical fields is not a recent tool, however early projects with old and inadequate methods have resulted arguable findings. Recently with new generation of ultra-sensitive IR cameras, knowledge about thermoregulation, powerful image processing algorithms, standardized reading protocol and controlling laboratory and certified trained thermologists, thermography opens its place in medical society especially in developed country. For example, today more than 170 certified breast thermography centers are only in the United States [79]. The objective of this modality is not to be an alternate for clinical measurement however to upgrade it. Experimental data of interaction between pathology and IR imaging is fundamental to further anticipate the worth of IR imaging of breasts. Depended on the convenience of breast thermography as a safe, non-invasive, and inexpensive first-line detection technique, it should be utilized as an adjunctive technique in breast examinations.

Unfortunately, in spite of the value of breast thermography, many specialists still are uncertain to recognize thermography as an appropriate technique in clinical practice. This viewpoint may be concluded since the physical and biological features of thermography are not known to most specialists whereas the other approaches investigating cancer introduce exactly subjects of medical teaching. Comparatively, radiography and ultrasonography indicate anatomy. However, thermography is relied on thermodynamics and bioheat transfer that are unknown to many specialists.

References

1. Adams, F.: The Genuine Works of Hippocrates. Williams and Wilkins, Baltimore (1939)
2. Lawson, R.: Implications of surface temperatures in the diagnosis of breast cancer. Can. Med. Assoc. J. **75**, 309–310 (1956)

3. http://www.worldcat.org/title/clinical-thermography/oclc/1324536. Last access 16 Nov 2015
4. http://www.mypinkimage.com. Last access 16 Nov 2015
5. http://womensacademyofbreastthermography.com/html/breast-health.html. Last access 16 Nov 2015
6. http://www.bk2health.com/docs/UtilizationofClinicalThermology.pdf. Last access 16 Nov 2015
7. www.miamiholisticcenter.com/services/BreastThermography.htm. Last access 16 Nov 2015
8. .http://www.iact-org.org/professionals/new-therm-tech.html. Last access 16 Nov 2015
9. Piana, A., Sepper, A.: Contemporary evaluation of thermal breast screening. Pan. Am. J. Med. Thermol. **1**(2), 93–100 (2015)
10. Usamentiaga, R., Venegas, P., Guerediaga, J., Laura Vega, L., Molleda, J., BulnesInfrared, F.G.: Thermography for temperature measurement and non-destructive testing. Sensors **14**:12305–12348 (2014)
11. Maldague, X.P.V., Jones, T.S., Kaplan, H., Marinetti, S., Prystay, M.: Fundamentals of infrared and thermal testing. In: Nondestructive Handbook, Infrared and Thermal Testing, p. 718. ASNT Press, Columbus (2001)
12. Archer, F., Gros, C.: Classification Thermographique des Cancers Mammaries. Bull. Cancer **58**, 351–362 (1971)
13. Lawson, R.N., Chughtai, M.S.: Breast cancer and body temperatures. Can. Med. Assoc. J. **88**, 68–70 (1963)
14. Head, J., Elliott, R.L.: Breast thermography. Cancer **79**, 186 (1993)
15. Anbar, M.: Breast cancer. In: Quantitative Dynamic Telethermometry in Medical Diagnosis and Management, pp. 84–94. CRC Press, Ann Arbor (1994)
16. Rodenberg, D.A., Chaet, M.S., Bass, R.C., Arkovitz, M.D., Garcia, B.F.: Nitric oxide: an overview. Am. J. Surg. **170**, 292–303 (1995)
17. Thomsen, L.L., Miles, D.W., Happerfield, L., Bobrow, L.G., Knowles, R.G., Mancada, S.: Nitric oxide synthase activity in human breast cancer. Br. J. Cancer **72**(1), 41–44 (1995)
18. Guidi, A.J., Schnitt, S.J.: Angiogenesis in pre-invasive lesions of the breast. Breast J. **2**, 364–369 (1996)
19. Gamagami, P.: Indirect signs of breast cancer: angiogenesis study. In: Atlas of Mammography, pp. 231–226. Blackwell Science, Cambridge (1996)
20. Ng, E.Y.K.: A review of thermography as promising non-invasive detection modality for breast tumor. Int. J. Thermal Sci. **48**, 849–855 (2009)
21. Gershon-Cohen, J., Haberman, J., Brueschke, E.E.: Medical thermography: a summary of current status. Radiol. Clin. North Am. **3**:403–431 (1965)
22. Hoffman, R.: Thermography in the detection of breast malignancy. Am. J. Obstet. Gynecol. **98**, 681–686 (1967)
23. Stark, A., Way, S.: The screening of well women for the early detection of breast cancer using clinical examination with thermography and mammography. Cancer **33**, 1671 (1974)
24. Amalric, R., Giraud, D., Altschule, C., Spitalier, J.M.: Value and interest of dynamic telethermography in detection of breast cancer. Acta. Thermogr. **1**, 89–96 (1976)
25. Hobbins, W.B.: Mass breast cancer screening. In: Proceedings of 3rd International Symposium, Detection and Prevention of Breast Cancer, New York City, NY, pp. 637 (1976)
26. Hobbins, W.B.: Abnormal thermogram significance in breast cancer. Interamer. J. Rad. **12**, 337 (1987)
27. Spitalier, H., Giraud, D., Altschuler, C., Amalric, F., Spitalier, J.M., Brandone, H., Ayme, Y., Gardiol, A.: Does infrared thermography truly have a role in present day breast cancer management? In: Biomedical Thermology (Proceedings of an International Symposium), Alan R. Liss, Inc., New York City, NY, pp. 269–278 (1982)
28. Isard, H.J., Becker, W., Shilo, R., Ostrum, B.J.: Breast thermography after four years and 10,000 studies. Am. J. Roentgenol. **115**, 811 (1972)
29. Moskowitz, M., Milbrath, J., Gartside, P., Zermeno, A., Mandel, D.: Lack of efficacy of thermography as a screening tool for minimal and stage I breast cancer. N. Engl. J. Med. **295**, 249–252 (1976)

30. Threatt, B., Norbeck, J.M., Ullman, N.S., Kummer, R., Roselle, P.F.: Thermography and breast cancer: an analysis of a blind reading. Ann. N. Y. Acad. Sci. **335**, 501–527 (1980)
31. Haberman, J., Francis, J., Love, T.: Screening a rural population for breast cancer using thermography and physical examination techniques. Ann. N. Y. Acad. Sci. **335**, 492–500 (1980)
32. Useki, H.: Evaluation of the thermographic diagnosis of breast disease: relation of thermographic findings and pathologic findings of cancer growth. Nippon. Gan. Chiryo. Gakkai. Shi. **23**, 2687–2695 (1988)
33. Gautherie, M.: Thermobiological assessment of benign and malignant breast diseases. Am. J. Obstet. Gynecol. **147**, 861–869 (1983)
34. Louis, K., Walter, J., Gautherie, M.: Long term assessment of breast cancer risk by thermal imaging. In: Biomedical Thermology (Proceedings of an International Symposium), Alan R. Lis, Inc., NY, pp. 279–301 (1982)
35. Jones, B.F.: A reappraisal of the use of infrared thermal image analysis in medicine. IEEE Trans. Med. Imaging **17**, 1019–1027 (1998)
36. Parisky, Y.R., Sardi, A., Hamm, R., Hughes, K., Esserman, L., Rust, S., Callahan, K.: Efficacy of computerized infrared imaging analysis to evaluate mammographically suspicious lesions. Am. J. Roentgenol. **180**, 263–269 (2003)
37. Nyirjesy, I., Ayme, T.: Clinical evaluation, Mammography, and thermography in the diagnosis of breast carcinoma. Thermology **1**, 170–173 (1986)
38. Thomassin, L., Giraud, D.: Detection of subclinical breast cancers by infrared thermograph. In: Recent Advances in Medical Thermology (Proceedings of the Third International Congress of Thermology), New York City, NY, Plenum Pres, pp. 575–579 (1984)
39. Etehadtavakol, M., Sadri, S., Ng, E.Y.K.: Application of K- and fuzzy C-means for color segmentation of thermal infrared breast images. J. Med. Syst. **34**, 35–42 (2010)
40. Jiang, L.J., Ng, E.Y.K., Yeo, A.C.B., Wu, S., Pan, F., Yau, W.Y., Chen, J.H., Yang, Y.: A perspective on medical infrared imaging. J. Med. Eng. Tech. **29**, 257–267 (2005)
41. Gold, J.E., Cherniack, M., Buchholz, B.: Infrared thermography for examination of skin temperature in the dorsal hand of office workers. Eur. J. Appl. Physiol. **93**, 245–251 (2004)
42. Kakuta, N., Yokoyama, S., Mabuchi, K.: Human thermal models for evaluating infrared images. Eng. Med. Biol. Mag. IEEE **21**, 65–72 (2002)
43. Mercer, J.B.: Infrared thermal imaging in modern medical research: a technique with extensive possibilities. In: The Kastelli Symposium: Oulu, Finland (2000)
44. Ammer, K.: The Glamorgan protocol for recording and evaluation of thermal images of the human body. Thermol. Int. **18**, 125–129 (2008)
45. Buchlin, J.M.: Convective heat transfer and infrared thermography. J. Appl. Fluid Mech. **3**, 55–62 (2010)
46. Steketee, J.: Spectral emissivity of skin and pericardium. Phys. Med. Biol. **18**, 686–694 (1973)
47. Planck, M.: On the law of distribution of energy in the normal spectrum. Ann. Phys. **4**, 553 (1901)
48. Maldague, X.P.V., Jones, T.S., Kaplan, H., Marinetti, S., Prystay, M.: Fundamentals of infrared and thermal testing. In: Nondestructive Handbook, Infrared and Thermal Testing, p. 718. ASNT Press, Columbus (2001)
49. Plassmann, P., Murawski, P.: CTHERM for standardized thermography. In: Proceedings of Abstracts, the 9th Congress of Thermology Poland, Krakow, Poland, pp. 27–29 (2003)
50. Plassmann, P., Ring, E.J.F., Jones, C.D.: Quality assurance of thermal imaging systems in medicine. Thermol. Int. **16**:10–15 (2006)
51. Selfe, J., Hardaker, N., Thewlis, D., Karki, A.: An accurate and reliable method of thermal data analysis in thermal imaging of the anterior knee for use in cryotherapy research. Arch. Phys. Med. Rehabil. **87**, 1630–1635 (2006)
52. Kattapong, K.R., Fogg, L.F., Eastmann, C.I.: Effect of sex, menstrual cycle phase and oral contraceptive use on circadian temperature rhythms. Chronobiol. Int. **12**, 257–266 (1995)

53. Zaproudina, N., Varmavuo, V., Airaksinen, O., Närhi, M.: Reproducibility of infrared thermography measurements in healthy individuals. Physiol. Meas. **29**, 515–524 (2008)
54. Hildebrandt, C., Raschner, C.: An intra-examiner reliability study of knee temperature patterns with medical infrared thermal imaging. Therm. Int. **19**, 73–77 (2009)
55. Owens, E.F., Hart, J.F., Donofrio, J.J., Haralambous, J., Mierzejewski, E.: Paraspinal skin temperature patterns: an inter-examiner and intra-examiner reliability study. J. Manipulative Physiol. Ther. **27**, 155–159 (2004)
56. Vardasca, R.: Symmetry of temperature distribution in the upper and lower extremities. Thermol. Int. **18**, 154–155 (2008)
57. Selfe, J., Whitaker, J., Hardaker, N.: A narrative literature review identifying the minimum clinically important difference for skin temperature asymmetry at the knee. Thermol. Int. **18**, 41–44 (2008)
58. Koehle, M.S., Lloyd-Smith, R., Taunton, J.E.: Alpine ski injuries and their prevention. Sports Med. **32**, 785–793 (2002)
59. Bergstrom, K.: Activity related knee injuries and pain in athletic adolescents, knee surgery. Sport Traumat. Arthros. **9**, 146–150 (2001)
60. Ammer, K.: Thermal evaluation of tennis elbow. In: Ammer, K., Ring, E.J.F. (eds.) The Thermal Image in Medicine and Biology, pp. 214–219. Uhlen Verlag Wien, Vienna (1995)
61. De Loes, M., Dahlstedt, L.J., Thomee, R.: A 7 year on risks and costs of knee injuries in male and female youth participants in 12 sports. Scand. J. Med. Sci. Sports **10**, 90–97 (2000)
62. Randall, W.V., Steadman, J.R., Mair, S.D., Briggs, K.K., Sterett, W.I.: Anterior cruciate ligament injury incidence among male and female professional alpine skiers. Am. J. Sports Med. **27**, 792–795 (1999)
63. Fisher, G., Hoyt, G.L., III, Lamberth, J.G., Joe, L.A., Chromiak, J.A., Chromiak, A.B., Willard, S.T., Ryan, P.L.: Determination of the typical digital infrared thermographic profile of the knee of distance runners. Med. Sci. Sports Exer. **39**:318 (2007)
64. Ring, E.F.J., Ammer, K.: Thermal imaging in sports medicine. Sport Med. Today **1**, 108–109 (1998)
65. Xiaojiang, X., Werner, J.: A dynamic model of the human clothing environment system. Appl. Human Sci. **16**, 61–75 (1997)
66. Elliott, R.L., Head, J.F.: Medical infrared imaging in the twenty first century. Thermol. Int. **9**, 111 (1999)
67. Diakides, N.A., Diakides, M., Lupo, J.C., Paul, J.L., Balcerak, R.: Medical infrared imaging. In: Diakides, N.A., Bronzino, J.D. (eds.) Advances in Medical Infrared Imaging, pp. 1–13. CRC Press, Boca Raton (2008)
68. Ring, E.F.J., Ammer, K.: The technique of infrared imaging in medicine. Thermol. Int. **10**, 7–14 (2000)
69. Thomas, R.A.: Reliability of medical thermography. In: Proceedings of Thermal Solutions Conference, Sarasota, FL, USA, pp. 23–26 (2006)
70. Mayr, H.: Korrelation durchschnittlicher und maximaler; Temperatur am Kniegelenk bei Auswertung Unterschiedlicher Messareale. Thermol. Int. **5**, 89–91 (1995)
71. Akata, T., Kanna, T., Yoshino, J., Higashi, M., Fukui, K., Takahashi, S.: Reliability of fingertip skin surface temperature and its related thermal measures as indices of peripheral perfusion in the clinical setting of the operating theatre. Anaest. Intensive Care **32**, 519–529 (2004)
72. Etehadtavakol, M., Ng, E.Y.K.: Breast thermography as a potential non-contact method in the early detection of cancer: a review. J. Mech. Med. Biol. **13**(2) (2013)
73. Amalu, W.C.: A review of breast thermography. Int. Acad. Clin. Thermol. http://clinicalthermography.co.nz/A_review_of_Breast_Thermography.php (2003)
74. Ng, E.Y.K., Rajendra Acharya, U.: A review of remote-sensing infrared thermography for indoor mass blind fever screening in containing an epidemic. IEEE Eng. Med. Biol. **28**(1): 76–83 (2009)
75. Acharya, U.R., Ng, E.Y.K., Tan, J.-H., et al.: Thermography based breast cancer detection using texture features and support vector Machin. J. Med. Syst. **36**(3):1503–1510 (2012)

76. Ng, E.Y.K., Sudharsan, N.M.: Numerical computation as a tool to aid thermographic interpretation. J. Med. Eng. Technol. **25**(2), 53–60 (2001)
77. Ng, E.Y.K., Sudharsan, N.M.: An improved three-dimensional direct numerical modelling and thermal analysis of a female breast with tumour. Proc. Inst. Mech. Eng. Part H J. Eng. Med. **215**(H1):25–37 (2001)
78. Ng, E.Y.K., Sudharsan, N.M.: Computer simulation in conjunction with medical thermography as an adjunct tool for early detection of breast cancer. BMC Cancer **4**(17), 1–26 (2004)
79. http://www.iact-org.org/links.html. Last access 16 Nov 2015

Registration of Contralateral Breasts Thermograms by Shape Context Technique

Mahnaz Etehadtavakol and Eddie Y.K. Ng

Abstract Comparison of breast temperature in the contralateral breast is very helpful in breast cancer diagnosis. Asymmetrical thermal diffusion might be a sign of early irregularity. Practically, most of the existent breast thermograms do not possess symmetric borders. Consequently, a suitable registration is required for comparing temperature distribution of two breasts by investigating in contrast the extracted features. In this book chapter, the proposed registration algorithm includes two steps. First, shape context, the technique as introduced by Belongie et al, was used to register two breast borders. Second, a mapping function of boundaries points was obtained and applied for mapping two breasts' interior points. Results are very encouraging. Boundary registration was accomplished perfectly for 28 out of the 32 cases.

Keywords Breast thermal images · Shape contexts · Registration

1 Introduction

One of the major issues in today's women health is breast diseases. It is remarkably important for physicians to identify potentially threatening malignant tumors in breasts. Thermography has a long and highly arguable history for breast cancer early detection. However, nowadays a renewed interest is obtained as a consequence of the accessibility of high-sensitive thermographic cameras that can provide the indicative thermograms showing breast vascular alterations, and also the existence of advanced image processing algorithms. The level of blood circulation influences the skin hotness that impacts the amount of the infrared heat radiate from

M. Etehadtavakol (✉)
Isfahan University of Medical Sciences, Isfahan, Iran
e-mail: mahetehad@gmail.com

E.Y.K. Ng
School of Mechanical and Aerospace Engineering, College of Engineering, Nanyang Technological University, Singapore, Singapore

E.Y.K. Ng and M. Etehadtavakol (eds.), *Application of Infrared to Biomedical Sciences*, Series in BioEngineering,
DOI 10.1007/978-981-10-3147-2_5

the human skin. To provide thermal imaging, a sensitive infrared camera is applied to catch the skin temperature alterations as a result of the blood perfusion changes [1–3]. Signals are sent by cancerous tumor cells to neighborhood normal cells and special genes stimulate to build proteins that accelerate expansion of additional blood vessels [4]. Consequently, malignant tumors are indicated by hot regions in thermograms. Since symmetricity generally shows healthy subjects [5], asymmetrical isotherms of the contralateral breasts perhaps is a powerful indicator of irregularities [6–11]. Practically most of the actual thermograms do not possess symmetric borders. Therefore, in analyzing the temperature diffusion relating to the opposite side of breasts, a proper registration for the two breasts is required. We first introduced the shape context method to register two contralateral breasts borders in this study. Then in order to align the points of inside of the contralateral breasts the obtained transfer function of borders points was applied. This chapter is arranged as follows: in Sect. 2, the shape context technique as well as the thin-plate spline is presented. Section 3 introduces dataset and the algorithm guidelines. Section 4 presents the experimental results and the findings are concluded in Sect. 5.

2 Methods

The mechanism of aligning two or more images of the same scene is image registration. This mechanism involves labeling one image as the reference, and using geometric transformations to the other images in order to align them with the reference. Misalignment of images could be due to a variety of reasons. Image registration is usually applied as a preliminary step in other image processing practices. Image registration provides assessing feasibility and comparison of common features in different images. Usually, an image is considered as a vector of dimension n designed by chaining pixels intensity. However, a vector of pixel intensity somehow is an insufficient descriptor of a shape. For example, very small changes in rotation, translation, and scale need adequate preprocessing in order to obtain necessary invariances. Then alternative suggestions like finding key points could be provoked. But all shapes do not have noticeable key points and this approach is insufficient for all cases. Hence, a general representation of an object as a set of points selected from the border of the object is appreciable. The shape context, a descriptor related to each point, represents the coarse description of the rest of the object concerning that point. We introduce shape context, a point-based registration technique next.

A. Shape Context

In 2002 Belongie et al. [12] proposed the shape context or point set matching algorithm. In this algorithm, shapes are described in a way that deals with measuring shape similarity and the point correspondences improving. To explain this

algorithm, one known and one unknown objects are considered. Supposing point set $l = \{l_1, \ldots l_n\}$ captured the form of the known object and $h = \{h_1, \ldots h_n\}$ the unknown object. The scattering over respective positions is compact, robust, and greatly selective. Therefore, the coarse histogram of the respective coordinates of the remaining $n - 1$ points for the point l_i is defined to be the shape context of l_i that is illustrated by Eq. (1):

$$m_i(k) = \#\{h \neq l_i : (h - l_i) \in \text{bin}(k)\}. \tag{1}$$

Primarily, the likeliness of two patterns is calculated. Patterns are presented by a group of finite sample points from pattern outlines as discussed earlier. These points are not needed to be certain points like curvature extrema or landmarks, etc. As the number of samples is getting bigger, the obtained closeness to the hidden pattern is becoming better. By applying the shape context, we enable to represent the rough distribution of the rest of pattern regarding to a given point on the pattern. For each sample point on one pattern, by discovering likeliness of two patterns, we detect the most analogous shape context for the sample point on the other pattern. With the given likeliness at sample points, the likeliness is continued to complete pattern by calculating a mapping transformation that aligns one pattern onto the other. Aligning patterns can be considered the degree of pattern likeliness. In attaining a total of corresponding errors between similar points, collected with an expression which calculates the magnitude of the mapping transform, then calculation of the dissimilarity between the two shapes is possible.

Assuming a point l_i and a point h_j are on the known pattern and on the unknown pattern, respectively, and $C(l_i, h_j)$ is the cost of matching point l_i and point h_j. Shape contexts are distributions introduced as histograms, it is statistically X^2 test:

$$C(l_i, h_j) = \frac{1}{2}\sum_{k=1}^{K} \frac{\left[m_i(k) - m_j(k)\right]^2}{m_i(k) + m_j(k)}, \tag{2}$$

where the k bin normalized histogram at l_i and h_j are indicated by $m_i(k)$ and $m_j(k)$, respectively. It designates the group of costs C_{ij} between all pairs of points l_i and h_j on the known and unknown patterns, respectively. The aim is minimizing the sum of matching cost denoted in Eq. (3):

$$G(\pi) = \sum_i C(l_i, h_{\pi(i)}), \tag{3}$$

where π is a permutation. It could be determined in $O(N^3)$ time applying the Hungarian approach.

Here we present examples of two original objects and their sample points on their borders shown in Fig. 1a, b. Furthermore, the compassion of the two objects is shown in Fig. 2.

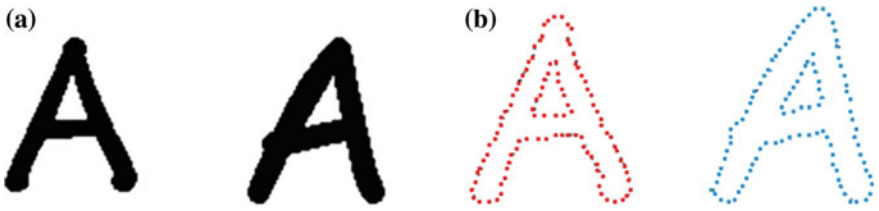

Fig. 1 Shape context matching. **a** Two original objects. **b** Sample points of two objects on their borders

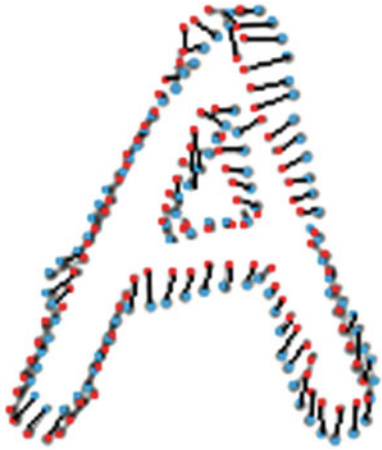

Fig. 2 The compassion of the two objects

By having a limited set of similarities between points on two patterns, we enable to continue estimating a plane transformation. Thin-plate spline (TPS) was employed in this work. A short explanation of TPS is presented in the following part.

B. Thin-Plate Spline (TPS)

Thin-plate spline (TPS) is an approach derived from a spline. It is applied to interpolate and smooth data and has generally been considered as a nonrigid mapping model to align two images and match two shapes. Bookstein discovered that TPS model is greatly powerful for modeling alterations in biological patterns [13]. The TPS model is the most extensively applied model in transformations when working with shape contexts. It can be used to map optional points from one pattern to the other. In other words, TPS is 2D observation of the cubic spline. Let that positions of (x_i, y_i) are all distinctive and are not collinear. The TPS interpolant $g(x, y)$ minimizes the bending energy E_f described in Eq. (4):

$$E_f = \iint \left(\frac{\partial^2 g}{\partial x^2}\right)^2 + 2\left(\frac{\partial^2 g}{\partial x \partial y}\right)^2 + \left(\frac{\partial^2 g}{\partial y^2}\right)^2 \mathrm{d}x\mathrm{d}y$$

$$g(x,y) = a_1 + a_x x + a_y y + \sum_{i=1}^{n} w_i O(\|(x_i, y_i) - (x, y)\|), \tag{4}$$

where $O(r)$ is expressed as follows:

$$O(r) = r^2 \log r^2. \tag{5}$$

3 Dataset and Processing Steps

In this study, thermal images, accessible from Sun State Thermal Imaging Center in Australia [14], Thermography of Iowa [15], American College of Clinical Thermology [16], Thermal imaging lab in the San Francisco Bay Area [17], and Ann Arbor thermography center [18], were used. The algorithm includes the following steps:

(1) Selecting randomly two sets of points that lie on the boundaries of two breasts separately.
(2) Determining similarities between points on the borders of the two breasts.
(3) Estimating a mapping function using the correspondences. The obtained mapping function of boundaries points is employed for mapping the inside points of the breast thermogram. In digital images, pixels are prescribed to lie on an experiencing lattice, captured to be in an integer network. Typically, the output grid does not accompany with the integer grid. Comparatively, the positions of the grid points may acquire any of the connected values which are appointed by the mapping function. Consequently, an interpolation must be suggested to convert discrete sample data to a connected surface. Then the connected surface may be sampled at noninteger positions of the output grid. The output image benefits of the accuracy of the interplant function.
(4) Determining the measure of R, G, B of the output grid accordingly by employing cubic spline for interpolation.

4 Experimental Results

We implemented the algorithm for 32 subjects. It thoroughly accomplished for 28 subjects. The proposed algorithm implementation for two typical subjects is shown in Figs. 3 and 4. Thermograms of the left breasts are shown in Figs. 3b and 4b,

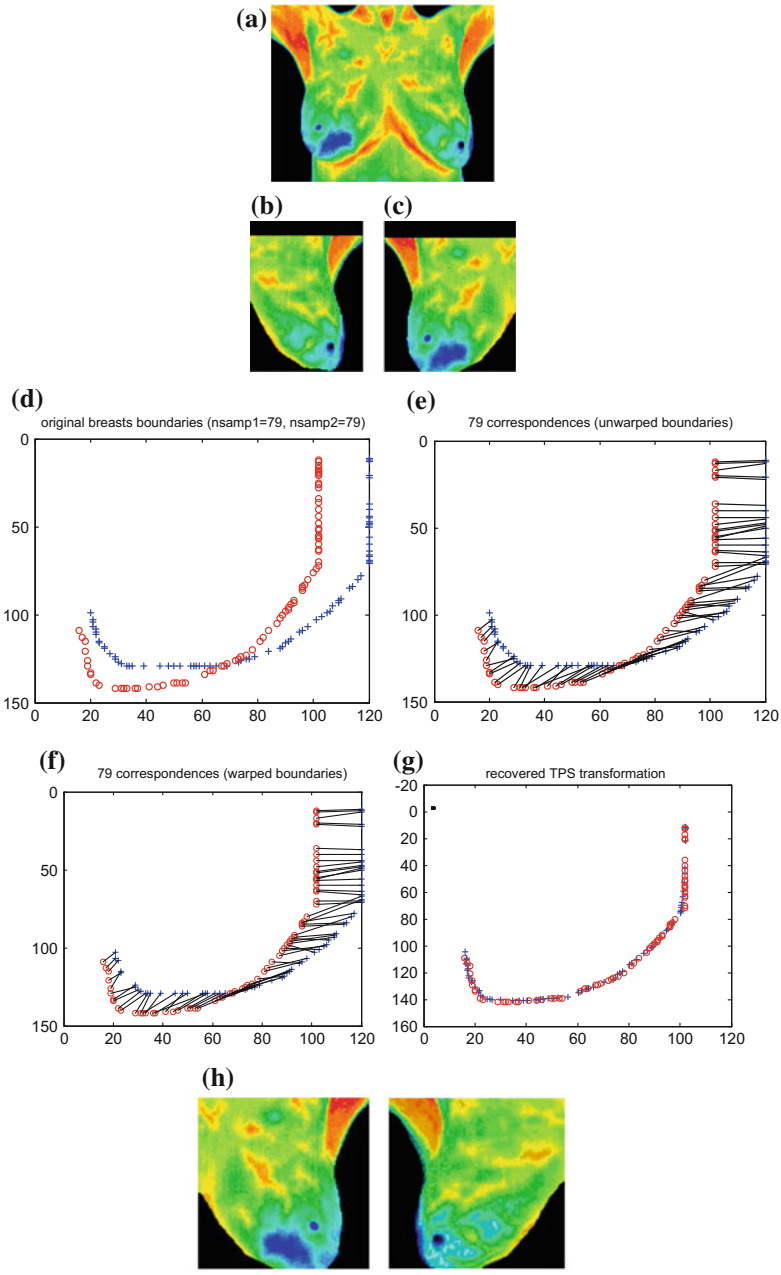

Fig. 3 Case I **a** original thermogram, **b** left breast, **c** right breast, **d** *Blue points* on borders of right breast, and *red points* on borders of left breast, **e** unwarped borders, **f** warped borders, **g** borders of two breasts after alignment, and **h** interpolated left and right breasts

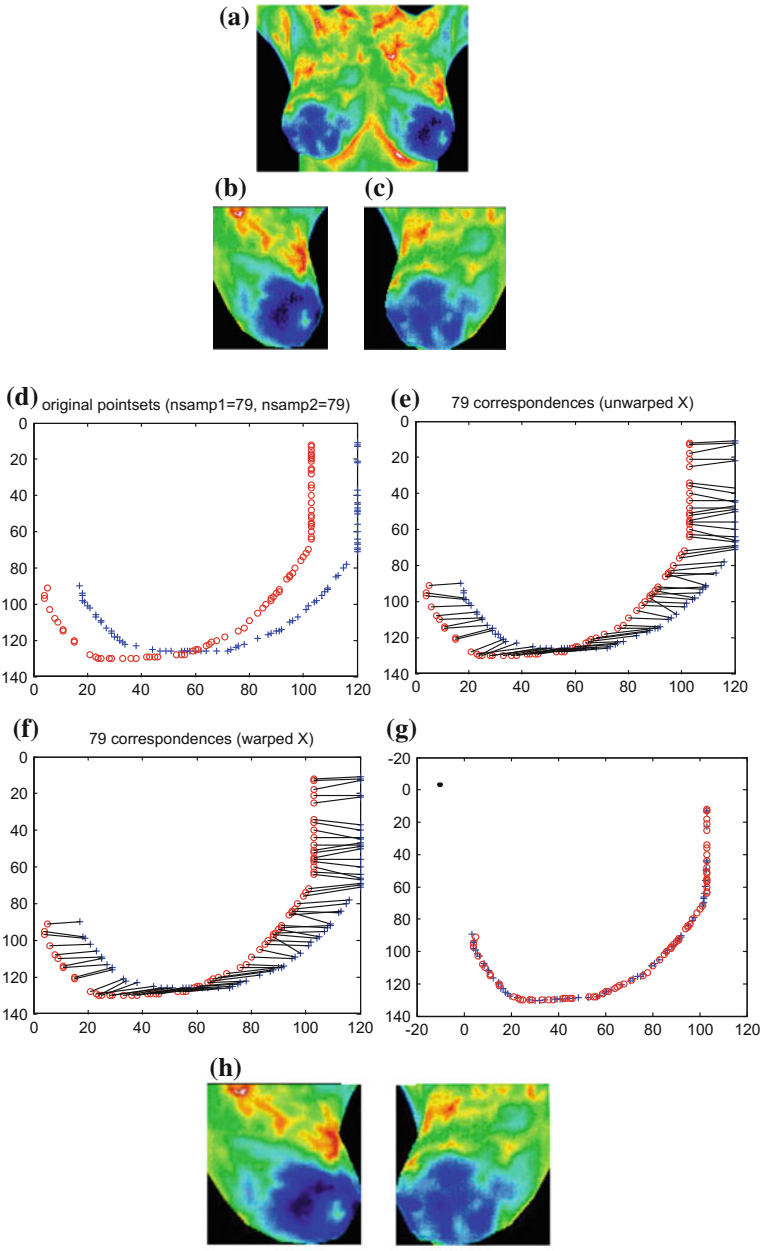

Fig. 4 Case II **a** original image, **b** left breast, **c** right breast, **d** *blue points* on borders of right breast, and *red points* on borders of left breast, **e** unwarped borders, **f** warped borders, **g** borders of two breasts after alignment, and **h** Interpolated left and right breasts

while the thermograms of the right ones are in Figs. 3c and 4c. The set of points on borders of right and left breasts are depicted in Figs. 3d and 4d. Unwarped boundaries are demonstrated in Figs. 3e and 4e and warped boundaries in Figs. 3f and 4f. Borders of two breasts after using the aligning function are shown in Figs. 3g and 4g. Furthermore, the interpolated left and right breasts are demonstrated in Figs. 3h and 4h.

5 Conclusion

We have proposed a technique in achieving symmetrical borders for thermograms of contralateral breasts. Shape context method was used in our proposed algorithm. After accomplishing registration of borders, then, the determined mapping function of borders points is applied for mapping of points of inside of two breast images. The benefits for employing shape context technique in this study include not requiring special land marks or key points, and progressing to all usual shape deformation. Although the technique is straightforward and not difficult to use it presents an especially rich descriptor for point sets notably improving point set registration. Findings are very hopeful. The proposed algorithm was accomplished for 32 subjects and perfect implementation was obtained for 28 of them.

6 Future Work

As long as we attain two symmetric breast thermograms, many works can be done for comparison of thermal distribution of the two breasts in future. The two obtained symmetric breast thermograms will be used for comparing their temperature diffusion by analyzing suitable obtained features from opposite side breasts to diagnose thermal unlikeness. Various features such as statistical features and geometrical features may be the suitable ones.

References

1. Ng, E.Y.K., RajendraAcharya, U.: A review of remote-sensing infrared thermography for indoor mass blind fever screening in containing an epidemic. IEEE Eng. Med. Biol. **28**(1), 76–83 (2009)
2. Etehadtavakol, M., Ng, E.Y.K.: Breast thermography as a potential non-contact method in early detection of cancer: a review. J. Mech. Med. Biol. **13**(2), pp. 1330001-1 to 1330001-20 (2013). doi:10.1142/S0219519413300019
3. Ng, E.Y.K.: A review of thermography as promising non-invasive detection modality for breast tumour. Int. J. Thermal Sci. **48**(5), 849–855 (2009). doi:10.1016/j.ijthermalsci.2008.06.015

4. Singh, Y.: Tumor angiogenesis: clinical implications. Nepal J. Neurosci. **1**(1), 61–63 (2004)
5. Uematsu, S.: Symmetry of skin temperature comparing one side of the body to the other. Int. J. Thermology **1**(1), 4–7 (1985)
6. Qi, H., Kuruganti, P.T., Snyder, W.E.: Detecting breast cancer from thermal infrared images by asymmetry analysis. In: Biomedical Engineering Handbook (ch. 27), pp. 1–14. CRC (2006)
7. Diakides, N., Bronzino, J.D.: Medical Infrared Imaging. CRC Press, Taylor & Francis Group (2008)
8. Tan, T.Z., Quek, C., Ng, G.S., Ng, E.Y.K.: A novel cognitive interpretation of breast cancer thermography with complementary learning fuzzy neural memory structure. Expert Syst. Appl. Int. J. **33**(3), 652–666 (2007)
9. Etehadtavakol, M., Ng, E.Y.K., Lucas, C., Sadri, S., Gheissari, N.: Estimating the mutual information between bilateral breast in thermograms using nonparametric windows. J. Med. Syst. **35**(5), 959–967 (2011)
10. Etehadtavakol, M., Sadri, S., Ng, E.Y.K.: Application of K- and fuzzy c-means for color segmentation of thermal infrared breast images. J. Med. Syst. **34**(1), 35–42 (2010). doi:10.1007/s10916-008-9213-1
11. Schaefer, G., Zavisek, M., Nakashima, T.: Thermography based breast cancer analysis using statistical features and fuzzy classification. Pattern Recogn. **42**(6), 1133–1137 (2009)
12. Belongie, S., Malik, J., Puzicha, J.: Shape matching and object recognition using shape contexts. IEEE Trans Pattern Anal. Mach. Intell. **24**(24), (2002)
13. Bookstien, F.L.: Morphometric Tools for Landmark Data: Geometry and Biology. Cambridge University Press (1991)
14. STImaging: http://www.stimaging.com.au/page2.html. Last accessed July 2009
15. http://www.thermographyofiowa.com/casestudies.htm. Last accessed July 2009
16. ACCT: www.thermologyonline.org/Breast/breast_thermography_what.htm. Last accessed July 2009
17. MII: http://www.breastthermography.com/case_studies.htm. Last accessed July 2009
18. AAT: http://aathermography.com. Last accessed July 2009

Color Segmentation of Breast Thermograms: A Comparative Study

Mahnaz Etehadtavakol and Eddie Y.K. Ng

Abstract Color segmentation of breast thermograms can have a crucial performance in tumor detection. There is a relation between blood vessel activity and the surrounding area temperature. Once a cancer increases blood vessel activity, the cancer cells and their surrounding tissue become hotter than normal tissue. Pre-cancer and cancer cells need plenty of nutrients to multiply and survive consequently; they are highly metabolic tissue and have different thermal patterns compared to the normal one. In this paper, a comparison work is presented for three modeled color segmentation approaches: *K*-means, mean shift (MS), and fuzzy *c*-means (FCM) applied to infrared breast images. There are some drawbacks for *K*-means and MS approaches. Almost empty clusters may be obtained in the segmentation results using *K*-means algorithm. In addition, we frequently confront almost empty clusters with MS algorithm due to its sensitiveness to the window size parameter. Choosing an appropriate window size parameter is not an easy task. On the other hand, the fuzzy inherent breast thermal images aid the FCM technique to obtain more precise outcomes. Malignant tumors show hotter thermal patterns than healthy tissues and even with benign tissues. Segmenting different parts of two breasts in terms of their temperature has potential helping to identify abnormal breast tissues.

Keywords Breast · Cancer detection · Thermogram · Pseudo-coloring · Color segmentation · *K*-means · Fuzzy *c*-means · Mean shift

M. Etehadtavakol (✉)
Isfahan University of Medical Sciences, Isfahan, Iran
e-mail: mahetehad@gmail.com

E.Y.K. Ng
School of Mechanical and Aerospace Engineering, College of Engineering,
Nanyang Technological University, Singapore, Singapore

E.Y.K. Ng and M. Etehadtavakol (eds.), *Application of Infrared to Biomedical Sciences*, Series in BioEngineering,
DOI 10.1007/978-981-10-3147-2_6

1 Introduction

Over 2000 years ago Hippocrates layered mud over a patient's body. He noticed the mud dried quicker where the internal disease generated heat. Actually he understood the diagnostic significance of body temperature changes.

Infrared energy wavelength is extended from 700 nm to 1 mm which human eyes sensors are not able to detect the all range, so it is not visible. Infrared energy is a sector of the electromagnetic spectrum that one recognizes as heat. All objects with a temperature above absolute zero radiate infrared electromagnetic energy. Objects with higher temperature radiate larger infrared radiations. One infrared camera can capture the heat pattern emitted from the object.

Breast thermal imaging is a radiation-free updating screening procedure that captures heat pattern of the breast helping early detection of cancer. The infrared radiation from an individual as an outcome of surface temperature is related to the amount of blood circulation. As a tumor grows it develops a blood supply that emits more heat [1].

Breast thermal imaging is a harmless physiological examination that presents the chance of earlier detection of breast disease than has been attainable through breast self-examination, and other breast screening tests alone.

Breast cancer if detected early can be taken out and stopped. Once a woman who has cancer is too late to start early detection, but if identified early enough, it can be removed in initial phases before it metastasizes and spreads to the neighboring area.

Breast thermal imaging is a painless, noninvasive, fast, low cost, passive, updating clinical examination without any risk of radiation. All subjects with any age with any breast size can benefit of this technique. Also women with dense breast as well as nursing or pregnant women can use breast thermal imaging [2–6].

Lawson declared in 1956 that the surface temperature of cancerous breast was higher than the normal one. Therefore, Lawson claimed that the cancerous cells can be recognized as hot regions in thermograms [7]. In infrared pseudo-color images distinct colors show distinct rate of hotness. Hence, breast thermograms' color segmentation can be beneficial in identifying the suspecting zones.

This study is arranged in this way: Pseudo-coloring of gray images is explained in Sect. 2. MS technique is discussed in Sect. 3. Numerical outcomes and discussions are given in Sect. 4 and finally the findings are achieved in Sect. 5.

2 Color Conversion of Gray-Scale Images

Pseudo-coloring or color conversion of gray-scale images is one of the possible means of upgrading digital image. The human eye is more sensitive to differences in color than to differences in shades of gray. It is a common task in image processing with the aim of upgrading visual quality, presenting a visual appeal and emphasizing specific features in the image.

Two limitations with gray-scale images which are related to specific characteristics of the individual discernable system lead to suggest the concept of pseudo-coloring. First, as the size of the feature composed of the alternate gray shade is reduced, a human's ability to discern gray-shade differences in an image decreases. As the size of the feature decreases, it takes larger differences in gray-scale intensity for a person to be able to see the alternate shade of gray. Second, humans are only capable of discerning between 60 and 90 separate shades of gray, suggesting much of the information in a typical 256 gray-shade image is lost on the viewer. Furthermore, individuals are capable of discerning more than 500 shades of color [8, 9].

Although it is controversial that the viewer allocates greater knowledge by pseudo-coloring of gray images, thoroughly produced pseudo-color image indeed allows tumor identification that is as good as gray scale and enhances fulfillment of other jobs like recognition and interpretation of a tumor. In the interest of rehearsing a thoroughly produced pseudo-coloring which can keep the whole knowledge of grey-scale images and derives no deformity in images, uniform color space is suggested [10].

In a uniform color space, identical alterations in the component of color space correlate to identical noticeable alterations in color chroma and color hue angle. However, many elements cause some difficulties. Some of these elements are as follows: (1) the color of an area relies on neighborhood colors; (2) chromatic accommodation impacts are influenced by eye motions, because colors are a head or come after other colors in time; and (3) color discriminability evaluates on the angular stretch of the investigation area. The 1976 CIELAB color space is suggested by the International Commission on Illumination (CIE).

The space of CIELAB is shown in Fig. 1.

It is an attempt to provide an intuitively uniform color space. In this color space, the amount of dissimilarities of the colors in terms of luminance, chroma, and hue can be nearly described by the two-point separation length. In addition, tristimulus values XYZ can obtain CIELAB coordinates (L^*, a^*, b^*) as expressed by the

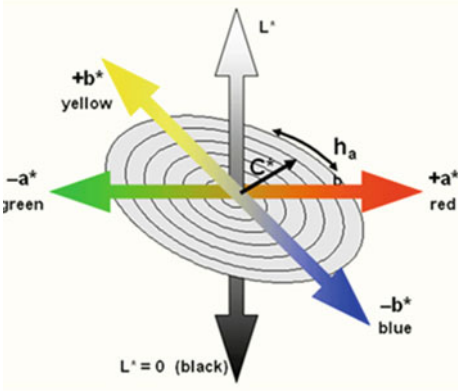

Fig. 1 CIELAB color space [11]

formulas in Eq. (1) where the white point values are denoted by the subscript n [12, 13]:

$$\begin{aligned} L^* &= 116g\left(\frac{Y}{Y_n}\right) - 16 \\ a^* &= 500\left[g\left(\frac{X}{X_n}\right) - g\left(\frac{Y}{Y_n}\right)\right] \\ b^* &= 200\left[g\left(\frac{Y}{Y_n}\right) - g\left(\frac{Z}{Z_n}\right)\right], \end{aligned} \tag{1}$$

where

$$g(m) = m^{1/3} \quad m > \left(\frac{6}{29}\right)^3 \tag{2}$$

$$g(m) = \frac{1}{3}\left(\frac{29}{6}\right)^2 m + \frac{4}{29} \quad m \leq \left(\frac{6}{29}\right)^3. \tag{3}$$

3 Mean shift clustering (MS)

MS is a nonparametric technique that was introduced in 1975, [14]. This technique does not need knowing about the number of clustering and does not force any format of the clusters in advance [15–18]. Supposing a set of feature vectors, y_i (i = 1,…, n), be in a feature space of dimension d. The relation between the density of any point y in terms of the kernel density evaluator $K(y)$ and the size of window h is obtained by Eq. (4):

$$f_{h,K}(y) = \frac{c_{k,d}}{nh^d}\sum_{i=1}^{n} K\left(\left\|\frac{y - y_i}{h}\right\|^2\right). \tag{4}$$

The zero gradient of Eq. (4) produces Eq. (5)

$$= \frac{2c_{k,d}}{nh^{(d+2)}}\sum_{i=1}^{n} q\left(\left\|\frac{y - y_i}{h}\right\|^2\right)\left(\frac{\sum_{i=1}^{n} y_i q\left(\left\|\frac{y-y_i}{h}\right\|^2\right)}{\sum_{i=1}^{n} q\left(\left\|\frac{y-y_i}{h}\right\|^2\right)} - y\right), \tag{5}$$

where $q(s) = -K'(s)$, supposing function q be the derivate of function K. Equation (5) is a product of two expressions. The first expression is proportional to the density estimate at y, and the MS vector which is the second expression is introduced by Eq. (6):

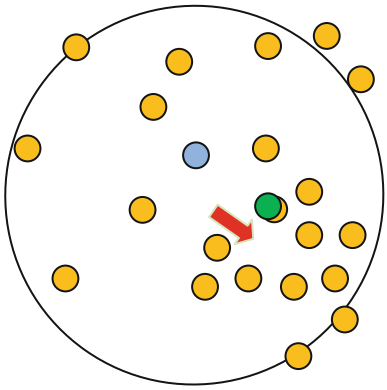

Fig. 2 Demonstration of mean shift algorithm; the *red arrow* shows the MS vector; the *green circle* shows the updated center of the cluster

$$m_h(y) = \frac{\sum_{i=1}^{n} y_i q\left(\left\|\frac{y-y_i}{h}\right\|^2\right)}{\sum_{i=1}^{n} q\left(\left\|\frac{y-y_i}{h}\right\|^2\right)} - y. \tag{6}$$

It is noticed that the direction of the greatest amount of growth in the density is certainly pointed by the MS vector. The MS algorithm is demonstrated in Fig. 2. The red arrow displays the MS vector while the updated center of the cluster is indicated by the green circle. It is noteworthy to mention that the window size variable h is the only variable of the MS technique. It has remarkable impact on the acquired results.

4 Experimental Results

In this study K-means [19] and FCM [20] were applied for color segmentation of breast thermograms [21, 22]. However, the three techniques K-means, MS, and FCM are applied and compared. Sixty breast thermal images accessible from five different breast thermography centers [23–27] were investigated in this work.

These three techniques put all cases into practice. With K-means algorithm, almost empty clusters are appeared in some experiments. Besides, if K-means is redone some times, the outcomes for distinct experiments are non-identical in accordance with the drawbacks of the K-means technique [28–31]. Figure 3b shows the experiment in which two almost empty clusters are obtained for a cancerous individual as shown in Fig. 3a. Nevertheless by performing the FCM technique (Fig. 3c), no empty cluster is obtained because fuzzy c-means technique measures the colors in a comparative way and categorize them in groups that are not with rigid borders. Consequently, data point is able to associate to more than one group although in hard clustering (K-means) data is collected to rigid groups suggesting each data point associates to particularly one group [32–34]. Also performance of

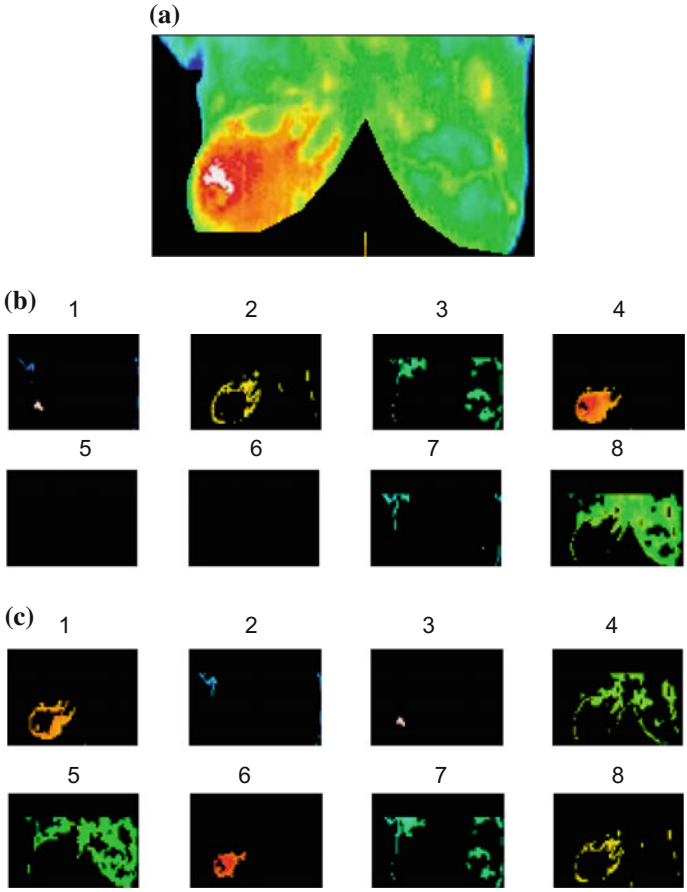

Fig. 3 **a** An inflammatory cancer breast thermogram. **b** Two almost empty clusters out of eight clusters obtained by *K*-means technique. **c** Eight non-empty clusters obtained by FCM clustering

FCM for a normal individual (Fig. 4a) is demonstrated in Fig. 4b. MS technique is easily affected by parameter h, the window size. In this work, MS algorithm was performed for a normal case. Figure 4b shows the results for $h = 12$ with eleven empty clusters while Fig. 4c for $h = 15$ with four empty clusters.

In this work, FCM technique has potential to identify the two first hottest areas by measuring their colors with respect to the provided palette spectrum colors. By color segmenting of breast thermograms, we are able to identify the two hottest clusters. Consequently providing some helpful data from the doubtful areas by measuring the color of the two hottest areas with the color of the provided palette spectrum is feasible.

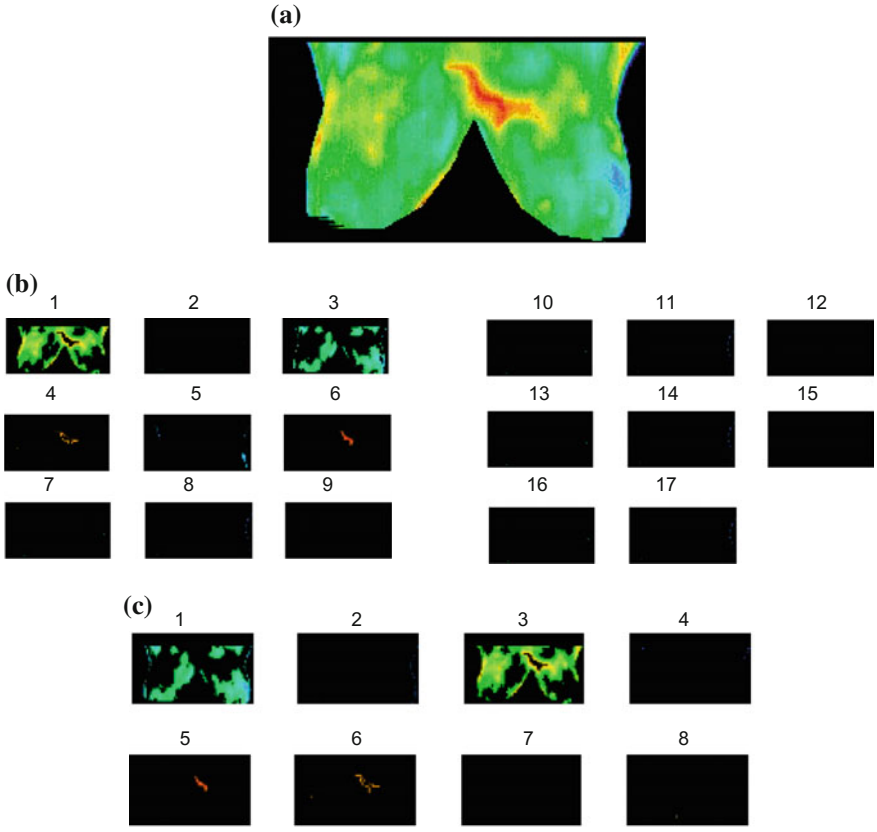

Fig. 4 **a** A normal breast thermogram. **b** Eleven almost empty clusters out of seventeen clusters obtained by MS with h = 12. **c** Four almost empty clusters out of eight clusters obtained by MS with h = 15

5 Conclusion

Although it is controversial that with pseudo-colored gray images more data can be allowed to the observer, but precisely produced pseudo-color image indeed is capable of tumor identification that is equivalent to the gray scale and upgrades accomplishment of other jobs like perception and judgment of a tumor. In this research, three techniques for breast thermograms color segmentation were used. MS technique is easily affected by parameter *h*, the window size, and accordingly, in this study, we usually challenged empty clusters and selecting a suitable *h* was not straight forward. *K*-means technique reduces the sum of within cluster outcomes numerically and clusters are tight and fully divided and produce precise outcomes. Due to the *K*-means drawbacks, nevertheless, for many cases, *K*-means technique is not practicable where clusters are not separated and an element in an image may

associate to various clusters. Choosing appropriate initial cluster centers is crucial for *K*-means clustering. Inadequate initial centers may produce empty clusters. In FCM technique, elements of the image are included in different clusters with disparate levels of association. By reason of the fuzzy nature of the breast thermograms, more faultless outcomes were resulted by FCM method to segment breast thermograms.

In this study, 60 breast thermograms were studied. By implementing FCM technique, we provided the two first hottest areas for each subject where convenient features are obtainable. There are some conveniences of breast thermograms color segmentation by FCM such as identification of irregular subjects by contrasting the analogous clusters from the contralateral breasts (over the symmetrical line), determination of level of malignity with identifying the two first hottest areas, and extraction of some useful features from them.

References

1. Etehadtavakol, M., Chandran, V., Ng, E.Y.K., Kafieh, R.: Breast cancer detection from thermal images using bispectral invariant features. Int. J. Thermal Sci. **69**, 21–36 (2013)
2. Jones, B.F.: A reappraisal of the use of infrared thermal image analysis in medicine. IEEE Trans. Med. Imaging **17**(6), 1019–1027 (1998). doi:10.1109/42.746635
3. Ng, E.Y.K.: A review of thermography as promising non- invasive detection modality for breast tumour. Int. J. Therm. Sci. **48**(5), 849–859 (2009)
4. Diakides, N., Bronzino, J.D.: Medical Infrared Imaging, 3rd edn. CRC, Taylor & Francis, New York (2008)
5. Ng, E.Y.K., Kee, E.C.: Advanced integrated technique in breast cancer thermography. J. Med. Eng. Technol. **32**(2), 103–114 (2008). doi:10.1080/03091900600562040
6. Etehadtavakol, M., Ng E.Y.K., Breast thermography as a potential non-contact method in early detection of cancer: a review. J. Mech. Med. Biol. **13**(2), 1330001-1–1330001-20 (2013)
7. Lawson, R.N.: Implications of surface temperature in the diagnosis of breast cancer. Can. Med. Assoc. J. **75**, 4309–4310 (1956)
8. Vaughn G., "Image Processing Class Notes", Texas Tech University Interdisciplinary Engineering Masters Program, 2007
9. Weeks, A.R., Fundamentals of Electronic Image Processing, 3rd edn. SPIE Press, Bellingham, Washington (2004)
10. Zhou, X., Zhang, C.: A perceptive uniform pseudo-color coding method of SAR images, Radar, CIE. International Conference, Oct. 2006 IEEE, pp. 1–4 (2006)
11. http://www.flexoglobal.com/flexomag/08-September/flexomag-ploumidis.htm
12. Li, H., Burgess, A.E., Evaluation of signal detection performance with pseudo-color display and lumpy backgrounds, JrnlID 10916_ArtID 9213_Proof# 1 - 08/09/2008. In: Kundel, H.L. (ed.) SPIE, Medical Imaging: Image Perception, vol. 3036, pp. 143–149. Newport Beach CA, USA (1997)
13. Connolly, C., Fliess, T.: A study of efficiency and accuracy in the transformation from RGB to CIELAB color space. IEEE Trans. Image Process. **6**, 1046–1048 (1997). doi:10.1109/83.597279
14. Fukunaga, K., Hostetler, L.D.: The estimation of the gradient of a density function, with applications in pattern recognition. IEEE Trans. Inf. Theory 2, 32–40 (1975)

15. Comaniciu, D., Meer, P.: Mean shift: a robust approach toward feature space analysis. IEEE Trans. Pattern Anal. Mach. Intell. 24(5), 603–619 (2002)
16. Cheng, Y.: Mean shift, mode seeking, and clustering. IEEE Trans. Pattern Anal. Mach. Intell. 17(8), 790–799 (1995)
17. Jin, H., Tao, W., Zhang, Y.: Color image segmentation based on mean shift and normalized cuts. IEEE Trans. Syst. Man Cyberetics 37(5), 1382–1389 (2007)
18. Mayer, A., Greenspan, H., Segmentation of brain MRI by adaptive mean shift, biomedical imaging: nano to micro 3rd IEEE International Symposium, pp. 319–322 (2006)
19. MacQueen, J.B., Some methods for classification and analysis of multivariate observations. In: Proceedings of Fifth Berkeley Symposium on Mathematical Statistical and Probability, vol. 1, pp. 281–297. University of California Press (1967)
20. Bezdek, J.C., Keller, J., Krisnapuram, R., Pal, N.R.: Fuzzy models and algorithms for pattern recognition and image processing. Kluwer, Norwell, MA (1999)
21. Forgy, E.W.: Cluster analysis of multivariate data: efficiency versus interpretability of classifications. Biometrics 21, 768–769 (1965)
22. Etehadtavakol, M., Sadri, S, Ng, E.Y.K., Application of K- and fuzzy c-means for color segmentation of thermal infrared breast images. J. Med. Syst. **34**(1), 35–42 (2010). doi:10.1007/s10916-008-9213-1
23. AAT: http://aathermography.com. Access Aug 2015
24. MII: http://www.breastthermography.com/case_studies. Access Aug 2015
25. ACCT: www.thermologyonline.org/Breast/breast_thermography_what.htm. Access Aug 2015
26. http://www.thermographyofiowa.com/casestudies.htm. Access Aug 2015
27. ST Imaging: http://www.stimaging.com.au/page2. Access Aug 2015
28. Deelers, S., Auwatanamongkol, S.: Enhancing K-means algorithm with initial cluster centers derived from data partitioning along the data axis with the highest variance. Int. J. Comput. Sci. **2**, 4247–4252 (2007)
29. Bradley, P.S., Fayyad, U.M., Refining initial points for K-Means clustering. In: Proceedings of 15th International Conference on Machine Learning, Morgan Kaufmann Publishers Inc., San Francisco, CA, USA, pp. 91–99 (1998)
30. Krishna, K., Narasimha, M., Genetic K-Means algorithm. IEEE Trans. Syst. Man Cybern. **29** (3), 433–439 (1999). doi:10.1109/3477.764879
31. Golestani, N., Etehadtavakol, M., Ng, E.Y.K.: Level set method for segmentation of infrared breast thermograms. Exp. Clin. Sci. **13**, 241–251 (2014)
32. Sowmya, B., Bhattacharya, S., Color image segmentation using fuzzy clustering techniques. IEEE Indicon, Conference, Chennai, India, pp: 41–45, Dec (2005)
33. Solvenia, K. R., Fuzzy C-means clustering and facility location problems. In: Proceeding of Artificial Intelligence and Soft Computing, Palma de Mallorca, Spain, p. 544 (2006)
34. Acharya, U.R., Ng, E.Y.K., Tan, J.H., et al.: An integrated index for the identification of diabetic retinopathy stages using texture parameters. J. Med. Syst. **36**(3), 2011–2020 (2012)

Potentialities of Dynamic Breast Thermography

Amina Amri, Anthony James Wilkinson and Susan Helen Pulko

Abstract Since the introduction of breast thermography into medicine, researchers have been interested in enhancing the thermal contrast in thermograms taken at steady state. It was found that cooling the surface of the skin during long acclimation periods produced better thermal contrast, although it was agreed that acclimation periods of up to 15 min may suffice to reflect functionalities of inner skin tissues. However, the use of artificial sources for cooling the skin has revealed new functional information that complements steady state thermography findings. The method has been referred to as 'Dynamic thermography' and is based on monitoring skin's thermal state after cold stress. Although dynamic thermography showed some promises in breast cancer diagnosis during the 70s, it has not received much interest till the advent of computer image processing techniques. Analytical tools such as sequential thermography, subtraction thermography, μ-thermography and thermal parametric images have been used in order to increase the accuracy of breast thermography. Other processing techniques used thermal transients of control points on the breasts to examine the change in blood perfusion induced by the presence of a breast disease. Autonomic cold challenge has also been used to identify a tumour's blood vessels. Recent numerical methods have investigated the effectiveness of dynamic breast thermography and revealed new parameters that are strongly correlated with tumour's depth. Here we review the state of the art in dynamic thermography as it is applied to breast diagnosis and identify some of the potential information that could be provided about breast diseases.

Keywords Breast cancer · Cold stress · Autonomic cold challenge · Subtraction thermography · Sequential thermography · μ-thermography · Dynamic thermography · Thermal recovery models

A. Amri (✉) · A.J. Wilkinson · S.H. Pulko
University of Hull, Hull, UK
e-mail: amri.amina@gmail.com

E.Y.K. Ng and M. Etehadtavakol (eds.), *Application of Infrared to Biomedical Sciences*, Series in BioEngineering,
DOI 10.1007/978-981-10-3147-2_7

1 The Concept of Dynamic Thermography

Breast thermography was introduced into medicine by Lawson [1] who observed that some breast cancers cause a rise in the temperature of the overlying tissue and argued that breast cancers could be detected at an early stage if thermal scan of the chest could be performed. Since then medical research has focused on the development of medical infrared scanning systems that could produce a quantitative temperature map of the breast [2, 3]. This interest in infrared scanning systems has been driven by the potential value of thermograms and was encouraged by the development of sensitive infrared detectors and sophisticated scanning systems for military requirements. Discussion about spurious thermography findings and possible errors that could affect thermal images have pointed out the importance of insuring that the temperatures measured at the surface of the skin are relevant to the physiological or pathological conditions of the body and not caused by artefacts [2–5]. It has been thus agreed that thermography should be performed using protocols during which thermal images of the unclothed part of the body be taken after 10–15 min acclimation period in a room of temperature between 18 and 24 °C, free of drafts, heat sinks or sources and that the patient be seated in an appropriate position. Under the foregoing conditions, better thermal contrasts have been observed. Further, faster scanning techniques and better thermal resolution are required for accurate thermal mapping.

At this stage, it was known that, in a healthy body any two symmetrically located areas of skin are at the same temperature under controlled environmental conditions [6–9]. Therefore, it was important to be able to correlate thermal contrast observed on thermograms with pathological conditions of the body in order to appraise the clinical value of thermography and to avoid subjective interpretation of thermograms. Barnes [5] has observed that the contrasts shown on thermograms are essentially caused by the generators of heat within the body and that thermograms can give information about pathological conditions from which the patient may be suffering. Subsequently, Williams [8, 9] proposed several causes for thermal contrast and stated that a range of breast diseases such as abscesses and some tumours induce a hot spot on the surface of a thermogram.

In the light of this, it was desirable to enhance the thermal contrast observed on thermograms given that the temperature of the skin is affected by environmental parameters and inner tissues characteristics. Barnes [10] demonstrated that the acclimation period is nothing but natural cooling of the skin and observed that better thermal contrasts are associated with longer acclimation periods which allow an equilibrium condition to be reached. Using the Barnes Mod I infrared scanner, a modified infrared instrument originally designed for military applications [11], Barnes [10] obtained a series of thermograms during natural cooling of the unclothed upper body of a patient in a room temperature of 29 °C and observed that the contrast was progressively increased after 15, 42, 65 and 94 min acclimation period while thermal details were still faithfully reproduced. In another experiment, Barnes [10] artificially cooled an arm by placing a damp towel on it for a few

seconds and then drying it quickly. A series of thermograms were taken during 27 min thermal recovery period at 3 min interval. An enhancement of contrast was observed during the first 9 min after which contrast decreased as the arm returned to thermal equilibrium.

Although heating the skin would obviously decrease the thermal contrast, Barnes [10] examined the effect of heating the arm progressively from ambient up to a temperature of 43 °C. Thermograms taken at temperatures of approximately 34, 37, 40, 41, 42 and 43 °C showed that at approximately body temperature, thermal contrast disappear. At elevated temperatures, a different thermal pattern emerged including cool areas directly over the veins. Consequently, Barnes [10] concluded that heating the skin could provide information about thermal conductivities of various tissues beneath it and suggested the use of superficial heating to study dermatological problems.

Concurrently, Williams [9] also reported that thermal contrast is accentuated by longer acclimation periods and by overcooling using artificial means. A steady state thermogram of a patient with advanced carcinoma of the right breast showed a temperature difference of 3.5 °C. When the chest wall was cooled using a towel soaked in iced water, the thermal contrast was observed to increase. The enhancement observed in the thermal contrast over a cancerous breast has marked the beginning of the use of superficial cooling as part of breast thermography protocols.

The advent of thermography as an adjunct technique for breast screening has spurred many medical researchers to establish its value in breast diseases with regard to known modalities of mammography and physical examination. Amalric et al. [12] compared thermography with physical examination, mammography and cytology. During thermography examination, the patient's chest was sprayed with a cooling liquid which was evaporated using a fan for 10 min. Thermograms were taken just after cooling. Thermographic findings were then compared with histological findings for evaluating thermographic usefulness. Out of 1879 confirmed cancers, 9% could not been identified either by physical examination or by mammography, but have been detected by the combination of cold stress and thermography.

2 Breast Dynamic Thermography Using Autonomic Cold Challenge

The early 80s witnessed the use of a protocol involving autonomic challenge before thermography. The method involved cooling of the extremities (hands or feet) by ice water immersion as part of breast thermography protocol. The cold challenge has been known as a test of sympathetic function and was used as a definitive diagnostic method for Complex Regional Pain Syndrome also known as Reflex Sympathetic Dystrophy (CRPS/RSD). The introduction of an autonomic challenge

was predicated on the fact that at some stage of its growth, cancerous tumours release angiogenic growth factor proteins that stimulate blood vessels to grow into the tumour, so that it can be supplied with nutrients and oxygen. However, angiogenesis growth does not continue throughout all stages of cancer. The autonomic cold test was intended to identify the development of a tumour's blood new vessels known as neoangiogenesis, and these could then be correlated with the development and existence of breast cancer. Since neoangiogenesis are devoid of a muscular layer and normal neural regulation, they would fail to constrict in response to a sympathetic stimulus. Therefore, a high blood perfusion rate is maintained in the tumour region as well as a high level of metabolic heat generation, while vasoconstriction occurs near the skin surface.

The concept was initiated in France where Gautherie et al. [13] used hand immersion in an attempt to make breast thermography more sensitive. The study used large sample data including over 10,000 patients. Thermograms could be taken prior to and after 45 s of cooling. It was reported that false positive rate decreased to 3.5%.

However, there have been theoretical claims that some anatomical factors can compromise the ability of the sympathetic nervous system to provoke vasoconstriction. Cockburn [14] argued that dilated vessels or capillary networks that resulted from surgery, incisional biopsy and lumpectomy, as well as local trauma and thoracic spine instabilities, would fail to respond to the autonomic cold challenge thus compromising the detection of tumour's neoangiogenesis. He also suggested that patient's own anxiety about the procedure may cause a sympathetic fight or flight response before the autonomic cold challenge and may lead to negative findings after applying cold stress. Therefore, researchers in the realm of breast thermography discontinued the use of the autonomic cold challenge in the early 90s after observing poor correlation between the results using cold stress and medical case histories [14–16].

Using advanced medical imaging systems, Amalu [17] has conducted a clinical study in order to reappraise the role of autonomic cold challenge as it might be applied to breast thermography. Breast thermograms of 23 patients with histologically confirmed breast cancers demonstrated positive and negative responses to cold stress. Amalu [17] found that excluding the autonomic cold test from breast thermography protocol does not affect the sensitivity or the specificity of thermography in the detection of breast cancers and concluded that more studies are needed to assess the validity of the autonomic cold test.

3 Characterisation of Thermal Recovery After Cold Stress

Barnes' observations during thermal recovery from superficial cooling and heating stimulated the interest of Japanese medical researchers to obtain information about the reaction of blood perfusion, metabolic heat generation and thermal conduction of the human skin to superficial stimulus. Nagasawa and Okada [18] referred to this

type of thermography as "dynamic thermography" because it is based on recording thermal transient during the dynamic thermal recovery of the skin.

Nagasawa and Okada [18] devised a spot cooling source consisting of a piece of ice in a film container of 30 mm diameter. A constant pressure of about 200 g insured that the cooling source was kept in contact with the skin. The part of the skin in contact with the device beyond the cooling area was insulated. Instead of taking several thermograms of the cooled area at different time intervals during thermal recovery, Nagasawa and Okada [18] recorded the thermal transient at the centre of the cooled area in a room that fulfilled thermography conditions. After cooling a pair of healthy human cheeks for 15 s, the thermal recovery curve of the right cheek was almost identical to the left cheek. After removal of the coolant, the temperature T of the centre of the spot recovered rapidly for the first minute and then its rise became more gradual ultimately reaching thermal equilibrium temperature, T_∞, which was almost the same as before cooling. The time needed to reach the final temperature was referred to as Recovery Time, *ReT*.

In order to calculate *ReT*, the thermal recovery curve was processed to a straight line using a logarithmic transformation of the difference between T and T_∞. The calculated and the measured values of *ReT* were found to be almost identical. The recovery time, *ReT*, was measured in cases of various diseases. In a case of hemangioma, *ReT* value of 3 min suggests active blood perfusion whilst for lipoma, the *ReT* was longer suggesting a low heat activity. Recovery time measurements were also used to track the acceptance of transplanted tissue in a deficient region on the cheek. It was found that after the first 20 days the recovery time was relatively slow but became faster after 80 days, which indicated its acceptance. Consequently, it was concluded that *ReT* depends on the kind of disease and its seriousness. Nagasawa and Okada [18] further investigated the value of dynamic thermography in observing the process of diseases and the effects of medication. Figure 1 shows a comparison of the linearized thermal recovery curves of a postoperative inflammation area, after removing an impacted mandibular third molar, and its

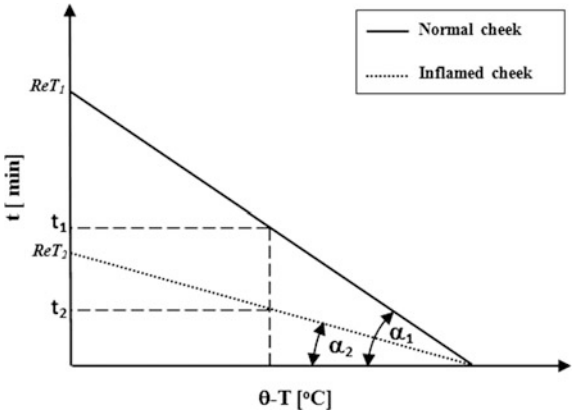

Fig. 1 Linear representation of thermal recovery curves of normal and inflamed cheeks after cooling [18]. The ratio $RtR = t_2/t_1 = \tan\alpha_2/\tan\alpha_1 = ReT_2/ReT_1$

symmetrical part. It was observed that the ratio of their corresponding slopes was equal to the ratio of their recovery times. This ratio was referred to as Recovery time Rate, *RtR*, and was used to observe the gradual recovery of the inflammation.

After examining various clinical experiments of dynamic thermography using cooling as well as heating stimuli, Nagasawa and Okada [18] concluded that a thermal recovery process could provide quantitative information about blood perfusion and heat activity of a tumour and that dynamic thermography could be applicable to differential diagnosis. It was also suggested that chemicals may be used as a stimulus for dynamic thermography in order to observe the reaction of specific diseases.

Concurrently with the clinical work of Nagasawa and Okada [18], Cary and Mikic [19] described a localised cooling method that could be used in differential diagnosis of human tumours. Although it was already known that thermal contrast is enhanced by cooling, the observed effects of cooling were not well understood at the time of the study. The method was established using the fact that the growth of tumours is usually associated with increases in the local blood perfusion and the local metabolic rate. These changes can produce an effect on skin temperature maps in the region above a tumour. Therefore, differential diagnosis of tumours could be made from comparison of temperature fields near tumours and in the corresponding region of the contralateral breast, on the basis that this is healthy tissue. Further, it was assumed that blood perfusion rates in healthy or normal tissue could differ significantly from blood perfusion rates through tumours during moderate cooling. Blood rate differences between cancerous and healthy tissue are thereby reflected in the observed thermal contrast.

The theoretical concept was later used to devise a simple, inexpensive local cooling system that could help in differential diagnosis of breast tumours [20]. The system comprises two cylindrical cooling units weighting approximately 500 g each. The units are filled with crushed ice at least 30 min prior to testing so that the cooling disk reaches 10 °C or less. The patient should be lying on her back with pen marks on the point where the tumour is closest to the surface. During a 10 min test, the units are held by the patient on the region of interest and on its symmetrical healthy part. Each unit insures a small surface cooling area of approximately 25 mm around which the skin in contact with the cooling device is insulated. Using such a system, relatively large temperature differences between the skin over cancerous tissue and that above healthy tissue could be obtained, without the heat loss from the patient being sufficient to affect patient comfort adversely and so limit the enhancement of the thermal contrast. The cooling units insure controlled cooling as well as recording the temperature of the cooling surface at one minute intervals. It was observed that thermal equilibrium was reached after 10 min and the thermal contrast ΔT after 10 min was calculated.

During cooling, the rate of variation of skin temperature T_s with time is influenced by blood perfusion of the tissue. When the temperature of a tissue does not vary significantly in space during cooling because of the inner fixed body temperature, the rate of variation of T_s could be expressed as:

$$\frac{dT_s}{dt} \propto \omega_b (T_a - T_s) \tag{3.1}$$

where ω_b is the blood perfusion rate and T_a is the temperature of the arterial blood perfusing the tissue. However, the rate of variation of T_s is nonlinearly related to blood perfusion due to the complex breast tissue structure that causes both spatially- and time-varying temperature field. Since the ratio $(dT_s/dt)/(T_a - T_s)$ is a monotonically increasing function of perfusion rate, a parameter M was defined as:

$$M = \frac{dT_{s2}/dt(T_a - T_{s1})}{dT_{s1}/dt(T_a - T_{s2})} \tag{3.2}$$

To quantify the response of the local cooling device to known breast diseases, M and ΔT values were used to define diagnosis criteria. If $\Delta T \geq 0.9$ °C or $M \geq 1.35$ then the test was assumed positive for cancer. On the other hand, if $\Delta T < 0.9$ °C and $M > 1.35$ then the tumour was classified as non-malignant. The local cooling method was tested on 130 women for whom xerographical, thermographical, clinical and pathological information was available. Fifty-two of the women were normal. There were 31 carcinomas, 14 solitary cysts, 4 benign tumours and 22 diffuse dysplexia. Other patients include 5 women with asymmetrical axillary tail and 2 with abscesses or inflammation. Masses were of average diameter of 17 mm and were 15 mm deep.

The foregoing criteria correctly diagnosed: 23 of 31 malignancies, which corresponds to 74%; 16 of 18 benign growths, which is 88%, and 46 of 52 normal cases which is also 88%. However, 10 of 22 women (45%) who had asymmetrical diffuse non-malignant disease would have been falsely diagnosed as having cancer. Some false negative results were caused by clinically occult carcinomas with insignificant thermal contrast and by large necrotic, inactive neoplasm. On the other hand, false negative findings were induced by large thermal contrasts observed in benign breast diseases such as sclerosing adenosis, cystic disease, fibroadenoma and abscesses. Cary et al. [20] have outlined some technical issues in the cooling unit and procedure that could have influenced the results including unequal initial disc temperature, improper location of the unit during testing and movement of the units during testing due to patient's breathing.

4 A Mathematical Model for Thermal Recovery After Cooling

Since the early 60s, the medical community has been aware that steady state thermography could produce false positive as well as false negative findings. It was, therefore, important to investigate theoretically whether dynamic thermography

could provide substantial information which could be useful for the clinical diagnosis.

Motivated by the findings of Nagasawa and Okada [18] during thermal recovery after cold stress, Steketee [21] subjected the skin of the forehead of 20 healthy subjects to a cold temperature T_{cold} and subsequently recorded the thermal recovery over a period of 15 min. The recovery curve shown in Fig. 2a was approximated by a mono-exponential function:

$$T - T_{cold} = (T_{\infty} - T_{cold})(1 - e^{-\mu t}), \tag{4.1}$$

where T_{∞} is the steady state temperature. The value of the decay constant, μ, was determined from a semi-logarithmic plot of $T_{\infty} - T$ as a function of time as shown in Fig. 2b. However, it has been noticed that the steady state temperature T_{∞} was

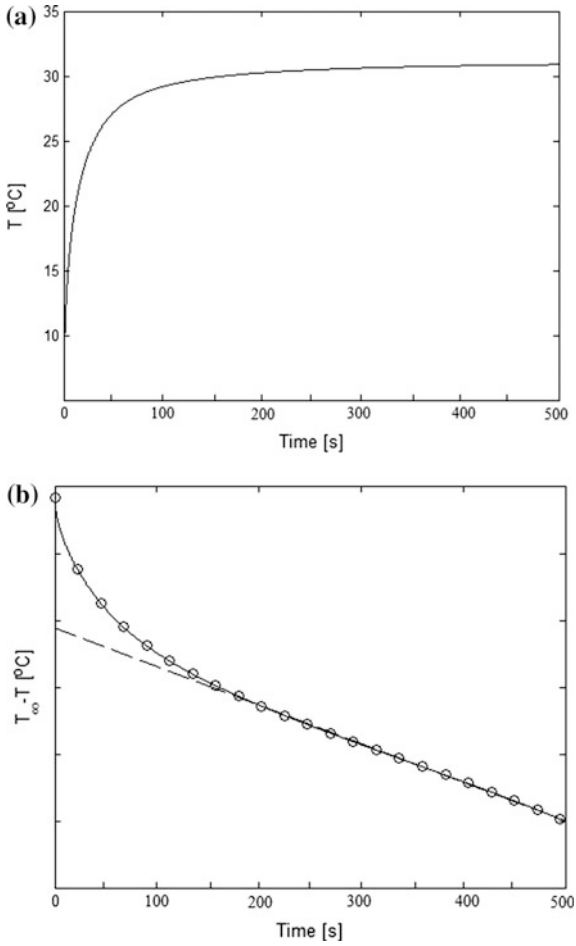

Fig. 2 Typical curves obtained by Steketee and Van Der Hoek [22] after cooling the forehead. **a** Thermal recovery and **b** semi-logarithmic linearization of $T_{\infty} - T$ versus time

lower than the temperature before cooling inconsistent with the observation of Nagasawa and Okada [18] that T_∞ was approximately the same before cooling. Furthermore, data obtained using thermal recovery measurements taken over a shorter period, couldn't be fitted by a mono-exponential curve as shown in Fig. 2b. The variance of the measured decay constants was also very high. Therefore, Steketee and Van Der Hoek [22] used a theoretical model based on the bioheat equation attributed to Pennes [23] in order to understand the character of the thermal recovery and improve the method.

The following Pennes [23] bioheat equation was used to model heat transfer during thermal recovery:

$$\rho c \frac{\partial T}{\partial t} = k \frac{\partial^2 T}{\partial x^2} - \omega_b \rho_b c_b (T - T_a) + Q_m \tag{4.2}$$

In Eq. (4.2), ρ (kg m^{-3}), k (W m^{-1} K^{-1}) and c (J kg^{-1} K^{-1}) denote the density, thermal conductivity, and specific heat capacity of tissue; ρ_b, c_b are density and specific heat capacity of blood; ω_b (s^{-1}) is the blood perfusion rate; Q_m is the metabolic heat generation; T_a is the supplying arterial blood temperature which is assumed constant, and T is the breast temperature.

A one-dimensional homogeneous skin model was used to study the thermal transient after cooling the surface at a temperature T_{cold}. Assuming that the skin is at body temperature, T_c, at a distance L from the surface and that the surface is exposed to ambient temperature, T_f, the following boundary conditions were prescribed

$$\begin{cases} k \frac{\partial T(x,t)}{\partial x}\Big|_{x=0} = h_0 [T(0,t) - T_f] \\ T(x,t) = T_c \quad \text{for} \quad x \geq L \end{cases} \tag{4.3}$$

In Eq. (4.3), h_0 is the effective heat transfer coefficient that combines the heat transfer attributable to convection and radiation as well as the cooling effect associated with evaporation. Defining $\theta = T - T_{cold}$, Eq. (4.2) becomes:

$$\frac{\partial \theta}{\partial t} = \alpha \frac{\partial^2 \theta}{\partial x^2} - \beta \theta + \gamma \tag{4.4}$$

where α is the thermal diffusivity $\alpha = k/\rho c$, $\beta = \omega_b \rho_b c_b / \rho c$ and $\gamma = (Q_m/\rho c) + \beta \theta_c$. The boundary conditions then become:

$$\begin{cases} \frac{\partial \theta(x,t)}{\partial x}\Big|_{x=0} = h' [\theta(0,t) - \theta_f] \\ \theta(L,t) = 37 - T_{cold} \quad \text{for} \quad x \geq L \end{cases} \tag{4.5}$$

where $h' = h_0/k$ (m^{-1}). Steketee and Van Der Hoek [22] solved the problem using the Laplace transformation method [24] and the complex inverse Bromiwich's integral formula [25] to obtain the thermal transient during recovery:

$$\theta(x,t) = \theta(x,0) + A\frac{\sinh\eta(L-x)}{\eta\cosh\eta L + h'\sinh\eta L} - 2\alpha A\sum_{n=1}^{\infty}\frac{\exp(-\mu_n t)p_n^2\sin p_n[1-(x/L)]}{\mu_n L[p_n^2 + h'L(1+h'\alpha)]\sin p_n} \tag{4.6}$$

where

$$A = \frac{\eta[\theta_c + (\gamma/\beta)(\cosh(L\eta)-1)]}{\sinh(L\eta)} + h'\theta_f \quad \text{and} \quad \eta = \sqrt{\beta/\alpha}$$

$$\mu_n = \beta + \frac{\alpha p_n^2}{L^2}; \quad \tan p_n = -\frac{p_n}{h'L} \text{ and } \beta \neq 0$$

The surface temperature $\theta(0,t)$ and the steady state value $\theta(0,\infty)$ were derived from Eq. (4.6).

$$\theta(0,t) = 2\alpha A\sum_{n=1}^{\infty}\frac{[1-\exp(-\mu_n t)]p_n^2}{\mu_n L[p_n^2 + h'L(1+h'\alpha)]} \tag{4.7}$$

$$\theta(0,\infty) = A\frac{\sinh\eta(L)}{\eta\cosh\eta L + h'\sinh\eta L} \tag{4.8}$$

Equation (4.7) can be used to study the effect produced by a variety of parameters on the steady state temperature and to estimate the time needed to reach that temperature that Nagasawa and Okada [18] refer to as *ReT*. Equation (4.8) shows that T_∞ depends on the temperature at depth L. The later varies among subjects implying that T_∞ cannot be used as a reliable measurement for blood perfusion. Furthermore, the theoretical solution (4.6) showed that the decay constants, μ_n, depends strongly on the thermal diffusivity of the tissue. It was also concluded that a two-exponential model should be used to fit the thermal recovery curve in order to better discriminate normal and pathological blood circulation.

5 Computer Assisted Dynamic Breast Thermography

Computers were introduced for the qualitative analysis of breast thermograms in the 70s [26–29] with the aim of improving the accuracy of diagnosis. It was a reasonable assumption that a computer-based system would be a fast way of diagnosing abnormality, and would be less expensive than visual interpretation in a large breast screening program. Winter and Stein [28] assessed the ability of three computer image processing techniques: spatial signature analysis, symmetry measurement using thermal density distributions and image coding by contour map data structure. Newman et al. [26] devised a simple automated technique for obtaining

the breast outline and investigated criteria for abnormality. Ziskln et al. [29] classified 85 thermograms into normal and abnormal categories using a statistical decision program based on a linear discriminant analysis technique. They reported an overall accuracy of 85%.

Over the years, different methods of dynamic breast thermography have been reported. After the application of an external cold stress, thermal recovery of the breast could be examined by means of sequential thermograms taken at time intervals, or/and subtracting sequential thermograms to produce a single contrasted thermogram. Another approach was to compare the thermal transients of particular areas of interest on the abnormality with its contralateral symmetrical part.

Using a standardised cooling procedure, Geser et al. [30] reduced the temperature of the breast by approximately 3 °C using two fans. A computer-assisted discriminant analysis was used to classify a sequence of 20 thermograms recorded during thermal recovery of the breast after cooling. This quantitative dynamic thermography was then able to correctly classify 80% of 162 patients with negative clinical and mammography findings and 72.5% of 51 patients with proven breast cancer. When combined with steady state thermography, the false positive rate was reduced to 40%, though this value remains high.

Usuki et al. [31] combined observation of steady-state thermal maps with dynamic thermography after cold stress in a clinical study that included 56 breast carcinomas and 320 diagnosed benign diseases. Unspecified imaging procedures were used. Thermographic measurements were taken in a room of temperature 24 ± 1 °C and 60 ± 10% humidity using a thermo-tracer 6T66 (NEC-Sanei Co.). After an acclimation period of 15 min, steady state thermograms were taken. Soon after, the breasts were cooled with 70% alcohol mist and thermograms were taken at 0, 1, 2 and 3 min after cooling. Thermograms were then processed using imaging software that subtracted thermograms obtained immediately after cooling from the thermograms obtained 3 min after cooling. Statistical analysis of steady state thermography findings provides a sensitivity of 85.7%, a specificity of 65.6% and a total accuracy of 68.6%. In contrast, subtraction thermography showed a sensitivity of 89.3%, a specificity of 78.4% and a total accuracy of 80.1%. It was then concluded that, although subtraction thermography after cold stress decreases the false positive rate, it cannot be used as an ultimate breast imaging method. It was also recommended that correlations between steady state and subtraction thermography findings required more studies and that image analysis techniques needed further development in order to be used in this context.

Uchida et al. [32] developed a physiological functional image processing system for the quantitative analysis of sequential thermograms obtained during thermal recovery of the breast after cooling. This system used models developed by Steketee and Van Der Hoek [22] which describe the rewarming of the skin after cold stress is removed. By assuming that this thermal recovery can be approximated by a mono-exponential function, the temperature T of a pixel (i, j) at a time t was given as:

$$T(i,j,t) - T(i,j,0) = [T(i,j,\infty) - T(i,j,0)] \times [1 - \exp(-\mu t)], \quad (5.1)$$

where the constant μ depends on the blood perfusion underneath the skin surface as well as the thermal conductivity of the tissue. The μ-value thermal imaging system provided a colour-coded 250 × 230 image of μ values of each pixel calculated from sequential thermograms. Despite the observation of Steketee and Van Der Hoek [22] that it is necessary to discard the initial part of the transient if a mono-exponential thermal recovery is to be useful, it was thought that μ-thermograms could reveal information about pathophysiological abnormality.

The effectiveness of the μ-value thermal imaging system was initially assessed for a patient with a proven cancer in the right breast and a false negative steady state thermogram performed after 20 min acclimation in a room temperature of 21 °C. After 2 min chilling by using cold air moved over the breast surface using an electric fan, the temperatures of the right and left nipples were recorded every 15 s during rewarming. Measurements were taken over a period of approximately 4 min. Thermal recovery curves showed that the temperature of the left nipple was lower than the temperature of the right one. Furthermore, the computer system processed a sequence of 6 thermograms taken every 15 s by subtracting the temperature values in each thermogram from corresponding values in the previous one in order to produce a colour-coded μ-value image.

Two years Later, Uchida et al. [33] used the μ-value thermal image processing system to analyse 18 patients with breast cancer which had been incorrectly diagnosed by steady state thermography and dynamic thermography (sequential and subtraction). Steady state thermograms were taken in a room temperature of 23 °C after 10 min acclimation. Then thermograms were taken sequentially at intervals of 15 s, following exposure to cold air applied using an electric fan for a period of 2 min. The diagnosis criteria used for breast thermography at steady state and after cooling depended on qualitative and quantitative findings of:

1. Asymmetric hot spot on the steady state thermogram
2. Asymmetric abnormal exaggeration of vascular pattern
3. Significant differences in the thermal map
4. Positive heat patterns in thermograms taken sequentially
5. A hot spot in the subtracted thermogram

The presence of sign 1 or sign 2 was considered positive in terms of diagnosis using steady state thermography. However, several problems including patient movement as well as breathing have limited the diagnostic value of μ-thermography which corrected 4 cases among 12 false negative thermograms and 4 cases among 6 false positive thermograms. The authors also pointed out thermal artefacts caused by uneven air flow distribution over the curved surface of the breast and suggested that better results could be produced using different cooling methods. The accuracy of μ-thermography was then reassessed after incorporating motion compensation analytical tools by examining 26 patients with non-palpable breast cancer [34].

A correct diagnosis was obtained in 55% cases using steady state thermography, 14% using dynamic thermography (sequential and subtraction) and 11% using μ-thermography.

Later, Ohashi and Uchida [35] reviewed the effectiveness of steady state and subtraction thermography in the diagnosis of 728 patients with proven breast cancer and 100 patients with benign breast diseases between 1989 and 1994. However, for patients with breast cancer, the diagnostic accuracy improved from 54% when steady state thermography was used to the much larger value of 82% in the case of dynamic thermography after cold stress, without any associated increase in the rate of false positives. For cases of benign breast diseases, the overall false positive rate of steady state thermography was 41% versus 29% using subtraction thermography. Although Ohashi and Uchida emphasised the merit of μ-thermography as a future diagnosis tool, the current authors are not aware of any further work that has been published since 1997.

More recently, Arora et al. [36] conducted a 2-year study to evaluate an advanced digital thermography system for cancer detection. The study involved 92 women whose average age was 51 years, the range being between 23 and 85, all of whom had a suspicious breast lesion which had been identified using mammography or ultrasound. Prior to thermography examination, the group of patients underwent biopsy in a prospective double-blind trial. 60 out of 94 biopsies suggested the presence of a malignancy and 34 suggested no malignancy. The majority of malignancies were infiltrating ductal carcinoma and the invasive tumours ranged in size from 0.5 to 14 cm. The clinical study used the Sentinel BreastScan, an advanced digital thermography system manufactured by Infrared Science Corporation comprising a digital camera with a sensitivity of 0.08 °C and a spatial resolution of 320×240 pixels. Unlike other infrared system, the Sentinel BreastScan is a fully automated diagnostic tool that employs artificial intelligence to provide a fully interpreted real-time test report to the doctor. During the thermography procedure, a series of more than 100 thermograms were collected while cool air was directed at the breasts for approximately 4 min. Specific thermal parameters for each breast were extracted and compared using asymmetry analysis during post-processing of thermograms recorded during cooling. The software then produced colour-coded images of the breast indicating suspicious areas as well as all measured thermal breast parameters. Dynamic thermography identified 58 of 60 malignancies; the sensitivity was 97% and the specificity 44%.

6 Active Dynamic Breast Thermography

Active Dynamic Thermography (ADT) refers to dynamic thermography in non-destructive evaluation of materials [37]. It is based on retrieving thermal parameters of a tested object from its surface thermal response to an active external excitation which involves heating or cooling. A series of thermal images are

processed for the calculation of parametric images mainly thermal constant profiles that are strongly correlated with the presence of defect in the tested object.

Advanced infrared imaging systems and image processing tools are being developed to retrieve information from thermal recovery response after removing the external excitation [38–40]. By assuming a Fourier heat conduction model in tissue, two-exponential models have been used to fit temperature transients at the surface of the tissue during thermal recovery after heating or cooling:

$$T_c(x,y,t) = T_e + \Delta T_1 \exp(-t/\tau_{1c}(x,y)) + \Delta T_2 \exp(-t/\tau_{2c}(x,y)) \tag{6.1}$$

$$\begin{aligned} T_h(x,y,t) = T_e &+ \Delta T_1(x,y).[1 - \exp(-t/\tau_{1h}(x,y))] \\ &+ \Delta T_2(x,y).[1 - \exp(-t/\tau_{2h}(x,y))] \end{aligned} \tag{6.2}$$

where T is the temperature transient during thermal recovery from heating or cooling, T_e is the temperature at steady state, τ_1 and τ_2 time constants, the subscripts c and h indicates cooling and heating phase, respectively. Time constants τ_1 and τ_2 of the models can be identified using readily available nonlinear fitting functions. In order to establish diagnosis criteria, averaged values for time constants of the healthy tissue, $\bar{\tau}_{ref}$, are used as references in normalised time constants defined by:

$$\tau_{norm} = \frac{\tau - \bar{\tau}_{ref}}{\tau + \bar{\tau}_{ref}} \tag{6.3}$$

Normalised values of time constant would eliminate any change in blood perfusion in a patient or between a group of patients [39].

Different types of excitations and cooling mode have been used. Forced convection was applied using two different cooling units. The first is a cryotherapeutic unit designed for clinical applications that uses expanded carbon dioxide mixed with air and provides a cooling stream from 0 °C to ambient temperature. The second industrial air conditioning unit blows air at temperatures in the range of 5 °C to ambient temperature. Both units are supplied with disposable air filters to insure aseptic conditions during cooling. Ice held in a thin plastic bag was used for localised cooling of the tested tissue. Controlled cooling periods were between 30 and 60 s. Halogen lamps were used to heat the surface of tissues to a maximum temperature of 48 °C.

Active Dynamic Thermography procedures have been applied for burns diagnosis [41], quality evaluation of cardio-surgery procedures [42] and post-surgery wound healing [43]. Despite the promising results that have been obtained [38], the use of ADT in breast diagnosis has received little attention [44, 45]. Active dynamic thermography was performed on a small-scale study group of three women with proven breast cancer (mammography and biopsy). In order to achieve heating, the breast surface was exposed to light from halogen lamps of electrical power of 1000 W located 50 cm from the breast surface, for a period of 30 s. Parametric images of time constants τ_{1c} and τ_{2c} were obtained but not presented for all the

three women's breasts. Further, interpretations of parametric images were not given because of the complex structure of breast tissue, limited heating power and limited depth of detectable cancers.

Generally, research studies have identified problems of implementing ADT in medicine caused by the complex structure of tissues, variability of thermal properties between patients, movement of patient during imaging due to breathing and technical limitations inherent to the type of external heating or cooling source. Therefore, the main challenges of the research studies were as follows [46]:

1. Define optimal excitation sources which induce the best thermal contrast in each specific medical diagnosis problem. Sources should be non-invasive, safe and aseptic, easy to use and reliable.
2. Determine the required characteristics of the imaging system (thermal resolution and spectral range) to be used with a particular excitation.
3. Identify sources of errors that may affect the final parametric images.

The performances of heating and cooling sources have been extensively investigated for medical applications. Cooling was found to be safer than heating [46]. The change of skin temperature up to 20 °C was found comfortable for a patient. The signal to noise ratio was higher for cooling than for heating. It was also suggested that heating should never exceed 42 °C and that the best condition for cooling is at room temperature to avoid thermal gradient and heat exchange with the environment. However, when electric fans were used for cooling, it was difficult to control the energy level and the uniformity of cooling. The later also depends on the shape of the tested tissue. Overall, cooling experiments showed that the excitation should not last for more than one minute in order to minimise the effect of the thermoregulatory mechanism. For the instrumentation requirement, a minimum infrared camera resolution of 0.1 °C and a recording rate of at least 30 images per second was recommended. Interference between the heating sources and the thermal radiation from the tested tissue should be avoided. To improve the quality of parametric images, thermal images should be pre-processed using algorithms for motion compensation caused by unintentional patient displacement and for noise filtering. In some applications of ADT, recording of thermal images have to be synchronised with natural movement of the body caused mainly by breathing or by heart beating in the case of cardiovascular surgery.

However, it has been reported that the main challenge to which are faced every application of ADT in medicine, is the interpretation of the parametric images of time constants. It has been observed that different stresses yield different parametric images reflecting information about blood perfusion, thermal diffusivity and metabolic heat generation. Nevertheless, promising clinical results were obtained by a versatile instrumentation that could be used for the quantitative and qualitative analysis of dynamic thermography in various medical applications [38].

7 Numerical Modelling of Breast Dynamic Thermography

Numerical simulations are a powerful means of understanding and optimising breast thermography. So far, several numerical techniques have been used to examine conditions that affect breast surface temperature and steady state thermal contrast in the presence of a tumour. The effect of factors such as blood perfusion, tumour characteristics including depth and diameter as well as environmental characteristics affecting thermography measurements, namely ambient temperature and heat transfer coefficient, have all been investigated [47–53]. Nevertheless, none of these numerical methods obtained the details of tumour characteristics from steady state and transient thermograms.

In the late 70s, Chen et al. [54] studied the feasibility of determining interior information from temperature transients, and investigated its limitations. It was shown that it is almost impossible to determine the metabolic heat of an embedded source from sequential thermograms. However, Chen et al. [54] proposed a theoretical method to determine blood perfusion of a volumetric heat source from time-dependent thermographic observations. A two-dimensional numerical model was used with no specific inversion technique. The procedure consists of varying the air flow and the ambient temperature impulsively and recording the temperature transients for a fixed duration. Computer-based harmonic analysis was then used to determine the blood perfusion.

Although it is useful to detect the presence of a tumour by determining the change in blood perfusion in the surrounding tissue after cooling, it is also interesting to use thermal recovery to derive information about tumour's parameters such as depth, diameter and blood perfusion. Such characterisation represents numerically an ill-posed inverse numerical problem that can be impractical to solve due to the complexity of the boundary conditions. Therefore, the main objectives of numerical modelling of breast dynamic thermography are to examine optimal conditions for cooling that induce larger thermal contrasts during thermal recovery of the breast and to identify thermal recovery parameters that could be correlated with tumour's characteristics.

To this end, it is necessary to describe a heat transfer model for the breast with and without a tumour and to implement a numerical scheme for a breast's model geometry. This later should provide a steady state solution for breast thermography and transient solutions during cooling and the subsequent thermal recovery.

7.1 A Heat Transfer Model for the Breast

Heat conduction, blood perfusion and metabolic heat generation all influence the mechanism of heat and associated temperature fields in biological materials. There is a general agreement that it is difficult to model the mechanism of blood perfusion, due to the complex structure of the perfused tissue. There have been two types of

approaches: a continuum approach and a vascular approach. In the continuum approach [23, 55–57], a single parameter is used to represent the effect of all blood vessels. On the other hand, in the vascular approach each blood vessel is considered individually in terms of its thermal effect [58, 59]. The earliest continuum model, Pennes [23] bioheat transfer equation, represents the effects of the blood flow using a single heat source, which is nonlinear in the sense that it is itself temperature dependent. Other models have been proposed to overcome the shortcomings of Pennes model by considering the influence on heat transfer of blood flow within elements of the vascular network. There are several critical reviews of heat transfer models in biological materials, including [60–64]. However, Pennes equation has been shown to have a high level of validity when vessels larger than 500 μm are concerned [65].

Because the use of a vascular model requires detailed knowledge of the breasts microvascular network which varies from one woman to another, continuum models are more attractive, and Pennes bioheat equation (7.1) has been extensively used to model heat transfer in the breast. We recall this as:

$$\rho c \frac{\partial T}{\partial t} = \nabla . k \nabla T - \omega_b \rho_b c_b (T - T_a) + Q_m, \tag{7.1}$$

where the symbols have the meanings given previously. Heat transfer between the surface of the breast and the surrounding ambient is by radiation and convection, with additional cooling as the result of evaporation of sweat. These processes can be expressed as [66]:

$$-k \frac{\partial T}{\partial n}\bigg|_{\text{skin}} = h_f (T_s - T_f) + \sigma \varepsilon \left(T_s^4 - T_f^4\right) + Q_e, \tag{7.2}$$

where n is the normal vector at the surface; h_f (W m^{-2} C^{-1}) is the convection heat transfer coefficient; T_s and T_f are temperature of the skin and the surrounding air, respectively; ε is the skin emissivity, and σ the Stefan–Boltzman constant; Q_e is the evaporative heat loss.

Since changes in air temperature, circulation and humidity all cause changes in the thermogram of a breast, a strict protocol is needed for recording thermograms. Protocols developed so far include environmental specification, as well as requirements relating to the patient's condition. Imaging room temperature should fall within the range 18–22 °C to promote cooling by vasoconstriction and the flow of heat to the breast surface by air convection needs to be minimized [66]. To this end, heat-generating equipment such as computers should be located outside the examination room. Amalu et al. [67] pointed out that such temperatures do not cause patients to either shiver or perspire. Patients are also ideally recommended to avoid consuming alcohol, tea or coffee, eating heavy meals, smoking, sunbathing, using cosmetic preparations or undertaking strenuous exercise before examination, since these can have an effect on skin temperatures [68, 69].

When appropriate protocols are followed, Draper and Boag [66] showed that total heat loss may be considered to be proportional to $(T_s - T_f)$, assuming that $(T_s - T_f)$ is small. Thus the boundary condition at the breast surface is reduced to

$$-k\frac{\partial T}{\partial n}\bigg|_{\text{skin}} = h_0(T_s - T_f), \tag{7.3}$$

where h_0 is a constant referred to as the surface conductance which combines the effect of radiative and convective heat coefficients:

$$h_0 = h_{\text{conv}} + h_{\text{rad}} \tag{7.4}$$

If the environment is suitably controlled, the heat loss associated with evaporation may be rendered negligible. It is difficult to estimate accurately the convection heat loss from the patient. However, Winslow et al. [70] studied the influence of air movement on convective heat loss from the whole body. For wind speeds between 2.6 and 0.46 m s^{-1} they derived the empirical formula:

$$h_{\text{conv}} = 12.1\left(v^{0.5}\right) \text{W m}^{-2}\,^{\circ}\text{C}^{-1}, \tag{7.5}$$

where v is the wind speed. This approach yields values of h_{conv} for the upper breast surface of 4.6 W m^{-2} °$C^{-1}$and for the lower surface of the breast of 5 W m^{-2} °C^{-1}. If $(T_s - T_f)$ is small in comparison to the average temperature T_m, then we can consider the heat loss due to radiation to be $4\sigma\varepsilon T_m^3$ where $T_m = (T_s + T_f)/2$, so that

$$h_{\text{rad}} = 4\sigma\varepsilon T_m^3 \tag{7.6}$$

Mitchell et al. [71] found that, at thermal radiation wavelengths, the emissivities of black and white skin were within 1% of unity throughout the whole range. Since T_m is likely to vary between a minimum of 22 °C and a maximum of 27 °C, Eq. (7.6) suggests that h_{rad} varies between 5.95 and 6.15 W m^{-2} C^{-1}.

Draper and Boag [66] recorded a total heat loss of $h_0 = 10.4$ W m^{-2} C^{-1} when ambient air is stationary and values in the range of $h_0 = 12$ and 24 W m^{-2} C^{-1} when air at speeds in the range of 0.2–2 m s^{-1} flows over the surface of the breast. Osman and Afify [72], on the other hand, evaluated the heat transfer coefficient representing the combined effect of radiation, convection and evaporation, as $h_0 = 13.5$ W m^{-2} C^{-1}.

The presence of a tumour in the breast can be accounted for by implementing the corresponding metabolic heat generation and blood perfusion or thermal conductivity. Gautherie et al. [73] showed that the time necessary for the tumour to double, τ, and the metabolic heat are related by a hyperbolic function:

$$Q_m = \frac{3.27 \times 10^6}{468.5\ln(100D) + 50} \text{W m}^{-3}, \tag{7.7}$$

where D is the diameter of the tumour assumed of spherical shape. Gautherie [74] estimated a global effective thermal conductivity for a cancerous breast tissue, the value of which was enhanced to include the effect of blood perfusion. The estimated value was 0.511 W m^{-1} °C^{-1}. By assuming that the thermal conductivity of the tumour tissue matches that of the glandular tissue at 0.48 W m^{-1} °C^{-1}, Ng and Sudharsan [51] used the enhancement in the thermal conductivity value of 0.03 W m^{-1} °C^{-1} to calculate tumour blood perfusion. Using mathematical and physical models, Priebe [75] established an incremental relationship between blood flow and thermal conductivity: a variation of blood flow of 150 ml min^{-1} per 100 g of tissue results in a change of thermal conductivity of about 0.05 W m^{-1} °C^{-1}. Correspondingly, the enhancement in the tumour blood perfusion is 90 ml min^{-1} per 100 g.

7.2 A Numerical Procedure for Transient Thermography

To solve the previous heat transfer model, a breast's model geometry needs to be defined. From a knowledge of breast anatomy [76, 53] developed a two dimensional model in which the various layers of the breast (subcutaneous, gland and fat), were modelled using layers of various thickness close to the actual shape. Later, a three dimensional breast model with an embedded tumour was used to examine numerically the effectiveness of subtraction thermography during breast thermal recovery after cold stress [77]. The cooling of the breast was not considered, although a lumped thermal analysis was used to estimate the extent to which the cold layer, induced by an instantaneous change in the ambient temperature, penetrated the breast and to develop an approximate model for vasoconstriction. During thermal recovery, a time-dependent model for blood perfusion was used for the three quadrants of the breast affected by vasoconstriction whilst the tumour of diameter 32 mm, was located at the upper quadrant of the breast that was assumed unaffected by cold stress. The model was numerically solved using FASTFLO calculator, which solves partial differential equations dedicated for CFD (computational fluid dynamics). The temperature's map observed after 60 min of recovery from cold stress was almost the same as the steady state temperature distribution. Unlike the observation of Usuki et al. [31] that subtraction thermography may enhance thermal contrast, subtraction of thermal profiles obtained for 1, 3 and 5 min during thermal recovery did not yield any improvement in the thermal contrast or give information not available using the steady state thermogram.

Numerical simulation of dynamic thermography using a three-dimensional model based on a hemisphere with and without a tumour could pose problems in terms of computer processing times and memory storage due to the large number of thermograms that would need to be captured and processed during the phase of thermal recovery. In addition, the use of such models for comparing the effectiveness of different cooling methods is rather impractical. An alternative breast

model geometry has been suggested by Amri et al. [47]. Based on the model of Ng and Sudharsan [51], the breast model shown in Fig. 3 consists of a 5 mm thick fat and gland which thickness H of at least 45 mm. The embedded tumour was assumed to be spherical and of diameter D and metabolic heat Q_m. The use of such a model for steady state thermography has shown consistency with the results obtained using hemispherical models. The breast model of Fig. 3 was recently used by Amri et al. [78] to examine numerically the dynamic breast thermography after cold stress using the Transmission Line Matrix (TLM) method [79].

The numerical procedure starts by solving Pennes bioheat equation (7.1) at steady state, subject to the following conditions:

$$-k\frac{\partial T}{\partial z} = h_0(T_f - T) \quad \text{at } z = 0 \text{ and } T = T_c \text{ at } z = H \tag{7.8}$$

$$-k\frac{\partial T}{\partial x} = 0 \quad \text{at } x = 0 \text{ and } -k\frac{\partial T}{\partial x} = 0 \text{ at } x = L \tag{7.9}$$

$$-k\frac{\partial T}{\partial y} = 0 \quad \text{at } y = 0 \text{ and } -k\frac{\partial T}{\partial y} = 0 \text{ at } y = L \tag{7.10}$$

Perfect thermal contact is assumed between the breast tissue and the tumour.

$$\begin{cases} T_b(x,y,z) = T_t(x,y,z) \\ \frac{\partial T_b}{\partial n} = \frac{\partial T_t}{\partial n} \end{cases} \tag{7.11}$$

Subscribes b and t denote breast and tumour respectively. The change in the temperature of the surface, associated with the presence of a tumour, is evaluated

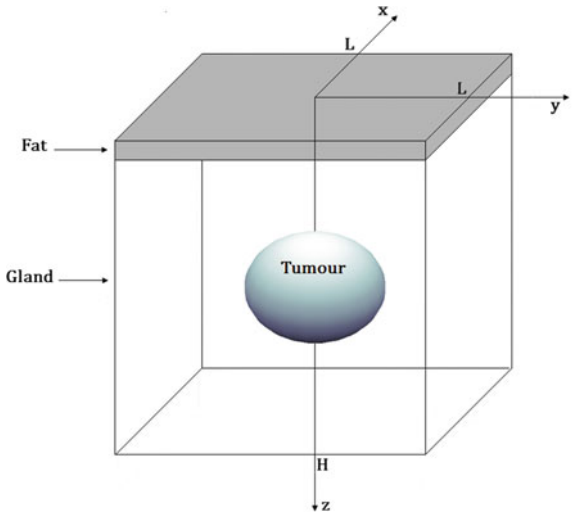

Fig. 3 A three-dimensional breast model geometry [78]

using a parameter known as the steady state thermal contrast, C_{ss}. This is defined as the difference between the maximum temperature reached in the presence of a tumour and the temperature at the surface of the normal breast.

$$C_{ss} = \max(T_{tumour}) - T_{healthy} \tag{7.12}$$

Tumour diameters of 10, 20 and 30 mm at depths of dp = 5, 7.5, 10, 15, 20 and 30 mm were considered. The depth is defined as the distance between the breast surface and the top of the tumour. The steady state thermal contrast C_{ss} illustrated in Fig. 4 shows that, irrespective of tumour diameter, steady state thermography is best suited to detect tumours at depths less than 20 mm. An infrared camera with a thermal resolution of 0.1 °C can be used, though higher resolution is desirable. Beyond this depth, it is difficult to distinguish the tumour diameter and depth as they lead to almost identical steady state thermal contrast C_{ss}. Thus, if the thermal contrast is small, this may indicate a deep tumour but does not give information about the tumour's diameter.

With the tissue initially in a state of thermal equilibrium, a cold stress temperature T_{cold} was applied on the surfaces of both the normal (healthy) breast and the cancerous breast during a cooling period t_{cool}. Pennes equation was then solved using a constant boundary condition:

$$T = T_{cold} \quad \text{for} \quad 0 < t \leq t_{cool} \tag{7.13}$$

To estimate how far into the breast tissue the effect of surface chilling penetrates, it is helpful to define the thermal penetration depth δ_p. The temperature of the tissue when the penetration depth has been reached should satisfy [24]:

$$\frac{\partial T(z,t)}{\partial z} = 0 \quad \text{at} \quad z = \delta_p(t) \tag{7.14}$$

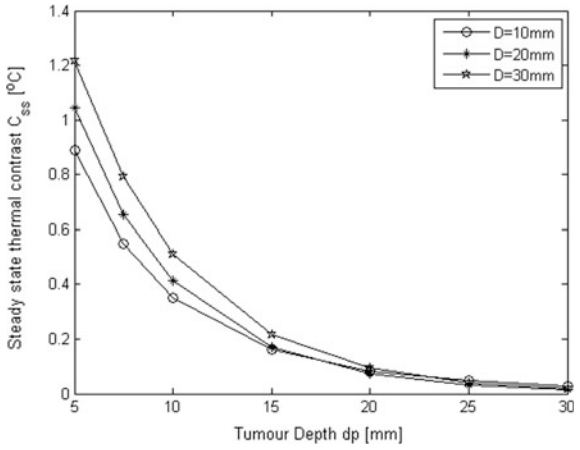

Fig. 4 Thermal contrast plotted against tumour diameter and depth at steady state

$$T(z,t) = T_i \quad \text{at} \quad z = \delta_p(t) \tag{7.15}$$

where T_i is the initial temperature. Although some clinical studies that have been reported in earlier sections used fan cooling of the breast, it has been criticised for producing nonuniform cooling and for being difficult to control. Therefore localised cooling seems to be an ideal choice as long as cooling is applied for short periods of time to avoid patient's shivering.

In order to study the effect of cold stress temperature T_{cold} and the cooling period t_{cool} on the thermal transients, cold temperatures of 5, 10 and 15 °C and cooling periods of 10, 20, 30, 60 and 120 s have been examined. Figure 5 represents the variation of the penetration depth versus the cooling time. The horizontal line represents the rear boundary of the fat layer. Equations (7.14) and (7.15) predict that a minimum cooling period of 20 s is required for the cold front to reach the gland region where a tumour is likely to be. When cooling for a maximum of 2 min, the thermal cold front penetrates about 14 mm into the breast, so that tumours located deeper in the breast are uncooled.

After the cold stress was removed, the surface temperatures on both breasts were recorded throughout the rewarming period of 60 min; this is consistent with [23] that skin temperature at the forearm needs 30–60 min to return to steady state after the end of chilling. During thermal recovery, both normal and cancerous breasts exchange with adiabatic ambient via radiation and convection. To evaluate the efficiency of the cold stress on the enhancement of temperature differences between the breasts, the transient thermal contrast is again defined by:

$$C_{max}(t) = \max[T_{tumour}(t)] - T_{healthy}(t) \tag{7.16}$$

To enable tracking of the maximum temperature, the steady state thermogram may help since the location of the maximum temperature can be identified. It might then be helpful to mark the hot spot location on the cancerous breast and on the

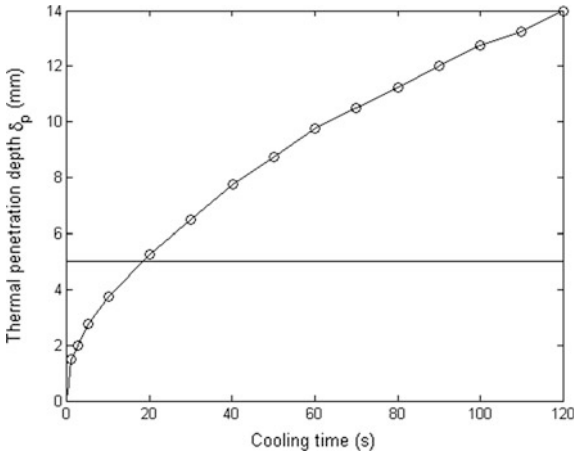

Fig. 5 Influence of cooling period on the thermal penetration depth. The *horizontal line* indicates the edge of the fat layer

corresponding contralateral symmetrical part of the normal breast. There is then no need to monitor the dynamic change in the surface temperature of the whole of the suspicious breast so storage of enormous amounts of data can be avoided.

The diagnostic value of cold stress was assessed by comparing the transient and steady state thermal contrasts and by extracting information about the tumour's size and depth. The effects of the temperature and the duration of the chilling process on the transients were examined for different tumours at different depths and of different diameters.

Figure 6 illustrates a typical transient thermal contrast during the rewarming transient. Since the objective of dynamic thermography is to enhance thermal contrast, it is useful to use the steady state thermal contrast as a reference. This is identified by the dash dotted line in Fig. 6. Initially, the contrast rises to the steady state thermal contrast C_{ss}, then increases further as time continues to reach a contrast peak, C_{peak}, at a peak time τ_{peak}. After this time, the thermal contrast decreases and thermal equilibrium is reached by the end of the monitored period.

To evaluate how useful dynamic thermography after cold stress can be, the magnitude of the contrast peak and its corresponding peak time, have been derived from thermal contrasts transients. This has been done for tumours having a range of diameters and being located at a range of depth. The data obtained are presented in Fig. 7.

Figure 7a shows similar trends as steady state thermal contrast shown in Fig. 4. It seems that the magnitude of the contrast peak is determined by the penetration depth of figure (Fig. 5). Higher contrast peak values have been obtained for tumours which have been affected by cooling located at depth less than 15 mm. Dynamic thermography was unable to enhance thermal contrast for tumours at depth 20 mm or more. It has also found that the use of lower temperatures does increase the transient peak for tumours located near the surface. This suggests that, chilling temperatures marginally less than ambient temperature are all that is necessary and chill duration needs to be no longer than 1 min. Such a protocol should not prove particularly uncomfortable or inconvenient to patients.

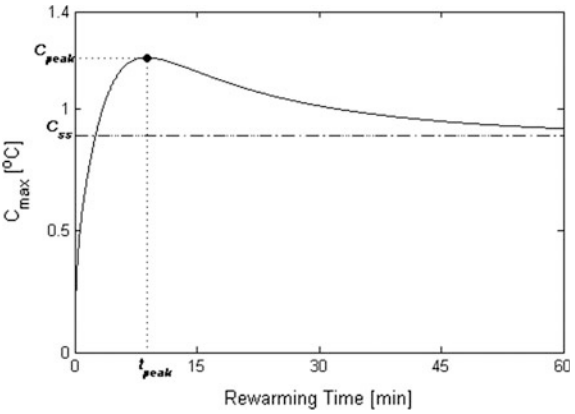

Fig. 6 Schematic of the variation of the maximum contrast as thermal recovery occurs after the end of cold stress. The *dashdot horizontal line* represents the steady state thermal contrast, and the *filled circle* corresponds to the contrast peak

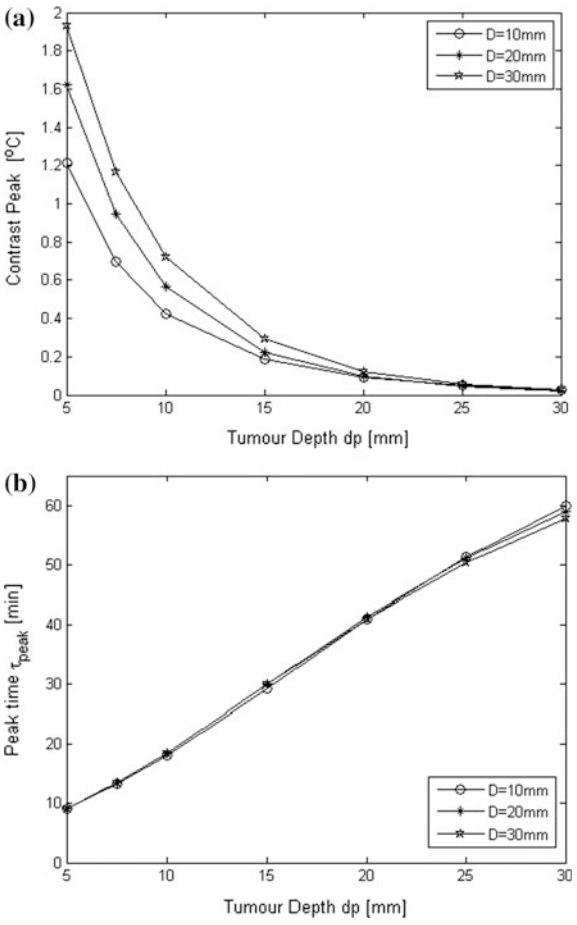

Fig. 7 Effect of tumour size and depth on **a** the contrast peak and **b** the corresponding peak time after cooling at T_{cold} = 5 °C during t_{cool} = 1 min

The measure of the corresponding peak time values shown in Fig. 7b would be critically dependent on the responsivity associated with the infrared camera in order to locate the contrast peak. This is particularly important for tumours located 20 mm deep and more. Nevertheless, the peak time seems to be directly related to the tumour's depth and independent of the tumour's diameters. It was also found that the peak time does not vary significantly with the magnitude of the cooling temperature or the period of cooling. This would make details of the measurement protocols in the clinical environment less important. In the light of the continuing progress in the infrared imaging technology and the development of software that include motion as well as noise compensation tools, measurements of the peak time may become more feasible in the near future.

8 Conclusion

Dynamic thermography techniques have been utilised in a variety of diagnostic applications including breast cancer. Clinical experiments have observed enhanced thermal contrast after artificially cooling the breast and have demonstrated the ability of increasing the accuracy of breast cancer diagnosis. Various computer techniques have been deployed to process sequential thermograms during thermal recovery of the breast including subtraction thermography and μ-thermography. These techniques have been applied to small-sample breast cancer studies and have revealed information pertaining to the change in thermal parameters of the breast associated with the presence of a tumour. The complexity of the thermal findings has caused major difficulties for the clinical interpretation of thermal parametric images. Some research studies investigated the change in blood perfusion caused by the presence of a tumour. These studies employed localised cooling on the area that shows hot spot on steady state thermograms and its contralateral part. Although results were promising, the rate of false positive was a major constraint to this technique and might relate to protocol and instrumentation issues. Other clinical studies used the autonomic cold challenge by cooling patient's extremities in order to identify new tumour's blood vessels known as neoangiogenesis but research findings did not correlate with the presence of the tumour.

In an attempt to understand skin's temperature transient after cold stress, a mathematical model for a homogenous one-dimensional skin slab was developed. The analytical solution showed that a two-exponential temperature transient model is a good fit for the thermal recovery of the skin after direct chilling and that the corresponding time constants are related to the thermal properties of the tissue as well as to its blood perfusion. When modelling skin with an embedded heat source representing a tumour, a numerical study showed that it is possible to extract a tumour's blood perfusion from temperature transients after cooling the skin by convection. However, it was not possible to extract the tumour's parameters such as metabolic heat, size and location during thermal recovery and that even the use of inverse numerical models would fail, due to the complexity of the problem. However, a more recent simulation study of dynamic breast thermography after cooling the breasts at a constant temperature for a period of time of two minutes or less, showed an enhancement in the contrast peak for tumours at depth 20 mm or less. Furthermore, it was found that the time corresponding to the contrast peak, referred to as the peak time, was directly related to the tumour's depth and independent of the tumour diameter. It was also shown that the peak time does not correlate with the cold stress temperature or the duration of the cooling phase which give it the potential to be an indicator of tumour depth. Although it might be interesting to obtain information about the tumour's diameter, depth is the more important parameter in breast tumours diagnosis as the tumour's diameter can be estimated by palpation during physical examination.

Until now, different techniques have been applied to cool the breast and to process the thermal recovery. Overall, each processing technique of breast thermal

recovery has contribute unique information about the presence of an abnormality in the breast such as a change in blood perfusion, an alteration in the breast thermal parameters or by estimating its depth. Therefore, in the light of the continuing progress in infrared imaging instrumentation, dynamic breast thermography justifies thorough research interest in order to conclude about its usefulness in breast cancer diagnosis.

References

1. Lawson, R.: Implications of surface temperatures in the diagnosis of breast cancer. Can. Med. Assoc. J. **75**, 309 (1956)
2. Williams, K.L., Williams, F.L., Handley, R.: Infra-red radiation thermometry in clinical practice. Lancet **276**, 958–959 (1960)
3. Williams, K.L., Williams, F.L., Handley, R.: Infra-red thermometry in the diagnosis of breast disease. Lancet **278**, 1378–1381 (1961)
4. Barnes, R., Gershon-Cohen, J.J.: Clinical thermography. JAMA **185**, 949–952 (1963)
5. Barnes, R.B.: Thermography of the human body. Science (Infrared-radiant energy provides new concepts and instrumentation for medical diagnosis) **140**, 870–877 (1963)
6. Freeman, H., Linder, F.E., Nickerson, R.F.: The bilateral symmetry of skin temperature: one figure. J. Nutr. **13**, 39–49 (1937)
7. Sheard, C., Williams, M.M.D.: Skin temperatures of the extremities and basal metabolic rates in individuals having normal circulation. Proc. Staff Meet. Mayo Clin. **15**, 758–762 (1940)
8. Williams, K.L.: Infrared thermometry as a tool in medical research. Ann. N. Y. Acad. Sci. **121**, 99–112 (1964)
9. Williams, K.L.: Pictorial heat scanning. Phys. Med. Biol. **9**, 433 (1964)
10. Barnes, R.B.: Thermography. Ann. N. Y. Acad. Sci. **121**, 34–48 (1964)
11. Astheimer, R.W., Wormser, E.M.: High-speed infrared radiometers. J. Opt. Soc. Am. **49**, 179–183 (1959)
12. Amalric, D., Giraud, D., Altschule, C., Spitalier, J.: Value and interest of dynamic telethermography in detection of breast cancer. Acta Thermograph **1**, 89–96 (1976)
13. Gautherie, M., Haehnel, P., Walter, J., Keith, L.: Long-term assessment of breast cancer risk by liquid-crystal thermal imaging. Prog. Clin. Biol. Res. **107**, 279–301 (1981)
14. Cockburn, W.: Announcement of Official Change in Thermal Reporting [Online]. Available: http://www.thermologyonline.org/breast/breast_q_a/bqa_coldstress.htm (2005)
15. Kane, R.L.: Considerations in the Applications of Various Cooling Methods During Breast Thermography Stress Studies [Online]. International Academy of Clinical Thermology. Available: http://www.iact-org.org/articles/articles-considerations.html (2002)
16. Leando, P.: Cold Stressing Breasts and Why Don't We Do It Anymore and the Thermal Rating System [Online]. American College of Clinical Thermology. Available: http://acct-blog.com/category/cold-stressing-breast/ (2003)
17. Amalu, W.C.: Nondestructive testing of the human breast: the validity of dynamic stress testing in medical infrared breast imaging. In: Engineering in Medicine and Biology Society, 2004. IEMBS'04. 26th Annual International Conference of the IEEE, pp. 1174–1177. IEEE (2004)
18. Nagasawa, A., Okada, H.: Thermal recovery. In: Atsumi, K. (ed.) Medical Thermography. University of Tokyo Press, Tokyo (1973)
19. Cary, J., Mikic, B.: A thermal analysis of human tissue with applications to thermography. In: 2nd International Symposium on the Detection and Prevention of Cancer, Bologna, Italy (1973)

20. Cary, J., Kalisher, L., Sadowsky, N., Mikic, B.: Thermal evaluation of breast disease using local cooling 1. Radiology **115**, 73–77 (1975)
21. Steketee, J.: Thermografie van het voorhoofd. *Jubilee edition of reports*. Erasmus University, Rotterdam (1978)
22. Steketee, J., Van der Hoek, M.: Thermal recovery of the skin after cooling. Phys. Med. Biol. **24**, 583 (1979)
23. Pennes, H.H.: Analysis of tissue and arterial blood temperatures in the resting human forearm. J. Appl. Physiol. **1**, 93–122 (1948)
24. Carslaw, H.S., Jaeger, J.C.: Conduction of Heat in Solids, 2nd edn. Clarendon Press, Oxford (1959)
25. Spiegel, M.: Schaum's Outline of Laplace Transforms. McGraw-Hill Education (1965)
26. Newman, P., Evans, A.L., Davison, M., Jackson, I., James, W.B.: A system for the automated diagnosis of abnormality in breast thermograms. Br. J. Radiol. **50**, 231–232 (1977)
27. Uchida, I., Onai, Y., Ohashi, Y., Tomaru, T., Irifune, T.: quantitative diagnosis of breast thermograms by a computer. J. Jpn Radiol. Soc. Radiol. **39**, 401–411 (1979)
28. Winter, J., Stein, M.A.: Computer image processing techniques for automated breast thermogram interpretation. Comput. Biomed. Res. **6**, 522–529 (1973)
29. Ziskln, M.C., Negin, M., Piner, C., Lapayowker, M.S.: Computer diagnosis of breast thermograms. Radiology **115**, 341–347 (1975)
30. Geser, H., Bosinger, P., Stucki, D., Landolt, C.: Computer-assisted dynamic breast thermography. Thermology **2**, 538–544 (1987)
31. Usuki, H., Teramoto, S., Komatsubara, S., Hirai, S., Misumi, T., Murakami, M., Onoda, Y., Kawashima, K., Kino, K., Yamashita, K.: Advantages of subtraction thermography in the diagnosis of breast disease. Biomed. Thermol. **11**, 286–291 (1991)
32. Uchida, I., Ohashi, Y., Onai, Y., Yamada, Y., Tomaru, T.: Quantitative analysis of sequential thermograms 1. In: Development of a Physiological Functional Image Processing System for Dynamic Thermography after Cooling (1988)
33. Uchida, I., Ohashi, Y., Sato, Y., Yamada, Y., Oyamada, H., Tomaru, T., Onai, Y., Ito, A.: Effectiveness of pathophysiological functional thermal images in the diagnosis of breast thermography. Jpn Radiol. Phys. **10**, 101–106 (1990)
34. Ohashi, Y., Uchida, I.: Some considerations on the diagnosis of breast cancer by thermography in patients with nonpalpable breast cancer. In: Engineering in Medicine and Biology Society, 1997. Proceedings of the 19th Annual International Conference of the IEEE, vol. 2, pp. 670–672, 30 Oct–2 Nov 1997
35. Ohashi, Y., Uchida, L.: Applying dynamic thermography in the diagnosis of breast cancer. Eng. Med. Biol. Mag. IEEE **19**, 42–51 (2000)
36. Arora, N., Martins, D., Ruggerio, D., Tousimis, E., Swistel, A.J., Osborne, M.P., Simmons, R.M.: Effectiveness of a noninvasive digital infrared thermal imaging system in the detection of breast cancer. Am. J. Surg. **196**, 523–526 (2008)
37. Maldague, X.P.: Theory and Practice of Infrared Technology for Nondestructive Testing. Wiley, New York (2001)
38. Kaczmarek, M., Nowakowski, A.: Active IR-thermal imaging in medicine. J. Nondestr. Eval. **35**, 1–16 (2016)
39. Nowakowski, A., Kaczmarek, M.: Active dynamic thermography—problems of implementation in medical diagnostics. Quant. InfraRed Thermogr. J. **8**, 89–106 (2011)
40. NowakowskI, A.: Quantitative Active Dynamic Thermal IR-Imaging and Thermal Tomography in Medical Diagnostics. Medical Infrared Imaging, CRC Press (2012)
41. Renkielska, A., Kaczmarek, M., Nowakowski, A., Grudzinski, J., Czapiewski, P., Krajewski, A., Grobelny, I.: Active dynamic infrared thermal imaging in burn depth evaluation. J. Burn Care Res. **35**, e294–e303 (2014)
42. Kaczmarek, M., Rogowski, J.: The role of thermal monitoring in cardiosurgery interventions. In: Bronzino, J.D., Peterson, D.R. (eds.) Biomedical Signals, Imaging, and Informatics. CRC Press (2014)

43. Moderhak, M., Nowakowski, A., Kaczmarek, M., Siondalski, P., Jaworski, Ł.: Active dynamic thermography imaging of wound healing processes in cardio surgery. In: Piętka, E., Kawa, J., Wieclawek, W. (eds.) Information Technologies in Biomedicine, vol. 4. Springer International Publishing, Cham (2014)
44. Kaczmarek, M., Nowakowski, A.: Analysis of transient thermal processes for improved visualization of breast cancer using IR imaging. In: Engineering in Medicine and Biology Society, 2003. Proceedings of the 25th Annual International Conference of the IEEE, pp. 1113–1116. IEEE (2003)
45. Kaczmarek, M., Nowakowski, A.: Active dynamic thermography in mammography. Task Quart. **8**, 259–267 (2004)
46. Nowakowski, A.: Limitations of active dynamic thermography in medical diagnostics. In: Engineering in Medicine and Biology Society, 2004. IEMBS'04. 26th Annual International Conference of the IEEE, pp. 1179–1182. IEEE (2004)
47. Amri, A., Saidane, A., Pulko, S.: Thermal analysis of a three-dimensional breast model with embedded tumour using the transmission line matrix (TLM) method. Comput. Biol. Med. **41**, 76–86 (2011)
48. Haifeng, Z., Liqun, H., Liang, Z.: Critical conditions for the thermal diagnosis of the breast cancer. In: Bioinformatics and Biomedical Engineering, 2009. ICBBE 2009. 3rd International Conference, pp. 1–3, 11–13 June 2009
49. Hu, L., Gupta, A., Gore, J.P., Xu, L.X.: Effect of forced convection on the skin thermal expression of breast cancer. J. Biomech. Eng. **126**, 204–211 (2004)
50. Jiang, L., Zhan, W., Loew, M.H.: Modeling static and dynamic thermography of the human breast under elastic deformation. Phys. Med. Biol. **56**, 187 (2011)
51. Ng, E.Y.K., Sudharsan, N.M.: An improved three-dimensional direct numerical modelling and thermal analysis of a female breast with tumour. Proc. Inst. Mech. Eng. [H] **215**, 25–37 (2001)
52. Sudharsan, N., Ng, E.: Parametric optimization for tumour identification: bioheat equation using ANOVA and the Taguchi method. Proc. Inst. Mech. Eng. [H] **214**, 505–512 (2000)
53. Sudharsan, N., Ng, E., Teh, S.: Surface temperature distribution of a breast with and without tumour. Comput. Methods Biomech. Biomed. Eng. **2**, 187–199 (1999)
54. Chen, M.M., Pedersen, C.O., Chato, J.C.: On the feasibility of obtaining three-dimensional information from thermographic measurements. J. Biomech. Eng. **99**, 58–64 (1977)
55. Chen, M.M., Holmes, K.R.: Microvascular contributions in tissue heat transfer. Ann. N. Y. Acad. Sci. **335**, 137–150 (1980)
56. Klinger, H.: Heat transfer in perfused biological tissue—I: general theory. Bull. Math. Biol. **36**, 403–415 (1974)
57. Wulff, W.: The energy conservation equation for living tissue. IEEE Trans. Biomed. Eng. **6**, 494–495 (1974)
58. Weinbaum, S., Jiji, L.: A new simplified bioheat equation for the effect of blood flow on local average tissue temperature. J. Biomech. Eng. **107**, 131–139 (1985)
59. Weinbaum, S., Jiji, L., Lemons, D.: Theory and experiment for the effect of vascular microstructure on surface tissue heat transfer—part I: anatomical foundation and model conceptualization. J. Biomech. Eng. **106**, 321–330 (1984)
60. Stańczyk, M., Telega, J.: Modelling of heat transfer in biomechanics-a review. P. 1. Soft tissues. Acta Bioeng Biomech. **4**, 31–61 (2002)
61. Arkin, H., Xu, L., Holmes, K.: Recent developments in modeling heat transfer in blood perfused tissues. Biomed. Eng. IEEE Trans. **41**, 97–107 (1994)
62. Zolfaghari, A., Maerefat, M.: Bioheat transfer. In: Bernardes, M.A.D.S. (ed.) Developments in Heat Transfer (2011)
63. Charny, C.K.: Mathematical models of bioheat transfer. Adv. Heat Transf. **22**, 19–155 (1992)
64. Khanafer, K., Vafai, K.: Synthesis of mathematical models representing bioheat transport. Adv. Numer. Heat Transf. **3**, 87 (2009)

65. Charny, C.K., Weinbaum, S., Levin, R.L.: An evaluation of the Weinbaum-Jiji bioheat transfer model for simulations of hyperthermia. In: Roemer, R.B., Mcgrath, J.J., Bowman, H.F. (eds.) Winter Annual Meeting of the American Society of Mechanical Engineers, pp. 1–10, 10–15 Dec. San Francisco, California, New York (1989)
66. Draper, J.W., Boag, J.: The calculation of skin temperature distributions in thermography. Phys. Med. Biol. **16**, 201 (1971)
67. Amalu, W.C., Hobbins, W.B., Head, J.F., Elliott, R.L.: Infrared imaging of the breast-an overview. In: Bronzino, J.D. (ed.) Biomedical Engineering Handbook, 3rd edn. CRC Press (2006)
68. Lahiri, B., Bagavathiappan, S., Jayakumar, T., Philip, J.: Medical applications of infrared thermography: a review. Infrared Phys. Technol. **55**, 221–235 (2012)
69. Ng, E.Y.K.: A review of thermography as promising non-invasive detection modality for breast tumor. Int. J. Therm. Sci. **48**, 849–859 (2009)
70. Winslow, C.-E., Gagge, A., Herrington, L.: Heat exchange and regulation in radiant environments above and below air temperature. Am. J. Physiol.-Leg. Content **131**, 79–92 (1940)
71. Mitchell, D., Wyndham, C., Hodgson, T., Nabarro, F.: Measurement of the total normal emissivity of skin without the need for measuring skin temperature. Phys. Med. Biol. **12**, 359 (1967)
72. Osman, M.M., Afify, E.M.: Thermal modeling of the normal woman's breast. J. Biomech. Eng. **106**, 123–130 (1984)
73. Gautherie, M., Quenneville, Y., Gros, C.: Metabolic heat production, growth rate and prognosis of early breast carcinomas. Biomedicine **22**, 328–336 (1975)
74. Gautherie, M.: Thermology of breast cancer: measurement and analysis of in vivo temperature and blood flow. Ann. N. Y. Acad. Sci. **335**, 383–415 (1980)
75. Priebe, L.: Heat transport and specific blood flow in homogeneously and isotropically perfused tissue. Physiol. Behav. Temp. Regul. 272–280 (1970)
76. Romrell L.J., Bland, K.I.: Anatomy of the breast, axilla, chest wall and related metastatic sites. Breast: Compr. Manag. Benign Malignant Dis. 22 (1998)
77. Ng, E.Y.K., Sudharsan, N.M.: Effect of blood flow, tumour and cold stress in a female breast: a novel time-accurate computer simulation. Proc. Inst. Mech. Eng. H. **215**, 393–404 (2001)
78. Amri, A., Pulko, S.H., Wilkinson, A.J.: Potentialities of steady-state and transient thermography in breast tumour depth detection: a numerical study. Comput. Methods Programs Biomed. **123**, 68–80 (2016)
79. De Cogan, D.: Transmission line matrix (TLM) techniques for diffusion applications. Gordon and Breach Science Publishers (1998)

In Vivo Thermography-Based Image for Early Detection of Breast Cancer Using Two-Tier Segmentation Algorithm and Artificial Neural Network

Asnida Abd Wahab, Maheza Irna Mohamad Salim and Maizatul Nadwa Che Aziz

Abstract Breast cancer is the most common form of cancer among women globally. Detecting a tumor at its early stages is very crucial for a higher possibility of successful treatment. Cancerous cells have high metabolic rate which generate more heat compared to healthy tissue and will be transferred to the skin surface. Thermography technique has distinguished itself as an adjunctive imaging modality to the current gold standard mammography approach due to its capability in measuring the heat radiated from the skin surface for early detection of breast cancer. It provides an additional set of functional information, describing the physiological changes of the underlying thermal and vascular properties of the tissues. However, the thermography technique is shown to be highly dependent on the trained analyst for image interpretation and most of the analyses were conducted qualitatively. Therefore, the current ability of this technique is still limited especially for massive screening activity. This chapter presented a proposed technical framework for automatic segmentation and classification of abnormality on multiple in vivo thermography-based images. A new two-tier automatic segmentation algorithm was developed using a series of thermography screening conducted on both pathological and healthy Sprague-Dawley rats. Features extracted show that the mean values for temperature standard deviation and pixel intensity of the abnormal thermal images are distinctively higher when compared to normal thermal images. For classification, Artificial Neural Network system was developed and produced a validation accuracy performance of 92.5% for thermal image

A.A. Wahab (✉) · M.I.M. Salim · M.N.C. Aziz
Faculty of Biosciences and Medical Engineering, Universiti Teknologi Malaysia, V01 Satellite Building, Skudai, Johor, Malaysia
e-mail: asnida@biomedical.utm.my

M.I.M. Salim
e-mail: maheza@biomedical.utm.my

M.N.C. Aziz
e-mail: nadwaaziz@gmail.com

E.Y.K. Ng and M. Etehadtavakol (eds.), *Application of Infrared to Biomedical Sciences*, Series in BioEngineering,
DOI 10.1007/978-981-10-3147-2_8

abnormality detection. In conclusion, this study has successfully demonstrated that for massive or routine screening activities, the proposed technical framework could provide a highly reliable clinical decision support to the clinicians in making a diagnosis based on the medical thermal images.

Keywords Thermography · Thermal image processing · Artificial neural network

1 Introduction

Breast cancer is the most common cancer experienced among women globally [1, 2]. The number of breast cancer incidences has steadily increased, and breast cancer has recently appeared to be the second leading cause of death in women [3]. National Cancer Institute of Canada has estimated that two out of five women will develop breast cancer during their lifetime, and approximately one out of four will die as a result of this disease [2]. Although breast cancer is highly treatable if it is detected at the early stages, the number of women diagnosed with breast cancer is at the later stage especially those in developing and third world countries due to the unavailability of portable breast imaging facilities and lack of awareness [4, 5].

Mammography technique is the current gold standard morphological-based imaging tool that is used in clinical practices globally. However, this technique exhibits low sensitivity in dense breast tissue composition or in young women. Additionally, it requires breast compression during screening and exposes to harmful radiation [6–9]. On the other hand, infrared thermography technique has shown to be a potential adjunctive tool for detecting breast cancer [10–12]. Previous studies show that the heat generated by cancerous cells due to the high metabolic rate will be transferred to the skin surface via heat conduction and heat convection through both tissue and blood vessel respectively. Infrared thermography will then measures the heat radiation emitted from the skin surface and converts it into a visual thermal image format with its respective temperature values [8, 13]. It is a non-invasive and effective alternative modality for early detection of breast cancer with simple screening procedure requirement, high accuracy for surface temperature measurement, low in cost and available in small sizes which allow mobility for bigger population coverage [10, 11, 14, 15].

With the advances in the infrared camera technology and computerized image processing system, the subtle alteration of temperature associated with underlying physiological changes is becoming more accessible in thermography, enabling high accuracy thermal-based breast cancer detection. However, this technique is highly dependent on trained analysts for thermal image interpretation which means, a single thermal image may be interpreted differently by different analysts relative to their respective skills, experiences, and health conditions [16, 17]. As a result, the clinical applicability of the thermography technique is still limited, and it is very crucial to further improve the technical aspects to increase the overall system reliability for high acceptance into a clinical practice.

Unlike any other applications of thermography (e.g., image from surveillance camera) which mainly focus on the presence of overall subject, thermal images obtained from medical thermography present a different temperature patterns and contours related to the underlying physiological changes which occur at a specific area within the subject. Thus, detecting and segmenting the symptomatic region from the rest could be a very challenging task due to the inhomogeneous nature and lack of clear limits in each subject. In addition, different camera settings and initialization that could vary the size of subject in each frame. As a consequence, most researchers prefer to manually segment or to use a semi-automatic region of interest (ROI) segmentation method for further measurement and analysis.

In the case of qualitative breast cancer diagnosis, the ROI segmented must include both breasts since clusters of lymph nodes are found in the axillar region, above the collarbone and chest. Herry and Frize have developed a contour detector using morphological operators, as a means of comparing the intensity distribution between both breasts. However, the initial segmentation of the subject has been carried out manually [18]. Lipari and Head have constructed a semi-automatic segmentation method, wherein each breast was divided into four distinct quadrants, and an asymmetrical pattern between the quadrants was used for further. But, lack of ideal body symmetry in the images has resulted in missing data for comparison [14]. Another semi-automatic segmentation has been proposed by Scales and others which comprised of eight different steps. They have reported that only 4 out of 21 images result in satisfactory ROI detection and errors were due to detection of inframammary fold and bad edge detection [19]. However, for large number of thermal images that need to be processed, both semi-automatic and manual segmentation will be time consuming with a high chance of result inconsistency due to fatigue. Motta and others have recently developed a fully automatic segmentation method based on automatic threshold and border detection, and extraction of infra mammary folds. They have used mathematical morphology and cubic spline interpolation to separate both breasts symmetrically. However, the ROI detected may exclude the portion of upper quadrant of the breast [20]. Therefore, most of the researchers are currently focusing on developing an autonomous method for breast segmentation.

Contrarily, in quantitative analysis, important features required to be extracted from the ROI and to be fed into a classification system for diagnosis purposes. In this particular case, the presence of breast images for processing is not necessary but accurate ROI detected is crucial in order to ensure that features extracted from the thermal images are highly reliable. In Schaefer and others' studies, the ROIs were segmented manually by an expert before fuzzy rule-based classification system was applied [21, 22]. On the other hand, Ng and Kee have performed manual segmentation on patients' thermal images prior feeding them in an advanced integrated breast thermography classification method [23]. However, fully automatic ROI segmentation is still preferred to reduce overall computational time and intervention by analysts especially when dealing with numerous thermal images.

Although infrared thermography has not yet been applied to clinical practice, this technique otherwise has shown to be an ideal modality for an upfront and routine breast screening due to its passive nature and simple screening procedure [10, 11]. However, a reliable classification of thermal image abnormalities would be a steadfast indicator for further assessment using other sophisticated imaging techniques. Therefore, this chapter proposed a new technical framework for thermal image computer-aided diagnosis which integrates automatic segmentation, feature extraction using both characteristics from visual and temperature data for image abnormality classification. The main focus is to assist the clinicians in analysing multiple thermal images accurately with minimal intervention and storage requirement for mass screening activities.

A process of selecting different features from both visual image (pixel based) and data temperature (temperature point) is compulsory in order to compose a feature vector for classification between abnormal and normal thermal images [24]. However, due to storage limitation, most researchers have chosen to process and extract the pixel related features available on the thermal images. Acharya and others have measured smoothness, coarseness and regularity of pixels from thermal images in order to further segregate these textures into two main classes, namely structural and statistical. Later, they have used support vector machine (SVM) method for classification [25]. Schaefer and others have extracted basic statistical features, histogram features, cross co-occurrence matrices and mutual information from the thermal images [21, 26]. In addition, Kuruganti and Qi have extracted features such as mean, variance, kurtosis, peak pixel intensity and entropy, in order to validate their proposed classification method [27]. Jakubowska and others have extracted four different image features based on histogram, co-occurrence matrix, gradient and run-length matrix. They have then utilized artificial neural network (ANN) method for classification. Nevertheless, extracting and analyzing the features from the pixel-based aspect alone for classification might introduce asynchronization of data especially when extensive preprocessing technique is carried out [28]. Therefore, Ng and Kee have extracted thermal information from the data temperature point with additional history information, to determine breast abnormalities [23]. Borchartt and others have considered features including range of temperature, mean temperature, and standard deviation of temperature in their study and used SVM to evaluate the selected features [29]. Both studies have achieved a high accuracy performance of 80.95 and 85.71% respectively.

It can be seen that different combinations and flows of image processing methods have been applied and proposed previously, in accordance with the specific objectives of each study. In general, the image segmentation and feature analysis techniques have been developed from a simple single method analysis to an advanced integration analysis techniques depending on the different objectives that need to be achieved and also the availability of image data types.

2 Data Collection

2.1 Animal Preparation

The use of animals in this study was approved by the institutional review board of the Universiti Kebangsaan Malaysia, Animal Ethics Committee (UKMAEC), Selangor Malaysia. Two groups of female Sprague-Dawley strain rats consisting of fifteen pathological (abnormal) rats and fifteen control (normal) rats weighing between 180 and 250 g were housed in polypropylene cages with wood shavings used as bedding at an ambient room temperature, as well as access to water and food ad libitum with a 12 h light/dark cycle. For pathological group, a single dose of 10 mg of 7, 12-dimethylbenz(α)anthracene (DMBA), a carcinogenic chemical used widely to produce mammary tumor, was dissolved in 0.5 mL of sesame oil purchased from Sigma-Aldrich and administered via a subcutaneous injection into the rats at the average age of 57 days [30]. All rats were palpated weekly to detect the presence of mammary tumors. The induced rats were then allowed to adapt to a new environment for two weeks before thermography screenings were carried out.

2.2 In Vivo Thermography Screening

The entire experiment has been conducted in a small preparation room with minimal light exposure located in the Clinical Animal Laboratory of the Faculty of Bioscience and Medical Engineering (FBME) at the Universiti Teknologi Malaysia (UTM) in Johor, Malaysia. The room temperature was controlled and maintained at a range of 20–22 °C, using an air-conditioning system with relative humidity of 60–65%. The fluorescent lights available in the room were turned off during acclimatization and screening processes [31]. This will ensure factors such as high variations in room temperature, different percentages of light exposure, and other possible factors that could influence the result in a significant way were minimized. With this approach, a higher result consistency could be achieved. The images were acquired using an Epidermal Thermal Imaging Professional (ETIP) infrared imaging camera system model 7640 P-Series, manufactured by Infrared Camera Incorporation, Texas USA, with a resolution of 640 × 480 pixel, and a field of view of 49°/18 mm × 36°/25 mm, using a focal plane array microbolometer type detector, a spectral range of 7–14 µm, a thermal sensitivity of 0.038 °C with a temperature range of −40 to 400 °C and an accuracy of ±1% of readings.

The camera was mounted on a flexible arm which was connected to the display monitor as shown in Fig. 1. The distance between the camera to the sample was manually controlled, in order to get the best display output. The initialization of the camera was carried out once prior to screening, in order to reduce noise and stabilize the system.

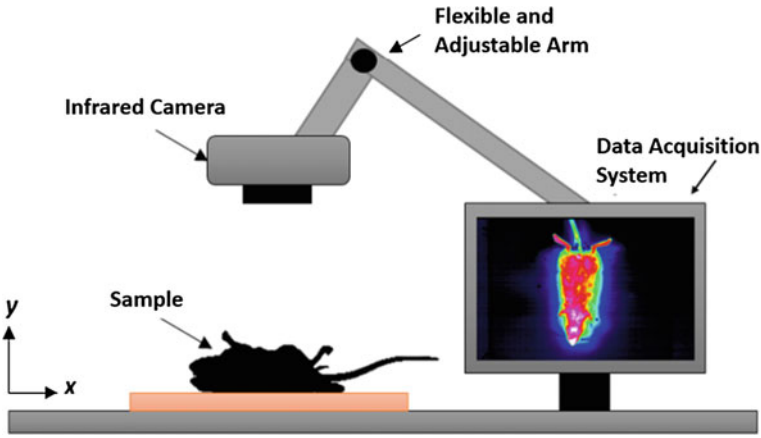

Fig. 1 In vivo thermography screening setup

All rats were allowed to acclimate to the room temperature of range from 20 to 22 °C for up to 15 min before screening. Since a still or minimal movement target is required during the screening process, a single dose of 0.1 ml/100 g of Ketamine–Zoletil–Xylazine (KTX) anesthetics combination was administered into each rat via an intramuscular route to provide a light anesthesia for 30–45 min [32]. A polyethylene decapicone restrainer was used for handling and approaching the rats. Anesthetized rats were placed back in their individual cage until they were fully unconscious. The rats were weighed and palpated to check for any lumps or tumor multiplicity as shown in Fig. 2 before the screening and all this data was measured and recorded accordingly.

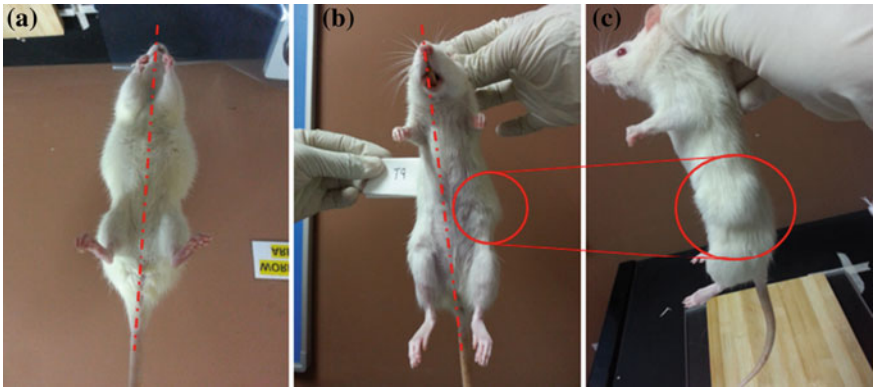

Fig. 2 Frontal view of **a** a normal rat with symmetrical body shape, **b** a pathological rat with palpated lump on the left side of the body and **c** side view of a pathological rat with palpated lump

Rats were then placed on the wooden plate in anterior position facing the camera for ten minutes. Images were captured at a rate of five frames per minute and thermal image in the *joint photographic expert group* (jpeg) format and temperature data point in the *comma separated values* (csv) file formats were stored for further analysis and processing. All screened rats were kept in their individual cages, and were monitored hourly for any post-procedure effects.

2.3 Disease Verification

After 12 weeks of consecutive screening, histology test and disease verification procedure were carried out to ensure that the symptomatic hotspot areas detected on the thermal images were due to the cancer disease and not any other pathologies. All surviving rats were euthanized by using drug overdose method to harvest the breast tissue sample. Before excision, the fur around the breast area was shaven and tissue samples were cut into smaller pieces and immersed inside 10% buffered formalin solution for fixation and preservation purposes. The tissue were processed, embedded in paraffin and section at 5 μm. The sections were then mounted on the

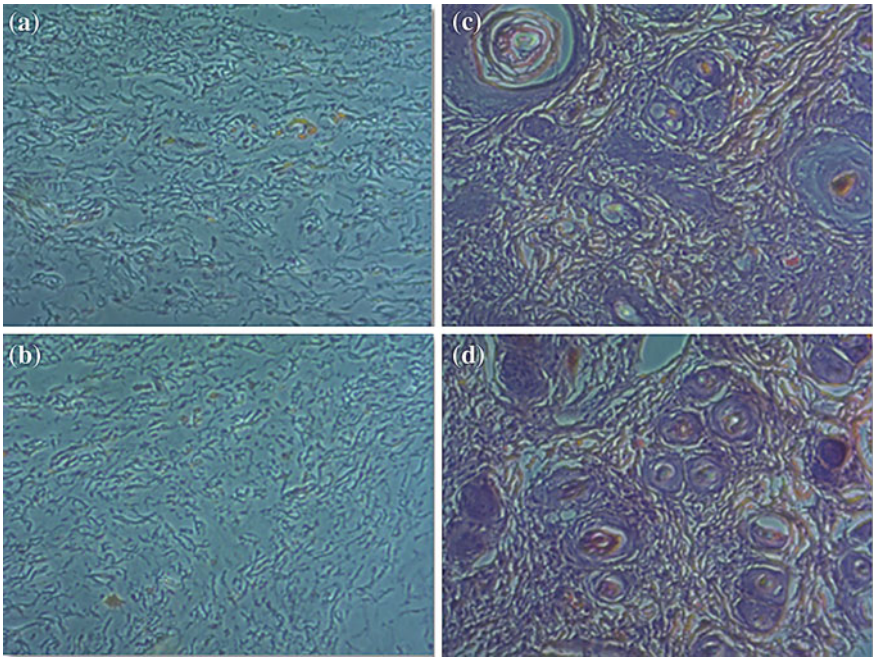

Fig. 3 Histological view of **a**–**b** cell arrangement in healthy breast tissue and **c**–**d** cell arrangement in cancerous tissue

glass slides and stained with haematoxylin and eosin to give contract to the tissue as well as to visualize the microscopic structures.

An expert from Pathology and Clinical Laboratory, Johor, Malaysia has classified both normal and pathological samples based on gross morphologic appearance of the tissue as shown in Fig. 3. Obtained histology results have confirmed that all specimens within the pathological group had high grade invasive ductal carcinoma of the mammary gland, with the presence of the syringomatous carcinoma component in certain samples, while healthy group specimens were confirmed to be normal without the presence of any cancerous cells.

3 Image Processing

A two-tier segmentation algorithm was developed in order to detect the symptomatic regions on the visual image and mapped them to the corresponding temperature data file for feature extraction and classification purposes. This will assist the clinician in diagnosing the thermal image by focusing only on the data extracted from affected area and not having to examine the whole image captured.

3.1 First Tier: Segmentation for Subject of Interest (SOI)

The first segmentation process involved separating the subject from the background in the thermal images using histogram based separation method. This eliminates the possibility of the system to detect any hot spot area in the background as one of the possible symptomatic region of interest since each pixel in the visual image corresponding one temperature value. Two vertical points namely x_1, y_1 and x_2, y_2 need to be chosen by the analyst once during system initialization, in order to approximately mark the subject position based on laboratory setting as shown in Fig. 4.

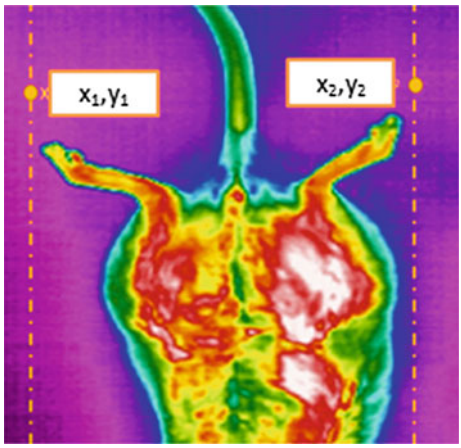

Fig. 4 Example of selection of two vertical points

Local information such as the overall intensity and vertical profile based on the selected vertical points were utilized in order to perform an individual image background correction. This particular step will allow flexibility alteration to different types of room and equipment settings including distance of the subject to the camera, the zooming function and the various physical sizes of the subjects.

Figure 5 shows a flowchart of new algorithms proposed for SOI segmentation. The raw image obtained from the thermography screening was preprocessed. Since different system have different color schemes (e.g., RGB, thermal, rainbow), analyst has to select one channel that suit the system best during initialization phase. The calculation of the mean intensity (μ_i) value as shown in Eq. 1 was used to generate a new matrix layout mapping with identical intensity value.

$$\mu_i = \frac{1}{N}\sum_{i=1}^{N} x_i \tag{1}$$

where N is the total pixel determined using vertical range (0—y_1 and y_2—max vertical pixel number) and x_i is the intensity value of each pixel measured.

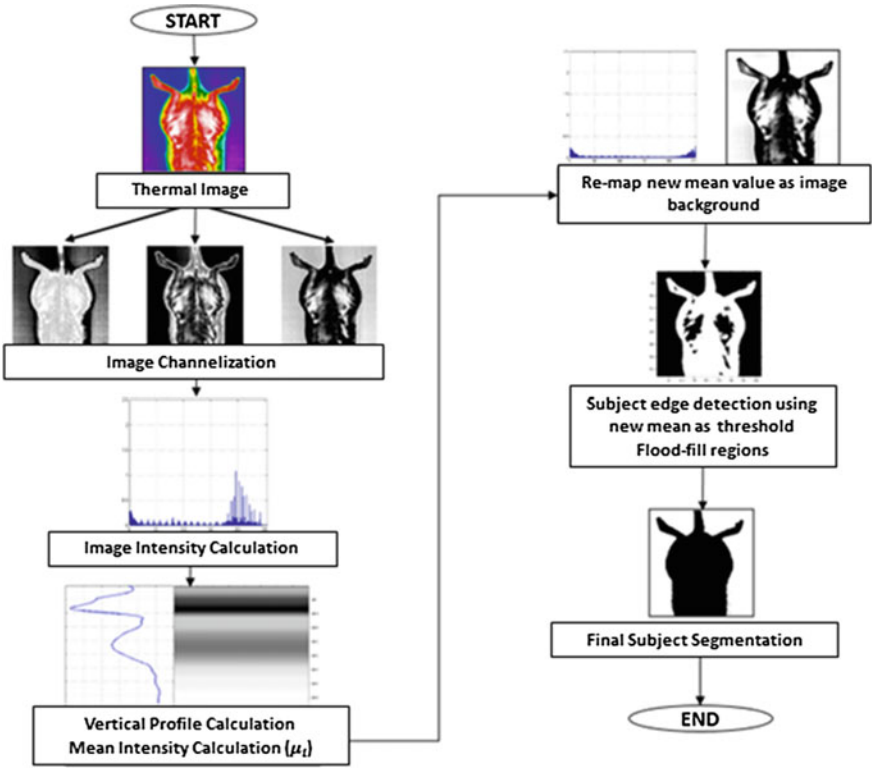

Fig. 5 Flowchart for SOI segmentation

Each pixel value in the output image, $I'_{(i,j)}$, was generated by the subtraction of the mean intensity value from the pixel value in the input image, $I_{(i,j)}$, as shown in Eq. 2.

$$I'_{(i,j)} = I_{(i,j)} - \mu_i \tag{2}$$

Next, the image was converted into a binary format background and was remapped onto a new image. Subject edge detection was performed within the subject with a flood-fill operation applied in order to eliminate any brightness discontinuity and to allow only one subject boundary to be detected. For performance evaluation, a comparative study between the proposed algorithm and the conventional segmentation methods namely the Otsu and Active Contours was performed.

3.2 *First Tier: Result and Discussion*

Figure 6 shows the output of the SOI segmentation carried out on multiple thermal images using the newly developed algorithm. It can be seen that although each thermal image has a different image background profile, the proposed algorithm is capable of detecting the SOI accurately, while manual segmentation requires longer time due to the complicated subject outline.

On the other hand, Fig. 7 shows the segmented image using Otsu's method. It can be clearly observed that the segmented image did not show any distinct boundary between the subject and the background. This is due to the default thresholding applied in Otsu's method which is not suitable for use in thermal

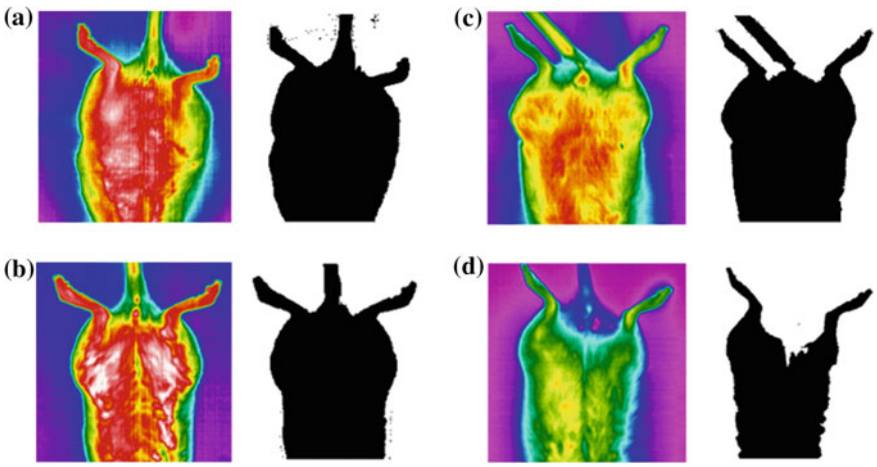

Fig. 6 Segmentation of multiple thermal images using a new developed algorithm

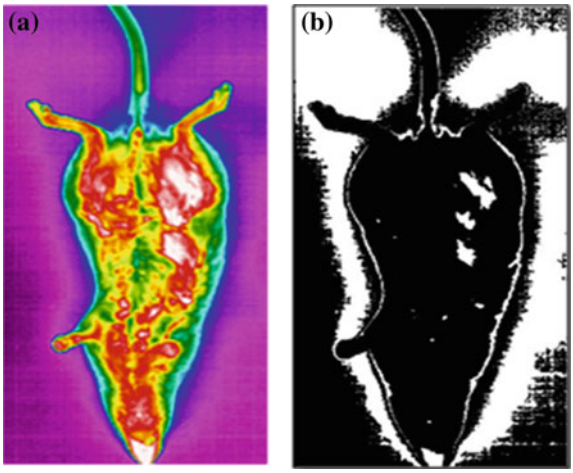

Fig. 7 Thermal image segmentation using Otsu's method

images due to its inhomogeneous color contours. However, for images with homogeneous objects and backgrounds Otsu's method has been shown to be very precise.

Figure 8 shows the segmented thermal image, using the Active Contour method with a different iteration number used. Interestingly, it can be observed that the higher the iteration, the detected edge becomes smoother and clearer. However, the disadvantage of larger iteration numbers is that they require higher computational loads and longer times to process. In addition, for the large number of images which need to be processed, single settings on iteration number may not be suitable to be used and could result in subject segmentation inconsistency.

Further morphological and quantitative comparisons were made based on the edge detection line drawn on each SOI segmented image and time taken for each segmentation as shown in Fig. 9 and Table 1 separately. It was observed that the

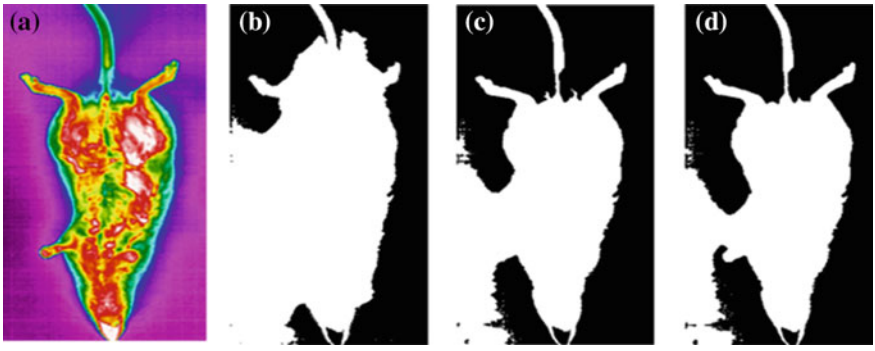

Fig. 8 Thermal image segmentation using the Active Contour method including **a** the raw thermal image **b** after 300 iterations **c** after 600 iterations and **d** after 700 iterations

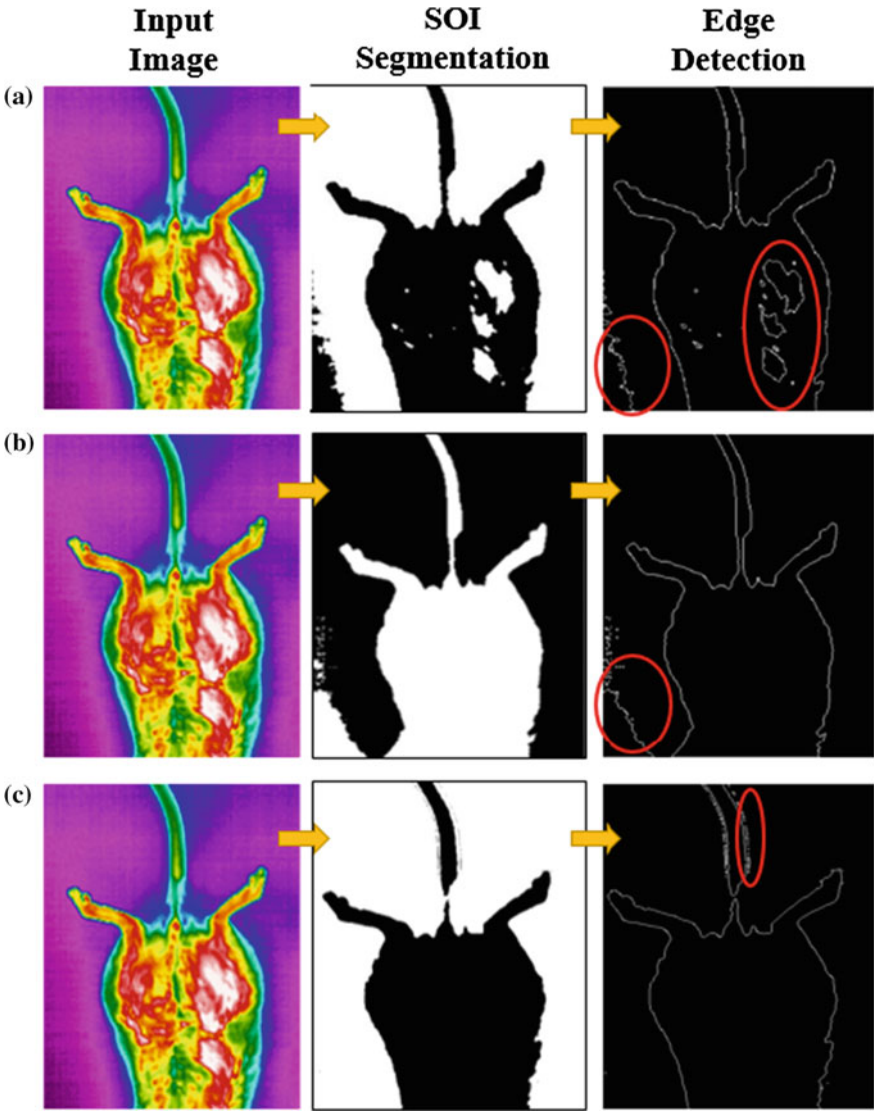

Fig. 9 Comparison of segmentation methods using **a** the Otsu's method **b** the Active Contour with 700 iterations and **c** the newly proposed SOI algorithm

Table 1 Processing time comparison

Method	Time (mean ± std) (s)
SOI segmentation	0.6415 ± 0.0429
Otsu's method	0.7130 ± 0.0651
Active Contour (700)	30.318 ± 1.0519

newly proposed SOI segmentation algorithm has outperformed the existing methods in both aspects, producing a distinguished boundary line between SOI and clear image background with lowest processing time. However, since initial image cropping can be controlled, analyst may choose to exclude the lower part of the body to minimize the undesirable noise captured along the tail. In previous clinical case study, areas such as face, neck and lower body were excluded during image processing. A corrected background profile shows a smooth and consistent pixel arrangement.

Segmented SOI from Otsu's method is shown to be the least accurate with a comparable processing time to the newly developed algorithm. The thermal image output was shown to capture the largest amount of background information. This may reduce the ROI segmentation accuracy in the later stage. Likewise, the background profile displayed a polluted pixel arrangement. Otsu's method has a drawback as it uses a single parameter setting, although this method is generally preferred in other digital image processing field, it seems to be not suitable for SOI segmentation in medical thermal image processing.

Contrariwise, the Active Contour method with 700 iterations produced a better cut-off line between the subject and background than Otsu's method with a small background area captured, but this method requires the longest processing time and highest load among others.

Therefore, the newly proposed SOI segmentation algorithm has proven to be capable for segmenting the SOI in different thermal images automatically with high accuracy and requires less processing load and time.

3.3 Second Tier: Segmentation for Region of Interest (ROI)

The second-tier segmentation algorithm was developed to detect the possible ROIs within the subject, where any presence of hotspots outside the SOI boundary will be disregarded in this stage.

Figure 10 shows the overall flow chart for the ROI segmentation process. By using the mean intensity value calculated previously in the SOI segmentation stage as a new threshold, all possible ROIs could be determined. Equation 3 shows the possible ROIs selection criteria where value '1' represents positive possible ROIs and value '0' represent non-ROI hotspots.

$$R_{\text{poss}} = \begin{cases} 1 & \text{if } R_i > \mu_i \\ 0 & \text{otherwise} \end{cases} \quad (i = 1, 2, 3 \ldots n), \tag{3}$$

where R_{poss} are the possible regions which have pixel value larger than the mean value and R_i are all hot spot in the SOI segmented. Figure 11 shows the output of possible regions detected within the subject using two different regions selection schemes.

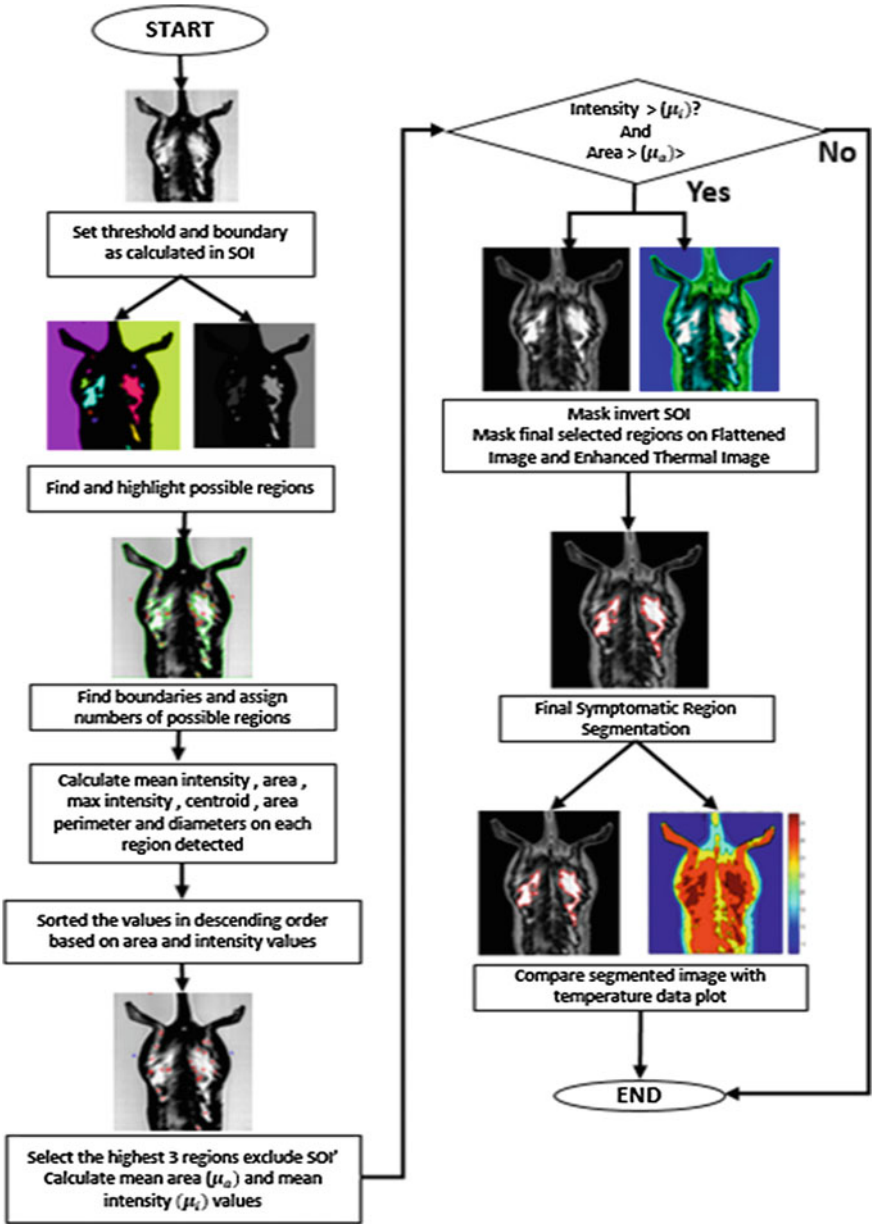

Fig. 10 Flowchart for ROI segmentation

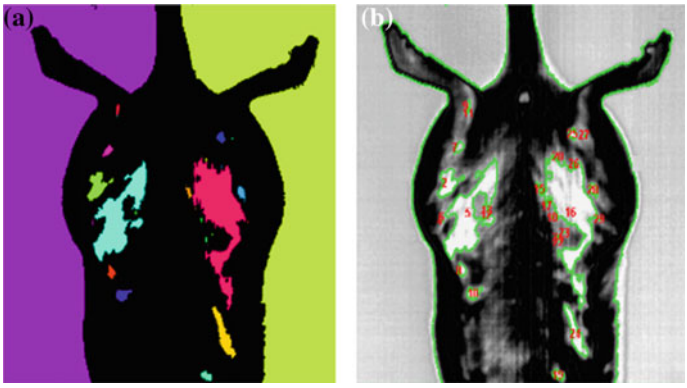

Fig. 11 Example of possible hotspot regions detected with **a** color highlighted and **b** numbered

Local parameter properties, such as the intensity, centroid value, diameter and area of each identified region were measured and tabulated for all possible symptomatic ROIs. Two parameters namely mean area (μ_a) and mean intensity (μ_i) were calculated and used to determine the final ROIs (R_{final}) selection as shown in Eq. 4.

$$R_{\text{final}} = R_{\text{poss}} > (\mu_a \cap \mu_i) \tag{4}$$

Mean area was used to eliminate the presence of smaller hotspots which are insignificant, while mean intensity was used to eliminate low temperature areas. Areas which satisfied both criterions were masked on the SOI segmented thermal image. Regions that not belong to these criterions were ignored, and if there were none detected, the image is considered normal and the algorithm will be terminated.

Finally, the output result of the ROI segmented image was compared to the temperature data contour plot, in order to validate and verify whether the final ROIs detected from the thermal image are in the same position as those generated from the raw temperature data file. This is a very important step as processing a raw temperate data file in the '*comma separated value*' or csv format can significantly increase the processing load requirement by thrice. However, qualitative comparison alone is insufficient to evaluate the performance of the developed ROI segmentation method. Hence, four different area based evaluation methods namely Dice Similarity Coefficient (DSC), Jaccard Index (JI), Relative Area Different (RAD) and Area Overlap Error (AOE) were used to analyze and compare ROI obtained via automated segmentation and using manual tracing for all samples [33–35].

DSC identifies the degree of area that is overlapping between automated and manual segmentation. On the other hand, Jaccard Index study the ratio of area in common of both automated and manual segmentation methods. RAD calculates the difference between area of the automated segmentation and the one from manual tracing where negative values indicate that the region segmented by the proposed

method is smaller than that by manual tracing. Positive values indicate that the region segmented manually is smaller than the one segmented by the system. AOE, which is based on JI, shows that ratio of the area that is not intersecting between both regions.

Hence, segmenting the ROI in its visual format and extracting features based on the ROI mapped onto the temperature data file will certainly increase the overall processing efficiency.

3.4 Second Tier: Results and Discussion

Figures 12 and 13 show the results of ROI segmented in both normal and abnormal thermal images respectively.

It was observed that for normal thermal image, no symptomatic region was detected and mapped onto the SOI segmented image. However, for the abnormal thermal image, few distinctive symptomatic regions were detected and mapped onto the SOI segmented image. Although a large hotspot could be seen clearly on the raw thermal image, only areas which satisfied the criterion set earlier were selected. This is crucial to guide and assist the clinicians in diagnosing a patient. As visual image only carries pixel information, it is important to ensure that ROI segmented corresponded to the highest temperature on the raw thermal image.

Based on the output result obtained in Fig. 14a, it is clearly shown that the ROIs detected have correspondingly matched their respective temperature data shown in Fig. 14b, c. In addition, an automated segmentation method developed shown to have high similarity coefficient to manual tracing with 97.38 and 94.89% for both DSC and JI respectively as shown in Table 2. RAD shows a positive value of 5.38 which indicates that bigger region segmented using manual tracing than the one segmented automatically. This is due to the small temperature changes along the border of symptomatic regions that was not able to be differentiated visually.

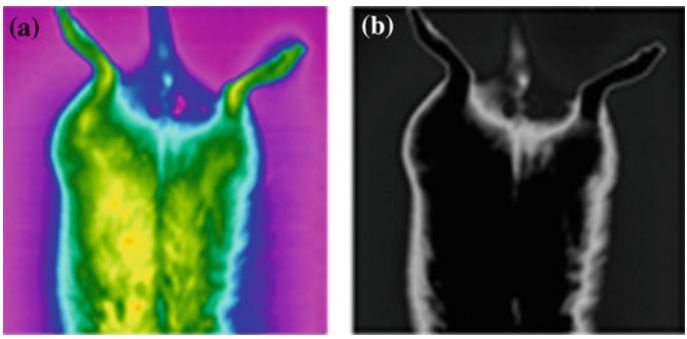

Fig. 12 ROI segmentation of normal thermal image **a** raw thermal image, and **b** ROI masked on raw image

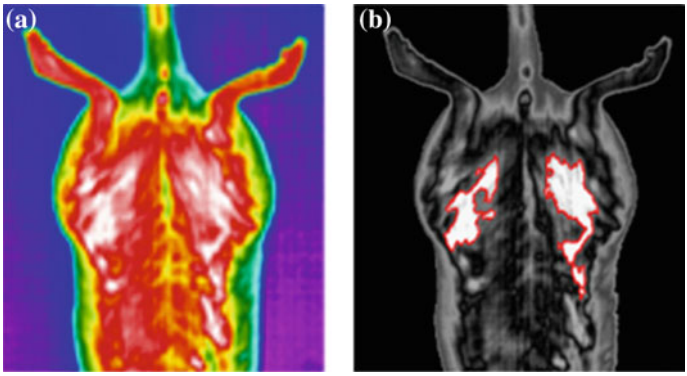

Fig. 13 ROI segmentation of abnormal thermal image **a** raw thermal image, and **b** ROI masked on raw image

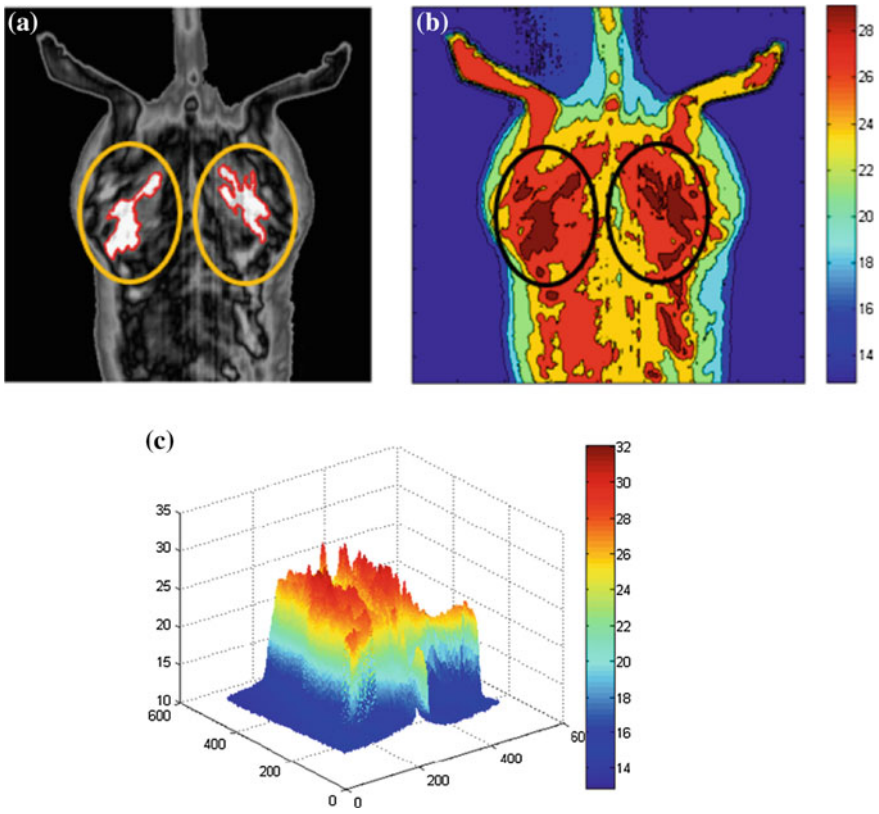

Fig. 14 Comparative analysis between **a** ROI segmented thermal image and **b**, **c** temperature data plot in 2D and 3D respectively

Table 2 Quantitative performance measurement between automated and manual segmentation

Dice similarity coefficient (%)	Jaccard index (%)	Relative area difference (%)	Area overlap error (%)
97.38	94.89	5.38	5.10

Finally, AOE result obtained shows that there was a high resemblance between both regions segmented using manual and automated methods.

4 Automatic Abnormalities Detection

Once the final ROIs were detected, the pixel number lies within the ROI boundary will be used as a reference to extract the temperature related information from the temperature data file. For normal thermal images with no ROI boundary detected, temperature information within an area of size 50 × 50 pixels from the subject midpoint were extracted. Five different features including mean intensity, mean temperature, maximum temperature, minimum temperature and standard deviation were extracted. These data which were taken from a total of 200 sets of thermal images and were then sampled into three different categories namely training, testing, and validation. Target value of '1' was assigned to all pathological images and target value '0' was assigned to all thermal images captured on normal samples. In this study, an artificial neural network (ANN), a widely used classification method in medical diagnosis has been utilized to classify whether the thermal image is belong to the abnormal group or otherwise [36, 37]. ANN processes the data in parallel distributed mainframe and has the ability to learn on the basis of the input data they fed. The network was first trained using back propagation algorithm which employs steepest gradient descent with momentum and consists of one input layer, two hidden layers and one output layer with sigmoid and linear transfer function were applied in the hidden layers. The network was then optimized to reduce over fitting before data testing and validation can be performed by varying the training parameters including number of neuron, learning rate, momentum constant, and iteration rate. The values of each parameter was considered optimum when the network produces the lower mean squared error (MSE) value with high prediction accuracy performance. The prediction values obtained from both testing and validation steps were further evaluated for group recognition and accuracy measurement. The MSE calculation is shown is Eq. 5.

$$E_k = \frac{1}{2}\sum_{j=1}^{N}\left(T_{kj} - O_{kj}\right)^2, \tag{5}$$

where E_k is the MSE value, T_{kj} represent target value for jth output neuron, O_{kj} is the actual output and N is the total output number of neuron. The range used for

both groups are shown in Eqs. 6 and 7. While the accuracy calculation was made based on conditions in Eq. 8.

$$-0.2 < \text{Pnormal} < 0.2 \tag{6}$$

$$0.8 < \text{Pabnormal} < 1.2 \tag{7}$$

$$\text{Accuracy } (\%) = \frac{\text{Total of Correct Detection}}{\text{Total Detection}} \times 100 \tag{8}$$

4.1 Features Extraction and Classification

Figure 15 shows the comparison of temperature and mean intensity values for all features extracted including maximum temperature, minimum temperature, mean temperature and standard deviation from data temperature file and mean intensity values from thermal image for both normal and pathological rats separately. The temperature standard deviation and mean intensity values for both groups were shown to be the most significant distinguishable features among others. Mean values (°C) of 0.433 ± 0.1547 and 0.109 ± 0.037 for both the abnormal and normal groups were observed in temperature standard deviation while distinctive values of 216.9417 ± 8.6471 and 167.0467 ± 3.708 were obtained in pixel mean intensity.

Maximum temperature and mean temperature showed a comparably significant difference with minimal correlation, while the minimum temperature was observed to have the least significant difference where values from the third quartile (Q3) of a normal group could be mistakenly assigned to the abnormal group. Data which have outlier values were excluded for classification. Nonetheless, these features have been considered with additional selected features from image processing to be used in the development of ANN as they fulfil the least requirements needed for robust prediction.

For classification, a total of 120 sets of data (60 normal and 60 abnormal images) were used in the training process, 40 sets of data (20 normal and 20 abnormal images) for testing and another 40 sets of data (20 normal and 20 abnormal images) were used for validation purposes. A final optimized network architecture consists of 5 network inputs, 2 neurons in the hidden layer and 1 network output with learning rate of 0.3, an iteration rate of 200,000 and momentum constant of 0.2.

Figure 16 shows the result plot between actual classification output value and the predicted classification output value for validation data set from the optimized network while Table 3 shows the final classification performance for both testing and validation data with a training performance of 98.45% and an MSE of 0.015.

The prediction results obtained showed that the ANN developed for the image abnormality classification was capable of achieving an overall accuracy of 97.5 and 92.5% for both testing and validation data, respectively, which is comparable to the

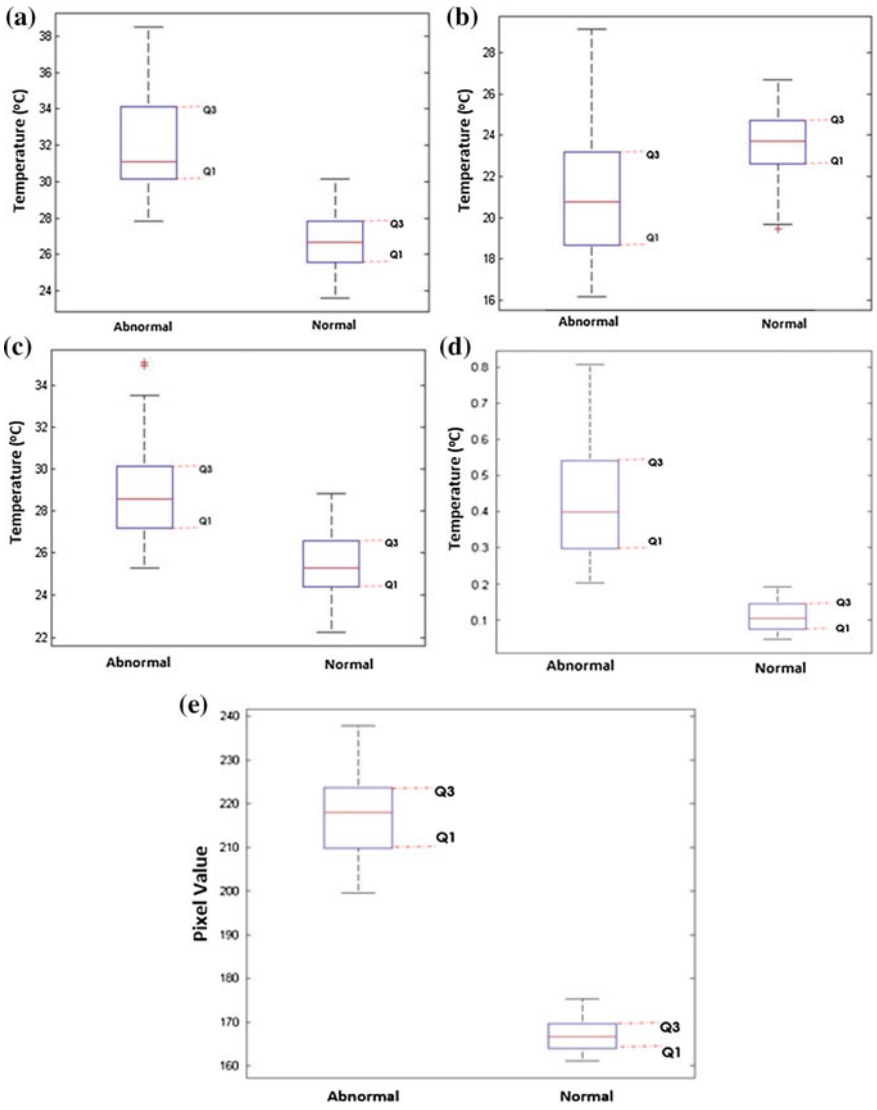

Fig. 15 Comparison of **a** maximum temperature, **b** minimum temperature, **c** mean temperature, **d** standard deviation of temperature and **e** mean intensity value for both abnormal and normal groups

performance achieved by other techniques [23, 29, 38]. This finding indicates the higher possibility of using features extracted from both visual image and temperature data in assisting clinicians to improve the current breast oncology diagnosis process.

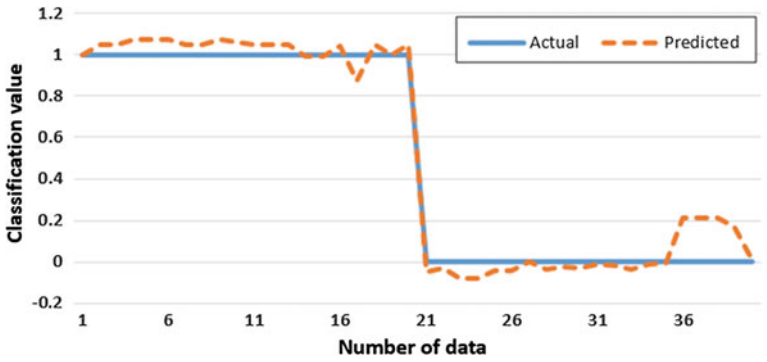

Fig. 16 Plot of actual classification value against predicted classification value for thermal image abnormality detection

Table 3 Classification results for abnormality detection

Data	Testing		Validation	
	Abnormal	Normal	Abnormal	Normal
Actual data	20	20	20	20
ANN prediction	20	19	19	18
Group accuracy (%)	100	95	95	90
Total accuracy (%)	97.5		92.5	

5 Conclusion

In this chapter, a two-tier segmentation method was proposed to automatically segment the symptomatic regions lie within the subject of interest. Features from both thermal visual image and data temperature file were extracted and fed into ANN classification system to assist the analyst in diagnosing multiple thermal images with low processing time and computational load required. A total of 200 thermal images were used to test the framework and show that the proposed method is capable in processing a large number of images from mass screening activities. This approach has produced a high accuracy of 92.5%. For future clinical study, a large data set from both healthy and cancer patients is required in both thermal visual and data temperature point formats to confirm the efficacy of this method.

Acknowledgements The authors would like to express gratitude to Universiti Teknologi Malaysia for supporting this research under the Institutional Research Grants Vote Number 05H92 and also to the Malaysian Ministry of Higher Education (MOHE) for providing the MyBrain scholarship to the author.

References

1. Saslow, D., Solomon, D., Lawson, H.W., Killackey, M., et al.: American Cancer Society, American Society for Colposcopy and Cervical Pathology, and American Society for Clinical Pathology screening guidelines for the prevention and early detection of cervical cancer. Am. J. Clin. Pathol. **137**, 516–542 (2012)
2. Canada Cancer Society, Canadian Cancer Statistics Special topic : Predictions of the future burden of cancer in Canada (2015)
3. American Cancer Society: Cancer Facts & Figures (2013)
4. Yip, C.H., Pathy, N.B., Teo, S.H.: A review of breast cancer research in Malaysia. Med. J. Malaysia **69**, 8–22 (2014)
5. Pathy, N.B., Yip, C.H., Taib, N.A., Hartman, M., et al.: Breast cancer in a multi-ethnic Asian setting: results from the Singapore-Malaysia hospital-based breast cancer registry. Breast **20** (Suppl 2), S75–S80 (2011)
6. Osako, T., Iwase, T., Takahashi, K., Iijima, K., et al.: Diagnostic mammography and ultrasonography for palpable and nonpalpable breast cancer in women aged 30 to 39 years. Breast Cancer **14**, 255–259 (2007)
7. Kavanagh, A.M., Giles, G.G., Mitchell, H., Cawson, J.N.: The sensitivity, specificity, and positive predictive value of screening mammography and symptomatic status. J. Med. Screen. **7**, 105–110 (2000)
8. Kennedy, D.A., Lee, T., Seely, D.: A comparative review of thermography as a breast cancer screening technique. Integr. Cancer Ther. **8**, 9–16 (2009)
9. Sree, S.V., Ng, E.Y.K., Acharya, R.U., Faust, O.: Breast imaging: a survey. World J. Clin. Oncol. **2**, 171–178 (2011)
10. Head, J.F., Elliott, R.L.: Infrared imaging: making progress in fulfilling its medical promise. IEEE Eng. Med. Biol. Mag. **21**, 80–85 (2002)
11. Keyserlingk, J.R., Ahlgren, P.D., Yu, E., Belliveau, N., Yassa, M.: Functional infrared imaging of the breast. IEEE Eng. Med. Biol. Mag. **19**, 3 (2000)
12. Foster, K.R.: Thermographic detection of breast cancer. IEEE Eng. Med. Biol. Mag. **17**, 6 (1998)
13. Borchartt, T.B., Conci, A., Lima, R.C.F., Resmini, R., Sanchez, A.: Breast thermography from an image processing viewpoint: a survey. Sig. Process. **93**, 2785–2803 (2013)
14. Lipari, C.A., Head, J.F.: Advanced infrared image processing for breast cancer risk assessment. In: Proceedings of 19th Annual International Conference IEEE Engineering Medical Biological Society Magnificent Milestones and Emergency Opportunities in Medical Engineering (Cat. No. 97CH36136), vol. 2, pp. 673–676 (1997)
15. Head, J.F., Wang, F., Lipari, C.A., Elliott, R.L.: The important role of infrared imaging in breast cancer. IEEE Eng. Med. Biol. Mag. **19**, 52–57 (2000)
16. Ng, E.Y.K., Fok, S.-C.: A framework for early discovery of breast tumor using thermography with artificial neural network. Breast J. **9**, 341–343 (2003)
17. Ng, E.Y.-K.: A review of thermography as promising non-invasive detection modality for breast tumor. Int. J. Therm. Sci. **48**, 849–859 (2009)
18. Herry, C.L., Frize, M.: Digital processing techniques for the assessment of pain with infrared thermal imaging. In: Proceedings of Second Joint 24th Annual Conference Annual Fall Meeting Biomedical Engineering Society [Engineering Med. Biol.], vol. 2 (2002)
19. Scales, N., Herry, C., Frize, M.: Automated image segmentation for breast analysis using infrared images. In: Conference Proceedings IEEE Engineering in Medicine and Biology Society, vol. 3, pp. 1737–1740 (2004)
20. Motta, L.S., Conci, A., Lima, R.C.F., Diniz, E.M.: Automatic segmentation on thermograms in order to aid diagnosis and 2D modeling. In: Proceedings of 10th Workshop em Informática Médica, Belo Horizonte, MG, Brazil, vol. 1, pp. 1610–1619 (2010)
21. Schaefer, G., Závišek, M., Nakashima, T.: Thermography based breast cancer analysis using statistical features and fuzzy classification. Pattern Recogn. **42**, 1133–1137 (2009)

22. Schaefer, G., Nakashima, T., Zavisek, M., Yokota, Y., et al.: Breast cancer classification using statistical features and fuzzy classification of thermograms. In: 2007 IEEE International Fuzzy System Conference (2007)
23. Ng, E.Y.K., Kee, E.C.: Advanced integrated technique in breast cancer thermography. J. Med. Eng. Technol. **32**, 103–114 (2008)
24. Ng, E.Y.K., Ung, L.N., Ng, F.C., Sim, L.S.J.: Statistical analysis of healthy and malignant breast thermography. J. Med. Eng. Technol. **25**, 253–263 (2001)
25. Acharya, U.R., Ng, E.Y.K., Tan, J.-H., Sree, S.V.: Thermography based breast cancer detection using texture features and Support Vector Machine. J. Med. Syst. **36**, 1503–1510 (2012)
26. Jones, B.F., Schaefer, G., Zhu, S.Y.: Content-based image retrieval for medical infrared images. In: Proceedings 26th Annual International Conference IEEE EMBS, pp. 1–5, San Francisco, CA, USA (2004)
27. Kuruganti, P.T., Qi, H.Q.H.: Asymmetry analysis in breast cancer detection using thermal infrared images. In: Proceedings of Second Joint 24th Annual Conference Annual Fall Meeting Biomedical Engineering Society [Engineering Med. Biol.], 2, pp. 7–8 (2002)
28. Jakubowska, T., Wiecek, B., Wysocki, M., Drews-Peszynski, C., Strzelecki, M.: Classification of breast thermal images using artificial neural networks. J. Med. Infomatics Technol. **7**, 41–50 (2004)
29. Borchartt, T.B., Resmini, R., Conci, A., Martins, A., et al.: Thermal feature analysis to aid on breast cancer diagnosis. In: Proceeding COBEM 2011, Brazil, 24–28 Oct 2011
30. Hakkak, R., Holley, A.W., Macleod, S.L., Simpson, P.M., et al.: Obesity promotes 7,12-dimethylbenz(a)anthracene-induced mammary tumor development in female zucker rats. Breast Cancer Res. **7**, R627–R633 (2005)
31. Bezerra, L.A., Oliveira, M.M., Rolim, T.L., Conci, A., et al.: Estimation of breast tumor thermal properties using infrared images. Sig. Process. **93**, 2851–2863 (2013)
32. Struck, M.B., Andrutis, K.A., Ramirez, H.E., Battles, A.H.: Effect of a short-term fast on ketamine-xylazine anesthesia in rats. J. Am. Assoc. Lab. Anim. Sci. **50**, 344–348 (2011)
33. Dice, L.R.: Measures of the amount of ecologic association between species. Ecology **26**, 297–302 (1945)
34. Jaccard, P.: La distribution de la flore dans la zone alpine. Rev. Générale des Sci. (1906)
35. Fleiss, J.L., Levin, B., Paik, M.C.: The measurement of interrater agreement. Stat. Meth. Rates Proportions **52**, 598–626 (2003)
36. Wishart, G.C., Campisi, M., Boswell, M., Chapman, D., et al.: The accuracy of digital infrared imaging for breast cancer detection in women undergoing breast biopsy. Eur. J. Surg. Oncol. **36**, 535–540 (2010)
37. Wiecek, B., Danych, R., Zwolenik, Z., Jung, A., Zube, J.: Advanced thermal image processing for medical and biological applications. In: 2001 Proceedings of 23rd Annual EMBS International Conference, pp. 2805–2807, Istanbul, Turkey, 25–28 Oct 2001
38. Etehadtavakol, M., Chandran, V., Ng, E.Y.K., Kafieh, R.: Breast cancer detection from thermal images using bispectral invariant features. Int. J. Therm. Sci. **69**, 21–36 (2013)

Detection of Breast Abnormality Using Rotational Thermography

Sheeja V. Francis, M. Sasikala and Sandeep D. Jaipurkar

Abstract Breast cancer is considered to be one of the major causes for high mortality rates in young women in the developing countries. Survival rate in breast cancer patients may be improved significantly by early detection. In order to detect cancer in its initial stages breast screening is recommended for women over 40 years of age. Due to the limitations of existing breast cancer screening techniques alternative modalities such as thermography are being explored. An elevation in local surface temperature due to an underlying pathology is considered as one of the earliest indications of an underlying cancer. Such regions are represented as hotspots on a conventional thermogram. Detection of these hotspots from conventional breast thermograms is quite challenging, mainly due to incomplete image acquisition. A novel technique called rotational thermography has been developed to address this issue. In this chapter, a frame work has been presented for developing a breast cancer screening system using thermograms acquired with this new imaging modality. Image features are extracted from rotational thermograms in spatial, bispectral, and multi-resolution domains. Optimal features are identified using genetic algorithm and automatic classification is performed using support vector machine. In addition to screening, attempt has been made to characterize a detected abnormality as benign or malignant. As rotational thermography acquires images of the breast in multiple views, study is carried out to locate the position of the tumor in correlation with ultrasound and biopsy findings. Thus the potential of the system for screening, characterization, and localization of breast abnormalities is explored.

S.V. Francis (✉)
Department of Electronics & Communication Engineering, MNM Jain Engineering College, Chennai, Tamil Nadu, India
e-mail: sheejavf@gmail.com

M. Sasikala
Department of Electronics & Communication Engineering, College of Engineering, Guindy, Anna University, Chennai, Tamil Nadu, India
e-mail: sasikala@annauniv.edu

S.D. Jaipurkar
Breast Clinic, Vijaya Health Centre, Chennai, Tamil Nadu, India
e-mail: sjaipurkar3@gmail.com

E.Y.K. Ng and M. Etehadtavakol (eds.), *Application of Infrared to Biomedical Sciences*, Series in BioEngineering,
DOI 10.1007/978-981-10-3147-2_9

Keywords Breast cancer · Breast thermography · Conventional thermography · Rotational thermography · Feature extraction · Classification

1 Introduction

Breast cancer is reported to be the most predominant of all cancers detected in women. Cancer facts and figures released by the American Cancer Society estimates that about 29% of all reported cancers in 2015 would be of the breast [1]. It is estimated that one in every eight women possesses the risk of developing breast cancer in their lifetime. The estimated mortality rates are also very high, with breast cancer contributing to 15% of all cancer deaths.

The mortality rate due to breast cancer is found to be rising in both the developed and the developing countries. These rates may be brought under control if the disease is detected early, leading to effective treatment and prognosis. As early detection can lead to better survival chances, women above 40 years of age are advised to undergo screening for breast cancer annually. Currently, mammography is used as the gold standard imaging technique for the purpose. However, the diagnostic ability of this technique is found to be compromised in women with dense breasts. Keyserlingk et al. [2] have reported that mammography fails to detect small tumors of size less than 1.66 cm on an average and hence is not able to detect cancer at an early stage. Further, patients who undergo mammographic procedure are at the risk of radiation hazards due to repeated X-ray exposures. Hence, continuous efforts are being made to develop radiation safe imaging techniques for the early detection of breast cancer. According to Gautherie et al. [3], thermography is one such technique that can detect breast cancer 8–10 years ahead of mammography. Although thermography is popularly used for mass screening of fever [4], several studies have reported on its early detection capability of breast cancer in the last two decades [5–8]. Understanding of the thermal profile of human breast is quite essential to evolve thermography for breast cancer detection.

1.1 Thermal Profile of Human Breast

The core temperature of human body is reported to be around 37 °C when the ambient temperature is maintained at 25 °C. The transfer of heat from core of the body to skin surface is a complex thermo-biological process. When subjected to extreme environmental temperatures, the vaso-regulatory system of our body helps to maintain the thermal equilibrium by triggering shivering or sweating as reflex mechanisms. The optimal temperature range in which a slightly dressed human body can maintain thermal equilibrium is 20–25 °C. Hence, thermographic studies are conducted in controlled environments maintained within this temperature range. The mean temperature of human breasts is found to vary from person to person based on several

factors such as environmental conditions, physical exertion, menstrual cycle, anxiety, etc. Also, different regions within the breast exhibit different temperatures. The average temperature of breast surface is reported to be around 30 °C in a controlled environment at 20 °C [9]. Several researchers have established that the surface temperature of a cancerous region is significantly higher than that of the surrounding normal regions. Hence, an abnormal breast condition may be detected by analyzing the temperature differences within a breast region. Further, a temperature difference of more than 0.5 °C between right and left breasts is reported to be indicative of abnormality [10]. Hence, exploring the thermal asymmetry between the contra-lateral breasts is widely practiced for breast cancer detection. Due to advancements in sensor technology, infrared cameras with enhanced thermal resolution of less than 0.1 °C are available. These are capable of sensing the subtle temperature variations and are used for evaluating breast conditions in breast thermography.

2 Breast Thermography

The first instance of using infrared imaging for cancer diagnostics can be traced to 1956, when it was discovered that surface temperature over cancerous tissues in a breast was higher than the surrounding normal regions [11]. The high rate of metabolic activity around cancerous tumors triggers a huge demand for supply of nutrients. Consequently, an increased blood flow is ensured in order to nourish these cancer cells by recruiting dormant vessels and creating new ones (neo-angiogenesis). This process leads to vascular asymmetry and increase in regional surface temperatures in the breasts, which may be considered as the earliest signs of breast cancer [12, 13]. Breast thermography involves capturing these variations and interpreting them for early detection of breast cancer or for monitoring its prognosis.

A large-scale study popularly known as breast cancer detection and demonstration project (BCDDP) was conducted in the United States in the early 70s to evaluate the diagnostic ability of breast thermography. According to the report of the working group, the diagnostic value of infrared imaging was considered to be poor [14]. This was followed by a period of uncertainty and waning interest in the procedure. However, poor study design, use of untrained technicians, improper environmental controls, and protocols led to the failure of the project [15].

Since mid-70s, significant improvements have been made in infrared technology, sensor arrays, and computing systems for military purposes. This has renewed the research interest in breast cancer detection through thermography. State-of-the-art breast thermography uses highly sensitive infrared cameras and software systems to represent thermal variations of the breast surface in the form of high-resolution images called breast thermograms. The procedure is noninvasive, comfortable, and radiation safe. An abnormal breast thermogram has been reported to be an important high-risk marker for cancers that might develop in the future [16].

Both passive and active methods are being practiced in breast thermography. In passive thermography, the regions of interest are naturally at a higher or lower

temperature than the background. Hence, the infrared rays emitted from these regions are picked up effectively by the camera system. An active approach is necessary when such regions are usually in equilibrium with the surroundings. Thus in active thermography, an energy source is used to produce a thermal contrast between the regions of interest and the background by applying a cold challenge. It is usually implemented as a blow of hot air or chemical vaporization on the skin surface. Though Amalu [17] has reported that application of cold challenge does not lead to performance improvement in active breast thermography-based systems, continuous research has been going on in this area.

Though thermography is a promising screening tool for breast cancer, diagnosis is usually done manually by skilled professionals. Hence, interpretations made from thermograms are highly subjective in nature. In order to overcome factors such as shortage of trained personnel and operator variability, a computer-aided diagnostic (CAD) system needs to be developed. The advancements made in thermal imaging systems and pattern analysis techniques may be used to build a reliable system for breast cancer detection based on thermography. Such a system can be used for breast cancer screening in developing countries, especially by primary health care professionals in rural areas where specialized health care is lacking. Several researchers have worked on developing CAD systems for breast cancer detection using thermograms acquired by conventional breast thermography technique.

2.1 Conventional Breast Thermography

In the conventional technique for breast thermography the patient is seated in front of the infrared camera at a distance of 80–100 cm. This distance is chosen so as to image the complete torso of the subject with good resolution at the field of view of the camera. The schematic representation of conventional breast thermography

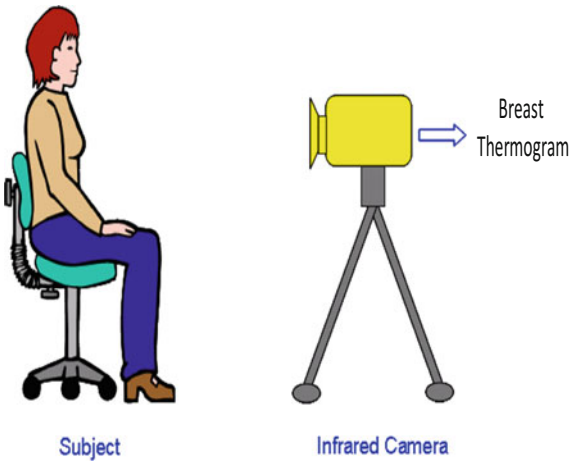

Fig. 1 Schematic representation of conventional breast thermography technique

technique is shown in Fig. 1. In this method infrared images of the breast are acquired in three views, viz., Contra-lateral, Medio-Lateral Oblique, and Axillary.

Most of the CAD systems presented in literature use contra-lateral or frontal thermograms and are confronted with two problems. First, tumors in the inferior regions of the breast are obscured behind the natural sag and often go undetected. Second, the neck carotid and infra mammary folds are visible in the images. These are normally hot regions that may lead to wrong diagnosis if not removed. Segmentation of the breasts from these areas is a pre-requisite for effective CAD systems and is quite a challenge till date. The image acquisition and interpretation processes are operator dependent and are found to vary across patients. In order to address these issues a new thermal imaging technique called rotational thermography has been evolved.

2.2 Rotational Breast Thermography

A novel setup known as the Mammary Rotational Infrared Thermogram (MAMRIT) unit [18] is used for acquiring rotational breast thermograms. The unit comprises an imaging chamber with a patient table on its top as shown in Fig. 2. The ambient temperature and humidity inside the chamber are controlled with an inbuilt air conditioner.

The subject lies in prone position on the patient table of the MAMRIT unit with one breast suspended through the small circular aperture into the imaging chamber beneath. An infrared camera is fixed at the free end of a robotic arm situated inside the MAMRIT chamber. The arm is programmed to revolve around the suspended breast in angular steps of 30°. The infrared camera captures images of breast at every step. Thus 12 views of the breast are obtained in one rotation ensuring complete imaging of the breast. Surface temperature information of the entire breast is captured and may be displayed by placing the cursor at required spatial positions. The acquisition of temperature information is repeated after lowering the ambient temperature to understand the tissue response to external stimuli. All the images are stored along with patient information, the camera position, ambient temperature, and time of acquisition. The set of thermograms obtained before and after lowering of ambient temperature are called precool and post-cool series, respectively. The same procedure is repeated for the other breast.

The images are acquired with patient consent and Institutional review board—approved protocol, using infrared camera ICI7320P [19]. The camera is an uncooled bolometer type with spatial resolution 480 × 640 pixels. The inbuilt software represents the raw temperature data picked up by the detector in the form of pseudo-color images. The ‘hot’ color palette is used which varies from blue to red in increasing order of temperature (heat). A temperature variation of around 10 °C is observed in the human breast. These variations are represented on thermogram images by grouping pixels into 10–12 bands, such that the temperature

Fig. 2 Views of MAMRIT Unit

variation between successive bands is around 1 °C. The minimum temperature resolution is 0.01 °C. At such resolution, the slight variations in intensity present within the bands are not perceived by the human eye. Nevertheless, these pixel intensities may be observed by placing the cursor on regions of interest and more so by computer vision techniques. A specific pattern of temperature variation is observed along the vertical direction in rotational breast thermograms of normal subjects. The nipple region is found to be the coldest and the temperature increases in regions closer to the chest wall. This pattern is found to extend across the breast when all twelve views are observed. In case of abnormality, bands that represent higher temperatures are found protruding into the zones of lower temperature thereby disturbing the characteristic temperature pattern. Figure 3 shows the complete sequence of precool rotational images of single breast (Left side) at angles 0°, 30°, 60°, 90°, 120°, 150°, 180°, 210°, 240°, 270°, 300°, and 330°, respectively.

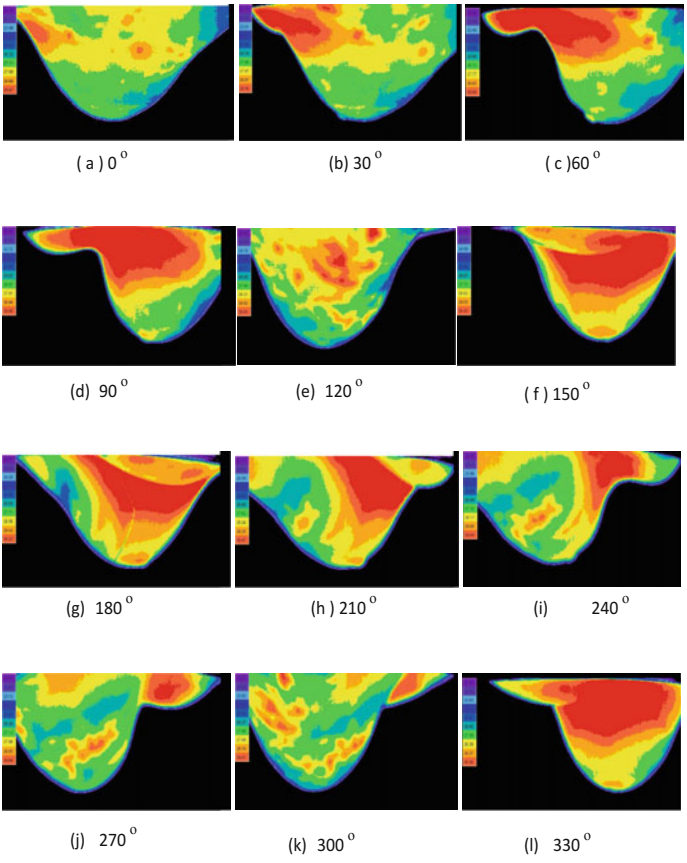

Fig. 3 Image sequence acquired by rotational breast thermography

The rotational breast thermography technique contains more diagnostic information than the conventional technique due to the following reasons.

- Chances of missing a tumor are much less as the breast is imaged completely.
- As images are captured by moving the camera around the suspended breast, all tumors that are located within 4.5 cm from breast surface are detected (at least in a few closest views), whereas, in the conventional method, the heat emissions from such depths are scattered and lost in the overlying tissues.
- Cold challenge may be easily implemented as the breast is imaged in a temperature-controlled chamber.
- Movement artifacts are greatly reduced as the patient is made to lie comfortably in prone posture during image acquisition.

2.3 Outline of the Chapter

The study is presented in two sections. In the first, a screening system is developed for detecting breast abnormality in rotational thermograms by exploring texture features in various domains. Optimal features are identified using genetic algorithm in order to design a reliable system for detection of breast abnormalities. Automatic classification of normal, benign, and malignant conditions is carried out to study the ability of rotational thermography-based system in characterizing the detected abnormality. The capability of the system to locate the abnormal region has been studied in correlation with ultrasound findings in the second section.

3 Screening and Characterization of Breast Abnormality in Rotational Thermograms

During the last two decades several computer-aided systems have been developed for screening of abnormality from conventional breast thermograms. Such systems include general image processing techniques such as segmentation, feature extraction, and classification. Several segmentation methods have been proposed to extract whole breasts and specific regions of interest as well [20–26]. Spatial-domain statistical features [27–31], wavelet-based features [32, 33], higher order spectral features [34], bispectral invariant features [35], and fractal dimension [36] have been employed for classifying breast thermograms. Numerical modeling of thermal properties of breast has been used to aid interpretation from breast thermograms [37–39]. The relationship between texture features and surface temperature changes has been well established in literature [40]. Hence, texture features are extracted from regions of elevated temperatures in rotational thermograms for

breast screening. As a preliminary study failed to prove the effectiveness of existing cold challenge mechanism, only rotational thermograms of precool series were used for the study.

Various breast abnormalities exhibit distinct temperature profiles and may be broadly characterized as benign or malignant. According to Jayashree et al. [9], the local temperature rise is less than 1 °C in benign regions while it is more than 1.5 °C in case of malignancy. This margin between benign and malignant conditions may be even less when malignancy is in its initial stages. Further, the patterns of thermal variations between normal and benign conditions are often indistinguishable. Hence, the characterization study is also important for detection of breast cancer. Examples of normal, benign, and malignant thermograms are shown in Fig. 4.

From the observations made from literature survey on conventional thermography-based systems and preliminary study on rotational thermography, a CAD system has been developed for screening and characterization of abnormality in rotational breast thermograms. The general block diagram of this system is shown in Fig. 5.

Breast cancer detection potential of rotational thermography is evaluated by extracting texture features from rotational breast thermograms in various domains, analyzing and classifying normal and abnormal breast conditions. The potential of these features in characterizing a detected abnormality as benign or malignant has also been studied. Principal component analysis (PCA) and genetic algorithm (GA) are used to identify the most discriminative features for improving the screening and characterization accuracy of the system.

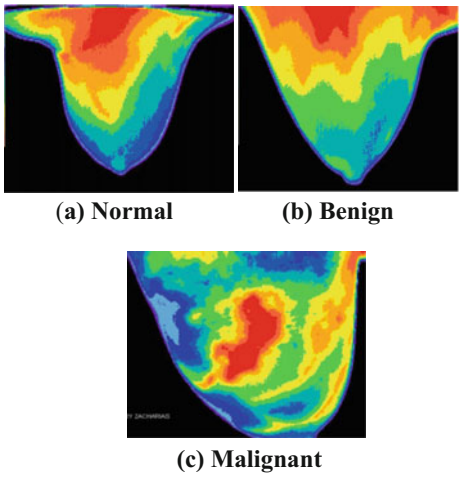

Fig. 4 Samples of rotational breast thermograms

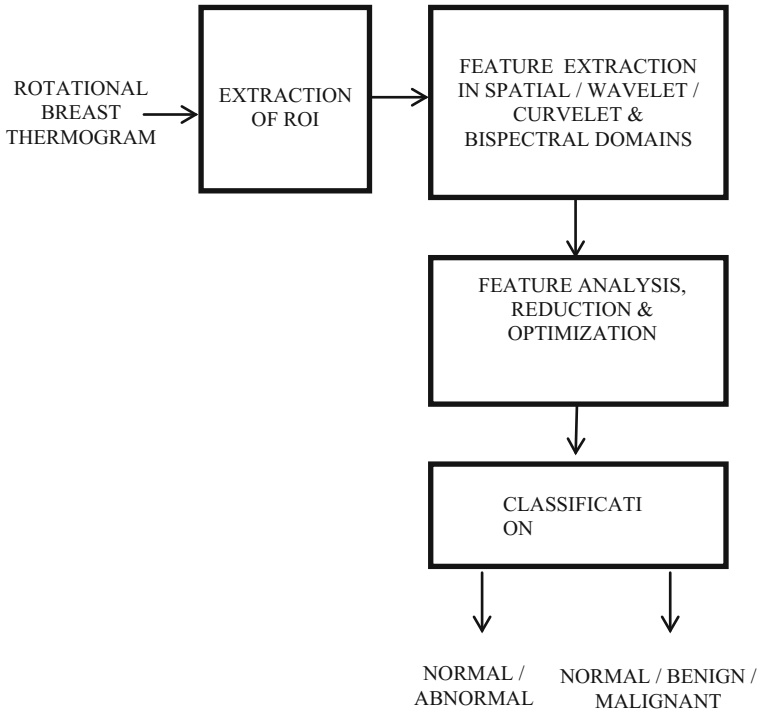

Fig. 5 Rotational breast thermography-based system for screening and characterization of abnormality

3.1 Preprocessing—Segmentation

As the first step, the regions of interest are extracted from rotational thermograms. Normal and abnormal breast thermograms are converted into gray scale as shown in Fig. 6. It is observed that the temperature variation in a normal breast follows a specific pattern in the vertical direction as discussed earlier: an increase in temperature from the nipple to the chest wall. The camera captures the images of breast at every angular increment of 30° by rotating around it, resulting in a series of 12 thermograms. Given the average size of breast, each successive view (image) in the series includes a region already covered in the previous one. Thus, there is partial overlap of regions in successive thermograms in a series.

The distance between the breast and camera is adjusted to obtain complete view of the breast within the frame. According to clinician's requirement, 30% of the total breast area is extracted at the center of image to form the ROI. This extraction is done on all 12 thermograms in a series to ensure that the entire breast area is examined.

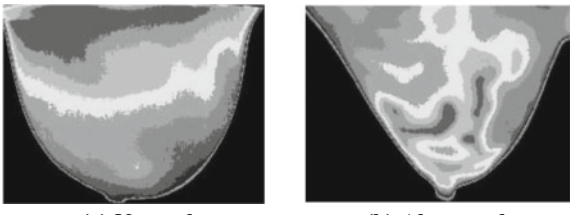

Fig. 6 Rotational breast thermograms in gray scale

Fig. 7 Regions of interest extracted from rotational breast thermograms

(a) Normal **(b) Abnormal**

ROI is extracted using the following steps.

- Obtain the whole breast region from thermogram and calculate its area.
- Identify a vertical axis, midway between the right and left extremes of the breast with nipple position as lower most reference.
- Extract a symmetrical rectangular region about the central axis as the ROI when its area becomes equal to 0.3 × total area of breast.

The central 30% of breast area is extracted from all 12 views in a series of thermograms to form regions of interest. As the entire breast area is covered by this process, no information is lost. The ROIs thus obtained from normal and abnormal thermograms in Fig. 6 are shown in Fig. 7.

3.2 Feature Extraction

Statistical features that best represent the thermal variations in thermograms are extracted as features. First- and second-order statistical features are obtained from the regions of interest of normal and abnormal thermograms. First, these features have been extracted and analyzed in the spatial domain, followed by multi-resolution domains such as wavelet and curvelet.

- **First-Order Statistical features**

First-order statistical features, viz., mean, variance, skewness, and kurtosis, represent the spatial distribution of gray-level intensities in a given ROI. These simple histogram-based statistical features extract global texture information from the thermograms [41]. Mean represents the average intensity of pixels in the ROI

and does not carry significant information. Variance feature represents the deviation of pixel intensities from the mean value of the ROI. Skewness and Kurtosis represent the third- and fourth-order deviations from the mean. Since abnormal regions contain large variations in intensity, features such as variance, skewness, and kurtosis contain significant information.

- **Second-Order Statistical Features**

Second-order statistical features also known as texture features are extracted from normalized gray-level co-occurrence matrices (GLCMs) constructed from the ROIs. Thirteen texture features described by Haralick et al. [42] have been computed. These include angular second moment (ASM), contrast, correlation, sum of squares, inverse difference moment, sum average, sum variance, sum entropy, entropy, difference variance, difference entropy, information measure of correlation 1, and information measure of correlation 2. The ASM feature represents the extent of uniformity in textures. Contrast represents the amount of local intensity variations in an image. Correlation measures linear dependencies in the image. Inverse difference moment is a measure of local homogeneity while entropy measures the range of randomness of the gray-level distribution in the image. All the features derived from normalized co-occurrence matrices contain information about the texture of an image. However, it is difficult to identify the specific texture characteristics represented by each of them.

3.2.1 Wavelet Transform

Wavelet transform is used in signal analysis to overcome the time–frequency localization limitations of Fourier transform. A wavelet is a waveform that exists for a limited duration and has a zero average value. A mother wavelet is a small wave of distinct signature. Wavelet analysis convolves shifted and scaled mother wavelets with the input signal. In two-dimensional signals (images), wavelet decomposition is performed with separable filtering along the rows and columns. At the first scale of decomposition, the image is represented by four sub-bands (three directional sub-bands and 1 approximate band). The wavelet coefficients in these sub-bands carry information about intensity variations in horizontal, vertical, and diagonal directions in the image. Thus wavelet analysis is considered as an image decomposition method that offers good space–frequency localization. Statistical features extracted from the wavelet sub-bands may be used to analyze the underlying characteristics of an image. Figure 8 illustrates image decomposition using wavelet transforms at levels (scales) 1 and 2.

Transformed domain features pose problems of high dimensionality and redundancy due to decomposition into multiple sub-bands. A sub-band is identified for each ROI based on maximum variance criterion. Statistical features are extracted from this sub-band, instead of using the coefficient values directly thereby leading to dimensionality reduction of the feature set. As Symlet mother wavelet is

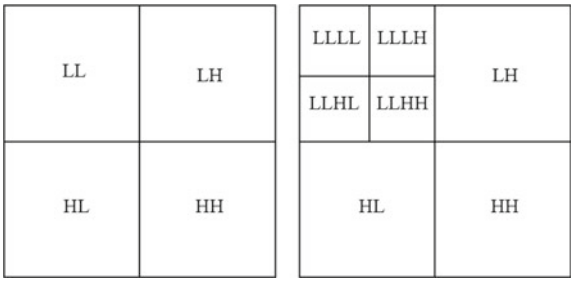

Fig. 8 Representation of 2D wavelet decomposition

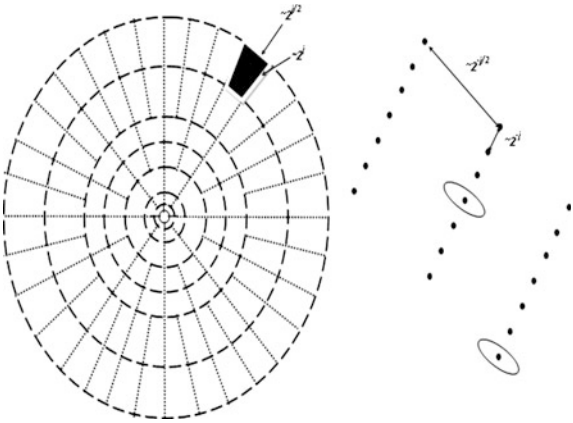

Fig. 9 Continuous curvelet transform decomposition in frequency domain

most suited to detect a deviation from symmetry, it is used to decompose the ROI at level 2. The sub-band with maximum variance was selected for extracting features at decomposition level 2.

3.2.2 Curvelet Transform

Curvelet transform developed by Candes and Donoho is a multi-resolution tool that includes directional aspect while decomposing an image in addition to the scale and position features of a wavelet transform [43]. Most biomedical images contain curvilinear structures. Curvelet transform at a predefined scale and orientation decomposes an image into smaller blocks so as to approximate curves as piecewise linear structures. Curvelet transform resolves the frequency domain into multidirectional and multiscale fan-shaped wedges as shown in Fig. 9. The scale becomes smaller from outside to inside and the number of directions gets reduced by a factor of two after an interval of one scale.

Candes et al. [44] proposed two distinct implementations of discrete curvelet transform: one using unequispaced fast Fourier transform (USFFT) and the other

using a wrapping method. The more common of them, the fast discrete curvelet transform (FDCT), implemented by the wrapping technique has been used in this work.

In curvelet domain, the ROI is decomposed at scale 2 and orientation 8. The sub-bands of curvelet decomposition comprise of curvelet coefficients. The directional sub-band with maximum variance was selected for extracting features. The extracted features are analyzed statistically using student's t test to study their discriminating ability and are classified using SVM classifier. The performance of the classifier is validated using the leave-one-out method.

3.2.3 Extraction of Bispectral Invariant Features

The potential of higher order spectral features (HOS) has been investigated with great interest in the analysis of medical signals such as EEG. The bispectrum of a random signal $x[k]$ is defined as the third-order spectral feature in the frequency domain as given in Eq. 1:

$$B(f_1,f_2) = X(f_1)X(f_2)X^*(f_1+f_2), \tag{1}$$

where$X$ (f) is the Fourier transform of $x[k]$ and f *is* the normalized frequency (between 0 and 1).

The bispectrum of a real-valued discrete-time signal exhibits symmetry properties. Hence, computation may be done over a triangular region in bi-frequency space as shown in Fig. 10.

The integral of bispectrum along a straight line of slope, 'a', gives a complex quantity, containing magnitude and phase information as shown in Eq. 2. This phase component is called the bispectral invariant feature ($\emptyset(a)$) as defined by Eq. 3:

$$I(a) = \int_{f_1=0^+}^{\frac{1}{1+a}} B(f_1, af_1)\mathrm{d}f_1 = I_{\mathrm{Re}}(a) + jI_{\mathrm{Im}}(a) \tag{2}$$

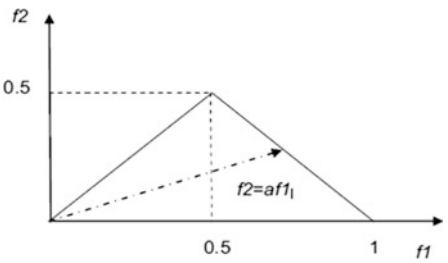

Fig. 10 Region of bispectrum computation in the bi-frequency space

$$\emptyset(a) = \arctan\left(\frac{I_{\mathrm{Im}}(a)}{I_{\mathrm{Re}}(a)}\right). \tag{3}$$

These features have been shown to be invariant to translation, scaling, and amplification [45]. Being sensitive to shape changes in input patterns, these may be used to detect deviations from normal patterns in thermograms. Signal processing principles have been extended to 2D (images) in order to extract bispectral invariant features from thermograms. The input image is first converted into a set of 1D projections using Radon transform at several angles. Bispectral invariant features are computed from each of these projections. In this work Radon transform has been computed at six angles with four slopes each. Thus each ROI is represented by a set of 24 bispectral invariant features.

3.3 *Feature Analysis*

Features extracted from normal and abnormal ROIs in various domains are analyzed and classified using SVM classifier. Average value of each feature is computed for both classes in all the domains. Features extracted in spatial domain and transformed domains are analyzed statistically using student's t test at 95% confidence level. The null hypothesis is framed such that the features extracted from normal and abnormal groups belong to the same class. If the p value returned by the test is found to be less than 0.05, this null hypothesis is rejected. Thus features with $p < 0.05$ are found to be statistically significant than the others and can discriminate an abnormal ROI from a normal one more effectively.

Feature analysis by student's t test proved that the first-order statistical features were statistically insignificant in almost all domains. It is also observed that among the 13 texture features, 8 were found to be significant in spatial domain, 4 in wavelet, and 9 in curvelet domains. The level of statistical significance was found to be highest with the curvelet features. Among the bispectral invariant features, those extracted from all angles were found to be statistically significant except at angle 0. This phenomenon may be explained from basic principles as given. The Radon transform at 0° produces the 1D projection of intensity variations along the horizontal direction at the center of the ROI. It may be observed that pattern changes on a thermogram are minimal in this direction, compared to the vertical and other (radial) angles. Finding the optimal number of angles and slopes for bispectrum computation is found to be a major issue in this domain. Statistical analysis reveals that among the features extracted, the curvelet transform-based co-occurrence features are more suited for the problem.

As the first-order statistical features were found to be statistically insignificant, these were eliminated from further investigation. A two-stage classification scheme has been implemented using texture and bispectral features. In the first stage, the screening ability of the system has been tested in all domains followed by the evaluation of characterization ability.

3.4 Classification

The Support Vector Machine (SVM) classifier is used for automatic detection of abnormal conditions in thermograms. SVM is a supervised learning algorithm that finds wide application in pattern recognition problems. It generates a robust mapping function from a set of training data [46]. SVM is of great use in classification problems where the input data is not linearly separable. In such cases, nonlinear kernel functions may be used to transform the input data to a higher dimensional feature space where the separability is better. The order of these functions may be varied iteratively until the distance between the decision surface and nearest sample is maximized. Thus SVM constructs N-dimensional hyper-plane for optimal separation of input data into classes [47].

In this work a binary SVM using polynomial kernel of order 3 has been used for the classification purpose. Performance of the classifier is validated using leave-one-out method. In this method, a single observation from the original sample is used as the test data, while the remaining observations form the training set. The validation scheme is complete when each observation in the sample has been used as the test data at least once. The performance of the classifier has been evaluated by finding accuracy, sensitivity, and specificity measures from confusion matrices. Traditionally, the classification results of a test under study are compared against those of a standard test. The observations made in four categories, viz., true positives (TP), true negatives (TN), false positives (FP), and false negatives (FN), are presented in a (2×2) matrix. Accuracy is the measure of true results (both true positive and true negative) obtained by the test in the entire population. Sensitivity represents the probability that a test will produce a positive result when used on diseased population. Specificity gives the probability that a test will produce a negative result when conducted on normal population.

3.4.1 Feature Reduction Using Principal Component Analysis

Principal component analysis is a statistical procedure used to convert a set of highly correlated input variables into a smaller set of uncorrelated variables popularly called as principal components [48]. This orthogonal transformation results in a reduced set of variables as the number of principal components obtained is usually less than the number of original inputs. These components are formed by linear combinations of all input features and are arranged in decreasing order of their variance. The composition of these principal components may be analyzed by observing their respective Eigen vectors. PCA is generally used as a feature reduction technique in classification problems when the input feature set is large and redundant.

3.4.2 Selection of Optimal Features Using Genetic Algorithm

Although PCA gives a reduced feature set, all features have to be extracted in the first place in order to form the principal components. PCA provides fewer discriminative inputs that reduce classifier complexity but fails to be of any aid in the exhaustive feature extraction process. Hence, an effective search algorithm may be employed to select the most discriminative subset of features. Genetic algorithm (GA) is used to identify the optimal features that can lead to best classification accuracy. GA is a search algorithm that models the natural process of biological evolution using operators such as selection, mutation, and crossover to find the optimal solution for the specific problem [49].

In GA, each feature set is represented as a chromosome. A chromosome is represented in form of a binary string of length equal to the number of features. A fitness function, usually a maximizing or minimizing function, is defined for the problem. The fitness value of each chromosome is computed. The selection of a chromosome is based on the ranking of its fitness value. The GA-based approach begins with creation of an initial random population and its evaluation using the fitness function based on the classifier error. The chromosomes in the population are ranked according to their fitness values. A few with highest fitness values (Elite) are directly transferred to the next generation. Using selection methods such as roulette wheel, tournament, etc., chromosome pairs are selected to undergo cross over and mutation to form new population. The process is repeated iteratively until the GA converges and the best chromosome is returned. The composition of the best chromosome may be examined to identify the optimal features.

3.5 Results of Classification

The SVM is trained and tested with a set of feature vectors extracted from normal and abnormal thermograms by the leave-one-out method first for screening and then for characterizing an abnormality as benign or malignant.

- **Screening of Abnormality**

The training set consisted of 36 normal and 36 abnormal thermograms (18 malignant and 18 benign). Classifier performance for screening of breast abnormality when features of various domains were used is presented in Fig. 11. It is observed that the screening performance of the system is at its best, when curvelet-based texture features are used, followed by bispectral invariant features. The system is able to detect an abnormal thermogram with a high accuracy of 94.4% in curvelet domain with sensitivity and specificity of 97.2 and 91.7%, respectively. In an earlier study, conventional thermography-based system had resulted in an accuracy of 90.91% when curvelet texture features were employed [50].

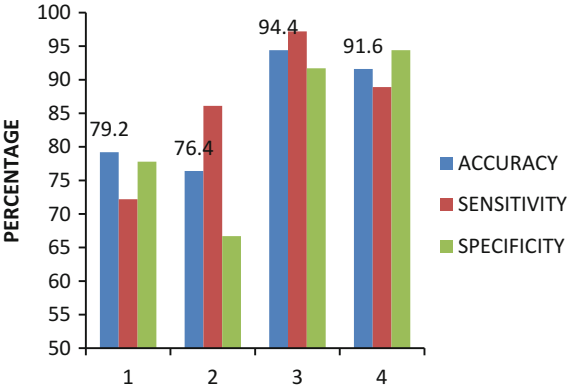

1. Haralick's texture features-spatial domain
2.Haralick's texture features-Wavelet domain
3. Haralick's texture features-Curvelet domain
4. Bispectral Invariant features

Fig. 11 Classifier performance for screening of breast abnormality in rotational breast thermograms

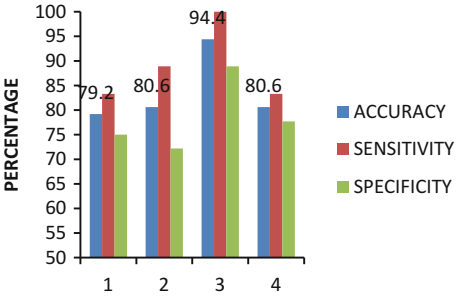

1. Haralick's texture features-spatial domain
2.Haralick's texture featureswavelet domain
3. Haralick's texture features-curvelet domain
4. Bispectral invariant features

Fig. 12 Classifier performance for characterization of breast abnormality in rotational thermograms

- **Characterization of Abnormality**

Features extracted from 36 rotational thermograms in each class have been used for classifying test inputs into benign-malignant, normal–malignant, and normal–benign classes using features extracted in all domains. Classifier performance for characterization of breast abnormality as benign/malignant is presented in Fig. 12. It is observed that the performance of the system for characterizing a detected abnormality as benign or malignant is also at its best when curvelet-based Haralick's texture features are used. An abnormal condition could be characterized as malignant or benign with an accuracy of 94.4% in the curvelet domain.

The results of binary classifications using curvelet-based texture features are shown in Fig. 13. It is observed that a malignant condition could be detected from

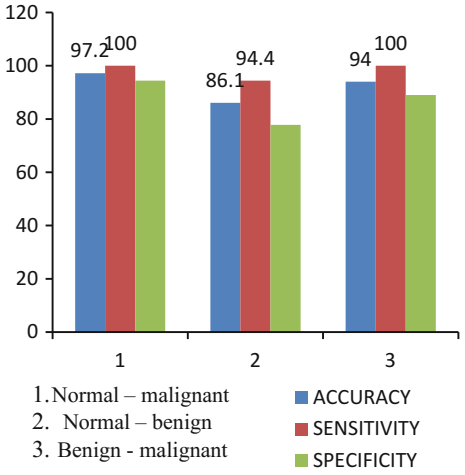

Fig. 13 Performance of SVM classifier using curvelet-based texture features for normal/malignant, normal/benign and benign/malignant classifications

Table 1 Classifier performance for screening and characterization of breast abnormality in rotational thermograms using optimal features selected by GA

Features	Classes	Accuracy (%)	Sensitivity (%)	Specificity (%)
Optimal curvelet transform-based texture features	Normal–abnormal (screening)	94.4	97.2	91.7
	Normal–malignant	98.6	100	97.2
	Normal–benign	88.9	94.4	83.3
	Benign–malignant	95.8	100	91.7

other classes with 100% sensitivity. As the tissue temperature in a malignant region is significantly higher than benign and normal conditions, the classifier is able to detect all malignant cases in the set of input images.

- **Classification using PCA- and GA-Based Feature Selection**

When PCA was used for feature reduction, it was observed that the first 3 principal components (formed from the 13 curvelet-based texture features) could produce an uncompromised classifier performance. As each component is a linear combination of all feature inputs, those which offered maximum contribution were identified from their Eigen vectors. It was found that features such as difference variance, sum of squares: variance, contrast, sum variance, and sum average had contributed significantly to the first principal component.

Incidentally, GA also identified three of these as optimal texture features: contrast, sum of squares—variance and difference variance. On correlating with the results of PCA, it is observed that these features had offered maximum contribution to the first principal component. These were also found to be statistically significant with least p values. Nevertheless, a global optimization technique such as GA has

validated the significance of these features. These features represent variations in the distribution of intensity values in thermograms, most effectively and may be considered to carry significant thermal signatures of abnormality. The results of classification with optimal features are presented in Table 1.

A significant improvement is observed in the classifier performance for characterization of abnormality with the use of optimal features. Although an improvement in classifier performance is observed with the use of optimal features, the accuracy of detecting benign abnormality from normal conditions is only 88.9%. This is observed to be lower than the accuracy in malignant–benign classes. On analyzing the sample thermograms used, the temperature difference between normal and benign conditions was found to be 0.7 ± 0.3 °C and that between malignant and benign conditions was found to be 1.7 ± 0.7 °C. As the margin of temperature difference between the benign–normal classes is lower, it is difficult to detect a benign condition from a normal condition in thermograms, resulting in lower accuracy in this class.

4 Localization Study Using Rotational Thermogram Series

As discussed earlier, images are acquired at spatial increments of 30° resulting in a series of 12 thermograms. Given the size of breast, there is partial overlap of regions in successive thermograms of a series. To ensure that the entire breast is examined, 30% of the total area is extracted as ROI from the center of the breast in each view. However, it is found that these ROIs cannot be identified uniquely with the respective breast views due to the overlaps with ROIs of succeeding and preceding views. Nevertheless, there is a non-overlapped central region in each ROI.

- If an abnormality is represented as hot spots in a confined small area, it will be detected in this central portion of one of the views. Thus, the accuracy of locating it is better.
- If an abnormality is observed at the periphery of breast at one view, it will be seen in the central portion of breast in one or two successive images down the series.
- If an abnormality is represented as a larger hot area, it will be seen in the central portion of more than one view. In such cases, the accuracy of locating it will be erroneous.

As curvelet-based texture features were found to perform best for classification purpose, these were extracted from the ROIs. These feature vectors are given as test inputs to SVM classifier in order to detect abnormal views. The classifier is trained with curvelet texture features extracted from 36 thermograms each in normal and malignant groups. The spatial views where an abnormality was detected by the system are noted for further analysis. Finally, optimal features selected by GA have also been used for improving the localization ability.

4.1 Results of the Localization Study

The study includes precool series—thermograms of 36 malignant patients (12 thermograms per patient). A report indicating hyper-thermal views, as interpreted by the thermographer, is made available for each subject. According to this report, several views are indicated to be hyper-thermal. After scrutiny by radiologist, 2–5 (views) thermograms were identified as abnormal for each patient. The details of thermograms used in the work are given in Table 2.

Table 2 establishes that the distribution of heat on the breast surface is based on the severity of the underlying tumor. It may be observed that hot regions are confined to only 2 views in 10 cases, while in others, 3–5 views may be involved. Thirty-six malignant cases with 12 thermograms each (a total of 432 thermograms, wherein 108 were abnormal) are used for locating the abnormality. For an abnormal patient, when all 12 images in a series were tested with a trained classifier, only thermograms acquired at certain views were detected as abnormal.

Results of the localization study are analyzed by evaluating the performance of the system from confusion matrices. It was observed that all (108) abnormal views were detected by the system when curvelet-based texture features were employed. Out of 324 normal thermograms, 288 were identified correctly by the system, resulting in an accuracy of 91.6%, sensitivity of 100%, and specificity of 88.9%. Improved performance was obtained when optimal features were used for classification as shown in Table 3.

The optimal curvelet texture feature-based system resulted in an accuracy of 93.5% with sensitivity and specificity of 100 and 90.7%, respectively. It is found that all the identified abnormal views were detected, while 30 normal views were misclassified as abnormal. Hence, detailed case studies were conducted to validate the performance of the system with the opinion of expert radiologist. The abnormal views detected by the system were compared with expert opinion and respective ultrasound findings.

Table 2 Details of thermograms used in the localization study

No. of malignant patients (36)	No. of abnormal views/patient	No. of abnormal views
10	2	20
20	3	60
2	4	8
4	5	20
Total no of abnormal views		108

Table 3 Confusion matrix for localization of abnormality using optimal curvelet-based texture features

		Detected class	
		Normal	Abnormal
True class	Normal (324)	(TN) 294	(FP) 30
	Abnormal (108)	(FN) 0	(TP) 108

All regions which were detected as abnormal by the proposed system, expert's interpretation, and ultrasound as well were found to be malignant, resulting in 100% sensitivity. This was verified with biopsy results in each case. It is found that a normal breast region with increased vasculature is reported to be hyper-thermal on a thermogram, but normal on ultrasound. Such cases result in false positives and reduce the accuracy and specificity of the system when used as a standalone unit.

From results of the localization study, it is found that the views where a thermogram was detected as abnormal could always be mapped to the abnormal quadrant identified by USG, unless when the abnormality was positioned along the periphery of two quadrants. In such cases, the location of the abnormality may be mapped to either of the quadrants, as it lies in the overlapped ROIs of two consecutive thermographic views. Thus, the maximum angular error of locating an abnormality is observed as $\pm 30^{\circ}$ (1 view) with respect to camera position. In order to improve the accuracy of classification, the proposed system may be used as an adjunct to USG. Hence, curvelet transform-based texture features may be used to develop a reliable system for localization of breast cancer.

5 Conclusion

A comprehensive study has been conducted on the relatively new breast imaging technique: Rotational Breast Thermography to evaluate its performance for screening and characterization of abnormal breast conditions. As rotational breast thermography acquires images of the breast in multiple views, its ability for localization of abnormality has also been explored.

Features have been extracted and analyzed in spatial, wavelet, curvelet, and bispectral domains. These features have been used for detection of abnormality in rotational thermograms with a SVM classifier. It has been found that curvelet transform-based Haralick's texture features are best suited for the problem.

Screening performance of rotational thermography is found to be superior with curvelet-based texture features. As abnormal regions on breast thermograms exhibit curvilinear properties, curvelet transform-based feature extraction has resulted in better screening. Also a detected abnormality could be effectively characterized as benign or malignant. The ability of rotational thermography for detecting malignancy from normal and benign conditions has also been found to be effective.

GA has been used to identify three optimal features from the curvelet-based texture feature set. An improved system performance, screening accuracy of 94.4%, characterization accuracy of 95.8, and 100% sensitivity for malignancy detection, is achieved when these optimal features were used for classification. Localization of abnormality is a promising area for further research in rotational thermography.

Acknowledgements Authors would like to register their profound gratitude to Mr. N. Kannan of M/s Tuscano Systems Pvt. Ltd., Chennai, India, for the installation of the Rotational Thermography unit and complete technical support for the same.

References

1. American Cancer Society: Cancer facts and figures. Available from www.cancer.org/acs/groups/content/@research/documents/document/acspc-042725.pdf. 10 May 2015
2. Keyserlingk, J.R., Ahlgren, P.D., Yu, E., Belliveau, B.: Infrared imaging of breast: initial reappraisal using high-resolution digital technology in 100 successive cases of stage I and II breast cancer. Breast J. **4**, 241–251 (1998)
3. Gautherie, M.: Atlas of breast thermography with specific guidelines for examination and interpretation. Milan, Italy, PAPUSA (1989)
4. Ng, E.Y.: Is thermal scanner losing its bite in mass screening of fever due to SARS? J. Med. Phys. **32**(1), 93–97 (2005)
5. Vinithasree, S., Ng, E.Y.K., Acharya, R.U., Faust, O.: Breast imaging: a survey. World J. Clin. Oncol. **2**(4), 171–178 (2011)
6. Ng, E.Y.K., Ung, L.N.: Statistical analysis of healthy and malignant breast thermography. J. Med. Eng. Technol. **25**, 253–263 (2001)
7. Etehad Tavakol, M., Ng, E.Y.K.: Breast thermography as a potential non-contact method in early detection of cancer: a review. J. Mech. Med. Biol. **13**(2) 1330001-1–1330001-20 (2013). doi:10.1142/S0219519413300019
8. Ng, E.Y.K.: A review of thermography as promising non-invasive detection modality for breast tumour. Int. J. Therm. Sci. **48**(5), 849–855 (2009). doi:10.1016/j.ijthermalsci.2008.06.015
9. Jayashree, M., Menaka, M., Venkatraman, B., Baldev, B.: Detection of breast lesions by infrared thermography. In: Proceedings of National Seminar on Medical Thermography, pp. 6–9, Chennai, India (2011)
10. Yang, H.Q., Xie, S.S., Lin, Q.-Y., Ye, Z., Chen, S.-Q.: A new infrared thermal imaging and its preliminary investigation of breast disease assessment. In: Proceedings of IEEE/ICME International Conference on Complex Medical Engineering, pp. 1071–1074, Beijing, China (2007)
11. Lawson, R.N.: Implication of surface temperatures in the diagnosis of breast cancer. Can. Med. Assoc. J. **75**, 309 (1956)
12. Gamagami, P.: Indirect signs of breast cancer: angiogenesis study. Atlas of Mammography, pp. 226–231. Blackwell Science, Cambridge, MA (1996)
13. Guidi, A.J., Schnitt, S.J.: Angeogenesis in pre invasive lesions of the breast. Breast Journal **2**, 364–369 (1996)
14. Report of the working group to review the national cancer institute breast cancer detection demonstration projects: J. Natl. Cancer Inst. **62**, 641–709 (1979)
15. Amalu, W.C., Hobbins, W.B., Head, J.F., Elliot, R.L.: Infrared Imaging of the Breast: A Review' in 'Medical Infrared Imaging', edited by Nicholas A Diakides, pp. 9–22. CRC Press, Joseph D. Bronzino (2008)
16. Gros, C., Gautherie, M.: Breast thermography and cancer risk prediction. Cancer **45**, 51 (1980)
17. Amalu, W.: The validity of the thermoregulatory stress test in infrared imaging of the breast. Presented at the 31st annual symposium of the American Academy of Thermology, Auburn University, Alabama (2004)
18. M/s Tuscano Systems Pvt Ltd.: Mammary rotational infrared thermographic system [MAMRIT], PCT/IN 2012/000778 (2012)
19. Camera Specifications: Available from http://www.meditherm.com. 10 December 2013
20. Kapoor, P., Prasad, S.V.A.V., Patni, S.: Automatic analysis of breast thermograms for tumor detection based on bio statistical feature extraction and ANN. Int. J. Emerg. Trends Eng. Dev. **2**(7), 245–255 (2012)
21. Kapoor, P., Prasad, S.V.A.V., Bhavana, E.: Real time intelligent thermal analysis approach for early diagnosis of breast cancer. Int. J. Comput. Appl. **1**(5), 33–36 (2010)
22. Kapoor, P., Prasad, S.V.A.V.: Image processing for early diagnosis of breast cancer, using infrared images. In: Proceedings of 2nd International Conference on Computer and Automation Engineering, pp 564–566, Singapore (2010)

23. Ng, E.Y.K., Chen, Y., Ung, L.N.: Computerized breast thermography: study of image segmentation and temperature cyclic variations. J. Med. Eng. Technol. **25**(1), 12–16 (2001)
24. Etehad Tavakol, M., Sadri, S., Ng, E.Y.K.: Application of k- and fuzzy c-means for color segmentation of thermal infrared breast images". J. Med. Syst. **34**(1), 35–42 (2010)
25. Ng, Eddie Y.-K., Chen, Y.: Segmentation of breast thermogram: improved boundary detection with modified snake algorithm. J. Mech. Med. Biol. **6**(2), 123–136 (2006)
26. Golestani, N., Etehad Tavakol, M., Ng, E.Y.K.: Level set method for segmentation of infrared breast thermograms. Exp. Clin. Sci. Dortmund Ger. **13**, 241–251 (2014)
27. Nurhayati, O.D., Widodo, T.S., Susanto, A., Tjokronagoro, M.: First order statistical features for breast cancer detection using thermal images. World Acad. Sci. Eng. Technol. **46**, 382–384 (2010)
28. Etehad Tavakol, M.: Estimating the mutual information between bilateral breast in thermograms using nonparametric windows. J. Med. Syst. **35**(5), 959–967 (2011)
29. Francis, S.V., Sasikala, M.: Automatic detection of abnormal breast thermograms using asymmetry analysis of texture features. J. Med. Eng. Technol. **37**(1), 17–21 (2013)
30. Acharya, U.R., Ng, E.Y.K., Tan, J.H., Sree, S.V.: Thermography based breast cancer detection using texture features and support vector machine. J. Med. Syst. **36**, 1503–1510 (2010)
31. Prasad, S.V.A.V., Kapoor, P., Patni, S.: Image segmentation and asymmetry analysis of breast thermograms for tumor detection. Int. J. Comput. Appl. **50**(9), 40–45 (2012)
32. Wiecek, B., Wiecek, M., Strakowski, R., Jakubowska, T., Ng, E.Y.K.: Wavelet-based thermal image classification for breast screening and other medical applications. In: Ng, E.Y.K., Acharya, U.R., Suri, J.S. (eds.) Chapter 12, Performance Evaluation Techniques in Multi-Modality Breast Cancer Screening, Diagnosis and Treatment. American Scientific Publishers (2010)
33. Etehad Tavakol, M., Ng, E.Y.K., Chandran, V., Rabbani, Hossien: Separable and non-separable discrete wavelet transform based texture features and image classification of breast thermograms. Infrared Phys. Technol. **61**, 274–286 (2013)
34. Rajendra Acharya, U., Ng, E.Y.K., Vinitha Sree, S., Chua, C.K., Chattopadhya, S.: Higher order spectra analysis of breast thermograms for the automated identification of breast cancer. Expert Syst. **31**(1), 37–47 (2014). doi:10.1111/j.1468-0394.2012.00654.x
35. Etehad Tavakol, M., Chandran, V., Ng, E.Y.K., Kafieh, R.: Breast cancer detection from thermal images using bispectral invariant features. Int. J. Therm. Sci. **69**, 21–36 (2013)
36. Etehad Tavakol, M., Lucas, C., Sadri, S., Ng, E.Y.K.: Analysis of breast thermography, using fractal dimension to establish possible difference between malignant and benign patterns. J. Healthcare Eng. **1**(1), 27–43 (2010)
37. Ng, E.Y.K., Sudharsan, N.M.: Numerical modelling in conjunction with thermography as an adjunct tool for breast tumour detection. BMC Cancer (Medline J.) **4**(17), 1–26 (2004)
38. Ng, E.Y.-K., Sudharsan, N.M.: An improved 3-D direct numerical modelling and thermal analysis of a female breast with tumour. Int. J. Eng. Med. Proc. IMechE, Part H **215**(1), 25–37 (2001)
39. Ng, E.Y.-K., Sudharsan, N.M.: Numerical computation as a tool to aid thermographic interpretation. J. Med. Eng. Technol. **25**(2), 53–60 (2001) (Published: MAR-APR)
40. Tan, J.-H., Ng, E.Y.K., Rajendra Acharya, U., Chee, C.: Study of normal ocular thermogram using textural parameters. Infrared Phys. Technol. **53**, 120–126 (2010)
41. Nurhayati, O.D., Widodo, T.S., Susanto, A., Tjokronagoro, M.: First order statistical feature for breast cancer detection using thermal images. World Acad. Sci. Eng. Technol. **70**, 1040–1042 (2010)
42. Haralick, R.M., Shanmugam, K., Dinstein, I.: Textural features for image classification. IEEE Trans. Syst. Man Cybern. **3**, 610–621 (1973)
43. Candes, E.J., Donoho, D.L.: Curvelets, multi-resolution representation, and scaling laws. In: Proceedings of SPIE 4119. Wavelet Applications in Signal and Image Processing VIII, vol. 1, San Diego, CA, USA, 4 Dec 2000

44. Candes, E.J., Demanet, L., Donoho, D., Ying, L.: Fast discrete curvelet transforms. Multiscale Model. Simul. **5**(3), 861–899 (2006)
45. Chandran, V., Carswell, B., Boashash, B.: Pattern recognition using invarients defined from higher order spectra: 2-D image inputs. IEEE Trans. Image Process. **6**, 703–712 (1997)
46. Tan, J.H., Ng, E.Y.K., Acharya, U.R.: Study of normal ocular thermogram using textural parameters. Infrared Phys. Techn. **53**, 120–126 (2010)
47. Hearst, M.A., Dumais, S.T., Osman, E., Platt, J., Scholkopf, B.: Support vector machines. IEEE Intell. Syst. **13**(4), 18–28 (1998)
48. Smith, L.I.: A tutorial on Principal component analysis. Cornell University, USA. **51** (52), 65 (2002)
49. Babatunde, O., Armstrong, L., Leng, J.: A genetic algorithm-based feature selection. Int. J. Electron. Commun. Comput. Eng. **5**, 899–905 (2014)
50. Francis, S.V., Sasikala, M., Saranya, S.: Detection of breast abnormality from thermograms using curvelet transform based feature extraction. J. Med. Syst. **38**(4), 1–9 (2014). doi:10.1007/s10916-014-0023-3

Author Biographies

Dr. Sheeja V. Francis is Associate Professor at Department of Electronics and Communication Engineering at MNM Jain Engineering College, Chennai—600097, Tamilnadu, India.

As a graduate research scholar, she has carried out research on diagnostic applications of near infra red light. She has worked on image processing approaches for automatic detection of abnormality in breast thermograms in her doctoral programme, at the Department of Electronics and Communication Engineering, College of Engineering, Guindy, Anna University, Chennai—600025. Her area of interests are Biomedical signal and image processing.

Dr. M. Sasikala is Associate Professor, at Centre for Medical Electronics, Department of Electronics and Communication Engineering, College of Engineering, Guindy, Anna University, Chennai—600025, Tamilnadu, India. She has been associated with this work as supervisor, right from its start and has been refining the same with her vast experience in medical image processing. Her area of interests are Biomedical signal and image processing, pattern recognition and Brain computer interface.

Dr. Sandeep D. Jaipurkar is consultant radiologist, at the Breast Clinic, Vijaya Health Centre, Chennai, Tamilnadu, India. He is a pioneer in the field of breast thermography and has provided the rotational breast thermograms. He has been associated with this work for the last three years and provided clinical validation of results.

Application of Infrared Images to Diagnosis and Modeling of Breast

Roger Resmini, Aura Conci, Lincoln Faria da Silva, Giomar Oliver Sequeiros, Francieric Araújo, Claudinéia de Araújo, Adriel dos Santos Araújo, Reinaldo Rodríguez-Ramos and Frédéric Lebon

Abstract This chapter presents some developments and researches on using breast infrared images in Brazil (Visual Lab group of the Federal Fluminense University). These researches focus on comparing protocols for data acquisition using a FLIR SC 620 infrared (IR) camera; preprocessing the acquired data (using operations such as region of interest or ROI extraction, image registration and some other operations to prepare the images or thermal matrices to be used in computations); 3D reconstruction and, diagnostic recommendations from the IR data. These are steps for development of computer tools for screening breast diseases, mainly, to be used on public health system (named in Brazil: "Sistema Único de Saúde"—SUS). After experimentations and comparisons among the diversity of recommendations and ways of data acquisition reported in the literature, we propose a new protocol to IR data capture and storage. With these, we developed a web site that can be used

R. Resmini (✉) · C. de Araújo
Instituto de Ciências Exatas e Naturais, Universidade Federal de Mato Grosso, Rodovia MT 270, Km 6, Bairro Sagrada Família, CEP: 78735-901 Rondonópolis, Mato Grosso, Brazil
e-mail: rogerresmini@ufmt.br; rogerresmini@gmail.com

A. Conci · L.F. da Silva · G.O. Sequeiros · A. dos Santos Araújo
Instituto de Computação, Universidade Federal Fluminense, Av. Gal. Milton Tavares de Souza s/n, CEP: 24210-346 Niterói, Rio de Janeiro, Brazil

F. Araújo
Diretoria-Geral, Diretoria de Administração e de Planejamento, Instituto Federal do Piauí, Praça da Liberdade, 1597 Teresina, Piauí, Brazil

R. Rodríguez-Ramos
Facultad de Matemática y Computación, Universidad de la Habana, San Lázaro y L, Vedado, Habana 4 CP10400, Cuba

F. Lebon
Laboratoire de Mécanique et d'Acoustique, Université Aix-Marseille, CNRS, Centrale Marseille, 4 Impasse Nikola Tesla, CS 40006 13453 Marseille Cedex 13, France

E.Y.K. Ng and M. Etehadtavakol (eds.), *Application of Infrared to Biomedical Sciences*, Series in BioEngineering,
DOI 10.1007/978-981-10-3147-2_10

by all researchers interested in development of works in such subject. The site has public access and presents several ground truths of intermediated developments of the research as segmentation of the ROI, sets of features to be used for comparing artificial intelligence methods for decision making, and some techniques for ROI registration. Our intension is to provide materials to those interested in infrared researches for breast disease. For the development of IR applications are very important compare outcomes in disease detection (and diagnosis) and to use different strategies for features extraction, decision-making, and dimensionality reduction. However, in order to promote fair conditions for comparisons, we have to begin in a more standardized way to go further and for this we invite all interest in the same theme to use a unified procedure for data acquisition.

Keywords Infrared images · Image registration · Breast diseases · Image segmentation

1 Introduction

Thermoregulation in humans is affected by their metabolic activity and sweating. Related to the temperature distribution, the human body can be considered as a symmetrical system around the sagittal plane. This is the idea behind the use of temperature for diagnosis or triage of diseases [7]. As Hippocrates said, "if the temperature of an area of the body diverges of its symmetrical, then diseases must be chased in these" [1]. It is especially related to the tumor growth when angiogenesis plays a fundamental part of in the processes of proliferation, migration and cellular differentiation, and when neovascularization increases the temperature in the region near to a cancer.

Thermography, like ultrasound (US), is a functional examination. Both present no risks to the patient and do not use ionizing radiation, and have safety and cost benefits. The use of US imaging or sonography in medicine requires very good operator training: such a person, in most countries, must be the same doctor that elaborates and signs the examination report. On the other hand, to aid the diagnosis of breast cancer, the most widely used imaging examination is mammography. This is, in part, due to the fact that mammography (like thermography) does not require a medical doctor for acquiring the patient images: only a well-trained nurse or assistant who follows an established and protocol of training is necessary; then, diagnosis can be done later by the specialists. This possibility allows performing examinations in a more efficient way in large hospitals, big clinics and in a very populated and poor country for triage proposes. Additionally, combining the two main positive aspects of these most used and traditional examinations in medicine, some authors have pointed out that thermography can detect cancer earlier than US imaging and mammography, due to their relation with fluid perfusion, neo vases formation and in the beginning of a disease [12, 15].

Historically, the computer was used for the first time to help with medical diagnosis around the year 1960. At that time, the key idea was to achieve a diagnosis elaborated by the computer. Due to several factors such as low processing power of computers and the lack of powerful algorithms, for decision making, the idea did not progress. By the 1980s, the idea of using the computer for the diagnosis reemerged, supported by the increase in the processing power of computers, advances in image processing and improvements in artificial intelligence algorithms. This second wave was supported on the premise that the computer system gives a second opinion or a complementary opinion for diagnostics, but never pretending to replace the human specialist. The first thermal sensors became available for diagnosis in the 60s. The 1990s promoted advances in infrared (IR) sensors (IR digital cameras allow the implementation of more elaborated software, accurate enough to be used for medical diagnostics) . During the current millennium, a new generation of sensors has arrived, being more rapid, sensitive and allowing images with more resolutions.

Although, the computational power of computers has increased continuously since then, allowing use of more sophisticated machine learning algorithms, such as support vector machines (SVM) [33], fuzzy neural networks, and deep learning. And, even though, big data treatments have grown in parallel, producing more techniques for storage, maintenance and retrieval, and allowing for use of not only an image per patient but a complete history of the patient's life with many sorts of examinations patients can have, included in their files along with many other significant data sets related to heath. The idea nowadays is to use the computer as a tool to help the physician save time, and to promote more efficient and correct diagnosis without taking from the physicians and patients the role of protagonists (i.e., continuing in the trend of the end of last century). With this in mind, this chapter suggests image processing techniques to help in the medical diagnosis of breast diseases by using thermal imaging. In the literature an inconsistent point among the articles using infrared breast imaging is the existence of multiple protocols for data acquisition, that is. These aspects are discussed in the next section. After acquisition, the images and data are stored and submitted to a number of techniques which generate the result of the examination, which is the report that is to be sent to the patients and their physician. These techniques are explained in the following sections, which consider storage and retrieval, preprocessing, 3D reconstruction, extraction of features, classification and performance evaluation.

2 An Overview on the Image Acquisition Protocols

Image acquisition protocols present at least three aspects: the preparation of the patient; the room environmental conditions and the procedures performed on the patient during the examination.

The preparation of the patient is related to recommendations to be followed before the exam (first aspect). Although, almost each hospital or health center uses

its own protocol, there are common patient recommendations. For instance, these are for patients do not do: smoke; drink caffeine or alcohol; practice physical exercises; and apply any cream or oil type in the region of the breast and armpit. A second aspect of recommendations is related to the environmental conditions of the examination room: Temperature, relative humidity and air circulation should be controlled during the examination and the same of all capture. This second aspect is, in some way, almost the same among the groups (excluding the room temperature) using thermal examinations over the world, as well.

However, considering the procedures performed on the patient (third aspect) there are much more variations. This third aspect ranges from the induction of changes in the body temperature of the patient (**Passive Static Thermography**), or no temperature alteration (**Active Dynamic Thermography**); duration of cooling or heating of the breasts; patient's position (lying, sitting or standing) during the examination; patient's position relative to the camera (angles and distance); position of the arms (on the head or supported at the waist, the named akimbo position), and number of examinations used on the diagnostic decision.

Related to the induction of changes in the breast temperature, the acquisition protocol may be classified as static or dynamic (passive or active). This nomenclature is considered in relation to the presence of the forced heat transfer in the patient body and consequent increase in the transient terms of the associated equations that describes the phenomena of thermal distribution on healthy and unhealthy tissues of the breast. In static protocols the patient is on stable temperature state with the environment of the examination room over the duration of the exam. This type of acquisition is suitable to identify hot and cold areas and to measure the symmetry in the distribution of skin temperature: it is the most used type. On the other side, an acquisition protocol is named dynamic when the camera is used for monitoring the recovery of skin surface temperature after a thermal stress (for example, heating or cooling) or chemical stress (e.g., on the use of some drug to promote vasodilatation or vasoconstriction in the vascular system). In other words: the dynamic case study the temperature of the skin surface in transient part of the processes and, allows to analyze changes over time, this turns important the acquisition of more than one frame at same position in the examination in order to enable the use of the transient set of data. That is, to promote the use of the information related to the changes of the skin surface temperature plus the interior temperature radiation and convection improves the identification of the age of the blood vases of the breast. This is important because normal veins (the one with almost the same age then the patient) present vasoconstriction (i.e., have constriction behavior) on the cold. However, this behavior is not visible for the bad formed and incomplete vein produced by the fast malignant proliferation of cells induced by the liquids perfusion near a cancerous region.

A fourth aspect related to the acquisition protocols is the dates or number of examinations used to promote the current diagnosis of a patient. In this aspect it can be classified as simple, sequential, or monitoring. In a simple acquisition, a unique examination (capture in a specific date or a single image) of the patient is used, that is, only a moment of time of her life is considered. In sequential mode, a series of

images are acquired sequentially at a time interval as in dynamic protocols for monitoring skin temperature variation do not in the same day, but after some interval of days, weeks, or months. That is, as the dynamic protocol more images are used, but in monitoring mode, images are captured over longer interval on the same type of examination, for instance every 6 or 12 months, in order to monitor suspicious region, for early detection of a disease, to verify the progress of a disease and treatment after an therapy [27, 29]. Of course, the fourth aspect can be considered as a repetition of the third. For this, the protocols which deserve more analysis and experimentations are the static and the dynamic (Passive or Active) acquisition protocol grouped in the third aspect commented before. In order to see what can be considered the best one for the interested community on promote the union of effort for better use of IR images on diagnosis, data from these two types of acquisitions, obtained by our group, are available in a database of breast thermal images, named Database for Mastology Research with Infrared Image—DMR-IR [27], and can be used by researchers on breast infrared images. This, as far as we known, have never be done before for breast diagnosis (for locating perforating vessels in breast reconstruction surgery the use of cold and hot stimulation was used and compared with static thermography by Kołacz et al. [16]). In both, the patient attempts the common preparation and we used to ask them for, before capturing the images, pass for acclimatization in a room with controlled temperature (between 20 and 22 °C for 10 min) with arms raised over the head and with the breast naked. The 2 acquisition forms used on experimentations are: (1) A static protocol, where five captures are

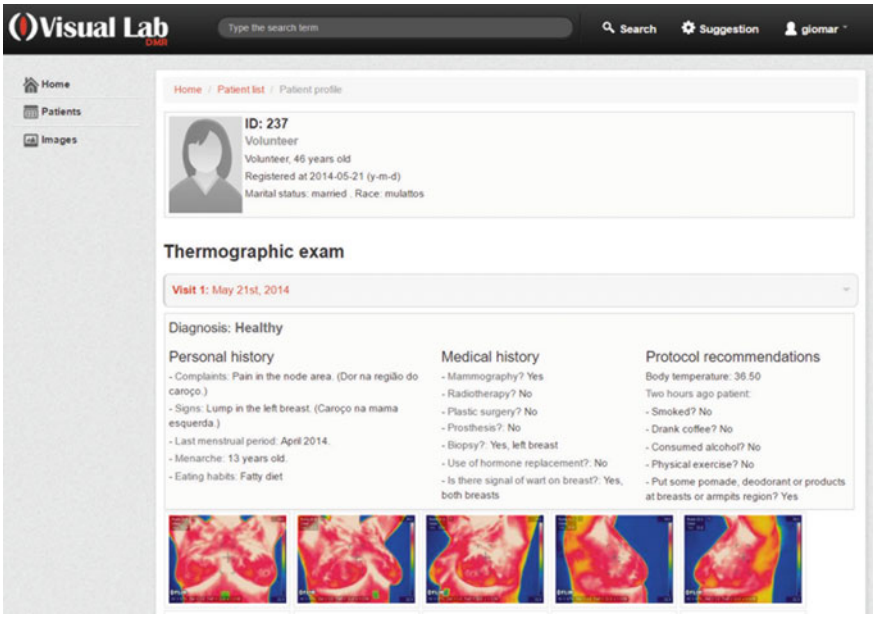

Fig. 1 User interface of DMR-IR database (http://visual.ic.uff.br/dmi)

done: 1 frontal, 2 laterals in an angle of 45° with the camera and 2 laterals in direction of the right and left sides of the body (Fig. 1). (2) A dynamic protocol, where an electric fan is turned on, in the breasts for 2 min and twenty frontal images are acquired, in fifteen seconds interval between them [28]. The resulting infrared images present 640 × 480 pixels and were captured using a FLIR thermal camera, model SC620, which sensitivity of 0.04 °C range from −40 to 500 °C.

3 Storage and Retrieval

The Database for Mastology Research with Infrared Image—DMR-IR contains infrared images and temperature matrixes, digitalized mammograms and clinical data acquired in the university hospital (Hospital Universitário Antônio Pedro—HUAP) of Federal Fluminense University, Rio de Janeiro, Brazil. The data are from patients of the gynecologic department of HUAP. There are data from healthy patients and from patients with a number of breast diseases, including cancer. This research is approved by the Ethical Committee of the HUAP and registered at the Brazilian Ministry of Health under number CAAE: 01042812.0.0000.5243. The DMR-IR is accessible through a user-friendly interface (http://visual.ic.uff.br/dmi) for managing and retrieving information. All data are from those patients that agree on signing a term of understanding and knowledge about the research details and consent on the use of their data for the research. Figure 1 illustrates one of the navigations pages of the static protocol with some patient information for filtering the wanted cases and images. Images can be downloaded in JPG or BMP format for mammograms and thermograms (infrared images). The thermograms can also be downloading as a 2D array of temperature. Reports of the exam can be downloaded in txt or xml format as well.

A relational model was employed to construct the database and a client–server application is used for data management. A retrieval tool was implemented using a client side application that provides a search dialog to compose the query. A server side application executes it using the tool and returns the results to the client [13, 31]. As in some cases, textual-based information is not enough for retrieval, especially when user's search requirements are about image visual features, a CBIR (Content-Based Image Retrieval) tool was implemented. The image retrieval is based on extraction of interest points. An interest point of an object represents a specific area on the object around which the local image structure is rich in terms of local information about the image content.

Figure 2 shows the CBIR model for image retrieval given an image as sample and performing ASIFT [20]. In this, we use the frontal position of the thermograms. For image representation, the local visual feature considered is the Bag of Words (BoW) [32]. The basic idea of BoW is that a set of local image patches is sampled using some detected features on key points. They are composed by a vector of visual descriptors for each patch independently. Then the patches created are included into a set of visual words which constitute a codebook. After that, an

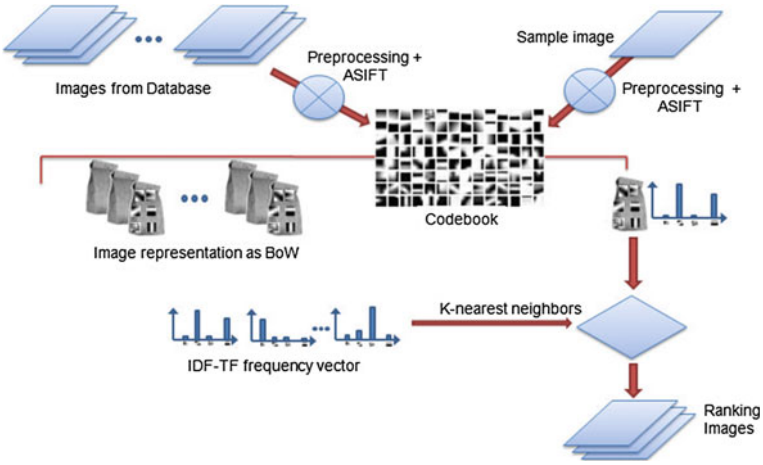

Fig. 2 Content-based image retrieval (CBIR) with bag of words (BoW) model [25]

image is described as a histogram-based representation of the codebook, and a classifier (the Support Vector Machine—SVM in the implemented tool) is used to find the image more similar to one associated to that the user have presented as sample for retrieval [25].

4 Preprocessing

Mainly, the preprocessing step performs the segmentation of the data that is the identification of the Region of Interest (ROI) of the images, and the separation of this from the rest of the frame (that will be considered no relevant or the background). For diagnosis purpose, the thermal matrix and image are exported by the camera. Both data can be used in an analysis. Images can use for segmenting visually the ROIs, and the thermal matrixes (i.e., the file with thermal values, one per point in the scene observed) are used for feature extraction to help in diagnosis.

The segmentation process (i.e., the ROI), in the breast application, frequently generates two areas or masks, one for the right breast and the other for the left breast. According to the physicians of our groups there are two possible ways to consider the breast analysis relating to ROI segmentation [4, 8]. Both exclude head and neck and begin in the inframammary fold. Figure 3 shows these two types of ROIs: including (Fig. 3a, b) in the ROI the area of possible lymph nodes related to breast and armpits or excluding this area (Fig. 3c, d) [23].

The purpose of inclusion of the armpits area is to investigate the ability to detect altered lymph nodes, like it is done in sentinel lymph node exams (that verifies if a cancer is in metastases) [18]. Ground truth (i.e., segmentation is done manually by specialist) for this type of segmentations and the results achieved by two automatic

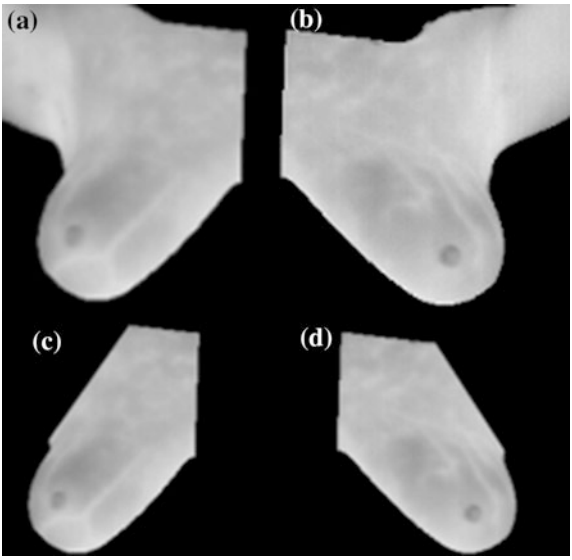

Fig. 3 Two possible breast regions of interests (ROI). **a** *Right* breast and **b** *left* breast of segmentation without armpits. **c** *Right* breast and **d** *left* breast of segmentation with armpits [23]

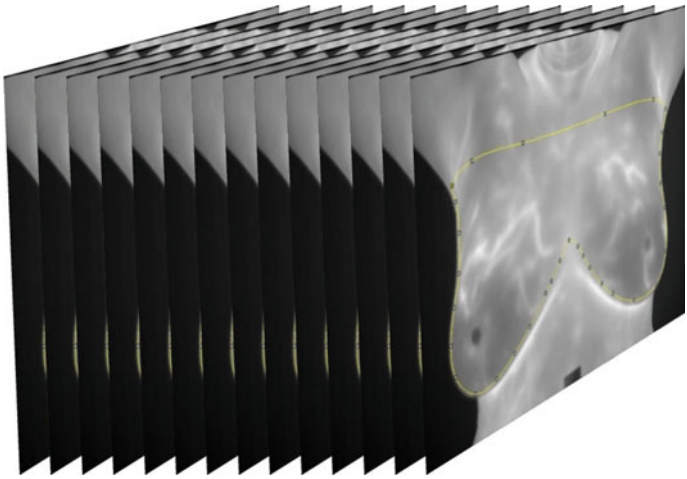

Fig. 4 Series do dynamic acquisition and the region of interest (ROI) on the images

approaches can be seen in http://visual.ic.uff.br/en/proeng/marques/ or downloaded in http://visual.ic.uff.br/en/proeng/marques/gt.php. Details about how they are done can be found in Marques et al. [19]. The same process of separation of relevant data can be applied over the array of temperature, i.e., the temperature to be analyzed can be cropped and the elements outside the region of interest (ROI) can not be used (Fig. 4).

For comparison of the influence of the use of this additional area on diagnosis, both ways of segmentation are performed in the same group of patients and the same methodologies for features extraction and diagnostic suggestion are conduced to a complete scheme by Resmini [23]. Segmentations used in this comparison are available in http://visual.ic.uff.br/en/proeng/rresmini_thesis.

5 Three-Dimensional Reconstruction

The geometric modeling of the patient breast is useful for many application such as: (1) to merge temperature information with others [5] specially with 3D exams which represent the same patient like magnetic resonance, (2) to represent a model of the breast with a 3D mesh for surgical reconstruction after mastectomy modeling, (3) to identify points of correlation between IR exams and models of the patient body for finite elements analysis or other forms of treatment of the inverse problem (i.e., what is inside of the body that can result in a thermal distribution of skin' surface) [3, 11, 24] and (4) for some numerical analysis and other examinations like Electrical Impedance Tomography (EIT) [14] and 3D Ultrasound [35]. Moreover, three dimensional meshes of the real model can be used in surgeries simulations, for the personal project of prosthesis, for breast reduction, and other procedures.

We proposed two approaches for reconstruction. The first one uses a frontal image and two lateral (orthogonal to this) images of the breast for shape reconstruction. Figure 5 shows some steps of this approach [34]. The second extends the first by proposing an apparatus to be used during the capture with thermal camera and two Kinects (MicroSoft Xbox 360), improving the quality of the 3D mesh generated [2]. The steps of the second one can be seen in Fig. 6.

From the two-dimensional thermal images (Fig. 5) it is possible to reconstruct the patient breast geometry. The 3D geometric model proposed is based on fitting two curves (for each breast a frontal and lateral view is used). The first step is the identification of the points of the inframammary fold of the patient's IR image). These points are computed from IR image adjusted by using the least-square method (LSM) [34]. These define the bottom curve used to define the size and

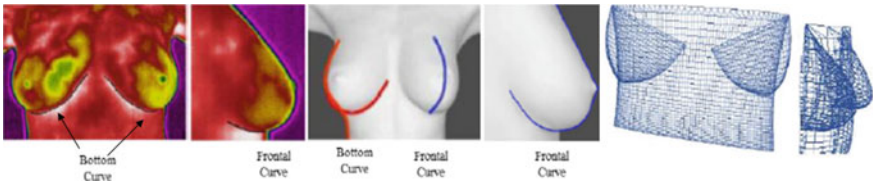

Fig. 5 Breast contour detection using a frontal and lateral view for each breast. Surface modeling from such curves are achieved after positioning the lateral curves on a plane parallel to the coronal over the nipple and using the bottom curve to define the size and shape of the breast [34]

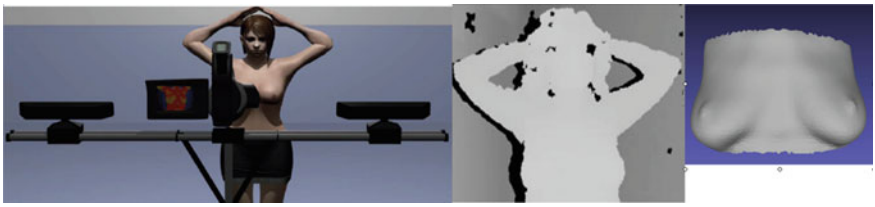

Fig. 6 Schemes for data acquisition the infrared image and at same time the range cameras (kinects) for breast geometric reconstruction, the range image achieved and the obtained result [2]

shape of the breast. The spatial shape is defined by positioning the border of the lateral views orthogonally to this over the nipple. The curves are joined as indicated in Fig. 5. A computer graphics border representation can be used to generate the 3D mesh. Then calculated curves and surfaces are compared with those obtained from the process of asking the patient to be inside a laser scanner device in order to capture the shape and measure how well the calculated curves and surface fits the patient breast shape. The steps for these are:

1. Identification of the 2D coordinates of the breast border from the IR image red line and blue line in Fig. 5;
2. Definition of the middle point (or nipple position) of the inframammary fold image (red line) that will joint this curve with the vertical points (blue line);
3. Translate coordinates of all the points to the same axis and origin, and calculation of the 3D representation of the coordinates of the points, i.e., the (x, y, z) representation for the frontal breast lower curve as can be seen in order to have an orthogonal spatial limits of the breast;
4. Creation of an NURB surfaces using this limits, and the a 3D model of the breast [34].

The validation of generated model was realized using 3 volunteers that have been submitted to 3D laser digitalization of their bodies. Then the model of the real bodies obtained with the scanner and the proposed "steps" re compared: i.e., the laser scanned points with the proposed model of reconstruction from thermal images. It was found that, on average, the differences between the 3D shape from this method and the acquired model by laser scanner differ between 4.42 and 6.03%. The maximum value of differences is between 4.77 and 6.08%. In addition, the general analysis about average of maximum value, and the minimum value found on the validation is considered small and very much acceptable, turning the 3D model created by this methodology very close to real patient breast [34].

Range images are the name of the outcomes of a collection of imaging devices available to produce a 2D image considering the distance of the points in a scene to a specific point. This is normally associated with some type of sensor of the device. These images have as pixel values a measure of the corresponding distance (e.g., brighter values mean shorter distance). If the sensor used to produce the range

image is properly calibrated, the pixel values can be used directly to compute distance in the desired length unit, such as centimeters or inch.

In the developed of a second technique for breast shape modeling we used two Kinects, and it consists of three stages: the first is calibration of the Kinects in an apparatus (Fig. 6 left); the second step carries out the registration of the clouds of points acquired by the sensors (Fig. 6 center); then, the reconstruction of the surface of the virtual object (Fig. 6 right). Comparison of this technique and the real breasts of five (5) volunteers and two (2) phantoms are done [2]. For the volunteers the breasts are captured by a laser scanner (as previous commented) and for the phantoms they are measured directly by a mechanical devise. The mean differences among the surfaces areas are 3.55%, or 0.93 considering the Dice similarity coefficient [9], in average, and we achieve mean differences among the distances of the real nipples and the reconstructed models of 3.51% in this technique.

6 Feature Extractions, Classification and Evaluation of Performance for Diagnostic Tools

The developed tools for diagnostic aid [10] can be divided as a function of time in static or dynamic. They originate from the use of data archived by the **Passive Static Thermography or by the Active Dynamic Thermography**, respectively.

Using the static protocol, 3 works to perform diagnosis have been developed by our group. In a first one [26], Lacunarity and the Hurst coefficient are calculated from each breast ROI. Both these features use the concepts of the fractal geometry and were computed in three approaches: using each ROI independently, combining both patient ROIs by subtracting one from the other or by feature subtractions. A total of 133 features were extracted in Serrano et al. [26] work from a sample of 28 volunteers. Classification algorithms of WEKA (http://www.cs.waikato.ac.nz/ml/weka/) were used. To identify the best result achieved, the performance of a cancer x normal classification were considered by plotting the true positive rates (sensitivity) against the false positive rates (specificity) of each used classifiers, i.e., the receiver operating characteristic (ROC) curve were considered. The Naïve Bayes technique achieved the best score for correctly identifying cancer using these features: it presented 0.958 of area under the ROC Curve (AUC).

In a second work [22], a total of 320 features were computed: most of them are from the geo statistic (Ripley's K function, Moran index, and Geary coefficient), but also features from fractal geometry (using Higuchi fractal dimension approach) and statistic (average and standard deviation and second order moments). They are computed from each breast separately without combination or subtraction of images or features. The same 28 patients are considered. These characteristics are grouped in an array of data processed by the WEKA (http://www.cs.waikato.ac.nz/ml/weka/) classifier software, as the previous one. The principal component analysis (PCA) is performed in two ways: with the base divided into four groups of features and with

the entire amount of data. The Support Vector Machine (SVM) was used for patient classification by the PCA best group. The best accuracy is 82.14 and 91.70% is the best sensitivity obtained [21].

In a third work [4], the used features were from fractal geometry (Higuchi fractal dimension and Succolarity), basic statistics (average, standard deviation, and thermal amplitude), histograms from the thermal matrix, geostatistics (Moran index and Geary coefficient), and Ripley Diversity Index, using a total of 40 features computed from 51 patient's ROIs. Some tests were performed to find the most expressive set of features by Principal Components Analysis (PCA) and genetic algorithm feature selection. The work used SVM for classification and the AUC to perform comparison of outcomes (resulting in 85.20%).

Using data from the dynamic protocol, Silva et al. [28] proposed a methodology for analyzing temperature variations in order to detect a number of breast abnormalities (including cancer), using unsupervised and supervised machine learning techniques, which characterizes the methodology as hybrid. The sequence of thermograms from each patient is firstly segmented and the ROIs are registered using the initial frame as reference. Then, for each point, functions representing the change of temperature during the examination are built and the k-means algorithm is applied on these functions using various values of k. Indices of clustering validation are applied to evaluate the possible groups for each value of k, generating values to be used in the classification model. Data mining tools and hyper parameter optimization (CASH) were used to combine groups in order to classify the patients' breast. Further, classifiers based on Bayesian networks, neural networks, SVM and decision tree were used. Among 39 tested classification algorithms, K-Star and Bayes Net obtained classification accuracy of 100%. Furthermore, among the Bayes Net, Multi-Layer Perceptron, LibSVM [6] and J48 classification algorithms, an average accuracy of 95.71% was obtained.

Dynamic protocol data were also used by Silva [30] to compute ROI features (first and second order statistical, clustering, histogram, fractal geometry, and diversity indexes) and then to organize temporal series. These were after reorganized in subseries with different cardinalities. The top subseries of features were selected and used in SVM to classify the breast. The leave-one-out technique is employed for validation using 64 patients (32 healthy and 32 with some disease). Two features were extracted from each series and submitted to the classifier, they are: the amplitude of the series and the square root of the sum to the square of the series. The values were normalized between 0 and 1. The SVM classifier in the WEKA tool was used with all their default parameters. The SVC (Support Vector Classification) learning was used (in both C-SVC and Nu-SVC). Detailed results of each group of feature (i.e., its sensitivity, specificity, accuracy, Youden index and the AUC, for each analysis, are presented in Appendix B of Silva [30]. The best results of the analysis are shown in Fig. 7.

The horizontal axis of Fig. 7 shows accuracy in percentage, it is possible to notice that the greatest accuracies were obtained by the features from simple statistical group and by the union of all the features, achieving 97%. On the other

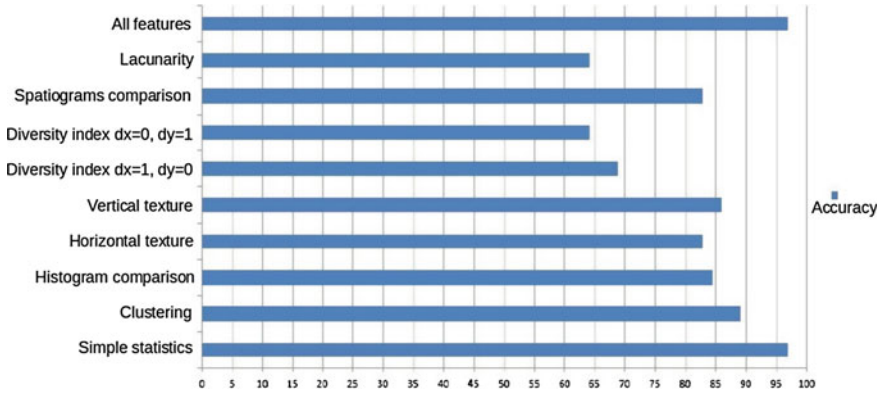

Fig. 7 Accuracy by group of features using active dynamic thermography [30]

hand, groups formed by the diversity index (horizontal and vertical) and lacunarity do not obtain good results.

7 Conclusions

In this chapter, we present several approaches that have been implemented related to the use of infrared images to breast modeling and diseases diagnosis; they consider all aspects of the process of diagnostic tool implementation: capture thermal matrix of patient body, storage and retrieval of images from a database, segmentation, 3D reconstruction, feature extraction and classification. The experiments and implementations were done by the Visual Lab group of the Fluminense Federal University in Niteroi, Rio de Janeiro, Brazil. The results are promising and it promotes diseases classification with very high accuracy. Each aspect considered in this chapter is an important application of infrared images for breast modeling and diagnosis. Test showed that the proposed methodology is able to detect breast anomalies, thus contributing to adopted thermography for breast cancer screening programs. For diagnostic recommendations the achieved results support the statement that IR analysis is able to detect breast anomalies and to insert the thermography in clinical routines for breast diseases screening. When considering the dynamic protocol versus the static one, tools for diagnosis implemented using the variation of the patient temperature (the dynamic protocol data) always achieve better results even when very simple approaches are used like only the temporal series of data [28, 29].

Acknowledgements This work was supported by Brazilian CAPES, CNPq, FAPERJ and FAPEMA agencies. This research has also been partially supported by project "Pro-Engenharia 021-2008," INCT-MACC and SiADE. We thank very much all collaborators of Visual Lab Group.

References

1. Adams, F.: The Genuine Works of Hippocrates. Williams and Wilkins, Baltimore (1939)
2. Araújo, F.A.: Metodologia para Reconstrução Tridimensional da Geometria da Mama Utilizando dois Sensores de Profundidade (in portuguese). PhD Thesis, Federal Fluminense University. Niteroi, Rio de Janeiro, Brazil (2014)
3. Bezerra, L.A., Oliveira, M.M., Rolim, T.L., Conci, A., Santos, F.G.S., Lyra, P.R.M., Lima, R. C.F.: Estimation of breast tumor thermal properties using infrared images. Sig. Process. **93** (10), 2851–2863 (2013)
4. Borchartt, T.B.: Análise de imagens termográficas para a classificação de alterações na mama (in portuguese). PhD Thesis, UFF, Niteroi, Rio de Janeiro, Brazil (2013)
5. Bukowska-Belniak, B., Lupa, M., Leśniak, A.: Fusion of infrared images with 3D GIS model for environmental imaging. In: Archives QIRT 2016, Quantitative InfraRed Thermography Conference, pp. 170–171. Gdansk, Poland (2016)
6. Chang, C.C., Lin, C.J.: LIBSVM: a library for support vector machines. ACM Trans. Intell. Syst. Technol. (TIST) **2**(3), 27 (2011)
7. Chernov, V., Martín-del-Campo-Mena, E., Chernov, G., Cirett-Galán, E., RuizDuarte, J.L., Torres-Peralta, R., Barboza-Flores, M.: Simplified grading scale for IR breast thermography using as a first-line component of a multi-imaging breast cancer detection strategy. In: Archives QIRT 2016, Quantitative InfraRed Thermography Conference, pp. 164–165. Gdansk, Poland (2016)
8. Conci, A., Galvão, S.L., Sequeiros, G.O., Saade, D.C., MacHenry, T.: A new measure for comparing biomedical regions of interest in segmentation of digital images. Discrete Appl. Math. **197**, 103–113 (2015)
9. Dice, L.R.: Measures of the amount of ecologic association between species. Ecology **26**(3), 297–302 (1945)
10. Doi, K.: Computer-aided diagnosis in medical imaging: historical review, current status and future potential. Comput. Med. Imag. Graph. **31**(4), 198–211 (2007)
11. Fellah, Z.E.A., Ogam, E., Masson, C., Gilbert, R.: Inverse problem of recovery of poro elastic parameters of cancellous bone by inversion of transmitted ultrasonic data. In: Proceedings of the NOISECON 2010 Conference, 159th Meeting of the Acoustical Society of America and NOISE, Baltimore, 2007–2007, 2010. Maryland, USA. https://hal.archives-ouvertes.fr/hal-00490794
12. Gautherie, M.: Thermobiological assessment of benign and malignant breast diseases. Am. J. Obstet. Gynecol. **147**(8), 861–869 (1983)
13. Isac, C., Viterbo, J., Conci, A.: A Survey on Ontology-Based Systems to Support the Prospection, Diagnosis and Treatment of Breast Cancer. Anais do Simpósio Brasileiro de Sistemas de Informação (SBSI), SBC (Sociedade Brasileira de Computação), ACM (Association for Computing Machinery) e AIS (Association for Information Systems), pp. 271–277 (2016)
14. Kantartzis, P.M., Abdi, M.P., Liatsis, P.: Stimulation and measurement patterns versus prior information for fast 3D EIT: a breast screening case study. Sig. Process. **93**(10), 2838–2850 (2013)
15. Keyserlingk, J.R., Ahlgren, P.D., Yu, E., Belliveau, N.: Infrared imaging of the breast: initial reappraisal using high-resolution digital technology in 100 successive cases of stage I and II breast cancer. Breast J. **4**(4), 245–251 (1998)
16. Kołacz, Sz., Moderhak, M., Jankau, J.: Comparison of perforator location in dynamic and static thermographic imaging with Doppler ultrasound in breast reconstruction surgery. In: Archives QIRT 2016, Quantitative InfraRed Thermography Conference, pp. 407–410. Gdansk, Poland (2016)
17. MacQueen, J.: Some methods for classification and analysis of multivariate observations. In: Proceedings of the Fifth Berkeley Symposium on Mathematical Statistics and Probability, vol. 1(14) (1967)

18. Marques, R.S.: Segmentação automática das mamas em imagens térmicas (in portuguese). Master Thesis, Federal Fluminense University. Niteroi, Rio de Janeiro, Brazil (2012)
19. Marques, R.S., Conci, A., Pérez, M.G., Andaluz, V.H., Mejía, T.M.: An approach for automatic segmentation of thermal images in computer aided diagnosis. IEEE Lat. Am. Trans. **14**(4), 1856–1865 (2016)
20. Morel, J.M., Yu, G.: ASIFT: a new framework for fully affine invariant image comparison. SIAM J. Imag. Sci. **2**(2) (2009)
21. Resmini, R.: Detecção de assimetrias em imagens térmica (in portuguese). Master Thesis, Federal Fluminense University. Niteroi, Rio de Janeiro, Brazil (2011)
22. Resmini, R., Borchartt, T.B., Conci, A., Montenegro, A., Lima, R.C.F., Fontes, C.A.P.: Extraction of features based on geostatistical measures using thermal images of breast. In: Anais do CONEM 2012, São Luiz, MA/Brazil (2012)
23. Resmini, R.: Classificação de Doenças da Mama Usando Imagens por Infravermelho (in portuguese). PhD Thesis, Federal Fluminense University. Niteroi, Rio de Janeiro, Brazil (2016)
24. Strąkowska, M., Strzelecki, M., Kaszuba, A., Więcek, B. Thermal parameter extraction for screening procedure of skin pathologies based on the cold provocation—10.21611/qirt.2016.125. In: Archives QIRT 2016, Quantitative InfraRed Thermography Conference, pp. 785–790. Gdansk, Poland (2016)
25. Sequeiros, G.O.: Desenvolvimento de um Banco de Dados de Imagens Médicas Acessíveis Via Web com Recuperação de Dados Baseada no Conteúdo (in portuguese). Master Thesis, Federal Fluminense University. Niteroi, Rio de Janeiro, Brazil (2013)
26. Serrano, R.C., Ulysses, J., Ribeiro, S., Lima, R.C.F., Conci, A.: Using hurst coefficient and lacunarity to diagnosis early breast diseases. In: Proceedings of IWSSIP 17th International Conference on Systems, Signals and Image Processing, Rio de Janeiro, Brazil, pp. 550–553 (2010)
27. Silva, L.F., Saade, D.C.M., Sequeiros, G.O., Silva, A.C., Paiva, A.C., Bravo, R.S., Conci, A.: A new database for breast research with infrared image. J. Med. Imag. Health Inform. **4**(1), 92–100 (2014)
28. Silva, L.F., Sequeiros, G., Santos, M.L., Fontes, C., Muchaluat-Saade, D.C., Conci, A.: Thermal signal analysis for breast cancer risk verification. In: MEDINFO 2015: eHealth-enabled Health, Ebook Series: Studies in Health Technology and Informatics, pp. 216 746–750 (2015)
29. Silva, L.F., Santos, A.A.S.M.D., Bravo, R.S., Silva, A.C., Saade, D.C.M, Conci, A.: Hybrid analysis for indicating patients with breast cancer using temperature time series. Comput. Meth. Programs Biomed. **130**, 142–153 (2016)
30. Silva, T.E.: Uma Metodologia de Auxílio ao Diagnóstico de Doenças de Mama a Partir de Termografias Dinâmicas (in portuguese). PhD Thesis, Federal Fluminense University. Niteroi, Rio de Janeiro, Brazil (2015)
31. Sparck Jones, K.: A statistical interpretation of term specificity and its application in retrieval. J. Documentation **28**(1), 11–21 (1972)
32. Tirilly, P., Claveau, V., Gros, P.: Language modeling for bag-of-visual words image categorization. In: Proceeding CIVR, 08 Proceedings of the International Conference on Content-Based Image and Video Retrieval, pp. 249–258 (2008)
33. Vapnik, V.N.: Statistical Learning Theory. Wiley-Interscience, New York (1998)
34. Vasconcelos, S., Borchartt, T.B., Resmini, R., Conci, A., Fontes, C.F.P., Lima, R.C.F.: On the breast reconstruction by thermal images. Thermol. Int. **20**(4), 134–135 (2010)
35. Zheng, R., Lasaygues, P.: Simultaneous assessment of bone thickness and velocity for ultrasonic computed tomography using transmission-echo method, ultrasonics symposium (IUS). IEEE Int. **2013**, 2084–2087 (2013)

A Semi-Analytical Heterogeneous Model for Thermal Analysis of Cancerous Breasts

A. Ramírez-Torres, R. Rodríguez-Ramos, A. Conci, F.J. Sabina, C. García-Reimbert, L. Preziosi, J. Merodio and F. Lebon

Abstract In the present work coupled stationary bioheat transfer equations are considered. The cancerous breast is characterized by two areas of dissimilar thermal properties: the glandular and tumor tissues. The tumorous region is modeled as a two-phase composite where parallel periodic isotropic circular fibers are embedded in the glandular isotropic matrix. The periodic cell is assumed square. The local problem on the periodic cell and the homogenized equation are stated and solved. The temperature distribution of the cancerous breast is found through a numerical computation. A mathematical and computational model is integrated by FreeFem++.

Keywords Temperature · Cancerous breast · Asymptotic homogenization · Finite element method

A. Ramírez-Torres (✉) · F.J. Sabina · C. García-Reimbert
Instituto de Investigaciones en Matemáticas Aplicadas y en Sistemas, Universidad Nacional Autónoma de México, CP 20-126, 01000 CDMX, Mexico
e-mail: ariel.ramirez@iimas.unam.mx

F.J. Sabina
e-mail: fjs@mym.iimas.unam.mx

C. García-Reimbert
e-mail: cgr@mym.iimas.unam.mx

R. Rodríguez-Ramos
Facultad de Matemática y Computación, Universidad de La Habana, CP 10400 La Habana, Cuba
e-mail: reinaldo@matcom.uh.cu

A. Conci
Instituto de Computação, Universidade Federal Fluminense, CEP:24210-346 Rio de Janeiro, Brazil
e-mail: aconci@ic.uff.br

L. Preziosi
Dipartimento di Matematica, Politecnico di Torino, CP 10129 Turin, Italy
e-mail: luigi.preziosi@polito.it

E.Y.K. Ng and M. Etehadtavakol (eds.), *Application of Infrared to Biomedical Sciences*, Series in BioEngineering,
DOI 10.1007/978-981-10-3147-2_11

1 Introduction

Actually, clinical examination, ultrasound, mammography, thermography, among others, are employed to identify and treat breast cancer [1, 2]. In particular, mammography is considered the standard procedure for detecting breast cancer. Yet, it presents difficulties for finding tumors in dense breasts. Thermography technique has arisen as a prospective method with the aim of increase the efficacy of the early discovery of breast cancer [3, 4]. Then, mathematical and numerical models have been proposed for studying thermal distribution on healthy and cancerous breasts, with the aim of using thermography as a complementary tool. For instance, [5] modeled a three-dimensional tumorous breast and sensitivity parameters are analyzed. Moreover, [3] were able to set a method to approximate thermal properties, where the physical process was ruled by a bioheat transfer equation. A three-dimensional breast, taking into account thermal and elastic properties, was modeled and the influence of both properties on the surface temperature was considered by [6]. In the aforementioned works, the numerical simulation was performed via FEM.

In the present study, a semi-analytical method is proposed for studying the breast thermal properties for different parameter data. Then, mathematical and computational modeling are integrated for solving two coupled stationary bioheat transfer equations. To separate micro and macro variables of the heterogeneous problem, the two-scale asymptotic expansion is used [7, 8]. In fact, multiscales methods have been successfully applied to various physical systems. For example, a formal two-scale asymptotic expansion for studying the macroscopic behavior of a porous and linear elastic solid was used in [9]. On the other hand, the homogeneous problem associated with the healthy breast tissues (without tumor) and the homogenized problem resulting by the application of the two-scale homogenization method to the heterogeneous tumor tissue, are solved using *FreeFem++*. Finally, numerical results are shown and discussed.

J. Merodio
Departamento de Mecánica de los Medios Continuos y T. Estructuras, E.T.S. de Caminos, Canales y Puertos, Universidad Politécnica de Madrid, CP 28040 Madrid, Spain
e-mail: jose.merodio@upm.es

F. Lebon
Laboratoire de Mécanique et d'Acoustique, Université Aix-Marseille, CNRS, Centrale Marseille, 4 Impasse Nikola Tesla, CS 40006, 13453 Marseille Cedex 13, France
e-mail: lebon@lma.cnrs-mrs.fr

2 Mathematical Model

The aim of the present work is to find the stationary temperature fields u and u^ε that are described by the following bioheat transfer equations [10].

$$\begin{cases} -\frac{\partial}{\partial x_i}\left(K_{ij}^g \frac{\partial u}{\partial x_j}\right) + \rho_b c_b \omega_b^g u = q_m^g + \rho_b c_b \omega_b^g u_a & \text{in } \Omega_1, \\ -K_{ij}^g \frac{\partial u}{\partial x_j} n_i = h(u - u_e) & \text{on } \partial\Omega_1^n, \\ u = u_c & \text{on } \partial\Omega_1^d. \end{cases} \tag{1}$$

$$\begin{cases} -\frac{\partial}{\partial x_i}\left(K_{ij}^\varepsilon \frac{\partial u^\varepsilon}{\partial x_j}\right) + \rho_b c_b \omega_b^\varepsilon u^\varepsilon = q_m^\varepsilon + \rho_b c_b \omega_b^\varepsilon u_a & \text{in } \Omega_2, \\ K_{ij}^\varepsilon \frac{\partial u^\varepsilon}{\partial x_j} n_i = -K_{ij}^g \frac{\partial u_g}{\partial x_j} n_i & \text{on } \partial\Omega_2, \\ u^\varepsilon = u_g & \text{on } \partial\Omega_2 \end{cases} \tag{2}$$

where $K_{ij}^g = k_g \delta_{ij}$ denotes glandular tissue thermal conductivity, ρ_b is blood mass density, c_b blood specific heat capacity, u_a is the arterial blood temperature, u_c the temperature at the boundary between breast and chest, u_e is the surrounding temperature and h represents the combined effective heat transfer coefficient due to convection, radiation and evaporation of 13.5 $\mathrm{W/m^2\,K}$ [11]. Besides, the rapidly oscillating coefficients $K_{ij}^\varepsilon, \omega_b^\varepsilon$ and q_m^ε are defined as follows

$$K_{ij}^\varepsilon(\mathbf{x}) = \begin{cases} k_g \delta_{ij}, \mathbf{x} \in \Omega_g^\varepsilon \\ k_t \delta_{ij}, \mathbf{x} \in \Omega_t^\varepsilon \end{cases}, \quad \omega_b^\varepsilon(\mathbf{x}) = \begin{cases} \omega_b^g, \mathbf{x} \in \Omega_g^\varepsilon \\ \omega_b^t, \mathbf{x} \in \Omega_t^\varepsilon \end{cases} \quad \text{and} \quad q_m^\varepsilon(\mathbf{x}) = \begin{cases} q_m^g, \mathbf{x} \in \Omega_g^\varepsilon \\ q_m^t, \mathbf{x} \in \Omega_t^\varepsilon \end{cases}.$$

Note that in the case of the healthy breast model only (P_1) has to be solved.

For the sake of simplicity, we will work in a two-dimensional section where the breast geometry is represented by a hemispherical shape with a diameter L as done in [11]. The healthy breast will be represented by a homogeneous tissue (glandular tissue) and associated with the open, bounded, and connected domain Ω_1 with Lipschitz boundary $\partial\Omega_1 = \partial\Omega_1^n \cup \partial\Omega_1^d$, where $\partial\Omega_1^n \cap \partial\Omega_1^d = \emptyset$. On the other hand, the cancerous tissue will be characterized by two regions of dissimilar thermal properties: the tumoral area (Ω_t^ε—fibers) and the glandular area (Ω_g^ε—matrix). In this sense, the cancerous region will consist of a periodic microstructure associated with the open, bounded, and connected domain $\Omega_2 = \Omega_g^\varepsilon \cup \Omega_t^\varepsilon \cup \partial\Omega_g^\varepsilon$ with Lipschitz boundary $\partial\Omega_2 = \partial\Omega_g^\varepsilon$ and with $\Omega_g^\varepsilon \cap \Omega_t^\varepsilon = \emptyset$. Then, the cancerous breast is represented by $\Omega = \Omega_2 \cup \Omega_1$ (Fig. 1). Let $\varepsilon > 0$ be the size of the microstructure and $\mathbf{y} = \mathbf{x}/\varepsilon$ the fast scale coordinate. The reference periodic cell will be denoted by Y, which contains one inclusion occupying the domain Y_t with Lipschitz boundary ∂Y_t such that $Y = Y_g \cup Y_t \cup \partial Y_t$, with $\overline{Y}_t \subset Y$ and $Y_g \cap Y_t = \emptyset$. It is also assumed that Ω_g^ε is connected and that the inclusions do not intersect the boundary $\partial\Omega_g^\varepsilon$. In previous works, soft tissues assume to present this type of arrangement. In fact, Penta et al. [9]

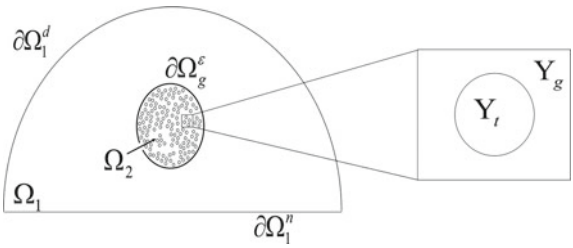

Fig. 1 Decomposition of the macroscopic domain (*left*) and the corresponding unit periodic cell (*right*)

used the same periodic geometry to depict a porous tissue microstructure. Boundary conditions for (1) are heat transfer by convection between the surface of the tissue and the external environment on $\partial\Omega_1^n$ and a prescribed temperature on $\partial\Omega_1^d$. In the case of (2) we assume heat and temperature continuity on $\partial\Omega_2$. Moreover, continuity conditions for temperature and heat flow are imposed on Γ^ε (boundary between the glandular tissue Ω_g^ε and the tumor inclusions Ω_t^ε), i.e.,

$$[\![u^\varepsilon]\!] = 0 \quad \text{on } \Gamma^\varepsilon \quad \text{and} \quad [\![\mathbf{K}^\varepsilon \nabla_x u^\varepsilon \cdot \mathbf{n}]\!] = 0 \quad \text{on } \Gamma^\varepsilon. \tag{3}$$

3 Two-Scale Homogenization

Here, the two-scale homogenization technique is applied to find the homogenized equation and corresponding effective coefficients. An overview of how this method is applied and its main assumptions can be found in [12]. Specifically, after finding the solution u of problem (1), an asymptotic expansion of u^ε [problem (2)] is sought as a function of ε for $\varepsilon \to 0$, namely

$$u^\varepsilon(\mathbf{x}) = u^0(\mathbf{x}) + \varepsilon\chi_p(\mathbf{y})\frac{\partial u^0(\mathbf{x})}{\partial x_p} + \varepsilon^2 u^2(\mathbf{x},\mathbf{y}) + \ldots, \tag{4}$$

where the functions $\chi_p(\mathbf{y}), u^2(\mathbf{x},\mathbf{y})$, are Y-periodic in $\mathbf{y}$. In particular, the vector function $\chi(\mathbf{y})$ satisfies the unit cell problem

$$\begin{cases} -\frac{\partial}{\partial y_i}\left(K_{ij}(\mathbf{y})\frac{\partial \chi_p(\mathbf{y})}{\partial y_j} + K_{ip}(\mathbf{y})\right) = 0 & \text{in } Y\backslash\Gamma, \\ [\![\chi]\!] = 0 & \text{on } \Gamma, \\ \left[\!\left[\left(K_{ij}(\mathbf{y})\frac{\partial \chi_p(\mathbf{y})}{\partial y_j} + K_{ip}(\mathbf{y})\right)n_i\right]\!\right] = 0 & \text{on } \Gamma \end{cases} \tag{5}$$

and $u^0(\mathbf{x})$ the homogenized problem solution

$$\begin{cases} -\frac{\partial}{\partial x_i}\left(\hat{K}_{ij}\frac{\partial u^0(\mathbf{x})}{\partial x_j}\right)+\left(\rho_b c_b \omega_b^g \frac{|Y_g|}{|Y|}+\rho_b c_b \omega_b^t \frac{|Y_t|}{|Y|}\right)u^0(\mathbf{x})=\left(q_m^g+\rho_b c_b \omega_b^g u_a\right)\frac{|Y_g|}{|Y|}+ \\ \quad +\left(q_m^t+\rho_b c_b \omega_b^t u_a\right)\frac{|Y_t|}{|Y|} \qquad \text{in } \Omega_2, \\ u^0(\mathbf{x})=u_g \qquad \text{on } \partial\Omega_2, \end{cases} \tag{6}$$

where $|\cdot|$ represents volume fraction. The effective constant coefficients $\hat{K}_{ip}$ are given by

$$\hat{K}_{ip}=\left\langle K_{ij}\frac{\partial \chi_p}{\partial y_j}+K_{ip}\right\rangle \tag{7}$$

where $p=1,2$ and $\langle\cdot\rangle$ denotes volume average.

3.1 Analytical Solution of the Unit Cell Problem

In particular, the theory of analytical functions by Muskhelishvili [13] is applied to solve the cell problem (5). In this sense, the solutions of the local problems are written as

$$\chi_1^{(g)}=\mathrm{Re}\left\{a_0^1 z+\sum_{k=1}^{\infty o} a_k^1 \frac{\zeta^{(k-1)}(z)}{(k-1)!}\right\} \quad \text{and} \quad \chi_1^{(t)}=\mathrm{Re}\left\{\sum_{l=1}^{\infty o} c_l^1 z^l\right\}, \tag{8}$$

$$\chi_2^{(g)}=\mathrm{Im}\left\{a_0^2 z+\sum_{k=1}^{\infty o} a_k^2 \frac{\zeta^{(k-1)}(z)}{(k-1)!}\right\} \quad \text{and} \quad \chi_2^{(t)}=\mathrm{Im}\left\{\sum_{l=1}^{\infty o} c_l^2 z^l\right\}, \tag{9}$$

where (γ) with $\gamma=g,t$ denotes the constituent, the superscript o specifies that the sum is carried out over odd indices, the coefficients a_0^p, a_k^p and $c_l^p (p=1,2)$ are real and ζ is the zeta quasi periodic Weierstrass function. Now, using Laurent's expansion of ζ and the quasi-periodicity property of ζ and its derivatives

$$\chi_1^{(g)}=\mathrm{Re}\left\{\sum_{l=1}^{\infty o}\left(a_l^1 z^{-l}-A_l^1 z^l\right)\right\} \quad \text{and} \quad \chi_2^{(g)}=\mathrm{Im}\left\{\sum_{l=1}^{\infty o}\left(a_l^2 z^{-l}-A_l^2 z^l\right)\right\}, \tag{10}$$

where for $p=1,2$

$$A_l^p=\sum_{k=1}^{\infty o} k a_k^p \eta_{kl} \quad \text{with} \quad \eta_{kl}=\begin{cases}(-1)^{p+1}\pi, & k+l=2 \\ \frac{(k+l-1)!}{k!l!}S_{k+l}, & k+l>2\end{cases}$$

and S_k are called the reticulate sums and are defined as $S_k = \sum_{w \in L*} \frac{1}{w^k}$ $(k \geq 3, k \text{ odd})$ with L^* representing the lattice excluding the number $w = 0$ and $w = mw_1 + nw_2$ where $m, n \in \mathbb{Z}$ and w_1, w_2 are the periods. In particular, in the present work $w_1 = 1$ and $w_2 = i$, due to we are in presence of square unit cells.

Substitution of (8)–(10) in boundary conditions of problem (5) and taking into account that on $\Gamma, z = Re^{i\theta}$ where R is the circumference radius give that coefficients a_k^p can be found through solution of the following infinite linear system (for finding the effective properties it is truncated into an appropriate order $k = N$)

$$\left(\xi^{-1}\mathbf{I} + (-1)^{p+1}\mathbf{W}^p\right)\hat{\mathbf{A}}^p = \mathbf{V}^p, \tag{11}$$

where $\hat{\mathbf{A}}^p = (\hat{a}_1^p, \hat{a}_2^p, \ldots)^{\mathrm{T}}, \hat{a}_k^p = a_k^p\sqrt{k}/R^k, \mathbf{V}^p = ((-1)^{p+1}R, 0, \ldots)^{\mathrm{T}}$,

$$\xi^{-1} = \frac{k_g + k_t}{k_g - k_t} \quad \text{and} \quad \mathbf{W}^p = \begin{cases} (-1)^{p+1}\pi R^2, & k+l=2 \\ \sum\limits_{k=1}^{\infty} \sqrt{k}\sqrt{l}\eta_{kl}R^{k+l}, & k+l>2 \end{cases}.$$

Now, from Eq. (7)

$$\hat{K}_{ip} = \left\langle K_{ij}\frac{\partial \chi_p}{\partial y_j} + K_{ip} \right\rangle.$$

Using the form of K_{ij}, Green's theorem, the double periodicity of χ_p and formulas (8)–(10), then

$$\hat{K}_{pp} = \begin{cases} k_g\left(1 - 2\pi a_1^1\right), & \text{if } p = 1 \\ k_t\left(1 + 2\pi a_1^2\right), & \text{if } p = 2 \end{cases}. \tag{12}$$

In fact, if $k_g = k_t$. Then, $\hat{K} = \hat{K}_{11} = \hat{K}_{22}$.

4 Numerical Solution and Analysis of Results

This section is devoted to find the temperature distribution of problems (1) and (6) where we define as $g = \rho_b c_b \omega_b^g$, $g^\varepsilon(\mathbf{x}) = \rho_b c_b \omega_b^\varepsilon(\mathbf{x})$, $f = q_m^g + \rho_b c_b \omega_b^g u_a$, $f^\varepsilon(\mathbf{x}) = q_m^\varepsilon(x) + \rho_b c_b \omega_b^\varepsilon(\mathbf{x}) u_a$. With this aim, we follow the following procedure.

4.1 Solution of (1)

For finding solution u of (1), we use *FreeFem++*. First, the problem must be written in its weak formulation. In this sense, let $H_d^1(\Omega_1) = \{u \in H^1(\Omega_1) \text{ s.t. } \gamma(u) = 0 \text{ on } \partial\Omega_1^d\}$. Using the trace theorem for $u_c \in H^{1/2}(\Omega_1)$, there exists a continuous linear operator $R_0 : H^{\frac{1}{2}}(\partial\Omega_1) \to H^1(\Omega_1)$ such that $\gamma(R_0 u_c) = u_c$. Now, we define $\tilde{u} = u - R_0 u_c \in H_d^1(\Omega_1)$. Then, on $\partial\Omega_1^d$

$$\gamma(\tilde{u}) = \gamma(u) - \gamma(R_0 u_c) = u_c - u_c = 0.$$

In this way, the equivalent variational formulation of problem (1) is

$$\begin{cases} \text{Find } \tilde{u} \in H_d^1(\Omega_1) \text{ such that} \\ a(\tilde{u}, v) = L(v), \quad \forall v \in H_d^1(\Omega_1) \end{cases}, \tag{13}$$

where

$$\begin{aligned} a(\tilde{u}, v) &= \int_{\Omega_1} \mathbf{K}^g \nabla_x \tilde{u} \cdot \nabla_x v \mathrm{d}x + \int_{\Omega_1} g\tilde{u} v \mathrm{d}x + \int_{\partial\Omega_1^n} h\tilde{u} v \mathrm{d}S, \\ L(v) &= \int_{\Omega_1} f v \mathrm{d}x - \int_{\Omega_1} g(R_0 u_c) v \mathrm{d}x - \int_{\Omega_1} \mathbf{K}^g \nabla_x (R_0 u_c) \cdot \nabla_x v \mathrm{d}x \\ &\quad + \int_{\partial\Omega_1^n} h(u_e - R_0 u_c) v \mathrm{d}S. \end{aligned}$$

In particular, the weak solution existence and uniqueness of problem (13) can be proved by standard methods using the Lax–Milgram theorem. In this sense, the following must be proved:

(i) The bilinear form $a(\tilde{u}, v)$ is continuous

In this sense, observe that $\mathbf{K}^g \in M(\alpha, \beta, \Omega_1)$ and by Cauchy–Schwartz

$$\begin{aligned} |a(\tilde{u}, v)| &\leq \beta \|\nabla_x \tilde{u}\|_{L^2(\Omega_1)} \|\nabla_x v\|_{L^2(\Omega_1)} + g\|\tilde{u}\|_{L^2(\Omega_1)} \|v\|_{L^2(\Omega_1)} \\ &\quad + h\|\tilde{u}\|_{L^2(\partial\Omega_1^n)} \|v\|_{L^2(\partial\Omega_1^n)}. \end{aligned}$$

Furthermore, by the Poincaré–Friedrichs II theorem

$$\|\tilde{u}\|_{L^2(\Omega_1)} \leq \tilde{C}_1 \|\nabla_x \tilde{u}\|_{L^2(\Omega_1)} = \tilde{C}_1 \|\tilde{u}\|_{H_d^1(\Omega_1)}.$$

On the other hand, by the trace theorem

$$\|\tilde{u}\|_{L^2(\partial\Omega_1^n)} = \|\gamma(\tilde{u})\|_{L^2(\partial\Omega_1^n)} = \left[\int\limits_{\partial\Omega_1^n} |\gamma(\tilde{u})|^2 + \int\limits_{\partial\Omega_1^d} |\gamma(\tilde{u})|^2\right]^{\frac{1}{2}}$$
$$= \|\tilde{u}\|_{L^2(\partial\Omega_1)} \leq C_2\|\tilde{u}\|_{H^1(\Omega_1)}.$$

Moreover,

$$\|\tilde{u}\|_{H^1(\Omega_1)} = \left[\|\tilde{u}\|^2_{L^2(\Omega_1)} + \|\nabla_x\tilde{u}\|^2_{L^2(\Omega_1)}\right]^{\frac{1}{2}} \leq \left[\tilde{C}_1\|\nabla_x\tilde{u}\|^2_{L^2(\Omega_1)} + \|\nabla_x\tilde{u}\|^2_{L^2(\Omega_1)}\right]^{\frac{1}{2}}$$
$$= (1+\tilde{C}_1)^{\frac{1}{2}}\|\nabla_x\tilde{u}\|_{L^2(\Omega_1)} = \tilde{C}_3\|\tilde{u}\|_{H^1_d(\Omega_1)}, \quad \tilde{u} \in H^1_d(\Omega_1).$$

Therefore,

$$\|\tilde{u}\|_{L^2(\partial\Omega_1^n)} \leq C_2\|\tilde{u}\|_{H^1(\Omega_1)} \leq \tilde{C}_4\|\tilde{u}\|_{H^1_d(\Omega_1)},$$

where $\tilde{C}_4 = C_2\tilde{C}_3 = C_2(1+\tilde{C}_1)^{\frac{1}{2}}$. Finally, for $\tilde{u} \in H^1_d(\Omega_1)$

$$|a(\tilde{u},v)| \leq \beta\|\tilde{u}\|_{H^1_d(\Omega_1)}\|v\|_{H^1_d(\Omega_1)} + g\tilde{C}_1C_1\|\tilde{u}\|_{H^1_d(\Omega_1)}\|v\|_{H^1_d(\Omega_1)} + h\tilde{C}_4C_4\|\tilde{u}\|_{H^1_d(\Omega_1)}\|v\|_{H^1_d(\Omega_1)}$$
$$\leq C_5\|\tilde{u}\|_{H^1_d(\Omega_1)}\|v\|_{H^1_d(\Omega_1)},$$

with $C_5 = \beta + g\tilde{C}_1C_1 + h\tilde{C}_4C_4$.

(ii) The bilinear form $a(\tilde{u},v)$ is H^1_d-elliptic

Let $u \in H^1_d(\Omega_1)$,

$$a(u,u) = \int\limits_{\Omega_1} \mathbf{K}^g(\nabla_x u)^2 \mathrm{d}x + \int\limits_{\Omega_1} gu^2\mathrm{d}x + \int\limits_{\partial\Omega_1^n} hu^2\mathrm{d}S$$
$$\geq C_6\left(\int\limits_{\Omega_1}(\nabla_x u)^2\mathrm{d}x + \int\limits_{\Omega_1} u^2\mathrm{d}x + \int\limits_{\partial\Omega_1^n} u^2\mathrm{d}S\right)$$
$$= C_6\left(\|\nabla_x u\|^2_{L^2(\Omega_1)} + \|u\|^2_{L^2(\Omega_1)} + \|u\|^2_{L^2(\partial\Omega_1^n)}\right)$$
$$\geq C_6\|\nabla_x u\|^2_{L^2(\Omega_1)} = C_6\|u\|^2_{H^1_d(\Omega_1)}, \quad \text{with } C_6 = \min(\alpha,g,h).$$

(iii) The linear form $L(v)$ is continuous in $H^1_d(\Omega_1)$

Let $v \in H^1_d(\Omega_1)$,

$$|L(v)| = \left| \int_{\Omega_1} fv\mathrm{d}x - \int_{\Omega_1} g(R_0u_c)v\mathrm{d}x - \int_{\Omega_1} \mathbf{K}^g\nabla_x(R_0u_c)\cdot\nabla_x v\mathrm{d}x + \int_{\partial\Omega_1^n} h(u_e - R_0u_c)v\mathrm{d}S \right|$$
$$\leq \int_{\Omega_1} |fv|\mathrm{d}x + \int_{\Omega_1} |g(R_0u_c)v|\mathrm{d}x + \int_{\Omega_1} |\mathbf{K}^g\nabla_x(R_0u_c)\cdot\nabla_x v|\mathrm{d}x + \int_{\partial\Omega_1^n} |h(u_e - R_0u_c)v|\mathrm{d}S.$$

But, by Cauchy–Schwarz inequality, the Poincaré–Friedrichs II theorem and the fact that $R_0u_c \in H^1(\Omega_1)$ and $\nabla_x(R_0u_c) \in (L^2(\Omega_1))^n$

$$|L(v)| \leq C_{10}\|v\|_{H_d^1(\Omega_1)},$$

where $C_{10} = C_1\|f\|_{L^2(\Omega_1)} + gC_1\|R_0u_c\|_{L^2(\Omega_1)} + \beta\|\nabla_x(R_0u_c)\|_{L^2(\Omega_1)} + (hC_7|u_e| + hC_8\|u_c\|_{H^{1/2}(\partial\Omega_1^n)})C_3$.

Thus, (i)–(iii) proves the existence and uniqueness of solution $\tilde{u}^0$ by using the Lax–Milgram theorem.

Now, it must be shown that the map $\langle f^\varepsilon\rangle \in L^2(\Omega_1) \rightarrow u \in H_d^1(\Omega_1)$ is continuous in order to prove the regularity of the weak solution. In fact, from the H_d^1-ellipticity of the bilinear form

$$|a(u,u)| \geq C_6\|u\|^2_{H_d^1(\Omega_1)}$$

and the continuity of the linear operator in $H_d^1(\Omega_1)$

$$|L(u)| \leq C_{10}\|u\|^2_{H_d^1(\Omega_1)}.$$

Then,

$$C_6\|u\|^2_{H_d^1(\Omega_1)} \leq |a(u,u)| = |L(u)| \leq C_{10}\|u\|^2_{H_d^1(\Omega_1)},$$

i.e.

$$\|u\|_{H_d^1(\Omega_1)} \leq \frac{C_{10}}{C_6} = C_{11}\|f\|_{L^2(\Omega_1)},$$

with

$$C_{10} = \frac{1}{C_6}\left(C_1 + \frac{gC_1\|R_0u_c\|_{L^2(\Omega_1)}}{\|f\|_{L^2(\Omega_1)}} + \frac{\beta\|\nabla_x(R_0u_c)\|_{L^2(\Omega_1)}}{\|f\|_{L^2(\Omega_1)}} + \frac{\left(hC_7|u_e| + hC_8\|u_c\|_{H^{1/2}(\partial\Omega_1^n)}\right)C_3}{\|f\|_{L^2(\Omega_1)}}\right).$$

Now, the contribution of R_0u_c may be difficult in some cases. However, *FreeFem++* replaces the Dirichlet condition by a Robin condition of the form

$\nabla_x u \cdot n + u/\varepsilon = u_c/\varepsilon$ on $\partial\Omega_1^d$ and solves the problem with a very small value of ε. In particular, we approximate the involved functions by piecewise linear continuous finite elements.

4.2 Solution of (6)

The last step in the homogenization procedure is to solve the homogenized problem (6). Here we prove that u^0 is its solution and that the problem is well posed. In this sense, let $H_0^1(\Omega_2) = \{u \in H^1(\Omega_2) \text{ s.t. } \gamma(u) = 0 \text{ on } \partial\Omega_2\}$. Using the trace theorem for $u_g \in H^{1/2}(\Omega_2)$ there exists a continuous linear operator $R_0 : H^{\frac{1}{2}}(\partial\Omega_2) \to H^1(\Omega_2)$ such that $\gamma\big(R_0 u_g\big) = u_g$. Now, we define $\tilde{u}^0 = u^0 - R_0 u_g \in H_0^1(\Omega_2)$. Then, on $\partial\Omega_2$

$$\gamma(\tilde{u}^0) = \gamma(u^0) - \gamma(R_0 u_g) = u_g - u_g = 0.$$

In this way, the equivalent variational formulation of problem (6) is

$$\begin{cases} \text{Find } \tilde{u}^0 \in H_0^1(\Omega_2) \text{ such that} \\ a(\tilde{u}^0, v) = L(v), \quad \forall v \in H_0^1(\Omega_2) \end{cases}, \tag{14}$$

where

$$a(\tilde{u}^0, v) = \int_{\Omega_2} \hat{\mathbf{K}} \nabla_x \tilde{u}^0 \cdot \nabla_x v \mathrm{d}x + \int_{\Omega_2} \langle g^\varepsilon \rangle \tilde{u}^0 v \mathrm{d}x,$$

$$L(v) = \int_{\Omega_2} \langle f^\varepsilon \rangle v \mathrm{d}x - \int_{\Omega_2} \hat{\mathbf{K}} \nabla_x (R_0 u_g) \cdot \nabla_x v \mathrm{d}x - \int_{\Omega_2} \langle g^\varepsilon \rangle (R_0 u_g) v \mathrm{d}x.$$

In particular, $\hat{\mathbf{K}} \in M(\alpha, \beta, \Omega_2)$ see Cionarescu and Donato [14], and $\langle f^\varepsilon \rangle \in L^2(\Omega_2)$ and $\langle g^\varepsilon \rangle > 0$. The existence and uniqueness of solution $\tilde{u}^0$ can be proved through the Lax–Milgram theorem. Then, we must show that:

(i) The bilinear form $a(\tilde{u}^0, v)$ is continuous

In this sense, observe that using the fact that $\hat{\mathbf{K}} \in M(\alpha, \beta, \Omega_2)$ and by Cauchy–Schwartz inequality

$$|a(\tilde{u}^0, v)| \leq \beta \|\nabla_x \tilde{u}^0\|_{L^2(\Omega_2)} \|\nabla_x v\|_{L^2(\Omega_2)} + \langle g^\varepsilon \rangle \|\tilde{u}^0\|_{L^2(\Omega_2)} \|v\|_{L^2(\Omega_2)}.$$

Now, from remark 3.37 p. 32 by Cionarescu and Donato [14], for $\tilde{u}^0, v \in H_0^1(\Omega_2)$,

$$\|\tilde{u}^0\|_{H_0^1(\Omega_2)} = \|\nabla_x \tilde{u}^0\|_{L^2(\Omega_2)},$$
$$\|v\|_{H_0^1(\Omega_2)} = \|\nabla_x v\|_{L^2(\Omega_2)}.$$

Furthermore, by the Poincaré–Friedrichs I theorem,

$$\|\tilde{u}^0\|_{L^2(\Omega_2)} \leq \hat{C}_1 \|\nabla_x \tilde{u}^0\|_{L^2(\Omega_2)} = \hat{C}_1 \|\tilde{u}^0\|_{H_0^1(\Omega_2)},$$
$$\|v\|_{L^2(\Omega_2)} \leq C_1 \|\nabla_x v\|_{L^2(\Omega_2)} = C_1 \|v\|_{H_0^1(\Omega_2)}.$$

Finally, for $\tilde{u}^0 \in H_0^1(\Omega_2)$

$$\begin{aligned} |a(\tilde{u}^0, v)| &\leq \beta \|\tilde{u}^0\|_{H_0^1(\Omega_2)} \|v\|_{H_0^1(\Omega_2)} + \langle g^\varepsilon \rangle \hat{C}_1 C_1 \|\tilde{u}^0\|_{H_0^1(\Omega_2)} \|v\|_{H_0^1(\Omega_2)} \\ &\leq C_2 \|\tilde{u}^0\|_{H_0^1(\Omega_2)} \|v\|_{H_0^1(\Omega_2)}, \end{aligned}$$

with $C_2 = \beta + \langle g^\varepsilon \rangle \hat{C}_1 C_1$.

(ii) The bilinear form $a(\tilde{u}^0, v)$ is H_0^1-elliptic

Let $u \in H_0^1(\Omega_2)$,

$$\begin{aligned} a(u,u) &= \int_{\Omega_2} \hat{\mathbf{K}} (\nabla_x u)^2 \mathrm{d}x + \int_{\Omega_2} \langle g^\varepsilon \rangle u^2 \mathrm{d}x \\ &= C_3 \left(\|\nabla_x u\|^2_{L^2(\Omega_2)} + \|u\|^2_{L^2(\Omega_2)} \right), \quad \text{with } C_3 = min(\alpha, \langle g^\varepsilon \rangle) \\ &\geq C_3 \|\nabla_x u\|^2_{L^2(\Omega_2)} = C_3 \|u\|^2_{H_0^1(\Omega_2)}. \end{aligned}$$

(iii) The linear form $L(v)$ is continuous in $H_0^1(\Omega_2)$

Let $v \in H_0^1(\Omega_2)$,

$$|L(v)| \leq \int_{\Omega_2} |\langle f^\varepsilon \rangle v| \mathrm{d}x + \int_{\Omega_2} |\hat{\mathbf{K}} \nabla_x (R_0 u_g) \cdot \nabla_x v| \mathrm{d}x + \int_{\Omega_2} |\langle g^\varepsilon \rangle (R_0 u_g) v| \mathrm{d}x.$$

But, using the Cauchy–Schwarz inequality, the Poincaré–Friedrichs I theorem and the fact that $R_0 u_g \in H^1(\Omega_2)$ and $\nabla_x (R_0 u_g) \in (L^2(\Omega_2))^n$

$$|L(v)| \leq C_6 \|v\|_{H_0^1(\Omega_2)},$$

where $C_6 = C_4 \|\langle f^\varepsilon \rangle\|_{L^2(\Omega_2)} + \langle g^\varepsilon \rangle C_5 \|R_0 u_g\|_{L^2(\Omega_2)} + \beta \|\nabla_x (R_0 u_g)\|_{L^2(\Omega_2)}$.

Thus, (i)–(iii) proves the existence and uniqueness of solution $\tilde{u}^0$ by using the Lax–Milgram theorem.

Now, it must be shown that the map $\langle f^{\varepsilon}\rangle \in L^2(\Omega_2) \rightarrow u \in H_0^1(\Omega_2)$ is continuous in order to prove the regularity of the weak solution. In fact, from the H_0^1-ellipticity of the bilinear form

$$|a(u,u)| \geq C_3 \|u\|^2_{H_0^1(\Omega_2)}$$

and the continuity of the linear operator in $H_0^1(\Omega_2)$

$$|L(u)| \leq C_6 \|u\|^2_{H_0^1(\Omega_2)}.$$

Then,

$$C_3 \|u\|^2_{H_0^1(\Omega_2)} \leq |a(u,u)| = |L(u)| \leq C_6 \|u\|^2_{H_0^1(\Omega_2)},$$

i.e.,

$$\|u\|_{H_0^1(\Omega_2)} \leq \frac{C_6}{C_3} = C_7 \|\langle f^{\varepsilon}\rangle\|_{L^2(\Omega_2)},$$

with

$$C_7 = \frac{1}{C_3}\left(C_4 + \frac{\langle g^{\varepsilon}\rangle C_5 \|R_0 u_g\|_{L^2(\Omega_2)}}{\|\langle f^{\varepsilon}\rangle\|_{L^2(\Omega_2)}} + \frac{\beta \|\nabla_x (R_0 u_g)\|_{L^2(\Omega_2)}}{\|\langle f^{\varepsilon}\rangle\|_{L^2(\Omega_2)}}\right).$$

Once the solution u of (1) is found, we proceed to solve (6). In particular, the homogenized problem (6) is solved using the aforementioned *FreeFem++*. As above, we approximate the involved functions by piecewise linear continuous finite elements.

4.3 Analysis of Results

Numerical calculations are carried out for three breast models *A*, *B,* and *C*, whose tissue parameters are shown in Table 1. Temperatures are fixed as $u_a = u_c = 37\,^{\circ}\mathrm{C}$ [5]. We fixed the surrounding temperature $u_e = 20$. The metabolic heat value for different tumor sizes follows the law given by Jiang et al. [6] as $q_m^t = C/(468.6\ \ln(100D) + 50)$, where $C = 3.27 \times 10^6\ \mathrm{Wday/m^3}$ and D is the tumor diameter.

Figure 2A–C show the temperature distribution of healthy breast tissues with $L = 0.14$ m, i.e., without a tumor. Now, in Fig. 3 it is shown how depth (in the present study the depth is stated as the distance between the tumor center and the point on the breast surface in the same axis) affects breast thermal distribution. In particular, in the zone "far" from the tumor area, no appreciable temperature

Table 1 Tissue parameters

Model	k (W/m °C)		ω_b (1/s)		c_b (J/Kg °C)	ρ_b (kg/m^3)	q_g (Wm^{-3})	Reference
	k_t	k_g	ω_b^f	ω_b^g				
A	0.48	0.48	0.0132	0.0006612	3300	1100	700	[5]
B	0.48	0.48	0.009	0.00018	4200	1060	450	[3]
C	0.511	0.48	0.0108	0.000539	4200	1060	700	[15]

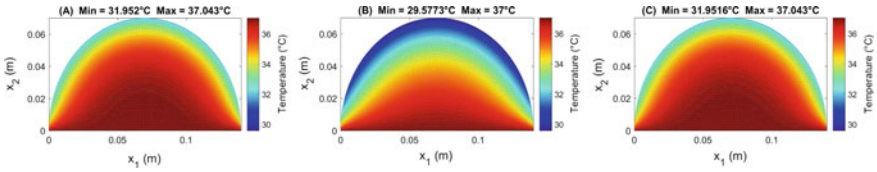

Fig. 2 Thermal distribution of a healthy breast tissue

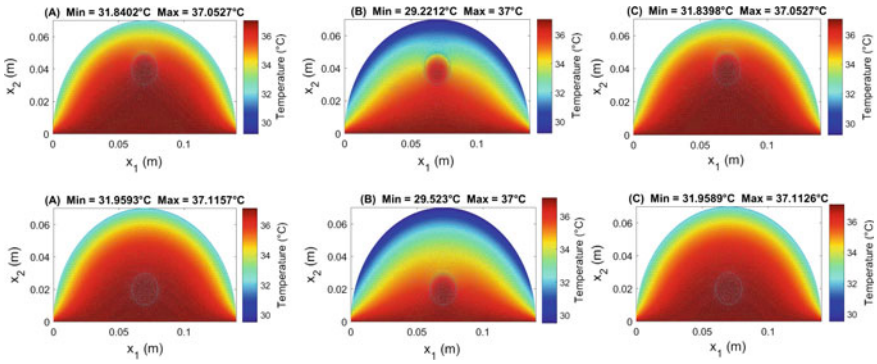

Fig. 3 Thermal distribution of a cancerous breast tissue with an embedded spherical tumor of radius $r = 0.01$ m located at depths $d = 0.03$ m (*first line*) and $d = 0.05$ m (*second line*), respectively

changes at the surface are observed. Which is not the case when the tumor is located near to the boundary where the temperature difference at the surface is higher if compared with Fig. 2. Indeed, when the tumor is nearer to the boundary, the surface temperature increases. This behavior is in accordance with the observations made by [5] and [6]. Figure 4 first line of graphs, center line and bottom line, present the steady-state temperature for a cancerous breast tissue with $L = 0.13$ m, $L = 0.15$ m and $L = 0.17$ m, respectively. In particular, a sphere with radius $r = 0.01$ m was inserted in the breast model to imitate the in situ tumor at a depth of $d = 0.04$ m. Moreover, a relative large tumor volume fraction $|Y_t| = 0.7$ is considered so that healthy breast tissue volume fraction is $|Y_g| = 0.3$ in the tumorous region. As observed, if the breast dimensions are bigger, the maximum temperature is higher,

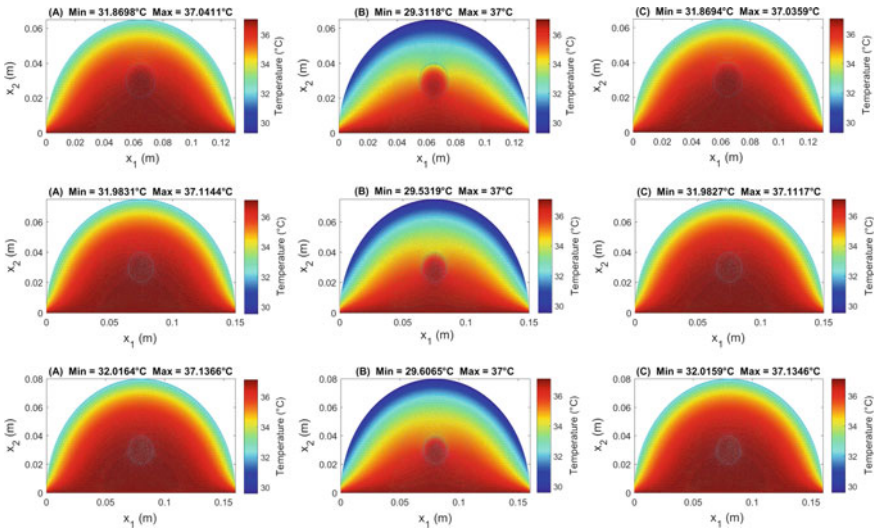

Fig. 4 Thermal distribution of a cancerous breast tissue with an embedded spherical tumor of radius $r = 0.01$ m for $L = 0.13$ m, $L = 0.15$ m and $L = 0.17$ m, respectively

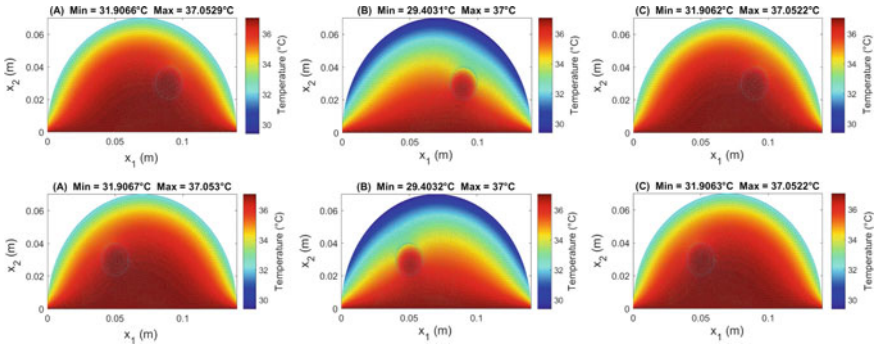

Fig. 5 Thermal distribution of a cancerous breast tissue with an embedded spherical tumor of radius $r = 0.01$ m located 0.02 m at the *right* and *left* of the central axis, respectively

where the temperature decreases from the chest wall to the front breast. Moreover, surface temperature varies with breast dimension. On the other hand, the first and second line of Fig. 5 show the temperature for a cancerous breast tissue where the tumor is not located on the central axis $x_1 = 0.07$ m, i.e., its center is situated 0.02 m at the right and left of the central axis, respectively. Even, when the tumor is found off central axis, it influences the temperature behavior on the nearest boundary, which is higher than that of the adjacent surface. Besides, for Figs. 4 and 5 a temperature variation is noticed in the tumor area and the region surrounding it.

5 Conclusions

Here, a semi-analytical method is used for studying breast thermography through coupled stationary bioheat transfer equations. One hand, the breast is assumed to be homogeneous and constituted by glandular tissue. On the other hand, the tumor area is represented by a periodic composite and comprised of glandular and cancerous tissue. In particular, the temperature distribution on both, breast and tumor tissue, was computed using a numerical algorithm implemented in FreeFem++. In summary, if the breast dimensions are bigger then the maximum temperature is higher and no appreciable changes in temperature difference were observed far from the breast boundary. The work results also indicate that the data parameter will influence the thermal distribution of the tumorous breast. The proposed method provides a helpful framework for studying the thermal profile of breast cancerous tissues. Moreover, it facilitates the understanding of the complex behavior of its surface temperature. Also, it improves the current premature discovery and analysis of breast tumors, integrating mathematical and computational tools. In fact, thermography together with mathematical and computational modeling bring an appropriate methodology in order to allow the assessment of rapidly growing neoplasm.

Acknowledgements AR gratefully acknowledges the Program of Postdoctoral Scholarships of DGAPA from UNAM, Mexico. The authors would like to thank Professor Sébastien Martin, Université Paris Descartes, Paris, France for helpful discussions during the course of this work. Also, we thank Departamento de Matemáticas y Mecánica IIMAS-UNAM for their support and Ramiro Chávez Tovar and Ana Pérez Arteaga for computational assistance. JM acknowledges support from the Ministerio de Ciencia in Spain under the project reference DPI2014-58885-R. Thanks to the Project (7515) Métodos Físico-Matemáticos para el estudio de nuevos materiales y la propagación de ondas. Aplicaciones. A.C. is grateful to CNPq (Projects INCT-MACC and 303240/2015-6)

References

1. Muralidhar, G.S., Bovik, A.C., Sampat, M.P., Whitman, G.J., Haygood, T.M., Stephens, T.W., Markey, M.K.: Computer-aided diagnosis in breast magnetic resonance imaging. Mt Sinai J. Med. **78**, 280–290 (2011)
2. Tang, J., Rangayyan, R.M., Xu, J., Naqa, I.E., Yang, Y.: Computer-aided detection and diagnosis of breast cancer with mammography: recent advances. IEEE Trans. Inf. Technol. Biomed. **13**(2), 236–251 (2009). http://scholar.google.com/scholar?hl=en&btnG=Search&q=intitle:Computer-Aided+Detection+and+Diagnosis+of+Breast+Cancer+With+Mammography+:+Recent+Advances#0
3. Bezerra, L.A., Oliveira, M.M., Rolim, T.L., Conci, A., Santos, F.G.S., Lyra, P.R.M., Lima, R. C.F.: Estimation of breast tumor thermal properties using infrared images. Signal Process. **93** (10), 2851–2863 (2013). http://dx.doi.org/10.1016/j.sigpro.2012.06.002
4. Kapoor, P., Prasad, S.V.A.V.: Image processing for early diagnosis of breast cancer using infrared images. In: The 2nd International Conference on Computer and Automation Engineering (ICCAE), vol. 3, pp. 564–566 (2010). http://ieeexplore.ieee.org/lpdocs/epic03/wrapper.htm?arnumber=5451827

5. Amri, A., Saidane, A., Pulko, S.: Thermal analysis of a three-dimensional breast model with embedded tumour using the transmission line matrix (TLM) method. Comput. Biol. Med. **41** (2), 76–86 (2011). http://dx.doi.org/10.1016/j.compbiomed.2010.12.002
6. Jiang, L., Zhan, W., Loew, M.H.: Modeling static and dynamic thermography of the human breast under elastic deformation. Phys. Med. Biol. **56**(1), 187–202 (2011)
7. Sanchez-Palencia, E.: Non-homogeneous Media and Vibration Theory, vol. 127. Springer, Berlin (1980). http://adsabs.harvard.edu/abs/1980LNP…127…..S
8. Bakhalov, N., Panasenko, G.: Homogenisation: Averaging Processes in Periodic Media. Kluwer Academic Publishers, Dordrecht (1989)
9. Penta, R., Ambrosi, D., Shipley, R.J.: Effective governing equations for poroelastic growing media. Q. J. Mech. Appl. Mech. **67**(1), 69–91 (2014)
10. Pennes, H.: Analysis of tissue and arterial blood temperatures in the resting human forearm. J. Appl. Physiol. **1**(2), 93–122 (1948)
11. Wahab, A.A., Salim, M.I.M., Ahamat, M.A., Manaf, N.A., Yunus, J., Lai, K.W.: Thermal distribution analysis of three-dimensional tumor-embedded breast models with different breast density compositions. Med. Biol. Eng. Comput. 1–11 (2015). http://dx.doi.org/10.1007/s11517-015-1403-7
12. Davit, Y., Bell, C.G., Byrne, H.M., Chapman, L.A.C., Kimpton, L.S., Lang, G.E., Leonard, K.H.L., Oliver, J.M., Pearson, N.C., Shipley, R.J., Waters, S.L., Whiteley, J.P., Wood, B.D., Quintard, M.: Homogenization via formal multiscale asymptotics and volume averaging: how do the two techniques compare? Adv. Water Resour. **62**, 178–206 (2013). http://dx.doi.org/10.1016/j.advwatres.2013.09.006
13. Muskhelishvili, N.I.: Some Basic Problems of the Mathematical Theory of Elasticity. Springer, Netherlands (1977)
14. Cionarescu, D., Donato, P.: An Introduction to Homogenization. Oxford University Press Inc., New York (1999)
15. Bardati, F., Iudicello, S.: Modeling the visibility of breast malignancy by a microwave radiometer. IEEE Trans. Biomed. Eng. **55**(1), 214–221 (2008)

Dynamic Angiothermography (DATG)

F. Casali, R. Brancaccio, F.P. Draetta, M.P. Morigi, M. Bettuzzi and G. Baldazzi

Abstract Dynamic Angiothermography (DATG) is a noninvasive technique for the diagnosis of breast cancer. The instrument consists of a thin plate with liquid crystals that changes color due to a change in temperature, consequently offering an image of breast vasculature. DATG is based on the angiogenesis theory on tumor initiation, development, and growth. A tumor needs new vessels. Therefore, by studying the changes in the pattern of vascular blood supply, it is also possible to diagnose neoplasms very early. In particular, it is shown that every human being has his or her own vascular pattern which, in the absence of disease, does not vary throughout the life time. By repeating DATG periodically, an efficient control of the onset of disease is possible, even in its early stages. This is not new but still little-known technique which is a component of the overall diagnostic techniques for the study and prevention of breast cancer that serves to offer a complete clinical picture of the patient. The great advantages of DATG are: it does not use radiation; it is not invasive or painful; it is low-cost and can be repeated periodically and successfully with no drawbacks. The angiothermographic examination thus makes it possible to visualize the breast vascularity pattern without using contrast medium. On the other hand, while highlighting changes in mammary vascularization, DATG is not able to indicate the size or depth of the tumor; even if recent researches (based on the approximated solution of the inverse Fourier heat equation) show the possibility to evaluate the depth of the tumor. This paper, after the introduction in

F. Casali
Academy of Sciences of the Institute of Bologna, Bologna, Italy

F. Casali · R. Brancaccio (✉) · M.P. Morigi · M. Bettuzzi
Enrico Fermi Center, Rome, Italy
e-mail: rossella_brancaccio@yahoo.it

R. Brancaccio · M.P. Morigi · M. Bettuzzi · G. Baldazzi
Department of Physics and Astronomy, University of Bologna, Bologna, Italy

R. Brancaccio · M.P. Morigi · M. Bettuzzi · G. Baldazzi
Istituto Nazionale di Fisica Nucleare (INFN), Bologna, Italy

F.P. Draetta
Gynecology and Obstetrics, Bologna, Italy

E.Y.K. Ng and M. Etehadtavakol (eds.), *Application of Infrared to Biomedical Sciences*, Series in BioEngineering,
DOI 10.1007/978-981-10-3147-2_12

Sect. 1, starts with a description of historical context in Sect. 2, and outlines the instrumentation in Sect. 3. Section 4 describes the technique, while a comparison with other diagnostic techniques is provided in Sect. 5. To close, Sect. 6 offers a practical guide on the use of this method.

Keywords Breast cancer · Diagnosis · Dynamic AngioThermoGraphy (DATG) · Liquid crystals · Contactthermography · Angiogenesis

1 Introduction

Despite the numerous diagnostic techniques, according to the WHO (World Health Organization) breast cancer as well as lung cancer and colorectal cancer, is the second leading cause of death in developed countries [1]. In recent years, breast cancer is the leading cause of cancer death among females in developing countries [2]. Each diagnostic technique has advantages and limitations, and only a proper synergy between the different techniques, together with forms of multidisciplinary collaboration, can lead to real progress. To this end, screening is an extremely important tool for prevention which, however, requires an extensive organization and considerable financial resources. There are several efficient diagnostic techniques (such as magnetic resonance imaging MRI) which are very expensive, and the use of which is justified only when there is a high probability of tumor [3]. Mammography is the gold standard in older women, but it is not effective in younger ones [4, 5]. Breast ultrasound is a radiation-free technique, but it is an auxiliary test and its specificity is lower than that of mammography [6–8]. The little-known Dynamic AngioThermoGraphy (DATG) has some attractive features [9–11]. This technique should not be confused with breast thermal imaging (or mammary thermography) [12–14], making use of a tool that shows the blood distribution (blood pattern) in the mammary gland. Any changes in this distribution, due to the presence of new blood vessels (*angiogenesis*), may be related to the presence of malignancy [15, 16]. The basic idea is that every human being has his or her own blood pattern, much like a fingerprint, when the person is healthy, does not change during his or her lifetime [17, 18]. Conversely, the alteration of this pattern might be evidence of a suspected tumoral or pretumoral activity [19, 20].

2 Historical Note

The importance of the influence of the vascular system in tumors was extensively studied and demonstrated by Judah Folkman in 1965. In 1992, he won the Wolf Prize for medicine for his research on angiogenesis. Studies on angiogenesis continued in France where, in the 1970s, J. Tricoire developed the first *contact thermography* technique. To display the temperature distribution on the breast surface,

he developed a kind of plate coated with liquid crystals [21–23]. The captured images by a camera were analyzed by physicians who were experienced in standard diagnostic techniques (usually gynecologists, oncologists, and radiologists). Studies on the vascular pattern showed a correlation between contact plate images and cancer. The method developed by Tricoire was based on the principle that emergent tumors can be detected by recording and mapping the heat generated by them.

The research on contact thermography, initiated by Tricoire, was continued in Bologna at the private "Madre Fortunata Toniolo" hospital by two gynecologists, Dr. Giancarlo Montruccoli and his son, Dr. Daniel Montruccoli. They used and studied contact thermography and found that the original technique gave rise to numerous false positives (low specificity), while the picture had a poor spatial resolution: characteristics confirmed by literature [24–26]. These physicians started to analyze the vascularity pattern and its changes rather than searching directly for the tumor as a heat source. In accordance with the angiogenesis theory, DATG does not use the quantitative measurements of emitted heat as a diagnostic criterion. Instead, it is based on the qualitative interpretation of breast blood flow lines, a feature that is making DATG increasingly more valuable from both a clinical and a scientific standpoint. In more than 30 years of clinical practice, approximately 4000 patients were followed up with a total of over 40,000 tests, of which around 1200 were histological examinations [27–30].

Thanks to the experience of these physicians, new plates were developed and the DATG instrumentation was improved [9, 31].

3 The Instrumentation for Contact Thermography

While in mammary thermography the temperature of the area to be investigated is recorded by an infrared camera, DATG analyzes the vascularization pattern. As an example of mammary thermography, Fig. 1a shows (in "false colors") a healthy breast, while Fig. 1b shows an advanced cancer in the left breast.

In DATG, the examination tool is made of two components: a thermographic sensor placed in contact with the breast, and a digital camera connected to a computer (Fig. 2) [31].

3.1 The Detector (Thermographic Plate)

The detector is a plate covered with cholesteric liquid crystals. Crystals orientate themselves in different ways depending on their temperature. Even though liquid crystals may work in a very broad temperature range (from −30 to 120 °C), for the DATG application their temperature range is designed to be that of the human body skin (32–38 °C). At room temperature only infrared radiation is reflected and

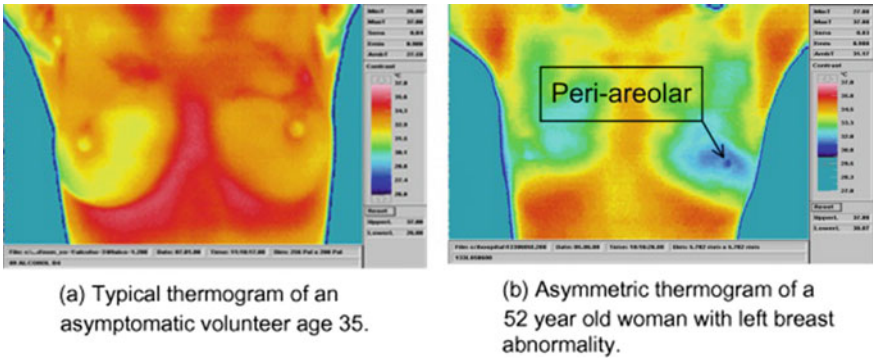

Fig. 1 Typical images of breast thermography (in "false color"): **a** healthy breast, **b** left breast with an advanced cancer [32] (Reprinted from Infrared Physics and Technology, Volume 66, Faust O, Acharya UR, Ng EYK, Hong TJ, Yu W, Application of infrared thermography in computer aided diagnosis, Pages 160–175, September 2014, with permission from Elsevier. doi: 10.1016/j.infrared.2014.06.001)

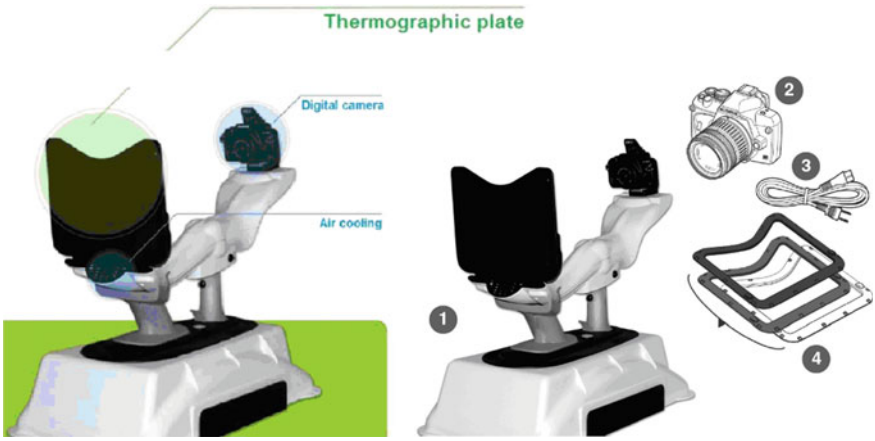

Fig. 2 *Left* Photo of Aura machine, (*Right*) *1* plastic support, *2* digital camera, *3* connecting cables, *4* removable plates, where the three colored frames are indicated in *white*, *gray*, and *black* [31] (Reprinted from http://www.breastlife.it/index.html with permission from BreastLife s.r.l)

crystals appear brown. When the temperature is increased, the crystal structure changes so that the reflected radiation becomes, successively, red, yellow, green and blue, and then returns to brown with the reflection of UV radiation.

When the physician places the plate in contact with the patient's breast, the plate is able to provide false color images of its vascularization. For good results, in order to eliminate superficial vein signals, the breast must be cooled with a current of cold air encapsulated within the plastic support (see Fig. 2).

Three plates with different sensitivities (with white, gray, or black frames, respectively) were available:

- Black frame plate: low sensitivity (34.0–37.5 °C)
- White frame plate: high sensitivity (31.5–34.0 °C)
- Gray frame plate: intermediate sensitivity (32.5–34.5 °C).

The difference in sensitivity is very important. The low-sensitivity plate (black frame) is used for young patients, whereas the high-sensitivity plate (white frame) is used for patients near or going through menopause.

At present, images can be interpreted visually by the doctor and/or evaluated with the aid of digital image enhancement techniques.

3.2 Physical Characteristics of the Plate

The physical characteristics of plates (spatial resolution of the image and its persistence) were measured by means of two Plexiglas phantoms, containing thermoresistors crossed by a current that brought them to a temperature of 37 °C (with a variation of no more than 1 °C). In the first phantom there is a series of thermoresistors with an increasingly close distance and the relative distribution of the temperature acquired from the plate (Fig. 3). With this instrument it was possible to evaluate a spatial resolution of a few tenths of mm. With the second phantom (Fig. 4), it was possible to verify that the time for the proper image formation is around just 3 s while the fade out image took only 1.2 s. Similar measurements were carried out using LCD (liquid crystal display) commercial plates, with much worse results [9].

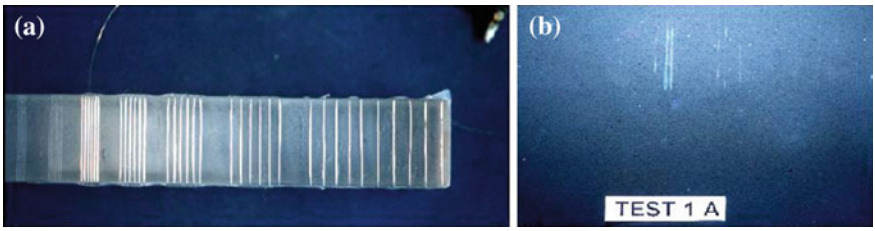

Fig. 3 Sequence of thermoresistors in the Plexiglas phantom (*left*) and the image on the crystal plate (*right*) [9] (Reprinted from Montruccoli et al. [9], with permission from Elsevier. doi: 10.1400/19286)

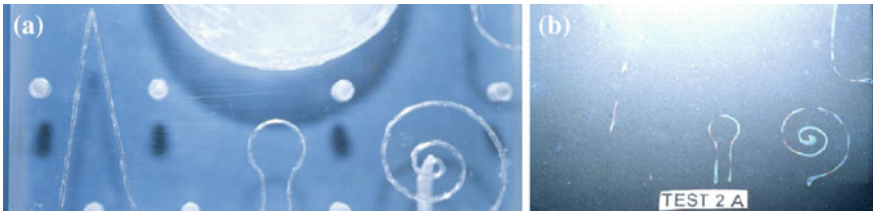

Fig. 4 Plexiglas phantom with thermoresistors to measure the acquisition time of the correct image [9] (Reprinted from Montruccoli GC, Montruccoli Salmi D, Casali F. A new type of breast contact thermography plate: a preliminary and qualitative investigation of its potentiality on phantoms. Phys Medica 2004; XX(1):27–31, with permission from Elsevier. doi: 10.1400/19286)

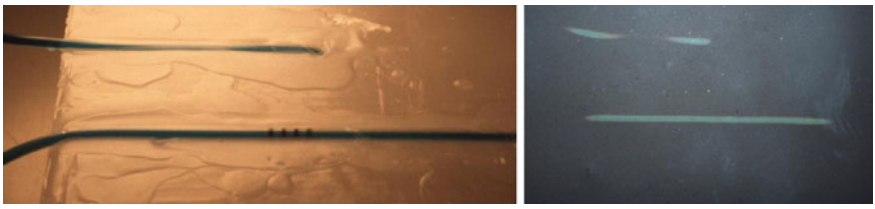

Fig. 5 Block of paraffin with two small hot water pipes (simulation of the breast blood circulation) [9] (Reprinted from Montruccoli et al. [9], with permission from Elsevier. doi: 10.1400/19286)

3.3 Simulation of the Breast Vascular Pattern

In a healthy breast the vascular pattern of a mammary artery is shaped like a small channel which ends with a tip in the direction of the nipple.

A third parallelepiped-shaped phantom made of paraffin was used to simulate the blood distribution in the breast and to assess its correct reproduction by the plate. Paraffin was chosen because of its thermal characteristics which are similar to the human tissues (Fig. 5). Two cannula, of a diameter of about 2 mm, were inserted into the block of paraffin introducing water at about 37 °C. The figure clearly shows that the cannula penetrates into the block, the same way as the vein descends toward the nipple, thus producing an image that ends in a "wedge" mode, indicating a proper blood circulation.

4 The Scientific Basis of Contact Thermography

Up until now, breast thermography was based on the evaluation of the cutaneous heat level and the research on its isotherms. This approach is very different from DATG for which, conversely, the morphological criterion is the diagnostic principle: knowing the normal perfusion of the healthy breast, any change in its shape is

an indication of some pathology. In fact, DATG studies the change in the blood perfusion both within the whole breast and within a well-defined area of it. In particular, a relationship between interpretative patterns and corresponding histological findings has been demonstrated, both for precancerous states and for in situ carcinomas or invasive cancers [29, 33–35].

4.1 Images of the Breast by Contact Thermography

The well-known characteristics of healthy mammary vascularity are a constant blood perfusion pattern for many years, its sudden change in a histologically demonstrated disease, its intense activity in the pubertal period versus its evident reduction in the postmenopausal period, the expansion of perfusion lines during pregnancy and lactation and, in the case of diseases, their focus within a single point corresponding to the tumor [17, 18]. These vascular behaviors suggest the opportuneness of using this method to study the pathophysiology of mammary gland also through its blood supply. Moreover, this approach has already been adopted by other methods, such as MRI and Doppler ultrasound to study precisely the various pathological aspects of the blood circulation within the gland.

Reading DATG results means to study the images created by currents of functional flow in relation to certain areas of the mammary gland, more than real blood vessels, where an indeterminate quantity of microvessels (capillaries and precapillaries) are present. This functional current, passing thorough a given area, is able to increase the tissue temperature just enough to distinguish it from the surrounding one. By conduction and by convection, precisely this temperature difference is transmitted through the skin to the plate that registers it. Thus, on the plate, we see some drawings that represent the path of prevalent blood flows and not others which are not visible because they are below the thermal detection threshold of the plate.

On the one hand the new interpretation of the thermographic pattern, on a functional basis, completely overlooks the quantitative aspect of the recorded temperature, moving increasingly away from the concept of "thermography" while, on the other, making it possible to highlight certain aspects of the blood circulation in the mammary gland which are so important that they become its basic diagnostic criterion.

These aspects are:

1. The angiothermographic pattern is unique and typical of each woman. In practice, this is the best explanation for the impossibility of developing a diagnostic–interpretative classification based on standard patterns, as had erroneously been done in the past.
2. In the absence of a disease this pattern remains identical, even for many years, during child-bearing age, up until menopause. This feature has a great predictive value and is one of the proofs of the technique's reproducibility.

3. There is no direct proportion between the detected pattern and the volume of the tumor, supporting in each case a clear sign of malignancy even in the presence of subclinical tumors. The latter aspect is of great importance for early diagnosis, and it is in relation to the phenomenon, presently well known, of angiogenesis whence the absolute need for an increased blood supply caused by the tumor, even in the earliest stage of carcinogenesis.

Figure 6 above on the left shows a scheme of the normal vascular pattern of the left mammary gland and the figure above on the right shows some cutaneous

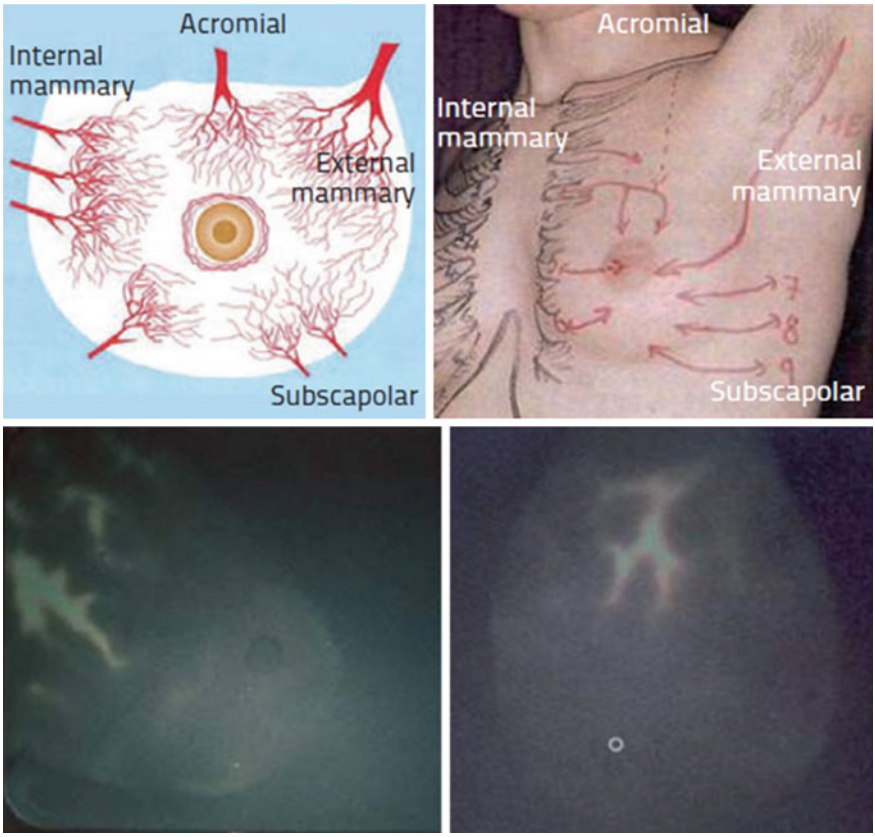

Fig. 6 *Above* (Reprinted from http://www.breastlife.it/index.html with permission from BreastLife s.r.l): *left* normal vascular pattern of the left mammary gland and (on the *right*) cutaneous projections of the main arteries in the mammary gland [31]. *Below* (Reprinted from http://www.breastlife.it/index.html with permission from BreastLife s.r.l): *left* angiothermographic image of the external mammary artery, perfectly representing the blood circulation in a healthy breast; *right* angiothermographic image of the acromial artery: there are lines of normal currents that follow the anatomy of the breast and head toward the nipple without leaving their quadrant of reference [31]

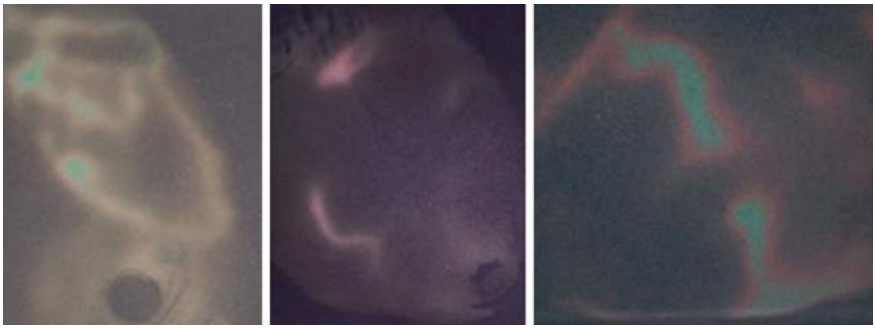

Fig. 7 Sample angiothermographic images of suspected cases. The current lines appear diverted, not speculated and pointing outward or toward a different quadrant from their own [31] (Reprinted from http://www.breastlife.it/index.html with permission from BreastLife s.r.l)

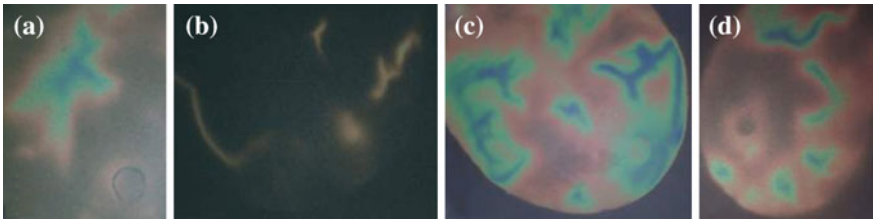

Fig. 8 Sample angiothermographic images of evidently malignant cases: **a** current lines that intersect to form a "malignant star"; **b** current lines that converge toward a "hotspot"; **c** and **d** current lines that converge from different points [31] (Reprinted from http://www.breastlife.it/index.html with permission from BreastLife s.r.l)

projections of the main arteries in the mammary gland [31]. Figure 6 below shows two images of healthy breasts. If a cancer or precancerous lesion is present, the image on the sensor either has a rounded shape or is the result of several converging channels for the tumor feeding. Figures 7 and 8, respectively, show some images of suspected and malignant cases.

4.2 The Role of Skin Cooling

To decrease the noise from superficial veins, the breast skin is cooled by a flow of fresh air. Figure 9 shows the venous network before and after cooling. These images of the superficial vein network before and after cooling show how DATG plates are able to record even minimum differences in blood flow. Moreover, the anatomical layout corresponds completely, both before and after cooling.

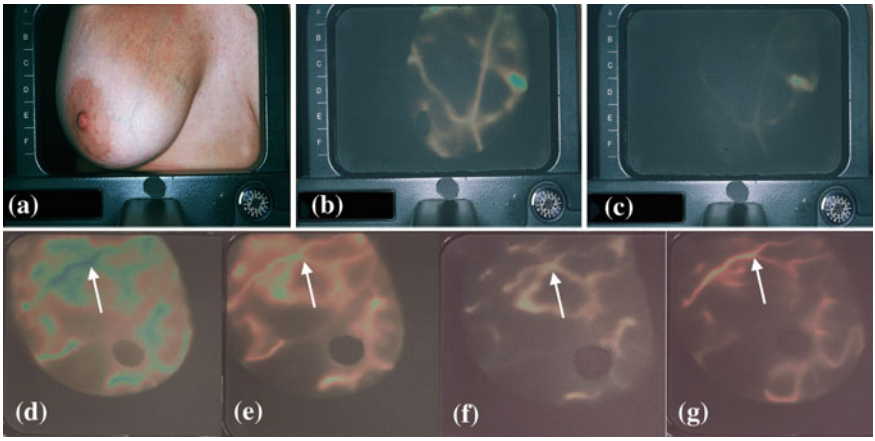

Fig. 9 Examples of skin cooling. In the first case the problem is generated by superficial veins. **a** Photo of the breast with evidence of superficial veins, **b** angiothermographic image without skin cooling, **c** angiothermographic image after skin cooling. In the second case the progressive cooling makes correct image interpretation possible: **d** first image, **e** the same after cooling, **f** after more cooling, **g** diagnostic image [31] (Reprinted from http://www.breastlife.it/index.html with permission from BreastLife s.r.l)

Like all diagnostic imaging techniques, DATG can present interpretation problems. An example is in Fig. 9e, where a quick interpretation of this highly congested breast is difficult. It is necessary to isolate the DATG signs by progressively cooling the breast and carefully selecting plates with appropriate sensitivity. In particular, at first glance, a possible malignant cross (white arrow) is indicated. In the second image (e), photographed after more cooling, the "cross" is indicated to be formed by an acromial flow line intersecting with an external mammary one. In the third image (f), taken after still more cooling, one of the two flow lines that seemed to form the "cross," is disappeared altogether. The fourth image (g) solves the problem: in a true "malignant cross," the two flow lines always have a similar intensity, but this is not the case here.

4.3 Persistence of the Vasculature in a Healthy Breast

As previously stated, in a healthy breast the vascular pattern remains unchanged over time, as shown by two images of the same patient acquired after 16 years, 20 years, and 33 years (Fig. 10). The reproducibility of the technique makes a long follow-up possible without pattern changes. Given the total lack of invasiveness of the DATG technique, tests can also be performed very close together in time, which is extremely useful in follow-ups after breast surgery.

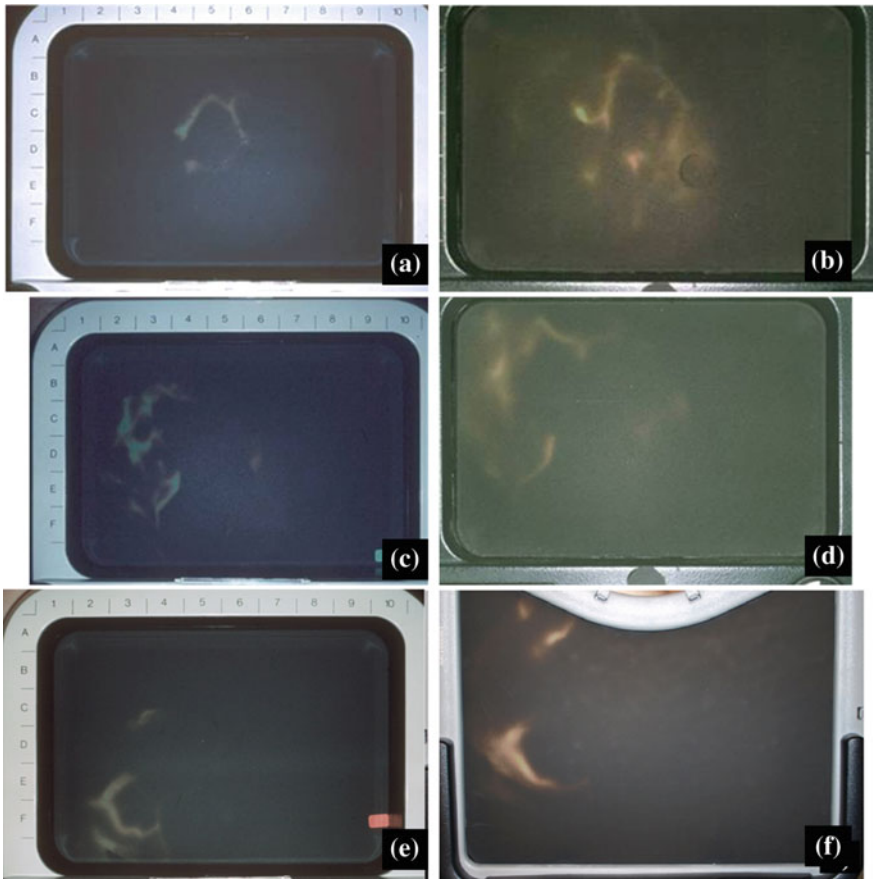

Fig. 10 Three examples of the long-lasting persistence of the shape of the blood pattern: DATG pattern remains the same over time in the absence of a disease. First woman: **a** angiothermographic test in 1979 and **b** in 1995 (after 16 years). Second woman: **c** angiothermographic image in 1979 and **d** in 1999 (after 20 years). Third woman: **e** angiothermographic image in 1978 and **f** in 2011 (after 33 years). It is evident that images represent, in all cases, the same blood diagram [31] (Reprinted from http://www.breastlife.it/index.html with permission from BreastLife s.r.l)

On the one hand, the pattern remains identical throughout life in the absence of malignancy, on the other hand, it can be more or less apparent in the various stages of a woman's life. During pregnancy and breastfeeding, an intensification of flow lines is expected, while after menopause they are gradually reduced (see Figs. 11, 12, and 13). It should be noted that, under any circumstances, these natural changes in a healthy woman involve the creation of new blood–vessels (angiogenesis).

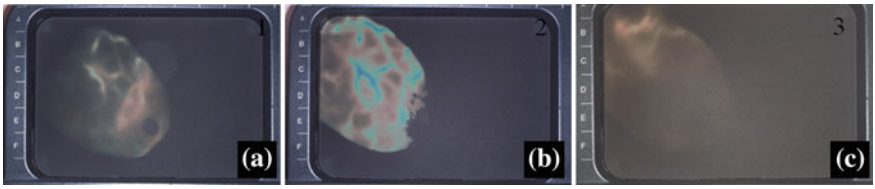

Fig. 11 Example of a DATG pattern change during pregnancy: 29-year-old woman: **a** before pregnancy, the test shows regular external mammary flow lines, mainly in the right breast, while the venous circulation is visible; **b** seven months later, during pregnancy, the functional blood circulation is much stronger; however, no completely new or abnormal flow lines have appeared; **c** sixteen months later the pattern has returned to its original appearance [31] (Reprinted from http://www.breastlife.it/index.html with permission from BreastLife s.r.l)

Fig. 12 Example of a DATG pattern change during breastfeeding: **a** DATG baseline; **b** after 2 years of breastfeeding; **c** after another 4 years, return to baseline pattern. It should be noted that during breastfeeding superficial veins are more congested, but there is no breast neoangiogenesis [31] (Reprinted from http://www.breastlife.it/index.html with permission from BreastLife s.r.l)

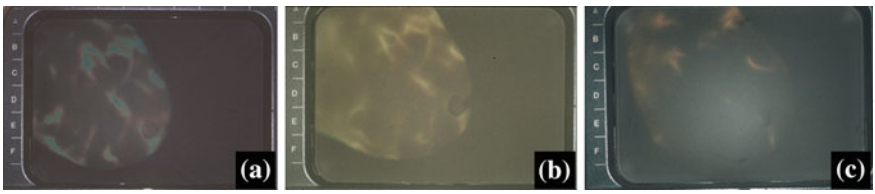

Fig. 13 Example of normal involution of flow lines with the onset of menopause: DATG images **a** at the onset of menopause; **b** after 6 years; **c** after 8 years [31] (Reprinted from http://www.breastlife.it/index.html with permission from BreastLife s.r.l)

5 DATG and Other Diagnostic Methods: Integrated Diagnosis

The comparison of DATG images with other previous acquired images or images acquired in the same laboratory via other methods (e.g. ultrasound, mammography, DOBI, MRI) is very important.

In the words of Doctor Daniele Montruccoli: "While DATG may be a useful diagnostic tool, I have always been mindful of the fact that with science in general, and medicine in particular, absolute certainty does not exist. As noted before, we used all three techniques together—mammography, ultrasound, and DATG—in our work, we aimed to arrive to the most accurate diagnosis possible, what we call it an *integrated diagnosis*."

There are many diagnostic techniques for breast cancer (with their advantages and disadvantages) including: mammography, tomosynthesis, ultrasound, MRI with contrast medium, positron emission tomography (PET), dynamic optical breast imaging (DOBI), and breast thermography. No single instrumental technique by itself, except in glaring clinical cases, offers an absolute certainty of the value of the histopathological examination. In most cases, it is precisely the set of information from various diagnostic techniques that makes it possible to isolate the cases to be submitted to histological examination, while differentiating them from the benign cases or the ones to be monitored during their lifetime; an integrated diagnosis is certainly the best way to tackle the diagnosis of breast cancer. In this context DATG, with its peculiarities, is a further aid to the combined efforts of other techniques for the study of breast cancer.

5.1 Mammography

Mammography is still considered the reference screening technique ("gold standard") for breast cancer, even though some recent publications claim that annual mammograms do not reduce breast cancer mortality in women and new screening programs should be stopped [36, 37]. Mammography highlights the different density of breast tissues. Modern mammography allows digital acquisitions with low- and high-energy X-rays (dual energy) after the administration of iodine-containing contrast media. This method offers a good resolution of the tissue density and is useful for identifying lesions in breasts characterized by high density [38]. A further improvement of mammography is the CT (Computed Tomography) of the breast [39]. This technique shows the tumor in 3D and avoids the compression of the breast. The radiation imparted to the breast is about twice that of a conventional mammography [40]. A new, very interesting, X-ray diagnostic technique for the breast is Digital Tomosynthesis (DTS). This is a sort of computed tomography of the breast done with a smaller number of acquisition angles. The breast image is reproduced in slices that are processed by a software program. For DTS, minimal pressure is needed, just enough to hold the breast in place. The results seem to be much better than for standard mammography [41, 42].

Figures 14 and 15 show an angiothermographic analysis in comparison with a mammogram of the same breast.

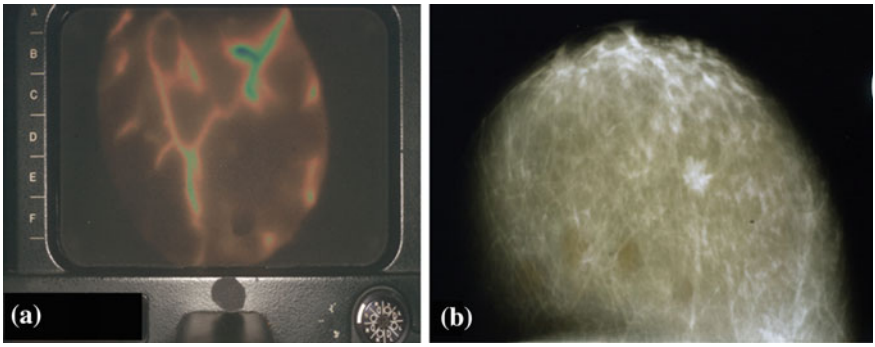

Fig. 14 Integrated diagnosis of DATG and mammography: **a** angiothermographic image and **b** mammography [31] (Reprinted from http://www.breastlife.it/index.html with permission from BreastLife s.r.l)

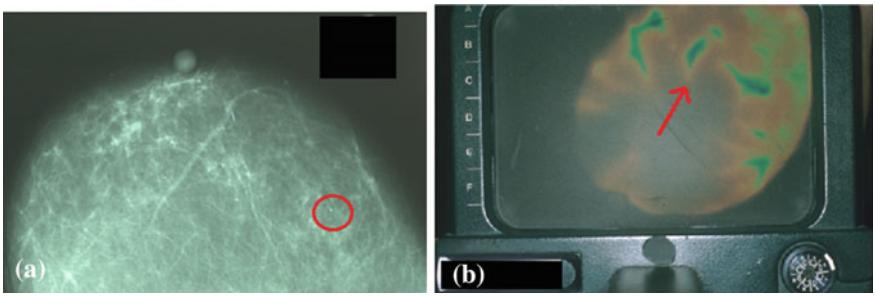

Fig. 15 Integrated diagnosis of DATG and mammography: **a** mammography, **b** DATG image [31] (Reprinted from http://www.breastlife.it/index.html with permission from BreastLife s.r.l)

The density of breast tissues in patients younger than 40 years of age degrades the radiographic image [40]. To acquire a good 2D mammogram, it is necessary to compress the breast, with a resulting discomfort for the patient. The risk of inducing breast cancer—small but not zero—is offset by the benefit of a possible early diagnosis [43, 44].

In conclusion, standard 2D mammography is a cheap, quick, and well-known technique, widely used for screening, albeit with the above-mentioned contraindications. In this field a better diagnostic technique is tomosynthesis [42] and, even better, breast CT [39].

5.2 Ultrasounds

With the development of modern probes, ultrasound has made significant strides forward. This technique has been proven to be very useful in the context of other

techniques; such as mammography, DATG, or clinical palpation that measure different physical parameters [45]. In particular, the DATG examination in combination with the ultrasound test can be very useful: in fact, the DATG can be a guide, highlighting the areas to be examined by ultrasound [46]. This is an example of the advantages of integrated diagnosis in breast examination [47]. Ultrasounds are able to measure the size of the tumor and to distinguish its liquid or solid nature within the breast tissue. The difficulty of distinguishing the acoustic impedance of various structures of the breast may produce some false positives. In some cases the cancer is manifested with characteristics of a benign nodule having a homogeneous structure and regular contours (such as in colloid, mucinous, and intracystic carcinomas). Also, when a tumor has poor cellularity, the answer is negative and we will have false negatives [48].

The technique requires considerable skills on the part of the operator, thus making it extremely "operator-dependent" [49].

In conclusion, ultrasound can be performed on women (and men!) of all ages and is totally non-invasive. The possibility of detecting a tumor remains high regardless of its size. A disadvantage of ultrasound scans is that they are admittedly unable to detect non-palpable tumors, such as microcalcifications [50].

5.3 Magnetic Resonance Imaging (MRI)

If Magnetic Resonance Imaging (MRI) performed with a suitable material to increase the contrast (for example, gadolinium), it can measure the distribution of blood within the breast in 3D. MRI can be performed on women of all ages (even those with dense breasts). It is recommended for women (also young ones) who have a family history of breast or ovarian cancer [51]. MRI sensitivity and specificity are very high [52]. Before surgery, an MRI test is very much appreciated by the surgeon for the good indications (spatial distribution) on the part of the tissue to be excised. Figure 16 shows the comparison between DATG and MRI.

MRI may be considered the best diagnostic technique for invasive cancer [53].

The disadvantages of MRI are that it is laborious (taking a long time) and requires expensive equipment. In order to produce good diagnostic images, contrast media that may cause allergic reactions must be used. There are several limitations to its performance [46]. Absolute contraindications regard the bearers of metal implants and cochlear implants, plates, screws or nails, mechanical valve prosthesis, neuroenhancers, cardiac pacemakers, tissue expanders (breast), and tattoos done less than six months earlier.

Among the relative contraindications are pregnancy in the first quarter and the possibility of claustrophobia during the test [54], even if the new MR equipment is designed for overcoming this problem.

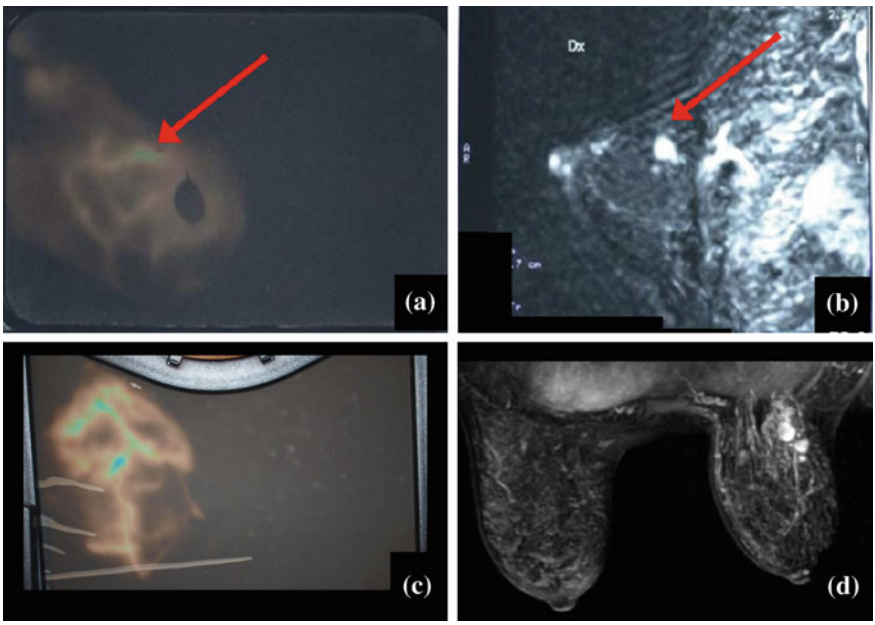

Fig. 16 Two examples of consistency between DATG and MRI tests. First woman: **a** angiothermographic image, and **b** resonance image. Second woman: **c** angiothermographic image, and **d** resonance image. MRI shows a local recurrence confirmed by DATG [31] (Reprinted from http://www.breastlife.it/index.html with permission from BreastLife s.r.l)

5.4 Positron Emission Tomography (PET)

Another way to highlight the bloodstream is the technique called Positron Emission Tomography (PET). A radioisotope, which emits positrons (positive electrons, β+), is injected into the blood. The emitted positron interacts with an electron, giving rise to the emission of two 511 keV photons (gamma rays) that exit the body in opposite directions. The two photons are detected by a series of counters that surround the organ on which the PET is performed. A specific software program reconstructs the digital images of the area of blood where the reaction takes place, thus creating a map of the vasculature as for MRI [55, 56].

The radiation dose, issued to the body from the beta + and by the two gamma rays, is much higher than that released in a mammographic test. The spatial resolution of the image is not too good [57].

5.5 DOBI (Dynamic Optical Breast Imaging)

Dynamic Optical Breast Imaging (DOBI) is a technique of optical mammography where, instead of X-rays, a light in the near-infrared spectrum is used. An array of Light Emitting Diodes (LEDs) illuminates the slightly compressed breast. A system with a fast digital camera, providing many images per second, records the light through the breast tissue; the amount of light depends on the ratio between hemoglobin and deoxyhemoglobin. A mathematical procedure reconstructs the 3D concentration of deoxyhaemoglobin in the breast tissues, thus making possible an evaluation of the vasculature [58]. This test can be performed on women of all ages (even those with dense breasts), and its cost is not very high and has a good tolerability [59, 60].

DOBI is a totally non-invasive technique, takes little time, and requires only a slight compression of the breast. This test can also be performed on women who have breast implants. It is a good test for monitoring recurrences, adjuvant chemotherapy, and hormone replacement therapy.

Its disadvantages are the multi-scattering of the light, with the wavelength of the near-infrared spectrum, and the poor spatial resolution in the image of blood distribution. Sometimes DOBI does not provide reliable results for: a) women who have undergone surgery less than one year before; b) after either less than three months from biopsy or less than one year after irradiation; c) lactating women (sometimes pregnant) due to the density of the milk secretion. Other causes of disturbance in the measurement can be the hyperpigmentation and inflammation of the skin [61].

5.6 Thermography (Or Tele-thermography)

The human body emits infrared radiation whose wavelength depends on the body's temperature. The distribution of the body's surface temperatures may be acquired by means of photo cameras with infrared sensors. Modern infrared cameras can detect variations in temperature of about 0.025 °C. For a better interpretation of the image, some temperature ranges are associated with different colors ("false color" images). Tumor tissues with high vascularization have a higher temperature than healthy ones. Figure 1a shows a thermal image of healthy breasts, while Fig. 1b shows the left breast affected by cancer at an advanced stage. In 1956, thermography started being considered as a method for breast screening; it obtained FDA approval in the U.S. and was well accepted by physicians. In 1977, a study gave less credit to thermography, stating that it produced too many false positives [62]. This study, which was partially rebutted [63], left a "stain" of unreliability on thermography. Today, with the development of new thermal imaging cameras, breast thermography has regained its credibility [64].

Thermography is an easy and inexpensive test. It is totally non-invasive and can be performed on women (and men) of all ages. Its best contribution is offered by its ability to report abnormalities in young patients in whom mammography does not provide reliable results.

Drawbacks are that the image does not properly define the place where biopsy should be performed. The majority of false negatives derive from microcalcifications, abnormalities that are not identified by thermography. The accuracy of measurements depends on environmental conditions (e.g., constant temperature in the location where measurements are performed). To perform these tests, patients must remain bare-chested in a room kept at a somewhat low temperature, for a relatively long time (about 15 min).

6 Other Interesting Applications of DATG

There are many other clinical cases other than breast cancer diagnosis in which DATG can be useful; for example: therapy monitoring, and diagnosis of other clinical cases. Here we will briefly explain some of the latter one. However, one should remember that, because of the physical conformation of plates (the sensors of DATG), this technique can provide diagnostic information only when the medical problem is generated, more or less, superficially in the body and in areas where the plate can be easily placed. In any case, it should be noted that it is not possible to diagnose a problem, for example, in the pancreas, which is located deep inside the abdomen.

6.1 DATG in a Child

DATG examination in a child of 29 months: early left breast development (Fig. 17a). Possible cause is the breastfeeding prolonged for over 24 months (maternal estrogens). After the abdomen ultrasound check of ovaries for pituitary adrenal stimulation, with negative results, breastfeeding was discontinued. The DATG examination after 7 months shows that the problem has been solved (Fig. 17b).

6.2 Checking and Monitoring Therapies

DATG can be very useful to check the efficacy of various therapies. Figure 18 shows an example of preoperative chemotherapy. Figure 19 shows the effect of antibiotic therapy in a case of mastitis. A third example is the monitoring of oral contraception therapy (see Fig. 20).

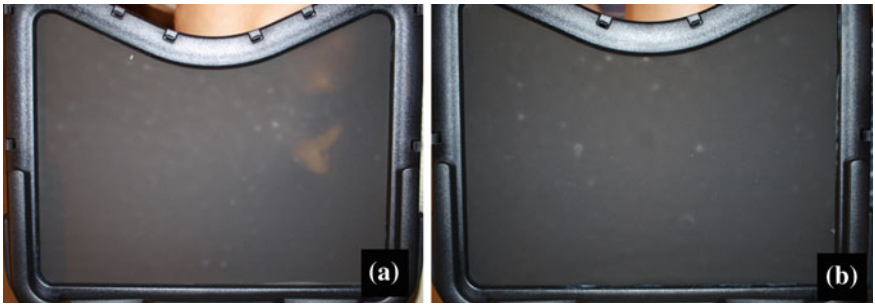

Fig. 17 DATG examination in a child of 29 months: **a** early left breast development; **b** normal pattern 7 months after the suspension of breastfeeding [31] (Reprinted from http://www.breastlife.it/index.html with permission from BreastLife s.r.l)

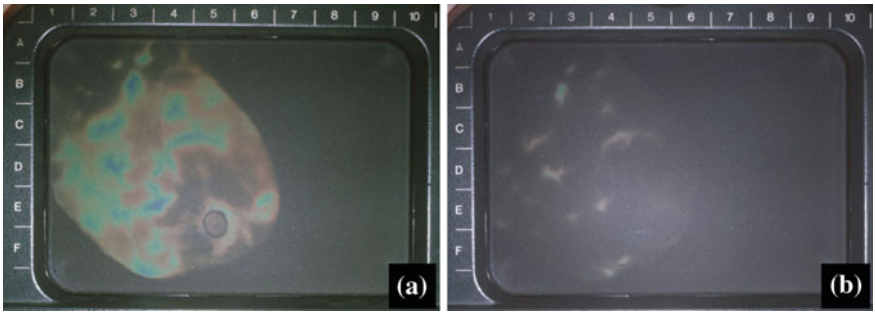

Fig. 18 Example of DATG applied to check the efficacy of a therapy: **a** at diagnosis, the external upper quadrant of the right breast shows an incomplete malignant ring made of numerous short flow lines in the external mammary gland, of acromial and internal mammary origin, all ending in spatula terminations; **b** after two months and two cycles of preoperative chemotherapy, the DATG pattern has become negative and all the abnormal flow lines have largely disappeared [31] (Reprinted from http://www.breastlife.it/index.html with permission from BreastLife s.r.l)

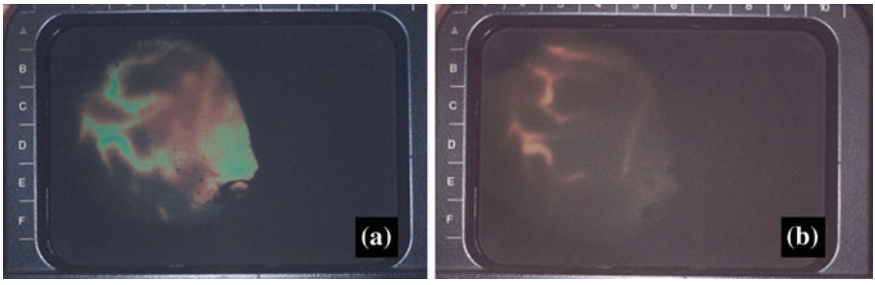

Fig. 19 Uncertain differential diagnosis between purulent and carcinomatous mastitis: **a** initial DATG examination; **b** after 14 days of antibiotics therapy the DATG pattern was completely negative [31] (Reprinted from http://www.breastlife.it/index.html with permission from BreastLife s.r.l)

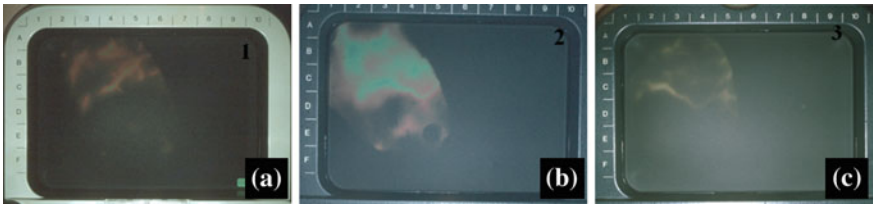

Fig. 20 Oral contraception in a 25-year-old woman. The initial DATG pattern **a** is almost completely normal. The only irregularity is the direction of an acromial flow line in the right breast, which runs toward the external upper quadrant. After 3 years of oral contraception, the DATG pattern **b**) shows a marked increase in the functional blood flow without any appearance of suspicious signs. Two years after suspension of the hormonal therapy, the DATG pattern **c** has returned to its initial appearance. Lastly, note that the initial abnormality of the acromial flow line, which was directed toward the external upper quadrant, has now completely disappeared. This was probably due to the presence of cysts, which may have disappeared because of the efficacy of the hormonal therapy [31] (Reprinted from http://www.breastlife.it/index.html with permission from BreastLife s.r.l)

Fig. 21 Example of a male breast cancer diagnosis. In a 74-year-old man, the left breast shows short abnormal flow lines with nonpointed terminations. These flow lines, covering nearly all the external upper quadrant, almost form an incomplete malignant ring around a hotspot. Note also the hot nipple. The histological test detected infiltrating ductal carcinoma [31] (Reprinted from http://www.breastlife.it/index.html with permission from BreastLife s.r.l)

6.3 Male Breast Cancer

Male breast cancer is a very rare event. Its annual prevalence in Europe and in the USA is of 1 or fewer in 100,000 and fewer than 1% of all breast cancer patients, while male breast cancer in Japan totals fewer than five per million [65]. Jewish men are the only racial group with higher incidence, two or three per hundred thousand. The main problem in diagnostic approaches and treatments for men is that techniques and therapy are generally extrapolated from those designed for women, due to inadequate research in male patients [66]. It is apparent that mammography is unfeasible for a man, while there are no contraindications or issues against the use of DATG. An example of a male breast cancer diagnosis is in Fig. 21.

7 Advantages and Disadvantages of DATG

Like all other diagnostic methods, DATG has advantages and disadvantages.

7.1 Advantages

DATG is non-invasive, does not require a contrast medium, and can be repeated as often as desired.

This technique is totally non-invasive (no ionizing radiation or contrast agents) and free from the painful compression of the breast. It can also be used in cases of acute or chronic mastitis, when other diagnostics tools cause great pain. Thanks to its total lack of side effects, it is particularly useful for monitoring patients at risk of familiarity and/or undergoing contraceptive and hormone replacement therapy, or estrogen–progestin ovarian stimulation for in vitro fertilization: all cases where a periodic examination is crucial.

As for the patient's age and conditions, DATG is also very useful for young patients or women with dense breasts, because its result is independent of the age and condition of menopausal or fertile status. Therefore it is not affected by glandularity or mammary fat. Dermatological diseases such as: herpes zoster, cutaneous hemangiomas, Recklinghausen do not affect the result. Pregnancy is not a limiting factor for diagnosis. Moreover, breast implants, plastic surgery procedures such as breast lifts, reductions, etc., are not absolute contraindications for exclusion.

The medical examination's run time is very fast: the entire procedure, which is called "angio test" includes taking the patient's history and a clinical examination, usually takes no longer than 15 min. Moreover, the test requires inexpensive and easy-to-move tools, if any. This rapid and inexpensive technique also makes possible a high number of angio tests per working day, and is matched by the immediate response, which is another big advantage.

As for diseases, the DATG examination provides signs of suspicious or malignant tissues that are independent of the size and shape of the lesion which also appear in cases of non-solid carcinomas. This technique is useful for screening, and it is also able to detect precancerous lesions where these have been highlighted by clinical examination (palpation) or other instrumental methods. DATG plays an important role in the differential diagnosis of lipoma and liposarcoma (showing the total absence of vascularization in the first, and vice versa in the second), and it is suitable for checking on therapy or following up: antiblastic chemotherapy when it would be useful to have presurgical DATG images. Certainly, it is also very useful in the difficult diagnosis of lobular, medullary, and colloidal carcinomas. The diagnostics of cutaneous melanoma is another interesting application of this technique. In fact, its DATG image is characteristic of cutaneous melanoma. Further studies will be carried out in the future.

Lastly, this technique—thanks to its low cost and ease of use—is indicated in screening programs, especially in "developing" countries.

7.2 Disadvantages

DATG shows the 2D vascular distribution, and not the 3D distribution, as with MRI, PET, and DOBI. It consequently provides no in-depth information and is therefore prone to errors caused by overlapping blood vessels and other vascularized structures. However, recent researches (based on the solution of the inverse Fourier heat equation) show the possibility to evaluate the depth of the tumor [67]. In fact, the temporal formation of the image on the plate can be processed to obtain information about the depth of the heat source (vasculature).

Moreover, DATG is not able to determine the size of a tumor, but indicates the presence of a suspicious lesion and points of the area looking at by using, for example, magnetic resonance imaging. Indeed, the intensity and size of the features in the image acquired by DATG, are not related to the shape and size of the tumor, but rather to the biological activity of its base.

Body lotion and ultrasound gel, when applied shortly before the test, can have a filter effect and cause an incorrect diagnosis, especially false negatives.

The existing blood flow lines immediately increase in diameter in early in pregnancy, and almost always new ones are generated, which do not, however, provide other predictive signs of disease. This gestational pattern remains more or less constant throughout pregnancy. Breastfeeding, instead, causes the maximum expression of flow lines: they become numerous, intersecting, almost indistinguishable from each other. During breastfeeding, DATG is not contraindicated but must be accompanied by other techniques.

Menopausal and postmenopausal conditions are characterized by a constant, very slow decrease in diameter and number of flow lines. But the situation differs greatly from woman to woman, as there are women who have a pattern corresponding to that of the reproductive age and others with an entirely quiescent one. Therefore, in many cases, the ovarian menopausal situation does not correspond to a "menopausal" breast. Consequently, each case should be evaluated independently.

8 Concluding Remarks

As happens with a work of art, observation from different points of view provides a greater chance of a better understanding; the same is true for DATG. This diagnostic technique, in fact, is not replacing with other techniques; but can combine with them in order to add information to the clinical picture from another viewpoint: that of the variation of blood distribution (angiography) which is linked to the

development of tumors. This technique is easy to learn for gynecologists, radiologists, sonographers, and oncologists. If they appropriately trained, they all can make correct diagnoses. It is affordable from the economic standpoint: thus it can play a very important role especially for young women and for those applicants who need frequent checks (follow-ups).

Acknowledgements The authors would like to thank Dr. Silvio Marino (working at the ANT foundation, Italian National Foundation for Cancer Research and Patient Care) for the information concerning DOBI results and the in vivo dynamic formation of the images by DATG, and Dr. Stefan Boeriu of the University of Santa Barbara (USA) for having kindly revised the English version of the paper. A great thank you to BreastLife, which supported our studies, providing us with the AURA equipment for DATG acquisition.

Lastly, we fondly remember Dr. Daniele Montruccoli, who died prematurely during the course of our research; he was the greatest world expert in DATG and introduced this technique even to the poorest countries.

References

1. Mathers, C., Fat, D.M., Boerma, J.T.: The global burden of disease: 2004 update. World Health Organization. Available http://www.who.int/healthinfo/global_burden_disease/2004_report_update/en/ (2008). Accessed 24 June 2016
2. Torre, L.A., Bray, F., Siegel, R.L., et al.: Global cancer statistics, 2012. CA Cancer J. Clin. **65**, 87–108 (2015). doi:10.3322/caac.21262
3. Pediconi, F., Catalano, C., Roselli, A., et al.: The challenge of imaging dense breast parenchyma: is magnetic resonance mammography the technique of choice? A comparative study with x-ray mammography and whole-breast ultrasound. Invest. Radiol. **44**, 412–421 (2009). doi:10.1097/RLI.0b013e3181a53654
4. Pinsky, R.W., Helvie, M.A.: Role of screening mammography in early detection/outcome of breast cancer. Ductal Carcinoma Situ Microinvasive/Borderline Breast Cancer, pp. 13–26. Springer, New York (2015)
5. Drukteinis, J.S., Mooney, B.P., Flowers, C.I., Gatenby, R.A.: Beyond Mammography: New Frontiers in Breast Cancer Screening. Am. J. Med. **126**, 472–479 (2013). doi:10.1016/j.amjmed.2012.11.025
6. Sree, S.V., Ng, E.Y.K., Acharya, U., Tan, W.: Breast imaging systems: a review and comparative study. J. Mech. Med. Biol. **10**, 5–34 (2010). doi:10.1142/S0219519410003277
7. Berg, W.A., Gutierrez, L., NessAiver, M.S., et al.: Diagnostic accuracy of mammography, clinical examination, US, and MR imaging in preoperative assessment of breast cancer 1. Radiology **233**(3), 830–849 (2004)
8. Sardanelli, F., Podo, F., Santoro, F., et al.: Multicenter surveillance of women at high genetic breast cancer risk using mammography, ultrasonography, and contrast-enhanced magnetic resonance imaging (the high breast cancer risk Italian 1 study): final results. Invest. Radiol. **46** (2), 94–105 (2011)
9. Montruccoli, G.C., Montruccoli Salmi, D., Casali, F.: A new type of breast contact thermography plate: a preliminary and qualitative investigation of its potentiality on phantoms. Phys. Medica **XX**(1), 27–31 (2004). doi:10.1400/19286
10. Longatto Filho, A., Costa, S.M., Milanezi, F., et al.: Immunohistochemical expression of VEGF-A and its ligands in non-neoplastic lesions of the breast sampling-assisted by dynamic angiothermography. Oncol. Rep. **18**(5), 1201–1206 (2007)

11. Cittadini, G.: Appendice 6: tra termografia e DITI. In: Edra (ed.) Diagnostica per immagini e radioterapia, pp. 1057–1065 (2015)
12. Ng, E.Y.-K.: A review of thermography as promising non-invasive detection modality for breast tumor. Int. J. Therm. Sci. **48**, 849–859 (2009). doi:10.1016/j.ijthermalsci.2008.06.015
13. Hankare, P., Shah, K., Nair, D., et al.: Breast cancer detection using thermography. Int. Res. J. Eng. Technol. **4**(3), 2395–2356 (2016)
14. John, H.E., Niumsawatt, V., Rozen, W.M., et al.: Clinical applications of dynamic infrared thermography in plastic surgery: a systematic review. Gland Surg. **5**, 122–132 (2016). doi:10.3978/j.issn.2227-684X.2015.11.07
15. Hanahan, D., Folkman, J.: Patterns and emerging mechanisms of the angiogenic switch during tumorigenesis. Cell **86**(3), 353–364 (1996)
16. Risau, W.: Mechanisms of angiogenesis. Nature **386**(6626), 671–674 (1997)
17. Naccarato, A.G., Viacava, P., Vignati, S., et al.: Bio-morphological events in the development of the human female mammary gland from fetal age to puberty. Virchows Arch. **436**(5), 431–438 (2000)
18. Andres, A.C., Djonov, V.: The mammary gland vasculature revisited. J. Mammary Gland Biol. Neoplasia **15**(3), 319–328 (2010). doi:10.1007/s10911-010-9186-9
19. Ando, Y., Fukatsu, H., Ishiguchi, T., et al.: Diagnostic utility of tumor vascularity on magnetic resonance imaging of the breast. Magn. Reson. Imaging **18**(7), 807–813 (2000)
20. Jesinger, R.A., Lattin, J.G.E., Ballard, E.A., et al.: Vascular abnormalities of the breast: arterial and venous disorders, vascular masses, and mimic lesions with radiologic-pathologic correlation. Radiographics **31**(7), E117–E136 (2011)
21. Rouvillois, C., Tricoire, J., Mariel, L., Portier, F.: Thermography using contact plates in the diagnosis of breast cancers. Chirurgie **99**(11), 866–872 (1973)
22. Tricoire, J.: Study of breast cancer by means of liquid crystals thermography. J. Gynecol. Obstet. Biol. Reprod. (Paris) **4**(SUPPL 2), 123–130 (1975)
23. Tricoire, J.: La thermografie en plaque. Technique nouvelle d'utilisation des cristaux liquides. Presse Med. **78**(55), 2481–2482 (1970)
24. Head, J.F., Elliott, R.L.: Thermography. Cancer **79**(1), 186–188 (1997)
25. Nyirjesy, I.: Breast thermography. Clin. Obstet. Gynecol. **25**(2), 401–408 (1982)
26. Kennedy, D.A., Lee, T., Seely, D.: A comparative review of thermography as a breast cancer screening technique. Integr. Cancer Ther. **8**(1), 9–16 (2009). doi:10.1177/1534735408326171
27. Montruccoli, G.C., Montruccoli, D.S., D'Errico, A., et al.: Angiothermography in an integrated diagnosis for secondary prevention of breast cancer. In: Lancet Conference—The Challenge of Breast Cancer, Brugge, 21–22 April 1994, vol. 49. The Lancet: London (1994)
28. Montruccoli, D., Casali, F., Schmitt, F.C., et al.: New advances in treatment of breast cancer. In: Proceedings of XVIII FIGO World Congress of Gynecology and Obstetrics; Kuala-Lumpur Malesia, 5–19 Nov 2006
29. Montruccoli, G.C., Montruccoli, D., Casali, F., et al.: Clinical application of a new thermographic plate: histophathological findings of 1027 breast lesions. In: 95th AACR Annual Meeting, March 27–31, Orlando, Florida, US. Cancer Res **64**(7), 215 (2004)
30. Montruccoli-Salmi, D., Casali, F., Draetta, F.G., et al.: Dynamic angiothermography a new functional technique in breast imaging, useful in gynecological practice. In: Abstracts of XX FIGO World Congress of Gynecology and Obstetrics, October 2012, Int J Gynecol Obstet 119(3):S642–S643 (2012)
31. Breast Life S.r.l.—Piazza San Martino, 1 40126 Bologna, Italy. http://www.breastlife.it/. Accessed 24 June 2016
32. Faust, O., Acharya, U.R., Ng, E.Y.K., et al.: Application of infrared thermography in computer aided diagnosis. Infrared Phys. Technol. **66**, 160–175 (2014). doi:10.1016/j.infrared.2014.06.001
33. Montruccoli, G.C., Montruccoli-Salmi, D., Barnabe, D., et al.: Early diagnosis of breast cancer by dynamic angiothermography. In: Taylor & Francis (ed.) Gynecology and obstetrics; New insights in gynecology & obstetrics research and practice. Parthenon Pub. Group, New York, London, pp. 296–300. ISBN 1850709661 (1998)

34. Montruccoli, G.C., Montruccoli-Salmi, D., Barnabe, D.: Value of functional blood supply pattern analysis in the detection of early breast cancer. Int. J. Gynecol. Obstet. **70**(5), E15 (2000). doi:10.1016/S0020-7292(00)82366-8
35. Montruccoli, G.C., Montruccoli-Salmi, D.: L'angiotermografia dinamica nella diagnosi senologica. In: Cosmi, E.V., Pinotti, J.A. (eds.) Neoplasie della Mammella – Dalla diagnosi al trattamento. SEE Editrice, Florence, pp. 205–218. ISBN 8884650151, 9788884650153 (2006)
36. Biller-Andorno, N., Jüni, P.: Abolishing mammography screening programs? A view from the Swiss Medical Board. N. Engl. J. Med. **370**(21), 1965–1967 (2014). doi:10.1056/NEJMp1401875
37. Miller, A.B., Wall, C., Baines, C.J., et al.: Twenty five year follow-up for breast cancer incidence and mortality of the Canadian National Breast Screening Study: randomized screening trial. BMJ **348**, g366 (2014). doi:10.1136/bmj.g366
38. Lewin, J.M., Isaacs, P.K., Vance, V., et al.: Dual-energy contrast-enhanced digital subtraction mammography: feasibility. Radiology **229**(1), 261–268 (2003)
39. Boone, J.M., Kwan, A.L., Yang, K., et al.: Computed tomography for imaging the breast. J. Mammary Gland Biol. **11**(2), 103–111 (2006)
40. Xia, Q.: Dedicated computed tomography of the breast: image processing and its impact on breast mass detectability. ProQuest, Duke University. ISBN 0549663193, 9780549663195 (2007)
41. Ciatto, S., Houssami, N., Bernardi, D., et al.: Integration of 3D digital mammography with tomosynthesis for population breast-cancer screening (STORM): a prospective comparison study. Lancet Oncol. **14**(7), 583–589 (2013). doi:10.1016/S1470-2045(13)70134-7
42. Sechopoulos, I.: A review of breast tomosynthesis. Part II. Image reconstruction, processing and analysis, and advanced applications. Med. Phys. **40**(1), 014302 (2013). doi:10.1118/1.4770281
43. Berrington de González, A., Reeves, G.: Mammographic screening before age 50 years in the UK: comparison of the radiation risks with the mortality benefits. Br. J. Cancer **93**(5), 590–596 (2005)
44. Yaffe, M.J., Mainprize, J.G.: Risk of radiation-induced breast cancer from mammographic screening. Radiology **258**(1), 98–105 (2011). doi:10.1148/radiol.10100655
45. Choi, B.B., Kim, S.H., Park, C.S., et al.: Radiologic findings of lobular carcinoma in situ: mammography and ultrasonography. J. Clin. Ultrasound **39**(2), 59–63 (2010). doi:10.1002/jcu.20772
46. Lee, C.H., Dershaw, D.D., Kopans, D., et al.: Breast cancer screening with imaging: recommendations from the Society of Breast Imaging and the ACR on the use of mammography, breast MRI, breast ultrasound, and other technologies for the detection of clinically occult breast cancer. J. Am. Coll. Radiol. **7**(1), 18–27 (2010). doi:10.1016/j.jacr.2009.09.022
47. Kelly, K.M., Dean, J., Comulada, W.S., et al.: Breast cancer detection using automated whole breast ultrasound and mammography in radiographically dense breasts. Eur. Radiol. **20**(3), 734–742 (2010). doi:10.1007/s00330-009-1588-y
48. Kornecki, A.: Current status of breast ultrasound. Can. Assoc. Radiol. J. **62**(1), 31–40 (2011). doi:10.1016/j.carj.2010.07.006
49. Leong, L.C., Sim, L.S., Lee, Y.S., et al.: A prospective study to compare the diagnostic performance of breast elastography versus conventional breast ultrasound. Clin. Radiol. **65**(11), 887–894 (2010). doi:10.1016/j.crad.2010.06.008
50. Soo, M., EL BakerJA, Rosen: Sonographic detection and sonographically guided biopsy of breast microcalcifications. AJR Am. J. Roentgenol. **180**(4), 941–948 (2003)
51. Saslow, D., Boetes, C., Burke, W., et al.: American Cancer Society Guidelines for breast screening with MRI as an Adjunct to mammography. CA Cancer J. Clin. **57**(2), 75–89 (2007)

52. Kul, S., Cansu, A., Alhan, E., et al.: Contrast-enhanced MR angiography of the breast: evaluation of ipsilateral increased vascularity and adjacent vessel sign in the characterization of breast lesions. AJR Am. J. Roentgenol. **195**(5), 1250–1254 (2010). doi:10.2214/AJR.10.4368
53. Morrow, M., Waters, J., Morris, E.: MRI for breast cancer screening, diagnosis, and treatment. The Lancet **378**(9805), 1804–1811 (2011). doi:10.1016/S0140-6736(11)61350-0
54. Dewey, M., Schink, T., Dewey, C.F.: Claustrophobia during magnetic resonance imaging: cohort study in over 55,000 patients. J. Magn. Reson. Imaging **26**(5), 1322–1327 (2007)
55. Bailey, D.L., Townsend, D.W., Valk, P.E., et al. (eds.): Positron emission tomography. Bascis Science, Springer, Berlin. ISBN 978–1-85233-798-8 (Print) 978-1-84628-007-8 (online) (2005)
56. Wilson, C.B., Lammertsma, A.A., McKenzie, C.G., et al.: Measurements of blood flow and exchanging water space in breast tumors using positron emission tomography: a rapid and noninvasive dynamic method. Cancer Res. **52**(6), 1592–1597 (1992)
57. Moses, W.W.: Fundamental limits of spatial resolution in PET. Nucl. Instrum. Methods Phys. Res. A **648**(1), S236–S240 (2011)
58. Gibson, A.P., Hebden, J.C., Arridge, S.R.: Recent advances in diffuse optical imaging. Phys. Med. Biol. **50**(4), R1–R43 (2005)
59. D'Aiuto, M., Frasci, G., Barretta, M.L., et al.: The dynamic optical breast imaging in the preoperative workflow of women with suspicious or malignant breast lesions: development of a new comprehensive score. ISRN Oncol. 2012: Article ID 631917, 9 pages (2012). doi:10.5402/2012/631917
60. Fournier, L.S., Vanel, D., Athanasiou, A., et al.: Dynamic optical breast imaging: a novel technique to detect and characterize tumor vessels. Eur. J. Radiol. **69**(1), 43–49 (2009). doi:10.1016/j.ejrad.2008.07.038
61. Tromberg, B.J., Pogue, B.W., Paulsen, K.D., et al.: Assessing the future of diffuse optical imaging technologies for breast cancer management. Med. Phys. **35**(6), 24432451 (2008)
62. Feig, S.A., Shaber, G.S., Schwartz, G.F., et al.: Thermography, mammography, and clinical examination in breast cancer screening. Review of 16,000 studies. Radiology **122**(1), 123–127 (1977)
63. Keyserlingk, J.R., Ahlgren, P.D., Yu, E., et al.: Functional infrared imaging of the breast. IEEE Eng. Med. Biol. **19**(3), 30–41 (2000). doi:10.1109/51.844378
64. Lahiri, B.B., Bagavathiappan, S., Jayakumar, T., et al.: Medical applications of infrared thermography: a review. Infrared Phys. Technol. **55**(4), 221–235 (2012). doi:10.1016/j.infrared.2012.03.007
65. Fentiman, I.S., Fourquet, A., Hortobagyi, G.N.: Male breast cancer. The Lancet **367**(9510), 595–604 (2006)
66. Ruddy, K.J., Winer, E.P.: Male breast cancer: risk factors, biology, diagnosis, treatment, and survivorship. Ann. Oncol. **24**(6), 14341443 (2013)
67. Brancaccio, R., Bettuzzi, M., Morigi, M.P., et al.: Preliminary results of a new approach for three-dimensional reconstruction of Dynamic AngioThermography (DATG) images based of the inversion of heat equation. Phys. Med. **32**(9), 1052–1064 (2016). doi:10.1016/j.ejmp.2016.07.637

Infrared Thermography for Detection of Diabetic Neuropathy and Vascular Disorder

B.B. Lahiri, S. Bagavathiappan, Baldev Raj and John Philip

Abstract Body temperature is a significant indicator of illness and hence is a useful parameter for clinical diagnosis. Among various techniques available for accurate and reliable measurement of subject temperature, infrared thermography is a relatively new methodology. However, it has become popular because of its noncontact, noninvasive, and real-time temperature measurement capability. During the last few decades, numerous applications of infrared thermography are reported in the field of medical sciences, which are rapidly growing. Diabetes is a metabolic disorder associated with high blood sugar levels over prolonged duration. One in every 11 adult population of the world is affected by diabetes and for every 6 s, one person dies from diabetes-induced complications. Therefore, a worldwide dedicated effort to prevent diabetic complications by early detection is important. Studies so far reveal that infrared thermography is capable of detecting subtle changes in skin temperature distribution in diabetic-at-risk foot and is capable of early detection diabetic-related peripheral neuropathy and vascular disorders. This chapter attempts to highlight the applications of infrared thermography in the early detection of diabetic neuropathy and vascular disorder. The basics of infrared thermography, classification of medical thermography techniques, details of infrared camera, ideal experimental conditions, data analysis, etc. along with typical case studies are discussed in detail.

Keywords Diabetic neuropathy · Vascular disorder · Classification · Experimental conditions · Data analysis

B.B. Lahiri · S. Bagavathiappan · J. Philip (✉)
Non-Destructive Evaluation Division, Radiography and Thermography Section, Metallurgy and Materials Group, Indira Gandhi Centre for Atomic Research, Kalpakkam, Tamil Nadu 603102, India
e-mail: philip@igcar.gov.in

B. Raj
National Institute of Advanced Studies, Indian Institute of Science Campus, Bangalore 560012, India

E.Y.K. Ng and M. Etehadtavakol (eds.), *Application of Infrared to Biomedical Sciences*, Series in BioEngineering,
DOI 10.1007/978-981-10-3147-2_13

1 Introduction

Temperature has been considered as a very good indicator of health and has been used as a parameter for clinical diagnosis since 400 BC [1–3]. Although thermometers were developed around seventeenth century [2], only in 1868, Wunderlich [4] first systematically studied the temperature of human subjects suffering from fever and compared the same with normal subjects and established the physiological and clinical importance of temperature. Till then, temperature has been considered as one of the most significant indicators of illness. Among various techniques being used for accurate and reliable measurement of subject temperature, infrared thermography is a comparatively new methodology that has become popular because of its noncontact, noninvasive, and real-time temperature measurement capability [5, 6]. Although infrared thermography is routinely used for nondestructive evaluation and condition monitoring studies [5–9], its application in the bio-medical field is huge and rapidly growing [10–16]. Numerous applications of infrared thermography in the medical sciences have been reported in the last few decades.

Some of the reviews highlighting the application of infrared thermography in medical science are by Jones [12], Ammer and Ring [13, 17], Jung et al. [18], Yang and Yang [19], Fauci et al. [20], Jiang et al. [21], Ring et al. [22], Lahiri et al. [10], and Faust et al. [23]. Infrared thermography has been extensively used in various fields of bio-medical sciences, viz., fever screening [24–31], breast cancer detection [32–37], brain imaging (thermoencephaloscopy) [38], dentistry and dermatology [39–42], muscular pain and shoulder impingement syndrome detection [43], dry eye syndrome detection [44, 45], diagnosis of rheumatologic diseases [46–49], evaluation of skin sympathetic dysfunction in Parkinson's disease [50], thermoregulation [14, 15, 51–53], detection and treatment of parasitic and metastatic liver diseases [54, 55], bowel ischemia [56], diagnosis of tuberculosis [57], renal transplantation [58, 59], gynecology [60–62], acupuncture [63], forensic medicine [64, 65], heart treatment [66], quantification of bacterial concentration [16, 67], and diagnosis and early detection of diabetic neuropathy and vascular disorder [68–77]. The developments in the field of medical thermography between 1989 and 2003 are reviewed by Ammer [78, 79]. An internet search in popular bibliometry service "Pubmed" [80] with the keywords, "Medical" and "Thermography" in all fields, yields in total 932 publications spanned over 1964–2016. Figure 1 shows the number of publication in the field of medical thermography as a function of publication year. It can be seen that in recent years (especially from 2000 onward), the number of publications per year clearly increased indicating a rapid growth in the use of infrared thermography in medical sciences. Figure 2a shows the year-wise number of publications on infrared thermography-based studies on diabetes, which was obtained from the "Pubmed" [80] database which clearly shows a surge of interest in infrared thermography-based detection of diabetes-related complications. Figure 2b shows the percentage of diabetes-related publication with respect to total

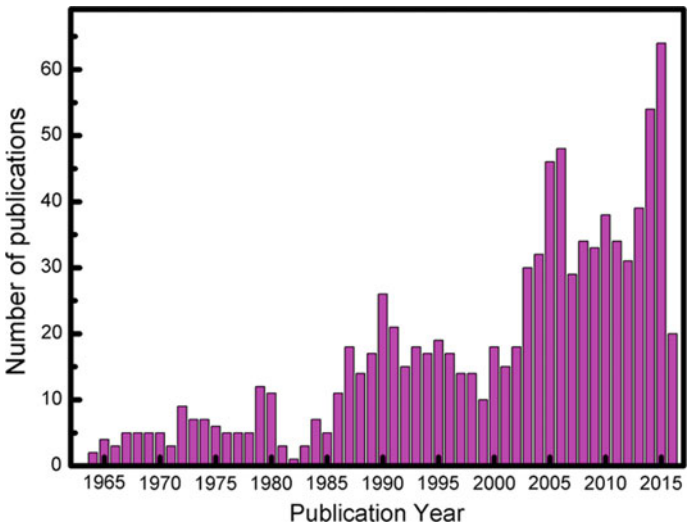

Fig. 1 Histogram distribution showing the number of publications in the field of medical thermography as a function of the year of publication. The data was obtained from "Pubmed" database [80] using the keywords: "Medical" and "Thermography" in all fields

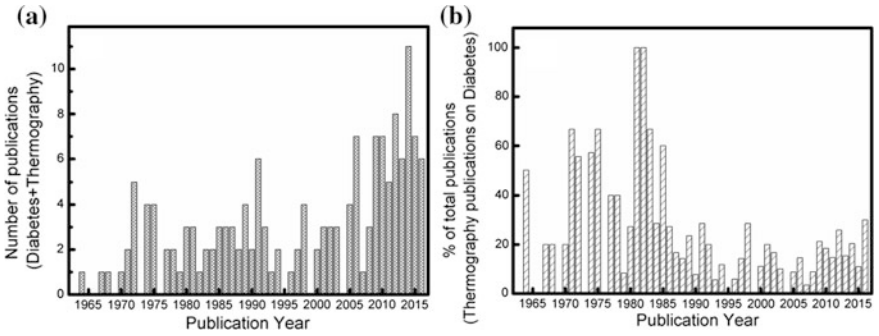

Fig. 2 **a** Histogram distribution showing the number of publications on application of thermography in diabetes. The data was obtained from "Pubmed" database [80] using the keywords "Diabetes" and "Thermography" in all fields. **b** Histogram showing the percentage of publications on application of thermography in diabetes with respect to the total number of publication in the field of medical thermography

number of year-wise publications in medical thermography which indicates diversified applications of infrared thermography in other medical fields, like breast cancer detection, fever screening, diagnosis of rheumatologic diseases, etc.

Diabetes is a metabolic disorder associated with high blood sugar levels over prolonged duration. 415 million cases of diabetes have been reported up to 2015 and the number is expected to rise to 642 million by 2040 [81]. One in every 11 adult population of the world is affected by diabetes and for every 6 s a person dies

from diabetes-induced complications [81]. It has also been reported that 1 in every 7 birth is associated with gestational diabetes [81]. Hence, a worldwide dedicated effort has been witnessed toward diagnosis, prevention, and early detection of diabetes. Bharara et al. [70, 82] reported that the incidence of diabetic foot diseases is growing worldwide leading to an increased socio-economic burden on health care systems of different countries. Diabetic foot with higher temperature patterns is indicative of early onset of diabetic neuropathy and subsequent ulceration, if not treated. Moreover, peripheral small fiber damages are often undetected using clinical and nerve conduction studies resulting in delayed diagnosis and detection of neuropathic symptoms. Infrared thermography is capable of detecting subtle changes in skin temperature distribution in diabetic-at-risk foot and hence, early detection is feasible using this technique which resulted in a renewed interest in application of infrared thermography in diagnosis of peripheral neuropathy and vascular disorder in diabetic subjects.

This chapter attempts to highlight the applications of infrared thermography in diabetic neuropathy and vascular disorder. For non-specialists, the basics of infrared thermography and classification of medical thermography techniques are discussed in detail, followed by a brief discussion on infrared camera, experimental conditions, and data analysis techniques. In the subsequent section, the physiological relationship of temperature with diabetic complications is discussed along with relevant literature survey. Finally, a few case studies on infrared thermography-based detection of diabetic neuropathy and vascular disorder are briefly presented.

2 Infrared Thermography

2.1 Basics of Infrared Thermography

Infrared thermography is a noncontact temperature measurement methodology where the electromagnetic radiation emitted by the surface of an object under observation is detected using a suitable infrared detector and surface temperature of the object is obtained from the intensity of the recorded radiation. The infrared radiation (wavelength ranging from 0.75 to 1000 μm) lies in between the microwave and visible regions of the electromagnetic spectrum. This vast range is further subdivided into three categories, viz., far infrared or FIR (wavelength range: 5.6–1000 μm), medium infrared or MIR (wavelength range: 1.5–5.6 μm), and near infrared or NIR (wavelength range: 0.75–1.5 μm). Although the theoretical understanding about infrared thermography was available from 1800, it took nearly 150–200 years for the technique to be available for routine use, due to lack of proper equipments and technical knowhow. The origin and theory of infrared thermography can be found elsewhere [5, 6].

Blackbody is a hypothetical object which absorbs all radiation incident on it and emits a continuous spectrum characteristic of its temperature and this continuous spectrum is governed by the well-known Planck's law [5]:

$$L_\lambda = \frac{C_1}{\lambda^5\left[\exp\left(\frac{C_2}{\lambda T}\right) - 1\right]}, \tag{1}$$

where λ is the wavelength (μm), L_λ is the power radiated by the blackbody per unit surface and per unit solid angle (W m^{-2} μm^{-1} sr^{-1}), T is the temperature of the blackbody in absolute scale (K), and C_1 and C_2 are the first and second radiation constants, respectively. Integrating Planck's law over all wavelength leads to the Stefan–Boltzmann's law which shows that the radiative power emitted per unit area is directly proportional to T^4, as described below [5]:

$$\frac{q}{A} = \sigma T^4, \tag{2}$$

where q is the rate of energy emission (W), A is the area of the emitting surface (m^2), and σ is the Stefan–Boltzmann's constant ($\sigma = 5.676 \times 10^{-8}$ W m^{-2} K^{-4}). For a real object the Stefan–Boltzmann's law is modified as $\frac{q}{A} = \varepsilon\sigma T^4$, where the parameter ε is known as emissivity which is defined as the ratio of spectral power radiated by a real surface at a particular temperature to that of a hypothetical blackbody maintained at the same temperature. For a hypothetical blackbody $\varepsilon = 1$ and for real surfaces $\varepsilon < 1$ [5]. It has been reported that the emissivity of human skin is $\sim 0.98 \pm 0.01$ in the wavelength range of 2–14 μm [83]. The skin emissivity does not vary with the color or texture of the skin or the nature of experiments, i.e., in vivo or in vitro [83]. On the other hand, studies show that the application of cosmetics or surface curvature may lead to a change in skin emissivity [84, 85]. Watmough et al. [86] have shown that the errors associated with surface temperature measurement are insignificant for viewing angles up to 45° which essentially rules out the variation of emissivity with skin curvature for medical thermography studies except for the cases of female breast imaging where silver, copper, or aluminized mylar mirrors have been used as reflectors with suitable correction factors [84].

The temperature of an object is measured using infrared camera using the following radiometric equation [5]:

$$M_{\text{cam}} = \tau\varepsilon M_{\text{obj}} + \tau(1-\varepsilon)M_{\text{env}} + (1-\tau)M_{\text{atm}}, \tag{3}$$

where M_{cam} is the radiance received by the infrared camera, M_{obj}, M_{env}, and M_{atm} are the radiance emitted by the surface of the object under investigation, surrounding environment and atmosphere, respectively. ε and τ are the surface emissivity of the object under investigation and atmospheric transmittance, respectively. Considering atmospheric transmittance to be nearly equal to unity for indoor experiments, Eq. 3 can be simplified to $M_{\text{cam}} = \varepsilon M_{\text{obj}} + (1-\varepsilon)M_{\text{env}}$.

Radiance received by the infrared camera is converted into an electrical signal by the infrared detector housed inside the camera casing and surface temperature of the object under investigation is obtained using suitable calibration curves [5].

Modern-day infrared cameras show the surface temperature distribution as visual images often pseudo-color coded where each pseudo-color indicates a range of temperature which aides in online visualization and fast analysis. Specifications of a typical infrared camera (FLIR SC5000) are shown in Table 1 [87].

2.2 Classification of Medical Thermography Techniques

On the basis of temperature measurement methodology, medical thermography can be primarily classified into four categories, viz., cutaneous temperature discrimination, electrical contact thermometry, liquid crystal thermography, and infrared

Table 1 Specifications of a typical high-end cooled type infrared camera (FLIR SC 5200)

Parameters	Values
Detector	Indium Antimonide (InSb)
Spectral range	3–5 μm (Detector response is from 2.5 to 5.1 μm)
Resolution	320 × 256 pixels
Pixel pitch	30 × 30 μm
Temperature range	5–300 °C (standard) −20 to 300 °C (very low temperature: additional) 5–1500 °C (high temperature: additional) 5–2500 °C (very high temperature: additional) 5–3000 °C (ultra high temperature: additional)
Accuracy	±1 °C or ± 1%
Noise equivalent temperature difference (NETD)	<25 mk (20 mK typical) @ 25 °C
Sensor cooling	Stirling closed cycle cooler
f/#	f/3.0
Power	12 V (DC)
Integration	Snapshot type
Integration time (electronic shutter speed)	3 μs–20 ms
Read-out mode	Asynchronous integrate then read
Dynamic range	14 bit
Full frame rate	Programmable 1–170 Hz
Sub-windowing	160 × 128/64 × 120/64 × 8 (minimum)
Well capacity	7.1 M electrons
Operability	99.5%
Dimension (L × W × H) (mm)	320 × 141 × 159
Weight (kg)	3.8

thermography [69]. Bertelsmann et al. have shown that cutaneous temperature discrimination threshold, which is a measure of small nerve fiber function, can be used for early diagnosis of diabetic subjects [88]. One of the most widely used instruments for the cutaneous temperature discrimination is the TipTherm (Axon GmBh, Germany) which is pen-like device without any external power supply and consist of two flat surfaces, one of them is metallic and the other one is synthetic [69]. Viswanathan et al. [89] used TipTherm for studying distal symmetrical polyneuropathy. In another study, Liniger et al. [90] used a thermo-resistance-based device, Thermocross (Medical School, Geneva, Switzerland) for thermal sensitivity in subjects with diabetic neuropathy. In electrical contact thermometry, individual or arrays of suitable transducers (thermistors or semiconductor sensors) are used for measuring skin temperature in contact mode [69]. A temperature difference of ± 1.5 °C was proposed as a limit of agreement between thermistor-based electrical contact thermometry and localized infrared thermometer [91]. Although the major drawback of electrical contact thermometry is due to fluctuation of skin temperature due to excessive contact pressure and lack of uniform contact with skin surface, small local arrangement of sensors in the size and shape of human foot to measure temperature of the plantar surface of the foot in diabetic neuropathy subjects is immensely beneficial [69]. In liquid crystal thermography, temperature-sensitive cholesteric liquid crystals are arranged in several layers between two flexible and heat sensitive rubber sheets for proper contact with skin surface [41, 69]. The liquid crystals change their color according to the temperature and the resultant pattern is a representation of skin surface temperature distribution. The major drawbacks of liquid crystal thermography are poor spatial resolution (>5 mm), low thermal sensitivity ($\sim$0.3–1.0 °C), slow response time (>60 s), and contact-based subjective temperature measurement [41, 92]. Two liquid crystal thermography-based commercial products, namely Spectrasole Pro 1000 (Sweden) [93] and Tempstat^{TM} (USA) [94], are available since 2004. Although Spectrasole is more focused on preventive diagnostics and monitoring of healing, Tempstat is a personal homecare product along with regular professional expertise. Taiwan-based Thermoscale is also a personal care device with integrated temperature-sensitive thermistors (electrical contact thermometry) for each foot, along with body weighing scale and fat measurement function. Piotr et al. [95] reported the development of a temperature measurement system for continuous monitoring of feet temperature using a data logger and wireless communication.

Infrared thermography, on the other hand, is a completely contactless temperature measurement technique where the infrared rays emitted by the skin surface are remotely detected in a noninvasive way. It is fast and can monitor temperature variations over a comparatively larger area. Modern infrared cameras are capable of real-time skin temperature measurement, with onboard image processing, which enables fast online data interpretations. The representation of skin surface temperature distribution in terms of pseudo-color-coded visual images also aides in data interpretation. Moreover, infrared thermography records naturally emitted radiations and no harmful radiation effects are present which makes this technique

perfectly suitable for prolonged and repeated use. In general, for medical applications, passive infrared thermography technique is used without the presence of external heat sources. An object at 27 °C emits a wavelength in the range of 2–20 μm with a peak around 10 μm. A narrow wavelength band of 8–12 μm is in general used for medical applications, which is also termed as body infrared rays. With the advent of newer generation infrared cameras near and mid-infrared bands are also used for medical thermography [68, 96]. Several commercial infrared cameras are available in the market as subsequently discussed.

3 Experimental Methods

3.1 Infrared Camera

The major requirements for medical thermography experiments are an infrared camera, a tripod, an image display, and processing unit. With advent of sophisticated computers, on-chip image processing is very common and most modern infrared cameras are equipped with inbuilt visual display and primary image analysis options. Personal computers equipped with necessary hardware and software configurations are the most widely used alternatives for detailed image processing and data analyses. Ring [74] stressed the need of a parallax-free mounting stand (not a common tripod) for medical infrared imaging for ensuring that reproducible camera positioning and reduced angular errors in the field of view between the infrared camera and the subject under investigation.

Development and detailed working principle of various infrared cameras and detectors have been described elsewhere [5, 97, 98]. Infrared cameras have undergone three major generations of advancements. The first-generation cameras were equipped with a single detector and two scanning mirrors for image production. These cameras were very slow and they suffered from saturation and calibration errors. Time delay integration was enabled in the second-generation cameras which improved image production. They were equipped with a small 2-D array or a large linear array of detectors along with two scanning mirrors. Third-generation cameras were free of any scanning mirrors and a focal plane array detector produced an image of the entire field of view in one snap. Modern-day infrared cameras are improved version of third-generation cameras with better and faster backplane electronics, sharpness controlled autofocus, on-chip image processing, variable integration time, and frame rate for image acquisition which make them suitable for real-time temperature measurement enabling online monitoring of dynamic temperature variation. Modern infrared detectors can be classified into two major categories, viz., cooled and uncooled. Traditionally cooled cameras are more stable and provide better spatial and temperature resolution but they are heavy and costly. On the other hand, uncooled cameras are light weight, portable, and cheap compared to the cooled cameras and with advancement of solid-state electronics,

the thermal sensitivity of uncooled cameras has reached ~0.05 °C, which is more than sufficient for majority of applications and mass manufacturing of such detector is possible using silicon wafer technologies [99]. It has been reported that infrared cameras equipped with focal plane arrays have spatial resolution of ~2 mm over a range of working distances and fields of view (e.g., 200 × 200 mm to 500 × 500 mm at a distance of 1 m) [100]. To provide a guideline for nonspecialist for selecting infrared cameras from various models available in the market, a few infrared cameras used for diabetes-related thermal imaging are tabulated in Table 2.

3.2 Experimental Conditions

Infrared radiation emitted from skin surface depends on several environmental factors like airflow, surrounding temperature, humidity, and the physiological condition of subjects. Hence, it is essential to perform medical thermography experiments in a controlled environment, especially when the main objective is to detect subtle temperature changes. The importance of a standard data acquisition protocol was stressed by Clark et al. [115] and Ring and Ammer [116] for reproducible and reliable results. According to their studies, the basic standards for examination room, subject information processing, imaging system, data acquisition, and data processing were very important for medical thermography. International Organization for Standardization (ISO) guidelines on human temperature screening [117, 118] were also found to provide additional useful information on test requirement and implementation guidelines for a proper and accurate medical thermography experiments.

Amalu et al. [32] reported that the temperature and humidity of the examination room must be selected in such a way that the physiology of the subjects is not "stressed into a condition of shivering or perspiring." A comfortable room temperature ensures mild thermal stress-induced vasoconstriction aided cooling of skin rendering the hot spots due to the underlying abnormalities to be clearly discernible [12]. A thermal acclimatization time is useful for the subjects to adjust with the environmental temperature and the duration of thermal acclimatization time is essential as it affects skin temperature profile. This thermal acclimatization procedure can be either nude or with normal dressing, depending on the requirements. For infrared thermography experiments on the lower or upper extremities, in most of the cases, disrobing is not required. Literature shows a wide variation in thermal acclimatization time adopted by various researchers, viz., nil duration [119], 1–5 min [68, 105, 120], 15–20 min [101, 107, 109, 111], and up to 30 min [104]. 15 min of thermal acclimatization time is more than sufficient in maximum cases as this is approximately 50% higher than the recommended duration for stabilization of infrared thermography images of human subject at rest [121]. Experimental conditions followed by a few research groups are highlighted in Table 3.

Table 2 List of infrared cameras used by various study groups (UCM indicates uncooled micro-bolometer type detectors) and their important features

Sl. No	Reference	Year	Camera make/Model	Spectral range/Temperature range	Thermal sensitivity	Detector type
1	Branemark et al. [101]	1967	AGEMA 780	3–5.6 μm	0.1 °C	Cooled
2	Cheng et al. [102]	2002	Thermo Tracer, Th2100 (NEC Co.)	8–13 μm	0.02 °C	UCM
3	Sun et al. [103]	2006	Spectrum 9000 MB	7–14 μm	0.05–0.08 °C	UCM
4	Bagavathiappan et al. [68]	2008	AGEMA THV550	3.6–5 μm	<0.1 °C	Cooled
5	Anburajan et al. [104]	2011	Thermacam T400	7.5–13 μm	<45 mK at 30 °C	UCM
6	Huang et al. [105]	2011	Spectrum 9000-MB	7–14 μm	0.05–0.08 °C	UCM
7	Szentkuti et al. [106]	2011	HEXIUM's MIDS (Medirlab Infra-diagnostic System)	8–14 μm	30 mK at 30 °C	FPA-UCM
8	Balbinot et al. [107]	2012	4010 IRYSIS, and T400 Flir	7–12 and 8–14 μm	0.08 and 0.01 °C	UCM
9	Bharara et al. [70]	2012	IRISYS- Model IRI 4010, UK	8–14 μm/(−10 to 250 °C)	0.15 °C at 21 °C ambient	160 × 120 pixels (UCM)
10	Balbinot et al. [108]	2013	IRISYS- Model IRI 4010, UK	8–14 μm/(−10 to 250 °C)	0.15 °C at 21 °C ambient	160 × 120 pixels (UCM)
11	Mori et al. [109]	2013	TH5108ME,	0–70 °C	0.08 °C at 30 °C	UCM
12	Netten et al. [110]	2013	FLIR SC305	7.5–13 μm	<0.05 °C at 30 °C	UCM
13	Oe et al. [111]	2013	Thermo-Shot F30S	8–14 μm	0.1 °C at 30 °C	UCM
14	Bandyopadhyay et al. [112]	2014	FLIR SC325	7.5–13 μm	<0.05 °C at 30 °C	UCM
15	Yavuz et al. [113]	2014	TiR2FT, Fluke Corporation	8–14 μm (−20 to 100 °C)	≤0.07 °C at 30 °C	160 × 120 FPA Vanadium oxide (UCM)
16	Alfred Gatt et al. [114]	2015	FLIR SC 7000	7.7–9.3 μm	<25 mK	Cooled

Table 3 Experimental parameters followed by a few research groups

Serial no.	Researcher	Year	Experimental conditions	
			Ambient room temperature (°C)	Acclimatization time (min.)
1	Branemark et al. [101]	1967	18–20	15–20
2	Armstrong et al. [71]	1997	21 ± 2	15
3	Hosaki et al. [75]	2002	20	15
4	Sun et al. [103]	2006	21 ± 1	15–20
5	Bagavathiappan et al. [68]	2010	25	5

Additionally, the examination room must be free from secondary sources of infrared radiation like incandescent lamps and direct sunlight to reduce the scattering and background temperature fluctuations. Moreover, the subjects should be advised to refrain from the use of cosmetics, deodrants, and antiperspirants. The ambient temperature of the experiment room can be varied between approximately 26–33 °C, i.e., within the limit of classical thermoneutral zone [122]. The physiological conditions of the subjects (like drugs, medications, alcohol, nicotine, exercise, etc.) may alter the skin temperature and hence, proper protocol must be followed in subject selection. Infrared thermography results are to be compared with clinical and medical data to establish possible correlations.

3.3 Data Analysis and Image Processing

Data analysis and image processing are important in medical thermography applications. Temperature data obtained from the acquired thermal images are in general presented as mean ± standard deviation (S.D.). The fluctuations in experimental conditions lead to such deviations and hence, statistical analysis is important obtaining reliable measurement of skin temperature distribution. The common statistical tools are hypothesis testing (Student's t test, Fischer's test), correlation analysis, χ^2 test, and analysis of variance (ANOVA) [71, 103, 123]. Selection of optimal statistical tool is very important as it varies with experimental protocol, data size, and primary objective of the study and design of experiments. Personal computer-based statistical software packages like IBM-SPSS, SAS/STAT statistical analysis software, R, Origin, and Microsoft Excel are in general used for statistical analysis.

Thermal waves attenuate exponentially in a medium and hence, skin surface thermal signatures, which represent underlying anomalies, are of comparatively low signal-to-noise ratio (SNR) [124]. Hence, image processing is fundamental to medical thermography and its importance in medical thermography was rightly

pointed out by Jones and Plassmann [11]. Nowadays, the image obtained from the infrared camera is directly fed into a personal computer where different filters, in time and frequency domains, for minimizing noise, preservation of edges, reducing blurring and for enhancing image quality, are used [112]. Soft computing techniques like artificial neural network (ANN), fuzzy logic, image fusion, etc. have significantly contributed to the development of the semi-automatic processing of medical thermography images [37, 112, 125]. Bandyopadhyay et al. [112] used histogram and Hough transform-based image processing algorithm for screening and monitoring of diabetic status from acquired infrared images of the subjects. Content-based automatic target localization and pattern matching has also been implemented in a few studies [126, 127]. Liu et al. [128] used asymmetric analyses for automatic detection of diabetic foot complications. They developed a robust algorithm for avoiding foot segmentation error using color images and used non-rigid landmark-based registration along with B-splines to circumvent contralateral differences arising out of shape or amputation. Hernandez-Contreras et al. [129] used 3D morphological pattern spectrum for automatic classification of thermal patterns in diabetic foot. Standardization of image capture by means of software masks have been reported by Ring [74]. These masks were designed for infrared imaging of subjects with diabetic neuropathy and vascular disorder where the masks fit the dorsal and plantar surfaces of the feet and hands along with other body parts. Recently, the concept of angiosome, which is defined as the "composite unit of skin and underlying deep tissue supplied by a source artery" [130], has emerged in thermographic monitoring of diabetic foot. Attinger et al. [131] have proposed four angiosomes in the plantar surface of foot, viz., the medial plantar artery angiosome, lateral plantar artery angiosome, medial calcaneal artery angiosome, and the lateral calcaneal artery angiosome. The concept of angiosome along with the aid of software mask will be immensely helpful for accurate monitoring and reliable measurement of temperature patterns in diabetic foot. Plassmann, Ring and Murawski [132, 133] have developed a modern PC-based software called CTHERM which is capable to acquire, store, and manipulate infrared images from both modern and older generation cameras. Modern software packages like Matlab, Labview, Altair, Thermacam-Researcher, etc. have multitude of options for image acquisition and image processing to suit the requirements of medical thermography researchers. The need for a digital database for medical thermography images was felt long ago and substantial work has been done in this direction [134–137]. Colantonio et al. [138] integrated infrared thermography data with 3D shapes to present a 3D image of diabetic foot. Netten et al. [110] have developed and implemented an automatic algorithm for differentiating between local and diffuse diabetic foot complications which was based on parameters captured by an infrared camera and was also capable of detecting absence of diabetic foot complications in healthy subjects. Nevertheless as of now, there is no dedicated database of medical thermography images for diabetic neuropathy and vascular disorder.

4 Infrared Thermography for Detection of Diabetic Neuropathy and Vascular Disorder

The term "diabetic foot" indicates physiological and clinical condition of lower extremities of human subject resulting from diabetes or its long-term complications [139]. The major issues of diabetic foot can be categorized into four types of complications, viz., peripheral neuropathy, peripheral arterial disease or vascular disorder, secondary infection, and soft tissue or bone deformity [140]. Mayfield et al. [141] discussed in detail the various complications of diabetes and preventive foot care methodologies.

Peripheral neuropathy in the lower extremity is one of the most common complications in diabetes subjects and approximately 60% diabetic subjects suffer from peripheral neuropathy [10, 68, 140, 142–144]. It has also been reported to be the most significant cause of pain in diabetic foot with burning or tingling sensation in the foot, which is often accompanied with radiating pain in the plantar regions [140]. In general, it has been observed that the severity of peripheral neuropathy increases with subject's age or duration of diabetes. Diabetic neuropathy affects large and small fibers affecting temperature discrimination and sensory functions [69, 70, 88, 103]. Sympathetic dysfunction in lower limbs often results in reduced sweating and dry skin leading to cracks, fissures, and thermoregulatory sweating abnormalities [103, 145, 146]. Cyclic and repetitive pressure, shear force during weight-bearing exercise or walking, etc. leads to an increased plantar pressure on diabetic foot leading to callus formation and skin breakdown [140]. Diabetic foot motor neuropathy is often associated with the imbalance of flexor and extensor muscles, which results in foot deformation along with prominent metatarsal heads, dry skin, and clawing of claws [140]. If left untreated, foot deformity may progress to joint deformity requiring conservative off loading or surgical intervention [140]. Charcot's neuropathy is a limb threatening advanced stage of joint neuropathy which involves small fiber neuropathy and the two major mechanistic processes involved in the pathogenesis are neurovascular theory and neurotraumatic theory which may ultimately lead to dislocation, disorganization, and changes in bone density [71, 140]. Sympathetic skin response is in general mediated through post-junctional unmyelinated small fibers via pseudo-motor pathways, which is anatomically distinct from vasomotor pathway, whereas skin temperature is regulated by vasomotor as well as pseudo-motor pathways [103, 147]. The elevated skin temperature in neuropathic foot is due to arteriovenous shunt flow [103, 148, 149]. Although the peripheral neuropathy affects somatic and sympathetic neural components in diabetic subjects, clinical and nerve conduction studies investigate only the somatic functions of large myelinated fiber [103, 150]. It has been reported that diabetic neuropathy can be identified in the early stage through detection of damage to unmyelinated small fibers [151] which is associated with change in skin temperature [103]. Studies show that infrared thermography can be reliably applied for early diagnosis of diabetic neuropathy and feet with elevated skin temperature in

diabetic subject is considered as an indication of early diabetic neuropathy [68, 69, 71, 103, 140, 145, 149]. Harding et al. [152] used infrared thermography for early detection of foot ulceration in diabetic neuropathic foot and observed that compared to radiation or isotope-based methods, infrared thermography is beneficial due to radiation protection, logistic, and cost reasons. Bharara et al. [69] reported that in early stages of diabetic neuropathy the skin temperature appears elevated, whereas in later stages the affected areas present lower skin temperature distribution due to significant vascular damage.

Branemark et al. [101] applied infrared thermography to study 16 (12 females and 4 males) diabetic subjects with an average history of 13 years and found that all of them presented abnormal temperature distribution in the feet and hands, like reduced temperature over the toes, fingers, and metatarsal regions. This is one of the first thermography-based studies on diabetic subjects and their studies indicated no variation in the temperature pattern over the dorsal aspect of the foot and tibia in the subjects. Bharara et al. [69] presented an excellent review on diabetes-induced complication in foot and the role of infrared thermography in diagnosis of diabetic foot. Sun et al. [103] used infrared thermography for studying the relationship between plantar skin temperature and sympathetic dysfunction in diabetic-at-risk foot in 29 diabetic subjects and compared the findings with temperature pattern of 25 control subjects. Their studies indicated that diabetes-at-risk subjects have significantly higher mean foot temperature (30.2 $\pm$ 1.3 °C) compared to the normal subjects (26.8 $\pm$ 1.8 °C). Mean foot temperature was obtained by averaging of the foot temperature over six regions, viz., hallux, lesser toes, forefoot, arch, lateral sole, and heel. Armstrong et al. [71] carried out comparative studies on the skin temperature of subjects affected with asymptomatic peripheral neuropathy (78 subjects), neuropathic ulcers (44 subjects), and Charcot's anthropathy (21 subjects) where contralateral limb was used as control. Their studies revealed significant contralateral temperature difference in the cases of neuropathic ulcers (5.6 °F) and Charcot's anthropathy (8.3 °F) whereas, no such temperature difference was observed in the cases of asymptomatic peripheral neuropathy. Vinik et al. [153] reported large temperature variation in extremities of diabetic subjects which was found to depend on several factors like environmental temperature and activity of the neurovegetative sympathetic nervous system. Papanas et al. [154] and Vinik et al. [155] studied the association of pseudo-motor dysfunction with foot temperature and dermal neurovascular dysfunction in diabetic subjects, respectively. Sivanandam et al. [156] studied 62 diabetic subjects using infrared thermography along with other clinical examinations and reported that infrared thermography was very successful in examining the extremities of the subjects and early diagnosis of foot ulceration was possible. This study also indicates a better sensitivity, accuracy, and specificity of infrared thermography-based diagnosis compared to conventional HBA1c-based measurements. Chan et al. [157] reported that diabetic subjects with painful peripheral neuropathy have higher forefoot temperature compared to normal subjects. Benbow et al. [73] and Stess et al. [158] reported that higher foot temperature in diabetic subjects was indicative of foot ulceration and temperature measurement aids in early diagnosis. Roback et al. [93] studied the feasibility of

thermography technique for early detection of foot complications in diabetic subjects. Fujiwara et al. [159] also used thermography for skin temperature measurement in diabetic subjects. Nishide et al. [160] applied thermography and ultrasonography for studying latent inflammation in diabetic foot callus. Recently, Kanazawa et al. [161] used a smartphone attached infrared thermography system (FLIR one) for assessment of pressure ulcer induced inflammation and diabetic foot monitoring and their results suggest that such ultra-lightweight alternative thermography systems can be reliably used for diabetic foot monitoring. Hazenberg et al. [162] combined digital photography and infrared thermography for assessment of foot infection in diabetic subjects and obtained high specificity (>79%) and high sensitivity (>60%) from the combined technique which was not possible to achieve with an individual technique alone. A typical case study [68] carried out in author's laboratory is described below. The infrared images were acquired using AGEMA Thermovision 550 infrared camera which is equipped with a focal plane array of platinum silicide (PtSi) detector elements cooled using an internal Stirling cycle. The spectral range was 3.6–5 μm and thermal sensitivity of the camera was better than 0.1 °C. Experiments were performed under controlled environment with an ambient temperature of 25 °C and 5 min of thermal acclimatization time during which the subjects were requested to remove their foot wears and socks and lie supine on a couch.

Randomly chosen 112 subjects suffering from type 2 diabetes were studied using infrared thermography. Anthropometric measurements like weight, height, waist, and hip sizes were carried out along with clinical measurements of vibratory perception threshold (VPT) using biothesiometry and pathological measurement of glycated hemoglobin (HBA1c). Mean foot temperature (MFT) was obtained from the infrared images of the plantar surface of the subjects by averaging the temperature over various locations, viz., hallux, lesser toes, arch, lateral sole ,and forefoot regions. It was also observed that neuropathic subjects (VPT > 20) have higher MFT compared to non-neuropathic subjects and the MFT showed a positive correlation with right and left great toes VPT values [68]. Figure 3 shows the variation of MFT values as a function of VPT values and it can be seen that 28 subjects with VPT values less than 20 (non-neuropathic) showed MFT values within the temperature range of 27–30 °C. On the other hand, 33 subjects were found with VPT values higher than 20 (neuropathic) and MFT values varying between 30 and 37 °C. Figure 4a, b shows the infrared images of the lower extremities of a 44-year-old neuropathic male diabetic (HbA1c value = 9.6%) and a 67-year-old non-neuropathic female diabetic (HbA1c value = 6.6%) subjects, respectively. The mean foot temperatures over the encircled regions were found to be 34.1 and 29.1 °C, respectively. It can be clearly seen that neuropathic subjects were associated with a higher mean foot temperature. The elevated skin temperature in neuropathic foot is attributed to arteriovenous shunt flow [103, 148, 149].

Diabetes often leads to peripheral arterial diseases (PAD) or vascular disorder which mainly affects the small and large blood vessels in the extremities, more commonly in the lower arteries resulting in varicose veins with inadequate

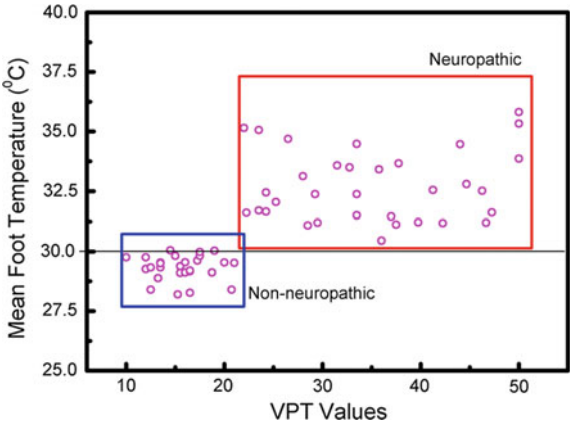

Fig. 3 Mean foot temperature (MFT) of diabetic subjects as a function of their vibratory perception threshold (VPT) values [68]. For non-neuropathic subjects (indicated by the *blue rectangle*) with VPT values less than 20, MFT values were distributed within 27–30 °C, whereas for neuropathic subjects (indicated by the *red rectangle*) with VPT values greater than 20, MFT values were within a range of 30–37 °C

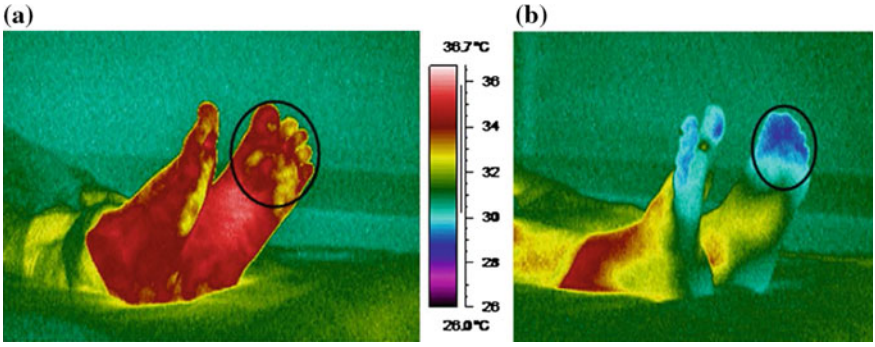

Fig. 4 Typical pseudo-color-coded infrared images of the plantar regions for two diabetic subjects [68]. **a** A 44-year-old neuropathic male subject and **b** A 67-year-old non-neuropathic female subject. The average temperature over the encircled regions were found to be 34.1 and 29.1 °C, for the neuropathic and non-neuropathic subjects, respectively

drainage. The major arteries that deliver blood to the lower extremities are posterior tibial, anterior tibial, and peroneal arteries and with progressing diabetes-induced vascular disorder these arteries may be affected [140]. It has been reported that progressing PAD primarily affect anterior tibial and peroneal arteries, whereas dorsalis pedis, posterior tibial, and plantar arteries are less affected resulting in normal pulsating responses in these arteries [76, 140]. Further complications of vascular disorder result in micro-arterial dysfunction, limited capillary capacity, increased arteriovenous shunting, and decreased neurogenic regulation, mild to

severe pain due to lack of oxygen and nutrient. Varicose veins are often associated with mild inflammation which can be detected using infrared thermography from the abnormally higher skin temperature over the affected regions [76]. Moreover, toe temperature at the distal positions appears to be lower in diabetic subjects suffering from vascular disorder due to inadequate drainage [76, 77] which can be reliably detected using infrared thermography. Historically, infrared thermography had been used for studying peripheral vascular disorder from mid-sixties. Probably, the first two studies on the application of infrared thermography in peripheral vascular disorder was reported by Skversky et al. [163] and Winsor and Bendezu [164] in 1964. In 1970, Robins and Bernstein [165] applied digital plethysmography and infrared thermography on subjects with peripheral vascular diseases and compared the efficacy of both the techniques. Application of infrared thermography for vascular disorder was also studied by Langer et al. [166] in 1972. Soulen et al. [167] compared angiography, ultrasonography, and thermography in the evaluation of peripheral vascular diseases in 166 subjects with suspected thrombophlebitis and 300 other subjects with peripheral arterial diseases and found that thermography aided in recognition of phlebitis and in assessment of post-operative vascular disorder. Holm et al. [168] reported the use of thermography in vascular surgery based on results obtained from 12 case studies. Henderson and Hackett [169] described thermography as a reliable, noninvasive and rapid methodology for investigating subjects with peripheral vascular disorders. Hosaki et al. [75] applied infrared thermography to quantitatively study peripheral vascular circulation in 27 diabetic subjects in which 14 were males and the rest were females. They observed temperature gradients, indicating abnormal blood flow in the affected regions which were found to be correlated with other clinical findings. This study also indicated that recovery ratio calculated from the infrared images were correlated with blood flow measured using laser Doppler flowmetry and it was suggested that infrared thermography can be used as a potential tool for early detection of arteriosclerosis obliterans (ASO) in diabetic subjects. Hitoi and Matsuoka [170] stressed the usefulness of infrared thermography-based monitoring of peripheral circulation in diabetic subjects. Balbinot et al. [108] applied IRT to diabetic subjects and found that rewarming index after cold stress presented good repeatability. The study also revealed that temperature difference (ΔT) measured using infrared thermography was clinically more relevant. Fushimi et al. [171] studied the abnormal vaso-reaction of peripheral arteries to cold stimulation in both hands of diabetic subjects. Huang et al. [105] applied infrared thermography for evaluating subjects with higher risk of lower extremity peripheral arterial disease (PAD) and observed that temperature changes in the soles of PAD versus non-PAD subjects were −1.25 versus −0.15 ($p < 0.001$). Mitchell et al. [172] applied thermography for studying skin blood flow and limited joint mobility in 32 insulin-dependent subject and 13 healthy control subjects at room temperature and after immersing in warm and cold water. They reported a predominantly distal rewarming pattern after withdrawal of cold stress with higher mean index finger temperature in the insulin-dependent subjects compared to the controls which was experimentally confirmed using

thermography. Toutouzas et al. [173] used an infrared thermography-based procedure for evaluating subjects with diabetes mellitus and coronary artery disease and reported that such subjects suffer from higher carotid inflammation. Uchikawa et al. [174] studied the effects of cilostazol (anti-platelet agent) on peripheral vascular disorder in diabetic subjects and reported that infrared thermography is beneficial in planning individual dose and monitor the effects of cilostazol and subject compliance during long-term drug administration. The effect of cilostazol in peripheral arterial occlusion was also studied by Ohashi et al. [175] using thermography techniques. Staffa et al. [176] applied infrared thermography for long-term monitoring of foot temperature in diabetic subjects. Three case studies, carried out by Bagavathiappan et al. [76, 77], on application on infrared thermography in detection of peripheral vascular disorder are described below. AGEMA Thermovision 550 infrared camera was used for acquiring the infrared images. Experiments were performed under controlled environment after 15 min of thermal acclimatization time.

Case: 1

First is a 48-year-old male subject reported recurring pain in the left calf muscle for past two years with the severity of pain continuously increasing over the last half a year. The pain was found to increase on walking or prolonged standing and presented symptoms of relief on comfortable seating posture. Clinical examinations revealed normal pulses in the left and right upper and lower limbs, normal dorsalis pedis and posterior tibial pulse in the right lower limb, and low volume of dorsalis pedis and posterior tibial pulse in the left lower limb. A non-healing ulcerous 8-month-old injury in the left great toe was observed with the presence of gangrenous tissue. The subject was occasional user of alcohol and nicotine. The respiratory system (RS), cardiovascular system (CS), central nervous system (CNS), and abdominal examinations were also found to be normal for this subject. Thermal imaging was carried out on the left leg of the subject.

Figure 5a shows the pseudo-color-coded infrared image of the medial view of the left leg of the subject along with the temperature scale. Figure 5b shows a horizontal line scan (as indicated in Fig. 5a) along the calf muscle which indicates a region of higher temperature at the middle portion which is also visually discernible from the thermal image [76, 77]. Such abnormal higher temperature regions were not present in healthy subjects used as control. This region of higher temperature was attributed to the presence of thrombosis which is an arterial obstruction to blood flow causing blood clotting within blood vessels. Such thrombosis may turn potentially life threatening if the dislodgement of the thrombus results in pulmonary embolism. This region of higher temperature was found to be associated with mild to severe inflammation and was coincident with the region of pain. Infrared thermography enabled noncontact detection of the region of pain and associated thrombosis. It was concluded that this may be due to thromboangiitis obliterans (or Buerger's disease) due to arterial insufficiency.

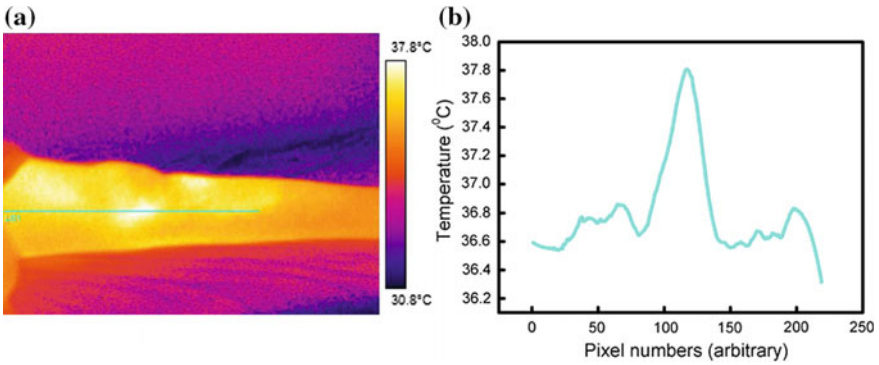

Fig. 5 **a** Pseudo-color-coded infrared image of the dorsal profile of the left leg of a 48-year-old male subject suffering from vascular disorder [77]. **b** Temperature profile along the horizontal line shown in the infrared image which indicated the presence of a higher temperature region that was attributed to the presence of thrombosis

Case: 2

A 31-year-old male subject with a long history (approximately five years) of swelling in both lower limbs on prolonged standing reported recurrent ulceration on the left lateral malleolus associated with pain and discharge of pus even after undergoing treatment and surgery (four years earlier). The RS, CVS, CNS, abdominal examination, and palpable arterial pulse were found to be normal for the subject. The subject was suffering from systematic hypertension and was under medication for the same for 6 months. Clinical examinations of the left lower limb revealed tortuous dilated veins and recurrent healing ulcers on the left lateral malleolus which were covered with slough and pus discharge. Thermal imaging was carried out on the left leg of the subject.

Figure 6 shows the pseudo-color-coded thermal image of the dorsal view of the left leg of the subject. It can be seen from the infrared image that clinically detected areas with varicosity presented an elevated temperature distribution (encircled by the black-dotted line) which was attributed to the varicosity-induced mild inflammation and slow passage of warm blood through the tortuous veins compared to normal veins. It was observed that the higher temperature regions (containing varicose veins) were presented in the lateral side of the left leg and not in the medial side of the leg (most commonly observed locations of varicose veins). It can be further seen from the infrared image that distal regions in the vicinity of the toes were at a significantly lower temperature (indicated by the white arrow) which was due to vascular disorder resulting in poor perfusion of blood [76, 77].

Case: 3

A 28-year-old male subject was suffering from a pain in the left lower limb which increased on prolonged standing. RS, CVS, CNS, abdominal examination, radial pulse, carotid pulse, dorsalis pedis, and posterior tibial pulse were found to be

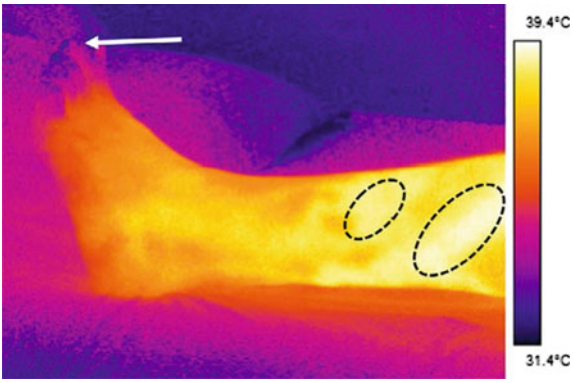

Fig. 6 Typical infrared image of the dorsal profile of the left leg of a 31-year-old male subject suffering from vascular disorder [76, 77]. Clinically diagnosed areas of varicosity were found to coincide with the regions of higher temperature (encircled by the *black-dotted lines*). The distal region was found to be at a lower temperature (indicated by the *white arrow*) due to inadequate blood flow

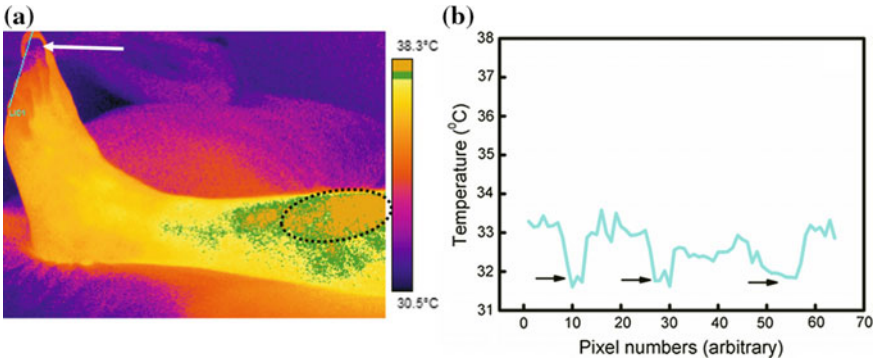

Fig. 7 **a** Typical infrared image of the left leg of a 28-year-old male subject suffering from vascular disorder. The image is shown in pseudo-color-coded isotherm scale and the region of higher temperature (encircled by the *black-dotted line*) corresponded to the mild inflammation of the varicose veins. The distal regions (indicated by a *white arrow*) presented a lower temperature due to inadequate blood perfusion. **b** Temperature profile along the line indicated in the infrared image. The periodic lower temperature confirmed slow blood perfusion in the distal regions (toes)

normal for the subject. Clinical examinations revealed varicosity of the long saphenous system of the left lower limb and the varicosity-related complications were predominant for the past one year. Thermal imaging was carried out over the left leg of the subject.

Figure 7a shows the pseudo-color-coded infrared image of the left leg of the subject. The line profile over the toe tips is shown in Fig. 7b. It can be clearly seen that distal position (indicated by the white arrow in the thermal image) had a

comparatively lower temperature, which was attributed to varicosity-induced inadequate venous drainage. Higher temperature regions (encircled by the black-dotted line) were observed over the left leg of the subject, which were found to be coincident with the varicosity-affected regions. It was observed that the temperature was 0.7–1.0 °C higher in these regions compared to the surrounding skin temperature. The affected regions presented an elevated temperature distribution due to varicosity-induced mild inflammation which was otherwise not detected during routine clinical examination.

Foot damages resulting from diabetic neuropathy, vascular disorder, or ischemia very often causes infection, which ultimately results in foot ulceration. Infection can be active (bacterial or fungal) or passive (biofilms). Most common species causing infection in diabetic foot are aerobic gram-positive cocci (*Staphylococcus aureus*), gram-negative bacilli (*Escherichia coli*), and anaerobic *Bacteroides* sp. and *Peptostreptococcus* sp. [140, 177]. Infrared thermography is successfully used for monitoring wound healing in the cases of foot ulcerations [178]. Apart from peripheral neuropathy and vascular disorder, infrared thermography has also been applied to diabetic retinopathy. Sodi et al. [179] performed a comparative study of the ocular surface temperature (OST) in 51 subjects with nonproliferative diabetic retinopathy (NPDR) and in 53 age and gender matched healthy subjects. They found that in diabetic subjects OST was significantly lower than the normal subjects. Although majority of the infrared thermography-based studies were conducted on subjects with type 2 diabetes, a few recent studies [180, 181] report the applicability of infrared thermography on type 1 diabetic subjects. Sejling et al. [180, 182] studied the changes in skin temperature during hypoglycemia in type 1 diabetic subjects and reported that skin temperature decreased during hypoglycemia over the nose and glabella regions. They indicated the suitability of infrared thermography to study the hypoglycemia-induced decrease in skin temperature which was observed to be higher in subjects with hypoglycemia awareness. Zotter et al. [181] applied infrared thermography to assess the abnormalities in skin blood flow before and after cold challenge on lower leg of 25 adolescent asymptomatic subjects with type 1 diabetes. Their studies revealed that adolescent type 1 diabetic subjects show abnormalities in skin blood flow over the tips of first and fifth toes and inner ankles after cold challenge which was successfully mapped using infrared thermography. Schindl et al. [183, 184] applied infrared thermography for monitoring low-intensity laser-induced improvement in peripheral circulation in subjects with diabetic microangiopathy.

The above case studies and literature survey clearly indicate that diabetic foot complications are associated with significant changes in skin temperature with definite patterns (e.g., lower temperature distribution in the distal position of the toes in the cases of vascular disorders and elevated foot temperature for the diabetic neuropathic subjects), which facilitates early diagnosis of diabetic complications using infrared thermography-based skin temperature monitoring. Therefore, periodic monitoring of skin temperature reduces the risk of foot ulceration [185]. Further, identifying individuals at high risk and treating for lower extremity

complications may reduce the number of amputations by 85% [186]. Pafili and Papanas [187] suggested that a 5-year use of infrared thermography or liquid crystal thermography for daily self-examination among high-risk group of subjects may significantly lower further complications in diabetic foot.

5 Conclusions

Among various techniques available for accurate and reliable measurement of subject temperature, infrared thermography is a relatively new methodology that has become popular because of its noncontact, noninvasive, and real-time temperature measurement capability. During the last few decades, numerous applications of infrared thermography are reported in the field of medical sciences. Considering the huge increase in diabetics cases worldwide, a dedicated effort for early detection of diabetes is essential. Studies reveal that infrared thermography is capable of the early detection of diabetic peripheral neuropathy and vascular disorders. This book chapter highlights the studies on diabetic neuropathy and vascular disorder using infrared thermography technique. The basics of infrared thermography, classification of medical thermography techniques, details of various infrared cameras available, ideal experimental conditions, data analysis, etc. along with typical case studies on the above two subjects are discussed. To become IRT as routine techniques for diagnosis of diabetic neuropathy and vascular disorder, more systematic case studies in large number of subjects from various continents and correlating the IRT results with clinical findings are a prerequisite. Further, refinements in the experimental protocols, automation, rapid, and reliable data analysis approaches are to be developed. One of the impeding issues in the use of this technique in the past was the higher cost of infrared camera but it has now surmounted because of the availability of infrared cameras at affordable rates.

Acknowledgements The authors wish to thank Dr. A.K. Bhaduri, Director, Metallurgy and Materials Group, IGCAR for his support and encouragement.

References

1. Houdas, Y., Ring, E.F.J.: Human Body Temperature. Plenum, New York (1982)
2. Ring, E.F.J.: The historical development of temperature measurement in medicine. Infrared Phys. Technol. **49**, 297–301 (2007)
3. Tan, J.H., Ng, E.Y.K., Acharya, U.R., Chee, C.: Study of normal ocular thermogram using textural parameters Infrared Phys. Technol. **53**, 120–126 (2010)
4. Wunderlich, C., Woodman, W.: On the Temperature in Diseases, A Manual of Medical Thermometry, vol. 71 The New Sydenham Society, London, England (1871)
5. Maldague, X.: Theory and Practice of Infrared Technology for Nondestructive Testing, 1st edn. Wiley, New York (2001)

6. Meola, C.: Infrared Thermography: Recent Advances and Future Trends. Bentham eBooks (2012)
7. Bagavathiappan, S., Lahiri, B.B., Saravanan, T., Philip, J., Jayakumar, T.: Infrared thermography for condition monitoring—A review. Infrared Phys. Technol. **60**, 35–55 (2013)
8. Lahiri, B.B., Bagavathiappan, S., Soumya, C., Mahendran, V., Pillai, V.P.M., Philip, J., Jayakumar, T.: Infrared thermography based defect detection in ferromagnetic specimens using a low frequency alternating magnetic field. Infrared Phys. Technol. **64**, 125–133 (2014)
9. Lahiri, B.B., Haneef, T.K., Bagavathiappan, S., Kulasegaran, N., Mukhopadhyay, C.K., Jayakumar, T., Philip, J.: Infrared thermography-based studies on hydrotesting of stainless steel pressure vessels. Insight **57**, 406–413 (2015)
10. Lahiri, B.B., Bagavathiappan, S., Jayakumar, T., Philip, J.: Medical applications of infrared thermography: a review. Infrared Phys. Technol. **55**, 221–235 (2012)
11. Jones, B., Plassmann, P.: Digital infrared thermal imaging of human skin. IEEE Eng. Med. Biol. Mag. **21**, 41–48 (2002)
12. Jones, B.F.: A reappraisal of the use of infrared thermal image analysis in medicine. IEEE Trans. Med. Imaging **17**, 1019–1027 (1998)
13. Ammer, K., Ring, E.F.J.: The Thermal Image in Medicine and Biology. Uhlen-Verlag, Vienna (1995)
14. Lahiri, B.B., Bagavathiappan, S., Nishanthi, K., Mohanalakshmi, K., Veni, L., Yacin, S.M., Philip, J.: Infrared thermography based studies on the effect of age on localized cold stress induced thermoregulation in human. Infrared Phys. Technol. **76**, 592–602 (2016)
15. Lahiri, B.B., Bagavathiappan, S., Soumya, C., Jayakumar, T., Philip, J.: Infrared thermography based studies on mobile phone induced heating. Infrared Phys. Technol. **71**, 242–251 (2015)
16. Lahiri, B.B., Divya, M.P., Bagavathiappan, S., Thomas, S., Philip, J.: Detection of pathogenic gram negative bacteria using infrared thermography. Infrared Phys. Technol. **55**, 485–490 (2012)
17. Ring, E.F.J., Ammer, K.: Infrared thermal imaging in medicine. Physiol. Meas. **33**, R33–R46 (2012)
18. Jung, A., Zuber, J., Ring, F.: A Case Book of Infrared Imaging in Clinical Medicine. MedPress, Warszawa (2003)
19. Yang, W.J., Yang, P.P.: Literature survey on biomedical applications of thermography. Biomed. Mater. Eng. **2**, 7–18 (1992)
20. Fauci, M.A., Breiter, R., Cabanski, W., Fick, W., Koch, R., Ziegler, J., Gunapala, S.D.: Medical infrared imaging-differentiating facts from friction, and the impact of high precision quantum well infrared photodetector camera systems, and other factors, in its reemergence. Infrared Phys. Technol. **42**, 334–344 (2001)
21. Jiang, L.J., Ng, E.Y., Yeo, A.C., Wu, S., Pan, F., Yau, W.Y., Chen, J.H., Yang, Y.: A perspective on medical infrared imaging. J. Med. Eng. Technol. **29**, 257–267 (2005)
22. Ring, E.F.J., Jung, A., Zuber, J.: New opportunities for infrared thermography in medicine. Acta Bio-Opt. Inf. Med. **15**, 28–30 (2009)
23. Faust, O., Acharya, U.R., Ng, E.Y.K., Hong, T.J., Yu, W.: Application of infrared thermography in computer aided diagnosis. Infrared Phys. Technol. **66**, 160–175 (2014)
24. Bitar, D., Goubar, A., Desenclos, J.C.: International travels and fever screening during epidemics: a literature review on the effectiveness and potential use of non-contact infrared thermometers. Eurosurveillance **14**, 1–5 (2009)
25. Mercer, J.B., Ring, E.F.J.: Fever Screening and infrared thermal imaging: concerns and guidelines. Thermol. Int. **19**, 67–69 (2009)
26. Ng, E., Kaw, G.: IR images and fever monitoring devices: physics, physiology, and clinical accuracy. In: Medical Devices and Systems, Biomedical Engineering Handbook. CRC Press, Boca Ranton (FL) (2006)

27. Ng, E.Y.K.: Is thermal scanner losing its bite in mass screening of fever due to SARS? Med. Phys. **32**, 93–97 (2005)
28. Ng, E.Y.K., Kaw, G., Chang, W.M.: Analysis of IR thermal imager for mass blind fever screening. Microvasc. Res. **68**, 104–109 (2004)
29. Ring, E.F.J., Jung, A., Zuber, J., Rutowski, P., Kalicki, B., Bajwa, U.: Detecting fever in Polish children by infrared thermography. In: 9th International Conference on Quantitative Infrared Thermography, Krakow, Poland (2008)
30. Ring, F.: Pandemic: thermography for fever screening of airport passengers. Thermol. Int. **17**, 67 (2007)
31. Ring, F., Mercer, J.: Thermal imaging for fever screening, pp. 33–35, ISO Focus, February (2007)
32. Amalu, W.C., Hobbins, W.B., Head, J.F., Elliot, R.L.L: Infrared imaging of the breast—an overview. In: Bronzino, J.D. (ed.) Biomedical Engineering Handbook, Medical Devices and Systems, 3rd edn, pp. 20. CRC Press (2006)
33. Louis, J.W.K., Gautherie, M.: Long term assessment of breast cancer risk by thermal imaging. Biomed. Thermol., 279–301 (1982)
34. Kennedy, D., Lee, T., Seely, D.: A comparative review of thermography as a breast screening technique. Integr. Cancer. Ther. **8**, 9–16 (2009)
35. Ng, E.Y.K.: A review of thermography as promising non-invasive detection modality for breast tumor. Int. J. Therm. Sci. **48**, 849–859 (2009)
36. Ng, E.Y.K., Kee, E.C.: Advanced integrated technique in breast cancer thermography. J. Med. Eng. Technol. **32**, 103–114 (2008)
37. Tan, T.Z., Quek, C., Ng, G.S., Ng, E.Y.K.: A novel cognitive interpretation of breast cancer thermography with complementary learning fuzzy neural memory structure. Expert Syst. Appl. **33**, 652–666 (2007)
38. Shevelev, I.A.: Functional imaging of the brain by infrared radiation (thermoencephaloscopy). Prog. Neurobiol. **56**, 269–305 (1998)
39. Fikackova, H., Ekberg, E.: Can infrared thermography be a diagnostic tool for arthralgia of the temporomandibular joint? Oral Surg. Oral Med. Oral Pathol. Oral Radiol. Endod. **98**, 643–650 (2004)
40. Carlo, A.D.: Thermography and the possibilities for its applications in clinical and experimental dermatology. Clin. Dermatol. **13**, 329–336 (1995)
41. Anbar, M., Gratt, B., Hong, D.: Thermology and facial telethermography. Part I: History and technical review. Dentomaxillofac. Radiol. **27**, 61–67 (1998)
42. Gratt, B., Anbar, M.: Thermology and facial telethermography: Part II. Current and future clinical applications in dentistry. Dentomaxillofac. Radiol. **27**, 68–74 (1998)
43. Park, J., Hyun, J.K., Seo, J.: The effectiveness of digital infrared thermographic imaging in patients with shoulder impingement syndrome. J. Shoulder Elbow Surg. **16**, 548–554 (2007)
44. Zelichowska, B., Rozycki, R., Tlustochowicz, M., Kujawa, A., Kalicki, B., Murawski, P.: The usefulness of the thermography in the dry eye syndrome. Klin. Oczna **107**, 483–487 (2005)
45. Tan, J.H., Ng, E.Y.K., Acharya, U.R., Chee, C.: Infrared thermography on ocular surface temperature: a review. Infrared Phys. Technol. **52**, 97–108 (2009)
46. Cosh, J.A., Ring, E.F.J.: Thermography and rheumatology. Rheumatology **10**, 342–348 (1970)
47. Jacobsson, H., Vesterskold, L.: The thermographic pattern of the lower back with special reference to the sacro-iliac joints in health and inflammation. Clin. Rheumatol. **4**, 426–432 (1985)
48. Vecchio, P.C., Adebajo, A.O., Chard, M.D., Thomas, P.P., Hazleman, B.L.: Thermography of frozen shoulder and rotator cuff tendinitis. Clin. Rheumatol. **11**, 382–384 (1992)
49. Will, R.K., Ring, E.F.J., Clarke, A.K., Maddison, P.I.: Infrared thermography, what is its place in rheumatology in the 1990s. Br. J. Rheumatol. **31**, 337–344 (1992)

50. Antonio-Rubio, I., Madrid-Navarro, C.J., Salazar-Lopez, E., Perez-Navarro, M.J., Saez-Zea, C., Gomez-Milan, E., Mínguez-Castellanos, A., Escamilla-Sevilla, F.: Abnormal thermography in Parkinson's disease. Parkinsonism Rel. Disord. **21**, 852–857 (2015)
51. Costello, J.T., McInerney, C.D., Bleakley, C.M., Selfe, J., Donnelly, A.E.: The use of thermal imaging in assessing skin temperature following cryotherapy: a review. J. Therm. Biol **37**, 103–110 (2012)
52. Bouzida, N., Bendada, A., Maldague, X.P.: Visualization of body thermoregulation by infrared imaging. J. Therm. Biol **34**, 120–126 (2009)
53. Tanda, G.: Skin temperature measurements by infrared thermography during running exercise. Exp. Therm. Fluid Sci. **71**, 103–113 (2016)
54. Milonov, O.B., Lebedeva, O.D., Pomelova, L.A.: The use of echography and thermography in patients with parasitic liver diseases. Sovet. Med. **4**, 62–67 (1980)
55. Mansfield, C.M., Farrell, C., Asbell, S.O.: The use of Thermography in the detection of metastatic liver disease. Radiology **95**, 696–698 (1970)
56. Brooks, J.P., Perry, W.B., Putnam, A.T., Karulf, R.E.: Thermal imaging in the detection of bowel ischemia. Dis. Colon Rectum **43**, 1319–1321 (2000)
57. Fiz, J.A., Lozano, M., Monte-Morenoc, E., Gonzalez-Martinez, A., Faundez-Zanuy, M., Becker, C., Pons-Rodriguez, L., Manzanoa, J.R.: Tuberculine reaction measured by infrared thermography. Comput. Methods Programs Biomed. **122**, 199–206 (2015)
58. Kopsa, H., Czech, W., Schmidt, P., Zazgornik, J., Pils, P., Balcke, P.: Diagnostic relevance of contact thermography in renal transplantation (author's translation). Med. Klin. **74**, 1067–1070 (1979)
59. Kopsa, H., Czech, W., Schmidt, P., Zazgornik, J., Pils, P., Balcke, P.: Use of thermography in kidney transplantation: two year follow up study in 75 cases. Proc. Eur Dial Transplant Assoc. **16**, 383–387 (1979)
60. Loriaux, C.: Role of thermography in gynecology. J. Radiol. Electrol. Med. Nucl., 56 (suppl.), 57–58 (1975)
61. Birnbaum, S.J., Kliot, D.: Thermography-obstetrical applications. Ann. N. Y. Acad. Sci. **121**, 209–222 (1964)
62. Topalidou, A., Downe, S.: Investigation of the use of thermography for research and clinical applications in pregnant women. Infrared Phys. Technol. **75**, 59–64 (2016)
63. Ernst, M., Lee, M.H.M.: Sympathetic vasomotor changes induced by manual and electrical acupuncture of the hoku point visualized by thermography. Pain **21**, 25–33 (1985)
64. Cattaneo, C., Giancamillo, A.D., Campari, O., Martrille, L., Jouineau, C.: Infrared tympanic thermography as a substitute for a probe in the evaluation of ear temperature for post-mortem interval determination: a pilot study. J. Forensic Leg. Med. **16**, 215–217 (2009)
65. Al-Alousi, L.M., Anderson, R.A., Worster, D.M., Land, D.D.: Multiple-probe thermography for estimating the postmortem interval: I. Continuous monitoring and data analysis of brain, liver, rectal and environmental temperatures in 117 forensic cases. J. Forensic. Sci. **46,** 317–322 (2001)
66. Manginas, A., Andreanides, E., Leontiadis, E., Sfyrakis, P., Maounis, T., Degiannis, D., Alivizatos, P., Cokkinos, D.: Right Ventricular endocardial thermography in transplanted and coronary artery disease patients: first human application. J. Invasive Cardiol. **22**, 400–404 (2010)
67. Salaimeh, A.A., Campion, J.J., Gharaibeh, B.Y., Evans, M.E., Saito, K.: Real-time quantification of viable bacteria in liquid medium using infrared thermography. Infrared Phys. Technol. **54**, 517–524 (2011)
68. Bagavathiappan, S., Philip, J., Jayakumar, T., Raj, B., Rao, P.N.S., Varalakshmi, M., Mohan, V.: Correlation between plantar foot temperature and diabetic neuropathy by using an infrared thermal imaging technique. J. Diab. Sci. Technol. **4**, 1386–1392 (2010)
69. Bharara, M., Cobb, J.E., Claremont, D.J.: Thermography and thermometry in the assessment of diabetic neuropathic foot: a case for furthering the role of thermal techniques. Int. J. Low. Extrem. Wounds **5**, 250–260 (2006)

70. Bharara, M., Schoess, J., Armstrong, D.G.: Coming events cast their shadows before: detecting inflammation in the acute diabetic foot and the foot in remission. Diabetes Metab. Res. Rev. **28**(Suppl 1), 15–20 (2012)
71. Armstrong, D.G., Lavery, L.A., Liswood, P.J., Todd, W.F., Tredwell, J.A.: Infrared dermal thermometry for the high-risk diabetic foot. Phys. Ther. **77**, 169–175 (1997)
72. Lavery, L.A., Higgins, K.R., Lanctot, D.R., Constantinides, G.P., Zamorano, R.G., Athanasiou, K.A., Armstrong, D.G., Agrawal, C.M.: Preventing diabetic foot ulcer recurrence in high-risk patients. Diabetes Care **30**, 14–20 (2007)
73. Benbow, S.J., Chan, A.W., Bowsher, D.R., Williams, G., Macfarlane, I.A.: The prediction of diabetic neuropathic plantar foot ulceration by liquid-crystal contact thermography. Diabetes Care **17**, 835–839 (1994)
74. Ring, F.: Thermal imaging today and its relevance to diabetes. J. Diab. Sci. Technol. **4**, 857–862 (2010)
75. Hosaki, Y., Mitsunobu, F., Ashida, K., Tsugeno, H., Okamoto, M., Nishida, N., Takata, S., Yokoi, T., Tanizaki, Y., Ochi, K., Tsuji, T.: Non-invasive study for peripheral circulation in patients with diabetes mellitus. In: Annual reports of Misasa Medical Branch, Okayama University Medical School, Tottori Japan, vol. 72, pp. 31–37 (2002)
76. Bagavathiappan, S., Saravanan, T., Philip, J., Jayakumar, T., Raj, B., Karunanithi, R., Panicker, T., Korath, M.P., Jagadeesan, K.: Infrared thermal imaging for detection of peripheral vascular disorders. J. Med. Phys. **34**, 43–47 (2009)
77. Bagavathiappan, S., Saravanan, T., Philip, J., Jayakumar, T., Raj, B., Karunanithi, R., Panicker, T.M., Korath, P., Jagadeesan, K.: Investigation of peripheral vascular disorders using thermal imaging. Br. J. Diabetes Vasc. Dis. **8**, 102–104 (2008)
78. Ammer, K.: Published papers on thermology or temperature measurement between 1989 and 2003. http://www.lla.if.sc.usp.br/art/public1989-2003.pdf
79. Ammer, K.: Thermology on the internet—An update. Thermol. Int. **19**, 15–28 (2009)
80. http://www.ncbi.nlm.nih.gov/pubmed.in
81. International Diabetes Federation: IDF diabetes atlas, 7th edn (2016). http://www.diabetesatlas.org/. Accessed on 24/05/2016
82. Reiber, G.E., Lipsky, B.A., Gibbons, G.W.: The burden of diabetic foot ulcers. Am. J. Surg. **176**, 5S–10S (1998)
83. Steketee, J.: Spectral emissivity of the skin and pericardium. Phys. Med. Biol. **18**, 686–694 (1973)
84. Webb, S.: The Physics of Medical Imaging, 1st edn. Institute of Physics Publishing, Bristol (1988)
85. Clark, J.A.: Effects of surface emissivity and viewing angle on errors in thermography. Acta Thermogr. **1**, 138–141 (1976)
86. Watmough, D.J., Fowler, P.W., Oliver, R.: The thermal scanning of a curved isothermal surface. Phys. Med. Biol. **15**, 1–8 (1970)
87. FLIR: FLIR Silver SC5000 MWIR (2009). http://www.flir.com/assets/e9d4e1d5563e4a54a7f220d7904e232e.pdf. Accessed on 6/6/2016
88. Bertelsmann, F.W., Heismann, J.J., Weber, E.J., van der Veen, E.A., Schouten, J.A.: Thermal discrimination thresholds in normal subjects and in patients with diabetic neuropathy. J. Neurol. Neurosurg. Psychiatr. **48**, 686–690 (1985)
89. Viswanathan, V., Snehalata, C., Seena, R., Ramachandran, A.: Early recognition of diabetic neuropathy: evaluation of a simple outpatient procedure using thermal perception. Postgrad. Med. J. **78**, 541–542 (2002)
90. Liniger, C., Albeanu, A., Moody, J., Richez, J., Bloise, D., Assal, J.: The Thermocross: a simple tool for rapid assessment of thermal sensation thresholds. Diabetes Res. Clin. Pract. **12**, 25–34 (1991)
91. Kelechi, T., Michel, Y., Wiseman, J.: Are infrared and thermistor thermometers interchangeable for measuring localized skin temperature? J. Nurs. Meas. **14**, 19–30 (2006)
92. Anbar, M.: Clinical thermal imaging today. IEEE Eng. Med. Biol. Mag. **17**, 25–33 (1998)

93. Roback, K., Johansson, M., Starkhammar, A.: Feasibility of a thermographic method for early detection of foot disorders in diabetes. Diabetes Technol. Ther. **11**, 663–667 (2009)
94. Frykberg, R.G., Tallis, A., Tierney, E.: Diabetic foot self examination with the Tempstat™ as an integral component of a comprehensive prevention program. J. Diab. Foot Complicat. **1**, 13–18 (2009)
95. Piotr, F., Piotr, L., Jan M.W., Martin, B., Julius, G., Karolina, M.-M., Maria, M., Stanislawa, S., Anna, C.: Continuous monitoring of feet temperature using a data logger with wireless communication. Biocybern. Biomed. Eng. **32**, 59–64 (2012)
96. Mansfield, J.R., Sowa, M.G., Payette, J.R., Abdulrauf, B., Stranc, M.F., Mantsch, H.H.: Tissue viability by multispectral near infrared imaging: a fuzzy C-means clustering analysis. IEEE Trans. On Med. Imaging **17**, 1011–1018 (1998)
97. Jones, D.P.: Biomedical Sensors. Momentum Press, New York (2010)
98. Zhang, Z.M., Tsai, B.K., Machin, G.: Radiometric Temperature Measurements. Academic Press, Oxford (2010)
99. Diakides, N.A.: New developments in low cost infrared imaging system. Eur. J. Thermol **7**, 213–215 (1997)
100. Ring, E.F.J.: High resolution infrared imaging. Eur. J. Thermol. **8**, 121 (1998)
101. Branemark, P.I., Fagerberg, S., Langer, L., Soderbergh, J.S.: Infrared thermography in diabetes mellitus. Diabetologia **3**, 529–532 (1967)
102. ISO/TR 13154:2009, http://www.iso.org/iso/catalogue_detail?csnumber=51236
103. Sun, P., Lin, H., Jao, S.E., Ku, Y., Chan, R., Cheng, C.: Relationship of skin temperature to sympathetic dysfunction in diabetic at-risk feet. Diabetes Res. Clin. Pract. **73**, 41–46 (2006)
104. Anburajan, M., Sivanandam, S., Bidyarasmi, S., Venkatraman, B., Menaka, M., Raj, B.: Changes of skin temperature of parts of the body and serum asymmetric dimethylarginine (ADMA) in type-2 diabetes mellitus Indian patients. In: 33rd Annual International Conference of the IEEE EMBS, Boston, Massachusetts, USA, pp. 6254–6259 (2011)
105. Huang, C.-L., Wu, Y.-W., Hwang, C.-L., Jong, Y.-S., Chao, C.-L., Chen, W.-J., Wu, Y.-T., Yang, W.-S.: The application of infrared thermography in evaluation of patients at high risk for lower extremity peripheral arterial disease. J. Vasc. Surg. **54**, 1074–1080 (2011)
106. Szentkuti, A., Kavanagh, H.S., Grazio, S.: Infrared thermography and image analysis for biomedical use. Period. Biol. **113**, 385–392 (2011)
107. Balbinot, L.F., Canani, L.H., Robinson, C.C., Achaval, M., Zaro, M.A.: Plantar thermography is useful in the early diagnosis of diabetic neuropathy. Clinics **67**, 1419–1425 (2012)
108. Balbinot, L.F., Robinson, C.C., Achaval, M., Zaro, M.A., Brioschi, M.L.: Repeatability of infrared plantar thermography in diabetes patients: a pilot study. J. Diab. Sci. Technol. **7**, 1130–1137 (2013)
109. Mori, T., Nagase, T., Takehara, K., Oe, M., Ohashi, Y., Amemiya, A., Noguchi, H., Ueki, K., Kadowaki, T., Sanada, H.: Morphological pattern classification system for plantar thermography of patients with diabetes. J. Diab. Sci. Technol. **7**, 1102–1112 (2013)
110. van Netten, J.J., van Baal, J.G., Liu, C., van der Heijden, F., Bus, S.A.: Infrared thermal imaging for automated detection of diabetic foot complications. J. Diab. Sci. Technol. **7**, 1122–1129 (2013)
111. Oe, M., Yotsu, R.R., Sanada, H., Nagase, T., Tamaki, T.: Screening for osteomyelitis using thermography in patients with diabetic foot. Ulcers, **2013** (2013)
112. Bandyopadhyay, A., Mondal, H.S., Chaudhuri, A.: Thermal imaging based diabetes screening using medical image processing techniques. Int. J. Eng. Res. Technol. **3**, 1298–1302 (2014)
113. Yavuz, M., Brem, R.W., Davis, B.L., Patel, J., Osbourne, A., Matassinie, M.R., Wood, D.A., Nwokolo, I.O.: Temperature as a predictive tool for plantar triaxial loading. J. Biomech. **47**, 3767–3770 (2014)
114. Gatt, A., Formosa, C., Cassar, K., Camilleri, K.P., Raffaele, C.D., Mizzi, A., Azzopardi, C., Mizzi, S., Falzon, O., Cristina, S., Chockalingam, N.: Thermographic patterns of the upper and lower limbs: baseline data. Int. J. Vasc. Med., **2015** (2015)

115. Clark, R.P., de Calcina-Goff, M.L.: International standardization in medical thermography. In: 18th International Conference of the IEEE Engineering in Medicine and Biology Society, Amsterdam, the Netherlands (1996)
116. Ring, E.F.J., Ammer, K.: The technique of infra red imaging in medicine. Thermol. Int. **10**, 7–14 (2000)
117. Standards Technical Reference for Thermal Imagers for Human Temperature Screening Part 1: Requirements and Test Methods, TR 15–1, Spring Singapore (2003)
118. Standards Technical Reference for Thermal Imagers for Human Temperature Screening Part 2: Users' implementation guidelines, TR 15–2, Spring Singapore (2004)
119. Boyko, E.J., Ahroni, J.H., Stensel, V.L.: Skin temperature in the neuropathic diabetic foot. J. Diabetes Complications **15**, 260–264 (2001)
120. Cheng, K.-S., Yang, J.-S., Wang, M.-S., Pan, S.-C.: The application of thermal image analysis to diabetic foot diagnosis. J. Med. Biol. Eng. **22**, 75–82 (2002)
121. Marins, J.C.B., Moreira, D.G., Cano, S.P., Quintana, M.S., Soares, D.D., da Fernandes, A.A., dos Silva, F.S., Costa, C.M.A., dos Amorim, P.R.S.: Time required to stabilize thermographic images at rest. Infrared Phys. Technol. **65**, 30–35 (2014)
122. Kingma, B.R., Frijns, A.J., Schellen, L., van Lichtenbelt, W.D.M.: Beyond the classic thermoneutral zone. Temperature, **1**, 10–17 (2014)
123. Pagano, M., Gauvreau, K.: Principles of Biostatistics, 3rd edn. Duxbury Press (1994)
124. Rajic, N.: Principal component thermography for flaw contrast enhancement and flaw depth characterisation in composite structures. Compos. Struct. **58**, 521–528 (2002)
125. Brioschi, M.L., Colman, D., Neto, H.M.: Fusing IR and magnetic resonance (MR) image. J. Korean Med. Thermol. **2**, 57–58 (2002)
126. Paul, J.L., Lupo, J.C.: From tanks to tumors. IEEE Eng. Med. Biol. Mag. **21**, 34–35 (2002)
127. Irvine, J.M.: Targeting breast cancer detection with military technology. IEEE Eng. Med. Biol. Mag. **21**, 36–40 (2002)
128. Liu, C., van Netten, J.J., van Baal, J.G., Bus, J.G., van der Heijden, F.: Automatic detection of diabetic foot complications with infrared thermography by asymmetric analysis. J. Biomed. Opt. **20**, 26003 (2015)
129. Hernandez-Contreras, D., Peregrina-Barreto, H., Rangel-Magdaleno, J., Ramirez-Cortes, J., Renero-Carrillo, F.: Automatic classification of thermal patterns in diabetic foot based on morphological pattern spectrum. Infrared Phys. Technol. **73**, 149–157 (2015)
130. Taylor, G.I., Palmer, J.H.: The vascular territories (angiosomes) of the body: experimental study and clinical applications. Br. J. Plast. Surg. **40**, 113–141 (1987)
131. Attinger, C.E., Evans, K.K., Bulan, E., Blume, P., Cooper, P.: Angiosomes of the foot and ankle and clinical implications of limb salvage: reconstruction, incisions, and revascularization. Plast. Reconstr. Surg. **117**, 261S–293S (2006)
132. Plassmann, P., Ring, E.F.J.: An open system for the acquisition and evaluation of medical thermological images. Eur. J. Thermol. **7**, 216–220 (1997)
133. Plassmann, P., Murawski, P.: CTHERM for standardized thermography. In: 9th European Congress of Medical Thermology, Krakow, Poland (2003)
134. Jones, C., Ring, E., Plassmann, P., Ammer, K., Wiecek, B.: Standardization of infrared imaging: a reference atlas for clinical thermography-initial results. Thermol. Int. **15**, 157 (2005)
135. Ring, E.F.J., Ammer, K., Wiecek, B., Plassmann, P.: Technical challenges for the construction of a medical IR digital image database. In: Chatard, J.P., Dennis, P.N.J. (Eds.) Proceedings of SPIE, Detectors and Associated Signal Processing II, pp. 191–198 (2005)
136. Fujimasa, I., Saito, I., Chinzei, T.: Far infrared medical image database on the world wide web. In: Proceedings of 19th International Conference IEEE/EMBS, Chicago, IL, pp. 652–653 (1997)
137. Ring, E.F.J., Ammer, K., Jung, A., Murawski, P., Wiecek, P., Zuber, J., Plassmann, P., Jones, C.D.: Standardization of thermal imaging. The Anglo-Polish reference database. In: 10th Congress of the European Association of Thermology, Zakopane, Poland (2006)

138. Colantonio, S., Pieri, G., Salvetti, O., Benvenuti, M., Barone, S., Carassale, L.: A method to integrate thermographic data and 3D shapes for diabetic foot disease. In: Proceedings of the 8th International Conference on Quantitative Infrared Thermography (QIRT 2006) ITC-CNR, Padova, Italy (2006)
139. Boulton, A.J.: The diabetic foot. Medicine **43**, 33–37 (2014)
140. Ahmad, J.: The diabetic foot. Diabetes Metab. Syndr. Clin. Res. Rev. **10**, 48–60 (2016)
141. Mayfield, J.A., Reiber, G.E., Sanders, L.J., Janisse, D., Pogach, L.M.: Preventive foot care in people with diabetes. Diabetes Care **21**, 2161–2177 (1998)
142. Zubair, M., Malik, A., Ahmad, J.: Clinico-microbial study and anti-microbial drug resistance profile of diabetic foot infections in North India. Foot **21**, 6–14 (2011)
143. Young, M.J., Boulton, A.J., MacLeod, A.F., Williams, D.R., Sonksen, P.H.: A multicentric study of the prevalence of diabetic peripheral neuropathy in the United Kingdom hospital clinic population. Diabetelogia **36**, 150–154 (1993)
144. Zubair, M., Malik, A., Ahmad, J.: Study of plasmid-mediated extended-spectrum β-lactamase-producing strains of enterobacteriaceae, isolated from diabetic foot infections in a North Indian tertiary-care hospital. Diabetes Technol. Ther. **14**, 315–324 (2012)
145. Watkins, P.J.: The diabetic foot. Br. Med. J. **326**, 977–979 (2003)
146. Springett, K., White, R.J.: Skin changes in the at risk foot and their treatment. Br. J. Community Nurs. **12**, 25–32 (2002)
147. Shahani, B.T., Halperin, J.J., Boulu, P., Cohen, J.: Sympathetic skin response—A method of assessing unmyelinated axon dysfunction in peripheral neuropathis. J. Neurol. Neusurg. Psychiatry **47**, 536–542 (1984)
148. Uccioli, L., Mancini, L., Giordano, A., Solini, A., Magnani, P., Manto, A., Controneo, P., Greco, A.V., Ghirlanda, G.: Lower limb arterio-venus shunts, autonomic neuropathy and diabetic foot. Diabetes Res. Clin. Pract. **16**, 123–130 (1992)
149. Flynn, M.D., Tooke, J.E.: Diabetic neuropathy and micro-circulation. Diabet. Med. **12**, 298–301 (1995)
150. Kimura, J.: Principles and variation of nerve conduction studies. In: Electrodiagnosis in Diseases of Nerve and Muscle: Principles and Practice, pp. 91–129. Oxford University Press, New York (2001)
151. Tack, C.J. ,van Gurp, P.J., Holmes, C., Goldstein, D.S.: Local sympathetic denervation in painful diabetic neuropathy. Diabetes, **51**: 3545–3553 (2002)
152. Harding, J.R., Wertheim, D.F., Williams, R.J., Melhuish, J.M., Banerjee, D., Harding, K.G.: Infrared imaging in diabetic foot ulceration. In: Proceedings of the 20th Annual International Conference of the IEEE Engineering in Medicine and Biology Society (Volume: 2) Hong Kong, pp. 916–918 (1998)
153. Vinik, A.I., Erbas, T., Park, T.S., Pierce, K.K., Stansberry, K.B.: Methods for evaluation of peripheral neurovascular dysfunction. Diabetes Technol. Ther. **3**, 29–50 (2001)
154. Papanas, N., Papatheodorou, K., Papazoglou, D., Kotsiou, S., Maltezos, E.: Association between foot temperature and sudomotor dysfunction in type 2 diabetes. J. Diab. Sci. Technol. **4**, 803–807 (2010)
155. Vinik, A.I., Erbas, T., Park, T.S., Stansberry, K.B., Scanelli, J.A., Pittenger, G.L.: Dermal neurovascular dysfunction in type 2 diabetes. Diabetes Care **24**, 1468–1475 (2001)
156. Sivanandam, S., Anburajan, M., Venkatraman, B., Menaka, M., Sharath, D.: Medical thermography: a diagnostic approach for type 2 diabetes based on non-contact infrared thermal imaging. Endocrine **42**, 343–351 (2012)
157. Chan, A.W., Macfarlane, I.A., Bowsher, D.R.: Contact thermography of painful diabetic neuropathic foot. Diabetes Care **14**, 918–922 (1991)
158. Stess, R.M., Sisney, P.C., Moss, K.M., Graf, P.M., Louie, K.S., Gooding, G.A., Grunfeld, C.: Use of liquid crystal thermography in the evaluation of the diabetic foot. Diabetes Care **9**, 267–272 (1986)
159. Fujiwara, Y., Inukai, T., Aso, Y., Takemura, Y.: Thermographic measurement of skin temperature recovery tim of extremities in patients with type 2 diabetes mellitus. Exp. Clin. Endocrinol. Diabetes **108**, 463–469 (2000)

160. Nishide, K., Nagase, T., Oba, M., Oe, M., Ohashi, Y., Iizaka, S., Nakagami, G., Kadowaki, T., Sanada, H.: Ultrasonographic and thermographic screening for latent inflammation in diabetic foot callus. Diabetes Res. Clin. Pract. **85**, 304–309 (2009)
161. Kanazawa, T., Nakagami, G., Goto, T., Noguchi, H., Oe, M., Miyagaki, T., Hayashi, A., Sasaki, S., Sanada, H.: Use of smartphone attached mobile thermography assessing subclinical inflammation: a pilot study. J. Wound Care **25**, 177–182 (2016)
162. Hazenberg, C.E.V.B., van Netten, J.J., van Baal, S.G., Bus, S.A.: Assessment of signs of foot infection in diabetes patients using photographic foot imaging and infrared thermography. Diabetes Technol. Ther. **16**: 370–377 (2014)
163. Skversky, N.J., Herring, A.B., Baron, R.C.: Thermography in peripheral vascular diseases. Ann. N. Y. Acad. Sci. **121**, 118–134 (1964)
164. Winsor, T., Bendezu, J.: Thermography and the peripheral circulation. Ann. N. Y. Acad. Sci. **121**, 135–156 (1964)
165. Robins, B., Bernstein, A.: Comparative studies of digital plethysmography and infrared thermography in peripheral vascular disease. Angiology **21**, 349–354 (1970)
166. Langer, L., Fagerberg, S.E., Johnsen, C.: Peripheral circulation in diabetes mellitus—a study with infrared thermography. Acta Med. Scand. **191**, 17–20 (1972)
167. Soulen, R.L., Lapayowker, M.S., Tyson, R.R., Korangy, A.A.: Angiography, ultrasound, and thermography in the study of peripheral vascular disease. Radiology **105** (1972)
168. Holm, J., Johnsen, C., Schersten, T.: Thermography in vascular surgery. A preliminary report based on a study in 12 cases. Acta Chir. Scand. **140**, 445–448 (1974)
169. Henderson, H.P., Hackett, M.E.J.: The value of thermography in peripheral vascular disease. Angiology **29**, 65–75 (1978)
170. Hitoi, A., Matsuoka, A.: patho-physiological analysis on peripheral circulation using thermography as an example of functional body imaging japan. J. Clinical Pathology **38**, 1119–1125 (1990)
171. Fushimi, H., Inoue, T., Yamada, Y., Matsuyama, Y., Kubo, M., Kameyama, M.: Abnormal vaso reaction of peripheral arteries to cold stimulus of both hands in diabetics. Diabetes Res. Clin. Pract. **32**, 55–59 (1996)
172. Mitchell, W.S., Winocour, P.H., Gush, R.J., Taylor, L.J., Baker, R.D., Anderson, D.C., Jayson, M.I.: Skin blood flow and limited joint mobility in insulin-dependent diabetes mellitus. Br. J. Rheumatol. **28**, 195–200 (1989)
173. Toutouzas, K., Benetos, G., Drakopoulou, M., Bounas, P., Tsekoura, D., Stathogiannis, K., Koutagiar, I., Aggeli, C., Karanasos, A., Panagiotakos, D., Siores, E., Stefanadis, C.: Insights from a thermography-based method suggesting higher carotid inflammation in patients with diabetes mellitus and coronary artery disease. Diabetes Metab. **40**, 431–438 (2014)
174. Uchikawa, T., Murakami, T., Furukawa, H.: Effects of the anti-platelet agent cilostazol on peripheral vascular disease in patients with diabetes mellitus. Arzneimittelforschung **42**, 322–324 (1992)
175. Ohashi, S., Iwatani, M., Hyakuna, Y., Morioka, Y.: Thermographic evaluation of the hemodynamic effect of the antithrombotic drug cilostazol in peripheral arterial occlusion. Arzneimittelforschung **35**, 1203–1208 (1985)
176. Staffa, E., Bernard, V., Kubicek, L., Vlachovsky, R., Vlk, D., Mornstein, V., Staffa, R.: Using noncontact infrared thermography for long-term monitoring of foot temperatures in a patient with diabetes mellitus. Ostomy Wound Manag. **62**, 54–61 (2016)
177. Sommer, T.C., Lee, T.H.: Charcot foot: the diagnostic dilemma. Am. Fam. Physician **64**, 1591–1598 (2001)
178. Mercer, J.B., Nielsen, S.P., Hoffmann, G.: Improvement of wound healing by water-filtered infrared-A (wIRA) in patients with chronic venous stasis ulcers of the lower legs including evaluation using infrared thermography. Ger. Med. Sci. **6**, 1–26 (2008)
179. Sodi, A., Giambene, B., Miranda, P., Falaschi, G., Corvi, A., Menchini, U.: Ocular surface temperature in diabetic retinopathy: a pilot study by infrared thermography. Eur. J. Ophthalmol. **19**, 1004–1008 (2009)

180. Sejling, A.S., Lange, K.H., Frandsen, C.S., Diemar, S.S., Tarnow, L., Faber, J., Holst, J.J., Hartmann, B., Hilsted, L., Kjaer, T.W., Juhl, C.B., Thorsteinsson, B., Pedersen-Bjergaard, U.: Infrared thermographic assessment of changes in skin temperature during hypoglycaemia in patients with type 1 diabetes. Diabetologia **58**, 1898–1906 (2015)
181. Zotter, H., Kerbl, R., Gallistl, S., Nitsche, H., Borkenstein, M.: Rewarming index of the lower leg assessed by infrared thermography in adolescents with type 1 diabetes mellitus. J. Pediatr. Endocrinol. Metab. **16**, 1257–1262 (2003)
182. Sejling, A.S., Lange, K.H.W., Frandsen, C.S.S., Diemar, S.S., Tarnow, L., Faber, J., Kjaer, T.W., Juhl, C.B., Thorsteinsson, B., Pedersen-Bjergaard, U.: Facial skin temperature measured by infrared thermography during hypoglycaemia in patients with longstanding type 1 diabetes. Diabetologia **57**, S260–S260 (2014)
183. Schindl, A., Heinze, G., Schindl, M., Pernerstorfer-Schon, H., Schindl, L.: Systematic effects of low-intensity laser irradiation on skin microcirculation in patients with diabetic microangiopathy. Microvasc. Res. **64**, 240–246 (2002)
184. Schindl, A., Schindl, M., Schon, H., Knobler, R., Havelec, L., Schindl, L.: Low-intensity laser irradiation improves skin circulation in patients with diabetic microangiopathy. Diabetes Care **21**, 580–584 (1998)
185. Armstrong, D.G., Holtz-Neiderer, K., Wendel, C., Mohler, M.J., Kimbriel, H.R., Lavery, L.A.: Skin temperature monitoring reduces the risk for diabetic foot ulceration in high-risk patients. Am. J. Med. **120**, 1042–1046 (2007)
186. Bharara, M., Fitzgerald, R., Rilo, H.R., Armstrong, D.G.: Practical thermal monitoring solutions: empowering diabetic foot care teams for prevention of lower extremity complications. Can. J. Diabetes **33**, 217–218 (2009)
187. Pafili, K., Papanas, N.: Thermographyin the follow up of the diabetic foot: best to weigh the enemy more mighty than he seems. Expert Rev. Med. Devices **12**, 131–133 (2015)

Exploratory Thermal Imaging Assessments of the Feet in Patients with Lower Limb Peripheral Arterial Disease

Daniel Kyle, John Allen, Klaus Overbeck and Gerard Stansby

Abstract Peripheral arterial disease (PAD) is an atherosclerotic condition that can result in reduced lower limb tissue perfusion. It is associated with significant comorbidity including coronary artery disease (CAD) and cerebrovascular disease. One of the most currently utilised diagnostic tools is the ankle brachial pressure index, which is time consuming, requires significant user training and is unreliable in diabetics due to vessel calcification leading to falsely elevated results. The aim of this pilot study was to explore the potential use of thermal imaging in identifying PAD. In 44 patients (24 male; mean (SD) age 67 [12] years) thermal images of three regions of interest (ROI's) on the feet were collected within a normothermic measurement room. The ROI's for each foot included the first toe (T), proximal foot (PF) and whole foot (WF). The ankle brachial pressure index (ABPI) reference test was collected to make a diagnosis of PAD (ABPI < 0.9). Parametric statistics were employed and a p value <0.05 considered statistically significant. Twenty-three patients had significant PAD in at least one leg (Mean ABPI 0.64; Range 0.32–0.86) while 26 patients had a normal ABPI (non-PAD) in at least one leg (Mean ABPI 1.14; Range 0.9–1.46). There were no significant ROI differences between PAD (Mean WF temperature 30.3 °C; SD 0.8) and non-PAD feet (Mean WF temperature 31.0 °C; SD 0.7) for their mean or SD values. The temperature gradient (toe-proximal foot) was close to −1 °C but this was not significantly different between the groups. Furthermore, right minus left whole foot temperature

D. Kyle · J. Allen (✉)
Microvascular Diagnostics, Freeman Hospital, The Newcastle upon Tyne Hospitals NHS Foundation Trust, Newcastle upon Tyne, UK
e-mail: John.Allen@nuth.nhs.uk

D. Kyle
e-mail: dankyle10@gmail.com; Daniel.Kyle@nuth.nhs.uk

D. Kyle · K. Overbeck · G. Stansby
The Northern Vascular Centre, Freeman Hospital, The Newcastle upon Tyne Hospitals NHS Foundation Trust, Newcastle upon Tyne, UK
e-mail: Klaus.Overbeck@chsft.nhs.uk

G. Stansby
e-mail: Gerard.Stansby@nuth.nhs.uk

E.Y.K. Ng and M. Etehadtavakol (eds.), *Application of Infrared to Biomedical Sciences*, Series in BioEngineering,
DOI 10.1007/978-981-10-3147-2_14

differences were not significant. Absolute, gradient, spatial and bilateral skin temperature differences of the feet have been quantified in PAD and non-PAD legs and have found no significant differences overall. This pilot study indicates that thermal imaging from resting measurements is unlikely to be of diagnostic value in detecting significant PAD. Furthermore, the study also raises questions about the apparent misconception that in PAD the foot temperatures are usually significantly reduced.

Keywords Thermal imaging · Peripheral Arterial Disease (PAD) · Vascular disease · ABPI · Cardiovascular disease · Skin temperature

1 Introduction and Research Context

1.1 Peripheral Arterial Disease (PAD): The Overlooked Cardiovascular Disease with Great Implications

Peripheral arterial disease (PAD), which is an atherosclerotic process effecting nearly 20% of all people aged over 70 years old worldwide, causes reduced lower limb tissue perfusion [1]. Atherosclerosis results from atheroma (fatty deposits) and can progress to thrombosis and vessel occlusion [2]. This can result in ischaemia, pain, tissue necrosis and potentially even limb loss or death [3].

Atherosclerosis can occur in any vessel within the arterial system leading to not only PAD but ischaemic heart disease (IHD) and cerebrovascular disease, which can result in myocardial infarction (MI) and stroke, respectively [4] (Fig. 1). These conditions are commonly grouped as cardiovascular diseases (CVD) and they have overlap in pathoetiology, diagnosis, prognosis and treatment [5]. The risk factors

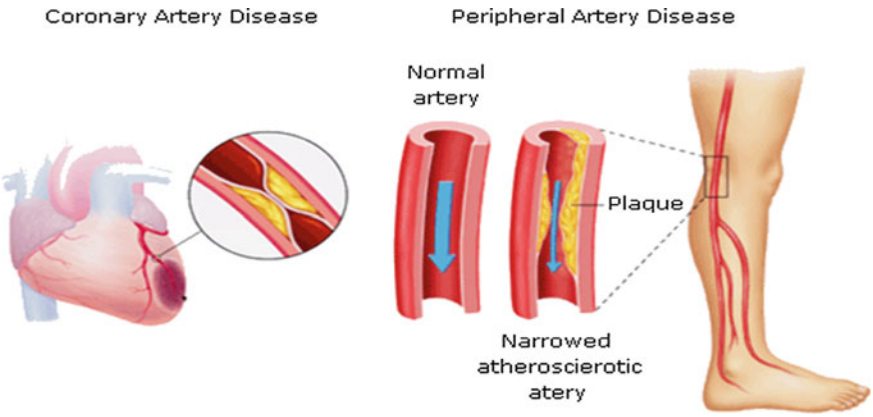

Fig. 1 Atherosclerosis affecting the periphery leading to PAD and the heart leading to CAD and MI. *Source* http://www.angioslide.com/USA/Patients/peripheral-artery-disease

for all CVD's include smoking, high blood pressure, diabetes, high cholesterol, obesity, renal disease and family history of vascular disease [3]. Therefore, diagnosis of PAD should alert to the patient's concurrent risk of MI and stroke. It was found that 65% of PAD patients also have coronary or cerebral artery disease [6]. Thus, improved diagnosis of PAD may have the added benefit of leading to earlier diagnosis of other CVD's and the improved outcomes secondary to earlier identification and management.

The most common symptom of PAD is intermittent claudication, defined as the repeatable, predictable onset of pain in the lower limbs (typically in the calf) that occurs on exertion as a result of impaired blood delivery and reduced oxygen supply to the muscles. The pain is characteristically worse uphill, and as disease progression occurs the distance a patient is able to walk before they have to stop due to pain will shorten. Pain resolves with rest and predictably re-occurs again on exertion. There are a number of classification systems of PAD which consider claudication distance such as the Fontaine and Rutherford classification systems [3]. As disease progresses, patients may suffer with rest pain and eventually develop arterial ulcers and gangrene, known as critical limb ischaemia (CLI), which once established leaves the patient with only a 50–60% five-year survival [7].

However, patients do not always give a clear history of their symptoms and especially in the early stages of the disease it can be difficult for the physician to confidently identify PAD. Other conditions that may produce similar pain include lumbar spinal stenosis (neurogenic claudication), osteoarthritis, chronic venous insufficiency and degenerative disc disease, which need to be excluded. On examination, the PAD patient's feet and legs may feel cold, hairless and a pulse may not be palpable. In severe disease, arterial ulcers and tissue necrosis/gangrene may be observed.

Investigations include screening for risk factors such as performing blood tests (total cholesterol, LDL cholesterol, triglycerides, blood glucose, HBA1c, C-reactive protein, urea and electrolytes) and electrocardiography (ECG). More specific investigations within a primary care setting include performing the ankle brachial pressure index (ABPI), which involves measuring the blood pressure from the upper and lower limbs of a patient in the supine position after they have rested for 10 min and calculated performing the following calculation:

$$\text{ABPI} = \frac{*\text{Leg systolic BP}}{\text{Highest arm systolic BP}}$$

* Performed on each leg to calculate an ABPI for both legs, usually using the highest of dorsalis pedis (DP) and posterior tibial (PT) arterial pressure measurements.

The value calculated can then be cross-referenced to the table below

ABPABPI score	Diagnosis
0.9–1.3	Normal
0.5–0.89	Mild/moderate PAD
<0.5	Severe PAD

Typically, values greater than 0.9 are considered normal, however, arterial calcification can lead to an ABPI result of greater than 1.3 due to reduced vessel compressibility. This can result in the arterial calcification masking arterial stenosis leading to a falsely reassuring ABPI. In addition, arterial calcification is common in diabetics who are also twice as likely to have PAD [8]. Therefore, the ABPI is potentially missing patients who have one of the highest risk factors for PAD, which is another limitation of the test. Furthermore, the ABPI requires the patient to lie in a supine position for 10 min before performing a measurement, which places a significant time commitment on a busy GP service. In order to perform the ABPI correctly also requires an element of formal training and expertise.

Once a patient is suspected to have PAD, they are referred to secondary care for definitive imaging via ultrasound Doppler of the lower limb arteries, often followed by either magnetic resonance angiography (MRA) or computed tomography angiography (CTA), which is able to identify the severity and level of an arterial stenosis/occlusion. First-line management is through modification of lifestyle factors followed by endovascular procedures such as angioplasty and stenting. Only in severe PAD, when a patient's quality of life is significantly impaired, surgery is considered an option. This would include bypass operations or amputation.

However, further objective, reliable screening tests for PAD that could be used in primary care are required due to the limitations of ABPI outlined above [9]. This is where the potential use of thermal imaging in identifying PAD arose. It is widely thought that a patient who has PAD would have reduced limb perfusion, leading to a reduction in skin temperature at the feet. We propose in this work that if a reduced skin temperature in PAD patients exists, then it would be identified using an infrared thermal imaging camera.

1.2 Thermal Imaging: The Fast, Non-contact Solution to Improved Diagnosis of PAD in Primary Care?

For thousands of years a raised body temperature, in the form of a fever, has been recognised as an indication of illness. Around 400 BC Hippocrates wrote "Whatever part of the body excess of heat or cold is felt, the disease is there to be discovered" [10]. A fever is the generalised, symptomatic manifestation of the presence of inflammation, infection or malignancy within the body. In addition,

increased localised skin temperature has also long been recognised as an indicator of local pathology, perhaps the most well known being the red, hot great toe which occurs in gout and or the hot, swollen joints of the hand in rheumatoid arthritis. Whether generalised or localised, the change in skin temperature is recognised as the presence of illness or pathology. This is because injury, infection, inflammation or malignancy is associated with localised vasodilation leading to tissue hyper-perfusion to the affected area and increased metabolic processes, all which lead to a higher emitted temperature [11]. The detection of increased body temperature in illness was purely subjective until the invention of the thermometer in the seventeenth century when objective measurements could then be made [12]. Traditional glass thermometers worked through detecting temperature changes via conduction but heat also leaves the body via radiation, evaporation and convection. It remained difficult to objectively measure the temperature of specific areas of the body until the invention of the first electronic sensor of infrared radiation in 1934 and the developments in infrared sensors since then [12].

Infrared thermal imaging involves the identification and quantification of naturally emitted infrared radiation from skin which is then represented as an infrared thermogram [13]. The different areas of skin temperature are represented as different colours on the thermogram making the image easily interpretable. It also has the advantages of being noninvasive, non-contact, quick and sensitive. The technology has progressed considerably since the first published paper which presented the use of infrared thermal imaging in preclinical diagnosis of breast cancer in 1956 [14]. Thermal imaging cameras are now able to detect differences in skin temperature at much smaller scales and with increased spatial accuracy. This has led to its increased use as a medical imaging tool with a vast number of potential applications including diabetes, Raynaud's Disease, the detection of breast cancer and the identification of flap viability in reconstructive surgeries [14].

However, despite the increasing research interest and potential clinical applications of thermography, often the clinical interpretation of the results remains challenging. This is because the relationship between skin temperature and skin perfusion is complex. It depends on many factors including site (central vs. peripheral), skin thickness, perspiration, core body temperature and ambient room temperature [9]. In addition, ingestion of caffeine or alcohol and certain drugs can affect skin temperature. Pertinently, the change in skin temperature in relation to blood flow may depend on whether the change in blood flow has occurred for physiological adaptation, for example due to a change in ambient temperature, or in response to pathology (Fig. 2).

Nonetheless, it is often taught to medical students learning to examine a patient for peripheral arterial disease to feel for skin temperature, as a limb with arterial disease may be cooler than a limb without blockage [1]. This is because it is thought, possibly incorrectly, that reduced blood flow to the limb may result in reduced cutaneous limb temperature that may provide the physician with a further clinical sign to help make a diagnosis. There have been a number of studies which have correlated skin temperature with PAD, however most studies have evaluated subjective assessments of skin temperature. A large scale cross-sectional study

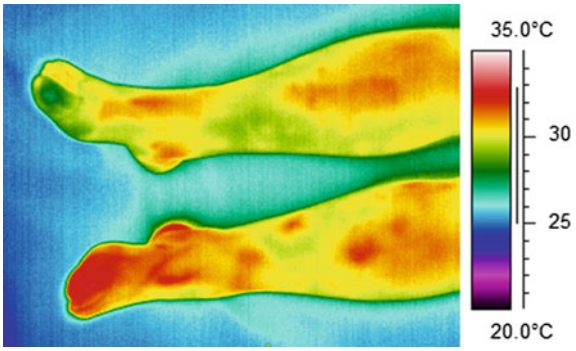

Fig. 2 Thermal imaging of a PAD patient. A PAD patient with a cool right foot (ABPI 0.53; whole foot temperature 30.4 °C) and a warmer left foot (ABPI 0.86; whole foot temperature 31.3 °C). There is only a physiologically small difference in skin temperature between the feet despite having clearly asymmetric PAD

performed in the Netherlands in 1997 which evaluated the diagnostic value of signs and symptoms of PAD in primary care found a relatively high specificity of palpating skin temperature and a diagnosis of PAD. Interestingly, in the same study, there was no diagnostic value in the patients reporting of cold feet [15].

The use of thermal imaging to detect peripheral vascular disorders including venous insufficiency, Raynaud's phenomenon and diabetes, has been studied previously, with some interesting observations. Bagavathiappan et al. [16] published a case series of four patients in which thermal imaging was concluded to reliably detect vascular diseases including chronic venous insufficiency and arterial obstruction. Distal tissues were found to be cooler than more proximal, surrounding tissue which was hypothesised to be due to arterial obstruction, whereas areas of venous compromise were warmer than surrounding skin, due to tissue inflammation [16]. In Clark et al. [17], the comparison of laser Doppler and thermal imaging in the detection of digital blood flow in Raynaud's was poorly correlated, however, in Schlager et al. [18] good correlation between thermal imaging and skin perfusion (determined using laser Doppler perfusion imager) was demonstrated in patients with Primary Raynaud's Phenomenon. In Cheng et al. [19] thermal imaging was demonstrated to be able to identify poor blood supply surrounding diabetic ulcers and Sivanandam et al. [20] demonstrated reduced peripheral foot temperature in type 2 diabetes mellitus, which correlated with HBa1c level. Ring [21] concluded in a review paper that thermal imaging is useful in the assessment of peripheral circulation in diabetes mellitus. In diabetic neuropathy, the thermoregulatory mechanisms are no longer functioning correctly leading to impaired neurovascular function and abnormal skin temperature [21].

However, there is limited evidence in the literature of the use of thermal imaging in detecting PAD. A study by Huang et al. [22] demonstrated that resting skin temperatures between PAD and control subjects were non-significant. However after a 6-min exercise test, the feet of PAD patients was either the same as or cooler than at rest but in the control group the feet were warmer or the same as at rest [22].

Therefore, the aim of this pilot study was to explore the potential of thermal imaging in identifying PAD. In this chapter, we describe the results of 44 patients who had thermal images taken of their feet, looking specifically at three regions of interest

(ROI) and the correlation of peripheral skin temperature with evidence of peripheral arterial disease, as diagnosed by ABPI. The results of this study may inform as to whether there is potential use of thermal imaging in the diagnosis of PAD.

2 Methods

Vascular measurements comprised ABPI and TI (thermal imaging). Thermal imaging was performed in a temperature-controlled microvascular imaging facility, based in the Medical Physics Department at Freeman Hospital, Newcastle upon Tyne. The room has a normothermic control which allowed all experiments to be performed at 25 °C.

Vascular patients were recruited from the Northern Vascular Centre (NVC) wards or NVC outpatient clinics. Healthy controls were recruited from hospital staff and local retired engineering groups. After consent was gained for the study, participants were asked to remove their shoes and socks, ensuring they were bare from the mid-shin down before lying supine on a standard medical examination couch. Participants were acclimatised at rest for at least 10 min in the measurement facility to allow for thermal equilibration before imaging took place.

Thermal imaging was performed using a FLIR SC300 (FLIR Systems) with standard view lens. The thermal camera was placed on an imaging stand that was placed approximately 1 m above a patient's legs so that both feet were captured in the same image. All images were taken by 1 thermal imaging operator (JA).

Ankle brachial pressure index (ABPI) measurements were performed shortly after the thermography using standard methods. An ABPI value of <0.9 was considered as diagnostic for significant PAD.

Thermal images of three regions of interest (ROI's) on the feet were collected from each patient. The ROI's for each foot included the first toe (T), proximal foot (PF) and whole foot (WF) (Fig. 3). The thermal imaging analysis was performed by a single operator (DK).

Thermal images were visualised and analysis was performed using FLIR ThermaCAM Researcher Pro 2.10 software. Temperature was colour-coded using a rainbow palette across a range of 18–36 °C.

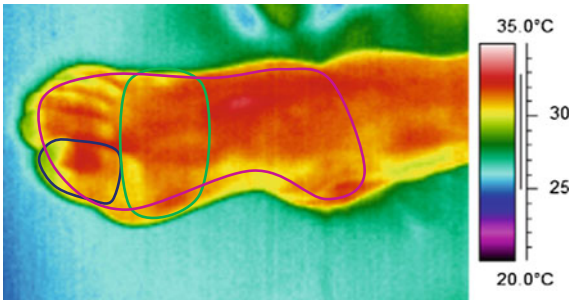

Fig. 3 Regions of interest (ROI). (1) First toe (T) (*blue outline*), (2) Proximal foot (PF) (*green outline*), (3) Whole foot (WF) (*purple outline*)

Three ROI's were measured, as described above. The mean temperature of each respective ROI was calculated and results were exported to a Microsoft Excel spreadsheet for analysis. Parametric statistics were employed using Minitab Statistical Software (Version 17) and a p value <0.05 considered statistically significant. Data were mainly displayed graphically using nonparametric statistical measures. Numerical summaries for the data were provided using parametric measures and with standard parametric statistical tests used throughout.

3 Results

A total of 44 patients were studied (24 male; 20 female) with a mean age of 67 ± 12 years (range 44–91 years old). The mean height was 168 cm [(Range 152–181 cm); mean PAD group 167.2 cm; non-PAD 168.2 cm)]. Mean weight was 78 kg [(Range 51–111 kg) mean PAD group 80 kg; mean non-PAD 76 kg)] Mean BMI 27.8 [(Range 20.8–38.4) mean PAD group 28.6; mean non-PAD 26.9)]. There were a total of eight patients with diabetes in the study, seven in the PAD group (five non-insulin dependent diabetic (NIDDM); two insulin dependent) and one in the non-PAD group (1 NIDDM).

Twenty-three had significant PAD in at least one leg [mean ABPI: 0.64 (SD 0.15)]. Five patients were found to have PAD in only one leg, which provided interesting individual comparison. There were no significant ROI differences between PAD and non-PAD legs for their mean or SD values (Figs. 4 and 5). However, the mean temperature of PAD feet at each ROI was close to 0.6 °C cooler

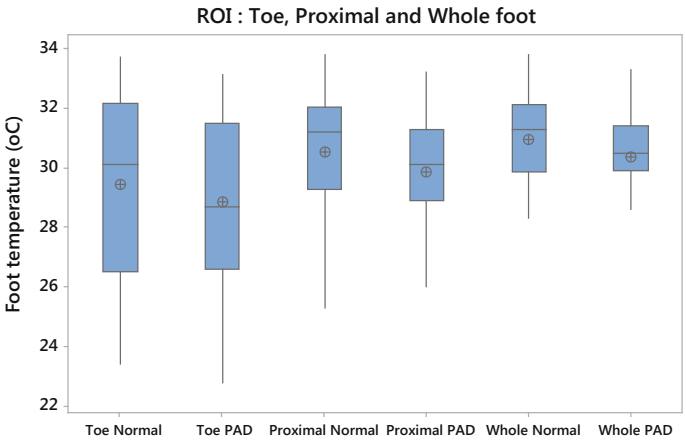

Fig. 4 ROI average temperature for PAD versus non-PAD. Figure shows the mean (as *cross within circle*), the median (as *line within boxplot*), interquartile range (*either ends of the main box*) (IQR (25–75%)), lower and upper quartile ranges with outliers removed (*either end of the lines*). There was no significant difference in ROI average between PAD and non-PAD legs ($p \geq 0.05$)

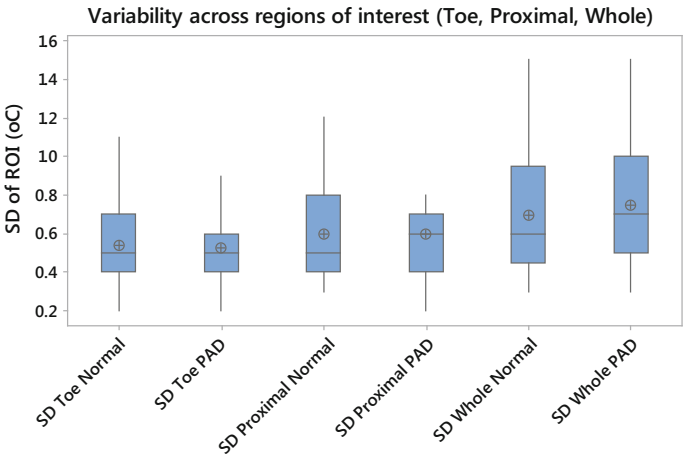

Fig. 5 Variation across each ROI (using SD values) for PAD versus non-PAD. Figure shows the mean (as *cross within circle*), the median (as *line within boxplot*), interquartile range (*either ends of the main box*) (IQR (25–75%)), lower and upper quartile ranges with outliers removed (*either end of the lines*). There was no significant difference in ROI SD between PAD and non-PAD legs ($p \geq 0.05$)

Table 1 Temperature gradients for each ROI expressed using mean and SD values for PAD and non-PAD groups

	Toe (°C) (SD)	Proximal (°C) (SD)	Whole foot (°C) (SD)
PAD	28.9 (0.53)	29.9 (0.60)	30.4 (0.75)
Non-PAD	29.4 (0.54)	30.6 (0.60)	31.0 (0.70)

The foot is progressively warmer as you move proximally, but there is no significant difference in temperature gradients between groups

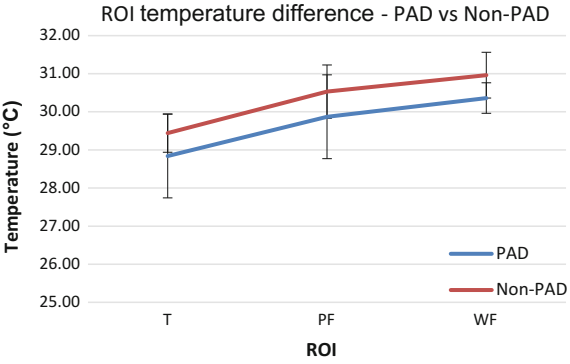

Fig. 6 ROI temperature difference between PAD and non-PAD patients. PAD feet are approximately 0.5 °C cooler than non-PAD feet across each ROI, which was non-significant. In addition, the temperature gradient from toe to proximal foot was close to −1 °C but this was also non-significant. (*T* First Toe; *PF* Proximal foot; *WF* Whole foot). *ROI* Region of interest

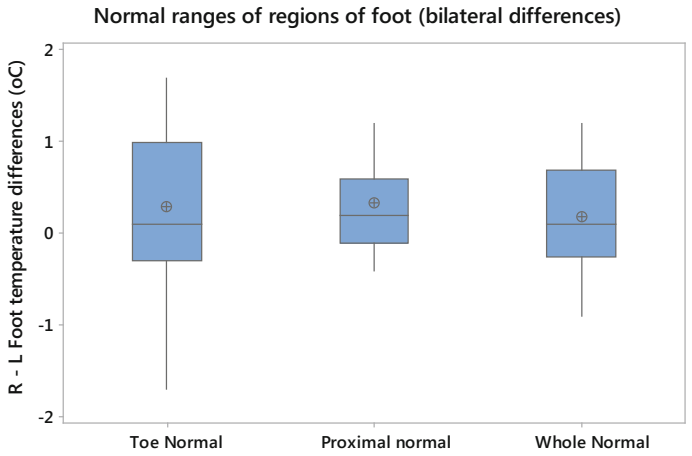

Fig. 7 The Bilateral differences in non-PAD patients. Figure shows the mean (as *cross within circle*), the median (as *line within boxplot*), interquartile range (*either ends of the main box*) (IQR (25–75%)), lower and upper quartile ranges with outliers removed (*either end of the lines*). There were no significant right minus left ($R - L$) differences in non-PAD patients. The 95% CI of the differences for the whole foot would be -0.9 to + 1.2 °C

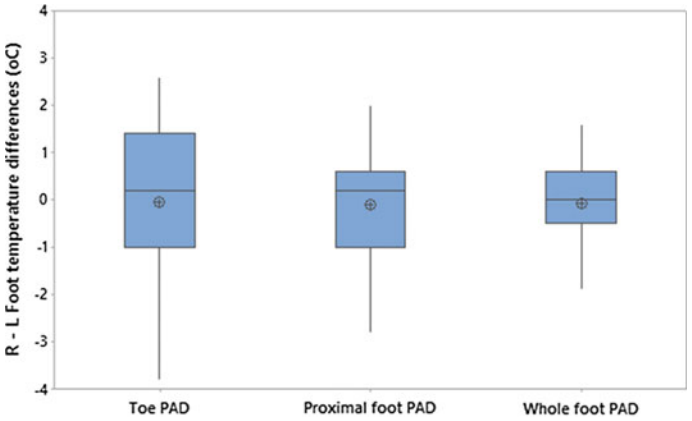

Fig. 8 The Bilateral differences in PAD patients i.e. with PAD in at least 1 leg. Figure shows the mean (as *cross within circle*), the median (as *line within boxplot*), interquartile range (*either ends of the main box*) (IQR (25–75%)), lower and upper quartile ranges with outliers removed (*either end of the lines*). Overall, there were no significant $R - L$ differences in PAD patients. However, there was significantly wider variance seen in PAD group ($p < 0.05$: for whole foot and proximal foot)

than non-PAD feet, which was statistically non-significant. The temperature gradient (toe-proximal foot) was close to −1 °C but this was not significantly different between groups (Table 1; Fig. 6). Right–left whole foot temperature differences were also not significant (Figs. 7 and 8).

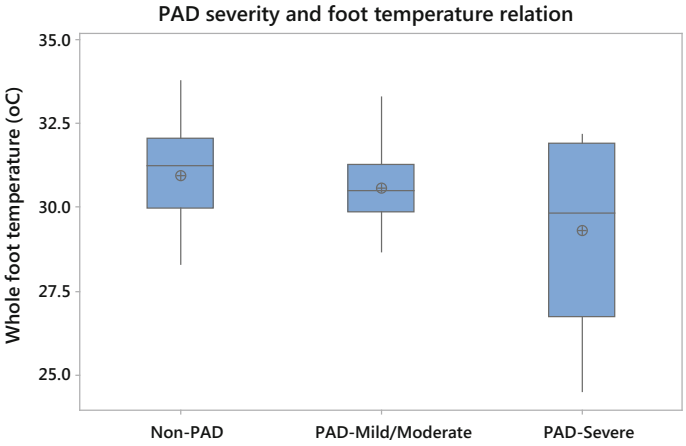

Fig. 9 The whole foot temperature is no different between healthy subjects and patients with mild/moderate PAD. Figure shows the mean (as *cross within circle*), the median (as *line within boxplot*), interquartile range (*either ends of the main box*) (IQR (25–75%)), lower and upper quartile ranges with outliers removed (*either end of the lines*). In the higher grade PAD (ABPI < 0.5) the foot temperature appears reduced only in a fraction of the patients

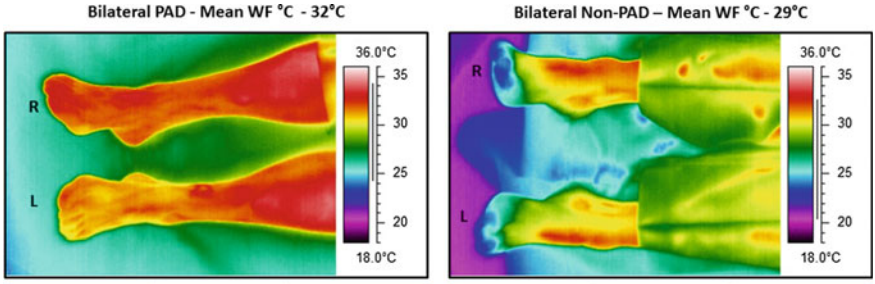

ROI	Right Leg (PAD; ABPI 0.58) °C (Mean ± SD)	Left leg (PAD; ABPI 0.63) °C (Mean)
Toe	32.6 ± 0.4	31.9 ± 0.2
Proximal foot	32.1 ± 0.4	31.2 ± 0.3
Whole foot	32.3 ± 0.4	31.3 ± 0.4

ROI	Right Leg (PAD; ABPI 1.07) °C (Mean ± SD)	Left leg (PAD; ABPI 1.07) °C (Mean)
Toe	24 ± 0.7	25.3 ± 1.1
Proximal foot	29.1 ± 1.1	28.5 ± 1.1
Whole foot	29.1 ± 2.7	29.1 ± 2.2

Fig. 10 Example thermograms highlighting the range of normal for toe temperatures since healthy subjects can have very cold toes without arterial pathology. In the cases shown the PAD patient has bilateral disease (*left panel*) with feet at 32 °C and the healthy subject has cooler feet at 29 °C

There was no significant difference between foot temperature in non-PAD subjects compared to PAD patients with mild/moderate disease, but appeared to be reduced in some of the severe PAD subjects but was not significant overall (Fig. 9). Individual patient examples of this point are given in Figs. 10, 11 and 12.

Some examples of patients who had one PAD (ABPI < 0.9) foot and one non-PAD (ABPI $\geq$ 0.9) foot

Example 1

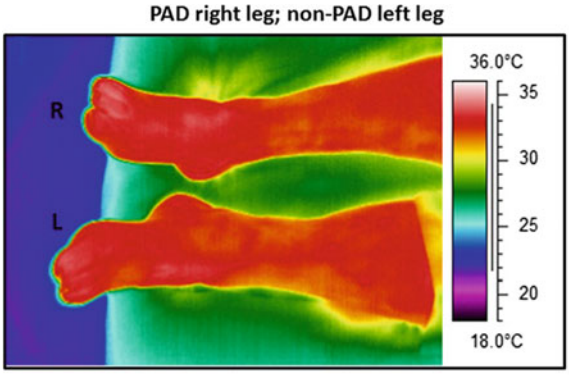

Fig. 11 No significant temperature differences between the right PAD leg (ABPI 0.77) and the left non-PAD leg (ABPI 1.02)

ROI	Right Leg (PAD; ABPI 0.77) °C (Mean ± SD)	Left leg (PAD; ABPI 1.02) °C (Mean ± SD)
Toe	33.1 ± 0.4	33.6 ± 0.3
Proximal foot	33.1 ± 0.4	33 ± 0.3
Whole foot	33.3 ± 0.3	33 ± 0.4

Example 2

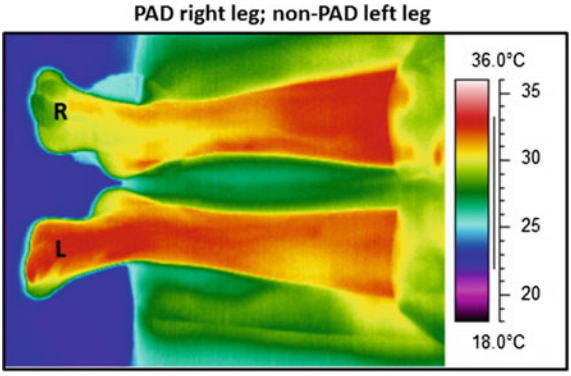

Fig. 12 The *right* PAD first toe (ABPI 0.51) is close to 4 °C cooler than the *left* non-PAD first toe (ABPI 1.06). In addition, the right foot is approximately 2 °C cooler for the proximal and whole foot ROI's

ROI	Right Leg (PAD; ABPI 0.51) °C (Mean ± SD)	Left leg (Non-PAD; ABPI 1.06) °C (Mean ± SD)
Toe	28.6 ± 0.5	32.3 ± 0.4
Proximal foot	30.1 ± 0.4	32.2 ± 0.7
Whole foot	30 ± 0.8	32.1 ± 0.8

4 Discussion and Summary

In this pilot study, we have quantified absolute, gradient, spatial and bilateral skin temperature differences in PAD and non-PAD legs and have found no significant differences between groups. However, a trend towards cooler feet in PAD patients of close to 0.6 °C was observed, but this was non-significant overall. Good perfusion of superficial tissues was maintained despite PAD. This pilot study indicates that thermal imaging is unlikely to be of diagnostic value in detecting significant PAD. The BMI of patients in the PAD group was approximately 2 kg/m^2 greater than the non-PAD group and patients in the PAD group were also more likely to be diabetic (PAD group 8; non-PAD 1). This is consistent with the expected co-morbidities of a PAD patient, as it well known that being overweight and diabetes are significant risk factors for the development of PAD.

There are a number of reasons as to why there were no significant differences observed between the temperature of PAD and non-PAD feet. First, it is possible that the sample size in this pilot study was insufficient to reach statistical power and with increasing patient numbers, significance may become apparent. However, temperature differences would still be small and detection through skin palpation as part of a clinical examination would be unlikely to sense a significant difference in individual patients.

The microcirculation of the peripheral tissues is partly controlled via the autonomic nervous system and thermoregulation mechanisms. Therefore, despite reduced gross tissue perfusion to the distal tissues in PAD, the superficial tissues are compensated via the autonomic response of the microcirculation, which results in maintained cutaneous temperatures. In addition, thermal imaging techniques are highly sensitive to detecting differences from so-called normal values. However, thermal imaging is not able to inform us as to why such a deviation exists. This is why care is always required when interpreting thermal images in the clinical context. For example, in PAD, as a consequence of impaired tissue perfusion, tissue necrosis may occur. Tissue necrosis may result in increased metabolic response of the tissue, leading to the accumulation of catabolic waste products which are known to be vasodilatory. As a consequence, tissue inflammation may be increased as part of the immune response towards necrosis, leading to increased heat production despite reduced gross perfusion to the tissues. Therefore, despite reduced perfusion to the feet due to PAD, thermal imaging is unable to detect the changes as cutaneous temperature is maintained and often even elevated, due to inflammation.

Furthermore, we have indicated that it is only at the extremes of PAD (e.g. ABPI < 0.5) that a reduced temperature begins to become apparent. Perhaps once such severe disease is established compensatory microcirculatory autonomic mechanisms that were maintaining skin perfusion and hence normal skin temperature are overwhelmed and the foot then becomes palpably cold. It is also possible that if the study was performed at a cooler room temperature, the effects of reduced tissue perfusion due to PAD would become more apparent. There is scope for

further work and future studies should consider disease severity across the spectrum of PAD in relationship to measurement room ambient temperature and thermal imaging diagnostic test accuracy in PAD.

Nevertheless, this study has revealed some interesting findings. Not least whether it is still valid to teach medical students, as part of a clinical examination of the vascular system, to palpate for skin temperature, as an indication of potential peripheral arterial disease. Perhaps, assessing skin temperature as part of a peripheral vascular examination has been a long held misconception that holds limited diagnostic weight.

However, it is apparent that further PAD detection tests are still required which may be informed from the observed findings in this pilot study. Other infrared-based technologies such as photoplethysmography (PPG) have been shown to possess diagnostic value although this is based on near infrared rather than far infrared technology [9, 23]. In PAD, the PPG waveform becomes damped and delayed, even for lower grade disease. The nature of PPG signals however is not well understood. We believe that a future cross-comparison of thermal imaging and PPG in PAD could help in the understanding of such technologies and the development of reliable tests.

In summary, we found no significant differences in the overall absolute, gradient, spatial or bilateral skin temperature differences between PAD and non-PAD legs. This pilot study indicates that thermal imaging from resting measurements is unlikely to be of diagnostic value in detecting significant PAD. Furthermore, it also raises questions about the apparent misconception that the foot temperatures are always significantly reduced in a patient with PAD. Finally, reliable fast, non-invasive devices for the detection of PAD are still required to aid the diagnosis of this under-diagnosed but significant cardiovascular disease.

References

1. Peach, G., Griffin, M., Jones, K., Thompson, M., Hinchliffe, R.: Diagnosis and management of peripheral arterial disease. BMJ **345**, e5208 (2012)
2. Falk, E.: Pathogenesis of atherosclerosis. J. Am. College Cardiol. **47**(8s1):C7–C12
3. Muller, M.D., Reed, A.B., Leuenberger, U.A., Sinoway, L.I.: Physiology in medicine: peripheral arterial disease. J. Appl. Physiol. **115**(9):1219–1226 (2013)
4. Hirsch, A.T., Criqui, M.H., Treat-Jacobson, D., Regensteiner, J.G., Creager, M.A., Olin, J.W., et al.: Peripheral arterial disease detection, awareness, and treatment in primary care. JAMA **286**(11), 1317–1324 (2001)
5. Criqui, M.H., Denenberg, J.O.: The generalized nature of atherosclerosis: how peripheral arterial disease may predict adverse events from coronary artery disease. Vasc. Med. **3**(3), 241–245 (1998)
6. Criqui, M.H., Langer, R.D., Fronek, A., Feigelson, H.S., Klauber, M.R., McCann, T.J., et al.: Mortality over a period of 10 years in patients with peripheral arterial disease. N. Engl. J. Med. **326**(6), 381–386 (1992)
7. icai Group T.: Long-term mortality and its predictors in patients with critical leg ischaemia. Eur. J. Vasc. Endovasc. Surg. **14**(2):91–95 (1997)

8. Norgren, L., Hiatt, W.R., Dormandy, J.A., Nehler, M.R., Harris, K.A., Fowkes, F.G.R., et al.: Inter-society consensus for the management of peripheral arterial disease. Int. Angiol. **26**(2), 81–157 (2007)
9. Allen, J., Howell, K.: Microvascular imaging: techniques and opportunities for clinical physiological measurements. Physiol. Meas. **35**(7), R91 (2014)
10. Thermology—History. [11/08/2016]; Available from: http://www.thermology.com/thermal_temperature_measurement_history.html
11. Qi, H., Diakides, N.A.: Infrared Imaging in Medicine. CRC Press, Boca Raton, FL (2007)
12. Ring, E.F.J.: Quantitative thermal imaging. Clin. Phys. Physiol. Meas. **11**(4A), 87 (1990)
13. Lahiri, B.B., Bagavathiappan, S., Jayakumar, T., Philip, J.: Medical applications of infrared thermography: a review. Infrared Phys. Technol. **55**(4), 221–235 (2012)
14. Lawson, R.: Implications of surface temperatures in the diagnosis of breast cancer. Can. Med. Assoc. J. **75**(4), 309 (1956)
15. Stoffers, H.E.J.H., Kester, A.D.M., Kaiser, V., Rinkens, P.E.L.M., Knottnerus, J.A.: diagnostic value of signs and symptoms associated with peripheral arterial occlusive disease seen in general practice a multivariable approach. Med. Decis. Making **17**(1), 61–70 (1997)
16. Bagavathiappan, S., Saravanan, T., Philip, J., Jayakumar, T., Raj, B., Karunanithi, R., et al.: Infrared thermal imaging for detection of peripheral vascular disorders. J. Med. Phys. **34**(1), 43 (2009)
17. Clark, S., Dunn, G., Moore, T., Jayson, M., King, T.A., Herrick, A.L.: Comparison of thermography and laser Doppler imaging in the assessment of Raynaud's phenomenon. Microvasc. Res. **66**(1), 73–76 (2003)
18. Schlager, O., Gschwandtner, M.E., Herberg, K., Frohner, T., Schillinger, M., Koppensteiner, R., et al.: Correlation of infrared thermography and skin perfusion in Raynaud patients and in healthy controls. Microvasc. Res. **80**(1), 54–57 (2010)
19. Cheng, K.-S., Yang, J.-S., Wang, M.-S., Pan, S.-C.: The application of thermal image analysis to diabetic foot diagnosis. J. Med. Biol. Eng. **22**(2), 75–82 (2002)
20. Sivanandam, S., Anburajan, M., Venkatraman, B., Menaka, M., Sharath, D.: Medical thermography: a diagnostic approach for type 2 diabetes based on non-contact infrared thermal imaging. Endocrine **42**(2), 343–351 (2012)
21. Ring, F.: Thermal imaging today and its relevance to diabetes. J. Diab. Sci. Technol. **4**(4), 857–862 (2010)
22. Huang, C.-L., Wu, Y.-W., Hwang, C.-L., Jong, Y.-S., Chao, C.-L., Chen, W.-J., et al.: The application of infrared thermography in evaluation of patients at high risk for lower extremity peripheral arterial disease. J. Vasc. Surg. **54**(4), 1074–1080 (2011)
23. Allen, J., Overbeck, K., Nath, A.F., Murray, A., Stansby, G.: A prospective comparison of bilateral photoplethysmography versus the ankle-brachial pressure index for detecting and quantifying lower limb peripheral arterial disease. J. Vasc. Surg. **47**(4), 794–802 (2008)

Reproducibility of Thermal Images: Some Healthy Examples

Audrey Macdonald, Nina Petrova, Suhail Ainarkar, John Allen, Peter Plassmann, Aaron Whittam, John Bevans, Francis Ring, Ben Kluwe, Rob Simpson, Leon Rogers, Graham Machin and Mike Edmonds

Abstract Thirty participants with healthy feet were imaged in the same way on two separate occasions (an average of 4 weeks apart). Overall, feet were found to be thermally symmetric although absolute temperature could vary considerably between visits. Temperature differences at specific sites on the foot sometimes exceeded the threshold of 2.2 °C regarded as clinically significant when looking for evidence of inflammation prior to skin breakdown in diabetes. At least one site exceeded this threshold in nine (30%) participants (the same figure for both visits). However, when looking for significant thermal asymmetry it is important to rule out transient changes by repeated imaging and to refer to baseline images.

keyword Thermal imaging · Thermal symmetry · Diabetic foot ulcer

A. Macdonald (✉) · J. Allen
Microvascular Diagnostics, Northern Medical Physics and Clinical Engineering Department, Freeman Hospital, Newcastle upon Tyne Hospitals Trust, Newcastle upon Tyne, UK
e-mail: Audrey.Macdonald2@nuth.nhs.uk

N. Petrova · M. Edmonds
Diabetic Foot Clinic, King's College Hospital Foundation Trust, London, UK

S. Ainarkar · J. Bevans
Community Podiatry Department, Pennine Acute Hospitals Trust, Manchester, UK

P. Plassmann
Photometrix Imaging Ltd., Pontypridd, UK

A. Whittam · R. Simpson · L. Rogers · G. Machin
National Physical Laboratory, Teddington, London, UK

F. Ring · B. Kluwe
University of South Wales, Pontypridd, UK

E.Y.K. Ng and M. Etehadtavakol (eds.), *Application of Infrared to Biomedical Sciences*, Series in BioEngineering,
DOI 10.1007/978-981-10-3147-2_15

1 Introduction

Thermal imaging has attracted attention as a fast, comprehensive and non-contact way to measure the fundamental physiological parameter, skin temperature. The colourful temperature 'maps' generated are capable of quick interpretation and easily comparable to 'healthy' or baseline images (see Fig. 1). However, it is important when interpreting images to be sure that the images are truly comparable and to have an understanding of what variability can be expected.

Thermal imaging of the skin is complicated by numerous factors. Some of these factors can affect how 'true' the temperature measurements are by affecting the emissivity of the skin. They include perspiration, hair and the use of skin creams. Physiological factors for an individual can affect actual skin temperatures and these include caffeine, certain medications, exertion and possibly time of day or point in menstrual cycle [1].

A good data collection study which seeks to establish baseline temperatures and 'maps' should be designed to minimise the impact of factors which affect accuracy of measurement. The protocol should be clear about which physiological factors it is controlling so that the relevance of the data to other studies or subject groups can be determined.

However, not all factors can be reliably controlled. As is the case with many types of test, thermal imaging would perform best in highly specific, controlled conditions which minimise normal variation but the simplicity and accessibility of thermal imaging and visual interpretation of images suits a fast test available in multiple settings [2]. For example, there have been studies on thermal imaging in operating theatres, podiatry clinics and even airports [3–5]. Measurements done in these settings will inevitably involve compromising some environmental and physiological factors which are known to affect variability.

In addition to this problem, published studies seldom describe the reproducibility of temperature measurements or maps on a day to day basis.

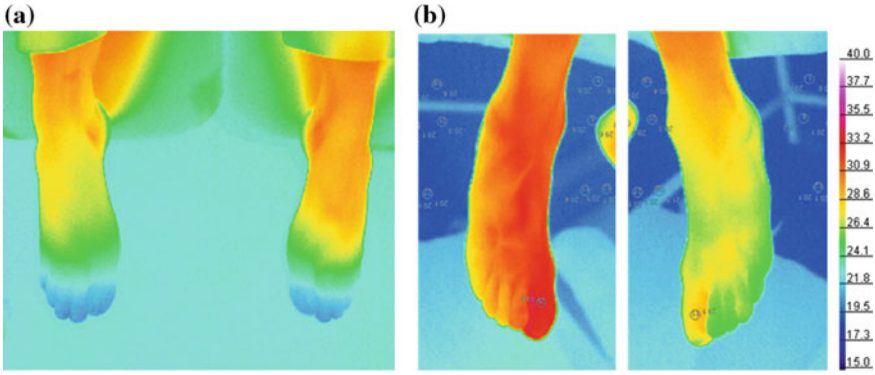

Fig. 1 Dorsal view of **a** healthy feet and **b** foot demonstrating increased temperature attributed to an ingrowing toenail on the right 1st toe (not one of the study group)

2 Research Context

2.1 Thermal Imaging, Spot Measurements, and the 'at Risk' Foot

Thermal imaging is gaining interest from practitioners who care for patients with diabetes. Foot ulcers are a serious complication for patients with diabetes who may also have neuropathy or peripheral or systemic vascular disease. In particular, patients with neuropathy are at increased risk of damaging their feet without the warning signs of discomfort or pain. Research has suggested that hotspots seen on the foot could give early warning of ulcer formation [6, 7]. These studies involved patients measuring spot temperatures with an infrared thermometer at corresponding sites on their feet at home and comparing right with left. Spot temperature differences greater than or equal to 2.2 °C were defined as significant. This threshold appears to have been widely accepted, considering the studies which have followed from the successful results reported [8]. Thermal imaging has the potential to compare all sites on the foot simultaneously and further studies have begun to investigate the possibility of imaging the feet in the podiatric clinic setting; however, regular checking of foot health is the goal of every podiatrist for patients with at risk feet. The aspiration is daily monitoring of foot health either in the patient's home or at least in accessible, non-specialist clinic settings such as GP surgeries.

The research which suggested patients' risk of foot ulceration improved if they monitored their skin temperatures daily could not rule out the effect of responding to random temperature differences [7]. The temperature monitoring group had reduced ulceration rates but also more contact with the study coordinator and more periods of rest (triggered by measuring temperature differences between right and left feet). The validity of comparing contralateral foot temperatures and images must depend on how consistent they are when no pathological change is suspected. Any measure of thermal asymmetry must be designed to be specific enough to confidently suggest pathology such as inflammation.

2.2 Diabetic Foot Ulcer Prevention System (DFUPS)

The Microvascular Diagnostics section of the Northern Medical Physics and Clinical Engineering Dept (part of Newcastle upon Tyne Hospitals NHS Trust) is in collaboration with King's College Hospital (London), Pennine Acute Hospitals Trust, Photometrix Imaging Ltd. and the National Physical Laboratory to complete a project funded by the National Institute for Health Research. The project aims to investigate the use of thermal imaging when managing patients at high risk of developing foot ulcers. Before patients were recruited however, an initial study was completed which was designed to collect data from participants with healthy feet. These feet had temperatures measured using the Thermofocus® infrared spot

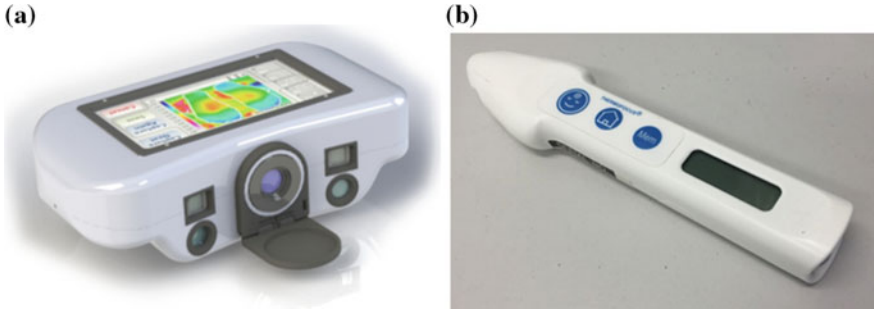

Fig. 2 **a** Diabetic Foot InfraRed Standard Thermography system (DFIRST), **b** Thermofocus® infrared spot thermometer

thermometer (see Fig. 2b) and also thermally imaged using the Diabetic Foot InfraRed Standard Thermography system (DFIRST) (see Fig. 2a). DFIRST is an experimental device that was developed by Photometrix Imaging Ltd specifically for this investigation. Visual images are captured simultaneously with the thermal information in order to aid placement of regions of interest when analysing the foot thermal image using a bespoke software package also written specifically for this investigation.

The study was approved by London-City Road and Hampstead Research Ethics Committee.

3 Method

3.1 Camera Description/Calibration

At the core of the battery-powered DFIRST device is a Micro-Epsilon TIM 400 thermal camera with a spatial resolution of 382 × 288 pixels and a thermal resolution of 0.08 °C. Before and after this investigation, the thermal camera was characterised by the National Physical Laboratory (NPL) for measurements errors such as temperature offset, start-up behaviour, short-term- and long-term measurement drift over time, and noise. Both the DFIRST thermal camera and the Thermofocus® infrared spot thermometer were calibrated by the NPL traceable to national standard blackbody references [9, 10]. Absolute temperature dependent calibration coefficients created by the work of NPL were applied as corrections to the measurements made. Overall, the DFIRST uncertainty was ±0.2 °C for the range 15–45 °C. The stated accuracy of the Thermofocus® 01500A3 thermometer used was ±0.2 °C for the range 20–35.9 °C.

3.2 Test Procedure

Healthy participants were asked to attend the Microvascular measurement facility at Freeman Hospital, Newcastle upon Tyne. The lab was set to a constant normothermic temperature of 23.5 °C. After consent was obtained for the test, participants were asked to remove their shoes and socks and rest for 10 min, seated on a podiatry couch with their legs supported and feet bare. Participants were excluded if they had active foot ulceration and/or infection or previous ulceration, a confounding foot deformity, past foot surgery, an implantable electronic device, history of high blood glucose levels, any symptoms of peripheral neuropathy or any symptom of ischemia. Intact feet and at least one palpable foot pulse (posterior tibial or dorsalis pedis) on each foot were requirements for inclusion.

The image capture order was a combined plantar foot image, combined dorsal view, right medial, right lateral, left medial and left lateral views. This required passively lowering each of the feet using the adjustable leg supports of the podiatry couch. A complete set of images were acquired at 10 min rest. Then a second set of images was acquired along with spot temperature measurements using a Thermofocus® infrared spot thermometer. The sites of the 33 spot measurements performed are illustrated in Fig. 3. The sites were chosen as the most frequent sites for ulcers to develop on the foot. The Thermofocus® measurements were performed in right/left pairs in order to keep contralateral measurements as close together as possible in time. After this, three more combined plantar views of the feet were acquired.

All 30 participants were asked to return for a second identical study. Although it is possible to obtain temperature data from the thermal images (by averaging over any selected region of interest) technical issues meant that this could not be done for all of the first visit data sets. The thermal variability results are therefore based on the Thermofocus® spot thermometer temperature measurements. However, the key conclusions are clearly illustrated by the thermal images taken at both visits.

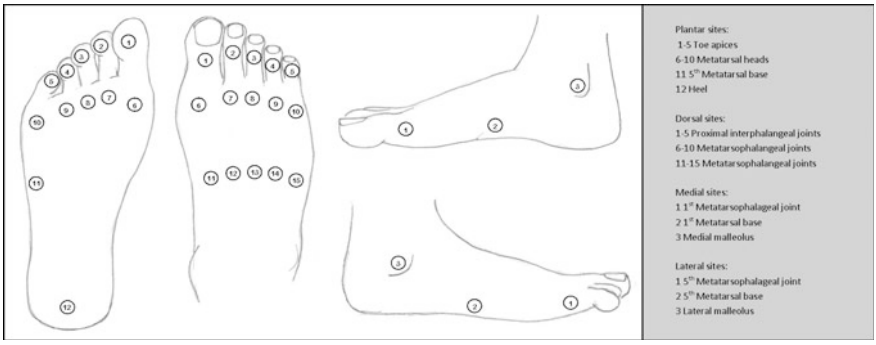

Fig. 3 The 33 measurement sites/regions of interest on the plantar, dorsal, medial and lateral aspects of the foot

4 Results

Thirty pairs of 'healthy' feet were studied at repeat visits. The average time between visits was 26.7 ± 8.2 days (3.8 ± 1.2 weeks). Table 1 details the demographics of the group studied and the results of the data analysis on whole feet. Whole foot temperature was taken to be the mean of all 33 spot temperatures measured on each foot (MFT33).

Conditions were similar at both visits and the mean foot temperatures (for the overall group) almost identical. However, individual mean foot temperatures differed between visits by up to ±4.6 °C. The symmetry between right and left feet overall for each of the two visits was comparable but greater asymmetry was demonstrated at the second visit. This is also seen when considering the individual spot measurements. Table 2 describes the distribution and number of hotspots found.

Hotspots were measured in nine participants at each visit. Five participants had at least one hotspot at both visits. Over three times as many hotspots were measured for visit 2 when compared with visit 1. However, 29 of the hotspots measured in visit 2 were accounted for by just three participants (in visit 1 these three participants only accounted for 1 hotspot).

Table 1 Demographics and temperature data statistics [expressed as mean ± standard deviation (range)]

	Visit 1	Visit 2
Age	42.6 ± 12.1 years (23–64 years)	
Height	1.7 ± 0.1 m (1.53–1.94 m)	
Weight	80.1 ± 15.2 kg (54–115 kg)	
BMI	26.7 ± 4.3 kgm^{-2} (20.9–38.9 kgm^{-2})	
Sex ratio	20 male:10 female	
Temp of room	23.5 ± 0.2 °C	23.5 ± 0.3 °C
Relative humidity of room	45.9 ± 5.3%	44.9 ± 8.9%
Mean foot temperature (An average of 33 spots: MFT33)	R: 28.3 ± 2.6 °C (24.2–33.4 °C) L: 28.2 ± 2.6 °C (24.3–33.4 °C)	R: 28.6 ± 2.5 °C (24.3–34.5 °C) L: 28.5 ± 2.5 °C (24.2–34.4 °C)
R-L MFT33	0.14 ± 0.70 °C (−0.5 to 1.0 °C)	0.16 ± 0.94°C (−1.7 to 1.7 °C)
Difference in mean foot temperatures between visits	R: 0.32 ± 1.96 °C (−4.29 to 4.41 °C) L: 0.31 ± 2.07 °C (−4.61 to 4.59 °C)	

Table 2 Hotspot distribution and spot measurement descriptive statistics [where relevant expressed as mean ± standard deviation (range)]

	Visit 1				Visit 2			
Total number of hotspots i.e. Spot measurements ≥2.2 °C or ≤−2.2 °C out of a possible total of 30 x 33 = 990	12 (1.2%)				40 (4%)			
Number of participants with at least one hotspot	9 (30%)				9 (30%)			
Number of participants with at least one hotspot at both visits	5 (17%)							
R-L difference between spot measurements	0.14 ± 0.70 °C (−2.8 to 2.8 °C)				0.16 ± 0.94 °C (−3.4 to 5.4 °C)			
Between visit difference between spot measurements	0.35 ± 2.19 °C (−8.8 to 7.8 °C)							
Number of hotspots by site (Site number/number of hotspots recorded) P-plantar D-dorsal M-medial L-lateral	P 1/1 2/2 3/0 4/0 5/2 6/1 7/1 8/0 9/0 10/0 11/0 12/1	D 1/1 2/0 3/0 4/0 5/1 6/1 7/0 8/0 9/0 10/0 11/0 12/0 13/0 14/0 15/0	M 1/1 2/0 3/0	L 1/0 2/0 3/0	P 1/0 2/3 3/4 4/2 5/5 6/1 7/0 8/2 9/2 10/0 11/0 12/0	D 1/1 2/0 3/2 4/4 5/3 6/1 7/0 8/0 9/2 10/2 11/0 12/1 13/0 14/0 15/0	M 1/2 2/1 3/0	L 1/2 2/0 3/0

The maximum temperature change measured for one of the spot sites between visits is −8.8 °C (fifth toe). The thermal images show the whole feet are much warmer at the first visit (see Fig. 5A). MFT33 for that participant cooled by 4.6 °C between visits.

The biggest temperature increase recorded between visits was 7.8 °C for the fourth toe. The thermal images show that the whole feet are much cooler at the first visit (see Fig. 5B). The MFT33 increased by 4.4 °C between visits.

Figure 4 is a Bland–Altman plot of MFT33 between visit variability [11]. A larger sample size would be needed to determine if there is a significant difference between male and female absolute temperatures, and their variability between visits.

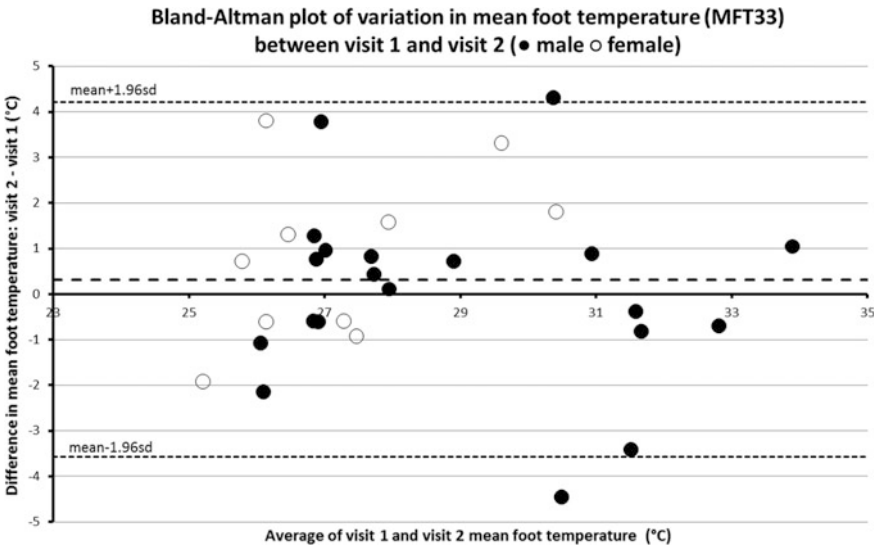

Fig. 4 Bland–Altman plot of mean foot temperature (MFT33) between visit variability. MFT33 is a measure of foot temperature derived from 33 spot temperature measurements from all four aspects of the foot (plantar, dorsal, medial and lateral)

5 Discussion

5.1 Right/Left Thermal Symmetry

It is important when discussing thermal symmetry between right and left regions of interest to be clear how the data has been presented. In our results relative temperature differences have been reported which preserves the sign or direction of the asymmetry. Unless a foot equivalent of handedness influences thermal symmetry we would expect a spread of thermal differences around zero, with the standard deviation giving information about the extent of asymmetry observed. Previously published studies have not always been clear about this, so it is not always possible to compare the results of similar studies. This study has demonstrated a thermal bias to the right of 0.15 °C (the average of the two visits). Although a bias due to handedness may be possible, analysis of equivalent regions of interest using the thermal image data acquired by the thermal camera for the second study generates a mean difference much closer to zero (0.03 °C ± 0.99 °C). This difference could have arisen due to the Thermofocus® measurements not being simultaneous. The analysis of regions of interest performed on the thermal images was predominantly performed on views which captured both feet simultaneously. Therefore the slight offset to the right seen in the Thermofocus® results could be due to gradual cooling of both feet (the right foot measurement was always performed first and 77% participants experienced their feet cooling over the course of the study in visit 2).

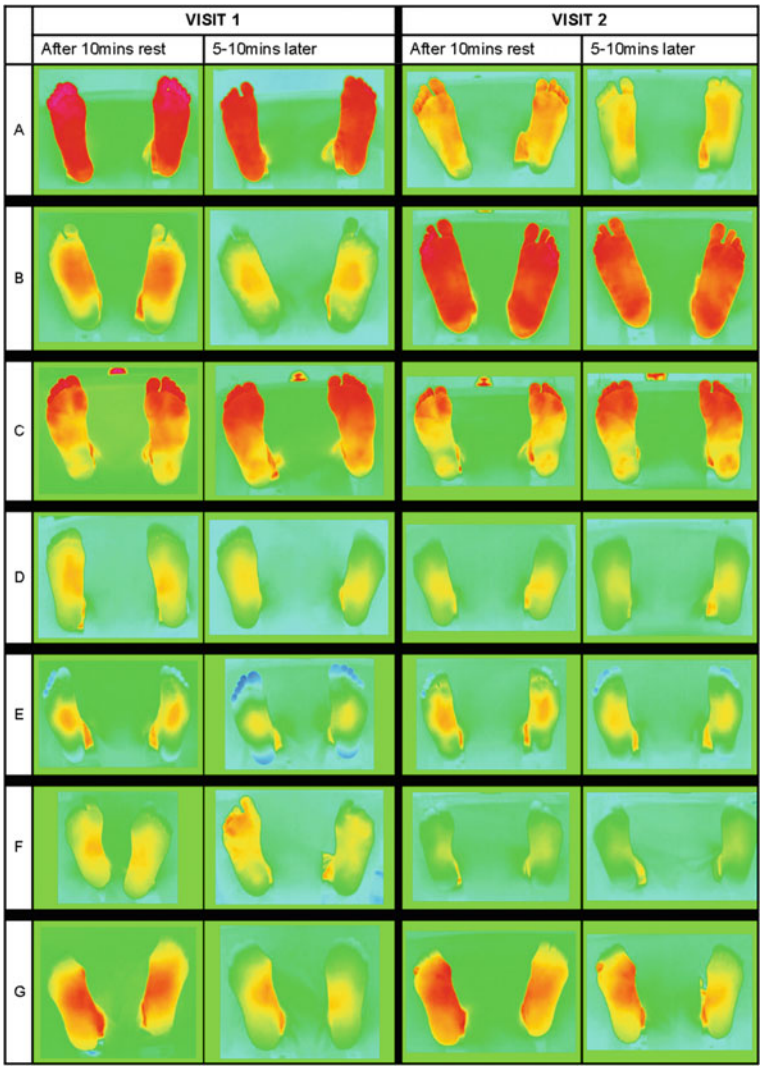

Fig. 5 Images from visit 1 and visit 2 for selected participants *A*–*G* (seven examples from the 30 studied). *A* and *B* exhibit large differences in mean foot temperature between visits whilst maintaining thermal symmetry. *C*, *D* and *E* are thermally symmetric and more consistent between visits although they illustrate the variety of thermal patterns seen. *F* and *G* exhibit thermal asymmetry. *F* undergoes vasodilation during visit 1 and *G* has a persistent asymmetry throughout visit 2 which is explained by a foot injury (see text). NB the thermal colour scale for the images is the same as that for the images in Fig. 1 (which ranges from 15 to 40 °C)

The results of this study demonstrate the large variability in foot temperatures of the feet of healthy participants. Figure 5 illustrates that although there can be big variations in mean foot temperatures from visit to visit, thermal symmetry can be preserved (see Fig. 5A, B). However, significant spot temperature differences (i.e. 2.2 °C or greater) were measured in 30% of participants. If temperature differences between contralateral areas of the feet are to be used as predictive indicators of pathology such as ulceration, the definition of a thermal hotspot needs to be refined.

5.2 Vasodilation

In our study, several factors known to influence thermography of the skin were not controlled. These factors included the consumption of caffeine, time of previous meal, footwear worn prior to the test and the level of exertion prior to the test. Consumption of caffeine, for example, can result in cardiovascular changes after a short delay. In several participants, over the sequence of images taken, it was possible to see vasodilation taking place. It often did so unevenly between the two feet and hotspot measurements were made because a snapshot of thermal symmetry captured the lag between right and left warming. The images in Fig. 5F illustrate this in visit 1. A refinement to the definition of a hotspot could be to ensure that the difference is not a transient feature. This can only be observed if more than one thermal image is taken. We recommend that taking at least two thermal images, several minutes apart, should be considered in a test to detect asymmetry.

5.3 Persistent Asymmetry

The images in Fig. 5G illustrate an example of persistent hotspots throughout a visit. At the first visit, the initially hotter first metatarsal head (MTH) cooled down over the course of the study. During the second visit, the first MTH and fifth toe on the right foot were consistently warm when compared with the rest of the same foot and the contralateral foot. Although there was no visible sign of skin trauma, the thermal images clearly show areas of increased temperature which can be explained by the participant reporting pain in those areas.

5.4 Thermal Symmetry

The images in Fig. 5C–E is examples of participants who were thermally symmetric throughout each study and were consistent between the two study visits. They are also examples of the variety of thermal patterns which can be observed in

healthy feet. Participant C had hot toes and forefoot. Participant D had fairly uniform feet throughout the study. Participant E had consistently cold toes.

5.5 Significance of Thermal Asymmetry or 'Hotspots'

The significance of thermal asymmetry or the measurement of hotspots on feet is dependent on the extent to which they can be observed in the 'healthy' population. Although several factors are known to increase thermal variability these cannot all be controlled, especially in the context of a quick test which is designed to be a monitoring tool to predict tissue damage onset. Our study has shown the importance of taking repeat images in order to rule out transient temperature differences.

5.6 Significance of Foot Temperature

Since all the participants (except perhaps G in Fig. 5) had apparently 'healthy' feet, our study suggests that there is no significance in overall foot temperature when screening for foot pathology. Some studies have found slight differences in the mean foot temperatures of different groups, but they did not follow this up with repeated measurements on the same participants [12, 13]. The magnitude of the variation we have seen between participants with healthy feet, and between visits for the same participants, makes it hard to believe that any significance can be attached to mean foot temperature at all. Foot temperature is naturally bounded by core body temperature and (roughly) room temperature (dependent on acclimatisation time). We have seen mean foot temperatures close to both extremes in just 30 participants.

6 Conclusion

The feet of healthy individuals can be very variable in absolute temperature on different days but thermal symmetry is generally maintained. Characteristic thermal patterns seem to be consistent so there may be some diagnostic value in a change in pattern or symmetry. Thermal asymmetry due to transient changes during the study period need to be ruled out with repeated images. These studies provide a baseline understanding of thermal symmetry in the feet of healthy participants which can be used when interpreting the images of the feet of patients with diabetes and neuropathy.

Acknowledgements The research was funded by the National Institute for Health Research (NIHR) II-LA-0813-20007 programme.

The views expressed are those of the author(s) and not necessarily those of the NHS, the NIHR or the Department of Health.

References

1. Fernández-Cuevas, I., Marins, J.C.B., Lastras, J.A., Carmona, P.M.G., Cano, S.P., García-Concepción, M.Á., Sillero-Quintana, M.: Classification of factors influencing the use of infrared thermography in humans: a review. Infrared Phys. Technol. **71**, 28–55 (2015)
2. Cook, R.J., Thakore, S., Nichol, N.M.: Thermal imaging–a hotspot for the future?: a case report. Inj. Extra **36**(9), 395–397 (2005)
3. Di Maria, C., Hainsworth, P.J., Allen, J.: Intra-operative thermal and laser speckle contrast imaging assessment of bowel perfusion in two cases of colorectal resection surgery. In: Ng, E.Y.K. (eds.) Application of Infrared to Biomedical Sciences, pp. TBC. Springer, Singapore (In press) (2016)
4. van Netten, J.J., Prijs, M., van Baal, J.G., Liu, C., van Der Heijden, F., Bus, S.A.: Diagnostic values for skin temperature assessment to detect diabetes-related foot complications. Diab. Technol. Ther. **16**(11), 714–721 (2014)
5. Mercer, J.B., Ring, E.F.J.: Fever screening and infrared thermal imaging: concerns and guidelines. Thermol. Int. **19**(3), 67–69 (2009)
6. Lavery, L.A., Higgins, K.R., Lanctot, D.R., Constantinides, G.P., Zamorano, R.G., Athanasiou, K.A., Armstrong, D.G., Agrawal, C.M.: Preventing diabetic foot ulcer recurrence in high-risk patients use of temperature monitoring as a self-assessment tool. Diabetes Care **30** (1), 14–20 (2007)
7. Armstrong, D.G., Holtz-Neiderer, K., Wendel, C., Mohler, M.J., Kimbriel, H.R., Lavery, L.A.: Skin temperature monitoring reduces the risk for diabetic foot ulceration in high-risk patients. Am. J. Med. **120**(12), 1042–1046 (2007)
8. Skafjeld, A., Iversen, M.M., Holme, I., Ribu, L., Hvaal, K., Kilhovd, B.K.: A pilot study testing the feasibility of skin temperature monitoring to reduce recurrent foot ulcers in patients with diabetes–a randomized controlled trial. BMC Endocr. Disord. **15**(1), 1 (2015)
9. Machin, G., Chu, B.: High quality blackbody sources for infra-red thermometry and thermography between—40 °C and 1000 °C. Imaging Sci. **48**, 15–22 (2000)
10. Machin, G., Simpson, R.C., Broussely, M.: Calibration and validation of thermal imagers. QIRTJ **6**, 133–147 (2009)
11. Bland, J.M., Altman, D.: Statistical methods for assessing agreement between two methods of clinical measurement. The Lancet **327**(8476), 307–310 (1986)
12. Bagavathiappan, S., Philip, J., Jayakumar, T., Raj, B., Rao, P.N.S., Varalakshmi, M., Mohan, V.: Correlation between plantar foot temperature and diabetic neuropathy: a case study by using an infrared thermal imaging technique. J. Diab. Sci. Technol. **4**(6), 1386–1392 (2010)
13. Papanas, N., Papatheodorou, K., Papazoglou, D., Monastiriotis, C., Maltezos, E.: Foot temperature in type 2 diabetic patients with or without peripheral neuropathy. Exp. Clin. Endocrinol. Diab. **117**(01), 44–47 (2009)

Thermal Imaging for Increasing the Diagnostic Accuracy in Fetal Hypoxia: Concept and Practice Suggestions

N.A. Urakova and A.L. Urakov

Abstract We developed a method for diagnosing fetal cerebral hypoxia with a thermal imaging camera. The method is based on the following detected principle: hypoxia and ischemia reduce the intensity of thermal radiation from tissues. Infrared thermography was performed in 35 pregnant women with a ThermoTracer TH9100XX thermal imaging camera (NEC, USA) in the temperature range of 26–36 °C. The research results showed that the local temperature of the skin in the parietal head part in live fetuses during delivery and immediately after birth ranged from 31.6 to 36.1 °C. It is found that normally an area of local hyperthermia might be observed on the top of the fetal head, and the temperature in this area might be 0.5–4.0 °C more than the temperature of the areas close to it. This area is located above the central suture of the skull, and has oblong shape. Monitoring the dynamics of temperature in the central suture allows us to evaluate the oxygen supply to fetal brain cortex during delivery. In this context, if the temperature drop areas are not observed in fetal head skin during his passing through the birth canals, it indicates the possibility of giving birth to a healthy child. In its turn, the occurrence of local hypothermia over the central suture of the skull indicates the hypoxic and ischemic damage to the fetal brain cortex and requires immediate hyper-oxygenation of the fetus blood. To increase the oxygen delivery to the fetus, we suggested giving the mother oxygen through a face mask and instruct her to breathe it in until "feeling drunk". We also suggest putting oxygen face mask on the fetus inside the mother's womb for artificial intrauterine ventilation of fetus lungs with breathing gas. In addition, in order to prevent fetal brain cortex cells from dying from hypoxia we suggested cooling the fetal head as soon as it comes out of the birth canal. We also propose to document the child health status in the final stage of childbirth by recording the dynamics of local temperature in the head skin area over the gap between the parietal skull bones with infrared thermography.

Keywords Physiological birth · Intrauterine hypoxia · Thermal imaging diagnostics · Newborn · Obstetric care

N.A. Urakova · A.L. Urakov (✉)
Institute of Mechanics, Ural Branch of the Russian Academy of Sciences, Izhevsk, Russia
e-mail: urakoval@live.ru

E.Y.K. Ng and M. Etehadtavakol (eds.), *Application of Infrared to Biomedical Sciences*, Series in BioEngineering,
DOI 10.1007/978-981-10-3147-2_16

1 Introduction

Hypoxia during childbirth is a major cause of perinatal damage to the cerebral cortex and is a leader in morbidity, disability and mortality rates in infants in the neonatal period [1]. Therefore, the threat of intrauterine fetal hypoxia in pregnancy and childbirth should be of great concern to obstetricians and gynecologists [2]. However, this problem remains unsolved, and the doctors lack safe methods for the diagnosis and monitoring of intrauterine fetal hypoxia.

With this aim in view, monitoring of the fetal heart rate is used to evaluate fetal status. Fetal heartbeat is monitored by cardiac heart murmur detection device or by measuring potential difference [1]. The murmur is detected during auscultation using a stethoscope and/or hand-held Doppler device. Ultrasound examination can also be used [3]. Electrical forces of fetal heart are detected by electrocardiograph with special sensors [4].

The informative value of these methods is reduced during labor due to the fact that the contractions of the uterus and other skeletal muscles cause electrical noise [5, 6]. This increases the error in monitoring sound and electric waves and results in the situation when sensors need to be replaced.

The study of the amniotic fluid collected by intubation is another common method for assessing fetal health [3]. This method is based on spectral changes of amniotic fluid associated with fetal excretion during severe hypoxia. It is monitored with an amnioscope or by visual observation after amniotomy. Such changes in amniotic fluid transparency are rare and exceptional [4]. Therefore, the diagnostic value of amniotic fluid transparency is limited and narrow.

At the same time, fetal hypoxia is dangerous not only for the heart, but also for the whole body. Moreover, the oxygen consumption in fetal brain is greater than in fetal heart [7–9]. The status of fetal brain cells defines future mental abilities [10]. Therefore, adequate oxygen and arterial blood supply to the fetal brain is an evidence of adequate obstetric support [1, 4, 11, 12].

In case of hemorrhagic shock in adult patients, this problem is solved by measuring the local temperature in fingertips with IR thermal imaging camera [13, 14]. However, this method is not applicable to neonates [15, 16]. In this case, the neonate's head can be used instead of the fingertips. Indeed, heat production by the neonate's brain is associated with aerobic metabolism intensity [17]. This allows us to use the dynamics of local temperature of fetal head for evaluating oxygen supply [4, 17]. However, monitoring the fetal head temperature in the delivery room and childbirth thermal imaging were not used previously for documentation of the labor process [1, 3, 10].

Nowadays continuous infrared thermal imaging of the visible part of the fetus's head skin after its appearance is not included in the list of compulsory procedures in childbirth control. As for methods for diagnosing hypoxia and/or ischemia of the fetal cerebral cortex during childbirth bearing down period, they are also unknown [18–22]. Based on the well-known role of general and local temperature in the preservation of life and health in warm-blooded mammals and humans [8, 9], recently we demonstrated high diagnostic value of infrared thermal imaging of various body parts surface for evaluating hypoxic, ischemic and drug damage in adults [5, 13, 23] and children [7, 16]. On this basis, we

developed a method for assessing the degree of hypoxic damage to the cerebral cortex and resuscitation efficacy in adults during clinical death [24]. However, this method is not suitable for diagnosis of hypoxia and/or ischemic brain injury in fetuses during bearing down labor stage. It was assumed that infrared thermography of the fetal head will reveal symptoms of hypoxic damage to the cerebral cortex in the fetus. Due to the fact that hypoxia and ischemia of any part of a human body is associated with local cooling and change in color of infrared radiation from multicolor palette of red-orange-yellow-green-blue to monocolor blue palette, the occurrence of local cooling in the skin area above the suture of fetal skull fontanel during the second labor stage may be a diagnostic symptom for brain hypoxia. Therefore infrared thermography of fetal head can be used to diagnose fetal brain hypoxia and/or ischemia in bearing down labor period and after head appearance out of the birth canals.

2 Results

Before beginning our research, we considered the following assumptions. Sudden fetal hypoxia can occur in case of placental abruption, uterine inertia and umbilical cord compression in the final stage of labor. This is due to the physiological characteristics of this stage of labor such as periodic muscular uterus contractions. When the uterine wall contracts, the uterus increases the pressure in the amniotic fluid inside it. Uterine muscles compress not only the fetus, but also the uterine blood vessels. This evacuates blood from the uterine vessels, thereby inducing hypoxia of uterus, placenta and fetus.

In the final stage of labor, there is a danger of mechanical compression of the umbilical cord. This is due to close mechanical contact between the fetus and the birth canal walls. The umbilical cord can sometimes be pressed against the birth canal wall by hard fetal body parts. This can lead to its mechanical compression, devascularization and result in fetal hypoxia.

In physiological childbirth, the fetus passes through the birth canal headfirst. Thus, during birth the fetal head comes first. The fetal head temperature is higher than ambient temperature (25–26 °C), which causes rapid evaporation of fluid. As a result of evaporation, the fetal head temperature decreases. The temperature decrease rate depends on the intensity of blood circulation in fetal head and brain. The dynamics of the head skin temperature depends on the oxygen supply to brain tissues. Local temperature of fetal head can be monitored using IR thermal imaging. This method is contactless and valid at a distance of 1–2 m. In addition, this method for monitoring fetal head temperature is virtually instantaneous.

Infrared thermography was performed in a maternity hospital in 35 pregnant women admitted for physiological birth. Preliminary ultrasonic examination of women and fetuses health status was performed before childbirth. The tests were performed using ultrasonic scanners ALOKA SSD—ALPHA 10 and Medison SonoAce_600_C with standard convex transducers with frequency 3–7 MHz in a

conventional way. The pregnant women were tested for fetal hypoxia using the Haussknecht method [25–29].

In this group, in 20 women in 30–32 weeks of pregnancy, fetuses demonstrated high adaptation to intrauterine hypoxia, which was confirmed by Gauskhneht test results (more than 30 s). In other 15 pregnant women in 30–32 weeks of pregnancy, fetuses demonstrated low adaptation to intrauterine hypoxia, which was confirmed by Gauskhneht test results (less than 10 s). Infrared thermometry was performed using Thermo Tracer TH9100XX thermal imager (NEC, USA) in the temperature range of +26 to +36 °C. The ambient temperature in the delivery room was in the range of +24 to +26 °C.

In our opinion, fetal health should be evaluated using digital parameters saved and stored as a document which can be accessed for 18 years after childbirth. In our study, this was achieved through recording digital IR images. For this purpose, we consider fetal head temperature to be the most informative parameter because the cortex has the highest intensity of oxygen metabolism and emits sufficient amounts of heat to the skin covering the skull fissures.

During our study, we found that infrared thermography of fetal head surface during labor ensures immediate delivery of accurate information on the dynamics of its local temperature values in the infrared radiation spectrum. It is shown that individual values of local skin temperature in the parietal scalp of live fetuses during labor and immediately after it were observed in the range of +31.6 to +36.1 °C. If the placental insufficiency symptoms are not observed, and the fetus has high resistance to hypoxia, then the infrared image of the parietal part of the head rarely has significant variations in colors.

In the absence of fetal hypoxia, the fontanel temperature is on the average 2.8 ± 0.21 °C ($P < 0.05$, $n = 20$) greater than cranium skin temperature. In case of severe hypoxia, the fontanel temperature is on the average only 1.5 °C greater than in the absence of hypoxia.

It was found that in normal pregnancy and normal physiological delivery, the head of live fetus is displayed on the thermal camera screen mostly in yellow-orange-red color palette. Besides, normally the temperature of infants' scalp is high (Figs. 1, 2, 3, 4, 5 and 6).

However, the scalp and body temperature in infants born with meconium-stained amniotic fluid was low. Moreover, normally an area of local hyperthermia might be observed on the top of the fetal head, and the temperature in this area might be 0.5–4.0 °C more than the temperature of the areas close to it. This area is located above the central suture of the skull, and has oblong shape (Figs 7, 8 and 9).

In the group of 15 pregnant women with placental insufficiency symptoms and with low fetal adaptation to hypoxia, the dynamics of temperature in the visible head surface during the bearing down labor stage in 10 fetuses had no fundamental differences from the dynamics of the temperature in the fetuses in the control group of mothers. But in other five fetuses we observed short periods of temperature drop in the central suture area of the scalp. The duration of these periods ranged from 30 to 120 s.

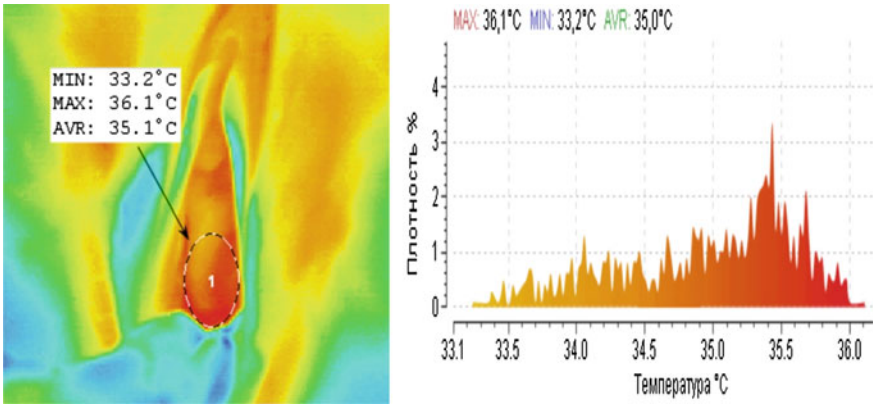

Fig. 1 Thermal camera image of perineum of mother P. and parietal part of the head surface of a live fetus at the beginning of his coming out of the birth canal in the norm

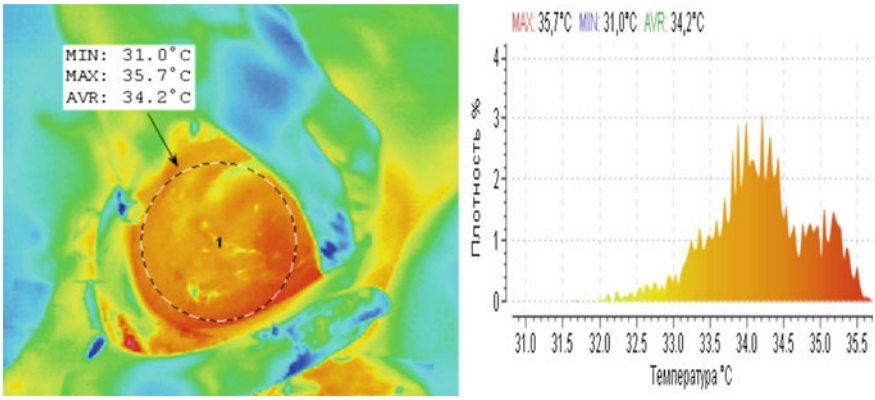

Fig. 2 Thermal camera image of perineum of mother P. and parietal part of the head surface of a live fetus at the delivery from the birth canal in the norm

We analyzed the circumstances of local hypothermia occurrence. It was found out that the immobile position of the fetus in the birth canal induced local hypothermia in the fetus' head above the central suture, whereas spontaneous labors induced rapid temperature increase (in 2–3 s) in five mothers.

The results showed that the immobility of the fetus in the birth canal enhances hypothermia in central suture area. We found that temperature image of the head in these fetuses was normalized only by artificially induced pushing of the fetuses inside the birth canal.

In addition, high informative value of thermal imaging was demonstrated during the first period after childbirth. For instance, in newly born infants the temperature during hypoxia was 32.2 ± 0.08 °C ($P \leq 0.05$, $n = 5$), while after 5 min of

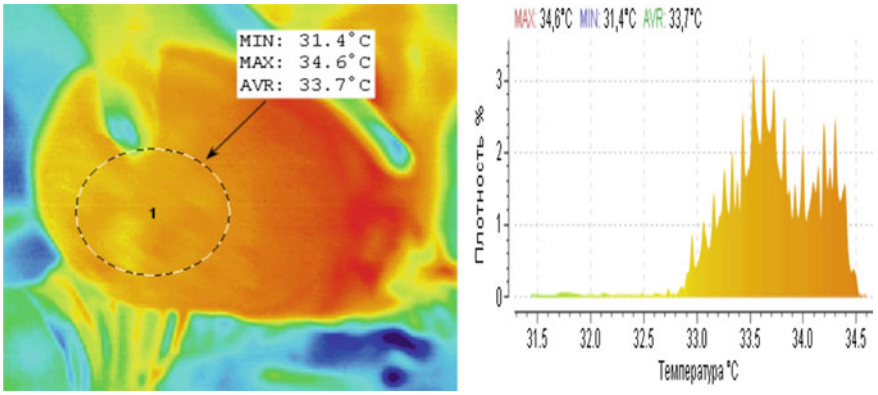

Fig. 3 Thermal camera image of parietal part of the head surface of a live fetus after delivery from the birth canal in mother P. in the norm

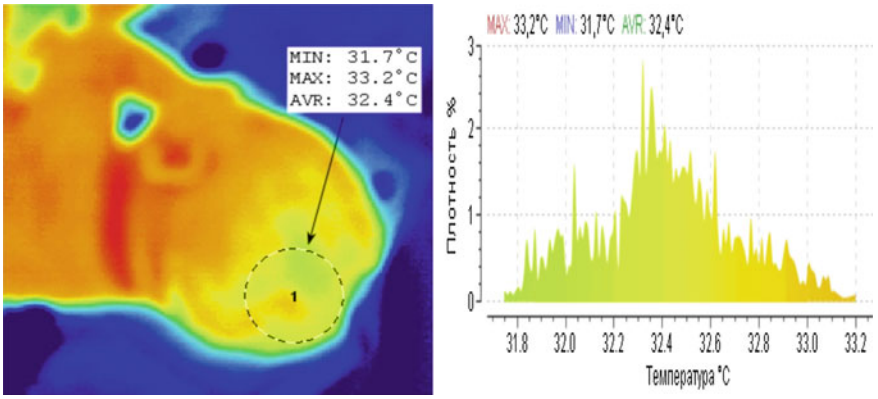

Fig. 4 Thermal camera image of the live newborn head immediately after birth from mother P. before cutting off the umbilical cord in the norm

artificial ventilation it was 34.15 ± 0.09 °C ($P \leq 0.05$, $n = 5$). In addition, neonatal hypoxia was associated with local hypothermia in their fingertips. This effect was observed together with blue skin in hands. The nose was the coolest area in the neonate's body. The average nose temperature was 30.85 ± 0.15 °C ($P \leq 0.05$, $n = 5$). The occurrence of local hypothermia in the nasolabial triangle was observed in one infant (Fig. 10).

We monitored neonates' health status during the first week after birth. From 20 neonates demonstrating high tolerance to hypoxia before birth and no signs of local hypothermia of the head skin area over central suture during labor, only one was found to have cerebral ischemia I. On the other hand, in five of 15 neonates with intrauterine hypoxia and local hypothermia of the head skin area over central suture

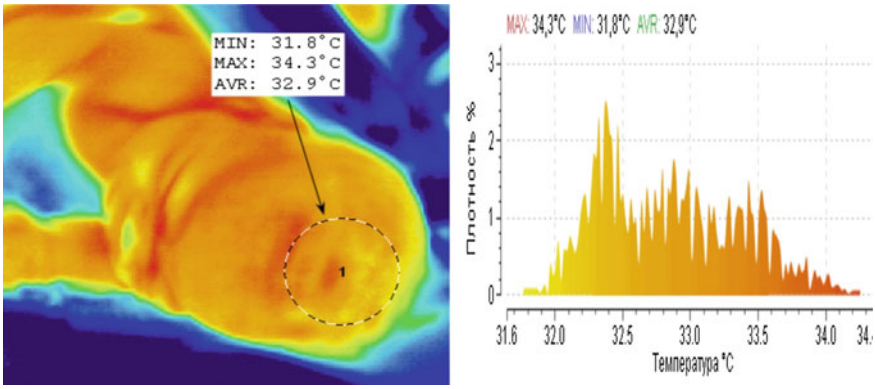

Fig. 5 Thermal camera image of the live newborn head after birth from mother P. after cutting off the umbilical cord in the norm

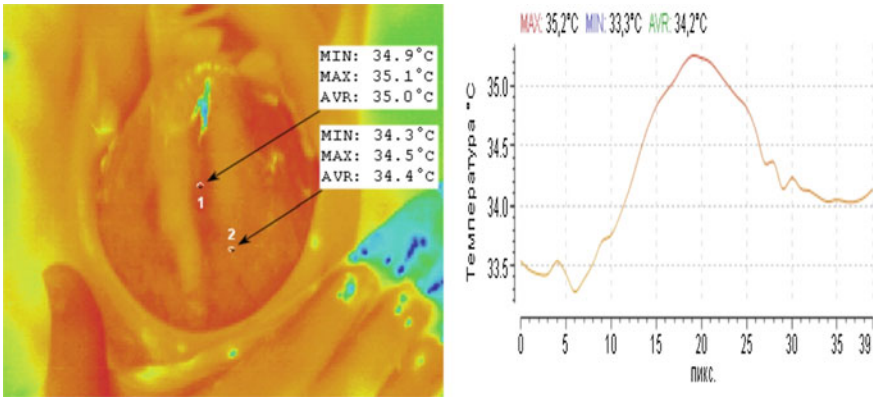

Fig. 6 Thermal camera image of perineum of mother C. and fetus head during the bearing down stage of labor. Before birth the fetus had a low resistance to intrauterine hypoxia. *Curve line* in the graph corresponds to the local temperature of the fetus head between the selected measurement points

cerebral ischemia I and II was observed. The five neonates were born with meconium-stained amniotic fluid and acrocyanosis.

Therefore, IR thermal imaging of neonate's head and body after delivery provides an informative approach to health monitoring and obstetric care quality control. Thermal imaging of the fetal head surface, performed with thermal imaging camera in the final period of labor, allows us to detect the occurrence and development of relative local hypo- and hyperthermia in the area of open central suture. In our opinion, the image of exposed and wet surface of the fetal head during its delivery surrounded by dry air at ambient temperature allows us to make conclusions about the intensity of oxidative metabolism in the brain cortex, as it is

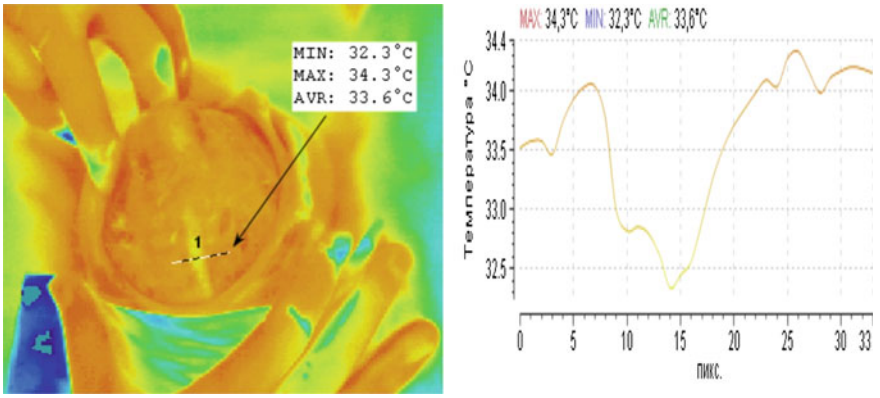

Fig. 7 Thermal camera image of perineum of mother C. and fetus head in 35 s after the termination of the uterus activity in labor. *Curve line* in the graph corresponds to the local temperature of the fetal head surface between the selected measurement points

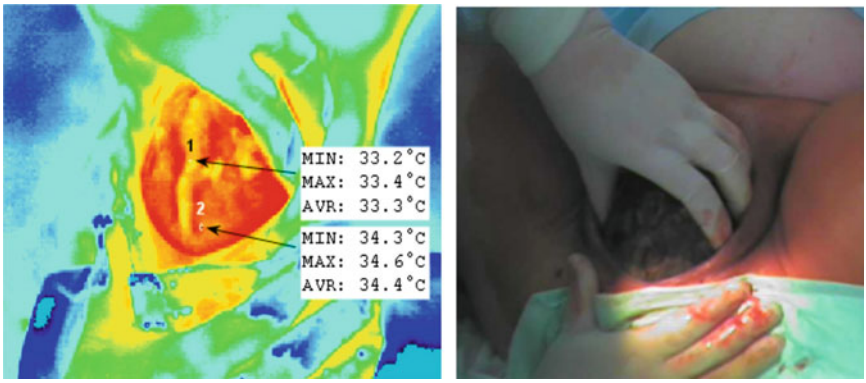

Fig. 8 Perineum of mother B. and the surface of fetal head at its coming out from the birth canal in 30 s after the termination of uterus activity during labor and the process of fetus passing through the birth canal in the infrared (**a**) and visible (**b**) ranges of the spectrum

associated with heat radiation. In its turn, the intensity of aerobic metabolism and thermal radiation enable us to make conclusions about the oxygenated arterial blood supply to cerebral cortex. Therefore, normal- and hyperthermia of the entire surface of the fetal head give bases for assuming that there is no threat of hypoxia and ischemia of the brain cortex.

Prolonged intrauterine hypoxia is the most probable cause of fetal death during abnormal labor and mental disability in newborns who underwent hypoxia and remained alive. The cells of cerebral cortex are known to be the most vulnerable to lack of oxygen, and the first to lose their functional activity and die. Nevertheless, modern standards of obstetric care still do not include methods for controlling the

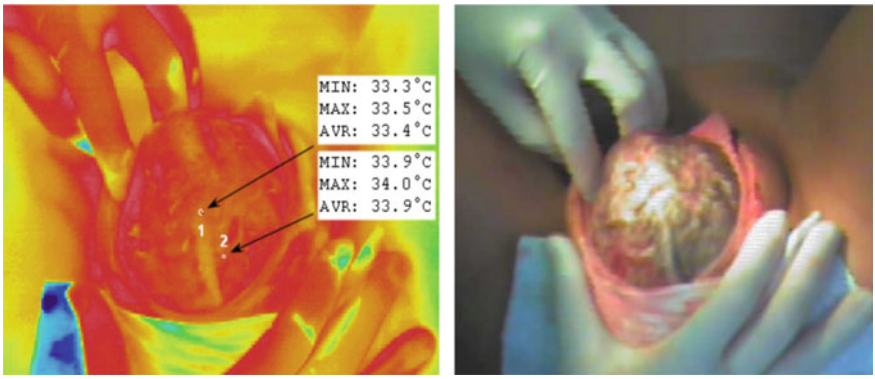

Fig. 9 Perineum of mother C. and the surface of fetal head at its coming out from the birth canal in 30 s after the completion of the uterus activity during labor and the beginning of the spot of the fetus in the birth canal in infrared (**a**) and visible (**b**) ranges of the spectrum

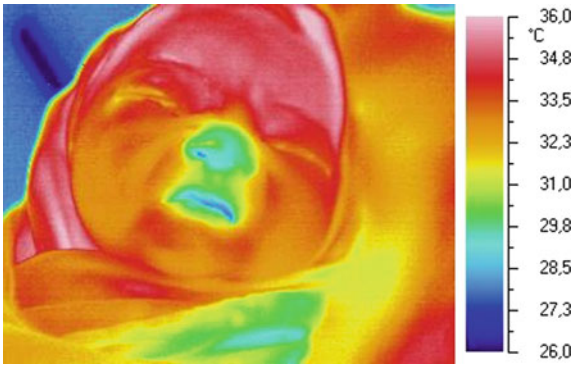

Fig. 10 IR image of neonate's face diagnosed with hypoxia in 30 min after birth

intensity of aerobic metabolism in fetal brain cortex in the final stage of physiological labor in real time.

Recently, with infrared thermography and thermal imaging cameras being introduced in medical practice, it has been revealed that monitoring the dynamics of local temperature of the body surface in humans and animals with a thermal imaging camera allows us to diagnose the occurrence and development of local hypothermia areas due to hypoxia and ischemia in a safe and contactless manner. We were the first to establish that the temperature of the parietal area of the head in newborns after coming out of the birth canal decreases in case of hypoxia and increases in case of hyperoxia.

At the same time, we found that the temperature of the head surface in adults with burr hole in the skull also depends on the efficiency of oxygen supply in real time. We found that local temperature drop is observed in 11–13 s in finger pads and in 50–60 s in the trepanation area after the beginning of voluntary apnea. The recovery of respiration begins to raise the local temperature in finger pads and in the

area of burr hole in the skull simultaneously after 2–5 s. Then, after 1–2 min, the local temperature returns to its initial value, and then continues to increase and may exceed its initial value by 0.1–1.5 °C. As a result, the area of local hyperthermia occurs in the former local hypothermia area (Figs. 11 and 12).

Thus, by monitoring the local temperature of the head surface over open suture and skull fontanelle in newborns and over the burr hole in adults, we can carry out inference about the sufficiency of oxygen supplied by the arterial blood to the cerebral cortex, and about the efficiency of lungs ventilation with breathing gas. Therefore, our data creates hope that monitoring local temperature of fetal head after its coming out of the birth canal and adult head with a burr hole with infrared imaging camera may become a new radiology method for evaluating oxygen supply to the cells of cerebral cortex.

Based on these results and on the theoretical concepts about the relationship between aerobic metabolism and the local temperature, we presented several inventions aimed at saving fetal brain cells from hypoxic damage during pregnancy and childbirth. To increase the oxygen delivery to the fetus, we suggested giving the mother oxygen through a face mask and instruct her to breathe it in until "feeling drunk" [21]. We also suggest putting oxygen face mask on the fetus inside

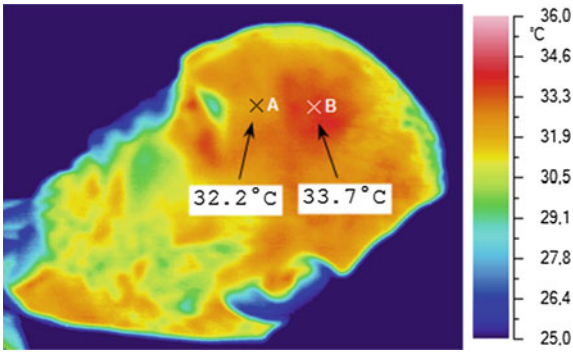

Fig. 11 The head of the patient V., 56 y.o., in 12 days after trepanation at normal blood oxygenation level (control). *Arrows* indicate the values of scalp surface temperature at point *A*—over the intact surface and at point *B*—over the burr hole

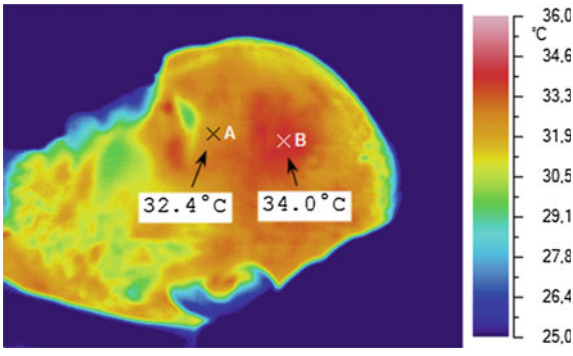

Fig. 12 The head of the same patient V., 56 y.o., with a burr hole in the skull in 60 s after voluntary apnea and in 3 min after the intensive recovery of respiration. *Arrows* indicate the values of scalp surface temperature at point *A*—over the intact surface and at point *B*—over the burr hole

the mother's womb for artificial intrauterine ventilation of fetus lungs with breathing gas [12]. In addition, in order to prevent fetal brain cortex cells from dying from hypoxia we suggested cooling the fetal head as soon as it comes out of the birth canal [20]. We also propose to document the child health status in the final stage of childbirth by recording the dynamics of local temperature in the head skin area over the gap between the parietal skull bones with infrared thermography [10]. Finally, we developed lymph substitute agent injected into the cerebral cortex and aimed at preserving cells viability during hypoxia and ischemia [30].

3 Conclusion

Out findings showed that infrared thermal imaging provides real-time monitoring of delivery process as well as the dynamics of local body temperature of the neonate; it is insensitive to acoustical, mechanical and electrical noises caused by sudden muscular contractions and electrical forces variation in the labor process. This technique allows monitoring the temperature variations in different areas of the fetal head skin, providing timely diagnosis of sudden intrauterine hypoxia and controlling its duration. Detecting local hypothermia areas over the central suture or frontal fontanel also contributes to prognosis of neonatal encephalopathy.

IR thermal imaging provides contactless monitoring of the neonate's head temperature, thereby providing real-time quality control of obstetric care during labor and immediately after delivery. The occurrence of local hypothermia area above the central suture and fontanel can be regarded as an evidence of oxygen deficiency and intrauterine hypoxia. In normal labor and in the absence of intrauterine hypoxia, the head skin temperature over the suture should not be lower than the temperature of the areas close to it. Local hypothermia over the central suture and/or fontanels is an evidence of insufficient arterial blood and oxygen supply to the brain, i.e. brain hypoxia and/or ischemia. Long-term local hypothermia increases the danger of neonatal encephalopathy.

Thus, IR thermal imaging of the neonate's head during the labor and immediately after delivery provides a new approach to labor monitoring and obstetric care quality control. During the final labor stage, this technique provides safe diagnosis of intrauterine hypoxia and its danger to the neonate's brain, and involves obstetric care correction. We believe this method might have favorable prospects in decreasing the neonatal mortality and neonatal encephalopathy.

Infrared thermal imaging also enables taking digital videos and photographs of the fetus, which can be saved and stored in USB flash drive.

References

1. Troiano, N.H., Harvey, C.J., Chez, B.F. (eds.): High Risk and Critical Care Obstetrics. Wolters Kluwer/Lippincott Williams and Wilkins Health, Philadelphia (2013)
2. Radzinsky, V.E., Urakov, A.L., Urakova, N.A., Gauskneht, M.Y.: Assessment of the sustainability of the fetus to intrauterine hypoxia during the period of breath-holding a pregnant woman reproductive health. East Eur. **1**, 119–127 (2012)
3. Kennedy, B.B., Ruth, D.J., Martin, E.J. (eds.): Intrapartum Management Modules: a Perinatal Education Program. Wolters Kluwer/Lippincott Williams and Wilkins Health, Philadelphia (2009)
4. Leveno, K.J., Alexander, J.M., Bloom, S.L., et al.: Williams Manual of Pregnancy Complications. McGraw Hill Professional, New York (2012)
5. Urakova, N.A., Urakov, A.L.: Heat radiation the surface of the head of the fetus as an indicator of security of the cerebral cortex oxygen delivery. Med. Exam. Probl. **3–4**, 32–36 (2012)
6. Urakova, N.A., Urakov, A.L., Gauskneht, Y.: Innovative features of the sustainability assessment of the fetus to hypoxia. In: Modern Problems of Science and Education 1. URL: www.science-education.ru/101-5328 (2012)
7. Urakova, N.A.: Decrease of the temperature of the head of the fetus during birth as a symptom of hypoxia. Thermol. Int. **23**(2), 74–75 (2013)
8. Urakov, A.L.: Cold in the heart protection. Sci. USSR **2**, 63–65 (1987)
9. Urakov, A.L.: Recipe for temperature. Science and Life **9**, 38–42 (1989)
10. Urakova, N.A., Urakov, A.L.: Diagnosis of intrauterine brain hypoxia using thermal imaging video monitoring of the fetus. Biomed. Eng. **48**(3), 111–115 (2014)
11. Evans, A.T., Niswander, K.R.: Manual of Obstetrics. Lippincott Williams and Wilkins Health, Philadelphia (2000)
12. Urakov, A.L., Urakova, N.A., Kasatkin, A.A., et al.: Vnutrimatochnyj akvalang N.A. Urakovoj i sposob ventilirovanija legkih ploda dyhatel''nymi gazami. RU Claim 2010134466/14, 27 Feb (2012)
13. Ammer, K.: Temperature of the finger tips in subjects with suspected Raynaud´s phenomen. In: Nowakowski,A., Mercer, J. (eds.) Advances of Infra-Red Thermal Imaging in Medicine (Warsaw, 30 June–3 July 2013). Lecture notes of the ICB Seminar, Warsaw, pp. 95–98 (2013)
14. Urakov, A.L., Kasatkin, A.A., Urakova, N.A., et al.: Infrared thermographic investigation of fingers and palms during and after application of cuff occlusion test in patients with hemorrhagic shock. Thermol. Int. **24**(1), 5–10 (2014)
15. Urakov, A.L., Urakova, N.A., Urakova, T.V., et al.: The impact of short-term hypoxia and ischemia on the temperature of the hands and color their images on the screen of the imager. Med. Almanac **2**, 299–301 (2010)
16. Urakov, A., Urakova, N., Kasatkin, A.: Temperature of newborns as a sign of life in Russia—time to change in World? J. Perinat. Med. **41**, 473 (2013)
17. Minamisawa, H., Smith, M.L., Siesjo, B.K.: The effect of mild hyperthermia and hypothermia on brain damage following 5, 10, and 15 minutes of forebrain ischemia. Ann. Neurol. **28**, 26–33 (1990)
18. Urakov, A.L., Urakova, T.V., Urakova, N.A., et al.: Sposob spasenija ploda pri vnezapnoj vnutriutrobnoj gipoksii. RU Claim 2011109952/14. 27 September 2012
19. Urakov AL, Urakova NA, Radzynsky VE et al (2014) Method for assessing fetus resistance to obstetric hypoxia. RU Patent 2,511,084, 10 April 2014
20. Radzynsky, V.E., Urakov, A.L., Urakova, N.A.: Method of protecting fetus from hypoxic damage in labor. RU Patent 2,503,414, 10 January 2014
21. Radzynsky, V.E., Urakov, A.L., Urakova, N.A.: Method of obstetric assistance in travails. RU Patent 2,502,485, 27 December 2013

22. Urakov, A.L., Urakova, N.A., Radzynsky, V.E., et al.: Sposob akusherskogo posobija. RU Claim 2014110156/14, 27 September 2015
23. Urakov, A.L., Urakova, N.A., Rudnov, V.A., et al.: Remedial and anesthetic thermocontrastable and thermal imaging termographiya tissues the groin area when vaginitis and phimosis. Ural Med. J. **10**, 152–156 (2010)
24. Urakov, A.L., Rudnov, V.A., Kasatkin, A.A., et al.: Method of determining stage of hypoxic injury and probability of recovery by Urakov, A.L. RU Patent 2,422,090, 27 June 2011
25. Urakova, N.A., Gauskneht, M.Y.: Forewarned is forearmed. Fetal hypoxia: new diagnostic possibilities. status praesens. Gynecol. Obstet. Barren Marriage **8**, 70–73 (2012)
26. Urakova, N.A., Urakov, A.L., Gauskneht, M.Y., et al.: Transabdominal ultrasound examination of the stability of the fetus to intrauterine hypoxia. Bull. Ural Med. Acad. Sci. **3**, 80–83 (2011)
27. Urakov, A.L., Urakova, N.A., Sokolova, N.V., et al.: Method for assessment of foetus resistance to hypoxia by Gauskneht, M.Y. RU Patent 2,432,118, 27 October 2011
28. Urakov, A.L., Urakova, N.A., Urakova, T.V., et al.: Method for labor by Sokolova, N.V. RU Patent 2,441,592, 10 February 2012
29. Urakov, A.L., Urakova, N.A., Kasatkin, A.A.: NA Urakova's method for antenatal assessment of foetal adaptation to repeated hypoxia. RU Patent 2,529,377, 27 September 2014
30. Urakov, A.L.: Lympho-substitute for local maintaining viability of organs and tissues in hypoxia and ischemia. RU Patent 2,586,292, 10 June 2016

Active Dynamic Thermography in Medical Diagnostics

Mariusz Kaczmarek and Antoni Nowakowski

Abstract This is an overview of active thermal imaging methods in medical diagnostics using external thermal stimulation. In this chapter, several clinical cases diagnosed using the active dynamic thermography method, ADT, are presented. Features of this technology are discussed and main advantages underlined. Applications in skin burn diagnostics and quantitative evaluation leading to modern classification of burned patients for further treatment are shown. Also the use of thermal imaging in cardiosurgery is discussed. A method of quantitative evaluation of the healing progress of post-cardiosurgery wounds is presented. The ADT method gives quantitative description of thermal structural data, supplementing well-established static thermal imaging that carry functional physiological information. Combination of both modalities supports the idea of modern multimodality approach in medical diagnostics.

Keywords Thermal imaging · Thermal stimulation · Signal processing · Thermography

1 Introduction—Thermal Non-destructive Testing Methods

InfraRed Thermal Imaging (TI), for the first time applied to medical diagnostics by Barnes [1] in sixties XX-century, allows to analyze physiological processes manifested by abnormal distribution of temperature at the surface of a human body. Overview of TI history may be found in many articles [2, 3]. Probably the most comprehensive handbook dealing with thermal imaging in medicine is the monograph [4]. Hot or cold spots indicate different metabolic processes but also strongly

M. Kaczmarek (✉) · A. Nowakowski
Gdansk University of Technology, Narutowicza 11/12, 80-233 Gdansk, Poland
e-mail: mariusz.kaczmarek@eti.pg.gda.pl

A. Nowakowski
e-mail: antowak@biomed.eti.pg.gda.pl

E.Y.K. Ng and M. Etehadtavakol (eds.), *Application of Infrared to Biomedical Sciences*, Series in BioEngineering,
DOI 10.1007/978-981-10-3147-2_17

depend on heat exchange conditions and are not specific. Therefore interpretation of diagnostic value of skin temperature distribution is difficult and requires careful preparation of a patient in stable environmental conditions.

Another thermal diagnostic value offer several methods using intentional heat exchange processes, known in industry since late eighties as *thermographic non-destructive testing* (TNDT) called also *infrared non-destructive testing* (IR-NDT). All of those methods using the same IR-thermal cameras and registration of dynamic temporal distribution of temperature, following external excitation, allow insight into internal structure of a tested object. Such analysis requires knowledge of boundary conditions and may be called model based. As the result analysis of transient thermal images existing at the surface of a tested object is giving structural information. In medicine we proposed one of such methods called *Active Dynamic Thermal IR-imaging (ADT)* as a new diagnostic modality, what we recently reported for the last 15 years [5]. In this chapter, we summarize this experience showing a few cases of practical value of ADT in clinical diagnostics.

The idea of material testing by any of active thermography methods is based on forcing heat flows in a tested structure and observation of transient thermal processes at its' visible surface, allowing further analysis of thermal transients using model-based approach. In effect visualization of material subsurface structure and existing abnormalities or failures is possible and leads to application of thermal testing in many technical fields [6]. There are numerous ways of excitation and following data treatment described in this book. Analysis of the progress of all quantitative thermal methods applied up to date is possible by studying materials of following Quantitative Infrared Thermography Conferences [7]. In medicine, one of the most frequently applied methods is pulse excitation, heating or cooling, here called Active Dynamic Thermography (ADT). For evaluation of tested structures parametric images are calculated mainly using multi-exponential approximation parameters as quantitative descriptors. The measurement procedure requires use of heat excitation, heating or cooling, to be applied to the object under test (OUT). Thermal response at the surface of OUT to external excitation is recorded using IR camera. Usually during excitation, the tested surface is of limited visibility by an IR camera, therefore the phase of natural recovery to initial conditions after excitation gives more reliable data for further analysis.

It is worth to mention that measurements of thermal transient processes allowed proposing the method called *thermal tomography* (TT). Vavilow and others, dealing with IR-NDT, proposed this term already 30 years ago [8–10]. According to the common meaning of the word *tomography,* this proposal was not correct as instead of using real reconstruction of a tested structure, existing in all tomographic procedures, they proposed so called *maxigrams* as diagnostic descriptors. Real thermal tomography approach was presented in 2003 [11]. The dynamic response recorded as a series of IR images allows reconstruction of properties of the equivalent thermal model. Either thermal properties of the model (for assumed structure of the OUT) or the internal structure (for known material thermal properties) may be determined and recognized. Even today the concept of using TT is not new; this modality may be practically regarded as a research tool only because

in real technical and medical applications it is not practical. Reconstruction algorithms are rather slow, 3D thermal models required to run the reconstruction are complicated and identification of boundary conditions is problematic. In consequence results of the research in TT are known, but it is difficult to find its' practical application in clinical or technical diagnostics.

Another more successful approach is the procedure called thermographic signal reconstruction (TSR) [12]. Here also pulse excitation is applied and shapes of transient thermal processes are approximated by multi-exponential functions. Additionally derivatives are calculated allowing enhanced visualization quality of tested structures. Recently this method was applied in medicine, based on analysis of the thermal processes after temporal occlusion stopping blood circulation. This experiment shows that even complicated physiology processes may be evidenced using this approach [13, 14].

In medicine, thermographic registration after external energy excitation was applied probably for the first time around 30 years ago [15]. To force heat flows the microwave excitation was applied *in vivo* on mice with induced tissue of the breast cancer. Again we proposed to use ADT in medicine and published early results of animal experiments [16–18]. As a handy procedure for visualization of affected regions we proposed the use of synthetic pictures of exponential model parameters, describing thermal transient processes at the phase of natural recovery to equilibrium after external pulse excitation [19, 20]. In this case, equivalent thermal model parameters of tested region of interest (ROI) are calculated allowing quantitative data visualization.

The main advantage of ADT in medicine is possibility of short thermal interaction with a tested region, as normally biofeedback processes may be activated strongly influencing on measurement results. On the other hand there are several practical issues limiting use of ADT in medical applications. For many years heating was regarded as almost ideal solution using optical or microwave energy, being fully aseptic and handy. Unfortunately, distribution of microwave energy is hardly controlled and optical excitation is usually nonuniform. Additionally the level of heating is strictly limited to 42 °C; higher value is damaging living cells and organs. Finally boundary conditions are usually uncontrolled, as temperature along superficial tissue is decreasing due to heat exchange at the skin surface. In such conditions, temperature gradient after heating may be low, what makes understanding of heat exchange difficult in interpretation. This leads to conclusions, that cooling, even technically more difficult, is a better solution. First, the amplitude of excitation may be higher comparing to the heating case; cooling down even to 4 °C is acceptable. For typical skin temperature equalling around 30 °C it is more than 20 °C difference; such gradient of temperature is easy and accurately measurable. Additionally the applied thermal camera shows the difference of the skin and the environment temperatures. If the tested ROI would be cooled only to the room temperature, the external heat exchange is minimized and internal heat flows are dominant, enabling better understanding of thermal phenomena and in consequence reconstruction of internal structure of a tested region. One has to remember that measurement results may strongly differ for ex vivo and in vivo experiments.

In medical diagnostics the concept and problems of validity of active dynamic thermal imaging (ADT) as well as thermal tomography (TT) or temperature signal reconstruction (TSR) are almost the same. In all three cases, the main element allowing quantitative evaluation of tested objects is the use of realistic thermal equivalent models. Practically the same instrumentation is applied in diagnostic procedure and only the data treatment and object reconstruction methods are different. Also the sources of errors influencing quality of measurements and limiting accuracy of reconstruction data are the same. Main limitations are due to necessity of using proper thermal models of living tissues, which are influenced by physiological processes and are not very accurate due to hardly controlled experiment conditions. One of important problems is correlation of thermal and physiological properties of living tissues essential for proper diagnostic interpretation of images.

ADT research results from phantoms, from in vivo animal experiments as well as from clinical applications performed in the Department of Biomedical Engineering Gdansk University of Technology and in co-operating clinics of the Medical University of Gdansk are discussed [20–27]. The results concern applications of thermal imaging in diagnostics of burns, skin transplants, cancer visualization and open-heart surgery, including study on healing processes of postoperative scars, evaluation and diagnostics. In this chapter, the problem of clinical use of ADT in skin burns and in analysis of post-cardiosurgery wound healing are presented for illustration.

2 Principles of Active Thermography Methods

The diagnostic instrumentation of all three dynamic thermography methods—ADT, TSR, and TT is the same. Central is the IR-thermal camera; most of modern research cameras with software allowing synchronization of image capture is sufficient for ADT experiments, of course the lower MRTD and higher geometry resolution the better for image quality. Very important is the excitation source, it should be able to force fast switching on and off pulses of constant energy lasting from seconds to even minutes. External thermal excitation source (heating or cooling) should be applied to a tested structure in fully controlled conditions. The basic data acquisition procedure is shown in Fig. 1.

What is very important, each patient should be carefully prepared for diagnostics. Environmental conditions should be controlled and registered, too. First, steady state temperature distribution on the region of interest (ROI) is registered using the IR camera. The following step requires pulsed thermal excitation application to the diagnosed region of interest and registration of temperature transients at the ROI surface. The driving unit synchronizes the processes of ROI excitation and thermal images registration. Usually the most important phase is recovery to the initial conditions after excitation as during excitation ROI may be not accessible. The ADT procedure may be repeated even in following days therefore careful determination of ROI is essential for proper data treatment. Visual camera (Fig. 3)

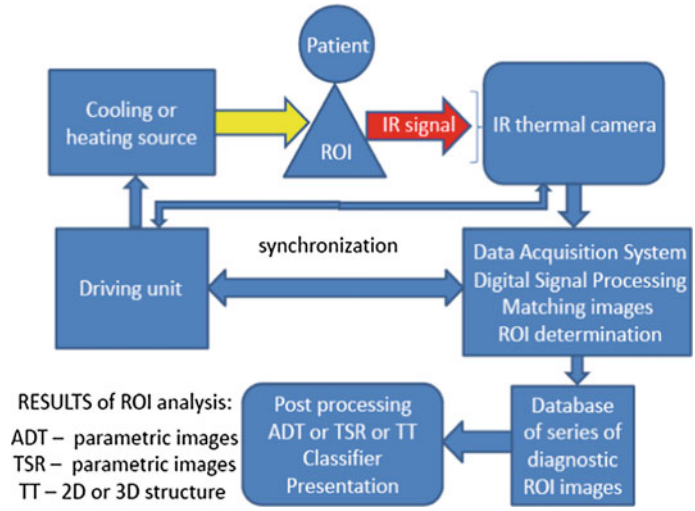

Fig. 1 Diagram of active thermography procedure

and fiducial markers may help to assure ROI determination the same in each image. All raw data are stored in the data acquisition system for further computer analysis, including geometry matching.

As in medicine, one is dealing with living patients problems of unintentional movements, breezing etc. must be solved. This requires synchronization of following images, determination of the region of interest—ROI—the same on all images in the series, and even in different days; therefore movement corrections are necessary. Usually diagnostic instrumentation is equipped in proper software packages allowing easy data manipulation and at least semiautomatic registration of images. Corrected series of images are stored in the image database for further application of ADT, TSR, or TT procedures.

In ADT, simplest equivalent multi-exponential models are applied. As the diagnostic descriptors mainly thermal time constants (τ_1, τ_2) are applied, though the magnitude Ts (temperature gradients) are also of important diagnostic values. Such descriptors are strongly correlated to a simple equivalent model, e.g., the three-layer structure described by thermal resistance $R_{\text{th}(1\text{-}3)}$ and thermal capacitance $C_{\text{th}(1\text{-}3)}$. The product $R_{\text{th}(1\text{-}3)}C_{\text{th}(1\text{-}3)}$ is equivalent to thermal time constants. In many cases, due to limited measurement accuracy only two exponential models applied are sufficient. It should be underlined that medical staff expectations concerning data manipulation is the simplest possible description!

Much more complicated is TT procedure as in this case reliable 2D or 3D structural thermal models must be applied and identified. Tomographic procedure of reconstruction and identification of model parameters is shown in Fig. 2. It may be performed after all of diagnostic images of series are properly registered and corrected serving as the reference measurement data (database of series of diagnostic ROI images). Reconstruction starts as an iterative process of identification

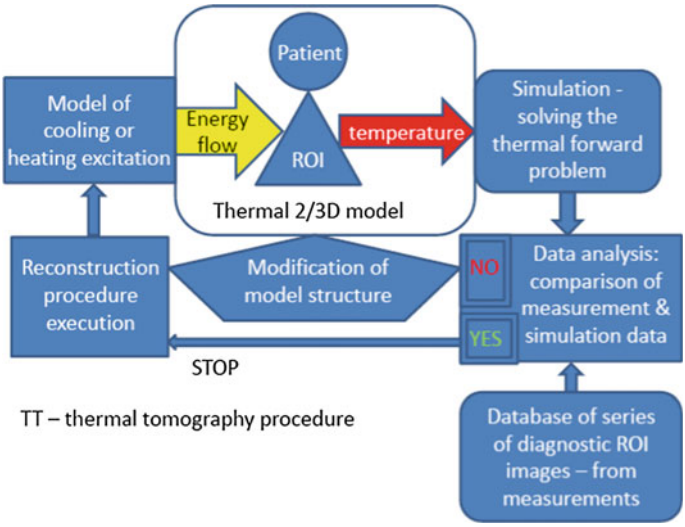

Fig. 2 Tomographic procedure of reconstruction and identification of a tested structure

parameters of the assumed model structure. Unfortunately only surface ROI temperature is known from measurements; therefore the reconstructive procedure strongly depends on the knowledge of boundary conditions and accuracy of measurements, in fact on the accuracy of reconstructed temperature transient signal in each pixel only. The simulated transient after solving the forward thermal problem is compared with measurement data. If the results of measurements and simulation are not satisfactory, the model parameters are changed and the following iterative procedure is continued. If results are convergent the reconstruction procedure stops. With a great probability the model is representing the tested structure. Unfortunately this reconstruction procedure is long and not always successful as the problem is mathematically ill posed and boundary conditions are not always properly identified. Those facts are responsible for limited interest of TT in practical applications.

In principle, the TSR method is using the same approach and instrumentation as ADT and is already broadly applied in industry IR-NDT. Heat exchange problems in medicine are much more complicated due to very complicated biological structures, additionally masked by biofeedback processes; therefore here we will stress our notice on practical discussion of ADT experiments only. In some medical experiments "internal" thermal excitation may be applied, e.g., clamping blood flow, instead of forced external cooling.

The set practically used in clinical diagnostics described in the following text is shown in Fig. 3. Two cameras—IR and RGB are applied for registration of thermal processes and visible images. Use of both cameras is essential for proper determination of ROI as RGB images are of much better spatial resolution than thermal images. Here cooling using two CO_2 cryotherapy units is applied to get relatively

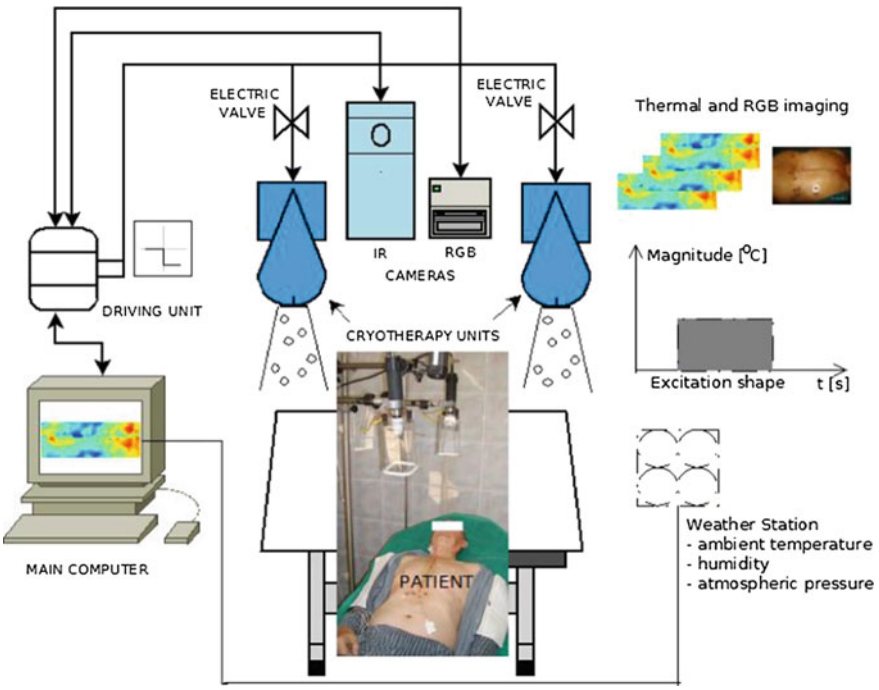

Fig. 3 ADT set in clinical environment; here diagnostics of a post-cardiosurgery wound

uniform ROI area for diagnostics. Usually excitation procedure (cooling) lasts up to 60 s, practically until ROI temperature decreases to the room temperature. At this moment coolers are switched off. The recovery phase is longer but registration of IR images is performed during no more than three cooling cycle times. This procedure was applied to skin burn diagnostics as well as to the analysis of post cardiosurgery wound healing, skin transplants, and others.

Additionally a weather station is installed to control environmental conditions such as temperature, air pressure and humidity. If necessary, ECG unit is applied for synchronization of thermal images with the heart action during open heart cardiosurgery interventions.

The temperature distribution at the ROI is composed of pixels which should be identified as the same on all following images in series. In ADT parametric images are calculated representing equivalent, usually the two exponential models. Chosen model parameter, mainly one of time constants allows quantitative description of ROI properties important in taking specific diagnostic decision.

To read more about this set see e.g., [5, 28, 29], where also issues related to applied software, data processing, model fitting, normalizing to the reference ROI are discussed.

3 Evaluation of Burns

It was almost natural to apply thermal imaging to assessment of burns [1]. The results have been encouraging giving for the first time an objective and quantitative tool in burn wound diagnostics. Still, the problem of undetermined burns diagnostics was not fully solved. Important progress using ADT is described in [27]. Here we comment main outcomes of this work. The research was performed at the Department of Biomedical Engineering Gdansk University of Technology in cooperation with the Department of Plastic Surgery, Gdansk University of Medicine. All experiments were performed with permission of the proper ethics commission.

In burn treatment it was typical to classify burn wound area to four degree classes of the Jackson scale [30]. According to present methodology only two class determinations of burns are important: the first class is when wounds will heal spontaneously within 3 weeks and the second class—those which will not heal within 3 weeks. Treatment of burn patients strongly improved over recent years with help of diagnostic instrumentation, but diagnostics of undetermined burns still requires definition of objective diagnostic descriptors to determine regions to be healing within three weeks after the burn.

Before treatment procedure of a burn wound can be applied, the patient should be properly and completely evaluated. Reliable diagnostics, evaluation, and management greatly help in minimizing suffering, optimizing healing results, and reduce economic costs. The best expected situation during the burn treatment would be if the physician could obtain a diagnostic image with clearly visible area of burn for surgical treatment (3) and area for conservative treatment (1) like it is shown in Fig. 4.

Burn wounds depth is regarded as the factor of crucial importance for the proper choice of treatment [31, 32]. Beside very imperfect, based only on visual inspection but the most frequently used clinical (visual) evaluation, several objective diagnostic methods have been proposed. Monstreya at all published [33] the review of methods used in evaluation of burn depth: (1) clinical evaluation; (2) histopathology of local biopsy as the reference; (3) methods based on evaluation of microcirculation in the burn wound, as: thermography, laser Doppler imaging (LDI) and other [34, 35]; (4) the group of research methods, as: optical, USG, photo-acoustic

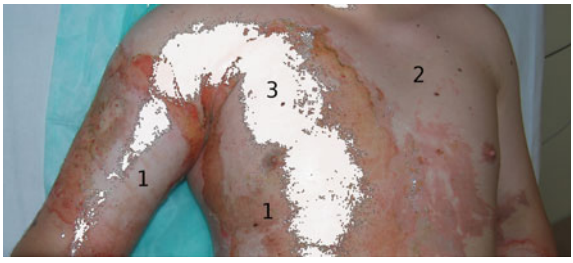

Fig. 4 Example of burn wound diagnostic results; *1* burn wound area; *2* healthy skin; *3* recognized and indicated area of full thickness burn requiring surgical intervention

and nuclear imaging [36, 37]. After 2008, papers devoted to development of the LDI method are most frequently published, see e.g., [38–41]. Our proposal allows determination of the burn depth using the ADT [27] and TT [11] approach.

Our recent ADT procedure of burn wound diagnosis comprises the cooling phase lasting about 60 s, then recording of the thermograms sequence within 3 min; the last step is the data fitting procedure. Using as a stimulus cooling medium one can get larger temperature gradients comparing to stimulation by heating using halogen lamps or incandescent IR sources, not worrying about the possibility of destructive action of the excitation to the tested tissue. However, be careful to avoid biofeedback reaction by inclusion of body's defense mechanisms counteracting becoming too cool and falsifying the test results. Another problem is to ensure uniform cooling of the entire ROI surface during the stimulus.

In the case of cooling the burnt skin surface to the ambient temperature the gradient between the inner tissue layer and the skin surface increases, while the temperature difference from the environment decreases. After switching-off the cooling source, the heating process occurs at the skin surface, largely due to the heat flow from deeper layers of the body. Value of the heat flux depends on factors characterizing the tissue, its structure, and physiology. This perfectly justifies the use of cooling in diagnosis of burn wounds and other types of diseases in which there are changes in the structure or functioning of tissues. It allows detection of particular changes in blood circulation or local changes of tissue structure, for example changes in tumor tissue depending on the stage of the disease, resulting in increased or decreased blood circulation. As an example, the case shown in Fig. 5 is discussed in details.

It is a case of burn wound by hot oil to the abdomen. Clinical diagnosis is shown in Fig. 5a, but the patient was treated conservatively only, as for assuring clinical diagnosis the histopathology of the biopsy specimen taken in the center of the undetermined burn area was 50.4% dtms (dermal thickness on measurement site) what should be healing spontaneously within three weeks. Interpretation of parametric ADT images differs. The magnitude—temperature T_s—gives the same score as the clinical method in the undetermined burn region. The time constant mean value of τ_{2n} in Ub area was −0.01; in the area diagnosed as superficial burn τ_{2n} was −0.09. This time is slightly longer than values for the unburned skin but shorter than the threshold value dividing burns into healed and unhealed in 3 weeks. The mean value for the undetermined area was −0.15 which is longer than for that part of the wound prognosis as superficial, but still shorter than the threshold value 0.00013. So, finally the diagnosis was following: ROI marked as "**1**" indeed was the first class wound which will heal in 3 weeks. The ROI marked as "?" finally appeared to be also the first class healing wound. Therefore the undetermined in visual inspection part of the wound was accurately diagnosed by means of the ADT method—the time constant parametric image. The whole abdomen area was healed in 3 weeks, which confirmed the earlier ADT diagnosis.

In order to verify quality of applied methodology in clinical tests several cases of burned patients were carried out, see, e.g., [21, 22, 27]. Patients were treated routinely, according to the workflows established in the clinic and in accordance

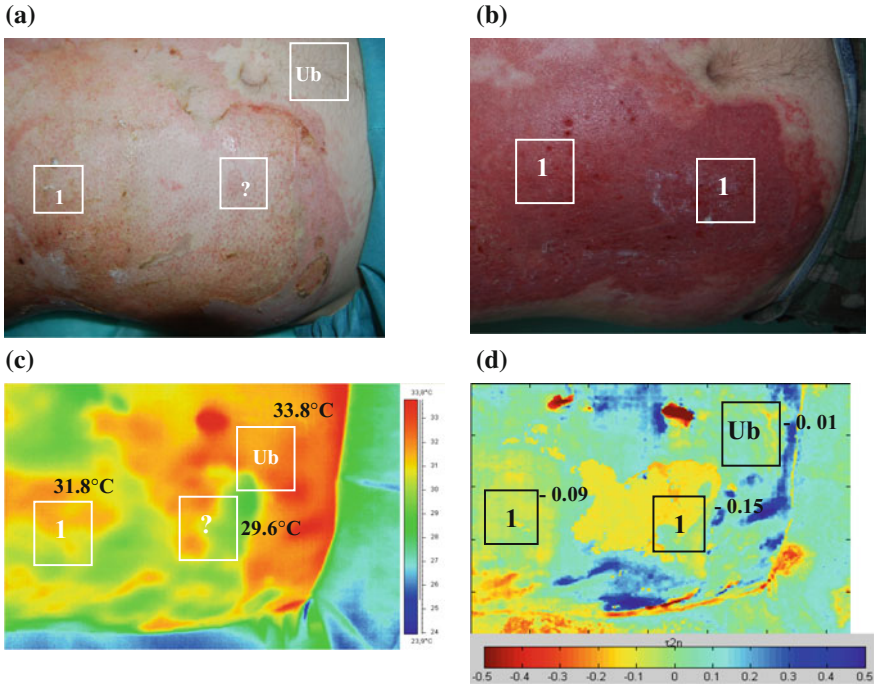

Fig. 5 Comparison of RGB diagnostic images of the burn wound to the abdomen in 19 year old man and ADT parametric images at the post burn day 2; applied descriptions: *Ub* unburned skin, *1* superficial burn which will heal within 3 weeks, *question mark* undetermined burn; **a** RGB after accident on the post burn day 2; **b** after 3 weeks; **c** temperature T_s [°C] and **d** time constant τ_{2n} descriptor at the day after burn accident

with common standards: before the test acclimated in an especially dedicated room for testing, which ensured controlled conditions; no drafts; no strong sources of radiation; the ambient temperature of 22 °C and normal humidity. Clinical evaluation of burns was performed by an experienced physician and compared with the results of IR-thermal imaging TI and ADT. Evaluation of the wound treatment three weeks after the accident proved validity of the clinical and thermal diagnostics. Detailed results are shown in cited papers [21, 22, 27].

4 Evaluation of Post-cardiosurgery Wound Healing

One of very interesting applications of IR-thermal imaging is in cardiosurgery [42]. In this chapter, we show results of a research project devoted to analysis of the value of ADT thermal IR-imaging in post-cardiosurgery wound healing evaluation. This research was performed at the Department of Biomedical Engineering Gdansk

University of Technology in cooperation with the Department of Cardiosurgery, Gdansk University of Medicine, financed by the Polish National Science Centre. All experiments were performed according to legal regulations and permission by the Gdansk Ethics Commission. Early results are already published in [28, 29].

There are several characteristic phases in the process of post-surgery wound healing, where cellular and chemical reactions interweave. The first is directed to stop the bleeding by contraction of damaged blood vessels; a clot is formed in this phase. In the second phase, a number of mechanisms are activated aimed at clearing the necrotic tissue, hematomas and foreign bodies in order to prepare the ground for the formation of scar tissue. The third phase smoothly develops new vessel, nerve, fiber, and the epithelial tissue formation. Cardiac treatment undoubtedly interferes with these processes. Patients undergoing cardiac procedures often have significantly impaired clotting because of the underlying disease anticoagulation. Typically during the treatment, drugs that affect coagulation are applied. Long-time use of extracorporeal circulation may have destructive influence on the function of platelets and other cellular components of the blood, too. In the first days after the operation, generalized unspecific inflammatory reaction of the body occurs. Undoubtedly, the described processes may lead to formation of interstitial edema and abscess fluid. The extent of surgical trauma often causes formation of large areas of necrosis. Long-time exposure of the operating field may affect microbial contamination, which can thrive on encountering the clot, tissue necrosis, ischemic topically with interstitial edema can cause infectious complications in healing wounds.

The diagnosis of complicated wound healing and/or infection uses standard definitions [43, 44]. The one consists of the following attributes: exude from the wound and its spontaneous dehiscence; positive results of bacteriological examination of exude or tissue taken from the wound; swelling, redness, pain, and an increase in temperature around the wound. At least one criterion should be fulfilled to recognize the complicated healing of the wound. It is often difficult to recognize and properly diagnose specific symptoms existing in a short postoperative period to six days after surgery. Early symptoms of deep wound infection with mediastinitis may remain unrecognized due to pain in the region of the wound, which is usually typical for a patient after the surgery, and often very strong inflammatory response and the possibility of other infections, such as the lung tissue, etc. Only a very experienced surgeon or doctor may determine proper diagnosis on wound healing after surgery.

The most significant additional examinations at a rapid diagnosis of deep wounds with inflammation of postoperative mediastinitis are cultures of secretions from the surgical wound and bacteriological examination of the blood. Proper prediction method of wound healing is very important. Currently, up to 10% of patients have problems with normal healing of surgical wounds, and they often require re-operation and costly treatment. This also has an impact on the deterioration of quality of life after surgery.

The goal of the reported research was to

1. Elaborate a simple diagnostic, qualification, and therapeutic routine in the case of patients with wound healing complications.
2. Provide a description of "natural history" of wound healing complications.
3. Evaluate effectiveness of the proposed ADT method.

It is well known that thermal processes accompany all metabolic changes related to blood deficit or increased circulation. Therefore it was natural to assume that thermal processes should be effective in subtle description of temporal changes of tissue thermal properties after surgical interventions and should be useful in terms of diagnostic evaluation of healing processes. We applied both, TI—temperature as a useful diagnostic descriptor, and ADT parametric images important in structure thermal properties determination in the vicinity of the postoperative wound.

The research presents a routine of qualification process and treatment applied to 400 cardiosurgery patients with sternotomy access, among them only five patients suffering from wound healing complications after cardiac surgery.

Patients were classified into two groups: the group 1—patients with no infected wound dehiscent; the group 2—only five patients with superficial wound infection and with acute deep wound infection and mediastinitis. Based on thermal investigation and data analysis we proposed the following classification method:

1. Thermal and visual investigation (TI, ADT, and RGB images) on the day before cardiosurgery—as the reference data—indicated as the day 1.
2. Thermal and visual investigation on the day after cardiosurgery intervention—the third day.
3. Thermal and visual investigation three days later—the sixth day.
4. Following step is data analysis and fitting of measurement results at each pixel to the two-exponential thermal model.

As descriptors the temperature as well as ADT parametric images are calculated. Most important is calculation of descriptor differences at following days and wound classification according to the proposed thresholds. For evaluation of the wound healing process the differences between the day 6 and the day 3 are chosen as diagnostically decisive

$$\Delta T_s = T_s(6\ \text{day}) - T_s(3\ \text{day})$$
$$\Delta \tau_2 = \tau_2(6\ \text{day}) - \tau_s(3\ \text{day}).$$

Such defined differences are finally analyzed as healing process diagnostic images and quality indicators.

In general, thermal images are of lower geometry resolution than RGB images. Therefore registration of IR images and matching with equivalent visual images allow for more precise interpretation of diagnostic content. As an example, the result of matching of a color photograph and a thermogram with additional determination of the ROI and parametric image of the descriptor in ROI is shown in Fig. 6. Only well identified and fitting to the reference ROI images are compared.

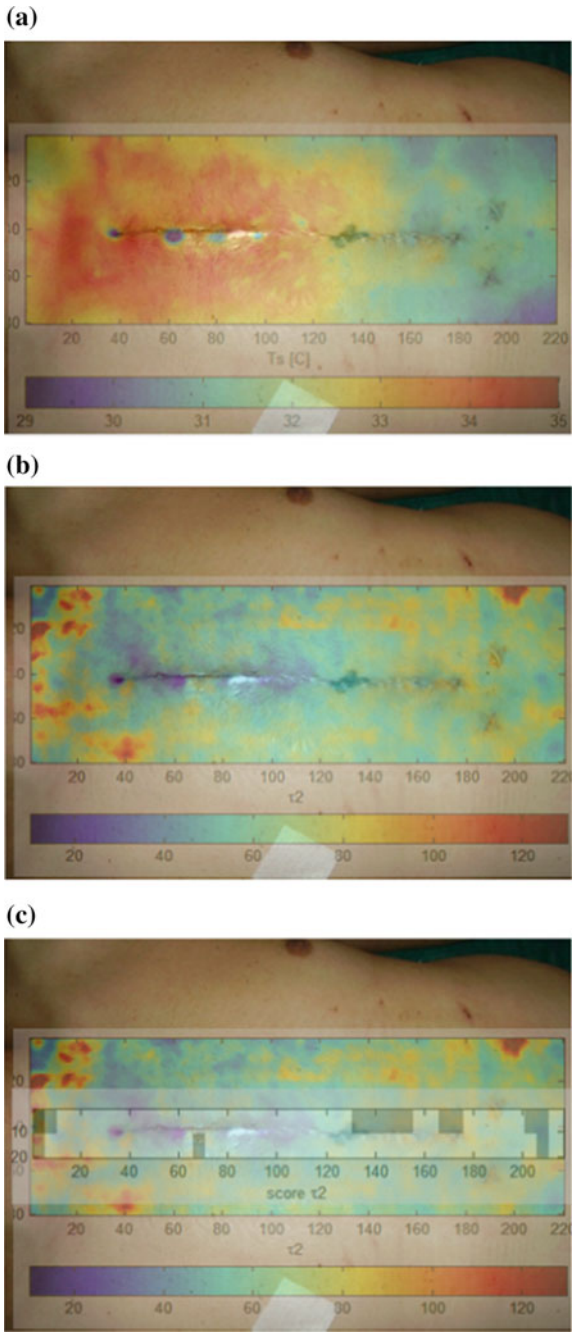

Fig. 6 Example of wound healing diagnostic results: the images fusion: **a** photo and static thermal image; **b** photo and τ_2 descriptor; **c** photo and τ_2 descriptor and score results

Table 1 Descriptors of patients without complications—reference data; mean value and standard deviation (sd) of the two exponential model

		Day 1		Day 3		Day 6		d6–d3
		Value	sd	Value	sd	Value	sd	Value
Wound area	T_s [°C]	33.42	1.36	34.34	1.10	33.75	1.03	-0.59
	τ_1 [s]	3.40	1.15	3.36	0.97	3.76	1.23	0.40
	τ_2 [s]	35.60	8.90	32.07	8.03	38.49	9.88	6.41
Healthy area around the wound	T_s [°C]	33.19	1.76	33.83	1.56	33.64	0.94	-0.19
	τ_1 [s]	3.51	1.20	3.48	1.16	3.88	1.18	0.40
	τ_2 [s]	35.11	8.87	36.03	9.75	41.57	11.97	5.53

Final ROI diagnostic visualization shows the same region on the patient chest surface in all images.

In Table 1 values of descriptors T_s (°C), τ_1 (s) and τ_2 (s), obtained for the controlled group of patients without the wound healing complications are collected.

According to Table 1 the value of the second (longer) time constant τ_2 parameter is taken as the decisive diagnostic figure of merit. The three stage classifier and classification thresholds are set as

$$\begin{array}{llll} \text{a/} & 1 & \text{for} & \Delta\tau_2 < -10 \\ \text{b/} & 0 & \text{for} & -10 < \Delta\tau_2 < 10 \\ \text{c/} & -1 & \text{for} & \Delta\tau_2 > 10 \end{array}$$

Based on this classification a diagnostic example is shown in Fig. 6c, where the RGB image, the parametric τ_2 descriptor, and the normalized score according to such defined thresholds are matched. The normalized and averaged in 5 by 10 pixels of ROI fields score is presented as

white (1)—"healing process with complication";
gray (0)—unrecognized—"hard to say";
black (−1)—"good (well) healing process".

Patients with wound healing complications are treated following special procedure. The treatment applied during the first phase, lasting from the moment of recognition up to 7 or 14 days, was similar for all the patients. The applied procedure combines application of antibiotics, surgical opening of the wound in order to place an antiseptic dressing and 10 sessions of HBO (HyperBaric Oxygenation) healing. On the following figures, two examinations are shown—first—a patient with wound healing complications (Fig. 7) and the second one—a patient without wound healing complications—proper wound healing (Fig. 8).

In following pages, diagnostic images allow to compare two patients: Fig. 7—wound healing with complications and Fig. 8—no complications of healing wound.

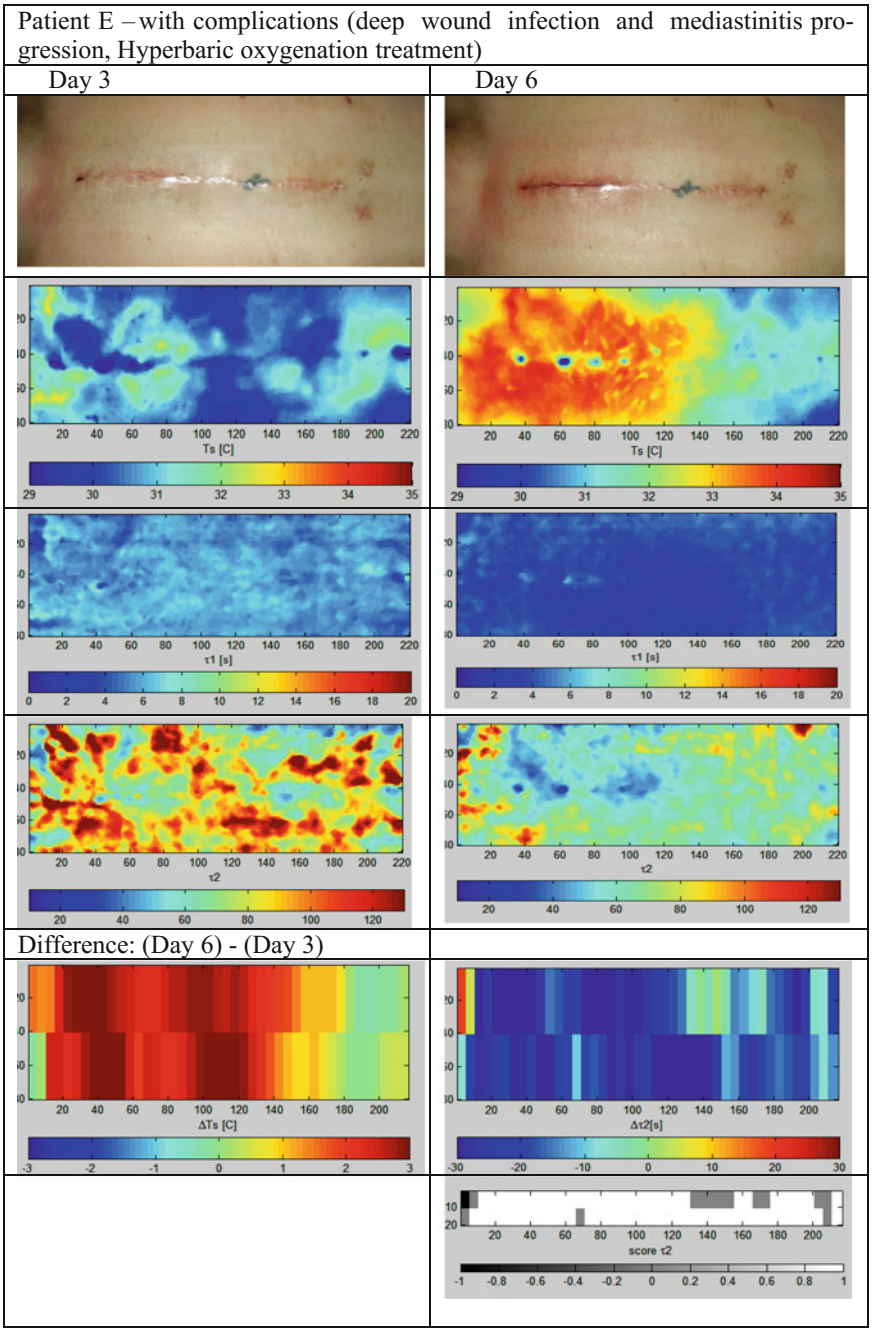

Fig. 7 Example of wound healing diagnostic results: photo; static thermal image; τ_1 and τ_2 descriptors and final score results—wound healing with complications

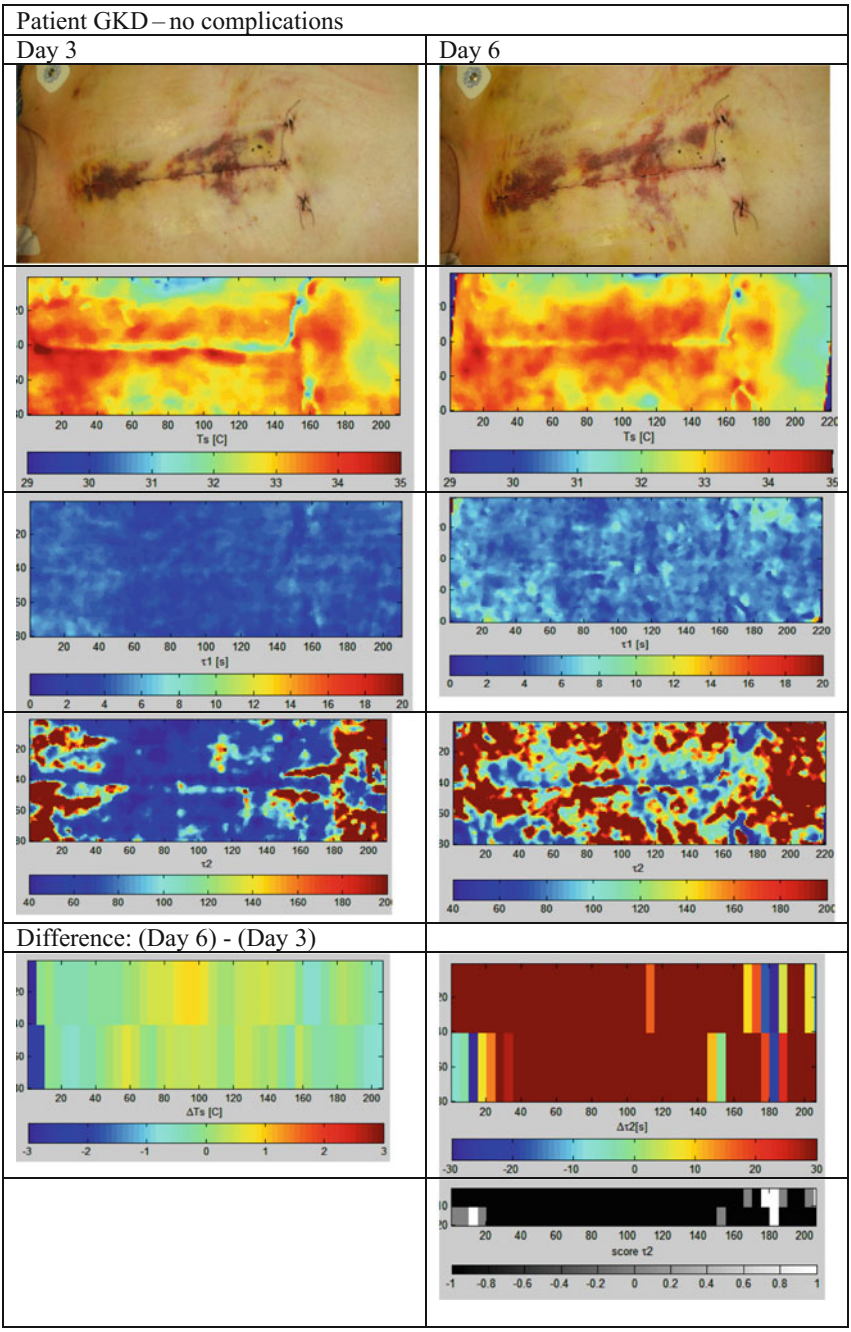

Fig. 8 Example of wound healing diagnostic results: photo; static thermal image; τ_1 and τ_2 descriptors and final score results—no complications wound healing

Results of measurements are shown for the days 3 and 6. Interpretation of thermal and parametric as well as RGB images is not easy, but the score—the lowest image—gives clear indication what to decide about a patient.

Figures above show typical diagnostic results. We present images of descriptors T_s (°C) and τ_2 following the fitting procedure for Day 3; Day 6 and differential images (Day 6–Day 3). The applied classifier of diagnostic decision is the differential image of the second time constant of the two exponent thermal model. For this classifier, only the closest to the wound region of the ROI is presented at the decisive image. The score is presented on matched RGB and parametric images of τ_2. There are two rows of pixels averaged in segments $\pm 5 \times 10$ along 200 pixel length covering the whole wound. Segmentation makes easy the classification and presentation of results. The diagnostic decision would be to keep the patient at the hospital for further treatment if the score is white (case no 1) or release him to recover at home if the score is black (case no 2).

In most of clinical cases, this decision is taken at the day 6 (4 days after operation), as due to economic reasons treatment and rehabilitation at home is strongly advantageous.

5 Summary

This overview shows importance of still new in medicine visualization modality called ADT—Active Dynamic Thermography. Assuming that classical thermal imaging TI is already broadly accepted, what in fact is only partly true as some clinicians still remember that this technology in breast cancer diagnostics failed in early stage of development [45, 46], the ADT increases the role of thermal imaging in medicine. To register static TI and dynamic ADT images the same IR camera is applied. Both modalities are supplementing each other as TI shows metabolic functional thermal images and ADT allows reconstruction of structural thermal properties adding to functional also structural diagnostic data. Therefore analysis and comparison of temperature distribution and images of ADT descriptors allow better understanding of diagnostic content and support multimodality concept of advanced diagnostics in medicine.

Acknowledgements Participation of coworkers from the Department of Biomedical Engineering Gdansk University of Technology, the Department of Plastic Surgery and the Department of Cardiac Surgery Gdansk University of Medicine is acknowledged; the research was financed by several research grants, recently NCN UMO-2011/03/B/ST7/03423 and partly from the statute funds of the Faculty of Electronics, Telecommunications and Informatics GUT.

References

1. Barnes, R.B.: Thermography. Thermography and its clinical applications. Ann. N. Y. Acad. Sci. **121**:34-48 (1964) (art.1)
2. Ring, E.F.J.: The historical development of temperature measurement in medicine. Infrared Phys. Technol. **49**, 297–301 (2007)
3. Ring, E.F.J., Ammer, K.: Infrared thermal imaging in medicine. Physiol. Measur. **33**:R33–R46 (2012)
4. Diakides, M., Bronzino, J.D., Petereson, D.R. (eds.): Medical Infrared Imaging—Principles and Practices. CRC Press, T&F Group, Boca Raton (2013)
5. Kaczmarek, M., Nowakowski, A.: Active IR-thermal imaging in medicine. J. Nondestr. Eval. **35**:19 (2016). doi:10.1007/s10921-016-0335-y
6. Maldague, X.P.V.: Theory and Practice of Infrared Technology for Nondestructive Testing. Wiley, New York (2001)
7. Proceedings of Quantitative InfraRed Thermography: Chatenay-Malabary-1992, Naples-94, Stuttgart-1996, Lodz-1998, Venice-2000, Reims-2002, and Brussels-2004, Padova-2006, Krakow-2008, QuebeckCity-2010, Naples-2012, Bordeaux-2014, Gdansk-2016; see the QIRT homepage—http://qirt.org
8. Vavilov, V., Shirayev, V.: Thermal Tomograph—USSR Patent no. 1.266.308, 1985
9. Vavilov, V.P., Kourtenkov, D., Grinzato, E., Bison, P., Marinetti, S., Bressan, C.: Inversion of experimental data and thermal tomography using "Thermo Heat" and "Termidge" Software, pp. 273–278 (1994)
10. Vavilov, V.P.: 1D-2D-3D transition conditions in transient IR thermographic NDE. In: Proceedings of QIRT'94, Seminar 64—quantitative infra-red thermography—QIRT'2000, Reims, 74 (2000)
11. Nowakowski, A., Kaczmarek, M., Hryciuk, M.: Tomografia Termiczna, 615–696. In: Chmielewski, L., Kulikowski, J.L., Nowakowski, A., Obrazowanie Biomedyczne, (Biomedical Imaging—in Polish) Biocybernetyka i Inżynieria Biomedyczna 2000, v. 8, Akademicka Oficyna Wydawnicza EXIT, Warszawa (2003)
12. Shepard, S.M., Lhota, J.R., Rubadeux, B.A., Wang, D., Ahmed, T.: Reconstruction and enhancement of active thermographic image sequences. Opt. Eng. **42**, 1337–1342 (2003)
13. Balageas, D.L., Roche, J.M., Leroy, F.H., et al.: The thermographic signal reconstruction method: a powerful tool for the enhancement of transient thermographic images. Biocybern. Biomed. Eng. **35**(1), 1–9 (2015)
14. Liu, W.-M., Maivelett, J., Kato, G.J., Taylor, V.I.J.G., Yang, W.-C., Liu, Y.-C., Yang, Y.-G., Gorbach, A.M.: Reconstruction of thermographic signals to map perforator vessels in humans. Quant. InfraRed Thermogr. J. **9**, 123–133 (2012)
15. Steenhaut, O., Van Denhaute, E., Cornelis, J.: Contrast enhancement in IR-thermography by application of microwave irradiation applied to tumor detection. In: MECOMBE, vol. 86, pp. 485–488 (1986)
16. Nowakowski, A, Kaczmarek, M.: Dynamic thermography as a quantitative medical diagnostic tool. Med. Biol. Eng. Comput. Incorp. Cell. Eng. Part 1 **37**(1):244–245 (1999)
17. Rumiński, J., Kaczmarek, M., Nowakowski, A.: Data visualization in dynamic thermography. J. Med. Inform. Technol. **5**:IT29–IT36 (2000)
18. Kaczmarek, M., Rumiński, J., Nowakowski, A.: Measurement of thermal properties of biological tissues—comparison of different thermal NDT techniques. In: Proceedings of Advanced Infrared Technology and Application, Venice, 1999, pp. 322–329 (2001)
19. Nowakowski, A., Kaczmarek, M., Rumiński, J., Hryciuk, M., Renkielska, A., Grudziński, J., Siebert, J., Jagielak, D., Rogowski, J., Roszak, K., Stojek, W.: Medical applications of model based dynamic thermography, Thermosense XIII, Orlando. Proc. SPIE **4360**, 492–503 (2001)
20. Nowakowski, A., Kaczmarek, M., Rumiński, J.: Synthetic pictures in thermographic diagnostics. In: Proceedings of EMBS-BMES Conference, Houston, pp. 1131–1132 (2002)

21. Kaczmarek, M., Nowakowski, A., Renkielska, A.: Rating burn wounds by dynamic thermography. In: Balageas, D., Beaudoin, J., Busse. G., Carlomagno, G. (ed.) Quantitative InfraRed Thermography, vol. 5, pp. 376–381. Reims (2000)
22. Kaczmarek, M., Nowakowski, A., Renkielska, A., Grudziński, J., Stojek, W.: Investigation of skin burns basing on active thermography. In: Proceedings of 23-rd Annual International Conference IEEE EMBS, CD-ROM, Istanbul (2001)
23. Hryciuk M., Nowakowski A., Multi-layer thermal model of healthy and burned skin. In: Proceedings of 2nd European Medical and Biological Engineering Conference, EMBEC′02, 3, Pt. 2, Vienna, pp. 1614–1617 (2002)
24. Hryciuk, M., Nowakowski, A.: Evaluation of thermal diffusivity variations in multi-layered structures. In: Proceedings of 6 QIRT, Zagreb, pp. 267–274 (2003)
25. Nowakowski, A., Kaczmarek, M., Wtorek, J., Siebert, J., Jagielak, D., Roszak, K., Topolewicz, J.: Thermographic and electrical measurements for cardiac surgery inspection. In: Proceedings of 23rd Annual International Conference IEEE EMBS, CD-ROM, Istanbul (2001)
26. Kaczmarek, M., Nowakowski, A.: Analysis of transient thermal processes for improved visualization of breast cancer using IR imaging. In: Proceedings of IEEE EMBC, Cancun, pp. 1113–1116 (2003)
27. Renkielska, A., Kaczmarek, M., Nowakowski, A., Grudziński, J., Czapiewski, P., Krajewski, A., Grobelny, I.: Active dynamic infrared thermal imaging in burn depth evaluation. J. Burn Care Res. **35**(5):e294–e303 (2014)
28. Moderhak, M., Nowakowski, A., Kaczmarek, M., Siondalski, P., Jaworski, Ł.: Active dynamic thermography imaging of wound healing process in cardiosurgery. In: Advances in Intelligent Systems and Computing, Information Technologies in Medicine, vol. 284, pp. 197–202. Springer, Berlin (2014)
29. Nowakowski, A., Siondalski, P., Moderhak, M., Kaczmarek, M.: A new diagnostic method for evaluation of cardiosurgery wound healing. Quant. InfraRed Thermogr. J. (2015)
30. Jackson, D.M.: The diagnosis of the depth of burning. Br. J. Surg. **40**, 588–596 (1953)
31. Engrav, L.H., Heimbach, D.M., Reus, J.L., Harnar, T.J., Marvin, J.A.: Early excision and grafting vs. non-operative treatment of burns of indeterminate depth: a randomised prospective study. J. Trauma **23**, 1001–1004 (1983)
32. Heimbach, D., Engrav, L., Grube, B., Marvin, J.: Burn depth: a review. World J. Surg. **16**, 10–15 (1992)
33. Monstrey, S., Hoeksema, H., Verbelen, J., Pirayesh, A., Blondeel, P.: Assessment of burn depth and burn wound healing potential. Burns **34**, 761–769 (2008)
34. Altintas, A.A., Guggenheim, M., Altintas, M.A., Amini, P., Stasch, T., Spilker, G.: To heal or not to heal: predictive value of in-vivo reflectance-mode confocal microscopy in assessing healing course of human burn wounds. J Burn Care Res. **30**(6), 1007–1012 (2009)
35. Alkhwaji, A., Vick, B., Diller, T.: Estimaiting burn depth from thermal measurements. Biomed. Sci. Instrum. **48**, 12–19 (2012)
36. Goertz, O., Ring, A., Köhlinger, A., Daigeler, A., Andree, Ch., Steinau, H.U., Langer, S.: Orthogonal polarization spectral imaging—a tool for assessing burn depths? Ann. Plast. Surg. **64**(2), 217–221 (2010)
37. Mihara, K., Shindo, H., Ohtani, M., Nagasaki, K., Nakashima, R., Katoh, N., Kishimoto, S.: Early depth assessment of local burns by videomicroscopy: 24 h after injury is a critical time point. Burns **37**, 986–993 (2011)
38. Merz, K.M., Pfau, M., Blumenstock, G., Tenenhaus, M., Schaller, A.E., Rennekampff, H.O.: Cutaneous microcirculatory assessment of the burn wound is associated with depth of injury and predicts healing time. Burns **36**, 477–482 (2010)
39. Hoeksema, H., Vaje, K., Tondu, T., Hamadi, M., Van Landuyt, K., Blondeel, Ph., Monstrey, S.: Accuracy of early burn depth assessment by laser Doppler imaging on different days post burn. Burns **35**, 36–45 (2009)

40. Wang, X.Q., Mill, J., Kravchuk, O., Kimble, R.M.: Ultrasound assessment thickness of burn scars in association with laser Doppler imaging determined depth of burns in pediatric patients. Burns **36**, 1254–1262 (2010)
41. Sharma, V., O'Boyle, C., Jeffery, S.L.A.: Man or machine? The clinometric properties of laser Doppler imaging in burn depth assessment. J Burn Care Res. **32**, 143–149 (2011)
42. Nowakowski, A., Kaczmarek, M., Rogowski, J.: The role of thermal monitoring in cardiosurgery interventions. In: Diakides, M., Bronzino, J.D., Petereson, D.R. (ed.) Medical Infrared Imaging—Principles and Practices, pp. 17-1–17-24. CRC Press, Taylor & Francis Group, Boca Raton (2013)
43. Bruce, J., Russell, E.M., Mollison, J., Krukowski, Z.H.: The quality of measurement of surgical wound infection as the basis for monitoring: a systematic review. J. Hosp. Infect. **49**:99–108 (2001)
44. Siondalski, P.: Algorytm leczenia powikłań gojenia się ran pooperacyjnych i ropnego zapalenia śródpiersia po operacjach kardiochirurgicznych [Algorithm dealing with the treatment of healing wound complications and mediastinitis after cardiac surgeries]. Annales Academiae Medicae Gedanensis. **39**(2), 303–413 (2009)
45. Feig, S.A., Shaber, G.S., Schwartz, G.F., et al.: Thermography, mammography, and clinical examination in breast cancer screening. Review of 16,000 studies. Radiology **122**, 123–127 (1977)
46. Kontos, M., Wilson, R., Fentiman, I.: Digital infrared thermal imaging (DITI) of breast lesions: sensitivity and specificity of detection of primary breast cancers. Clin. Radiol. **66**(6), 536–539 (2011)

Evaluation of Respiration Rate Using Thermal Imaging in Mobile Conditions

Jacek Ruminski and Alicja Kwasniewska

Abstract Respiratory rate is very important vital sign that should be measured and documented in many medical situations. The remote measurement of respiration rate can be especially valuable for medical screening purposes (e.g. severe acute respiratory syndrome (SARS), pandemic influenza, etc.). In this chapter we present a review of many different studies focused on the measurements and estimation of respiration rate using thermal imaging methods. Additionally, we present results of our research focused on the evaluation of different respiration rate estimators for the needs of data processing of image sequences recorded by small, mobile thermal cameras. We used small thermal camera modules in the prototypes of smart glasses for the evaluation of different parameters related to respiration activities. The chapter presents the used methodology and results of the respiration rate analysis, detection of apnea events, description of respiration patterns and other parameters that can be analyzed for respiration waveforms derived from the regions of the nostrils or mouth in thermal video sequences.

Keywords Thermal imaging · Vital signs · Image processing · Medical imaging

1 Introduction

In physiology, respiration can be defined as the two directional exchange of gases. Oxygen is delivered from the outside air to the cells in tissues and carbon dioxide is transported from cells to the outside air. The exchange of gases is caused by differences in the pressure between lungs and surrounding atmosphere. During the inspiration (inhalation), air enters the lungs, because the air pressure in lungs (within the alveolar spaces) is lower than the atmospheric pressure. When the air pressure becomes higher than the atmospheric pressure the expiration (exhalation) is observed. Therefore, the breathing process can be monitored by the observation

J. Ruminski (✉) · A. Kwasniewska
Gdansk University of Technology, Narutowicza 11/12, 80-233 Gdansk, Poland
e-mail: jacek.ruminski@pg.gda.pl
http://www.biomed.gda.pl/~jwr

E.Y.K. Ng and M. Etehadtavakol (eds.), *Application of Infrared to Biomedical Sciences*, Series in BioEngineering,
DOI 10.1007/978-981-10-3147-2_18

of two fundamental activities: mechanical changes of chest/abdomen volumes and airflow changes in nose/mouth regions. Such observations can be described using quantitative parameters representing properties of the breathing process: respiration rate, respiration regularity, presence and length of apnea events, etc. Respiration rate (RR) can be defined as the number of breaths for one minute or "breaths per minute" (bpm). Respiratory rate can characterize the breathing process indicating if the respirations are normal, too fast (tachypnea), too slow (bradypnea), or nonexistent (apnea). However, threshold values that could be used in differentiation of different categories of abnormal respiratory rates are sometimes defined for different categories of subjects. For example, normal respiration rate is changing with age. Therefore, some organizations propose tachypnea threshold values as [1, 2]:

- Newborn to 2 months: 60 bpm
- Infant 2 months–1 year: 50 bpm
- Preschool Child 1–5 years: 40 bpm
- School age Child: 20–30 bpm
- Adults: 20 bpm.

Respiratory rate is one of three fundamental vital signs (body temperature, heart rate and RR) and it is a very important parameter indicating potential health problems. For example, the value of the RR above 27 bpm could be a predictor of cardiac arrest [3]. The increased RR is used in the prediction of pneumonia [4] or for the prediction of lower respiratory tract infection [5]. In basic epidemiology, WHO's guidelines recommend that pneumonia case detection can be based on clinical signs alone, mainly respiratory rate [6]. It has been also shown that the respiratory rate is more discriminatory between stable and unstable patients than pulse rate [3]. Cretikos et al. [7] specified many recommendations about the measurement of respiratory rates for patients staying in hospitals. For example, they claimed "the respiratory rate should be measured and documented accurately in all hospital patients at least once a day, and should always be documented when other vital signs are measured".

Apnea is defined by the cessation of respiratory airflow and it is especially dangerous during sleep. The length of time required to classify the cessation of respiratory airflow as a true apneic episode is measured in seconds [8], e.g., >10 s for Central Sleep Apnea [9].

Respiration regularity is characterized by periodical appearance of inspiration/expiration events and similar amplitudes (depth) of those events. Abnormalities in respirations may occur in rate, rhythm, and in the effort of breathing. Different respiration patterns have been observed for some illnesses or injuries, including [10, 11]: Cheyne-Stokes respirations, Biot's breathing, Kussmaul's respirations, Apneustic respirations, and Ataxia respirations. Cheyne-Stokes respirations are characterized by periods of respirations, during which breathing gets progressively deeper and then gets progressively shallower (crescendo–decrescendo pattern). Similar series of variable in depth breaths are separated by periods of significant apnea (Fig. 1a). This respiration pattern can be a result of strokes, brain tumors or injuries, carbon monoxide poisoning, high altitude sickness and can be observed as a side-effect of morphine administration. Biot's breathing (or cluster respiration) pattern has clusters of similar rapid respirations

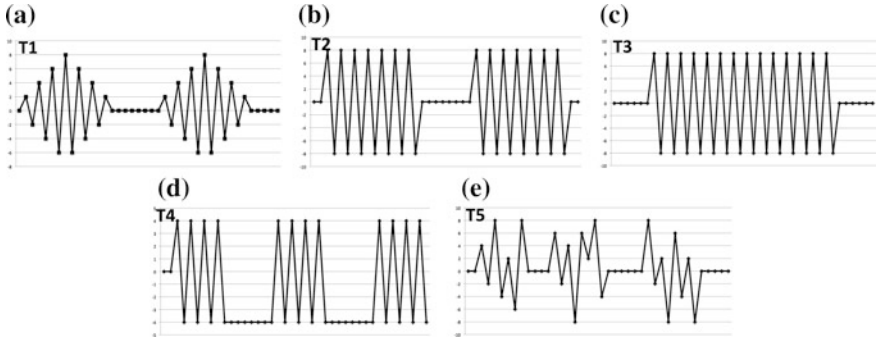

Fig. 1 Respiration patterns: **a** T1—Cheyne-Stokes respirations, **b** T2—Biot's breathing, **c** T3—Kussmaul's respirations, **d** T4—Apneustic respirations, **e** T5—Ataxia respirations

separated by apnea periods (Fig. 1b). It could be also a result of stroke or trauma. Kussmaul's respirations are characterized by deep and fast breathing (hyperventilation) (Fig. 1c). It is typically observed in the late stages of a severe metabolic acidosis, for example in diabetic ketoacidosis. Prolonged inspiration and expiration phases are observed in apneustic respirations (Fig. 1d). The prolonged expiration phase and following pause phase are interpreted as apneic phases due to long cessation of air inflow. It is commonly caused by some damages in central nervous system (CNS). Finally, ataxia (chaotic) respirations constitute a very irregular respiration pattern with irregular pauses and increasing episodes of apnea (Fig. 1e). It could be caused by damages in CNS, typically to the medulla oblongata.

Parametric description of respiration patterns should represent changes in rate and the depth of breathings and should describe the presence and timing of apnea events. Different methods have been proposed in literature for the monitoring and description of respiration-related parameters. In this chapter, we are focusing on the application of thermal imaging for remote monitoring of respiration rhythm. As it was presented earlier, respiration activities can be analyzed observing mechanical changes of chest/abdomen volumes or airflow changes in nose/mouth regions. Both categories of changes can be usually recorded using thermal cameras and analyzed to present respiration waveforms (patterns) and related parameters. This will be described in the following sections of this chapter.

2 Review of the Current State of the Art

2.1 Respiratory Rate Estimation and Respiration Patterns Analysis

Thermal imaging has been often used to analyze different dynamical changes that could be observed in medical diagnostics or treatment. Some examples include:

wound healing [12, 13], support in cardiosurgery interventions [14, 15], detection of tumors [16–18], and many other [19, 20]. Thermal imaging was also applied to the monitoring of respiration activities.

In [21] authors used a narrow band-pass filter to analyze thermal recordings. The side-view technique was used observing breathing-jet dynamics in the volume of interest (or region of interest, ROI, in a frame) close to the nostrils or mouth. For the ROI of each frame the average value was calculated and normalized in reference to the mean and standard deviation. The autocorrelation sequence was calculated for the extracted and filtered thermal waveform. Finally, the Fourier Transform was applied and power density spectrum (PDS) was calculated. The frequency for the dominated peak in PDS was used as a breathing frequency. The method was experimentally verified with the participation of 9 subjects (19 thermal clips). Results showed good correlation between breathing rate measured with the reference system (respiratory belt with piezo-strap transducer). In both methods the medium wave infrared (MWIR) camera was used (Focal Plane Array, FPA, resolution 640 × 512, 120 fps, 55 fps used in experiments, sensitivity 0.025 C).

Similar measurement technique was presented in [22]. Statistical methodology was used to label thermal video frames as expiratory or nonexpiratory. In the training phase the variant of *K*-means clustering algorithm was used to cluster "hot" pixels (expiratory) and "cold" pixels (nonexpiratory) in first, *M* frames of the thermal video. Hot and cold pixel values were modeled using normal distributions with separate parameters (e.g. a mean) for expiratory (hot) and nonexpiratory (cold) pixels. In each iteration the statistical distance was calculated to expiratory (D_e) and nonexpiratory (D_n) distributions from the previous step. The Jeffreys divergence measure was used with the smallest distance as a criterion. The parameters of the winning distribution were updated using averaging operation. In the testing phase each analyzed pixel in the ROI was modeled as a mixture of two distributions: $D_e + D_n$. Initially, both distributions were equiprobable. In next iterations ($t > 0$), the current distribution is compared to previous, existing expiration and nonexpiration distributions using the Jeffreys divergence measure and minimal distance criterion. Finally, pixels in the ROI are labeled as expiratory or nonexpiratory and frames are also labeled accordingly. Breathing rate is calculated by counting the labeled framed for each breathing cycle. The method was verified during experiments with 3 subjects (8 thermal clips) for 3 different sizes of ROI. The results showed that the medium size ROI (21 × 9 pixels) outperformed other ROI sizes. The achieved accuracy for the small number of subjects was 96.43%.

Later, the same group [23, 24] used the thermal sequences recorded collinear to the subject's face. They proposed the use of wavelet transformation on the resampled and normalized thermal signal to analyze it at different scales. It was assumed that the breathing component exists at a scale S_{max}, which is identified for the local maximum of the wavelet energy coefficients. The frequency, f_c, that maximizes the transform for mother wavelet is used to calculate the estimated respiration rate:

$$eRR * S_{\max} = f_c * \delta, \tag{1}$$

where: *eRR*—estimated respiration rate, δ—downsampling factor (= 10 fps).

Experiments with the participation of 20 subjects [24] were performed using the same MWIR thermal camera as described for previous works. The mean of the absolute normalized difference between values obtained using the thermal imaging method and using the thermistor was 1.73% (accuracy 100 − 1.73% = 98.27%). The method was also used in experiments with pathological subjects [23].

Many papers of the same group (e.g., [24–26]) present the problem and possible solutions for the automatic tracking of the nostrils or mouth ROI. Some methods will be described in the next section.

Abbas et al. [27] proposed to use the long wave infrared (LWIR) camera underling that in this range (7–14 μm) the emitted energy dominates the total signal and it is better to measure absolute or relative object irradiance or radiance. The proposed data acquisition and processing method was similar to previously proposed methods by Pavlidis et al. It extracts the respiratory waveform for the ROI of the nostrils, performs filtration and the wavelet transform. This is probably the first time that the method was used for the remote monitoring of neonates. The method was applied for 5 subjects extracting RR from the ECG signal as a reference. The mean absolute error was 1.32 bpm.

The automatic detection of respiration-related ROIs in thermal sequences was proposed by Pereira et al. [28]. First, the face image was segmented using three stages: multi-level Otsu thresholding. Next, background noise was removed and the largest area in the binary image was assumed to be a face region, The final stage was focused on finding the chin contour using method described in [29] and selecting the ROI after detection of nose edges with the use of Canny edge detector. The values in each ROI of the thermal video were averaged producing the digital respiration waveform. After band-pass filtration the adaptive short analysis window w, was applied to the signal to estimate the local breath-to-breath interval. Three estimators were used to calculate these local intervals: adaptive window autocorrelation, adaptive window average magnitude difference function, and maximum amplitude pairs. The adaptive window autocorrelation method calculates the correlation between m interval samples to the right of the analysis window $w[v]$ and to the left $w[v - m]$ of the center of the window $w[0]$. The second estimator locates the absolute difference between samples. The last estimator is a version of a peak detector. It calculates the maximum amplitude of any two samples. It reaches its maximum if two peaks (in a distance of m) are included in the analysis window w. In experimental verification the LWIR camera was used (resolution 1024 × 768, sensitivity 0.05 K, 30 fps). Eleven volunteers participated in the study. The reference measurement was preformed using piezo plethysmograph. The average breathing rate error for the experiment without user movements was 0.33 bpm with the mean error spread 0.71 bpm.

The general method for the monitoring of respiration with a thermal imaging system was also described in the US Patent Application Publication (Xu,

US2012/0289850 A1) [30]. In the method temperatures of extremities of the head and face (nose, mouth) are used to locate features, which are associated with respiration. RGB values of pixels related to those features are tracked over time to generate pattern of respiration. The respiration rate could be determined from the pattern of respiration counting peaks over pre-defined period of time. Two methods are mentioned: Fourier analysis and peak and valleys detectors. However, only general methods are mentioned. In the document authors underline the use of R, G, B channels suggesting that R and G channels are more important since these channels are "associated with warmer temperatures" and "exhaled air is warmer". It assumes that the use of colorful (pre-processed) images with the mapping of temperature values to colors. This is not a case in most other methods operating on single matrixes with measured temperature values or intensities of radiation. Color is not a carrier of information in this case, but it is used for the visualization. Additionally, the dynamics of respiration waveform depends on the temperature gradient, so inhalation and exhalation phases are both important and can be monitored as a change of temperature with the sign depending on the ambient temperature.

Lewis et al. [31] used similar methodology to estimate respiratory rate detecting the frequency with the greatest spectral density after Fourier transformation of the average respiration signal obtained for the ROI of the nostrils. However, authors additionally proposed the "integration of the thermal time series generated a transformed time-series, which contained a component assumed to be linearly related to tidal volume". The cubic-polynomial filter was used to remove sources of variance in thermal time series (existing due to thermal noise). The estimates were compared to results of the reference method, which was the LifeShirt inductance plethysmograph. Two LWIR cameras were used: TVS-700 with the resolution of 320 × 240 (sensitivity 0.08 C) and SC-6000 with the resolution 640 × 480 (sensitivity 0.02 C). Sampling rate was about 30 fps for both cameras. Thermal sequences were measured for 12 subjects with the TVS-700 camera and for 6 subjects with the SC-6000 camera. Similar mean, within-subject correlations were obtained (≥ 0.90) between results generated for thermal-based data (eRR an relative tidal volume) and for the reference system.

In a series of papers, AL-Khalidi et al. [32–35] presented the similar methods of respiration rate estimation by monitoring of skin surface temperature variations in the area located around (centered) the tip of the nose. This round area (circle, ellipse) was divided into eight segments. Pixel values in each segment were averaged for each frame. As a result, 8 signals were obtained and filtered using low-pass filter (5th order Butterworth filter) with the cutoff frequency of 1 Hz. The respiration rate was estimated calculating the average of distances between peaks. The validation of the method was performed experimental with the participation of 20 children. High correlation was obtained ($R^2 = 0.994$) between the thermal aiming method and the standard respiratory monitoring method.

Hanawa et al. [36] proposed similar breath detection system using the FWIR camera (NEC/Avio, TH7102MX, resolution 320 × 240, sensitivity 0.06 C, 30 fps). The camera detects the temperature change at the nasal hole caused by

respiratory activities. Authors focused on the practical use of the system, analyzing different factors that can contribute the results: head rotation, the distance between camera and human, and camera angle. Their used templates ROIs representing nasal cavity area that were extracted from the first frame. Templates differed in size of the rectangle. Template matching was then performed on each frame of the video recording. In all detected regions the average temperature was calculated. Thresholding operation was applied to calculated average temperature values to detect frames that indicate breaths. The method was verified with the participation of 5 subjects. Participants counted their breath during the experiment. The mean absolute error was about 0.12 bpm. In their later papers [37, 38] they focused on nasal cavity detection methods that are described in the next section.

2.2 *Facial Tracking Methods for the Estimation of Respiratory Rate*

Recently, research of face recognition has rapidly expanded because of a wide range of possible applications. Face and facial features detection is a first step in many automatic face-processing systems [39], not only in computer vision communication or access control systems, but also in medicine. However, face detection is a quite challenging task because it may suffer from lots of variations of image appearance. These variations include environment influence, for example illumination conditions and object influence like facial expressions or pose variation. Regardless of a kind of image (formed for different ranges of electromagnetic spectrum) many novel solutions were proposed in literature to resolve object influence variations, like the template-matching methods [40], the feature invariant approaches [41] or the appearance-based methods [42]. Some solutions for eliminating typical problems (the effect of the background and of disturbances caused by the haircut) were also described by Marzec et al. [43]. Nevertheless, coping with environment influence variations in visible light images is not straightforward and majority of the existing solutions are not robust enough to be used for face detection in visible light in uncontrolled environments [44, 45]. Whereas thermal infrared (IR) record the temperature distribution making them insensitive to variance in illumination conditions [44]. It makes thermal images processing solutions really attractive for various applications.

Considering non-contact estimation of respiration rate, there is a need to detect and track facial features automatically [32]. Some approaches have been already proposed and described for detecting and tracking human face and its characteristic points in thermal images. Many of them are threshold-based methods or at least use binarization in preprocessing stage [32, 43–46], utilizing the fact that face has intensities higher than other regions [43]. Different ideas for proper temperature value determination were performed and described in [43]. Some of them were not satisfactory, but in some cases setting the threshold to 28.3 °C allowed eliminating

most of the problems related to the background and haircut. Al-Khalidi et al. [32] proposed to use image processing techniques that include segmentation and median filter to enhance the recorded thermal images and remove unwanted noise. The segmentation stage consisted of thresholding and edge detection. Then, the nostril ROI was identified by extracting two warmest regions (points where eye corners meet the nose) within selected boundary (region between the bridge pointed by the nose and inner of each eye). The results indicate that the ROI had not been successfully located in a very small percentage of images (in almost all cases failure was less than 1%). Another method for detecting face in thermal images was described by Bhattacharjee et al. [46]. The preprocessing phase involved binarization of acquired image, marking face area and its centroid. After this phase specific facial features were extracted and classified using two techniques: Haar Wavelet Transform and Local Binary Pattern.

Some other approaches are based on Haar-like features [39, 44], which are descriptors of the local appearance. These features are the main concept of the Viola–Jones algorithm that is often used because of its high efficiency and precision. In [44] authors proposed an automatic eye localization method from long wave infrared images. Described method included eyeglass detection based on a Support Vector Machine classifiers trained from eyeglass features vector. Before eye localization, the face region was firstly detected according to intensities difference between this region and the background. Intensity variations of specific facial regions were described by Haar features. Proposed algorithm allowed achieving accurate rate of eye localization around 85%. Similar methodology was used by Mostafa et al. [39]. In the presented approach Haar features and AdaBoost algorithm were used to model a local texture around a given facial feature and create texture based model. The classifier was learned from labeled examples and used to detect a face. The face recognition process was performed by using nearest neighbor classifier in feature space defined by three signature extraction approaches: LBP, SIFT and Binary Robust Independent Elementary Features (BRIEF). Presented results indicate that thermal images have better performance under different illumination conditions but worse under expression variation. It is better to solve object (expressions) variations in visible images as geometric and appearance features in thermography are more blurred [44]. Different approach takes advantage of temperature distribution together with some considerations about face symmetry [43]. This analysis allows determining characteristic facial points on thermograms and applying specially prepared pattern to it. As a result, head orientation may be determined with satisfactory accuracy.

In order to estimate the respiration rate in mobile conditions, face detection and tracking algorithm should be able to run in real time. Although some methods have been already proposed for detecting face and its features in thermography, the time of processing one frame has not been specified in most of them. However, this parameter is required in order to determine whether the computational performance of the methods allows to run robustly in real time while achieving reliable feature detection.

3 Analysis of Respiration Waveforms

3.1 Heat Flow Near Nasal Cavities

Temperature differences observed at the nostrils or mouth level are a result of heat flow caused by respiration activities and several components describing the local environment. Abbas [27] described the total heat flow rate that is related to one respiration cycle inside the nasal cavity at the nostrils level, as:

$$Q_{\mathrm{RR}}(t) = Q_{\mathrm{conv}}(t) + Q_{\mathrm{rad}}(t) + Q_{\mathrm{perf}}(t) + Q_{\mathrm{evap}}(t) + Q_{\mathrm{other}}(t), \tag{2}$$

where:

$Q_{\mathrm{conv}}(t)$ convective heat flow related to airflow in nasal cavities, proportional to the temperature difference between the body (nasal cavity tissue) and the environment.
$Q_{\mathrm{rad}}(t)$ the radiation heat flow.
$Q_{\mathrm{perf}}(t)$ heat flow as a result of blood perfusion/flow.
$Q_{\mathrm{evap}}(t)$ heat flow caused by evaporation at the nasal surface.
$Q_{\mathrm{other}}(t)$ other, secondary heat flow/loss sources

The convective heat transfer is a result of temperature differences between the body (nasal cavity tissue) and the environment:

$$Q_{\mathrm{conv}}(t) = k \cdot (T_{\mathrm{e}}(t) - T_{\mathrm{nc}}(t)) \cdot A_{\mathrm{nc}} = -k \cdot \Delta T(t) \cdot A_{\mathrm{nc}}, \tag{3}$$

where: k is the heat transfer coefficient, T_{e} is the local environment temperature, T_{nc} is the temperature of nasal cavity tissue, A_{nc} is the internal surface area of the nasal cavity.

The net radiation loss rate at the nostrils region can be described by

$$Q_{\mathrm{rad}}(t) = \varepsilon \cdot \sigma \cdot (T_{\mathrm{nc}}^4 - T_{\mathrm{e}}^4) \cdot A_{\mathrm{nc}}, \tag{4}$$

where: ε is the emissivity of the nasal tissue, σ = 5.6703 10^{-8} × (W/m^2 K^4) is the Stefan-Boltzmann Constant.

The heat flow related to blood perfusion can be usually treated as a distributed heat source:

$$Q_{\mathrm{perf}}(t) = \omega \cdot \rho_{\mathrm{b}} \cdot c_{\mathrm{b}} \cdot (1 - k) \cdot (T_{\mathrm{a}}(t) - T_{\mathrm{nc}}(t)), \tag{5}$$

where: ω is the perfusion rate (volumetric flow rate of blood per volume of tissue), ρ_{b} is the blood density factor, c_{b} is the specific heat capacity of the blood, $k < 1$ is the factor representing the incomplete thermal equilibrium between blood and tissue; T_{a} is the arterial blood temperature.

The overall heat flow is therefore mainly related to changing air temperature and blood perfusion. The initial state or hypothetical steady state can be defined here as

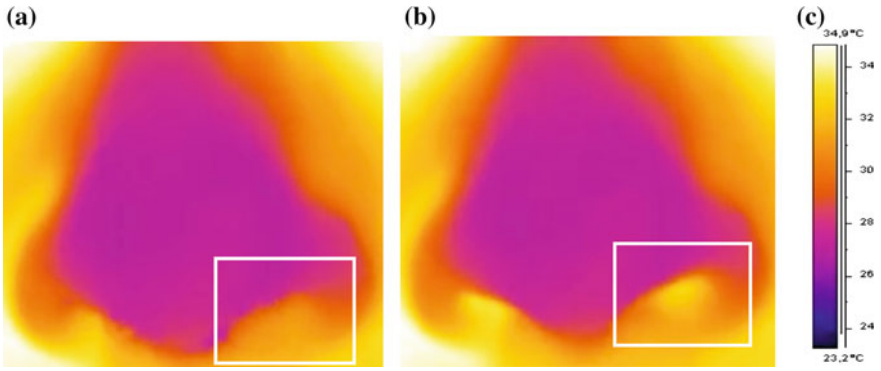

Fig. 2 Examples of thermal images taken during inspiration (**a**) and during expiration (**b**). Color legend is presented in (**c**). The ambient temperature was 25 °C

a lack of airflow due to the apnea (cessation of respiratory actions). Inspiration or expiration actions result in airflow that depending on values of parameters in Eqs. 3–5 and can produce observable changes of intensity of radiation or temperature in nasal/nostrils region of interest (ROI). Due to dynamic character of this process the observable intensity ($I(x, y, t)$) or temperature ($T(x, y, t)$) change is a function of time and location. In Fig. 2 examples of thermal images are presented, taken during inspiration (a) and during expiration (b). There is an observable difference of temperature distributions between both thermograms visible in the highlighted region of the nostrils.

The heat flow dynamics at nostrils or mouth levels can be observed in measured sequences of thermal images. These sequences are further processed to extract respiration-related waveforms (signals).

3.2 Data Acquisition and Preprocessing

Sequences of thermal images are recorded using thermal camera, usually using LWIR detectors. The goal of the presented work was to evaluate accuracy of respiration rate analysis using small and portable thermal cameras that can be embedded in smart glasses. Under the eGlasses platform we are developing the experimental smart glasses platform that is dedicated to research activities. It can be easily modified, for example, different electronic modules can be changed; it is possible to print another cover using 3D printer, add sensors or electrodes, change the display, etc. The current prototype of eGlasses uses OMAP 4460 processor with 1024 × 768 transparent display (Elvision Company), 1 GB RAM, 5 MPx camera, WiFi and Bluetooth 4 wireless interfaces, additional sensors (accelerometer, gyroscope, magnetometer, etc.), eye-tracker and extension slots. The Android 4.1 OS and Linux Ubuntu OS have been already tested. For the goals of this work two

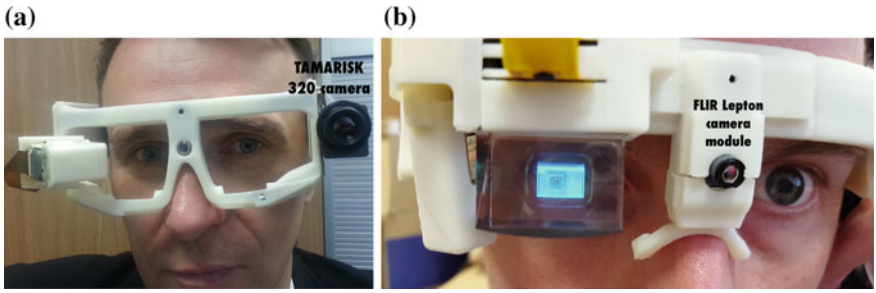

Fig. 3 Smart glasses with thermal cameras: **a** TAMARISK 320, **b** FLIR Lepton module

thermal cameras were used: the TAMARISK 320 LWIR camera and FLIR Lepton LWIR camera module. The first camera, TAMARISK 320, has a spatial resolution 320 × 240, sensitivity <50 mK and was connected using the frame grabber. The second camera, FLIR Lepton, has smaller spatial resolution 80 × 60, sensitivity <50 mK, has a 14-bit dynamics and was connected using SPI (Serial Peripheral Interface) interface with the use of specially designed electronic circuit. Figure 3 presents both cameras located is frames of two prototypes of the eGlasses platform.

In the experimental studies it was assumed that thermal cameras are observing subjects from short distances (<1.1 m) with at least partially visible nostrils. Thermal sequences were recorded for several groups of healthy volunteers. Measurements took place in laboratory rooms at ambient temperature between 23–27 °C. All subjects were asked to rest and not move during the experiment. Thermal images were recorded during 60 s with the sampling frequency (f_s or frames per seconds, fps) set to about 25 Hz (frame grabber, TAMARISK 320) and 13 Hz (Lepton). In parallel, during all experiments, respiration activities were additionally monitored using the respiration, pressure belt (Vernier RMB).

The first step of data preprocessing was the extraction of intensity of radiation changes that could represent respiration changes. Since in this experiment motion compensation was not used therefore changes were observed inside region of interests (ROI) manually selected at the level of the nostrils or mouth. It was assumed that due to respiration activities intensities of radiation are changing in the region of the nose or/and mouth. For each video frame the region of interest is extracted and corresponding values are averaged (one value for a frame):

$$s(t_i) = \frac{1}{N_{\mathrm{ROI}}} \sum_{x=C_s}^{C_e} \sum_{y=r_s}^{r_e} I(x, y), \tag{6}$$

where: N_{ROI}—number of pixels in the nose ROI, r_s, c_s—first (start) row and column of the ROI rectangle, r_e, c_e—last (end) row and column of the ROI rectangle, $I(x, y)$—pixel value of the data matrix of the ROI, i—the frame number ($i = 0 \ldots K - 1$, K—number of frames).

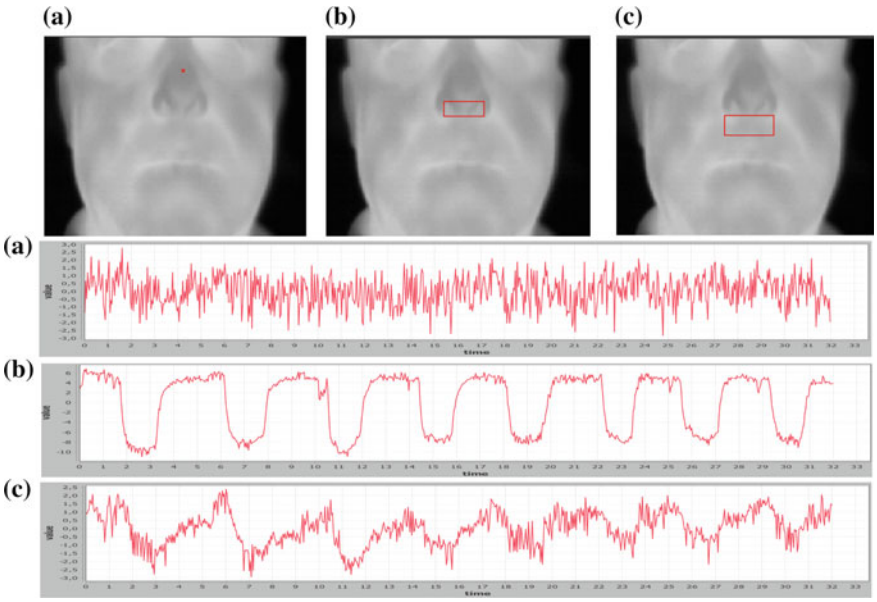

Fig. 4 The location of ROIs and extracted (using the average operator) signals for: **a** the single pixel ROI in the middle of the nose (no respiration waveform expected), **b** the ROI covering nostrils, **c** the ROI below nostrils. Data acquired using the TAMARISK 320 camera. Decrease in the periodical signals (**b**, **c**) is caused by inspirations (cooling—lower intensity values)

Finally the set of digital values (respiration-related waveform) are calculated and normalized to the mean value:

$$s_n(t_i) = s(t_i) - \mu(s(t)). \tag{7}$$

The ROI selection plays very important role in the extraction of respiration-related waveforms. In Fig. 4 examples of 3 different ROI locations or sizes are presented together with the derived $s(t_i)$ signals.

In the state of the art the averaging operation is commonly used to calculate the final aggregate of intensities of pixels inside a ROI. This is justified as it is very fast operation to implement (near real time estimation of respiration rate) and can spatially filter (low pass) data. To obtain high signal (respiration-related waveform) to noise (thermal interferences) the ROI should contain many pixels that represent skin surface where the respiration-related heat flow changes the local temperature. Therefore, the size of the ROI should be big enough to compensate small movements of the subject (and other related small temperature interferences) and small enough to contain majority of pixels representing respiration-related change of intensity. However, other aggregation operators could be used. For example, we have experimentally verified that higher 1st order moments can be successfully used to extract respiration waveforms, assuming that the ROI covers relatively large

area, where there are not other that respiration-related changes. The best results where obtained for the adjusted Fisher-Pearson coefficient of skewness, calculated as:

$$s_s(t_i) = \frac{N_{\mathrm{ROI}}}{(N_{\mathrm{ROI}} - 1) \cdot (N_{\mathrm{ROI}} - 2)} \cdot \sum_{x=C_s}^{C_e} \sum_{y=r_s}^{r_e} \left(\frac{I(x,y) - \mu_{\mathrm{ROI}}}{\sigma} \right)^3, \tag{8}$$

where: μ_{ROI} is an average pixel value in the ROI, σ_{ROI} is a standard deviation of pixel values in the ROI.

Skewness is a measure of symmetry or the lack of symmetry. The skewness for a normal distribution is zero, and any symmetric around mean data should have a skewness coefficient value near zero. Inspiration causes the local changes of data distribution in the analyzed ROI and data are skewed more left or right in reference to "expiration" or "pause" frames. Subtracting mean value of the skewness lead to the representation of skewness changes that represent temperature changes in the ROI. In Fig. 5 some examples of respiration-related signals extracted using the skewness operator are presented.

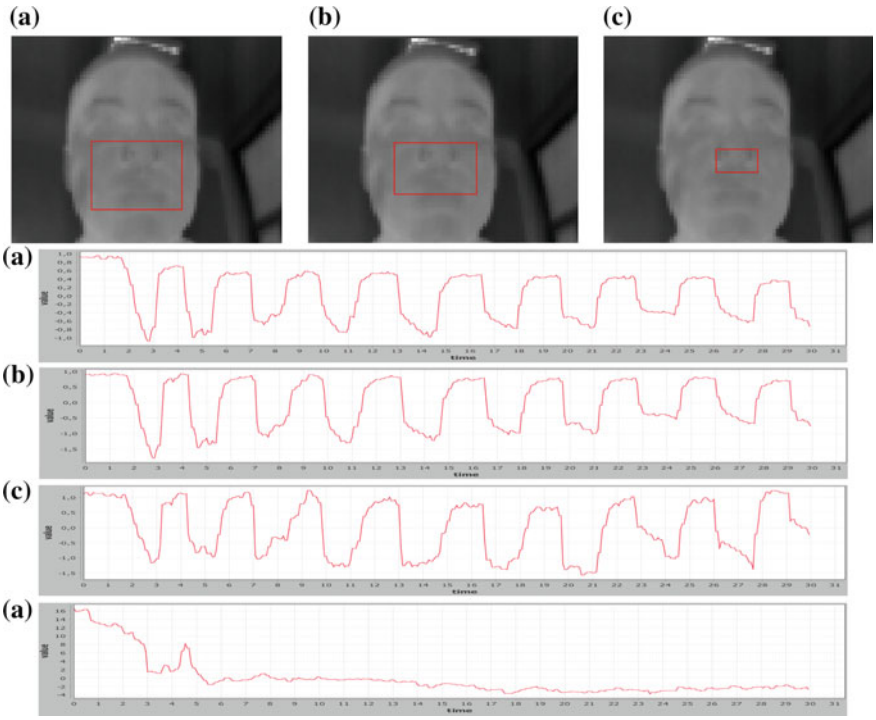

Fig. 5 The location, size and extracted (using skewness operator) signals for: **a** the biggest ROI covering nostrils, mouth and cheeks, **b** the middle size ROI covering the nostrils but not mouth, **c** the small ROI covering nostrils. The waveform on the *bottom* was extracted for the biggest ROI using the average operator. Data acquired using the FLIR Lepton camera

As it can be observed in Fig. 5 there are only small differences in extracted signals for different sizes of ROIs. For comparison, the last waveform shown in Fig. 5 presents the extracted waveform using the averaging operator for the biggest ROI in the Fig. 5a. It is practically useless for the analysis of respiration changes since the averaging operation performed on many pixels smoothed the changes generated by respiration activities. In the contrary, for the skewness operator extracted waveforms are practically not very sensitive on the size of the ROI, assuming that (1) it covers nostrils and (2) it is not too small. It was experimentally verified, that the width of the ROI should be at least equal to the width of nose and the height of the ROI could be set equal to width (what simplifies calculations). It is important to underline that using the skewness operator it is not necessary to precisely locate the ROI or classify the pixels as respiration-related or not. The ROI could be automatically detected using some predefined proportions in reference to the detected face area. Methods of face detection for thermal images are described later in this chapter.

Extracted, respiration-related waveforms are usually corrupted by higher frequency noise and by baseline drift. Therefore, the additional signal filtration is typically used. Baseline removal was performed using 4th-order high pass Butterworth filter with cutoff frequency set to 0.1 Hz. The low-pass filtration was implemented using repeated moving average operation with the window size of $f_s/2$. The preprocessed signals are further analyze to estimate the respiration rate and other parameters describing the respiration waveform.

3.3 Respiration Rate Estimators

Different methods have been previously proposed for the determination of the main frequency (period) of the periodical signal. In the presented studies short time windows were analyzed in the context of the respiration rate estimation using a thermal camera embedded in smart glasses. The typically used frequency estimator is based on the detection of the frequency value (f_{RR}) for the dominating peak (maximum value) in the frequency domain. It assumes that the respiration signal is dominating in the analyzed signal spectrum. The method has some disadvantages. For short time signals it has low frequency resolution. For example, assuming that the acquisition time T_a is equal to 15 s, sampling frequency f_s = 15 Hz, and number of samples N = 225 then the frequency resolution in frequency domain is equal to:

$$\begin{aligned} \Delta f &= \frac{1}{T_a} = \frac{f_s}{N} = \frac{1}{15} = 0.066(6)\ \text{Hz or} \\ \Delta f &= 0.066(6) * 60\ \text{s} = 4\ \text{bpm}. \end{aligned} \tag{9}$$

Therefore, to increase the estimation accuracy of respiration rate longer acquisition times are required. For example, assuming T_a = 30 s the resolution would be

Δf = 1/30 * 60 s = 2 bpm. Such resolution is practically related to the accuracy of ±1 bpm (the actual value is moved to the nearest left or right discrete frequency). In most medical applications, especially used for screening purposes, such accuracy is acceptable and could be much better than clinical observations. For example, in [47] 54 doctors from London were asked to evaluate 3 video recordings of different respiration activities of mock patients. The observed mean difference between values measured by doctors and known respiration rate values where up to 5.43 bpm (i.e., 0.02 for video no. 1, 2.46 for video no. 2, and 5.43 for video no. 3).

The RR estimation method based on the dominated peak in the frequency spectrum (it will be later labeled as *eRR_sp*) has also other disadvantage. It practically always returns the result even for a signal that doe not represent respiration activities (e.g. noise). Therefore, additional measures are required to evaluate the reliability that the analyzed signal represents respiration activities and the estimated RR value is probable. It will be analyzed later in this chapter.

Respiratory rate is clinically determined by counting the number of times the chest rises or falls per minute. Therefore, other respiration rate estimators could rely in counting events that are related to inspiration and/or expiration. Some examples were described in the state of the art section. Here, we analyze three additional estimators that are used in the analysis of signals in time domain: *eRR_zc*—estimator based on the number of zero-crossings, *eRR_pk*—estimator based on the number of detected peaks, and *eRR_ap*—estimator based on periodicity of peaks locations for the autocorrelation function in the time domain.

The respiratory rate estimator based on the total number of zero-crossings (*nZC*) in the filtered signal computes the frequency as:

$$f_{ZC} = 0.5 \cdot \left(nZC\left(\bar{s}_{fn}(t)\right) - 1\right) \cdot f_s/N \tag{10}$$

$$eRR\_zc = f_{ZC} \cdot 60 \tag{11}$$

The reliable use of this estimator assumes that the analyzed signal is smooth (without high frequency noise/interferences) without baseline drift.

Another respiratory rate estimator that is based on signal morphology uses detection of signal peaks. Typically, it calculates the number of inspiration/expiration peaks in the filtered signal. Assuming that inspiration activities are more easily detected in thermal-bases respiration waveforms (ambient temperature is lower that body temperature) then respiration frequency can be estimated as:

$$f_{PK} = \left(nPK_d\left(\bar{s}_{fn}(t)\right) - 1\right) \cdot f_s/N_d \tag{12}$$

$$eRR\_pk = f_{PK} \cdot 60 \tag{13}$$

where: nPK_d—number of inspiration peaks, N_d—the total number of samples between the first detected inspiration start and the last one.

The method requires the use of a peak detector, so in practice many algorithms could be proposed. In presented studies, the multistep detector was used. First, it is looking for the local minimum and the following local maximum of the analyzed signal, for which their difference is greater than the threshold value T:

$$d_j = \bar{s}_{fn}(t_{J+1}) - \bar{s}_{fn}(t_J), \quad d_j > T \tag{14}$$

where: $\bar{s}_{fn}(t_J)$—filtered signal value of the local minimum at j, $\bar{s}_{fn}(t_{J+1})$—filtered signal value of the local maximum at $j + 1$.

Peak and valleys points are labeled in two phases. In the first phase the threshold value

$T = T_1$ is calculated as:

$$T_1 = T_{K1} \cdot \left(\max\left(\bar{s}_{fn}(t)\right) - \min\left(\bar{s}_{fn}(t)\right)\right) \tag{15}$$

where T_{K1} was the scaling value set to 0.33.

The calculated threshold value is used to detect valleys and corresponding peaks in the analyzed signal. In the second phase, gradients between the corresponding valleys and peaks are calculated and the median value is computed. Next, the calculated median value is used to find the value of the T_2 threshold as:

$$T_2 = T_{K2} \cdot \text{median}(\{\Delta i\}) \tag{16}$$

where $\{\Delta i\}$ is a set of gradient values between the corresponding peaks and valleys.

The new threshold value T_2 is next used in the detector based on the first derivative estimator (4). In the reported study the scaling factor $T_{K2} = 0.25$ was used. The detected peaks are used to calculate the number of peaks () and points in time of the first inspiration event in the analyzed signal window and of the last inspiration event. It enables to calculate the total number of samples between the first detected inspiration start and the last one (N_i).

The next respiration rate estimator used in this study was based on the autocorrelation function. It is known that the autocorrelation sequence of a periodic signal has the same cyclic characteristics as the signal itself. Therefore, the autocorrelation for different time lags is calculated. The period can be further calculated using Fourier Transform and similar analyzes as for the *eRR_sp* estimator. This estimator will be designed further as *eRR_af*. This method has the practically the same disadvantages as the *eRR_sp*. However, the period can be also determined computing the average time period between detected peaks in time domain. Therefore, the next estimator is further used (*eRR_ap*) that detects peaks of the autocorrelation function using the peak detector method presented above.

The estimated frequencies were multiplied by 60(s) to obtain results in beats per minute (bpm). All estimators were calculated for thermal-based signals and signals measured using the reference pressure belt. Reference signals were visually inspected to manually calculate the respiration rate as a number of respiration events in time. The first and the inspiration events were visually detected in the

analyzed signal window. It was assumed that one respiration event longs between two successive starts of inspiration events. The number of respiration events in the analyzed time segment was counted (N_{RE}) and the total time of all respiration events was calculated (T_{RE}). The reference respiration rate was calculated as

$$\mathrm{RR} = (N_{\mathrm{RE}} * 60)/T_{\mathrm{RE}} \tag{17}$$

The Mean Absolute Error (MAE) was used in the evaluation of different estimators. It is defined as:

$$\mathrm{MAE} = \frac{1}{L}\sum_{l=1}^{L} |eRR\_xx_l - \mathrm{RR}_l| \tag{18}$$

where: L—number of data recordings, *eRR_xx*—the evaluated estimator (e.g. *eRR_sp*), RR—manually calculated respiration rate using belt data (the reference).

Similarly the standard deviation of absolute errors was calculated.

In [48] we have demonstrated the results of the study focused on the analysis of different respiration rate estimators. Sequences of thermal images were recorded for 16 healthy volunteers (avg. age = 34.75 years ± 13.16) using the TAMARISK 320 LWIR camera. All subjects were asked to breathe naturally and not to move during the acquisition time (1 min). In parallel reference data were collected using the chest pressure belt (Vernier RMB). Next, data were processed using methods described above in this section (the average operator was used as an aggregation operator in ROIs). The mean absolute error was calculated as a difference between manually calculated respiration rates and values computed using different respiration rate estimators. The best results were achieved for the *eRR_ap* estimator MAE = 0.415 bpm (std. dev. 0.398). The worst results were obtained for the estimator that was based on counting zero-crossings, *eRR_zc*. The achieved MAE was 1.291 bpm (std. dev. 0.93). The same estimators applied to data collected using the reference belt gave very similar results as for thermal-based data. For example the MSE for the *eRR_ap* estimator was 0.295 bpm (std. dev. 0.368), but for the worst *eRR_zc* the MSE was 1.584 bpm (std. dev. 0.816). The error lower that 2 bpm is fully acceptable for medical screening what is the main application of the proposed methodology. It is worth to underline that the implemented estimators worked properly giving similar results for thermal-based data and for belt-data. Small differences in results between the best estimator and manually calculated values were also caused by different number of samples that were analyzed by those methods. The estimators automatically analyzed the whole 30 s long data window. For manually calculated respiration rates only full respiration periods were manually selected from 30 s long data windows.

Similar experiments were described in [49]. Sequences of thermal images were recorded for 11 healthy volunteers (mean age: 39.73 years ± 11.98) using the FLIR Lepton LWIR camera. All subjects were asked to breathe naturally and not to move during the acquisition time (1 min). Also in this experiment reference data

were collected using chest pressure belt (Vernier RMB). All data were processed using methods described above in this section (the average operator was used as an aggregation operator in ROIs). However only two estimators were evaluated: *eRR_sp* and *eRR_ap*. The mean absolute error was calculated as a difference between manually calculated respiration rates (using Eq. 10) and values computed using two respiration rate estimators. Similar, good results were obtained for both estimators. For thermal-based data the MAE for the *eRR_ac* estimator was 0.501 bpm (std. dev. 0.504) and for the *eRR_sp* estimator it was 0.525 bpm (std. dev. 0.454). For belt data results were a little bit better: MAE for the *eRR_ac* estimator was 0.194 bpm (std. dev. 0.143) and for the *eRR_sp* estimator it was 0.418 bpm (std. dev. 0.368).

The above shown results were achieved assuming that subjects do not move and do not speak. In [50] we wanted to investigate if it is possible to estimate respiration rate when subjects are talking. We asked 12 healthy volunteers (avg. age = 36.25 years ± 12.08) to continuously speak (small head movements were allowed). This condition was similar to such situation, when a patient, during the interview, describes his/her problem. Analyzing the breathing patterns during natural speech could be interesting for medical purposes but also for proper speech training. In this study, the general methodology used in data processing was the same as previously described. However, the average operator was used for ROIs covering mouth areas. Three respiration rate estimators were evaluated: *eRR_zc*, *eRR_sp* and *eRR_ap*. The interesting finding of this study was that results automatically obtained for thermal-based data were generally better than for belt-data. The MAE for the best *eRR_ac* estimator was 0.728 bpm (std. dev. 0.597), for the *eRR_sp* estimator it was 2.089 bpm (std. dev. 2.346) and for the *eRR_zc* estimator it was 3.575 bpm (std. dev. 2.864). Results obtained for belt data were: for the *eRR_ac* estimator MAE = 2.553 bpm (std. dev. 2.373), for the *eRR_sp* estimator it was 2.496 bpm (std. dev. 2.153) and for the *eRR_zc* estimator it was 1.423 bpm (std. dev. 1.377). The overall results are worse than those when subjects were not speaking. This is because the extracted respiration related signals were much more noisy and sometimes respirations were irregular. In such conditions signals were not stationary. Some examples are presented in Fig. 6.

The described results were obtained using an average as the aggregation operator applied for ROIs of the nostrils or mouth. However, we have also compared previously described estimators for signals extracted using the skewness operator. In this study the FLIR Lepton camera was used. Data were recorded for 10 healthy volunteers (age: 38 years ± 9.3; recording time 1 min, sampling frequency f_s = 13 Hz). The respiration, pressure belt (Vernier RMB) was used for reference measurements. The best results were obtained for three estimators: *eRR_sp*, *eRR_af*, and *eRR_ap*. In most cases the results of the *eRR_sp* and *eRR_af* were similar due to the used similar method of the frequency estimation. Theoretically, for periodical signals without noise, values calculated by these estimators should be the same because the autocorrelation sequence of a periodic signal has the same cyclic characteristics as the signal itself. So the dominated peaks should be observed for the same frequency in the frequency spectrum. In Fig. 7 examples of filtered

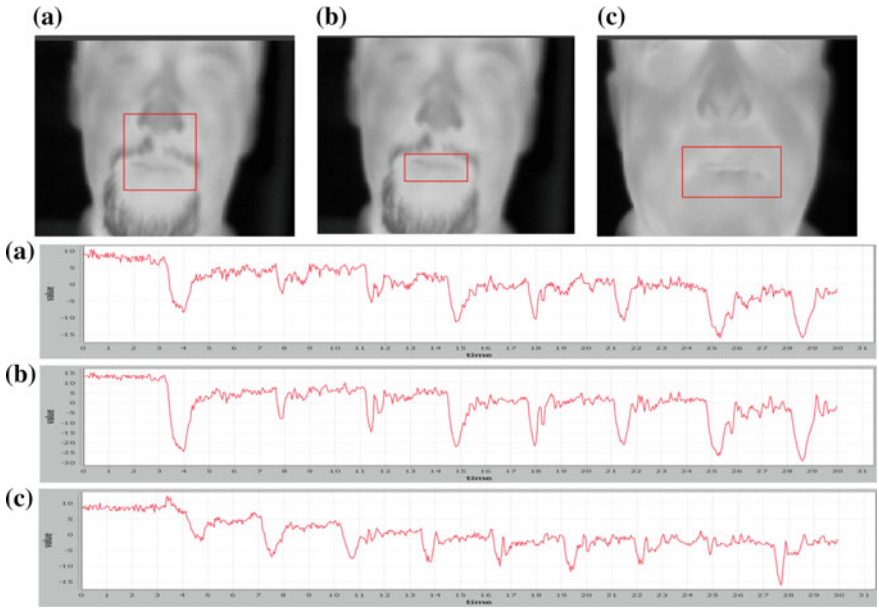

Fig. 6 Results of extracted respiration waveforms for speaking subjects. S02, S08

signals, their frequency spectrum and autocorrelation signal as a function of time lags are presented.

In Table 1 values of the mean absolute error, the standard deviation of absolute error and the coefficient of determination, denoted R^2, (representing the correlation between estimated and reference data) are presented for best estimators in the study.

The best results were achieved using the signals extracted from thermal recordings as a sequence of normalized skewness values of ROI data. It should be also underlined that these good results were observed for all estimators. The results obtained using the skewness operator for thermal data were almost identical to those obtained for reference belt data. The *eRR_ap* estimator gave best results for belt data and for thermal data processed using the skewness operator. In Fig. 8 the values of MAE are illustrated and graphically compared.

Other aggregation operators were proposed in [51], however the better results were obtained for the skewness operator.

The obtained results indicate that respiration rate can be reliable estimated using the analysis of thermal recordings. Different estimators were evaluated for thermal sequences recorded using two small, portable cameras: TAMARISK 320 and FLIR Lepton. In all cases the most accurate estimates of respiration rates were achieved for the *eRR_ap* estimator. This estimator is based on the calculation of autocorrelation for different time lags. Peaks of the derived signal are detected in time domain so there are not such limitations as for methods based on the analysis in frequency domain (e.g. limited frequency resolution). The periodicity of the derived signal is analyzed so

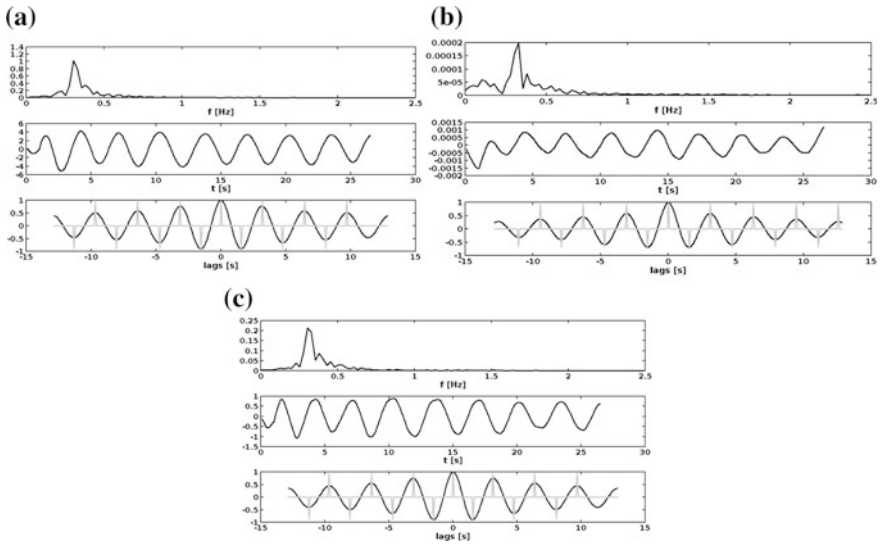

Fig. 7 The frequency spectrum, the filtered signal and (*bottom*) the autocorrelation signal as a function of time lags for the subject S09 for: **a** belt data, **b** thermal data—processed using the average operator, **c** thermal data—processed using the skewness operator

Table 1 Results of the study with the analysis of signals extracted using the skewness operator

Method	Belt			Thermal camera (average)			Thermal camera (skewness)		
Estimator	*eRR_sp*	*eRR_ap*	*eRR_af*	*eRR_sp*	*eRR_ac*	*eRR_af*	*eRR_sp*	*eRR_ac*	*eRR_af*
MAE (bpm)	0.350	0.182	0.428	0.468	0.529	0.622	0.350	0.236	0.350
Std. dev (bpm)	0.314	0.139	0.404	0.440	0.514	0.627	0.314	0.193	0.314
R^2	0.991	0.998	0.987	0.982	0.982	0.970	0.991	0.997	0.991

additional measures could be proposed to evaluate if the analyzed signal is periodically enough to reliable estimate respiration rate. It is also important to underline that if respirations are irregular then better results should be obtained using estimators based on the detection (and counting) of peaks in time domain. In such cases respiration signals are not stationary and results based on the dominating frequency analysis could lead to higher errors of respiration rate estimates.

Additionally, the very interesting finding is the possibility of estimation of respiration rate when the observed subject is speaking. In practice, smart glasses with the embedded thermal camera and required software could be a very useful tool for a healthcare professional. It can estimate respiration rate more naturally, during typical interview, without "artificially" connected devices to a patient.

Another interesting observation was related to data aggregation in ROIs. For thermal sequences recorded using the FLIR Lepton camera module better results were obtained calculating the skewness value instead of the average value for the ROI of each frame. It was also important, from the practical point of view, that the size of the ROI was not so important for obtaining the signal that contained

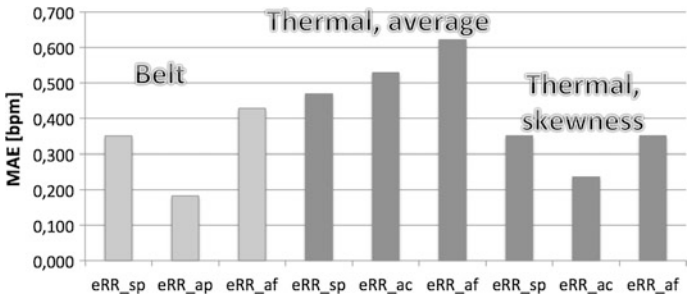

Fig. 8 The comparison of values of mean absolute error for particular methods

respiration related changes. It could partially reduce the computational complexity related to the determination of the best ROI size and location in data frames. However, this still does not solve a problem of patient movements. In such situations face/nostril detection and tracking algorithms are required.

3.4 Respiration Pattern Analysis

Respiration rate is the most important parameter that can be computed from the respiration signal. However, other parameters could be valuable for medical diagnostics. Some examples include: the number and length of apnea events, the depth of breathing or amplitudes of inspiration/expiration event, the length of inspiration phase, the length of expiration phase, the regularity of respiration events, etc. These parameters can also describe and can allow discriminating between different respiration patterns presented in Sect. 1. Most of the parameters are mainly based on the detection of three events: start of the inspiration event, start of the expiration event and end of the expiration event. For example, the apnea period can be defined here as a time period between the start of the inspiration event and the end of previous expiration event.

In the study presented in [49] we investigated whether it is possible to reliable detect apnea events from respiration waveforms extracted from sequences of thermal images. During the experiments 12 healthy participants (avg. age = 37.15 years $\pm$ 9.16) were asked to follow the T1–T5 respiration patterns. Thermal sequences were recorded using the TAMARISK 320 camera using the procedure described earlier for the analysis of respiration rate. To analyze the possibility of apnea events detection volunteers were asked to hold breath to simulate apnea periods in T1, T2, T4, and T5 patterns. They could decide when hold the breath and how long the apnea event should long. In apnea periods of the extracted signals from thermal recordings the temperature variations were observed. It is caused many internal (e.g. blood flow) and external (heat flow due to ambient temperature changes) thermal conditions. In reference to the baseline such changes can be positive (trend with the positive slope), negative (trend with the negative slope) or

neutral (without slope, normalized mean about 0). The observed rate of such changes is typically smaller that for respiration rate and the observed temperature gradient is also significantly smaller than for respiration activity. We proposed the apnea events detection algorithm (Algorithm 1).

Algorithm 1: DetectApneaEvents(filteredSignal, Fs, K, Tapnea)

```
sDiff=FirstDerivative(filteredSignal);
absSDiff=abs(sDiff);
nAbsSDiff=1/max(absSDiff) * absSDiff;
IQR=CalculateInterQuartileRange(nAbsSDiff);
T=K*IQR;
i=0, tStart=0;
for j=1:length(nAbsSDiff)
        if (nAbsSDiff (j) <T)
                if (counter==0)
                        tStart=j;
                else    counter++;
                endif;
        else    if(counter>0){
                        if((counter/Fs)>Tapnea)
                                apneaStart[i]=tStart;
                                apneaStop[i]=j;
                                apneaPeriods[i]=counter/Fs;
                        endif;
                endif;
                tStart=0;
                counter=0;
        endif;
endfor;
return [apneaStart apneaStop apneaPeriods]
```

It was based on the first derivative of the filtered signal. The absolute values of the first derivative signal were normalized in reference to maximum signal value. Then the algorithm is counting all successive samples, for which values are smaller than the threshold value. The threshold value, T, is calculated as the weighted (K) value of the interquartile range (IQR) for the processed signal. The apnea event is detected if the number of samples (or time period) is higher than the assumed parameter value, *Tapnea* (e.g. >10 s).

Some results for the apnea detection algorithm are presented in Fig. 9a, b.

The very interesting result can be observed from the analysis of signals presented in Fig. 9. For example, the first train of respiration events for thermal recording has more events (8 inspiration events) than the signal measured using the respiration belt (7 events). Similar situation can be observed for the last, 3rd, train. For the pattern T1, subjects were asked to first increase the respiration effort and then decrease. Very shallow respirations in the end of 1st and 3rd trains were not observed using the respiration belt. The pressure difference was too small to be observable. Probably, if the initial air pressure in the belt were higher then the pressure difference would be visible. However, that would be very uncomfortable for the participant of the experiment. It can be concluded that respiration monitoring using the thermal imaging is sensitive to inspirations even when the respiration effort is small.

In Fig. 10 examples of the results of apnea detection algorithm are presented for different respiration patterns extracted from recorded sequences of thermal images.

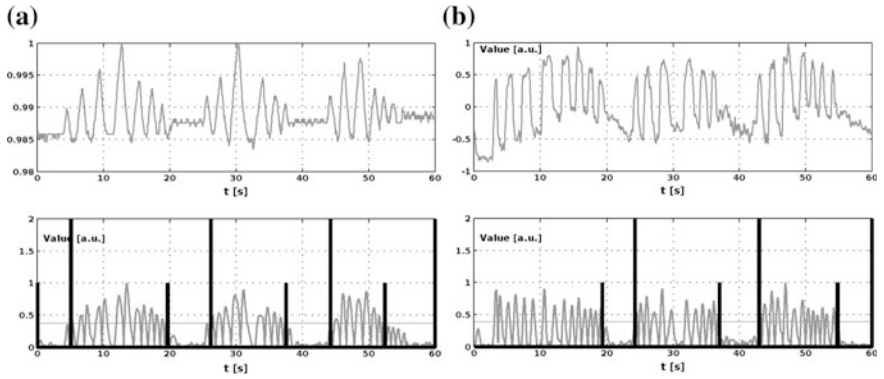

Fig. 9 Original respiration waveforms (*top*) and detected apnea periods using the Algorithm 1 for: **a** the signal recorded using the pressure belt, **b** the signal derived from the thermal recording. Presented signals were recorded for a subject S01 using the T1 respiration pattern

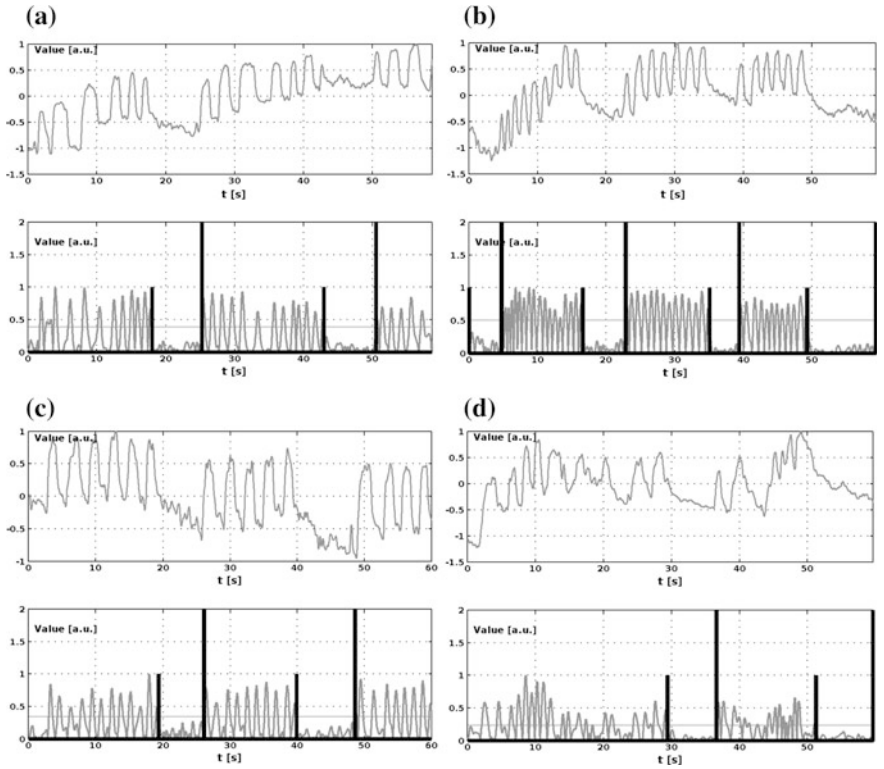

Fig. 10 Original respiration waveforms (*top*) and detected apnea periods using the Algorithm 1 for signals derived from the thermal recording for subject S09 and for: **a** T1 pattern, **b** T2 pattern, **c** T4 pattern, and **d** T5 pattern. The results for the T3 pattern is not presented since it does not contain simulated apnea periods

The mean absolute error calculated for differences between automatically detected lengths of apnea periods in thermal-based signals and manually calculated lengths of apnea events for belt-based signals was 0.44 (assuming *Tapnea* = 4 s and $K = 0.6$ in the Algorithm 1). The standard deviation was 0.39. Obtained results were very similar to the results of automatic processing of belt-based data. Therefore, it can be concluded that apnea periods can be reliable detected from different respiration patterns that can be extracted from thermal recordings. In the description of respiration patterns we proved that respiration rates (in given time windows) and length of apnea events could be accurately detected from signals extracted for thermal recordings. Additionally, relative amplitude values of respiration waveforms obtained using the reference belt and using the thermal camera were analyzed. The amplitudes were compared manually by the comparison of signal plots in time domain (for the pattern RP1). As it can be observed from Fig. 9 signals derived from thermal recordings do not follow the crescendo–decrescendo pattern than is easily observable in the signal recorded by the pressure belt. Results obtained for all volunteers confirmed that it is not possible to reliable correlate amplitude variations between signals measured with the pressure belt and signals extracted from thermal recordings. As it was described earlier, the thermal recording is sensitive to small temperature changes (respiration with very small effort) but it is not proportional to different effort levels. It can be explained by the heat flow mechanism assuming the cooling process during the inspiration (in room temperatures lower that body temperature). In the first phase of inhalation there is a high gradient of temperatures (air to nasal cavity tissue) that decreases with time of inhalation. Since the ambient temperature is not changing and, in parallel, nasal cavity tissue is heated by blood perfusion (and also by other mechanisms) therefore the observable temperature change is becoming saturated. Therefore, it is practically impossible to quantitatively compare breathings with different efforts (depths).

In [51] we additionally compared methods of detection of inspiration periods and expiration periods comparing the results obtained for signals recorded with the respiration belt and extracted from thermal recordings (using the TAMARISK 320 camera). The peak-and-valleys detector was used twice: analyzing the signal from the start to the end and from the end to the start. In the first phase starts of inspiration events and ends of inspiration events were detected. In the second pass (from the last sample towards the first sample) the end of expiration and the start of expiration events were detected. The inspiration period I_t was calculated as the difference between the time of inspiration end and inspiration start. The same method was used to calculate the expiration period E_t. Values of I_t and E_t were calculated for signals recorded with the respiration belt and extracted from thermal recordings. The mean absolute difference was calculated as a normalized mean absolute difference between values calculated for the belt-based signal and for the thermal-based signal. The normalization was performed by dividing the absolute difference value by the inspiration or expiration period value obtained for signals recorded using the reference pressure belt, i.e.:

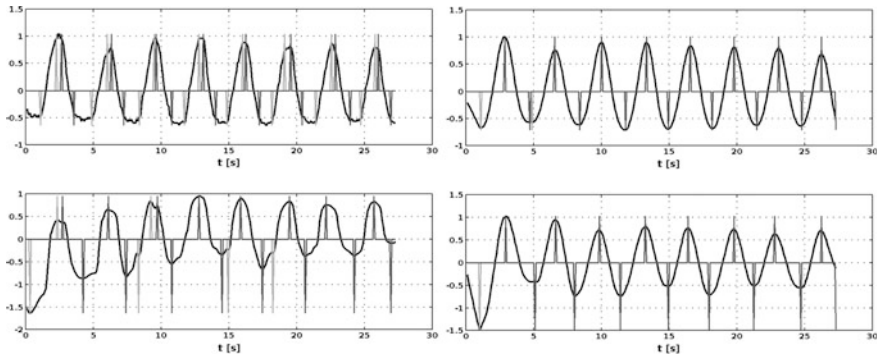

Fig. 11 Examples of original (*left*) and filtered (*right*) respiration waveforms obtained for the respiration belt (*top*) and extracted from the thermal recording (*bottom*). Automatically detected inspiration/expiration beginnings and ends are indicated. After low pass filtration inspiration ends are practically the same as expiration beginnings and expiration ends are the inspiration beginnings

$$\Delta I_t = |I_{t\mathrm{B}} - I_{t\mathrm{T}}|/I_{t\mathrm{B}}; \quad \Delta E_t = |E_{t\mathrm{B}} - E_{t\mathrm{T}}|/E_{t\mathrm{B}}; \tag{19}$$

where:

$I_{t\mathrm{B}}$, $E_{t\mathrm{B}}$ inspiration/expiration period calculated for the belt signal,
$I_{t\mathrm{T}}$, $E_{t\mathrm{T}}$ inspiration/expiration period calculated for the signal extracted from the thermal recording.

In Fig. 11 examples of respiration waveforms with automatically detected inspiration/expiration beginnings and ends are presented. It can be observed that for the original belt signal the respiration pause can be observed due to small pressure changes measured in the end of expiration and at the beginning of inspiration.

The results obtained for data recorded for 12 healthy volunteers (avg. age = 36.25 years ± 12.08) shown that inspiration and expiration beginnings and ends events can be detected with certain accuracy. Some differences were obtained between inspiration and expiration periods calculated for signals recorded using the respiration belt and signals extracted from thermal recordings. The normalized, mean absolute difference was about 19% for inspiration periods and about 15% for expiration periods. This relatively big difference is caused by several issues. First, there is a difference between both measurement methods. The start of inspiration can be earlier detected by the thermal imaging since even very small inspiration effort is clearly visible as cooling (if the ambient temperature is lower that the body temperature). For the respiration belt the small pressure change is visible only if the belt firmly adheres to the body and the initial air pressure in the belt is high enough to observe the difference related to very small respiration movements. Another reason for the observed values of mean absolute differences was the role of signal filtration. The proper use of the peak detector assumes that the signal is smoothed. The filtered signal has smoothed edges so the accuracy of the detection of exact

points in time when the change starts is lower that for the ideal step signal. Additionally, the analyzed signals have limited resolution. For example, if the inspiration period longs 1 s (13 samples) then shift by 1 sample in inspiration start and stop events leads to 2/13 = 14.4% of total difference.

Additionally, inspiration-related slopes (*S*) were calculated and compared for signals recorded with the thermal camera and using the reference, pressure belt. The values of slopes were calculated as the relation of the signal gradient for the corresponding inspiration start/end events to the time difference between points of time when those events occurred. The mean difference between inspiration-related slopes calculated between values obtained for signals recorded using the respiration belt and signals extracted from thermal recordings was 5.04° (±5.24). The smallest difference was 0.97, but the highest value was 18.32. Again, reasons of such differences are similar as described previously, since the calculation of slopes is based on accurate detection of inspiration beginning and end.

3.5 Automatic Detection of the Nostril Region

To estimate the respiration rate of subjects, the thermal facial image sequences have to be preprocessed for detecting and tracking face and nostril region. Some approach for real time nostril area tracking has already been discussed and described in details [52, 53]. The flow of described solution is presented in Fig. 12. In face-processing systems face detection is usually a first step [39]. After extracting facial area from the background it can be processed further in order to analyze its features.

In thermal imagery, the face is usually distinct from other part of image and can be easily marked. Most of existing methods extract face by segmentation, which can be easily achieved with thresholding [32]. On the other hand, Haar-like features

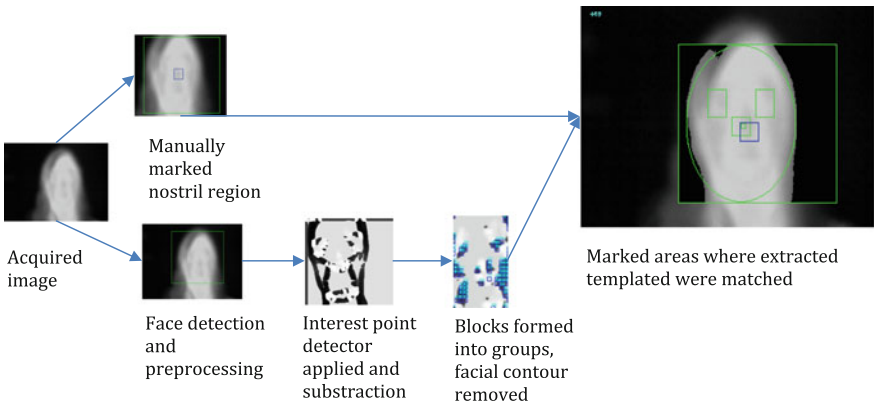

Fig. 12 The flow of proposed solution for tracking nostril region

Fig. 13 Examples of acquired images: *from the left*—2 positive and 2 negative cases

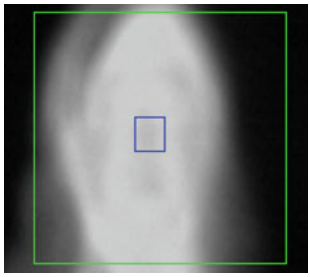

Fig. 14 The nostril area marked manually

are often used as a descriptor of the local appearance, because of high precision and computation speed of Viola-Jones algorithm [39, 44, 54]. This algorithm, which can run practically in real time, consists of two steps: training and detection. In a first phase a special classifier with cascade structure is trained from labeled images. Features from each image are extracted by encoding the presence of oriented contrasts between two regions with Haar-features. The resulted classifier is then used to detect objects in test data set.

In the study presented in [53], thermal video sequences were recorded by using TAMARISK 320 long wave thermal camera (resolution 320×240, sensitivity <50 mK, 25 fps) on a group of 19 volunteers (age: 23.7 ± 5.2). During the experiment each volunteer was asked to stand still, turn head slightly left and turn head slightly right. Then, 12,000 thermal images that portray male and female faces (positive cases) and 3000 images of other objects (negative cases) were extracted from recorded sequences and used to train the classifier. Examples of acquired images are presented in Fig. 13. The result of the training step was the Haar-feature classifier capable for face detection in the test data set that consisted of 480 images (20 for each volunteer).

The presented research [53] aimed at validating possibilities of tracking nostril region with acceptable accuracy in real time. In order to measure the precision of the algorithm, the mean value of pixel intensities in detected and tracked area was compared with the mean value of pixel intensities in nostril area marked manually in fixed position (not tracked), see Fig. 14.

Moreover, mean squared error (MSE) and root mean squared error (RMSE) of mean values were calculated separately for series of images that portray each volunteer during performing each movement (quiescence, turn left or turn right).

In thermography most of facial features are usually blurred and undistinguishable [39]. Moreover, usable data may be represented by close contrast values. To make the detection algorithm more robust authors of [53] increased image contrast by making following improvements: the image conversion to a gray scale and a histogram equalization. After extracting facial region and enhancing valuable data, interest points detectors (ORB, SIFT, SURF and Harris Corner Detector) were applied to this area to find specific facial features. Each detector was tested for processing time and accuracy, that was measured as a displacement of detected area from its expected location (specified by an expert) divided by the image height. For each interest point detector, the subtraction between image with found features and original image was calculated. The resulted image is presented in Fig. 15.

Then, the image was divided into blocks (30×30) and the mean value of pixel intensities in each block was calculated. In next step, authors applied thresholding as a segmentation technique, which aimed at partitioning an image into different components. The image was divided into parts with values higher and lower than selected threshold. This operation allowed marking blocks that contain interest points. After that, blocks that were close to each other were classified to the same group. The most numerous groups were formed from facial contour and they did not contain information about facial features, so they were removed. From the remaining groups, interest areas templates were extracted. The whole procedure was repeated for N initial frames and the average location of each template was calculated. The resulted locations and sizes were used to extract final templates, which were matched in next frames using pattern matching technique. The best match was defined as global minimum of all comparisons between templates and image patches slid across tested image. At each location, the template was compared against overlapped patch by calculating its metric using 'CV_TM_SQDIFF' method from OpenCV library [55].

The number of matched regions was limited to two, by preserving only these, which distance to nostril area (marked manually) was smallest. Next, the detected nose area was located in the middle of the horizontal distance between two matched areas (in all cases they represented eyes) and directly underneath them. Then, this nostril area was tracked by applying the same pattern matching method.

Fig. 15 The subtraction of original image and image with detected interest's points (Harris corner detection)

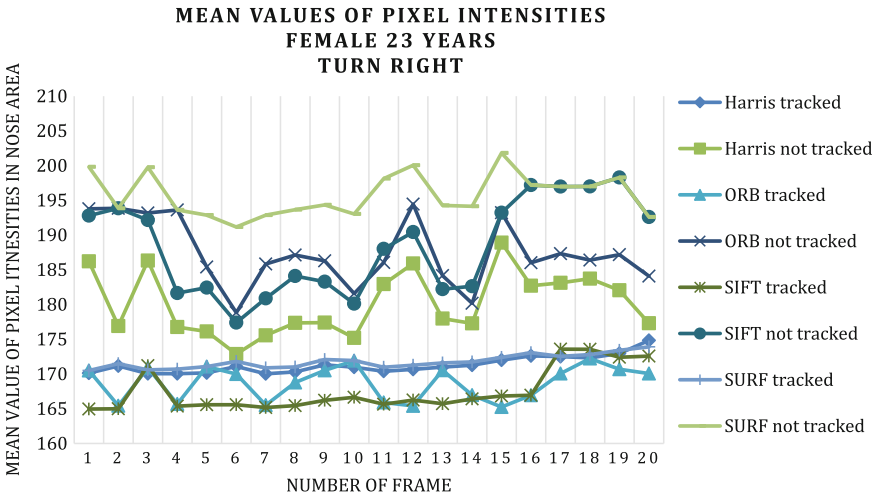

Fig. 16 Mean values of pixel intensities for one volunteer while turning head slightly right (all methods for tracked and fixed localization of nostril region)

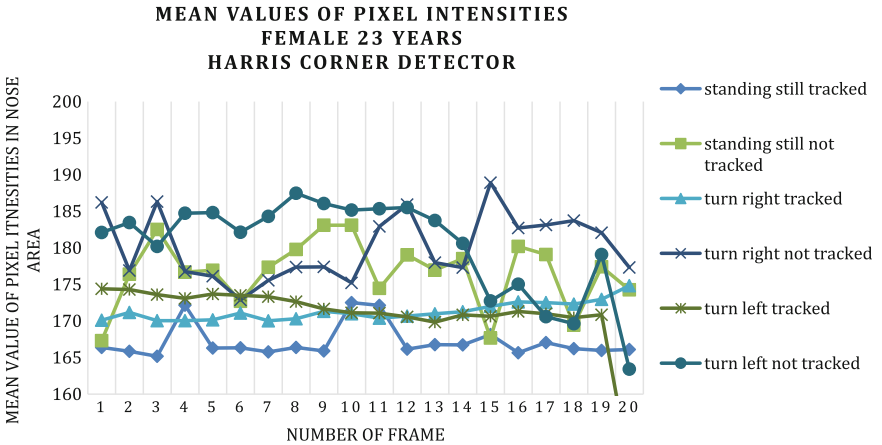

Fig. 17 Mean values of pixel intensities for one volunteer for chosen detector (all movements for tracked and fixed localization of nostril region)

Undoubtedly, the biggest advantage of described system for automatic tracking of nostril area is really short processing time [27.7 ms (Harris), 23.9 ms (ORB), 19.7 ms (SIFT), 27.6 ms (SURF)] while preserving satisfactory accuracy of region detection (displacement for Harris $7.2 \pm 4.3\%$, ORB $9.9 \pm 2.2\%$, SIFT $7.0 \pm 1.9\%$, SURF $8.9 \pm 2.7\%$).

Each interest point detector was used to detect nostril area separately for each movement. Taking it into account, mean value of pixel intensities in tracked and

Table 2 RMSE for each movement: rows represent each volunteer (Female F; Male M followed by age) T—tracked region, NT—not tracked region

Person	Standing still				Turning left				Turning right			
	Harris	ORB	SIFT	SURF	Harris	ORB	SIFT	SURF	Harris	ORB	SIFT	SURF
	T/NT	T/NT	T/NT	T/NT	T/NT	T/NT	T/NT	T/NT	T/NT	T/NT	T/NT	T/NT
F 22	0.3/1.6	0.4/4.9	1.9/3.8	1.7/4.4	7.2/9.2	1.6/4.1	7.6/5.6	1.6/3.6	3.8/3.3	1.7/5.0	0.4/2.1	0.5/2.6
F 23	2.2/4.5	2.7/4.1	1.8/5.3	2.7/6.2	1.2/4.5	2.4/4.6	3.0/6.6	0.9/3.0	2.6/5.5	1.2/3.9	1.8/2.8	1.7/2.4
F 23	2.2/2.8	2.1/5.5	6.3/20.5	17.5/22.6	9.3/14.7	21.6/25.5	8.5/15.6	8.5/14.8	11.1/21.6	10.5/21.3	1.2/3.3	1.2/2.8
F 23	1.6/2.5	0.5/1.6	4.0/8.7	4.0/11.2	1.4/5.0	0.6/2.2	0.6/6.0	0.6/1.9	0.5/4.1	5.7/6.2	0.5/6.1	0.5/2.4
F 23	1.3/2.7	5.7/3.1	12.5/46.9	20.6/45.6	2.5/2.5	6.5/4.1	4.6/6.5	3.5/4.1	14.8/45.3	14.7/46.7	0.5/5.5	2.2/5.2
M 19	1.7/2.2	2.3/2.4	4.2/4.3	3.8/3.6	4.5/4.7	3.3/7.4	3.1/5.9	5.9/5.8	3.3/3.6	5.3/3.9	1.0/2.9	2.6/2.7
M 24	2.2/3.8	0.5/4.0	5.5/5.7	8.4/7.0	5.3/6.8	4.1/9.0	6.8/9.0	8.3/8.3	6.3/7.5	4.6/4.6	0.7/3.4	1.1/4.0
M 44	1.8/2.0	1.8/2.3	2.7/3.1	2.3/3.4	5.3/6.2	5.8/7.7	5.2/4.8	2.8/6.9	1.9/4.5	7.7/3.8	2.0/2.2	3.6/3.1

nostril area marked in fixed position vary depending on used detector and pose of volunteer. Example values of pixel intensities for all detectors while turning head slightly right are presented in Fig. 16.

Values of pixel intensities for chosen detector depending on performed movement are presented in Fig. 17.

As can be seen, changes in the mean values were much more considerable for nostril regions marked in fixed positions. This result was also confirmed by calculated RMSE values (see Table 2). Almost in all cases (instead of 2 pairs of values marked in table with red color) errors were higher for not tracked areas. Similar situation may be observed for different pose variations. For tracked regions fluctuations of mean values were smaller. However, the movements analyzed in [53] were quite inconsiderable and achieved results may be different for other disturbances (for example background or haircut influence, as described in [43]). Currently, algorithm similar to solution presented by authors of [53] is tested for more noticeable movements (also in other planes) by us.

4 Conclusions

In clinical observations, the respiratory rate is often estimated by counting the number of times the chest rises or falls per minute [56]. Other, quantitative methods use different algorithms and techniques, including inductive plethysmographs or thoracic impedance systems [57], oxygen masks [58], bioacoustic sensors [59], accelerometers or gyroscope sensors [60], etc. Respiration activities are often recorded together with other biomedical signals. For example in the sleep studies a set of signals could be recorded, including electroencephalogram, electro-oculogram, electromyogram, nasal airflow, abdominal and/or thoracic movements, body position, snore acoustic signal, electrocardiogram, and blood oxygen saturation [61, 62]. Respiration rate can be estimated not only from one of those methods (e.g. nasal airflow) but also from other recorded signals (body movements, electrocardiogram, etc.). Additionally, in [63] 3D breathing waveforms can be also recovered out of thermal sequences allowing visualization of subtle pathological patterns.

The remote measurement of respiration rate is another very important and useful possibility. It can be especially valuable for medical screening purposes (e.g. severe acute respiratory syndrome (SARS), pandemic influenza, etc.). In this chapter we presented many different studies focused on the measurements and estimation of respiration rate using thermal imaging methods. All of the methods demonstrated the very good results of the estimation of respiratory rates. In our works we focused on the evaluation of different respiration rate estimators for the needs of data processing of image sequences recorded by small, mobile thermal cameras. The miniaturization of thermal camera allowed embedding such cameras in smart glasses. In several studies we demonstrated that using image sequences recorded by

thermal cameras of smart glasses not only respiration rate can be reliable estimated by also some other parameters that describe respiration patterns.

Respiration rate estimation should be performed as fast as possible. However, this requires data acquisition during a specific period of time. This is especially important for typically used data analysis in frequency domain (due to limited spatial resolution). The presented results of our experiments shown that the best accuracies had been obtained using the analysis of autocorrelation as a function of time lags (*eRR_ap* estimator). Ideally, the correlation of the signal with its shifted version should produce a value of 1 if the shift is equal to the signal period. In practice, except for the time offset equal to 0 (the same signal), the values are lower than 1. However, the absolute correlation values obtained for time offsets equal to the next multiplicities of signal period can be further used to evaluate if the original signal is really periodical or not. This could be used to evaluate if it is possible that the signal contains respiration-related information. Other similar measures or parameters can be used to evaluate if the signal is less or more periodical. Some examples include Hijorth parameters [64] or spectral "purity" indexes [65]. We have used them with success in the evaluation of signals for pulse rate estimation [66, 67].

In the analysis of respiration rate it is also important to locate pixels, which values change due to respiration activities. Sometimes data classification procedures are used but it requires relatively more computational resources. More often pixels are aggregated in the manually or automatically specified region of interests. In all papers presented in the state of the art the average operator was used. This requires that the ROI should contain majority of pixels that values are changing due to respiration activities. In such cases the specification of ROI location and size could be critical. In our works we asked if other aggregation operators assuming that differences in the parameters describing the distribution of values in the ROI could be useful. We successfully evaluated the skewness parameter calculated for ROI data of thermal sequences recorded using FLIR Lepton camera. It was interesting that the extracted signals using the skewness operator were not so highly dependent on the size of ROI, as it was observed for the average operator. Other parameters could be analyzed in the future.

Automatic detection and tracking of respiration-related sources of thermal changes (nostrils, mouth) are also very important for the context of mobile applications, especially when a patient is not cooperating. Different methods were presented in the state of the art. In our works we focused on methods that could be fast and have been previously successful for image sequences captured in visible-light.

Analysis performed for detecting and tracking nostril region showed that it is possible to process one frame in less than 30 ms for all detectors [27.7 ms (Harris), 23.9 ms (ORB), 19.7 ms (SIFT), 27.6 ms (SURF)]. This high computational performance is indicator for the assumption that analyzed methods could be used for tracking nostril region in applications running in real-time. Moreover, accuracy of tracking algorithm was also measured by calculating root mean squared error of pixel intensities in tracked and fixed localization of nostril area. Almost in all cases errors for tracked regions were smaller than corresponding not tracked area (for

chosen movement, volunteer and method), what allowed for reliable feature tracking. However, analyzed movements were rather small and achieved results are only preliminary. Considering future work in this area, in order to ensure correctness of results, algorithm should also be tested for more noticeable movements and other disturbances. Furthermore, for reliable and efficient medical applications we would like to track facial features without manual alignment, calibration or initialization. Therefore, a fully automatic system for detection, tracing and calculating respiration rate parameters should be designed and implemented in future. Recently, very small thermal cameras have been developed, so a system of this kind could use them after embedding them into wearable devices, like smart glasses.

In this chapter we analyzed respiration rate estimators that can be used to processed sequences of thermal images captured from small thermal camera modules embedded or connected to smart glasses. After calibration of thermal camera modules and using the algorithms to estimate pulse rate from video (recorded in visible light) [68] additional vital signs can be estimated. This could allow obtaining three the most important vital signs: body temperature, pulse rate and respiration rate. Using the intelligent patient identification [68, 69] such data can be automatically stored in the Hospital Information System [70] or other system for the management of Electronic Health Records or Personal Health Records.

Acknowledgements This work has been partially supported by NCBiR, FWF, SNSF, ANR and FNR in the framework of the ERA-NET CHIST-ERA II, European project *eGLASSES—The interactive eyeglasses for mobile, perceptual computing* and by Statutory Funds of Electronics, Telecommunications and Informatics Faculty, Gdansk University of Technology.

References

1. Moses, S.: Tachypnea (increased respiratory rate). Family Practice Notebook (2016). http://www.fpnotebook.com/lung/exam/Tchypn.htm. Accessed 20 Apr 2016
2. World Health Organization. Geneva, Switzerland: The Management of Acute Respiratory Infections in Children: Practical Guidelines for Outpatient Care (1996)
3. Smith, I., Mackay, J., Fahrid, N., Krucheck, D.: Respiratory rate measurement: a comparison of methods. Br. J. Healthc. Assistants **05**(01), 18–23 (2011)
4. Neuman, M.I., Monuteaux, M.C., Scully, K.J., Bachur, R.G.: Prediction of pneumonia in a pediatric emergency department. Pediatrics **128**, 246–253 (2011)
5. Nijman, R.G., Thompson, M., van Veen, M., Perera, R., Moll, H.A., Oostenbrink, R., et al.: Derivation and validation of age and temperature specific reference values and centile charts to predict lower respiratory tract infection in children with fever: prospective observational study. BMJ **2012**(345), e4224 (2012)
6. Bonita, R., Beaglehole, R., Kjellstrom, T.: Basic Epidemiology, 2nd edn. WHO, Geneva (2006)
7. Cretikos, M.A., Bellomo, R., Hillman, K., Chen, J., Finfer, S., Flabouris, A.: Respiratory rate: the neglected vital sign. Med. J. Aust. **188**, 657–659 (2008)
8. Nelson, N.M.: Members of task force on prolonged apnea. Reports of the task force on prolonged apnea of the American Academy of Pediatrics. Pediatrics **61**, 651–652 (1978)
9. Eckert, D.J., Jordan, A.S., Merchia, P., Malhotra, A.: Central sleep apnea. Pathophysiology and treatment. Chest **131**(2), 595–607 (2007)

10. Stanifer, J.W.: A peculiar type of dyspnea: Kussmaul, Cheyne-Stokes, and Biot respiration. Historia Med. **3**(1), 1–7 (2015)
11. Braun, S.R.: Respiratory rate and pattern. In: Walker, H.K., Hall, W.D., Hurst, J.W. (eds.) Clinical Methods: The History, Physical, and Laboratory Examinations (Chapter 43), 3rd edn. Butterworths, Boston. Available from: http://www.ncbi.nlm.nih.gov/books/NBK365/
12. Ruminski, J., Nowakowski, A., Kaczmarek, M., Hryciuk, M.: Model-based parametric images in dynamic thermography. Pol. J. Med. Phys. Eng. **6**(3), 159–165 (2000)
13. Ruminski, J., Kaczmarek, M., Renkielska, A., Nowakowski, A.: Thermal parametric imaging in the evaluation of skin burn depth. IEEE Trans. Biomed. Eng. **54**(2), 303–312 (2007)
14. Kaczmarek, M., Nowakowski, A., Suchowirski, M., Siebert, J., Strojek, W.: Active dynamic thermography in cardiosurgery. QIRT J. **4**(1), 107–123 (2007)
15. Nowakowski, A., Kaczmarek, M., Stojek, W., Trzeciak, B., Topolewicz, J., Rogowski, J., Siebert, J.: IR-thermal monitoring of cardiosurgery interventions. In: Sloten, V., et al. (eds.) Proceedings of the 4th European Conference of the International Federation for Medical and Biological Engineering; IFMBE, vol. 22, pp. 1329–1333. ISSN 1680-0737; CD-ROM, Springer (2008)
16. Ng, E.Y.K., Acharya, U.R., Suri, J.S.: Performance Evaluation of Breast Cancer, Screening, Diagnosis and Treatment. American Scientific Publishers, California, USA (2010)
17. Arora, N., Martins, D., Ruggerio, D., Tousimis, E., Swistel, A.J., Osborne, M.P., Simmons, R.M.: Effectiveness of a noninvasive digital infrared thermal imaging system in the detection of breast cancer. Am. J. Surg. **196**(4), 523–526 (2008). doi:10.1016/j.amjsurg.2008.06.015
18. Han, F., Shi, G., Liang, C., Wang, L., Li, K.: A simple and efficient method for breast cancer diagnosis based on infrared thermal imaging. Cell Biochem. Biophys. **71**(1), 491–498 (2015). doi:10.1007/s12013-014-0229-5
19. Ring, E.F.J.: The historical development of temperature measurement in medicine. Infrared Phys. Technol. **49**, 297–301 (2007)
20. Ring, F., Jung, A., Żuber, J.: Infrared Imaging. IOP Publishing (2015). doi:10.1088/978-0-7503-1143-4
21. Fei, J., Zhu, Z., Pavlidis, I.: Imaging breathing rate in the CO_2 absorption band. In: Proceedings of the 27th Annual International Conference of the IEEE Engineering in Medicine and Biology Society, 1–4 September 2005
22. Murthy, R., Pavlidis, I.: Non-contact monitoring of respiratory function using infrared imaging. IEEE Eng. Med. Biol. Mag. **25**, 57–68 (2006)
23. Murthy, J.N., van Jaarsveld, J., Fei, J., Pavlidis, I., Harrykissoon, R., Lucke, J.F.: Thermal infrared imaging. A novel method to monitor airflow during polysomnography. Sleep **32**, 1521–1527 (2009)
24. Fei, J., Pavlidis, I.: Thermistor at a distance: unobtrusive measurement of breathing. IEEE Trans. Biomed. Eng. **57**(4), 988–998 (2010)
25. Zhu, Z., Fei, J., Pavlidis, I.: Tracking human breath in infrared imaging. In: Proceedings of IEEE BIBE 2005, pp. 227–231, Minnesota, USA (2005)
26. Zhou, Y., Tsiamyrtzis, P., Lindner, P., Timofeyev, I., Pavlidis, I.: Spatio-temporal smoothing as a basis for facial tissue tracking in thermal imaging. IEEE Trans. Biomed. Eng. **60**(5), 1280–1289 (2013)
27. Abbas, K., Heiman, K., Orlikowsky, T., Leonhardt, S.: Non-contact respiratory monitoring based on real-time IR-thermography. In: Proceedings of WC2009 IFMBE, 25/IV, pp. 1306–1309 (2009)
28. Pereira, C.B., Yu, X., Czaplik, M., Rossaint, R., Blazek, V., Leonhardt, S.: Remote monitoring of breathing dynamics using infrared thermography. Biomed. Opt. Express **6**(11), 4378–4394 (2015)
29. Pereira, C.B., Yu, X., Blazek, V., Leonhardt, S.: Robust remote monitoring of breathing function by using infrared thermography. In: Proceedings of IEEE Engineering in Medicine and Biology Society (IEEE 2015), pp. 4250–4253 (2015)
30. Xu, B., Mestha, L.K., Pennington, G.: Monitoring respiration with a thermal imaging system, US20120289850 A1 (2012)

31. Lewis, G.F., Gatto, R.G., Porges, S.W.: A novel method for extracting respiration rate and relative tidal volume from infrared thermography. Psychophysiology **48**(7), 877–887 (2011)
32. AL-Khalidi, F.Q., Saatchi, R., Burke, D., Elphick, H.: Tracking human face features in thermal images for respiration monitoring. In: ACS/IEEE International Conference on Computer Systems and Applications—AICCSA 2010, pp. 1–6, Hammamet (2010)
33. AL-Khalidi, F.Q., Saatchi, R., Elphick, H., Burke, D.: An evaluation of thermal imaging based respiration rate monitoring in children. Am. J. Eng. Appl. Sci. **4**(4), 586–597 (2011)
34. AL-Khalidi, F.Q., Saatchi, R., Burke, D., Elphick, H., Tan, S.: Respiration rate monitoring methods: a review. Pediatr. Pulmonol. **46**, 523–529 (2011)
35. AL-Khalidi, F.Q., Elphick, H., Saatchi, R., Burke, D.: Respiratory rate measurement in children using a thermal imaging camera. Int. J. Sci. Eng. Res. **6**(4), 1747–1756 (2015)
36. Koide, T., Yamakawa, S., Hanawa, D., Oguchi, K.: Breathing detection by far infrared (FIR) imaging in a home health care system. In: Proceedings of IEEE ISBB 2009 [USB-Memory], pp. 206–209, Melbourne, Australia (2009)
37. Hanawa, D., Yaginuma, Y., Enomoto, Y., Koide, T., Terada, S., Oguchi, K.: Automation of non-intrusive nasal breathing detection by using far-infrared imaging. In: Proceedings on u-Healthcare 2010 (2010)
38. Hanawa, D., Morimoto, T., Terada, S., Sakai, T., Shimazaki, S., Igarashi, K., Oguchi, K.: Nose detection on far infrared image for non-contact measurement of breathing. In: Proceedings on IEEE-EMBS BHI 2012 [USB-Memory], pp. 878–881, Hongkong and Shenzhen, China (2012)
39. Mostafa, E., Hammoud, R., Ali, A., Farag, A.: Face recognition in low resolution thermal images. Comput. Vis. Image Underst. **117**(12), 1689–1694 (2013)
40. Dawoud, N.N., Samir, B.B., Janier, J.: Fast template matching method based optimized sum of absolute difference algorithm for face localization. Int. J. Comput. Appl. **18**(8), 30–34 (2011)
41. Poorna, B., Priscilla, C.V.: Invariant recognition of face. In: 2010 International Conference on Computing Communication and Networking Technologies (ICCCNT), pp. 1–6, Karur (2010)
42. Kith, V., El-Sharkawy, M., Bergeson-Dana, T., El-Ramly, S., Elnoubi, S.: A feature and appearance based method for eye detection on gray intensity face images. In: International Conference on Computer Engineering and Systems, ICCES 2008, pp. 41–47, Cairo (2008)
43. Marzec, M., Koprowski, K., Wróbel, Z.: Detection of selected face areas on thermograms with elimination of typical problems. J. Med. Inform. Technol. **16** (2010)
44. Wang, S., Liu, Z., Shen, P., Ji, Q.: Eye localization from thermal infrared images. Pattern Recognit. **46**(10), 2613–2621 (2013)
45. Chieh-Li, C., Bo-Lin, J.: Infrared thermal facial image sequence registration analysis and verification. Infrared Phys. Technol. **69**, 1–6 (2015)
46. Bhattacharjee, D., Seal, A., Ganguly, S., Nasipuri, M., Kumar Basu, D.: Comparative study of human thermal face recognition based on Haar wavelet transform and local binary pattern. Intell. Neurosci. **6,** 1 pp (2012)
47. Philip, K.E.J., Pack, E., Cambiano, V., Rollmann, H., Weil, S., O'Beirne, J.: The accuracy of respiratory rate assessment by doctors in a London teaching hospital: a cross-sectional study. J. Clin. Monit. Comput. **29**(4), 455–460 (2015)
48. Rumiński, J.: Analysis of parameters of respiration patterns extracted from thermal image sequences. Biocybern. Biomed. Eng. **2016**, 1–12 (2016)
49. Ruminski, J.: Estimation of respiration rate using an accelerometer and thermal camera in eGlasses. In: Proceedings of the 2016 Federated Conference on Computer Science and Information Systems, 4 pp, Gdansk (2016)
50. Ruminski, J.: Evaluation of the respiration rate and pattern using a portable thermal camera. In: Proceedings of the 13th Quantitative Infrared Thermography Conference, pp. 1–6, Gdansk (2016). doi:10.21611/qirt.2016.107
51. Ruminski, J.: Analysis of the parameters of respiration patterns extracted from thermal image sequences. Biocybern. Biomed. Eng. (2016) doi:10.1016/j.bbe.2016.07.006

52. Kwasniewska, A., Ruminski, J.: Face detection in image sequences using a portable thermal camera. In: Proceedings of the 13th Quantitative Infrared Thermography Conference, pp. 1–7, Gdansk (2016) doi:10.21611/qirt.2016.071
53. Kwasniewska, A., Ruminski, J.: Real-time facial feature tracking in poor quality thermal imagery. In: 9th International Conference on Human System Interactions (HSI) IEEE Xplore, pp. 504–510, Portsmouth, United Kingdom, (2016). doi:10.1109/HSI.2016.7529681
54. Viola, P., Jones, M.: Robust real-time face detection. Int. J. Comput. Vis. **57**(2) (2004)
55. OpenCV documentation. http://docs.opencv.org/. Accessed 02 May 2016
56. Wiley Publishing, Inc., Hoboken, New Jersey: Webster's New World Medical Dictionary, 3rd edn. MedicineNet.Com (2008). Accessed 25 May 2016
57. Brouillette, R.T., Morrow, A.S., Weese-Mayer, D.E., Hunt, C.E.: Comparison of respiratory inductive plethysmograpy and thoracic impedance for apnea. J. Pediatr. **111**(3), 377–383 (1987)
58. Anaxsys Technology Ltd.: RespiR8. http://www.respir8.com/about_respiR8.html (2011). Accessed 23 May 2016
59. Macknet, M.R., Kimball-Jones, P.L., Applegate, R.L., Martin, R.D., Allard, M.W.: Accuracy and tolerance of a novel bioacoustic respiratory sensor in pediatric patients. Anesthesiology **A84** (2007)
60. Hernandez, J., McDuff, D., Picard, R.W.: Biowatch: estimation of heart and breathing rates from wrist motions. In: 9th Pervasive Health Conference, pp. 167–176, Istanbul (2015)
61. Standards of Practice Committe of the American Sleep Disorders Association: Practice parameters for the indications for polysomnography and related procedures. Sleep **20**, 406–422 (1997)
62. Przystup, P., Bujnowski, A., Ruminski, J., Wtorek, J.: A multisensor detector of a sleep apnea for using at home. In: The 6th HSI Conference, IEEE Xplore, pp. 513–517 (2013)
63. Duong, D., Shastri, D., Tsiamyrtzis, P., Pavlidis, I.: Spatiotemporal reconstruction of the breathing function. In: Medical Image Computing and Computer Assisted Intervention—MICCAI 2012, pp. 149–156, LNCS 7510, Springer (2012)
64. Sörnmo, L., Laguna, P.: Bioelectrical Signal Processing in Cardiac and Neurological Applications. Academic Press (2005)
65. Barlow, J.S.: The Electroencephalogram: Its Patterns and Origins. MIT Press (1993)
66. Rumiński, J.: Reliability of pulse measurements in videoplethysmography. Metrol. Measur. Syst. **23**(3), 359–371 (2016)
67. Ruminski, J.: The accuracy of pulse rate estimation from the sequence of face images. In: 9th International Conference on Human System Interactions (HSI) IEEE Xplore , pp. 518–524, Portsmouth, United Kingdom (2016). doi:10.1109/HSI.2016.7529683
68. Smiatacz, M., Rumiński, J.: Local texture pattern selection for efficient face recognition and tracking. In: Proceedings of the 9th International Conference on Computer Recognition Systems CORES 2015, Advances in Intelligent Systems and Computing, pp. 359–368, Springer International Publishing (2016)
69. Ruminski, J., Smiatacz, M., Bujnowski, A., Andrushevich, A., Biallas, M., Kistler, R.: Interactions with recognized patients using smart glasses. In: Proceedings of HSI 2015 Conference, IEEE Xplore, pp. 187–194 (2015)
70. Ruminski, J., Bujnowski, A., Kocejko, T., Andrushevich, A., Biallas, M., Kistler, R.: The data exchange between smart glasses and healthcare information systems using the HL7 FHIR standard. In: 9th International Conference on Human System Interactions (HSI) IEEE Xplore, pp. 525–531, Portsmouth, United Kingdom, (2016). doi:10.1109/HSI.2016.7529684

Applications of Infrared Thermography for Noncontact and Noninvasive Mass Screening of Febrile International Travelers at Airport Quarantine Stations

Guanghao Sun, Takemi Matsui, Tetsuo Kirimoto, Yu Yao and Shigeto Abe

Abstract Infrared thermography (IRT), one of the most valuable tools, is used for noncontact, noninvasive, and rapid monitoring of body temperature; this has been used for mass screening of febrile travelers at places such as airport quarantine stations for over 10 years after the 2003 severe acute respiratory syndrome (SARS) outbreak. The usefulness of thermography for mass screening has been evaluated in many recent studies; its sensitivity varies from 40 to 89.4% under various circumstances. In this chapter, we perform IRT evaluations for detecting febrile international travelers entering Japan at Nagoya Airport, immediately after the SARS epidemic, from June 2003 to February 2004, and at Naha International Airport from April 2005 to March 2009. The correlation of body surface temperature measured via thermography with the axillary temperature was significant. Through IRT, febrile individuals were detected with good accuracy and the detection accuracy was improved by corroborating surveillance with self-reporting questionnaires. However, there are several limitations associated with the use of IRT for fever screening. For instance, taking antifebrile medications results in rapid modification of the body temperature and directly affects the efficiency of IRT. To solve this unreliability and obtain higher accuracy in mass screening, we have developed a novel infection screening system using multisensor data, i.e., heart and respiration rates are determined by microwave radar in noncontact manner and facial skin temperature is monitored through IRT. The detection accuracy of the system improved, which is notably higher compared to the conventional screening method using only IRT.

G. Sun (✉) · T. Kirimoto
The University of Electro-Communications, Tokyo, Japan
e-mail: guanghao.sun@uec.ac.jp

T. Matsui
Tokyo Metropolitan University, Tokyo, Japan

Y. Yao
ZEA-2, Electronic Systems, Research Center Jülich, Jülich, Germany

S. Abe
Takasaka Clinic, Fukushima, Japan

E.Y.K. Ng and M. Etehadtavakol (eds.), *Application of Infrared to Biomedical Sciences*, Series in BioEngineering,
DOI 10.1007/978-981-10-3147-2_19

Keywords Infrared thermography · Non-contact · Mass screening · Fever

1 Introduction

Infrared thermography (IRT) is a powerful tool for two-dimensional temperature mapping and thereby creating a thermal image. Due to noncontact, noninvasive, and rapid features of IRT monitoring, it has been widely used in clinical medicine and research. For instance, thermal image is an effective indicator for the diagnosis of breast cancer [1], peripheral vascular disorders [2], diabetes [1], fever screening [3] etc. In particular, it has been successfully applied to mass screening of febrile travelers at many quarantine stations of international airports after the severe acute respiratory syndrome (SARS) outbreak in 2003 [4–8].

Conventionally, entry quarantine was carried out in various ways, i.e., self-report from passengers, questionnaires on health condition, visual inspection by quarantine officers; this was done for reducing risks due to the entry of infected passengers into the country. However, quarantine screening by self-reporting questionnaires related to medical state do not provide accurate rate of infected individuals and true symptoms of those infected with epidemic diseases. For this reason, IRT was proposed for non-contact and rapid monitoring of body temperature for mass screening of international travelers. The usefulness of IRT for mass screening has been evaluated in many recent studies; its sensitivity varies from 40 to 89.4% under various circumstances [9–11].

In this chapter, we perform IRT evaluations for detecting febrile international travelers at Nagoya Airport, immediately after the SARS epidemic, from June 2003 to February 2004, and at Naha International Airport from April 2005 to March 2009. Our results indicated that IRT sufficiently detected febrile individuals and its detection accuracy was improved by corroborating surveillance with self-reporting questionnaires. However, there are several limitations associated with the use of IRT for fever screening. IRT deterred inspectors from utilizing due to its unreliability originated from following three causes:

(i) Individual-related causes would alter body surface temperatures. Internal causes such as water and alcohol consumption, pregnancy, estrus cycle, and hormone treatment would increase body temperature and external causes such as sweat and thick makeup would decrease body temperature. In addition, glasses and hats would cover the parts used for detection and body movements while scanning would result in unsuccessful image extraction.
(ii) Machine parameters may be influenced by factors such as ambient temperature, humidity, air ventilation, and performance differential.
(iii) Staff alternation would result in differences in judgment of images; these will be due to untrained or inexperienced inspectors, setting of inaccurate cutoff body surface temperature, and incorrect distance between the subject and IRT equipment.

Considering these issues with using IRT, we proposed a noncontact infection screening system for medical examinations that can be performed within 10 s by measuring vital signs (i.e., heart rate, respiration rate, and facial skin temperature) [12–15]. If a person is infected, not only the body temperature but also heart and respiration rates will invariably increase. Thus, our system automatically detects infected individuals within 10 s by a discriminant function using the measured vital signs. Heart and respiration rates are determined using microwave radar in a noncontact manner, and facial skin temperature is monitored through IRT. By adding heart and respiration rates as the new screening parameters, our infection screening system provides higher sensitivity than that of using only IRT.

This chapter is organized as follows. In Sects. 2 and 3, we introduce IRT evaluations for detecting febrile international travelers at Nagoya and Naha International Airports in Japan. In Sect. 4, we provide an overview of the hardware of the multiple vital sign based infection screening system, as well as the classification algorithm for screening of potentially infected patients. Finally, we draw conclusions in Sect. 5.

2 Fever Screening for SARS Symptoms at Nagoya Airport Through IRT in 2003

Between November 2002 and July 2003, there was an outbreak of SARS in southern China [16]. Nationwide surveillance for SARS in Japan was reinforced and IRT was set up at Nagoya Airport on May 12, 2003. On July 5, 2003, even though WHO announced that all known chains of person-to-person transmission of the SARS virus had been broken, quarantine stations at airports in Japan sustained their thermal scanning for febrile passengers. According to the data collected at Nagoya Airport in 2003 and 2004, we evaluated the efficiency of IRT as a means for quarantine.

2.1 Subjects and Methods

Out of a total of 137,473 subjects, 135,020 were passengers and 2453 were crew members from the 1280 flights arriving from Asian countries and Northern America to Nagoya Airport between June 2003 and February 2004; all these subjects were scanned through IRT (Neo Thermo TVS-700, Avio. Co., Ltd.). The isotherm low temperature was set at 35.4 °C, displaying the subjects above the set temperature in red (see Fig. 1). The distance from the subjects was approximately 3 m. The temperature accuracy was ±2 °C in an indoor environment. The subjects displayed in red on the screen were led to the Health Consultation Room for further measurements of either axillary or tympanic temperature by digital thermometers.

Using the Chi-squared test, we compared fever detections of temperature above 37 °C as detected by thermal scanning and those by self-reported questionnaires.

2.2 IRT Screening Results at Nagoya Airport

A total of 226 subjects (223 passengers and 3 crew members) were displayed in *red* by IRT scanning. Figure 2 shows a histogram of the axillary temperature of the above-mentioned subjects using digital thermometers; 31% of them had temperature 37.0–37.4 °C.

One of the symptoms for diagnosing SARS was a fever of above 38 °C. In this study, 0.054% of the scanned individuals met this criterion. Our follow-up survey found that 60% of these subjects had temperature between 38.0–38.9 °C along with influenza-like symptoms and acute upper respiratory inflammation. Three febrile

Fig. 1 Isotherm low temperature was set at 35.4 °C, displaying targeting subject in *red* above the set temperature

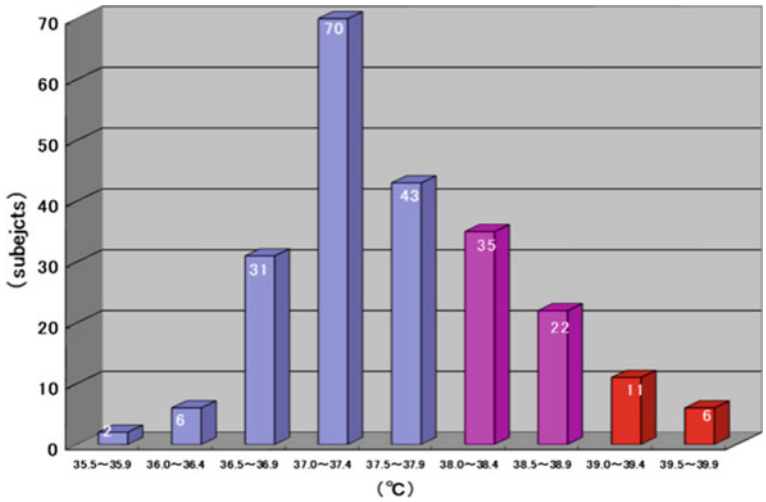

Fig. 2 Histogram of axillary temperature for 226 subjects (223 passengers and 3 crew members, all displayed in red by IRT) measured using digital thermometers

subjects with no clear explanation other than alcohol intake and one subject with sunburn were assumed to be detected as false positive. A self-reporting diarrhea subject, displayed in red by IRT, was diagnosed with dysentery. Sixty percent of the subjects with temperature between 39.0 and 39.9 °C also had influenza-like symptoms and acute upper respiratory inflammation. One subject without self-reporting diarrhea was found to be feverish by IRT and was revealed to have dysentery through a fecal examination.

By adopting the Chi-square test, we compared the detection rate of IRT with a temperature threshold of 37 °C to the detection rate obtained by self-reporting questionnaires. The detection rate of the IRT scan stochastically showed significant difference (significance level under 0.01%) from that of the questionnaires; thereby thermal scan was proved to be efficient for quarantine screening.

This indicates that active surveillance of feverish passengers and examinations at the Health Consultation Room will work efficiently for extracting patients in early stages or incubation period of infection.

3 Four-Year Large-Scale Evaluation of IRT at Naha International Airport in Japan[1]

Two years after the installation of IRT at quarantine stations of major airports in Japan, we conducted a large-scale test for IRT evaluation. A total of 617,289 international passengers who underwent quarantine screening at Naha International Airport from April 2005 to March 2009 were the subjects, out of which 7% of the passengers submitted self-reporting questionnaires.

3.1 Subjects and Methods

Facial skin temperature of all the passengers was measured at quarantine stations through IRT (Infra-eye 2000 DM-IN2000-05, Fujitsu Tokki Systems Limited, Japan). Passengers were made to stand at a distance of 2 m from the IRT to acquire the image for each passenger. The surface temperature of median forehead was measured for those who showed a temperature of above 35.4 °C by Thermofocus (Tecnimed Srl, Italy). Passengers who had a fever of above 37.0 °C as detected by Thermofocus were asked to fill questionnaires and their axillary temperature was measured by a digital thermometer (Thermo Digital Thermometer C202, Terumo Corp.). Clinicians examined those passengers who self-reported symptoms and axillary temperature was measured for those who consented.

[1]Dr. Shigeto Abe was chief of Naha Quarantine Station in these period.

3.2 IRT Screening Results at Naha International Airport

(i) The effect of seasonal changes on detecting the temperature of feverish subjects

Feverish subjects are defined as passengers having fever as detected by IRT and Thermofocus with an axillary temperature of above 37.0 °C. The number of feverish subjects was 391 (0.063% of all subjects). We investigated the effect of seasonal changes on the detection of the temperature of feverish subjects. Figure 3 shows significant fluctuation in the detection of feverish subjects. We assumed this fluctuation was affected by age and destination of passengers during long holiday seasons, i.e., Golden Week, summer vacation, and New Year's holiday in Japan, and not affected by internal and external conditions of passengers.

(ii) Correlation between axillary temperature and facial skin temperature

The mean value of facial skin temperature scanned by IRT was 35.1 °C and that of axillary temperature measured by thermometer was 37.8 °C. The difference between these temperatures was 2.7 °C, which was greater than the difference of 1.6 °C between IRT set point (35.4 °C) and axillary temperature (37.0 °C). This shows the possibilities of IRT detecting false negatives for febrile subjects. Figure 4 shows the correlation plot of the facial skin temperatures monitored by IRT and the axillary temperatures measured by thermometer. The IRT measurement exhibited a

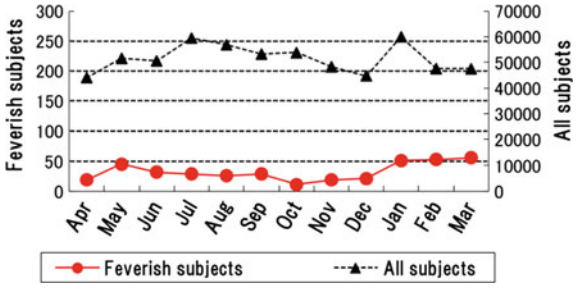

Fig. 3 Effect of seasonal changes on the detection of the temperature of feverish subjects

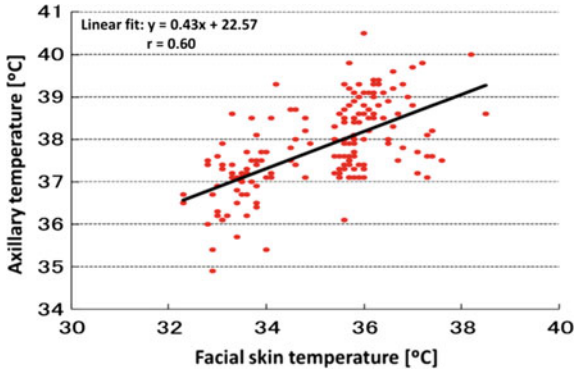

Fig. 4 Relationship between the facial skin temperature measured by IRT and the axillary temperature measured by thermometer

positive correlation with that of the thermometer ($r = 0.60$); the linear least square fitting equation is as follows:

$$y = 0.43x + 22.57 \quad (1)$$

Body surface temperature and axillary temperature, which is assumed to be core temperature, correlated significantly. The result is very similar to that obtained by Ng et al. [4]. In order to increase the correlation between body surface temperature and axillary temperature and maintain detection accuracy of thermography, standard operating procedure must be strictly conducted by quarantine inspectors.

The results indicated that IRT could sufficiently detect febrile individuals and the detection accuracy was improved by corroborating surveillance with self-reporting questionnaires. Questionnaires can be highly reliable when used in combination with thermal scanning that detects feverish passengers negligent to report their symptoms in the questionnaires. By excluding passengers in early stages or incubation period of infection, active border control can be reinforced and precautionary measures will prevent the infection from spreading within country.

4 Multiple Vital Sign Based Infection Screening System

4.1 Fundamental Idea of Infection Screening System

Since fever is one of the major symptoms of infectious diseases such as SARS and influenza, IRT is adopted for febrile passenger screening by monitoring their body temperature. However, facial skin temperature measured through IRT can be affected by many factors, such as antifebrile and alcohol intake, and ambient temperatures. Specifically, taking antifebrile medication results in rapid modification of body temperature and directly affects the efficiency of IRT. In order to achieve more accurate infection screening, we have developed an infection screening system, which monitors infection-induced alternation of heart and respiration rates as well as body temperature in a noncontact manner in our previous studies. The idea of using vital signs stems from the fact that infectious diseases are associated with inflammation and the increased rates of body temperature, heart, and respiration are included in the diagnostic criteria for the systemic inflammatory

Table 1 Diagnostic criteria for systemic inflammatory response syndrome

Criteria	Range
Body temperature	More than 38 °C or less than 36 °C
Heart rate	More than 90 beats per minute
Respiration rate	More than 20 breaths per minute
White blood cell count	>12,000/mm^3, <4000/mm^3, or >10% bands

Two or more of above criteria

response syndrome (Table 1) [17]. One of the criteria for infection is the white blood cell (WBC) count; however, this requires blood samples, which precludes its use as a fast and efficient screening parameter.

4.2 System Design of Infection Screening System for Airport Quarantine Stations

The proposed system automatically detects infected individuals within 10 s via a discriminant function by measuring vital signs, i.e., heart rate, respiration rate, and facial skin temperature.

Our first prototype was designed for airport quarantine stations in 2009 [18]; the schematic diagram of the noncontact infection screening system is shown in Fig. 5. The system consists of a laser Doppler blood flow meter (ALF21N, Advance, Tokyo), a 10-GHz microwave radar (Tau-giken, Yokohama), and an IRT (NEC SANEI, IS7800, Tokyo). The laser Doppler blood flow meter measures the pulse within a range of 3 cm from palmar surface. In order to monitor the respiratory motion of a subject's chest, the microwave radar radiates 10-GHz microwaves with an output power of 7 mW. The subject's facial skin temperature is measured via IRT, which is placed at a distance of 2 m from the target face. The pulse wave measured by laser Doppler blood flow meter, the respiratory curve measured by microwave radar, and the thermal image measured by IRT are displayed in real time.

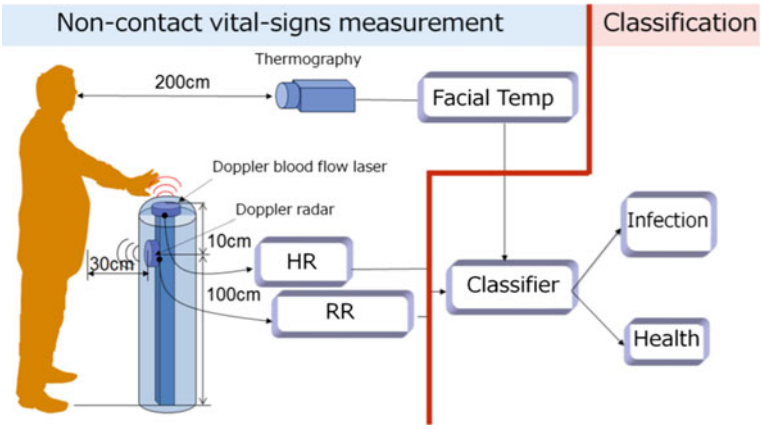

Fig. 5 Diagrammatic illustration of the noncontact infection screening system [18]

4.3 Classification Algorithms for Screening of Potential Infected Patients

In order to execute automatic detection of the patients with potential infection from measured vital signs, we proposed classification algorithms including linear discriminant analysis (LDA), quadratic discriminant analysis (QDA), support vector machine (SVM), k-nearest neighbors (kNN), logistic regression (LR), naive Bayes (NB), and Kohonen's self-organizing maps (SOM) with k-means clustering [19, 20]. In this section, we provide a short introduction of the SOM with the k-means clustering algorithm, which had the most reliable screening accuracy.

The unsupervised algorithm was created by a two-layer neural network, i.e., SOM combined with a k-means clustering method. The input layer had three inputs: heart rate, respiration rate, and facial skin temperature (Fig. 6). First, the preprocessing of the input layer for these three parameters was conducted. Data from all subjects was used to construct an ASCII file, which contained four columns, i.e., three parameters and one label. Whereas the scale of the parameters is important in determining the nature of SOM, we normalized all the parameters using the logarithmic scale. After preprocessing of the input layer, the ASCII file was used to create various SOM clusters. The SOM clustering result was visualized on a two-dimensional color-coded map using the unified distance matrix (U-matrix). The U-matrix shows the distance between neighboring map units by a color tone. This classification is composed of various clusters corresponding to a variety of U-matrix distances (color tone). Second, the k-means clustering algorithm was employed to reduce the SOM clusters into two clusters ("Potential infection group" and "Normal group").

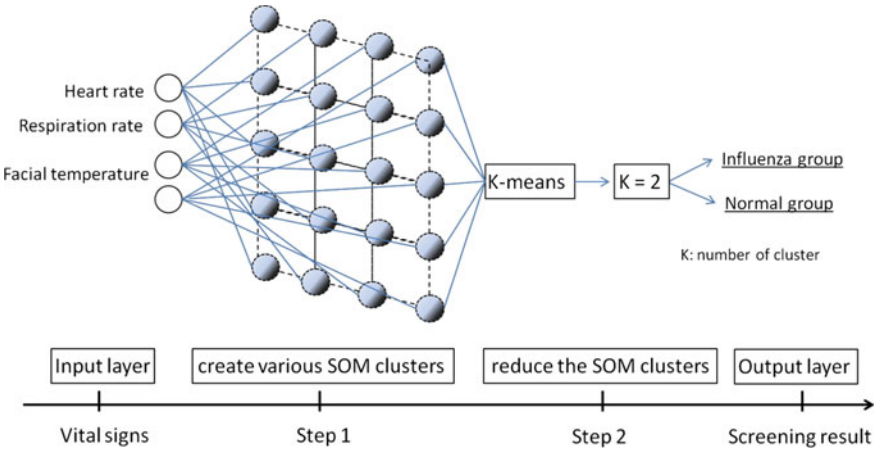

Fig. 6 Schematic representation of SOM combined with a k-means clustering algorithm to generate a nonlinear discriminant function [20]

Table 2 Classification results [21]

Method	Error rate (%)	Sensitivity (%)	Specificity (%)
LDA	10.9	91.2	85.7
QDA	9.8	93	85.7
SVM	9.8	93	85.7
kNN	10.9	93	82.9
LR	12	89.5	85.7
NB	14.1	89.5	80
SOM + k-means	9.7	98	77

We tested these classification algorithms on clinical data, i.e., 57 medicated influenza patients and 35 normal control subjects at the Japan Self-defense Forces Central Hospital. Moreover, we also compared the performance of all the proposed classification algorithms with the data (Table 2). Acquiring heart and respiration rates in addition to facial skin temperature allowed us to reduce the misclassification rate by more than 50%. In addition, mutual information scores and classification results indicate that the multiple vital sign approach for infection screening can present a solution to the problem of identifying infected individuals treated with antipyretics.

5 Conclusions and Future Work

In this chapter, we introduced the applications of IRT for mass screening of international travelers at airport quarantine stations. IRT could sufficiently detect febrile individuals in noncontact manner and the detection accuracy was improved by corroborating surveillance with self-reporting questionnaires. IRT is efficient in detecting infected passengers or those who come in contact with infected individuals in early seasons of epidemic; IRT will play an important role in avoiding the spread of infections with unclear characteristics. The benefits of implementing IRT for quarantine purposes can be summarized as follows:

(i) Fever at entry will be recorded and the collected data will be used as a reference in other fields of medicine.
(ii) Questionnaires can be highly reliable when conducted with thermal scanning that detects feverish passengers who were negligent in reporting their symptoms in the questionnaires. By excluding passengers in the early stages or incubation period of infection, active border control can be reinforced and these precautionary measures will prevent infection from spreading within the country.

Furthermore, to overcome the limitations associated with the use of IRT for fever screening, we developed a novel infection screening system based on noncontact acquisition of heart rate, respiration rate, and facial skin temperature. Multiple vital

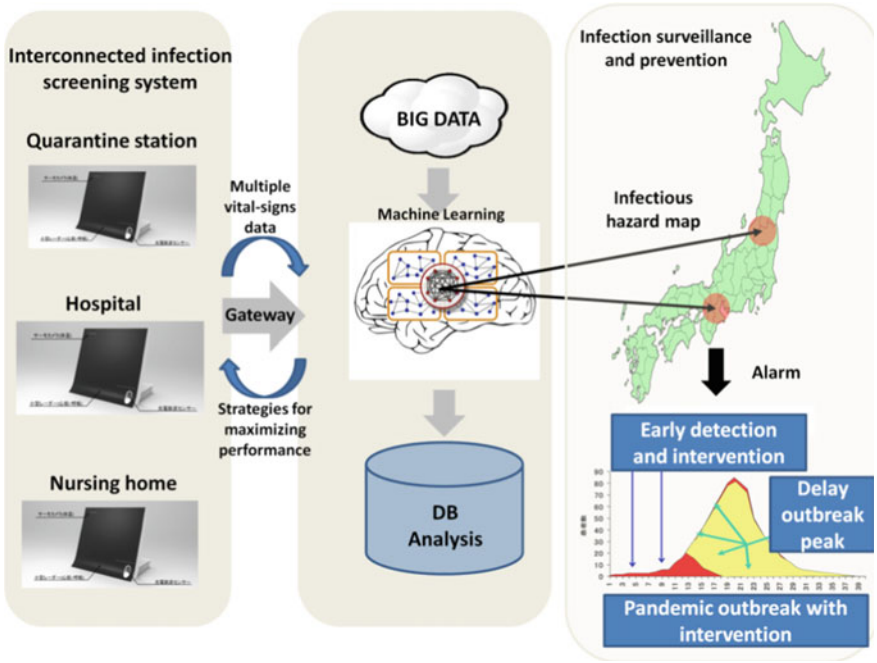

Fig. 7 Network of infection screening system used for early detection and prediction of pandemic outbreak of infectious diseases

sign based infection screening has a much higher potential to increase the detection rate than the traditional IRT-based screening.

To improve screening performance, as a part of future work, one of the most promising approaches is to connect multiple infection screening systems, which enables information sharing between different systems. This will allow us to apply big data analysis techniques, which can be used to predict outbreaks of infectious diseases much earlier than the existing methods (Fig. 7).

References

1. Ng, E.Y.K., Sudharsan, N.M.: Computer simulation in conjunction with medical thermography as an adjunct tool for early detection of breast cancer. BMC Cancer **4**, 17 (2004)
2. Bagavathiappan, S., Saravanan, T., Philip, J., et al.: Infrared thermal imaging for detection of peripheral vascular disorders. J. Med. Phys. **34**(1), 43–47 (2009)
3. Ring, F.: Thermal imaging today and its relevance to diabetes. J. Diabetes Sci. Technol. **4**(4), 857–862 (2010)
4. Ng, E.Y.K., Kaw, G.J., Chang, W.M.: Analysis of IR thermal imager for mass blind fever screening. Microvasc. Res. **68**(2), 104–109 (2004)

5. Nguyen, A.V., Cohen, N.J., Lipman, H., et al.: Comparison of 3 infrared thermal detection systems and self-report for mass fever screening. Emerg. Infect. Dis. **16**(11), 1710–1717 (2010)
6. St John, R.K., King, A., de Jong, D., et al.: Border screening for SARS. Emerg. Infect. Dis. **11**, 6–10 (2005)
7. Chiu, W.T., Lin, P.W., Chiou, H.Y., et al.: Infrared thermography to mass-screen suspected SARS patients with fever. Asia Pac. J. Public Health **17**, 26–28 (2005)
8. Chan, L.S., Cheung, G.T., Lauder, I.J., et al.: Screening for fever by remote-sensing infrared thermographic camera. J. Travel. Med. **11**, 273–279 (2004)
9. Chiang, M.F., Lin, P.W., Lin, L.F., et al.: Mass screening of suspected febrile patients with remote-sensing infrared thermography: alarm temperature and optimal distance. J. Formos. Med. Assoc. **107**, 937–944 (2008)
10. Ng, D.K., Chan, C.H., Lee, R.S., et al.: Non-contact infrared thermometry temperature measurement for screening fever in children. Ann. Trop. Paediatr.: Int. Child Health **25**(4), 267–275 (2005)
11. Liu, C.C., Chang, R.E., Chang, W.C.: Limitations of forehead infrared body temperature detection for fever screening for severe acute respiratory syndrome. Infect. Control Hosp. Epidemiol. **25**(12), 1109–1111 (2004)
12. Sun, G., Akanuma, M., Matsui, T.: Clinical evaluation of the newly developed infectious disease/fever screening radar system using the neural network and fuzzy grouping method for travellers with suspected infectious diseases at Narita International Airport Clinic. J. Infect. **72** (1), 121–123 (2016)
13. Sun, G., Miyata, K., Matsuoka, A.: A compact and hand-held infection-screening system for use in rapid medical inspection at airport quarantine stations: system design and preliminary validation. Med. Eng. Technol. **39**(3), 185–190 (2015)
14. Sun, G., Matsui, T., Hakozaki, Y.: An infectious disease/fever screening radar system which stratifies higher-risk patients within ten seconds using a neural network and the fuzzy grouping method. J. Infect. **70**(3), 230–236 (2015)
15. Matsui, T., Hakozaki, Y., Suzuki, S.: A novel screening method for influenza patients using a newly developed non-contact screening system. J. Infect. **60**(4), 271–277 (2010)
16. Cherry, J.D., Krogstad, P.: SARS: the first pandemic of the 21st century. Pediatr. Res. **56**, 1–5 (2004)
17. Kaukonen, K.M., Bailey, M., Pilcher, D., et al.: Systemic inflammatory response syndrome criteria in defining severe sepsis. N. Engl. J. Med. **372**(17), 1629–1638 (2015)
18. Matsui, T., Suzuki, S., Ujikawa, K., et al.: Development of a non-contact screening system for rapid medical inspection at a quarantine depot using a laser Doppler blood-flow meter, microwave radar and infrared thermography. J. Med. Eng. Technol. **33**(5), 403–409 (2009)
19. Sun, G., Hakozaki, Y., Abe, S., et al.: A novel infection screening method using a neural network and k-means clustering algorithm which can be applied for screening of unknown or unexpected infectious diseases. J. Infect. **65**(6), 591–592 (2012)
20. Sun, G., Abe, N., Sugiyama, Y., et al.: Development of an infection screening system for entry inspection at airport quarantine stations using ear temperature, heart and respiration rates. Conf. Proc. IEEE. Eng. Med. Biol. Soc. 6716–6719 (2013).
21. Yao, Y., Sun, G., Matsui, T., et al.: Multiple vital-sign based infection screening outperforms thermography independent of the classification algorithm. IEEE Trans. Biomed. Eng. **63**(5), 1025–1033 (2016).

Evaluation of Evaporative Dry Eye Disease Using Thermal Images of Ocular Surface Regions with DWT and Gabor Transform

Vidya K. Sudarshan, Joel E.W. Koh, U. Rajendra Acharya, Jen Hong Tan, Muthu Rama Krishnan Mookiah, Chua Kuang Chua and Louis Tong

Abstract Tear film instability is a major cause of dry eye (DE) disease. The lack of stability of the tear film may be associated with optical aberrations, visual disturbances, and ocular surface damage. It is clinically important to detect tear instability in DE as the treatment may involve specific measures such as chronic eyelid warming therapy. To achieve this, a practical and rapid method to analyze the relevant features from different regions of the ocular surface in DE will be useful. Thus, in this chapter, efficiency of using the upper half and lower half regions of the ocular surface (cornea + conjunctiva) in the detection of evaporative dry eye is assessed using infrared thermography images. Here, we define the ocular surface as the exposed area of the cornea and the bulbar conjunctiva during natural

V.K. Sudarshan (✉) · J.E.W. Koh · U.R. Acharya
J.H. Tan · M.R.K. Mookiah · C.K. Chua
Department of Electronics and Computer Engineering,
Ngee Ann Polytechnic, Clementi 599489, Singapore
e-mail: vidya.2kus@gmail.com

U.R. Acharya
Department of Biomedical Engineering, School of Science
and Technology, SIM University, Clementi 599491, Singapore

U.R. Acharya
Department of Biomedical Engineering, Faculty of Engineering,
University of Malaya, Kuala Lumpur, Malaysia

L. Tong
Singapore Eye Research Institute, Singapore 168751, Singapore

L. Tong
Singapore National Eye Center, Singapore 168751, Singapore

L. Tong
Duke-NUS Medical School, Singapore 169857, Singapore

L. Tong
Yong Loo Lin School of Medicine, National University of Singapore,
Singapore 117597, Singapore

E.Y.K. Ng and M. Etehadtavakol (eds.), *Application of Infrared to Biomedical Sciences*, Series in BioEngineering,
DOI 10.1007/978-981-10-3147-2_20

blinking conditions. Infrared thermography images are acquired from each eye of normal and DE participants. Discrete wavelet transform (DWT) and Gabor transform are used to extract the salient features from the 1st, 5th, and 10th frames of the infrared thermography images after the first blink is subjected to segmentation to obtain the upper half and lower half ocular regions. Each segmented region is decomposed up to three levels using DWT and Gabor transform is performed on the DWT coefficients. Principal component analysis (PCA) is performed on these extracted features to reduce the number of features, and PCA coefficients are ranked using t-value and fed to support vector machine (SVM) classifier. Using the 1st, 5th, and 10th frames of the upper half of ocular region after the first blink, we achieved classification accuracies of (i) 82.3, 89.2, 88.2% for the left eye and (ii) 93.4, 81.5, 84.4% for the right eye, respectively. Similarly, using 1st, 5th, and 10th frames of lower half of ocular regions we achieved accuracies of (i) 95.0, 95.0, 89.2% and (ii) 91.2, 97.0, 92.2% for the left and right eyes, respectively. This study shows that the lower half of the eye is superior to the upper half for the purpose of DE detection using our technique. The proposed algorithm is efficient, simple, and may be employed in polyclinics or hospitals for faster DE assessment.

Keywords Dry eye · Gabor transform · DWT · Thermogram · Feature · Classifier · SVM

1 Introduction

Dry eye (DE) may be caused by enhanced tear film evaporation and/or reduced tear production [1]. The tear film subserves important functions including the lubrication and continuous moisture necessary for maintaining optimal vision and comfort of the eye. The tear film's outer layer (lipid layer) maintains tear stability and prevents excessive tear evaporation. Any imbalance arising in the tear film components triggers DE symptoms in at risk individuals [2]. In addition, DE disturbs the homeostasis of the tear film, and significantly damages its defense capability such as preventing microbial invasion and supporting the ocular surface epithelium [3].

Clinically DE disease is diagnosed by indirect assessment of tear production and tears film stability measurements. For the measurement of tear production, the most commonly employed method is the Schirmer's test [4, 5]. In this test, a filter paper is placed inside the lower lid of eye to quantify the amount of wetting of the strip over a 5 min duration. The fluorescent breakup time (FBUT) method is used to evaluate the tear film stability. To perform this test, fluorescent sodium drops are applied onto the ocular surface and the time needed for dry spots to appear on the cornea is assessed [4, 5]. However, both of these tests may disturb the tear film and have other drawbacks, including inconvenience for patients.

Recent studies have been conducted to evaluate the health of the eye using IR images and tear film stability [6, 7]. The ocular surface temperature (OST) is disturbed by tear film instability [8, 9] and is one of the factors associated with DE symptoms [10, 11]. Studies have observed that the OST decreases significantly in DE patients group compared to the control group [12–14] and also rate of cooling is higher in the DE patients due to excessive tear evaporation [15]. Conversely, the pattern of the IR thermal images in DE patients appears to be more unstable and asymmetrical compared to those from normal research participants [9, 12, 15–17]. The temperature sketch of the normal eye is found to be more uniform as compared to the situation in DE [18, 19]. Nevertheless, the asymmetry present in the tear film's IR thermal image has not been quantitatively investigated. Previously, we have shown using OST derived tear evaporation rates that a specific treatment modality for evaporative DE, chronic eyelid warming, will benefit patients who present with increased evaporative loss. If patients have abnormally increased tear evaporation prior to treatment, they are more likely to achieve greater symptomatic relief and restoration of beneficial tear lipids such as O-acyl-ω-hydroxy-fatty acids (OAHFAs), at three months after commencement of treatment [20]. However, this method of tear evaporation assessment is computationally cumbersome for routine clinical use and can be simplified.

The existing diagnostic approaches are subjective, invasive, and uncomfortable. In the current work, we extract Gabor transform-based features from the DWT coefficients of lower and upper half regions of the eye to identify DE efficiently. The region-based DE assessment system developed will decrease the need for conventional DE tests currently used by ophthalmologists, and provide faster and more objective interpretation of tear film status. Assessing these different regions of the ocular surface on the thermograms instead of the entire ocular surface may hasten the evaluation of DE. Furthermore, this approach may be even more suitable when large numbers of people are to be screened for DE. The proposed method highlights the regional differences in the tear status in DE diagnosis and may increase our understanding of the tear physiology in DE.

Figure 1 shows the block diagram of proposed method. During off-line, thermogram images of normal and DE patients obtained during 1st, 5th, and 10th frames after blink are subjected to preprocessing and segmentation to extract lower half and upper half of ocular surface regions. Subsequently, the segmented images are subjected to discrete wavelet transform (DWT) up to three levels of decomposition to obtain the DWT coefficients. Gabor Transform is performed on each DWT coefficient, and 48 Gabor features are extracted, obtaining a total of 48×12 (DWT coefficients) Gabor features. These features are reduced using principal component analysis (PCA) and coefficients are ranked using t-value. These ranked features are used to feed the support vector machine (SVM). During on-line, from the unknown (test) thermogram images, the important Gabor features are extracted from the input (unknown) thermography images at various locations (lower and upper half) after going through DWT process. The features extracted are then classified automatically using support vector machine (SVM) classifier.

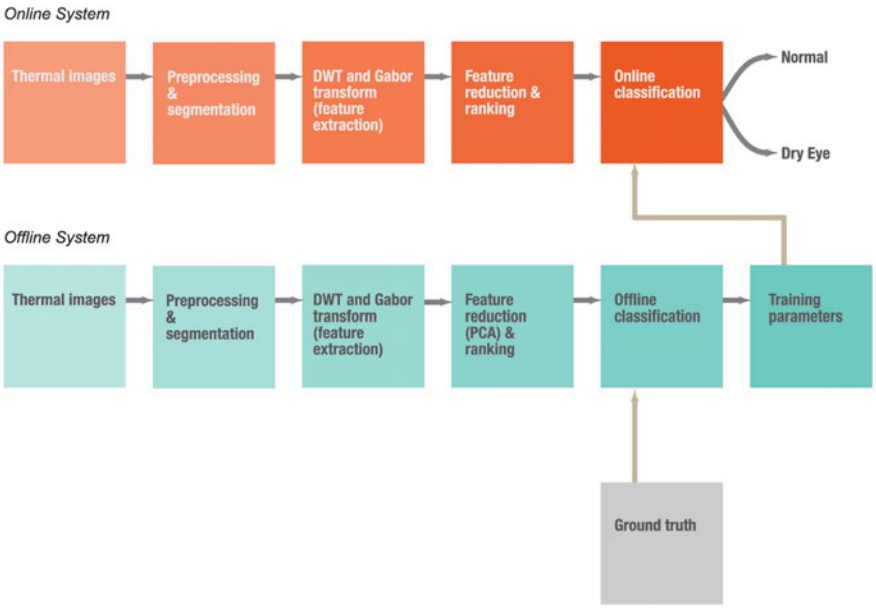

Fig. 1 Block diagram of the proposed methodology

2 Methodology

2.1 Materials

In this study, IR thermal images were obtained from normal and DE patients using the VarioTHERM head II device (Dresden, Germany) located at the Singapore Eye Research Institute (SERI), Singapore. This study has acquired ethical permission from the Singapore Health Services Centralized Institutional Review Board (IRB), Singapore, and written informed consent was obtained from all participants. The study recruited 83 DE participants and 21 normal volunteers. The recordings were captured from 10 AM to 4 PM, at 20 to 23 °C room temperature and 60 to 68% humidity. Twenty-five thermal images were taken over 20 s sequentially. Each thermal image was kept at a size of 442 × 299 pixels, and stored in JPEG format. Figure 2 shows a typical thermographic image of normal and DE subjects.

2.2 Preprocessing and Segmentation

We have taken the 1st, 5th, and 10th frames of IR thermography images after the first blink and manually delineated an ocular region as previously described [17].

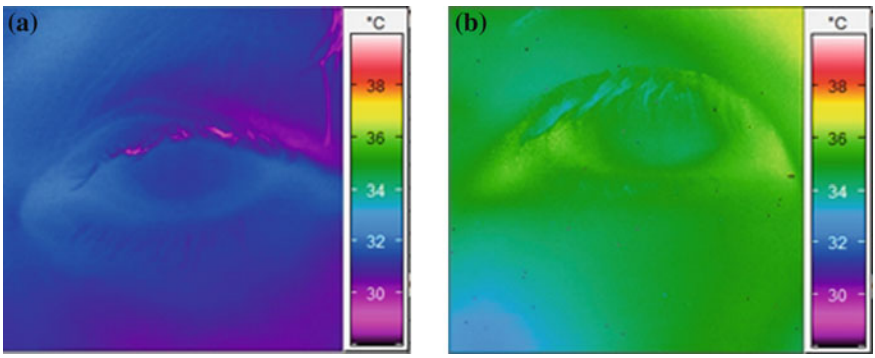

Fig. 2 Typical thermogram eye image: **a** normal, **b** DE

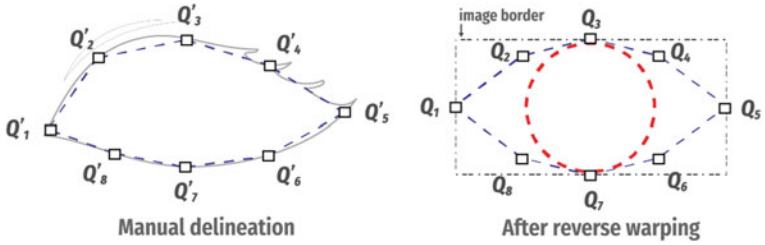

Fig. 3 Region of interest selection

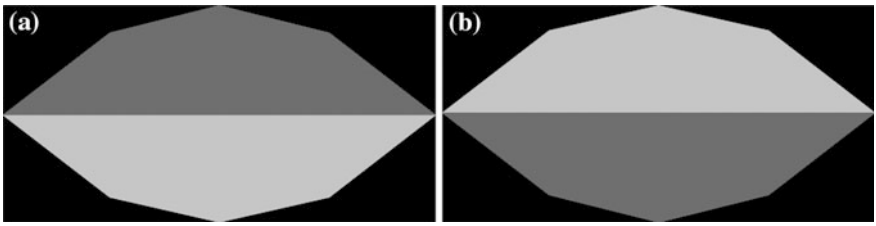

Fig. 4 Shows the selection of ocular region **a** lower half segmented IR thermography image, and **b** upper half segmented IR thermography image

On the delineated ocular region, reverse warping method [21] is used to obtain a standardized image. This new algorithm is described briefly in Fig. 3. To enhance the image quality, an adaptive histogram [22] is constructed.

Once the ocular surface region is outlined, the images are segmented into upper half and lower half ocular region. Figure 4 shows the upper and lower half of ocular region of the IR thermography images used for this study.

2.3 Feature Extraction

Feature extraction is a significant step in developing an automated detection system using IR thermography images. This paper proposes a new feature extraction method in which Gabor Transform features are extracted from the DWT coefficients of thermograms. A brief description of the methods used is as follows.

2.3.1 Discrete Wavelet Transform (DWT)

The DWT is performed on each segmented image (upper and lower regions) up to the three levels of decomposition prior to feature extraction [23, 24]. Thus, total of 12 subband coefficients are obtained from which Gabor features are extracted. In this study, DWT is performed on the segmented upper and lower ocular surface regions. From the DWT coefficients of upper and lower regions, Gabor Transform parameters are computed for each subband using the procedure detailed in the next section. In this work, we used Daubechies 8 (db8) wavelet function [25].

2.3.2 Gabor Transform—Features

The Gabor features help to identify fine variations occurring in the pixels [26–28]. A 2D Gabor function $(g_{l,k}(p,q))$ is obtained as follows,

$$g_{l,k}(p,q) = \left(\frac{1}{2\pi\sigma_p\sigma_q}\right)\exp\left[-\frac{1}{2}\left(\frac{p^2}{\sigma_p^2}+\frac{q^2}{\sigma_q^2}\right)+2\pi j\omega p\right], \tag{1}$$

where ω is the frequency of sinusoid, $\sigma_m = 1/2\pi\sigma_x$ and $\sigma_n = 1/2\pi\sigma_y$ represents the standard deviation (SD) of the Gaussian envelopes [29]. From the mother wavelet $(g_{l,k}(p,q))$ the 2D Gabor wavelets are obtained as follows,

$$g_{l,k}(p,q) = a^{-l}g\left[a^{-l}(p\cos\theta + q\sin\theta)a^{-l}(-p\sin\theta + q\cos\theta)\right], \quad a > 1, \tag{2}$$

where a^{-l}, is the scale factor; l and k are the integers; $\theta = q\pi/K$ represents the orientation and K represents the total number of orientations [29]. σ_p and σ_q are the filter parameters.

Let us consider that $I(p,q)$ is a given IR image. Gabor transform of $I(p,q)$ is calculated as,

$$G_{l,k}(p,q) = I(p,q) * g_{l,k}(p,q) \quad \text{for} \quad l = 1,2,\ldots,S \text{ and } k = 1,2,\ldots,K, \tag{3}$$

where $*$ is convolution operator. μ_{lk} (*mean*) and σ_{lk} (standard deviation) of the transform coefficients are used as features [29]. They are computed as follows,

$$\mu_{l,k} = \frac{1}{P^2} \sum_{p=1}^{P} \sum_{q=1}^{Q} \left| g_{l,k}(p,q) \right| \tag{4}$$

$$\sigma_{l,k}(p,q) = \left(\frac{1}{P^2} \sum_{p=1}^{P} \sum_{q=1}^{Q} \left(\left| g_{l,k}(p,q) \right| - \mu_{l,k} \right)^2 \right)^{1/2} \tag{5}$$

In this paper, we used $K = 6$ orientations and $S = 4$ scales, extracting a total of 48 features, which are denoted as,

$$f = (\mu_1, \sigma_1, \ldots, \mu_{48}, \sigma_{48}) \tag{7}$$

2.4 Feature Reduction

Gabor transform features are calculated from each DWT coefficients of segmented images (lower and upper regions); a total of 48 Gabor features are obtained for each coefficient (total of 12 coefficients). These features are reduced to 101 PCA coefficients.

2.4.1 Principal Component Analysis (PCA)

The PCA is a linear dimensionality reduction technique [30, 31] used to evaluate the paths of highest deviations and then projecting these signals onto the paths. Eigenvectors of covariance matrix are used as the basis vectors for these paths. In this work, the PCA is performed on the Gabor transform features (48 × 12 features) obtained at each coefficient. We have obtained total of 101 PCA components. Only the significant PCA components are tabulated in the results section.

2.5 Feature Ranking

It is very tedious to identify distinct and clinically significant image features to classify DE from normal. In order to select unique and highly discriminating features the Student *t*-test is used. ***t-test*** calculates the *mean* values of the two groups to determine difference existing between them [31]. This test returns the *p*-value and the *t*-statistic; the latter can be used to rank the classes since a high *t*-value suggests better discrimination of DE from normal.

2.6 Classification

This step is significant in the development of computer-aided diagnostic system. During classification process, highly ranked extracted features from upper and lower half regions are fed to classifier SVM with linear, quadratic, third-order polynomials and radial basis function (RBF) kernels [31] and the performance in classifying normal DE features is validated using tenfold cross-validation method.

3 Results

Tables 1, 2, 3, and 4 present the results of ranked features from lower and upper halves of the right and left eye regions, in thermography images from normal and DE individuals. The features are tabulated as *mean* and standard deviation (SD) and those features with p-values < 0.05 are chosen as clinically significant features.

Next, we evaluated the classifiers with the ranked features from upper and lower regions of 1st, 5th, and 10th IR images after the blink. We tested several combinations of the features to train the classifiers using tenfold cross validation technique. We found that four highly ranked features from left and right lower half of ocular surface resulted in the highest accuracy for DE detection. Table 5 shows the results of the classification using features extracted from left lower half, right lower half, left upper half, and right upper half, using 1st, 5th, and 10th frames after the

Table 1 Results of (mean and SD) of features extracted from lower half of left eye ocular region ($p < 0.05$)

PCA coefficients	Normal		DE		t-Value
	Mean	SD	Mean	SD	
1st frame after the blink					
PCA2	−0.2711	0.0236	−0.3272	0.0313	7.6535
PCA10	0.0764	0.0108	0.0828	0.0060	3.5764
PCA9	−0.4697	0.0085	−0.4753	0.0076	2.9394
PCA6	0.2579	0.0129	0.2501	0.0106	2.8332
5th frame after the blink					
PCA2	−0.2805	0.0163	−0.3436	0.0310	8.9700
PCA5	−0.0667	0.0106	−0.0568	0.0147	2.8935
PCA9	−0.4964	0.0082	−0.5010	0.0078	2.3381
PCA19	−0.0297	0.0028	−0.0282	0.0025	2.2934
PCA8	−0.1411	0.0104	−0.1369	0.0081	1.9882
10th frame after the blink					
PCA2	−0.2748	0.0174	−0.3396	0.0314	9.0592
PCA5	−0.1152	0.0094	−0.1054	0.0149	2.8561
PCA8	0.1587	0.0100	0.1642	0.0081	2.5975

Table 2 Results (mean and SD) of features extracted from lower half of right eye ocular region ($p < 0.05$)

PCA coefficients	Normal		DE		*t*-Value
	Mean	SD	Mean	SD	
1st frame after the blink					
PCA3	0.1098	0.0278	0.0567	0.0314	7.0582
PCA2	−0.3924	0.0289	−0.4274	0.0407	3.7019
PCA6	−0.1913	0.0123	−0.2013	0.0127	3.1997
PCA12	−0.0875	0.0067	−0.0843	0.0060	2.0689
5th frame after the blink					
PCA3	0.1762	0.0283	0.1272	0.0321	6.3702
PCA2	0.3706	0.0248	0.4125	0.0385	4.7174
PCA6	0.2941	0.0106	0.3050	0.0122	3.7244
PCA18	0.0636	0.0028	0.0656	0.0032	2.6608
PCA24	−0.0283	0.0024	−0.0294	0.0020	2.0810
10th frame after the blink					
PCA2	−0.2864	0.0178	−0.3419	0.0351	6.9979
PCA3	−0.2848	0.0308	−0.2473	0.0350	4.4711
PCA6	0.2905	0.0097	0.2995	0.0117	3.2055
PCA18	−0.1045	0.0026	−0.1066	0.0030	2.8517

blink with SVM. The SVM classifier with RBF kernels performed consistently well for all frames and features. Table 5 shows that the proposed method is able to detect DE using the 5th frames after each blink, with an accuracy of 97% using only four features. In addition, the lower half of ocular surface is more effective for diagnosing DE.

4 Discussion

In this paper, the effectiveness of different regions of the eye in DE diagnosis is evaluated using Gabor Transform features extracted from DWT coefficients from different ocular surface regions of IR thermography images. First- and second-order statistics are not sufficient to analyze the features of the image, so Gabor transform has been used to extract the more subtle variations in the image.

Different techniques such as Schirmer's test, fluorescein dye, tear stability analysis system (TSAS), IR thermometer, and IR thermography have been explored by various researchers to compute imaging indices such as, tear function index (TFI), temperature difference value (TDV), tear stability regularity index (TSRI), mean ocular surface temperature (MOST), radial temperature difference (RTD), tear stability asymmetry index (TSAI), higher order spectra (HOS) bispectrum and HOS cumulants features in the assessment of DE patients. A summary of these studies

Table 3 Results (mean and SD) of features extracted from upper half of ocular region left eye ocular region ($p < 0.05$)

PCA coefficients	Normal		DE		*t*-Value
	Mean	SD	Mean	SD	
1st frame after the blink					
PCA3	−0.1606	0.0225	−0.1324	0.0264	4.4783
PCA14	0.1109	0.0077	0.1177	0.0059	4.3648
PCA4	−0.0278	0.0269	−0.0137	0.0226	2.4516
PCA19	0.0352	0.0040	0.0327	0.0042	2.4342
PCA5	−0.0399	0.0236	−0.0489	0.0157	2.0713
PCA16	0.1197	0.0083	0.1172	0.0041	1.9352
5th frame after the blink					
PCA5	0.0154	0.0136	0.0296	0.0145	4.0426
PCA16	−0.3273	0.0043	−0.3317	0.0046	3.8892
PCA3	0.2415	0.0243	0.2197	0.0255	3.5143
PCA42	−0.1254	0.0007	−0.1247	0.0008	3.2368
PCA12	−0.1793	0.0075	−0.1746	0.0066	2.7459
10th frame after the blink					
PCA5	0.0701	0.0137	0.0592	0.0144	3.1100
PCA16	0.1760	0.0047	0.1791	0.0040	3.0180
PCA11	−0.1277	0.0049	−0.1325	0.0073	2.8312
PCA3	−0.2693	0.0253	−0.2518	0.0260	2.7459
PCA13	−0.0347	0.0077	−0.0314	0.0044	2.5358
PCA34	0.0071	0.0013	0.0064	0.0010	2.3030

which focusses on DE diagnosis using different ocular surface regions is summarized in Table 6.

Xu et al. [32] assessed the entire ocular surface clinically to assess tear dynamics for diagnosis of DE using TFI. They showed that TFI is able to identify the DE with 91.8% sensitivity and 78.9% specificity. Vico et al. [33] also utilized the same TFI method and detected DE with 74% sensitivity and 63% specificity. TFI is comparatively inexpensive and simple, but is tedious and potentially biased, and instillation of fluorescein dye performed during the test causes an artificial increase in tear volume and can also cause irritation and induce reflex tear production.

Tai et al. [34] evaluated the two parameters TDV and CV from the region of interest in the ocular surface using a linear discriminant function to discriminate DE from normal eyes. These indices evaluate respectively, the degree of temperature change and the degree of tear film stability for >6 s. The study reported 84% sensitivity and 83% specificity. While both parameters represent stability of the tear film, the CV is a useful parameter which measures the asymmetry of the relatively lower temperature region which corresponds to the region of the tear film with excessive evaporation. A larger TDV corresponds to larger amounts of tear evaporation.

Table 4 Results (mean and SD) of features extracted from upper half of right eye ocular region

PCA coefficients	Normal		DE		*t*-Value
	Mean	SD	Mean	SD	
1st frame after the blink					
PCA2	0.5182	0.0280	0.4830	0.0307	4.7540
PCA4	0.1930	0.0263	0.2064	0.0135	3.2405
PCA6	0.1453	0.0134	0.1387	0.0101	2.4797
PCA13	0.1278	0.0081	0.1316	0.0058	2.4042
PCA8	−0.0114	0.0115	−0.0165	0.0084	2.3021
PCA15	0.0112	0.0072	0.0084	0.0043	2.2818
5th frame after the blink					
PCA2	−0.5521	0.0256	−0.5211	0.0293	4.4365
PCA14	−0.0632	0.0051	−0.0667	0.0039	3.3167
PCA9	0.1224	0.0109	0.1276	0.0057	2.9973
PCA17	0.0822	0.0050	0.0844	0.0035	2.2762
PCA63	−0.0040	0.0003	−0.0038	0.0003	2.2052
PCA21	0.1582	0.0036	0.1597	0.0029	1.9399
10th frame after the blink					
PCA2	−0.5508	0.0203	−0.5182	0.0290	4.8532
PCA12	0.1731	0.0059	0.1760	0.0045	2.4682
PCA7	0.0372	0.0100	0.0425	0.0087	2.3703
PCA14	0.0060	0.0060	0.0083	0.0040	2.0452
PCA5	0.3642	0.0104	0.3587	0.0110	2.0347
PCA18	−0.0548	0.0048	−0.0565	0.0032	2.0129

Excessive tear evaporation increases the rate of cooling in the eyes of a DE patient [9, 17, 35, 36]. Chiang et al. [13] evaluated decreasing ocular surface temperatures (OST) using an IR thermal imager system for the DE identification. They reported 79.3% sensitivity, 75% specificity, and the area-under-curve (AUC) in the Receiver Operating Characteristic (ROC) of 0.841.

Takashi et al. [37] assessed the entire eye using the TSAS for the evaluation of tear film stability in DE patients. This equipment produced two indices TSRI and TSAI for the tear film stability analysis, showing promising results in distinguishing DE subtypes using dynamic changes in tear stability. The TSAS quantifies dynamic alterations in tear stability for 10 s by evaluating regions of asymmetry, and greater tear asymmetry is associated with more severe DE. Unfortunately the TSAS method is rather time-consuming and expensive, resulting in limited studies.

Dorota et al. [38] assessed tear film surface quality using three different techniques during suppressed and natural blinking condition (SBC and NBC) to predict DE. They obtained and analyzed ocular surface images using three non-invasive methods. Among them, the Lateral Shearing Interferometry (LSI) method outperformed (AUC = 0.80, 0.73 under SBC, NBC respectively) the other methods, even though the LSI instrument analyzes only a small portion of the ocular surface.

Table 5 Classification using features extracted from specific ocular regions of eyes with SVM classifier

Frames	No of features	Accuracy (%)	Sensitivity (%)	Specificity (%)
Left lower half				
1st	4	95.0	98.7	80.9
5th	5	95.0	95.0	95.2
10th	2	89.2	87.6	95.2
Left upper half				
1st	3	82.3	82.7	80.9
5th	5	89.2	90.1	85.7
10th	7	88.2	90.1	90.9
Right lower half				
1st	3	91.2	90.2	95.2
5th	4	97.0	97.5	95.2
10th	2	92.2	91.4	95.2
Right upper half				
1st	2	93.4	82.9	85.7
5th	3	81.5	84.1	71.4
10th	3	84.4	86.5	76.1

Morgan et al. [39] analyzed OST in five anatomical locations of the eye in DE patients using IR thermography. They calculated *Mean* OST (MOST) from OST values obtained in the five regions. In addition, the radial temperature difference (RTD), which is the temperature difference between the center of the cornea and average of two limbal readings, is evaluated. They found a higher MOST and RTD in DE than normal controls respectively. They also presented that RTD is higher in severe DE patients with TBUT ≤ 6 s compared to moderate DE patients with TBUT >6 s. Tear evaporation rate is suitable for predicting the usefulness of treatment strategies that target evaporative dry eye. We showed that thermography-derived evaporation rates are correlated to symptomatic response to eyelid warming three months after therapy [20]. In that study, we also showed that TBUT at baseline is not predictive of this symptomatic response, suggesting that this conventional test for dry eye alone is not sufficient to detect cases of evaporative DE that will benefit from eyelid warming. Most physicians and patients are aware of the use of lubricants for DE, but many may not be aware of the role of eyelid warming or how to select appropriate patients for eyelid warming treatment.

We have previously proposed the HOS method to analyze the ocular surface of the eye using IR thermography to detect DE [24]. The study extracted third-order cumulant (bispectrum) features from the ocular surface region of interest and reported 99.8% sensitivity, 99.8% specificity, and 99.8% accuracy using probabilistic neural network (PNN) and k-nearest neighbor (KNN) classifiers. Similar classification accuracies have been obtained using the SVM classifier (polynomial order 2 kernel). That proposed system extracts features automatically from the

Table 6 Summary of studies on analysis of ocular surface regions and or different locations of the eye to detect DE

Authors (year)	Modality	Data used	Features/Locations	No. of features	Classification	Results
Xu et al. [32]	Schirmer test with anesthesia, and fluorescein dye test	352 DE patients and 55 normal subjects	TFI/entire eye	Not mentioned	Statistical analysis	Sen: 78.9% Spec: 91.8%
Morgan et al. [39]	IR thermography images	36 DE patients and 27 normal subjects	Mean OST and RTD/the center of the cornea, the two intersections at the limbus, and two conjunctival sites (one temporal and one medial)	Not mentioned	Statistical analysis	Mean OST and RTD are greater in DE
Hiroshi Fujishima et al. [40]	IR thermometer readings	20 DE patients and 20 normal subjects	Corneal temperature change (for 10 s without blinking)/central cornea	Not mentioned	Statistical analysis	DE = 0.21 °C Normal = 0.61 °C
Vico et al. [33]	Schirmer's test and fluorescein dye test	85 adults (51 adults with DE symptoms)	TFI/entire eye	Not mentioned	Statistical analysis	Sen: 74% Spec: 63%
Takashi et al. [37]	TSAS test and obtained images captured by Videokeratoscopy	27 DE patients and 26 normal subjects	TSRI and TSAI/entire eye	Not mentioned	Statistical analysis	TSRI Normal = 0.72 ± 0.3 DE = 1.3 ± 0.4 TSAI Normal = 1.1 ± 0.9 DE = 2.1 ± 1.3
Chiang et al. [13]	IR thermal imager system	82 DE patients and 26 normal subjects	Cooling of the OST/ocular surface	Not mentioned	Statistical analysis	Sen: 79.3% Spec: 75%
Dorota et al. [38]	3 methods: dynamic area high-speed videokeratoscopy (HSV), wavefront sensing (DWS), and LSI	12 DE patients and 22 normal subjects	NBC and SBC blinking conditions/ocular surface	Not mentioned	Statistical analysis	LSI AUC = 0.80 in SBC and 0.73 in NBC

(continued)

Table 6 (continued)

Authors (year)	Modality	Data used	Features/Locations	No. of features	Classification	Results
Tai et al. [34]	IR thermal image system	76 DE eyes and 47 normal eyes	TDV and CV/ocular surface	2 features	Statistical analysis	Sen: 84% Spec: 83%
Acharya et al. [24]	IR thermography images	83 DE patients and 21 normal subjects	HOS texture parameters/ocular surface	37 (left eye) 34 (right eye) features	SVM, KNN and PNN	Left eye Acc, Sen, and Spec: 99.8% Right eye Acc: 99.8%, Sen: 99.9% and Spec: 99.4%
Current study	IR thermography images	21 normal and 83 DE subjects	DWT and Gabor transform/lower half and upper half of ocular surface regions	2 (left lower half) 7 (left upper half) 4 (right lower half) 2 (right upper half)	SVM	Left lower half Acc: 95% Sen: 95% Spec: 95.2% for 10th frame Left upper half Acc: 88.2% Sen: 90.1% Spec: 90.9% for 10th frame Right lower half Acc: 97% Sen: 97.5% Spec: 95.2% Right upper half Acc: 93.4% Sen: 82.9% Spec: 85.7% for 1st frame

Acc Accuracy; *Sen* sensitivity; *Spec* specificity

entire ocular surface, and since not much user interaction is required, the analysis is faster and reproducible. However we used 37 features in the left eye and 34 in the right eyes to achieve the high accuracy. In addition, the system uses about 10 frames after the blink to achieve the maximum classification accuracy, resulting in a computationally intensive approach.

To address this issue, we only utilized the 1st, 5th, and 10th frames after the blink in the infrared thermography images using Gabor Transform features. We achieved an accuracy of (i) 95.0, 95.0, and 89.2%, and (ii) 91.2, 97.0, and 92.2% for 1st, 5th, and 10th left and right lower halves of the ocular surface, respectively. Similarly, left and right upper halves resulted in an accuracy of (i) 82.3, 89.2, and 88.2%, and (ii) 93.4, 81.5, and 84.4% in identifying DE, respectively. The 5th and 10th frames after blink have provided better results compared to the 1st frame. This proposed method uses only one image frame after the first blink to detect DE efficiently, thus reducing computational time, which is a very important consideration for any algorithms used in point-of-care diagnostics. Clinicians need to know if eyelid warming is to be recommended for a patient a few minutes into the consultation.

The main advantages of this proposed method are,

(i) Only one frame (1st or 5th or 10th frame after the first blink) in lower half of the eye is used to detect DE. Also, the detection of DE is faster and computation time shorter, as we need to analyze only half the area of the exposed ocular surface.
(ii) It is semi-automatic compared to manual interpretations of tear film quality, ocular surface assessment, and TFI which may be more susceptible to inter-observer variation.
(iii) Our approach is more accurate compared to conventional tests as demonstrated by tenfold cross validation.
(iv) The proposed algorithm may have application in any polyclinics or situations economically, where the use of dyes and specialized consumables are not available.

5 Conclusion

In this chapter, the significance of limited ocular surface regions for the identification of DE using IR thermography images is proposed by extracting Gabor transform features from DWT coefficients. The method shows accuracy of (i) 82.3, 89.2, and 88.2%, for the left eye, and (ii) 93.4, 81.5, and 84.4%, for the right eye, upper half of 1st, 5th, and 10th frames after blink, respectively, using the SVM classifier. Similarly, using the 1st, 5th, or 10th frames obtained after the blink in the lower half of ocular regions we achieved accuracies of (i) 95.0, 95.0, 89.2% (left eye), and (ii) 91.2, 97.0, 92.2% (right eye) respectively in DE detection using SVM classifier. Our proposed algorithm helps in DE detection using IR thermography,

and assessment time is reduced without analyzing the entire ocular surface. In the future, the authors will explore the possibility of further limiting the analyzed regions to quarters of the ocular surface.

References

1. IDEWS, The International Dry Eye WorkShop Study Group: The definition and classification of dry eye disease: report of the definition and classification subcommittee of the international dry eye workshop. Ocul. Surf. **5**, 75–92 (2007)
2. Whitcher, J.P.: Clinical diagnosis of the dry eye. Int. Ophthalmo. Clin. **27**, 7 (1987)
3. Johnson, M.E., Murphy, P.J.: Changes in the tear film and ocular surface from dry eye syndrome. Prog. Retin Eye Res. **23**, 449–474 (2004)
4. Perry, H.D.: Dry eye disease: pathophysiology, classification, and diagnosis. Am. J. Manage Care **14**, S79–S87 (2008)
5. Savini, G., Pinita, P., Takashi, K., Martin, G., Edgar, E., Eiki, G.: The challenges of dry eye diagnosis. Clin. Ophthalmol. **1**, 31–55 (2008)
6. Tan, J.H., Ng, E.Y.K., Acharya, U.R., Chee, C.: Infrared thermography on ocular surface temperature: a review. Infrared Phys. Technol. **52**, 97–108 (2009)
7. Tan, J.H., Ng, E.Y.K., Acharya, U.R.: Automated study of ocular thermal images: comprehensive analysis of corneal health with different age group subjects and validation. Digit. Signal Process **20**, 1579–1591 (2010)
8. Purslow, C., Wolffsogn, J.: The relation between physical properties of the anterior eye and ocular surface temperature. Optom. Vision Sci. **84**, 197–201 (2007)
9. Tan, J.H., Ng, E.Y.K., Ahcarya, U.R.: An efficient automated algorithm to detect ocular surface temperature on sequence of thermograms using snake and target tracing function. J. Med. Syst. 1–10 (2010)
10. Lemp, M.A., Baudouin, C., Baum, J., et al.: The definition and classification of dey eye disease: report of the definition and classification subcommittee of the international dry eye workshop. Ocul. Surf. **5**, 75–92 (2007)
11. Hosaka, E., Kawamorita, T., Ogasawara, Y., Nakayama, N., Uozato, H., Shimizu, K., Dogru, M., Tsubota, K., Goto, E.: Interferometry in the evaluation of precorneal tear film thickness in dry eye. Ann. J. Ophthalmol. **151**, 18–23 (2010)
12. Morgan, P.B., Tullo, A.B., Efron, N.: Ocular surface cooling in dry eye—a pilot study. J. Br. Contact Lens Assoc. **19**, 7–10 (1996)
13. Chiang, H.K., Chen, C.Y., Cheng, H.Y., Chen, K.H., Chang, D.O.: Development of infrared thermal imager for dry eye diagnosis, in Infrared and photoelectronic imagers and detector devices II. In: Longshore, R.E., Sood, A. (eds.) Proceedings of SPIE, p. 6294 (2006)
14. Mori, A., Oguchi, Y., Okusawa, Y., Ono, M., Fujishima, H., Tsubota, K.: Use of high speed, high resolution thermography to evaluate the tear film layer. Am. J. Ophthalmol. **124**, 729–735 (1997)
15. Mathers, W.: Evaporation from the ocular surface. Exp. Eye Res. **78**, 389–394 (2004)
16. Craig, J.P., Singh, I., Tomlinson, A., Morgan, P.B., Efron, N.: The role of tear physiology in ocular surface temperature. Eye **14**, 635–641 (2000)
17. Tan, J.H., Ng, E.Y.K., Acharya, U.R.: Evaluation of tear evaporation from ocular surface by functional infrared thermography. Med. Phys. **37**, 6022–6034 (2010)
18. Acharya, U.R., Ng, E.Y.K., Yee, G.C., Hua, T.J., Kagathi, M.: Analysis of normal human eye with different age groups using infrared images. J. Med. Syst. **33**, 207 (2009)
19. Tan, J.H., Ng, E.Y.K., Acharya, U.R., Chee, C.: Study of normal ocular thermogram using textural parameters. Infrared Phys. Technol. **53**, 120–126 (2010)

20. Lam, S.M., Tong, L., Duan, X.R., Acharya, U.R., Tan, J.H., Petznick, A., Wenk, M.R., Shui, G.H.: Longitudinal changes in the levels of tear fluid lysophospholipids and O-acyl-omega-hydroxy fatty acids brought about by eyelid warming treatment in a cohort of Meibomian Gland Dysfunction patients. J. Lipid Res. P051185 (2014)
21. Beier, T., Neely, S.: Feature-based image metamorphosis. Comput. Graph. **26**, 35–42 (1992)
22. Gonzalez, R.C., Woods, R.E.: Digital Image Processing. Prentice Hall, USA (2002)
23. Addison, P.S.: Wavelet transforms and the ECG: a review. Physiol. Meas. **26**(5), R155–R199 (2005)
24. Acharya, U.R., Sudarshan, V.K., Ghista, D.N., Eugene, W.J., Molinari, F., Sankaranarayanan, M.: Computer-aided diagnosis of diabetic subjects by heart rate variability signals using discrete wavelet transform method. Knowl. Based Syst. **81**, 56–64 (2015)
25. Acharya, U.R., Faust, O., Vinithasree, S., Molinari, F., Suri, J.S.: Thyroscreen system: high resolution ultrasound thyroid image characterization into benign and malignant classes using novel combination of texture and discrete wavelet transform. Comput. Methods Programs Biomed. **107**, 233–241 (2012)
26. Ma, W., Manjunath, B.: Texture features and learning similarity. In: Proceedings of IEEE Computer Society Conference on Computer Vision and Pattern Recognition. CVPR, pp. 425–430 (1996)
27. Acharya, U.R., Chowriappa, P., Fujita, H., Bhat, S., Dua, S., Koh, J.E.W., Eugene, L.W.J., Kongmebhol, P., Ng, K.H.: Thyroid lesion classification in 242 patient population using Gabor transform features from high resolution ultrasound images. Knowl.-Based Syst. **107**, 235–245 (2016)
28. Raghavendra, U., Acharya, U.R., Fujita, H., Gudigar, A., Tan, J.H., Chokkadi, S.: Application of Gabor wavelet and locality sensitive discriminant analysis for automated identification of breast cancer using digitized mammogram images. Appl. Soft. Comput. **46**, 151–161 (2016)
29. Manjunath, B.S., Ma, W.Y.: Texture features for browsing and retrieval of image data. IEEE Trans. Pattern Anal. Mach. Intel. **18**, 837–842 (1996)
30. Andrew, R.: Webb, Statistical Pattern Recognition, 2nd edn. Wiley, Chichester, UK (2002)
31. Duda, R.O., Hart, P.E., Stork, D.G.: Pattern Classification, 2nd edn. Wiley, New York (2001)
32. Xu, K.P., Yagi, Y., Toda, I., Tsubota, K.: Tear function index. A new measure of dry eye. Arch. Ophthalmol. **113**, 84–88 (1995)
33. Vico, E., Benitez, C.J.M., Gimenez, R.A., Fernandez, C., Garcia, S.J.: Tear function index validation for dry eye diagnosis. Arch. Soc. Esp. Ophthalmol. **79**, 265–271 (2004)
34. Tai, Y.S., Hwa, C.K., Liu, P.H., Wu, M.H., Chang, D.O., Su, P.F., Chang, S.W., Chiang, H.K.: Noncontact detection of dry eye using a custom designed infrared thermal image system. J. Biomed. Opt. **16**, 046009 (2011)
35. Acharya, U.R., Tan, J.H., Sudarshan, V.K., Yeo, S., Too, C.L., Lim, W.J.E., Chua, K.C., Tong, L.: Diagnosis of response and non-response to dry eye treatment using infrared thermography images. Infrared Phys. Technol. **67**, 497–503 (2014)
36. Acharya, U.R., Tan, J.H., Koh, J.E.W., Sudarshan, V.K., Yeo, S., Too, C.L., Chua, K.C., Ng, E.Y.K., Tong, L.: Automated diagnosis of dry eye using infrared thermography images. Infrared Phys. Technol. **71**, 263–271 (2015)
37. Takashi, K., Reiko, I., Murat, D., Eiki, G., Yoji, T., Yukhihiro, M., et al.: A new noninvasive tear stability analysis system for the assessment of dry eye. Invest. Ophthalmol. Vis. Sci. **45**, 1369–1374 (2004)
38. Dorota, H.S., David, A.C., Iskander, D.R., Read, S.A., Collins, M.J.: Predicting dry eye using noninvasive techniques of tear film surface assessment. Invest. Ophthalmol. Vis. Sci. **52**, 751–756 (2011)
39. Morgan, P.B., Tullo, A.B., Efron, N.: Infrared thermography of the tear film in dry eye. Eye **9**, 615–618 (1995)
40. Fujishima, H., Toda, I., Yamada, M., Sato, N., Tsubota, K.: Corneal temperature in patients with dry eye evaluated by infrared radiation thermometry. Br. J. Ophthalmol. **80**, 29–32 (1996)

Infrared Thermal Mapping, Analysis and Interpretation in Biomedicine

Arul N. Selvan and Charmaine Childs

Abstract Measurement of body temperature is one of the cornerstones of clinical assessment in medicine. Skin, the largest organ of the human body, is essentially a temperature *mosaic* determined by the rate of blood flow through arterioles and capillaries adjacent to the skin. This makes the conventional methods of 'spot' measurement rather limited in providing detailed information of regional skin temperature. Infrared (IR) thermal imaging however has the potential to provide a robust method of surface temperature mapping in disease states where pathology disturbs the 'normal' distribution of blood flow to skin. To advance image interpretation from the conventional qualitative narrative to a quantitative and robust system, analytical developments focus on digital images and require computer-aided systems to produce results rapidly and safely. Hierarchical clustering-based segmentation (HCS) provides a generic solution to the complex interpretation of thermal data (pixel by pixel) to produce clusters and boundary regions at levels not discernible by human visual processing. In this chapter, HCS has been used to aid the interpretation of wound images and to identify variations in temperature clusters around and along the surgical wound for their clinical relevance in wound infection.

Keywords Infrared · Temperature · Thermal mapping · Wound infection · Image analysis · Hierarchical Clustering-based Segmentation (HCS) · Isotherm · Boundary outlining

A.N. Selvan
Materials and Engineering Research Institute, Sheffield Hallam University, Howards Street, Sheffield S1 1WB, City Campus, UK

C. Childs (✉)
Centre for Health and Social Care Research, Sheffield Hallam University, Montgomery House, Collegiate Campus, Sheffield S10 2BP, UK
e-mail: c.childs@shu.ac.uk
URL: http://www.shu.ac.uk

E.Y.K. Ng and M. Etehadtavakol (eds.), *Application of Infrared to Biomedical Sciences*, Series in BioEngineering,
DOI 10.1007/978-981-10-3147-2_21

1 Human Temperature Measurement

Measurement of the temperature of the tissues of the human body is probably one of the most well recognised clinical activities in modern medicine. A change in body temperature, notably fever, has long been regarded as a classical sign of inflammation and infection in man which for centuries was measured with a variety of instruments. In recent years, clinical thermometry has undergone an evolution with a variety of "*liquid in glass, liquid crystal and electronic*" '*thermometers*' in everyday use. The sites for measurement are limited and, by convention, confined to body cavities (mouth, oesophagus, rectum) skin folds and crevices of the groin and axilla (armpit) [21].

However, over the last few decades, advances in thermometry and accompanying technology has evolved such that we are now able to implant temperature sensors deep inside the human body, previously possible only in the experimental laboratory. In the brain for example, being able to implant sensors into injured white matter and/or cerebral ventricles [9] has shown variations in organ temperature from deep to superficial structures [14] and across the brain [8] and has revolutionised our understanding of the pathophysiology of brain damage [27, 36]. Similar variations in regional tissue temperature have also been reported, with non-invasive imaging of healthy brain using ^{1}H magnetic resonance spectroscopy (^{1}HMRS) and imaging (^{1}H MRSI) [7]. That said, we have to recognise the limitations of in situ sensor technology for whole organ temperature measurement. Since the insertion of multiple probes and sensors are not feasible in the clinical setting, the measurement site is generally restricted to just a single '*spot*'. The same is true for skin temperature measurement. When it comes to surface temperature, the skin has long been regarded as a thermal '*mosaic*' [17]. With the knowledge that skin temperature can vary widely across the body, what value might there be in a single skin measurement? More useful would be skin temperature "*mapping*" in body regions where disease manifests upon the skin. Infrared (IR) thermometry provides a solution to both temperature measurement and regional temperature mapping and can be undertaken rapidly and relatively simply.

Non-ionising IR thermal imaging has many advantages. Although not used routinely as a diagnostic clinical tool, it does have potential as a future imaging modality provided that image analysis can be developed to provide reliable routes to interpretation, assessment and diagnosis in medicine. In this chapter, methods for the interpretation of digital thermal imaging in biomedical applications are presented.

2 Infrared Thermal Imaging in Medicine

The use of infrared thermal imaging in health care is not a recent phenomenon. Thermography in breast cancer screening began in 1956 when Lawson [19] observed that skin temperature overlying a breast tumour was higher than that of

'*normal*' skin. However, using thermography without a standardised protocol for imaging, patient preparation, control of ambient temperature or physician training led to scepticism; the technique not being perceived well for "*diagnostic/screening*" accuracy. It subsequently suffered a demise [42]. Alternative imaging modalities at this time; X-ray, proton magnetic resonance imaging (^{1}HMRI) computed tomography (CT) whilst costly had a superior reputation for reliability and clinical utility. However, it is now recognised that when used repeatedly in diagnostics, all incur a degree of hazard to health due to ionising radiation load; particularly for neonates and young children [22, 26]. By contrast, IR thermography does not penetrate structures below the skin and is non-ionising.

The utility of IR thermal imaging is underpinned by its penetration depth. IR radiation is not emitted by skin at depths greater than 5.0 mm [20] thus it is unable to "*image*" deep tissue and organs. That said, many physiological and pathophysiological changes "*trigger*" alterations in skin dermis via capillary networks, particularly in acral regions (toe, finger, ear, tip of nose). Such changes occur either intrinsically through local biochemical stimuli, and/or by external factors (heat/cold for example) via vascular, neurological and/or neurovascular pathways [20]. This makes IR imaging at the surface of real value for a number of prognostic and diagnostic capabilities where changes in skin blood flow, and thus skin temperature, provide clinically relevant information. The significant advances in IR detectors and technology, along with improvements in the development of image processing techniques have, over the last 5 years, seen a re-emergence of interest in IR imaging with a successful reported use in oncology, pain management, vascular disorders, arthritis/rheumatism, neurology, sports and rehabilitation medicine [11].

3 Digital Medical Thermal Imaging Interpretation

Typically, thermal images are inspected and interpreted using the following methods:

- Qualitative or a narrative report determined by visually inspecting the image to identify differences in the colour map corresponding to temperature (°C/°F) (Fig. 1a).
- Quantitative analysis of a region of interest (ROI) or "*spot*" (pixel) measures (Fig. 1b) with options for including average, maximum and minimum values within a ROI.
- Image analysis, in its most simple form, relies solely on the variation in colour of the thermogram which corresponds to a temperature range [39].

3.1 Issues Associated with Visual Inspection of Thermal Images

Until recently, IR thermal cameras were constructed with sensors having low resolution only (e.g. 160 × 120 pixels) but, with advances in detector technology,

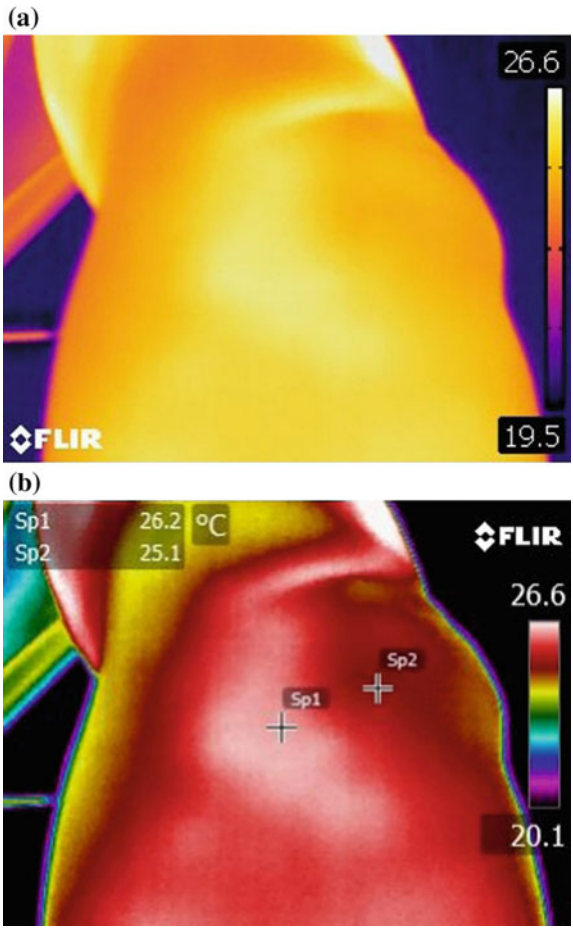

Fig. 1 Temperature values in a thermal image displayed using different colour palettes (**a**, **b**). The locations of interest *Sp1* and *Sp2* are better differentiated visually when the temperature values are displayed using colour palette (**b**) versus (**a**) and reveals the potential impact of colour palette choice for interpretation. To choose the right colour palette the user may need to know what they would like to highlight by differentiating from the surrounding area. For example in this case, the pain site (approximate location provided by the patient)

improved thermal sensitivity with possible pixel resolution of (640 × 480–1024 × 768) are available as affordable thermal imaging systems. The problem is that human visual processing is not capable of perceiving all of the subtle information present in such high resolution images. Thermal pattern-recognition computer software systems are therefore required to "*extract*" information of thermal values "*hidden*" within the data provided by the thermal camera manufacturers' dedicated software. For example in Fig. 1a, the skin surface temperature over this anatomical region appears relatively homogeneous in colour. However, post-processing with camera software identifies two distinct regions which differ by approximately 1 °C when using measurement spots to provide temperature values at each selected pixel location (SP1 and SP2) and referenced with the temperature key (Fig. 1b). This simple image analysis can be advanced further but requires far greater systems complexity to identify temperature variations over very small areas; for example, between groups of pixels. A system for defining (pixel) areas of

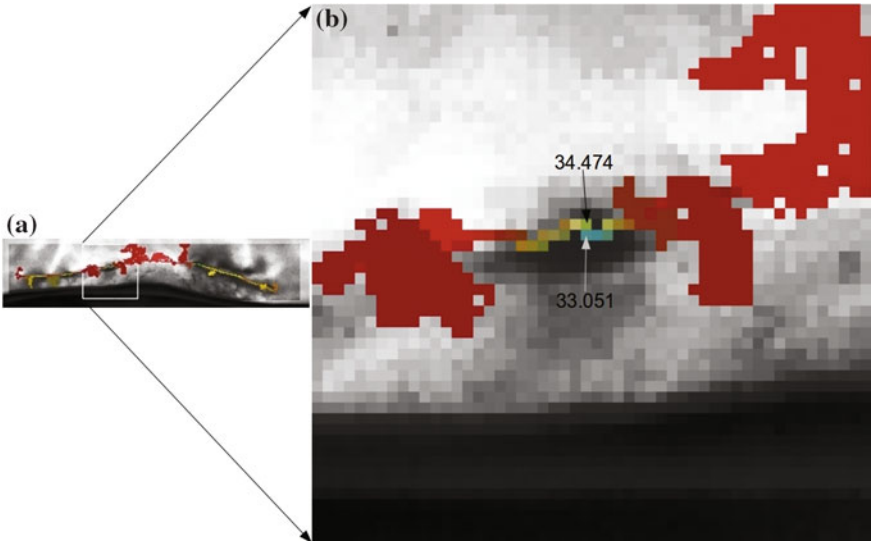

Fig. 2 A typical thermal image where there is a temperature variation of almost 1.5 °C across a single pixel distance. These locations might be missed on casual visual inspection and may need software tools to highlight the dissimilarity

similarity may then be required. As an example, Fig. 2 shows temperature variation of approximately 1.5 °C across single pixel locations. This temperature variation could be lost or overlooked on visual inspection but may be identified easily with a computer-aided pixel highlighting process.

In medicine, clues to the identification of skin/body regions where disease or injury may exist can be provided by the patient him/herself. In Fig. 3a, the patient had complained of pain at the muscles of the thenar eminence. In Fig. 3a, the painful region is identified by an arrow. An adjacent spot measure (SP2) reveals the temperature value; one of a number of regions in this thermogram close to the maximum value in the field of view (maximum being 34.4 °C). In Fig. 3b much greater detail is provided by exploring pixel boundaries around the site (arrow). At least three different colour coded regions can be identified within which the temperature values are similar. By using computer-aided software, it is possible to distinguish each of these regions as a separate temperature "*boundary*". Furthermore, the boundaries make the size and shape of each region, having similar temperature values, become evident. In this way, these images have the potential to map areas of skin temperature linked to the anatomical distribution of pain. This method for outlining areas of similar temperature will aid the objective assessment of the size and position of the area of interest because accuracy of diagnosis depends on how well the segmentation of the ROI is performed in a thermogram [18].

Comparing the ROI from images in Fig. 4a, b, it can be seen how the loss of visual detail inherent in human visual perception can be overcome by further

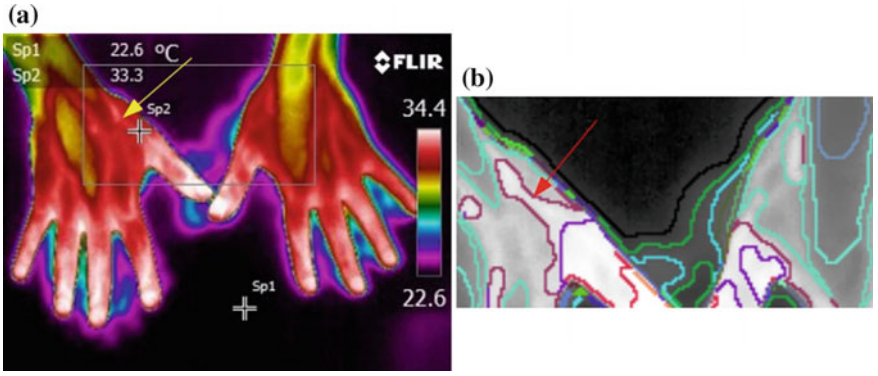

Fig. 3 Hand thermal image showing location of patient-reported pain thought due to underlying inflammation (*yellow arrow*). In **a,** pixel spot (*Sp2*) indicates the pixel temperature at adjacent skin site to the painful area. Computer-aided software tools system applied to (**a**) defines the areas of similar temperature and noting the extent and pattern of the temperature region commensurate with the painful area (*red arrow*) **(b)**

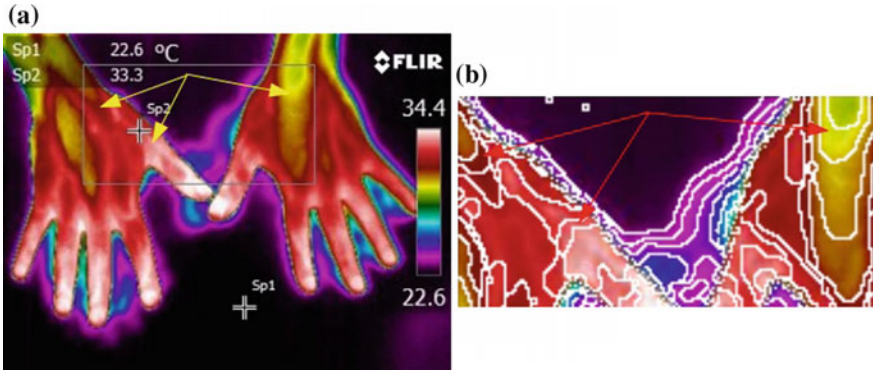

Fig. 4 Isotherms plotted by a computer programme aids visualisation of fine gradations of temperature in the region (defined by the "box") in (**a**). For example, around the locations identified at the (*yellow arrows*) (**a**) the fine gradations of temperature changes are highlighted by using isotherms (*Red arrows*) (**b**)

discrimination of pixels and boundary patterns achieved by the use of isotherms. In this context, isotherms are curves which enclose regions of similar temperature patterns. The isothermal patterns of Fig. 4b show greater detail than information in Fig. 4a and have been produced by a boundary outlining software [29] to enhance image information and to reveal the size and shape of regions with the same (and different) temperature characteristics. By using isothermal patterns and boundary regions, fine resolution and greater information from the same original image can be obtained. Thus, computer generated boundaries aid the visualisation of fine gradations of temperature changes within an area having a seemingly uniform temperature.

Given the potential for computer-aided image analysis to reveal details of the user-drawn ROI (not possible on visual inspection using the software provided by proprietary systems), there is an emerging interest in the development of '*smart*' image processing algorithms to enhance the interpretation and analysis of thermal signatures.

We have previously reported the variation in temperature along two different surgical wound types; wounds produced after closure of enterostoma [34] and after caesarean section [10]. We piloted the use of an image processing algorithm; Hierarchical Clustering-based Segmentation (HCS) [29], in detecting anomalies in temperature along the scar [10].

4 Computer-Assisted Medical Thermal Image Interpretation

Anomaly detection in infrared (IR) images is a challenging task. Frize et al. [15] have identified a number of factors which can confound the accuracy of the temperature values acquired, including emissivity, external conditions (temperature, humidity) and imaging surface factors (material, surface properties, orientation) all of which produce IR images of low signal-to-noise ratio [4]. This introduces inaccuracy in obtaining the actual temperature values and contributes to measurement uncertainty.

The most important step in developing a computer-assisted anomaly detection system and application for analysis of thermal images is to segment relevant thermal information from thermal noise. Numerous algorithms are available in the literature for detecting boundaries to segment ROI in visible and optical images. However, because of the non-uniformity of IR images, revealed by varied pixel values representing similar temperature across the image [6], boundary regions in thermal images are not defined clearly. Software techniques used successfully in detecting boundaries in optical (visible) images have the drawback of being unable to form continuous, distinct and meaningful boundaries around an ROI in thermograms; they are therefore unreliable for segmenting IR images [44].

Designs for computer-assisted methods for the interpretation of thermal images are available, for example, to assist the user in objective identification of skin '*hot*' spots. Snekhalatha et al. [35] implemented an automated thermal image segmentation of a hot spot region of the hand. Similarly, because a regular ROI such as a rectangle, square, circle or elipse, poorly outlines certain anatomical regions [13]. Vardasca et al. [40] designed an automated ROI fitting method to address the issues associated with obtaining a representative temperature value from a user-drawn regular ROI from thermal images of limbs. These examples suggest that automation of thermal images are typically for "*bespoke*" applications.

In this chapter, we discuss the development of a generic thermal image segmentation process to extract thermal features considered to be '*abnormal*' and using a Hierarchical Clustering-based Segmentation (HCS) design and process [29]. HCS segments an image as a set of regions with each region composed of sub-regions and which are, themselves, composed of sub-regions, and so on [16]. In this way, HCS is a dissimilarity highlighting process that yields a hierarchy of segmentation results. It is well suited to address the issues associated with the segmentation of 'noisy' thermal image data.

In separating out the ROI, *thresholding* is used. The separation is based on the variation of pixel values between the regions' pixels and the surrounding pixels. For example in a grey scale image with pixel values ranging from zero to 255, the variation of (difference in) pixel values between parts (regions) can be between zero and 255. In the thresholding process, a part of the image is segmented as a separate region if its pixel values vary from the surrounding pixel values by a threshold value (T). For a low threshold value, pixels having even the smallest difference from the surrounding pixel values will be *segmented* as a separate region. Thus, a low threshold value will locate boundaries of regions having the most subtle of differences. As these small pixel value differences may be because of the non-uniformity of IR images, the detected boundaries will be spurious [12]. By contrast, higher threshold values will detect only the boundaries of regions where there are major difference with the surroundings but by using a higher threshold, the downside is that there are likely discontinuities in the detected boundaries [12].

Identifying boundaries where only a single threshold value is employed has two problems [1, 2]. First, the most appropriate threshold value will depend greatly on the application, i.e. whether identification is required for major boundaries or subtle boundaries only. Second, and importantly, thresholding using a single threshold will result in loss of useful boundary information, which might otherwise be found for different threshold values.

Unlike other segmentation processes which favour identification of the boundaries between different regions by choosing a (single) threshold value, the HCS process is based on a non-thresholded boundary identifying process. That is, no threshold value is used. However, recognising that the process does, indeed, need some form of "*thresholding*" approach to identify the boundaries of different regions in an image, the HCS process rather than using a single threshold value, instead uses a "*hierarchical*" level of thresholding to identify the boundaries between different regions in the image.

4.1 Design of Hierarchical Clustering-Based Segmentation (HCS) as an Aid to Interpret Medical Thermal Images

The human visual system processes images at varying resolutions; coarse to fine. For example, given an anatomical image of the cross section of a skull, at a coarse level a radiologist can visualise the image as distinct regions belonging to soft

tissues or bone. At a fine level, different types of soft tissues are also identified. At a still finer level and, given the appropriate imaging modality, the radiologist will be able to distinguish "*abnormal*" regions (e.g. commensurate with ischaemia) within the same tissue type. This example illustrates a "*resolution*" hierarchy from coarse (bone) fine (tissue) and still finer (blood within tissue) within an image. Since the early days of computer vision, this hierarchical structure of visual perception has motivated clustering techniques for image segmentation [25]. So in a computer model representation, the segmentation process is modelled as a process of grouping visual information, where the details are grouped into objects, and objects into classes of objects. Thus, starting from the composite segmentation, the perceptual organization of the image can be represented by a tree of regions, ordered by inclusion. The root of the tree is the entire scene, the leaves are the finest details and each region represents an object at a certain scale of observation [1].

Hierarchical Clustering-based Segmentation (HCS) [28–30] implements the traditional agglomerative clustering [23] where the regions of an initial partition are iteratively merged and automatically generate a hierarchy of segmented images (Fig. 5); for example, Fig. 6 (top row of images; left to right).

The hierarchy of segmented images is generated by partitioning an image into its constituent regions at hierarchical levels of "*allowable dissimilarity*" (threshold value) between its different regions. At any particular level in the hierarchy, the segmentation process will cluster together all the pixels and/or regions which have dissimilarity value among them; less than or equal to the dissimilarity allowed for that level (Fig. 5).

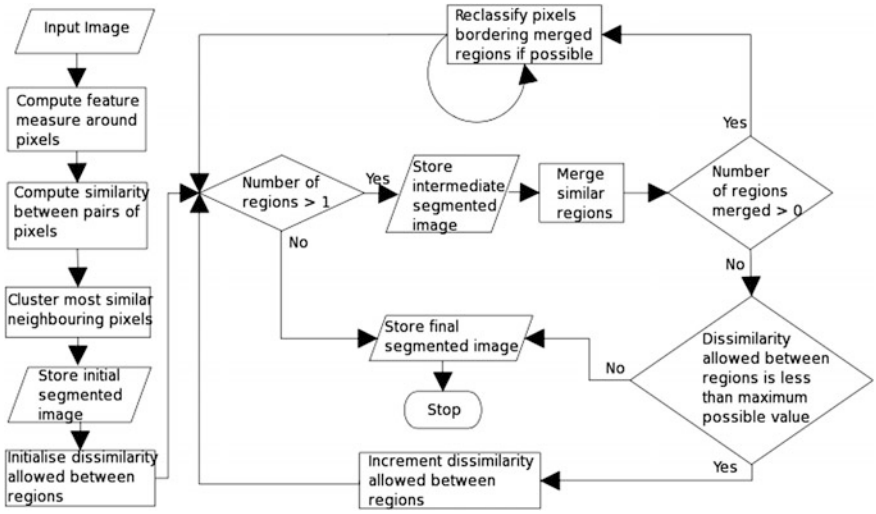

Fig. 5 Flow chart illustrating the working of the HCS process. The input image is initially segmented into regions by clustering similar neighbouring pixels. The initial segmentation of the region is merged for different *allowable dissimilarities*, between regions, yielding a hierarchy of segmented images. Reproduced from [28]

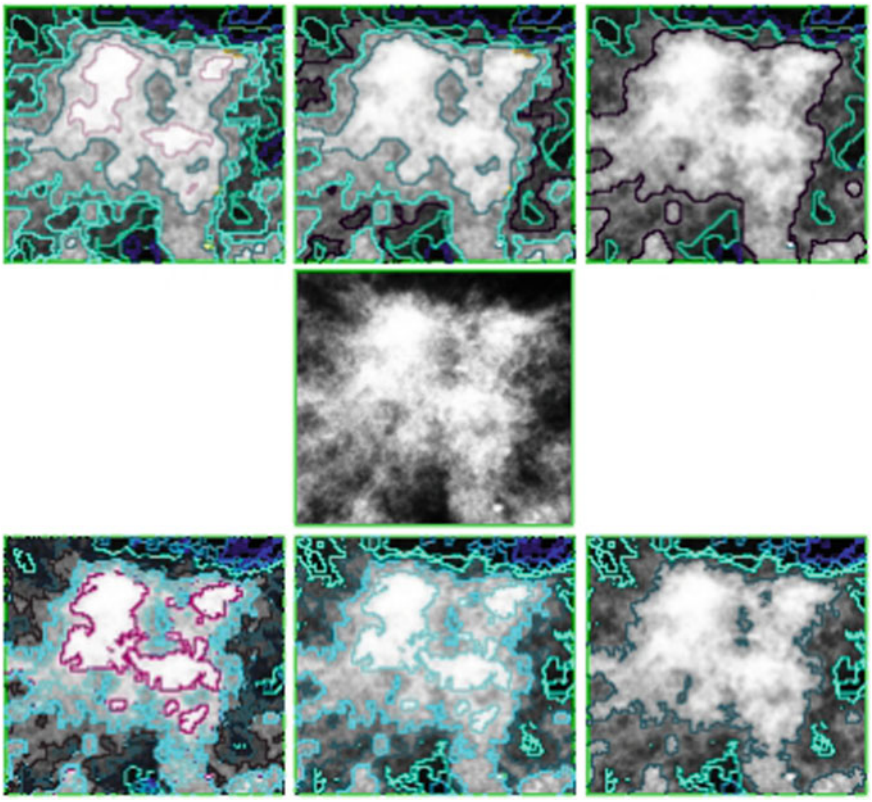

Fig. 6 Comparison of segmentation output of an ill-defined "*abnormality*" from an X-ray mammogram image (*middle row*) **with** border-pixel-re-classification (*top row*) and **without** border-pixel-re-classification(*bottom row*). The delineated cluster boundaries with border-pixel-re-classification (*top row*) are more easily visualised as distinct visual clusters when compared to the cluster boundaries delineated without border-pixel-re-classification (*bottom row*) and is an example of HCS process' capability

A unique feature of the HCS process is the border pixel classification operation (flow-chart Fig. 5). Border pixel reclassification is considered only for those pixels on the boundary of the clusters which had been merged with other clusters. These boundary pixels are removed one at a time from their original clusters. The pixel removed is considered as a region of its own and the similarity between the one pixel region and the regions bordering it (which include the original cluster to which it belonged) are found and the single pixel region merged with the most similar bordering region. Border pixel reclassification aides in over-riding local inhomogeneity while clustering similar pixels/regions.

An example of HCS border pixel re-classification in use can be demonstrated by the visually smooth border delineation obtained in Fig. 6. The central image (middle row) is the image of an abnormality having ill-defined boundaries presented in an

X-ray mammogram. It can be seen from the border outlined images that the HCS process (with border pixel reclassification—top row) achieves far better results in delineating the different regions within the abnormality when compared to the segmentation without border-pixel-re-classification (bottom row). The border pixel re-classification operation of the HCS process generates visually smooth boundaries and also identifies more appropriate boundaries when compared to other similar segmentation processes such as Tilton's [37] Hierarchical Segmentation (HSEG) [38]. For further details with relevant example see Selvan [29].

Since the HCS process is a generic segmentation process, it is applicable and equally successful at segmentation and outlining boundaries of ROI in digital images from any source whether from X-ray or thermal image. This makes HCS a versatile process which has been demonstrated successfully and without any modifications (e.g. parameter tuning) to segment images of the natural environment (e.g. birds, trees) [29] and diagnostic images obtained using different modalities; ultrasound images [28], CT [31], X-ray mammograms [32], magnetic resonance imaging [33] and digital medical thermal image (DMTI) [10].

5 HCS Process in Thermal Image Analysis of Surgical Wounds

In clinical practice, the assessment of surgical wounds for surgical site infection is largely undertaken using wound scoring tables and criteria (e.g. [5, 41, 43]). There are currently no independent quantitative technologies for wound assessment. Typically, however, descriptive narratives are used to describe the state of a wound and to undertake wound healing assessments [24].

Here we describe a novel method to aid the user to:

- visualise the thermal pattern to report information for a more robust qualitative analysis
- provide quantitative measures for wound analysis.

5.1 HCS Process Aided Evaluation of the Temperature Variation of the Surgical Wound

Previous studies report a relationship between temperature and skin viability during inflammation and infection. For example, raised skin temperature is recognised as a sign of inflammation [5]. By contrast, a fall in skin temperature can occur during vascular insufficiency, ischaemia and necrosis [24]. In surgical wounds, we have recently observed '*cold spots*' in the thermograms of surgical wounds which

subsequently were shown to be infected [34]. More recently, we have designed and used the HCS process-based method to obtain quantitative measures to undertake an objective and independent assessment of healthy and infected surgical wounds [10]. For detailed information of the technique see Childs et al. [10] but a brief description is provided here where the steps involved in the designed HCS process include the following:

(a) HCS processing of a ROI around the wound site. A box shaped ROI around the wound site is chosen by the user (Fig. 7a)
(b) comparison of the wound site with a nearby healthy area.

(a) HCS Processing of a ROI Around the Wound Site The main purpose of this step is to highlight regions of different temperature values in an automated and objective manner. The HCS process is applied within the user outlined ROI (Fig. 7a) around the wound site.

The HCS process generates a hierarchy of segmentation output, for different values of allowable dissimilarity, amongst the pixels collated to form regions of similar temperature profiles. From the hundreds of segmentations, the user may make use only of the relevant segmentations having useful segmentation outputs. Briefly, in this example, the user has chosen four different segmentation outputs ranging from the segmentation having 253 regions to the segmentation having 11 regions only (Fig. 7b).

The segmentation having 253 regions will be produced when a low threshold of dissimilarity is allowed between regions. Hence a lesser number of regions will be merged. The segmentation with 11 regions will be produced when a higher value for the dissimilarity threshold is allowed for merging. This facilitates a higher number of regions to merge. In each of the cases (low or high threshold dissimilarity) the region images were produced by mapping the average temperature value of the pixels contained within a region to 256 grey scale levels. The boundary images were produced by plotting the border of the different regions onto the 256 level representations of the radiometric data (Fig. 7a).

From the different segmentation outputs generated, the user may choose segmentation(s) of interest to generate quantitative measures for each of the regions. On inspecting the different segmentations (Fig. 7b), the segmentation with 253 regions was chosen for further analysis and to extract the quantitative (temperature) measurements (Fig. 8). The upper panel shows the locations of interest (locations 1–11) and the corresponding temperature boundary regions (lower panel). In this way, the user can identify the variability in temperature regions across the ROI. In summary, the usefulness of the HCS process in outlining regions of similar temperature profile are as follows:

- The highlighted (boundary outlined) areas will aid the user to visualise, in detail, ROI including the shape and size of "*abnormal*" regions and the variability in temperature within regions which "*at first sight*" appear similar (Fig. 7).

- The process will aid the user to automatically derive quantitative measures of the highlighted (boundary outlined) areas in an objective manner (Fig. 8).

The process can also be used to automatically estimate the summary statistics of the temperature difference between two ROIs; in this example, the regions of the wound and of undamaged skin (Fig. 9c). In this example, marked differences in temperature are evident across the wound and in excess of 1.5 °C.

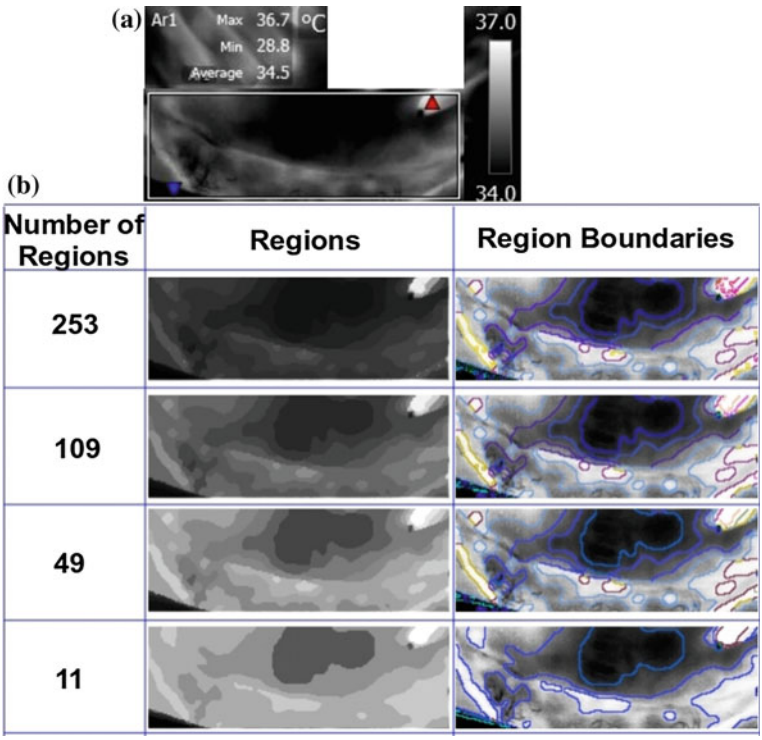

Fig. 7 Thermal image of a surgical wound site in grey scale with user outlined (*white*) box. The ROI is marked around the wound site (**a**). The summary statistics (maximum, minimum, average) of the temperature values within the ROI are estimated by the camera software (**a**); in this example, FLIR systems, Sweden. In (**b**) the region images display the average temperature value within the region mapped to 256 grey levels. The boundaries are marked on the grey shade thermal image (**a**). The HCS process will generate hundreds of segmentation outputs. The regions and boundary images shown in (**b**) are a sample output to illustrate that, when the *allowable dissimilarity value* is increased, the number of regions decrease because more regions will merge. For example when there are 253 regions, the central region (*locations 9, 10 upper panel* Fig. 8) reveals three bounded and segmented regions which range from *34.1* to *34.7 °C*

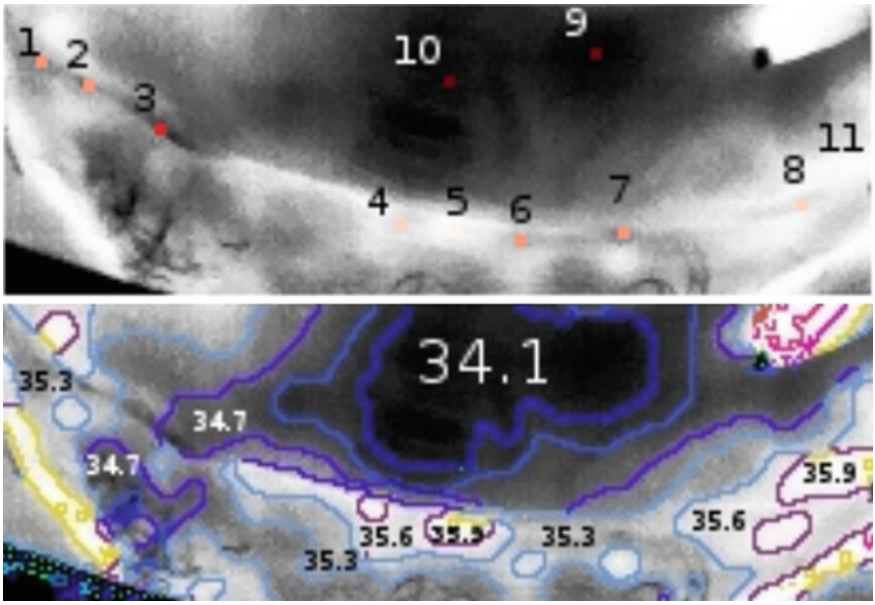

Fig. 8 HCS process' boundaries aid the user to visualise the different temperature patterns and estimate objective measures; average temperature values of different regions with similar temperature. This is much more appropriate when compared to the summary statistics estimated by the camera software for regular shape ROI (Fig. 7a)

(b) Comparison of the Wound Site with a Nearby Healthy Area Locations of interest along the wound site are noted as are adjacent locations marking healthy areas (Fig. 9a). From the output of the HCS process, regions over the area of healthy skin and the regions over the surgical wound are selected/identified for a user-chosen "*low*" dissimilarity level of 10% (i.e. each segmented region allows inclusion of pixels which differ from each other by not more than 10%) (Fig. 9b). The process automatically estimates the summary statistics of the temperature difference between the regions of the wound and the regions of the healthy area (Fig. 9c). In this example, there are wide variations between wound and adjacent healthy skin. For example, from the summary statistics generated from the HCS process for the image shown in Fig. 9, the wound site was maximally 1.6 °C lower, and maximally 1.2 °C higher, than healthy skin at loci shown (average differences being 0.53° and 0.45°, respectively). In addition, the temperature values along the wound estimated by the HCS process are average (34 °C), lowest (33.8 °C) and highest (35.4 °C) at loci shown in the figure and reveal significant temperature gradients within the ROI of the surgical wound.

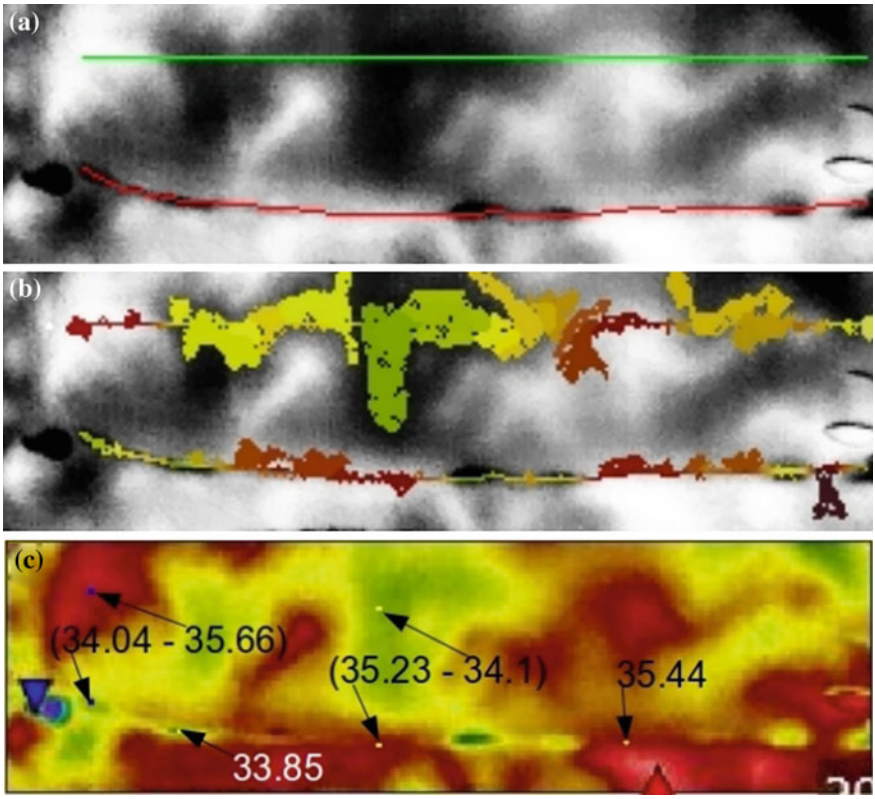

Fig. 9 User tagged locations along the wound (*red curve*) and along a healthy area nearby (*green line*) (**a**). Regions identified by the HCS process containing user tagged locations along the healthy area and along the wound (**b**) at a *dissimilarity level* of 10%. (**c**) Comparisons of temperature values of the regions along the wound and along the healthy area are identified and at three loci differ by 1.2–1.6 °C

6 Summary

Although the temperature of mammalian internal organs are considered relatively uniform (and constant), recent studies have shown that significant temperature gradients do occur [7, 8, 14]; even in a thermally "*shielded*" organ, brain. Whilst temperature shielding, due primarily to the effects of incoming arterial blood [45] would be expected to obviate large temperature gradients within internal structures, this is not the case for skin.

Since the seminal works of Aschoff and Wever in 1968 [3] variability of the body "*shell*" with temperature in excess of 10 °C are not unusual in healthy subjects. Furthermore, a variable counter current heat exchange between arterial and venous blood in limbs and digital extremities (hands, feet) enhances the temperature gradient of the peripheral "*shell*".

By undertaking a comprehensive assessment of healthy and injured skin by IR thermal mapping, combined with a computer-aided system to aid visual processing, we have exploited a variety of well-established image analysis techniques (e.g. hierarchical clustering, isotherm patterning) to produce an objective, robust method to obtain a hierarchy of thermal segments and boundaries to improve upon "*what we see*". Our work has allowed us to "*see more*" of the surgical wound and to set-in-train a quantitative, independent HCS technique of wound imaging systems to explore further the temperature mosaic which exists along the surgical wound for its potential future clinical utility.

Acknowledgements Our grateful thanks to Dr. Jon Willmott, Senior Lecturer in Sensor Systems, University of Sheffield UK, for his constructive comments during the preparation of this manuscript.

We would also like to thank the Machine Learning and Signal Processing Group, Centre of Telecommunication Research and Innovation (CeTRI), Universiti Teknikal Malaysia, Melaka (UTeM) for their contribution in providing the service of their High Performance RAM farm system for processing the thermal images.

References

1. Arbelaez, P.: Boundary extraction in natural images using ultrametric contour maps. In: Proceedings 5th IEEE Workshop on Perceptual Organization in Computer Vision (POCV'06), New York, USA, June 2006 (2006)
2. Arbelaez, P., Fowlkes, C., Martin, D.: The Berkeley segmentation dataset and benchmark June, 2007 (2007). http://www.eecs.berkeley.edu/Research/Projects/CS/vision/bsds/. Accessed 24 June 2016
3. Aschoff, J., Wever, R.: Cited in Stainer MW, Mount LE, Blight J. Energy balance and temperature regulation. Cambridge University Press, 1984 (1958)
4. Bal, A., Alam, A.S.: Automatic target tracking in FLIR image sequences using intensity variation function and template modelling. IEEE Trans. Instrum. Meas. **54**(5), 846–852 (2005)
5. Bharara, M., Schoess, J., Nouvong, A., Armstong, D.G.: Wound inflammatory index: a "proof of concept" study to assess wound healing trajectory. J. Diabet. Sci. Technol. **4**(4), 773–779 (2010)
6. Budzan, S., Wyzgolik, R.: Remarks on noise removal in infrared images. Measur. Autom. Monitor. **61**(06) (2015)
7. Childs, C., Hiltunen, Y., Vidyasagar, R., Kauppinen, R.A.: Determination of regional brain temperature using proton magnetic resonance spectroscopy to access brain-body temperature differences in healthy human subjects. Magn. Reson. Med. **56**, 1–9 (2006)
8. Childs, C., Shen, L.: Regional Pressure and temperature variations across the injured human brain: comparisons between intraparenchymal and ventricular measurements. Crit. Care **19**, 267 (2015). doi:10.1186/s13054-015-0982-x
9. Childs, C., Wang, L., Neoh, B.K., Goh, H.K., Zu, M.M., Aung, P.W., Yeo, T.T.: Multi-parameter brain tissue microsensor and interface systems calibration, reliability and user experiences of pressure and temperature sensors in the setting of neurointensive care. J. Med. Eng. Technol. Early Online, 1–12 (2014). doi:10.3109/03091902.2014.937834
10. Childs, C., Siraj, M.R., Fair, F.J., Selvan, A.N., Soltani, H., Wilmott, J., Farrell, T.: Thermal territories of the abdomen after caesarean section birth: infrared thermography and analysis approaches to surgical site assessment. J. Wound Care **25**(9), 499–512 (2016)

11. Diakides, N.A., Bronzino, J.D. (eds): Medical infrared imaging. CRC Press ISBN 9780849390272 (2008)
12. Dougherty, G.: Digital Image Processing for Medical Applications. Cambridge University Press (2009)
13. Duarte, A., Carrão, L., Espanha, M., Vianad, T., Freitas, D., Bártolod, P., Fariaa, P., Almeidaa, H.A.: Segmentation algorithms for thermal images. Procedia Technol. **16**, 1560–1569 (2014)
14. Fountas, K.N., Kapsalaki, E.Z., Felets, C.H., Smisson III, H.F., Johnston, K.W., Robinson, J. S.: Intracranial temperature: Is it different throughout the brain? Neurocritical Care **4**(2):195–200 (2004)
15. Frize, M., Karsh, J., Herry, C., Adéa, C., Aleem, I., Payeur, P.: Preliminary results of severity of illness measures of rheumatoid arthritis using infrared imaging. In: MeMeA 2009—International Workshop on Medical Measurements and Applications Cetraro, Italy May 29–30, 2009 (2009)
16. Griffin, L.D., Colchester, A.C.F., Roll, S.A., Studholme, C.S.: Hierarchical segmentation satisfying constraints. In: British Machine Vision Conference, UK,1994 (1994)
17. Henane, R., Bittel, J., Bansillon, V.: Partitional calorimetry measurements of energy exchange in severely burned patients. Burns **7**(3), 180–189 (1981)
18. Kapoor, P., Prasad, S.V.A.V., Patni, S.: Image segmentation and asymmetry analysis of breast thermograms for tumor detection. Int. J. Comput. Appl. **50** (2012)
19. Lawson, R.: Implications of surface temperatures in the diagnosis of breast cancer. Can. Med. Assoc. J. **75** (1956)
20. Leando, P.: Digital infrared thermal imaging (DITI) for referring health care practitioners. Meditherm Inc. (2003)
21. Lefrant, J.-Y., Muller, L., Emmanuel Coussaye, J., Benbabaali, M., Lebris, C., Zeitoun, N., Mari, C., Saissi, G., Ripart, J., Eledjam, J.-J.: Temperature measurement in intensive care patients: comparison of urinary bladder, oesophageal, rectal, axillary, and inguinal methods versus pulmonary artery core temperature. Intensiv. Care Med. **29**, 414–418 (2003)
22. Matthews, J.D., Forsythe, A.V., Brady, Z., Butler, M.W., Georgen, S.K., Byrnes, G.B., Giles, G.G., Wallace, A.B., Anderson, P.R., Guiver, T.A., McGale, P., Cain, T.M., Dowty, G.J.G., Bickerstaffe, A.C., Darby, S.C.: Cancer risk in 680,000 people exposed to computed tomography scans in childhood or adolescence: data linkage study of 11 million Australians. BMJ **346**, f2360 (2013)
23. Nadler, M., Smith, E.P.: Pattern Recognition Engineering. Wiley, New York (1993)
24. Nowakowski, A., Kaczmarek, M., Moderhak, M., Siondalski, P.: Thermal imaging in wound healing diagnostics. Measur. Autom. Monitor. **61**(06) (2015)
25. Ohlander, R., Price, K., Reddy, R.: Picture segmentation by a recursive region splitting method. Comput. Graph. Image Process. **8**, 313–333 (1978)
26. Pearce, M.S., Salotti, J.A., Little, M.P., McHugh, K., LeeC, Kim K.P., deGonzalez, A.B., et al.: Radiation exposure form CT scans in childhood and subsequent risk of leukaemia and brain tumours: a retrospective cohort study. Lancet **380**, 499–505 (2012)
27. Sacho, R.S., Childs, C.: The significance of altered temperature after traumatic brain injury: an analysis of investigations in experimental and human studies: Part 2. Br. J. Neurosurg. **22** (4), 497–507 (2008)
28. Selvan, A.N.: Highlighting dissimilarity in medical images using hierarchical clustering-based segmentation (HCS). MPhil. Dissertation, Faculty of Arts Computing Engineering and Sciences, Sheffield Hallam University, Sheffield, UK (2007)
29. Selvan, A.N.: Boundary extraction in images using hierarchical clustering-based segmentation (HCS). In: British Machine Vision Conference (Student workshop) Dundee, UK, Sept 2011 (2011)
30. Selvan, A.N.: Hierarchical clustering-based segmentation (HCS) aided diagnostic image interpretation and monitoring. Doctoral Dissertation, Faculty of Arts Computing Engineering and Sciences, Sheffield Hallam University, Sheffield, UK (2012)

31. Selvan, A.N., Saatchi, R., Ferris, C.M.: Improving medical image perception by hierarchical clustering based segmentation. In: 9th International Conference on Information Technology and Applications in Biomedicine, Larnaka, Cyprus, 4–7 Nov 2009 (2009)
32. Selvan, A.N., Saatchi, R., Ferris, C.M.: Computer aided monitoring of breast abnormalities in X-ray mammograms. In: Medical Image Understanding and Analysis Conference, London, UK (2011)
33. Selvan, A.N., Pettitt, S., Wright, C.: Hierarchical clustering-based segmentation (HCS) aided interpretation of the DCE MR images of the prostate. In: Medical Image Understanding and Analysis Conference, Lincoln, UK, July 2015 (2015)
34. Siah, C.J.R., Childs, C.: Thermographic mapping of the abdomen in healthy subjects and patients after enterostoma. J. Wound Care **24**(3) (2015)
35. Snekhalatha, U., Anburajan, M., Sowmiya, V., Venkatraman, B., Menaka, M.: Automated hand thermal image segmentation and feature extraction in the evaluation of rheumatoid arthritis. Proc. Inst. Mech. Eng. [H] **229**(4), 319–331 (2015)
36. Soukup, J., Rieger, C., Holz, C., Miko, I., Nemeth, N., Menzel, M.: Temperature gradient between brain tissue and arterial bloof mirrors the flow-metabolism relationship in uninjured brain: an experimental study. Acta Anaesthesiol. Scand. **51**, 872–879 (2007)
37. Tilton, J.C.: Hierarchical image segmentation. On-line Journal of Space Communication Issue No. 3 Winter 2003 Research and Applications (2003)
38. Tilton, J.C.: Hierarchical image segmentation (2016). http://science.gsfc.nasa.gov/606.3/TILTON/hseg.html. Accessed 11 Aug 2016
39. Vardasca, R., Bajwa, U.: Segmentation and noise removal on thermographic images of hands. Thermol. Int. **18**(3), 99–104 (2008)
40. Vardasca, R., Gabriel, J., Jones, C.D., Plassmann, P., Ring, E.F.J.: A template based method for normalizing thermal images of the human body. In: The 12th International Conference on Quantitative infrared Thermography, at Bordeaux, France, 2014 (2014)
41. van Walraven, C., Musselman, R.: The surgical site infection risk score (SSIRS): a model to predict the risk of surgical site infections. PLoS ONE **8**(6), e67167 (2013). doi:10.1371/journal.pone.0067167. (Editor: Emma S. McBryde, Royal Melbourne Hospital)
42. Wiecek, M., Strkowski, R., Jakubowska, T., Wicek, B.: Software for classification of thermal imaging for medical applications (2016). https://www.researchgate.net/publication/237215535_Software_for_classification_of_thermal_imaging_for_medical_applications. Accessed 24 May 2016
43. Wilson, A.P., Treasure, T., Sturridge, M.F., Gruneberg, R.N.: A scoring method (ASEPSIS) for postoperative wound infections for use in clinical trials of antibiotic prophylaxis. Lancet **1** (8476), 311–313 (1986)
44. Zhou, Q., Li, Z., Aggarwal, J.K.: Boundary extraction in thermal images by edge map. In: ACM Symposium on Applied Computing SAC'04, Nicosia, Cyprus March 14–17 (2004)
45. Zhu, M., Ackerman, J.J.H., Sukstanskii, A.L., Yablonskiy, D.A.: How the body controls brain temperature: the temperature shielding effect of cerebral blood flow. J. Appl. Physiol. 101:1481–1488 (2006). First published Jul 13. doi:10.1152/japplphysiol.00319.2006

Medical Thermal Tomography—Different Approaches

B. Więcek, M. Strakowska, P. Więcek, R. Strakowski and G. De Mey

Abstract Thermal tomography is a new tool in medical diagnosis. It is based on so-called cold provocation. It is practically realized be a weak cooling of an upper layer of the skin. As it is noninvasive and harmless it can be applied as a screening procedure and repeated frequently. Using thermographic camera, the temperature recovery of the skin in time is measured and analyzed. In this chapter, three new methods of thermal tomography are presented. First, one is based on the analysis in time domain. The temperature versus time is approximated by the function which is a combination of exponential and error functions. The chosen parameters of this approximation that can be interpreted as the time constants are used then to visualize the blood vessels. The second approach uses the thermal modeling of the multilayer skin structure. The inverse thermal problem in frequency domain is solved to estimate the thermal parameters of each layer of the skin, including perfusion. The last procedure uses the wavelet transform (WT) to convert the large sequence of thermal images and reduce it just one amplitude and one phase image for an appropriate scale. The new two-step algorithm of WT for the image sequence is presented. This approach speeds up the analysis significantly.

1 Introduction

Medical tomography is a very useful tool in medical diagnosis and treatment. Nowadays, there are many methods and apparatuses available for medical tomography, but most of them are not neutral for an alive tissue and invasive. Some of them are based on the harmful radiation or isotopes that injected into the body. They cannot be repeated periodically and frequently, so they cannot be classified as

B. Więcek (✉) · M. Strakowska · P. Więcek · R. Strakowski
Institute of Electronics, Lodz University of Technology,
Wolczanska str. 211/215, 90-924 Lodz, Poland
e-mail: boguslaw.wiecek@p.lodz.pl

G. De Mey
University of Gent, Ghent, Belgium

E.Y.K. Ng and M. Etehadtavakol (eds.), *Application of Infrared to Biomedical Sciences*, Series in BioEngineering,
DOI 10.1007/978-981-10-3147-2_22

the screening methods. In addition they are costly, and can only be made in a clinic, in many cases in the special rooms, equipped with an additional expensive equipment. In many countries the patients are waiting a long time for the tomography tests (e.g., a few months).

Among the known and routinely used tomography methods, there is the thermal tomography, which seems to be still unappreciated. Certainly, it has some constrains, especially due to the limited depth of the body penetration by the heat waves, but on the other hand, it can be recommended for daily screening of skin tissues pathologies, burns during healing, and superficial tumors [1–5]. Thermal tomography is very well suited wherever the skin or upper layers of the tissues change their perfusion or vascularization. Thermal tomography is already well developed and used in *Nondestructive Testing (NDT)* of nonmedical objects [6, 7]. *NDT* is mainly used for defect detection and material characterization. An alive tissue is the special object, and most of the *NDT* methods cannot be applied directly. The tissue is neither solid nor fluid, and is closer to the porous material. Perfusion and the blood flow through the vessels may influence the heat transfer in the tissue. In addition, the tissue in a nonhomogenous, anisotropic material with an external thermal feedback called thermoregulation [8–10].

For medical thermal tomography, one proposes the cold provocation applied to the skin tissue and the measurements of body temperature recovery by thermography [1, 2, 11]. Then, by applying the inverse thermal modeling of the tissue, the internal structure can be reconstructed. Inverse thermal modeling requires the forward thermal models and the optimization [1, 11, 12]. Both of these elements can be implemented today in a software to perform the screening. Thermal cameras are cheaper and widely available today. It makes possible to establish a new medical protocol for thermography screening. This chapter presents the different original approaches in medical thermal tomography developed by the authors recently. Although the results presented are coming from the research projects, the presented protocols can be easily and fast adapted to the practical use in the medical diagnosis.

2 Time-Domain Thermal Tomography

2.1 Cold Provocation Test

Cold provocation (also known as cold stress) is a simple medical protocol using a slight cooling of a selected part of the body. After cooling, the recovery of the surface temperature of the skin is recorded using the infrared technique. Almost any part of the human body can be cooled. For practical reasons, the limbs are often used for the diagnosis. The cooling can be performed using the metal blocks, water, gel, stream of gas, or electronically controlled Peltier coolers [1, 3, 11, 13, 14]. In order to get the repetitive results, it is important to assure the same cooling

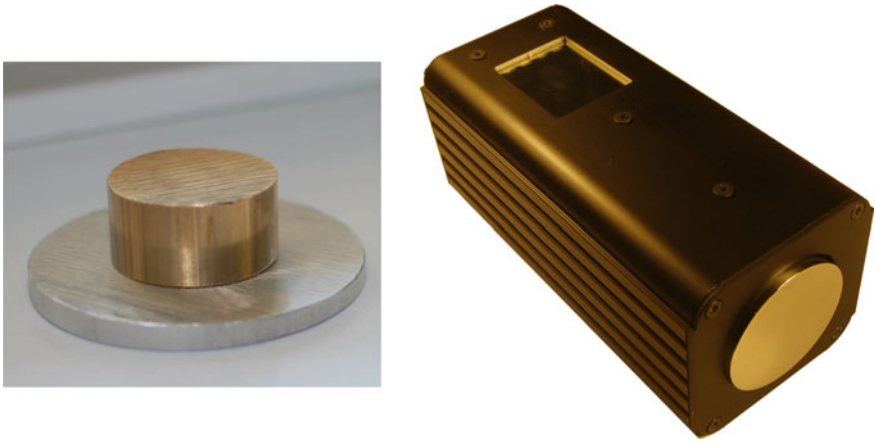

Fig. 1 A metal block and Peltier temperature stabilizer for cold provocation experiments

conditions during diagnosis of different patients. It can be done either by the same initial temperature of the cooling device or by keeping the constant temperature during cooling. It is accomplished better by the electronically controlled Peltier cooler. The exemplary metal block and the Peltier cooler developed recently are presented in Fig. 1 [1].

During the cold provocation tests, temperature of the upper surface of the skin decreases by a few degrees (3–10 °C). In order to get such a temperature decay, it is sufficient to keep the cooling active for a few minutes (1–2 min). The cooling is the noninvasive, safe, and aseptic method. In some cases (e.g., burns healing), the cooling is recommended and helps the treatments. Due to the thermal inertia of human body, the long-time temperature recovery is a certain inconvenience of this approach. This recovery can last several minutes. Typically, the tissue reaches the steady thermal state after 20–30 min. During this period, the patient should stay calm, without any rapid movement. Practically, it is impossible to get the full stability of an object during the diagnosis. This problem can be solved by the movement tracing and correction [15]. It is a preprocessing, offline operation, which is performed before the main images analysis. The algorithms and software for it are now available [15].

The exemplary thermal images selected from the long sequence recorded are presented in Fig. 2. In this test, the cooling was made by a cold gel put on the arm. Four black markers visible on the arm were prepared for the movement correction.

2.2 Temperature Approximation in Time Domain

Cold provocation in the medical diagnosis is based on cooling the skin. It can be done using the different devices such as cold solid blocks, water bath, gels, or cold

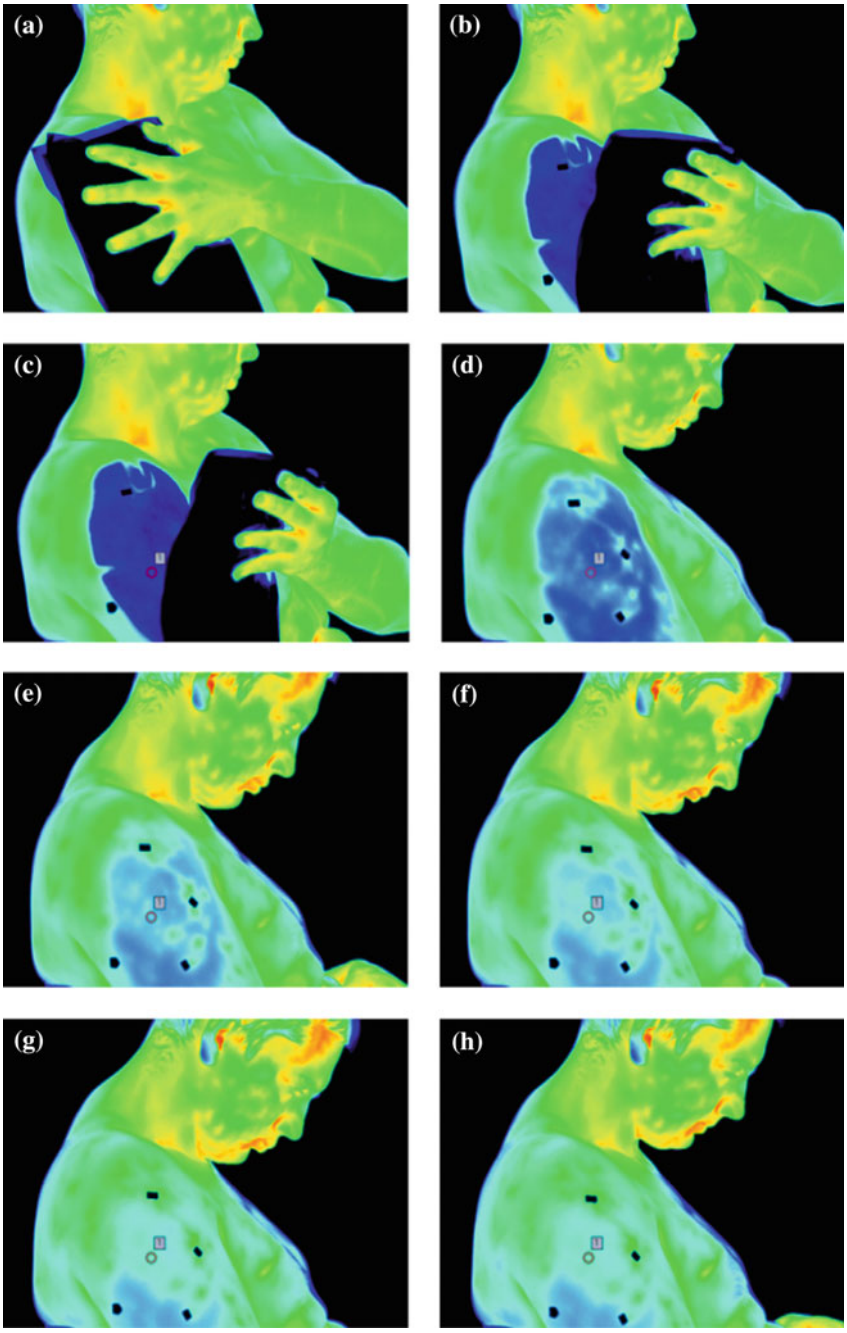

Fig. 2 Thermal images recorded during the cold provocation test, frame no.: **a** 0, **b** 40, **c** 41, **d** 1000, **e** 3000, **f** 5000, **g** 10,000, **h** 15,000

stream of nontoxic gases [1–3, 6, 11, 14]. Typically, the skin gets colder by a few degree Celsius comparing to the initial state. Then, using a thermographic camera or a pyrometer, the temperature recovery is recorded. Due to the thermal time constants of the tissue, this process is going on within hundreds of seconds. It is obvious that the patient cannot remain stable for such a long time. That is why, the movement correction on thermal images has to be performed. It is offline procedure using the different methods [15]. One of them applies the correlation of each frame with the selected region from one of the first thermal images in the sequence [15]. After movement correction, the approximation in time (smoothing) can be performed for the temperature rise in time for each or selected pixels in the sequence—Fig. 3.

Temperature evolution in time is due to the heating from inside of the body. This is a thermal process involving the perfusion. From the heat transfer theory in solids, one knows that the temperature rise in time can be approximated by the finite sum of the exponential components—Eq. (1). These components correspond to the time constants that are represented by the R_{th}–C_{th} sections in the thermal model for a solid in the dynamic state (R_{th}—thermal resistance, C_{th}—thermal capacitance)

$$T(t) = \sum_{i=0}^{\infty} T_i\left(1 - \mathrm{e}^{-\frac{t}{\tau_i}}\right) \approx \sum_{i=0}^{N} T_i\left(1 - \mathrm{e}^{-\frac{t}{\tau_i}}\right). \tag{1}$$

One can notice that the time constant τ_i can be replaced by angular frequency $\omega_i = 1/\tau_i$. The perfusion makes the thermal process in a tissue different to the heating of the solid materials. The major difference is in the very beginning of the heating. At first, the temperature rise is much faster than in the quasi-stable state. One can conclude that the heating of an alive tissue is 2-time-constant thermal process. It is not always the case. After many experiments we have noticed that the combination of the exponential and the error functions is the satisfactory

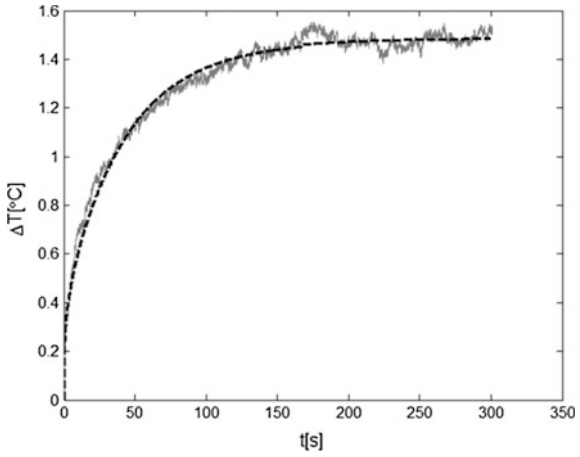

Fig. 3 Exemplary temperature evolution in time after cold provocation and its approximation by the combination of exponential and error functions

approximation of temperature rise for a human tissue after a weak cooling—Eq. (2) [12, 13]:

$$T(t) = T_0(1 - e^{-\omega_0 t}) + T_1(1 - e^{\omega_1 t} \cdot erfc(\sqrt{\omega_1 \cdot t})). \quad (2)$$

2.3 Time Constant Imaging—Superficial Vessel Visualization

The time constants both from the model (1) and the approximation (2) can be applied for visualization the internal structure of the measured object. Infrared thermography allows to measure the temperature on the exposed surface only. Obviously, temperature on the surface depends on the thermal process inside the body, and therefore both time constants in Eq. (2), i.e., $\tau_0 = 1/\omega_0$ and $\tau_1 = 1/\omega_1$, as well as the temperature coefficients T_0 and T_1 depend on the internal structure of an investigated object. One should notice that the thermal coefficients (T_0 and T_1) strongly correspond to the level of cooling, which is rather difficult to keep constant for every measurement. Time constants are independent of the different cooling conditions. Consequently, they relate directly to the internal structure of a tissue.

Figure 4a presents a raw thermal image, one selected from a large sequence containing thousands of frames. One can notice in Fig. 4a two markers used for the movement compensation. They are made of aluminum foil of low emissivity, and they are clearly visible in infrared as the dark areas. There is no much information on the skin structure from the direct thermal imaging. However, the temperature rise in time is different due to the place on the skin, especially if the larger vessel is beneath—Fig. 4b.

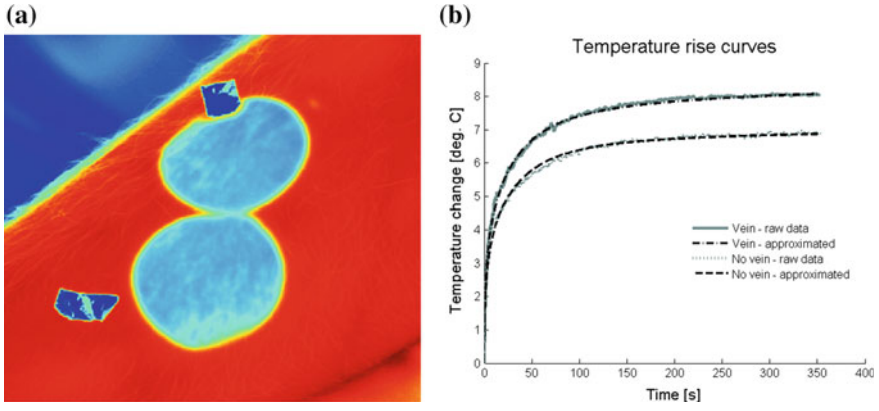

Fig. 4 Raw thermal image—one from the long sequence (**a**) and temperature rise for (raw and approximated) for a tissue with and without the blood vessel inside (**b**)—model (2)

In order to present the potential application of time constant imaging, the experiment was performed for a tissue with and without the blood vessel beneath the skin surface. As it is expected, the time constant distribution corresponds to the internal structure of an object. Especially, the distribution of $\omega_0 = 1/\tau_0$ clearly presents the vessel shape and its position in the tissue—Fig. 5.

Distribution of the temperature coefficients (T_0 and T_1) looks rather noisy. It can be explained that the cooling was nonuniform—Fig. 6. It could be indeed, as it was made by touching the skin with the cold metal blocks. The forearm is not the flat and stiff object, so the contact quality between the cooling device and the tissue can is vary.

The *method of time constants* has been already used in the previous research works. It was successfully applied to breast cancer detection and burn healing [2, 11].

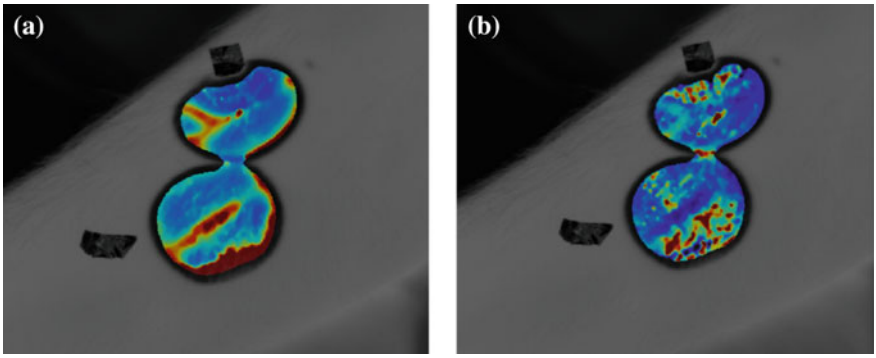

Fig. 5 Distribution of ω_0 (**a**) and ω_1 (**b**) in a cooled area on a forearm with visible vessels underneath

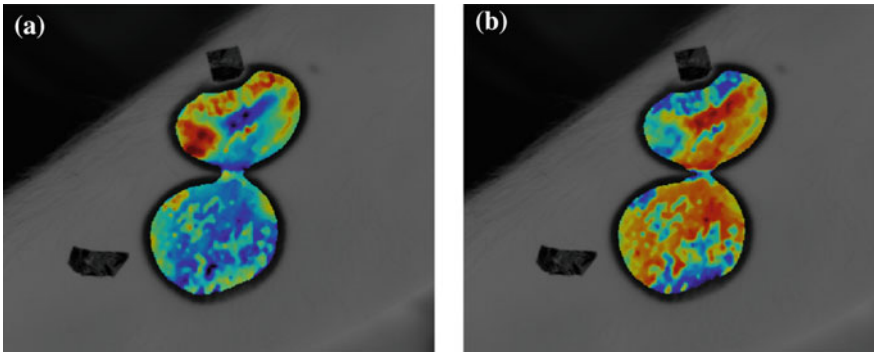

Fig. 6 Distribution of T_0 (**a**) and T_1 (**b**) in a cooled area on a forearm—model (2)

3 Inverse Thermal Modeling of a Tissue—Frequency-Domain Tomography

Thermal modeling of a tissue is not an easy task. A tissue is the nonhomogenous multilayer structure. In addition, the thermal parameters of a tissue strongly depend on perfusion and external conditions due to the thermoregulation. Generally, the heat transfer in a tissue is not one dimensional, rarely reaching the steady state. In the literature, there are a few fundamental achievements in the modeling of heat transfer in an alive body [8, 9, 12, 16–20]. In many cases the thermal models presented already in literature cannot be used for the screening because they are not real-time procedures with rather complex numerical calculations [20].

For practical reasons we propose a simplified one-dimensional thermal modeling of a tissue including perfusion in the dynamic conditions. It is well suited for cold stress diagnosis with the use of the IR thermography. The well-known approach in thermal management of electronics based on the thermal impedance Z_{th} is proposed [21]. The thermal impedance can be considered either in time or frequency domain. By definition, the concept of thermal impedance assumes that the object is powered by $P(t)$ excitation and the temperature evolution in time is measured $T(t)$—Fig. 7. It is exactly the case of the medical cold provocation. In order to normalize and unify the results as well as to simplify the calculations, the step function excitation $P_0 1(t)$ is typically used—Fig. 7. In some cases, it is very useful to present the thermal impedance in frequency domain—Eq. (3). Then, $Z_{th}(j\omega)$ is drawn in the graphical form as the so-called *Nyquist* plot [21].

By the definition, the thermal impedance in frequency domain takes the form (3)

$$Z_{th}(j\omega) = \frac{j\omega}{P_0} \int_0^\infty e^{j\omega t} T(t) dt, \tag{3}$$

where $T(t)$ is the temperature surplus over the ambient.

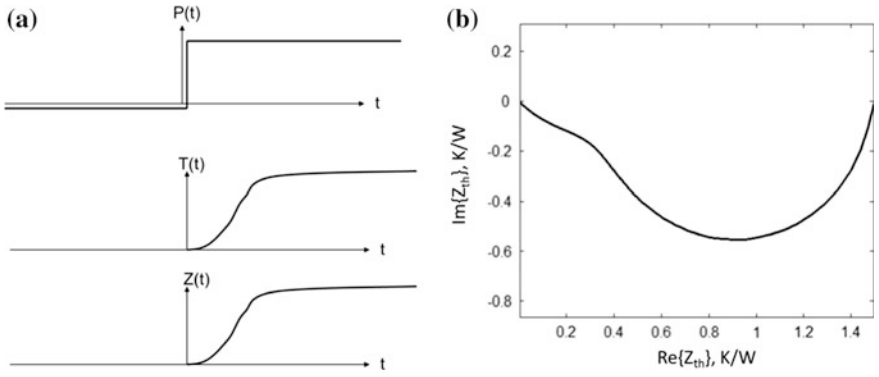

Fig. 7 The concept of thermal impedance in time (**a**) and frequency domains (Nyquist plot) (**b**)

The main reason of using the frequency domain for the analysis is the simplification of thermal modeling. In many cases for a simple geometry, the thermal model can be solved analytically in frequency domain. Such an approach can be easily used for the multilayer heat transfer modeling in a tissue [12].

3.1 Thermal Model of Multilayer Tissue Structure with Perfusion

Let us consider a tissue as three-layer structure (epidermis, dermis, and hypodermis) with three sets (one for each layer) of thermal parameters: density ρ_i, specific heat c_{si}, thermal conductivity k_i, and perfusion coefficient w_i, where $i = 1, 2, 3$—Fig. 8. During the cold provocation, a certain volume of a tissue is cooled down. One assumes that in the middle of this region, the heat coming from the internal part of the body propagates perpendicularly to the skin surface, along one axis only. It significantly simplifies the calculations. The heat transfer is described by the heat diffusion equation. By adding the perfusion we refer to the well-known Pennes formulae (4) [16]:

$$\rho \cdot c \cdot \frac{\mathrm{d}T}{\mathrm{d}t} = \lambda \cdot \frac{\mathrm{d}^2 T}{\mathrm{d}x^2} + w \cdot c_\mathrm{b} \cdot \rho_\mathrm{b}(T_\mathrm{b} - T), \tag{4}$$

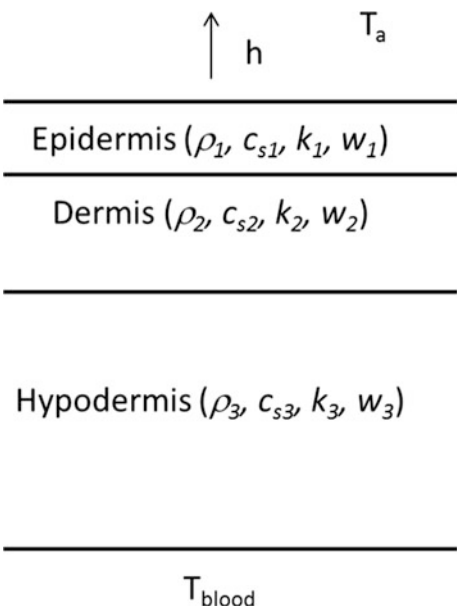

Fig. 8 Three-layer structure of the skin tissue

where w is the perfusion coefficient (1/s), c_b and ρ_b are the specific heat and density of the blood, and T_b is the blood temperature.

The next simplification in the model is made by performing Laplace transform of Eq. (4). It moves the model into the frequency domain. Simultaneously, one reduces Eq. (4) by eliminating the temperature derivative in time, Eq. (5). Consequently, it allows to solve the diffusion equation analytically:

$$\begin{aligned} k\frac{\mathrm{d}^2T}{\mathrm{d}x^2} - T(\rho \cdot c_s \cdot s + w \cdot c_{\text{blood}} \cdot \rho_{\text{blood}}) &= 0 \\ \frac{\mathrm{d}^2T}{\mathrm{d}x^2} - \frac{T}{L^2} &= 0 \\ L(s) &= \frac{1}{\sqrt{(\rho \cdot c_s \cdot s + w \cdot c_{\text{blood}} \cdot \rho_{\text{blood}})/k}}, \end{aligned} \tag{5}$$

where L (in m) is called diffusion length and it is a complex number.

Equation (5) is presented for all three layers with different values of the thermal parameters and solved independently for each layer.

The thermal model (5) has the analytical solution (6):

$$T(s) = A(s)\mathrm{e}^{\frac{x}{L(s)}} + B(s)\mathrm{e}^{-\frac{x}{L(s)}}, \tag{6}$$

where $A(s)$ and $B(s)$ are the integration constants.

The integration constants are calculated using the boundary and interface conditions. For three layers, there are six unknown integration constants and six boundary and interface equations [12]. It leads to the set of linear equations that can be solved analytically or numerically. Typically, it is solved numerically, and therefore the overall modeling presented here can be classified as the semi-analytical one. The boundary and interface conditions describe the continuity of temperature and heat fluxes at all interfaces between the layers. In addition, at the upper surface of the skin, the convection is taken into account (using the heat transfer coefficient h). At the bottom of third internal layer (hypodermis), we consider isothermal surface due to the internal body temperature T_b—Fig. 8. This heat transfer model is implemented in *Matlab* software, and it gives the solution in the complex number domain. The results can be graphically presented in the form of the *Nyquist* plots. In order to get the temperature variation in time, one has to calculate the inverse Laplace transform. Unfortunately, not always it is possible in the analytical way. On the other hand, in the cases of medical screening presented in this chapter, it is not necessary to get the thermal impedance and temperature versus time.

3.2 Screening Procedure

Inverse thermal problem is solved to get the values of the thermal parameters for the multilayer skin structure. It is performed by the numerical optimization in frequency domain, as it is presented in Fig. 9.

For thermal parameter estimation of multilayer skin structure, the *Nyquist* plot as the result of thermal modeling is sufficient, and no temperature versus time is required. The approximation of temperature rise during the cold provocation given by Eq. (2) has its analytical *Laplace-domain* representation (7):

$$T = \frac{T_0}{1 + j\frac{\omega}{\omega_0}} + \frac{T_1}{1 + \sqrt{\frac{\omega}{\omega_0}}}. \tag{7}$$

It denotes that the optimization and the overall inverse thermal problem can be performed in the frequency domain. The program in *Matlab* environment was prepared to perform the experiments. The main window of the program is shown in Fig. 10. The program calculates the multilayer thermal model in *Laplace* domain. It uses the optimization to get thermal parameter of the skin layers. A few optimization methods were tested. Among them, the method called *Patternsearch* was the most effective and fast [12]. The *Nyquist* plots are calculated for different angular frequencies, typically in the range 0.001–10 1/s. The optimization allows to match the *Nyquist* plots for each frequency obtained from the measurements and simulations—Fig. 10. It ensures the high credibility of the obtained results. The

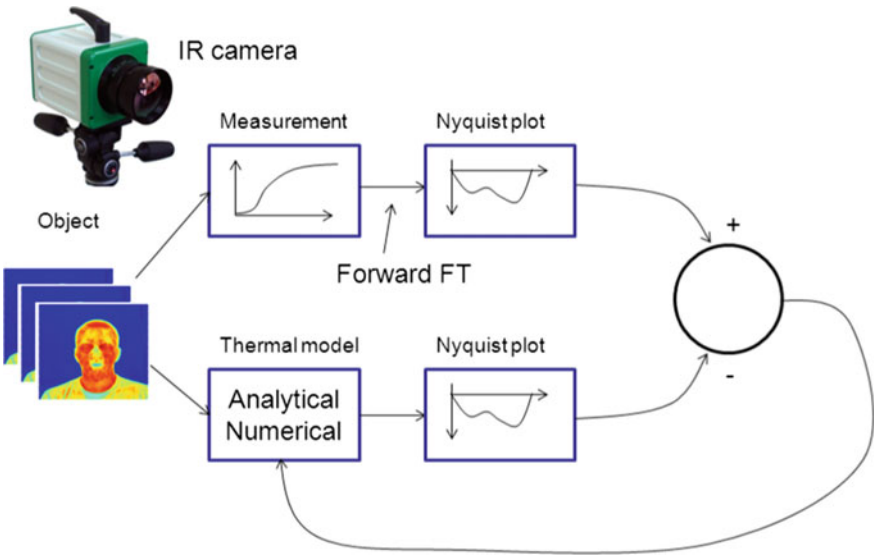

Fig. 9 Estimation of thermal parameters of the skin—screening procedure

optimization allows to evaluate not only the thermal parameters of the skin layers, but their thickness, convective heat transfer coefficient, and the effective heating power applied in the thermal cold provocation test [12].

3.3 Application to Skin Pathologies Screening (Psoriasis)

The inverse thermal modeling presented above can be applied for different screening procedures. One is to evaluate the perfusion in the skin tissue [6, 13]. In this research we neglect the perfusion in the upper layer—epidermis. In addition we assume the same perfusion w_{23} for two deeper layers: dermis and hypodermis—Fig. 8. The experiments were performed for the patients with psoriasis in a clinic for dermatology diseases. In order to verify the protocol, one chooses the healthy and unhealthy parts of the skin. For psoriasis it is easy to select two regions: with inflammation and inflammation-free because it is visible—Fig. 11. As usual, the aluminum foil is for the movement correction. The temperature rise was measured in the middle of the cooled regions—Fig. 11.

The quantitative results of the perfusion measurements are presented in Fig. 12. For eight of nine measurement (patients), the perfusion is higher for the region of skin with inflammation. Only once, the perfusion was lower for the unhealthy part of the skin. Probably, it is due to the highly advanced disease and the upper tissue layer necrosis.

In some practical cases the proposed protocol can be used for evaluation of thermal parameters for three- or four-layer skin tissue structure. It allows to monitor healing process of the injuries or burns. The exemplary sets of thermal parameters

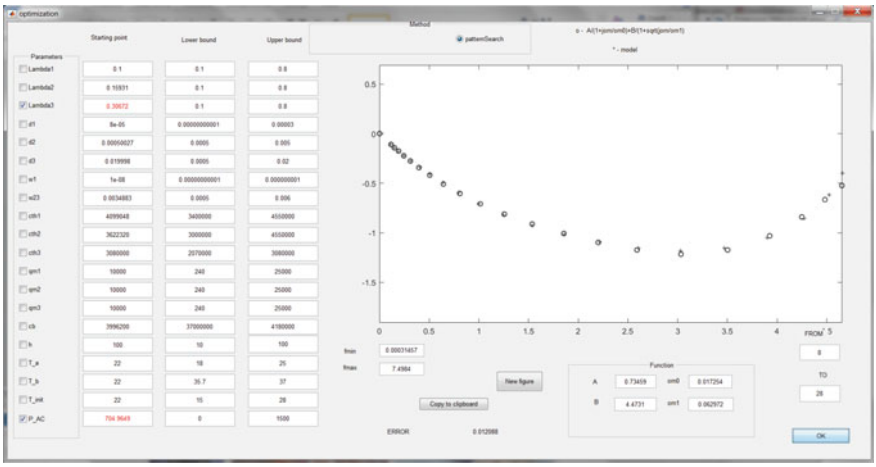

Fig. 10 Main window of the Matlab program for thermal medical screening

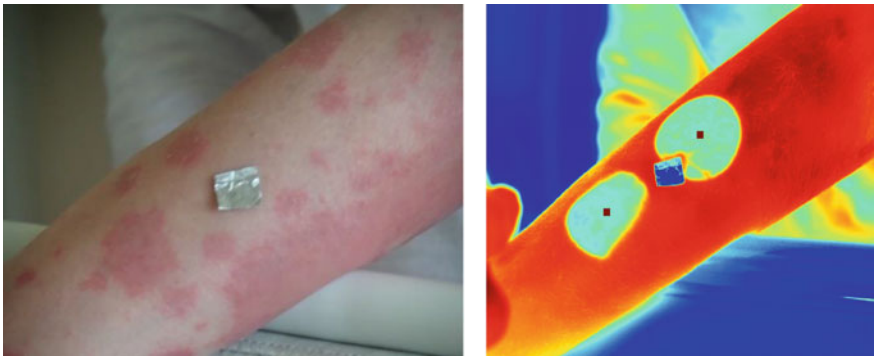

Fig. 11 The upper limb of the patient with psoriasis

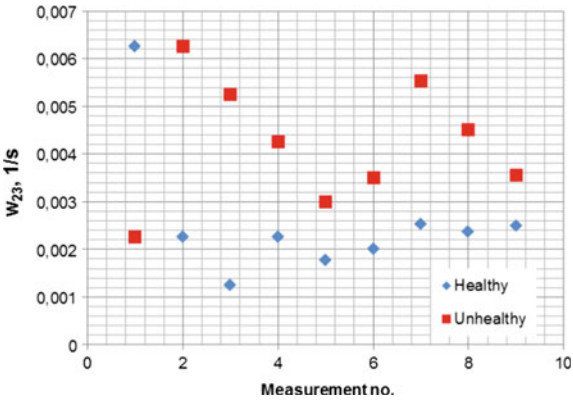

Fig. 12 The results of perfusion evaluation using cold provocation and thermography measurement

Table 1 Thermal parameter of three-layer skin tissue calculated using inverse thermal modeling (data corresponding to the Nyquist plots in Fig. 10)

Parameter	Epidermis	Dermis	Hypodermis
Thermal conductivity (W/m K)	0.1	0.16	0.3
Thermal capacity (J/Km^3)	4.1×10^6	3.6×10^6	3.1×10^6
Perfusion coefficient (1/s)	–	0.0034	0.0034

evaluated by the method presented, for all three layers, are presented in Table 1. In addition, the thermal capacity of the blood is evaluated as well, $C_b = 4 \times 10^6$ J/K m^3.

4 Wavelets Transform-Based Thermal Tomography

Wavelet transform (*WT*) is a powerful tool for signal and image processing. Nowadays, it is widely used for signal filtering, data compression, and feature detection. There are continuous and discrete, one- and two-dimensional *WTs*. One can use *WT* both for signals versus time and 2D images where the time axis is replaced by the spatial coordinates. There is a relevance between Fourier (*FT*), short-time Fourier (*STFT*), and wavelet transforms [6]. There are many applications of frequency analysis using *FT*, *STFT,* and *WT* in *Nondestructive Testing* (*NDT*) using IR thermography [7].

WT is the analysis either in the complex or the real number domain and can generate the results in the form of the real and imaginary part or/and modulus and phase. The frequency analysis allows to shift the considerations from time to frequency domain. In many practical cases, the interpretation of the temperature response in frequency domain is faster and easier. For example, one can consider the phase as a delay between the temperature response and the power excitation. In fact, it corresponds directly to the time constant approach presented above. *WT* has an important additional feature comparing to classical *FT*. It can be applied to the signals with spectrums varying in time. *WT* and *STFT* preserve time in the analysis. There are many different wavelets, e.g., Morlet, Shannon, Gauss, and B-spline ones. Choosing the appropriate wavelet gives another degree of freedom in the analysis and makes *WT* more flexible and adjustable for the different practical diagnostic cases.

4.1 2-Stage Algorithm of Thermal Image Processing

Application of *WT* for a long sequence of thermal mages is the time-consuming task. For all pixels $P_i(x, y)$ in each i-th image in the sequence, one can establish the discrete signals $s_{xy}(i)$—Fig. 13. For each $s_{xy}(i)$ signal, the frequency analysis (*FT*, *STFT*, *WT*) can be performed, for $(x, y) = (1, 1) \ldots (M \times N)$, where $M \times N$ is the image resolution. It needs a very powerful computer, even that it is not the real-time procedure. This is the reason that 2-stage approach has been recently developed and presented to simplify and speed up the calculations [6].

- First, the user manually selects the pixel for the primary 1-pixel frequency analysis—Fig. 13. Then the primary frequency analysis is performed—Fig. 14. It generates the results in the form of imaginary and real parts, modulus, and phase—Fig. 15. It allows to select the most suitable scale (*WT*) or frequency (*FT*, *STFT*) for the further processing—Fig. 15.
- Next, the final analysis for all $N \times M$ pixels is performed for previously chosen scale or frequency, giving four final images: imaginary, real, modulus, and phase ones (if the wavelet is complex)—Fig. 16.

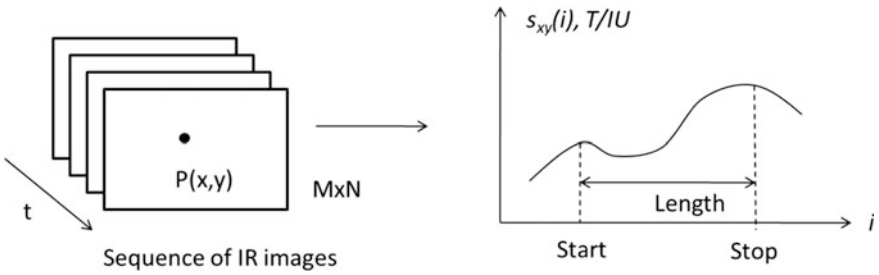

Fig. 13 One-pixel temperature evolution in time during cold provocation screening

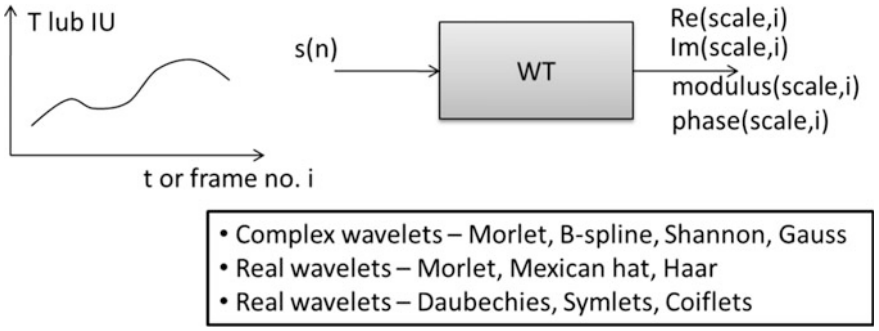

Fig. 14 Frequency analysis of one-pixel temperature evolution in time—the result of first step of the algorithm

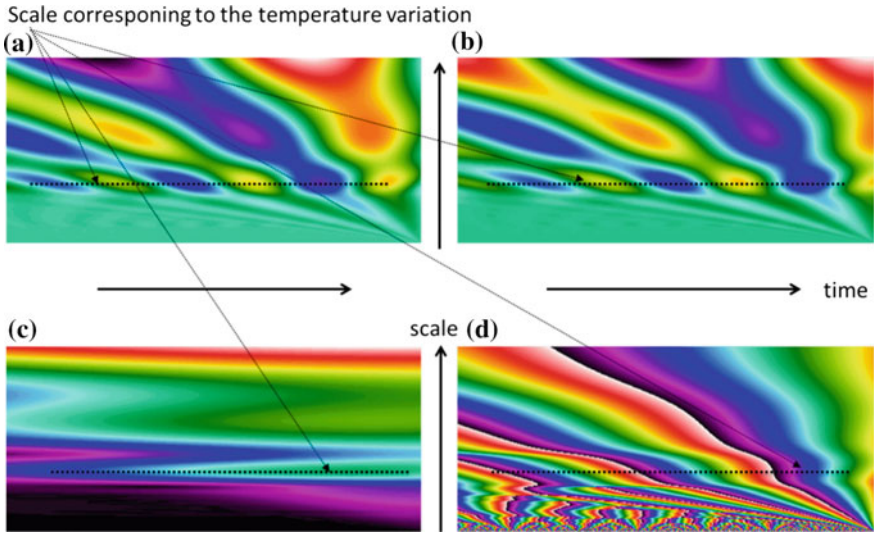

Fig. 15 Exemplary results of first step of the algorithm for WT with the chosen scale, **a** real part image, **b** imaginary part image, **c** modulus image, **d** phase part image

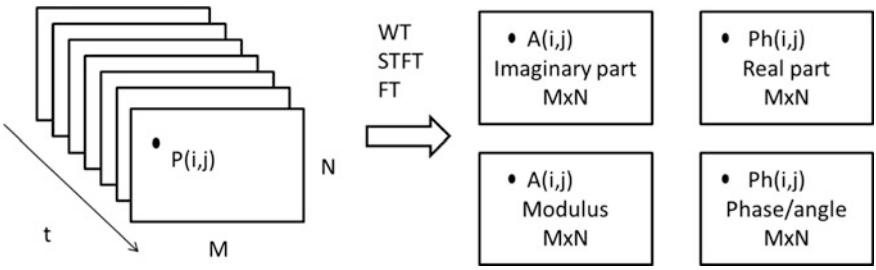

Fig. 16 Final-step frequency analysis for pixels and one chosen frequency (FT, STFT) or scale (WT)

The algorithm implements windowing in time before the frequency analysis. Besides the rectangle window, the user can select either Hamming, Hanning, or Blackman window. There are complex and real wavelets available to choose—Fig. 14.

The primary analysis generates either 1 or 4 images depending on the type of analysis (real or complex). Typically, the user selects the scale or frequency for which the signal varies the most—Fig. 15. By changing the position in time (horizontal axis) the wavelet starts to move over the signal, the different contrasts of the images of the final analysis can be obtained.

The chosen scale or frequency is then used for the second step of the screening method. Consequently, according to the resolution of the IR system, M x N analyses are performed, for the specified one scale or frequency—Fig. 15. For complex wavelets there are four-image result—imaginary part, real part, modulus, and phase images. In the practice, the modulus and the phase are the most useful because of the natural meaning and easy interpretation. Modulus image corresponds to the level of temperature of an object, while the phase represents the delay between the temperature response and the power excitation. One should take into account that the delay is for a certain frequency. If the excitation is periodic (lock-in approach), the user selects the frequency of the excitation for the analysis. If the excitation is like the step function (transient thermography), the frequency selection depends on the size and the depth of a detail one wants to visualize. The lower the frequency, the deeper the heat penetrates the object. The smaller the detail, the higher the frequency has to applied in measurement. The right selection of the frequency is upon the user.

4.2 Program for Medical Screening—Data Analysis Examples

The proposed algorithm of cold provocation data analysis is implemented in the program *TEndt* [6]. This tool can be used for detection, monitoring, and

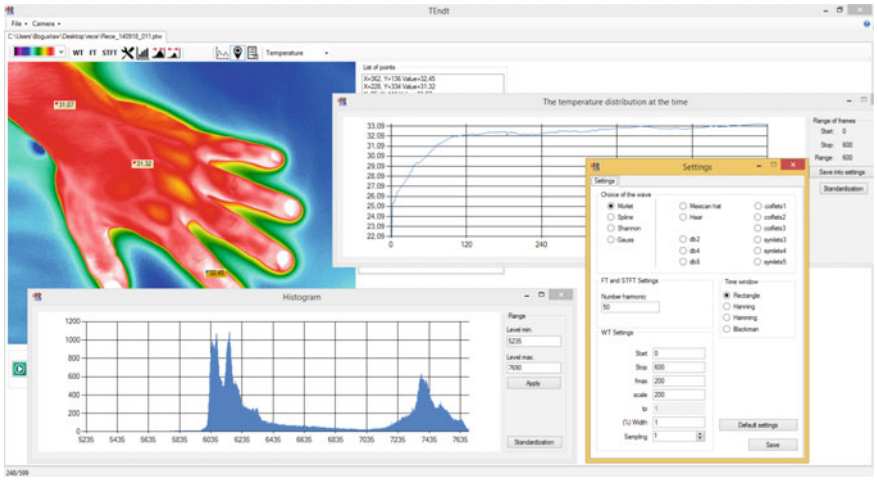

Fig. 17 The main window of TEndt program (pio)

differentiation the skin tissue pathological and physiological states. *TEndt* application can be adapted to any existing IR camera, under the condition the *Software Development Kit* (*SDK*) is provided by the manufacturer. The program is written using C# Visual Studio.NET platform. The main window of the application is shown in Fig. 17.

Two exemplary results are presented in this chapter. The first one concerns the diagnosis of the vascularization. The second example presents the application of cold provocation to thermal tomography to visualize the internal blood vessels.

Typically, the cold provocation tests and temperature recovery measurement are performed for limbs. In the exemplary test, the upper limb of a patient in the gloves was put in a water bath at the room temperature for about 1–2 min. Then the thermal recovery of a tissue was recorded by a thermographic camera. The sequence of thermal images is long and can contain hundreds or thousands of images. Practically, it is impossible to analyze such a long sequence of thermal images. One frame of the sequence of thermal images is presented in Fig. 18. One can hardly see that there is the nonuniform heating and temperature distribution of the different fingers.

A physician can have the better insight into the thermal process if one displays the temperature evolution in time—Figs. 19 and 20. Both the forefinger and small one (Fig. 19) react slower in comparison with the middle and ring fingers as well as the thumb (Fig. 20).

This effect can be also presented in the graphical form by applying the frequency analysis concept described in this chapter. By performing 2-step *NDT* analysis using the *WT*, one can get the result shown in Figs. 21 and 22. The areas of slower thermal reaction are clearly recognizable in the phase image using, e.g., the Morlet wavelet. For higher frequencies, one can monitor the heating effects in the

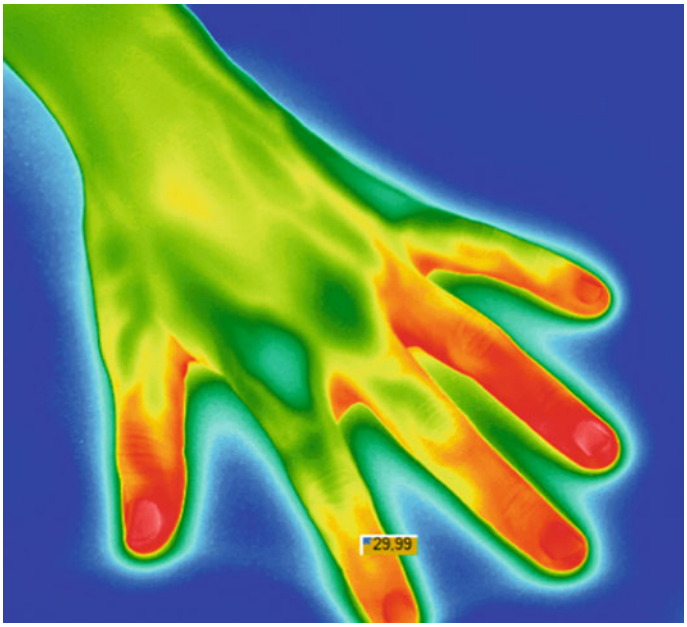

Fig. 18 One frame from a long sequence of thermal images after cold provocation

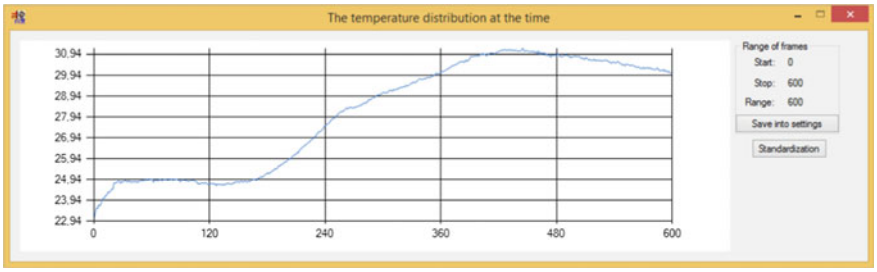

Fig. 19 Temperature versus time for forefinger, *r* time scale 0–600 s

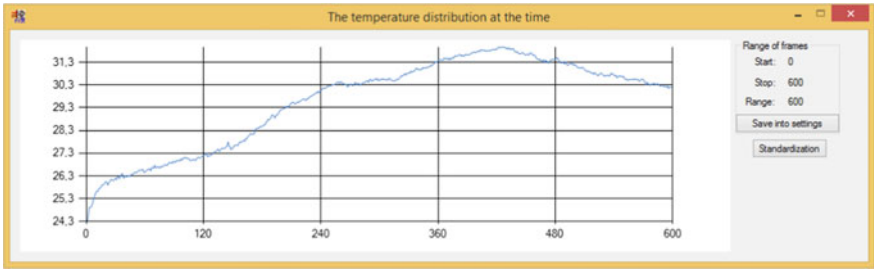

Fig. 20 Temperature versus time for ring finger time scale 0–600 s

superficial thin skin tissue layers. Figure 21 presents the phase for the scale = 81. The maximum scale was set to 200 in this example. The lower scale corresponds to the higher value of frequency in the *WT* notation. The tips of the forefinger and the small finger remain colder in the beginning of the recovery process. It corresponds to the heat transfer in the superficial layers of the tissue.

The lower frequency of the excitation allows to heat up the deeper parts of the tissue. As it is shown in Fig. 22, the inner layers of the tissue stay colder after the longer period. By choosing the higher value of the scale = 133 (the lower value of frequency), the thermal inertia of the deeper layers is visualized. Even the middle finger is slightly impaired due to the weaker vascularization after longer time—Fig. 22. In experiment presented here, the complex Morlet wavelet was used with an appropriate center frequency and the initial width chosen by the user.

The second example shows the application of *WT* analysis to the thermal tomography and visualization of the blood vessels—Fig. 23. The blood vessels full of moving fluid cause the additional temperature delay. Depending on the depth of the vessel, the user has to choose the appropriate frequency (scale) of the analysis. In addition, by selecting the different wavelets, one can visualize the appropriate details of the internal objects. The exemplary thermal tomography image is presented in Fig. 23. This result was obtained by performing *WT* using Gauss complex wavelet. In this case, the image of modulus for the scale = 24 presents well the vessels' structure—Fig. 23.

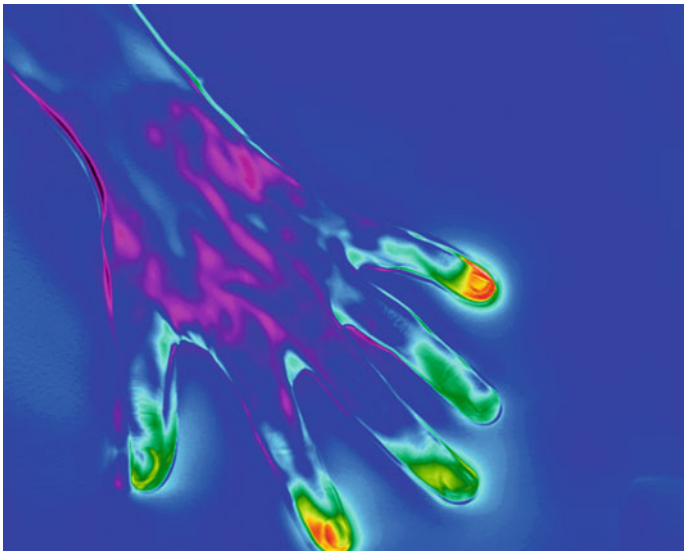

Fig. 21 Phase distribution for wavelet transform with the complex Morlet wavelet, scale = 81 (max. scale = 200)

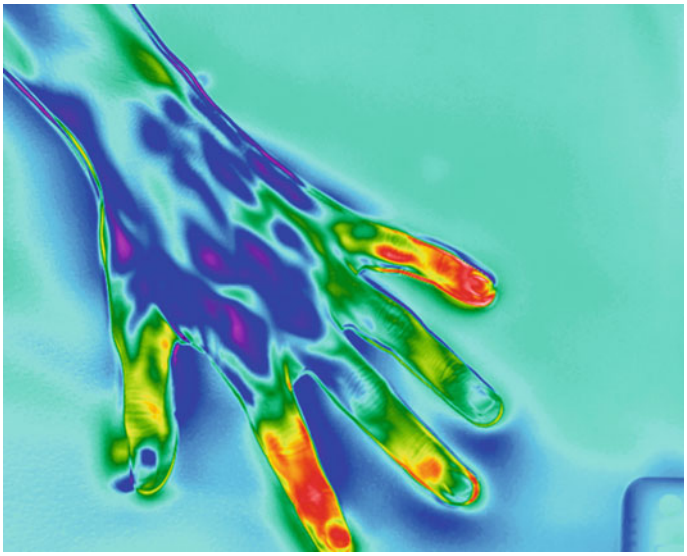

Fig. 22 Phase distribution for wavelet transform with the complex Morlet wavelet, scale = 133 (max. scale 200)

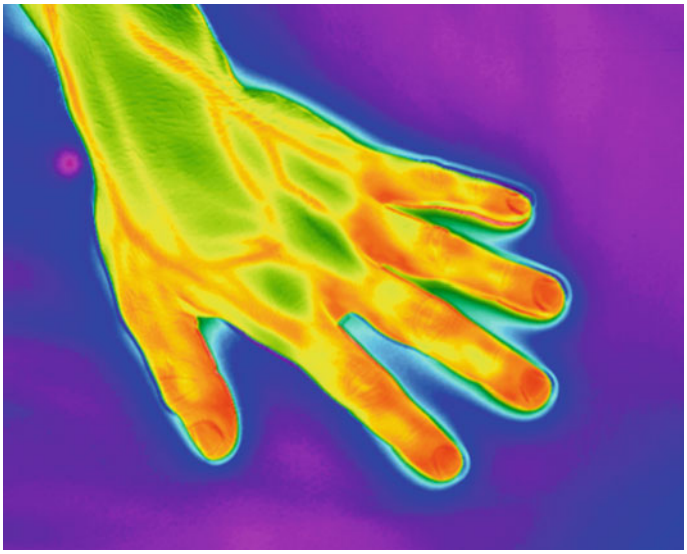

Fig. 23 Modulus for WT using Gauss complex wavelet, scale = 24 (max scale = 200)

5 Conclusion

This chapter presented the potentialities and limits of thermal tomography in medical diagnosis. As thermal tomography is based on heat propagation in a tissue, the depth of penetration the tissue by heat is limited. This depth strongly depends on the frequency of the provocation. Since the cold provocation is typically performed by the step-like excitation, the wide spectrum of the temperature signal is available for the analysis. This is the well-known concept of the thermal impedance of an object, but implemented in the frequency domain. We have shown that the thermal tomography can be applied for medical diagnosis, but it requires the powerful computers and advanced image processing. The IR imaging using thermography is the recommended tool for the temperature measurements. Thermal tomography can be applied wherever vascularization of the upper layers of the skin provides the diagnostic information. Forward and inverse thermal modeling of a tissue including the perfusion is very helpful in this applications. It can lead to the thermal characterization of the skin layers and measurement the perfusion rate. The proposed methods can be used to elaborate the medical protocol for the screening of skin diseases, including tumors and cancers.

References

1. Strakowska, M., Kaszuba, A., Strzelecki, M.: Novel methodology of medical screening using IR thermography. In: Signal Processing Algorithms, Architectures, Arrangements, and Applications—SPA 2014, Poznan, Poland (2014)
2. Laaperi, E., Laaperi, A.-L., Strąkowska, M., Więcek, B., Przymusiała, P.: Cold provocation improves breast cancer detection with IR thermography—a pilot study. Thermol. Int. **22**(4), 152–156 (2012). ISSN 1560-604X
3. Kaczmarek, M., Nowakowski, A.: Analysis of transient thermal processes for improved visualization of breast cancer using IR imaging. In: Proceedings of the 25th Annual International Conference of the IEEE on Engineering in Medicine and Biology Society, vol. 2, pp. 1113–1116 (2003)
4. Ring, E.F.J., Ammer, K.: The technique of infrared imaging in medicine. Thermol. Int. **10**(1) (2000)
5. Buzug, T.M., Schumann, S., Pfaffmann, L., Reinhold, U., Ruhlmann, J.: Functional infrared imaging for skin-cancer screening. In: EMBS Annual International Conference, New York City, USA, 30 Aug–3 Sept 2006
6. Więcek, P., Strakowska, M.: A novel tool for non destructive testing using frequency analysis of IR image sequences. Measur. Autom. Monit. MAM **61**(06), 219–222
7. Maldague, X.: Theory and Practice of Infrared Technology for Nondestructive Testing. Wiley, New York (2001)
8. Zolfaghari, A., Maerefat, M.: In: Bernardes, M.A.D.S. (ed.) Bioheat Transfer, Developments in Heat Transfer, InTech, 2011. ISBN 978-953-307-569-3. Available from: http://www.intechopen.com/books/developments-in-heat-transfer/bioheat-transfer
9. Valvano, J.W.: Bioheat transfer. In: Wiley "Encyclopedia of Medical Devices and Instrumentation", 2nd edn. The University of Texas Austin, Texas (2005)

10. Mariotti, A., Di Carlo, L., Orlando, G., Corradini, M.L., Di Donato, L., Pompa, P., Iezzi, R., Cotroneo, A.R., Romani, G.L., Merla, A.: Scrotal thermoregulatory model and assessment of the impairment of scrotal temperature control in varicocele. Ann. Biomed. Eng. Feb. **39**(2), 664–673 (2011)
11. Rumiński, J., Kaczmarek, M., Nowakowski, A.: Medical active thermography—a new image reconstruction method, In: Lecture Notes in Computer Science, pp. 274–181, LNCS 2124, Springer, Berlin-Heidelberg (2001)
12. Strakowska, M., De Mey, G., Wiecek, B., Strzelecki, M.: A three layer model for the thermal impedance of the human skin: modelling and experimental measurements. J. Mech. Med. Biol. **15**(3) (2015)
13. Strąkowska, M., Strąkowski, R., Strzelecki, M.: Thermal-time constant imaging in cold-stress screening. In: IEEE Conference on Signal Processing, Algorithms, Architectures, Arrangements, and Applications, SPA 2015, Poznan, Poland, 23–25 Sept 2015
14. Rumiński, J., Nowakowski, A., Kaczmarek, M., Hryciuk, M.: Model-based parametric images in dynamic thermography. Pol. J. Med. Phys. Eng. **6**(3), 159–164 (2000)
15. Strakowska, M., Strakowski, R., Wiecek, B., Strzelecki, M.: Cross-correlation based movement correction method for biomedical dynamic infrared imaging. In: 11th International Conference on Quantitative InfraRed Thermography, QIRT 2012, Naples-Italy, 11–14 June 2012, ISBN 9788890648441
16. Pennes, H.H.: Analysis of tissue and arterial blood temperatures in the resting human forearm. J. Appl. Physiol. **I**(2) 1948
17. Chen, M.M., Holmes, K.R.: Microvascular contributions in tissue heat transfer. Ann. N. Y. Acad. Sci. **335**, 137–150 (1980). ISSN 0077-8923
18. Weinbaum, S., Jiji, L.M.: A new simplified bioheat equation for the effect of blood flow on local average tissue temperature. ASME J. Biomech. Eng. **107**, 131–139 (1985). ISSN 0148-0731
19. Jasiński, M.: Modelling of 1D Bioheat Transfer with Perfusion Coefficient Dependent on Tissue Necrosis (vol. 7), Scientific Research of the Institute of Mathematics and Computer Science, Czestochowa University of Technology (2008)
20. Khanafer, K., Vafai, K.: Synthesis of mathematical models representing bioheat transport. In: Advances in Numerical Heat Transfer (Chapter 1), vol. III, pp. 1–28. CRC Press, New York (2009)
21. Vermeersch, B., De Mey, G.: Thermal impedance plots of micro scaled devices. Microelectron. Reliab. **46**, 174–177 (2006)

Vapotranspiration in Biological System by Thermal Imaging

Nicola Ludwig

Abstract Transpiration from porous materials such as leaves, stones, or human skin plays an important role in thermographic analysis due to evaporation. The change of physical state from liquid to vapor takes place at the interface of materials with surrounding air exactly where thermal infrared radiation is radiated. This chapter studies with the possibility to obtain quantitative evaluation of evaporation rate from non contact temperature measurements. The use of the localized high-intensity cooling on surface caused by evotranspiration has to be considered as a tool of inspection in diagnostics. A wide review of applications in plant physiology is here presented and some cases of follow-up of trauma in athletes are as well reported.

Keywords Leaf · Evaporation · Skin · Stomata conductance · Injuries

1 Forewords

Thermal imaging is the most immediate way to visualize evaporation in every porous material both in normal condition and under induced stress. Biology defines transpiration as the way plants carry water from roots to leaves where it finally evaporates. Evaporation flux intensity depends on ambient stress factors mainly wind and relative humidity. In this process water transformation from liquid to gas regulates also foliar temperature. To highlight the importance of physical state change and the relative energy transfer occurring in transpiration we will introduce the term *vapotranspiration*.

For many years, infrared thermography (IRT) has been recognized as an effective tool to monitor leaves vapotranspiration in conditions of controlled environment [8]. Basically, the temperature of a leaf is the result of energy exchange between environment and the leaf surface. The plant can react to thermal stresses by

N. Ludwig (✉)
Department of Physics, State University of Milano,
via Celoria 16, 20133 Milan, Italy
e-mail: nicola.ludwig@unimi.it

E.Y.K. Ng and M. Etehadtavakol (eds.), *Application of Infrared to Biomedical Sciences*, Series in BioEngineering,
DOI 10.1007/978-981-10-3147-2_23

means of evaporation of water through the stomata positioned on the foliar surface; this process produces cooling. Temperature modifications of a leaf are generated by changes in vapotranspiration rate and can be used to measure evaporation rate (i.e., vapor mass lost per surface and time units) in single leaf or to evaluate crop vitality.

This technique can also detect water content in specific areas of a leaf (necrosis, treatments with water repellent, etc.). In a leaf, changes of the water content (W_C) caused by severe climatic conditions lead to alterations in transpiration rate through an active regulation mechanism of the stomatal opening. Thermography can visualize the effects of these changes in real time [12], thanks the low thermal capacity of a thin leaf (see Fig. 1). IRT application is based on the direct dependency between transpiration and leaves temperatures. Figure 2 illustrates clearly this relationship showing evaporation rate of bean leaves in the same environmental conditions but treated with different products the enhance or reduce stomata aperture and evaporative flux.

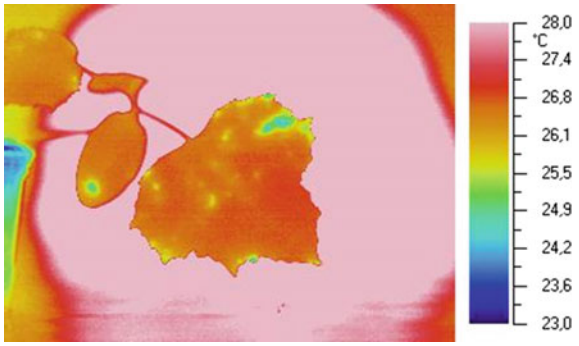

Fig. 1 Cucumber leaves, *green spots* are due to a local treatment with paralyzing abscisic acid (ABA) stomata in open position during a water stress condition (RH < 40%)

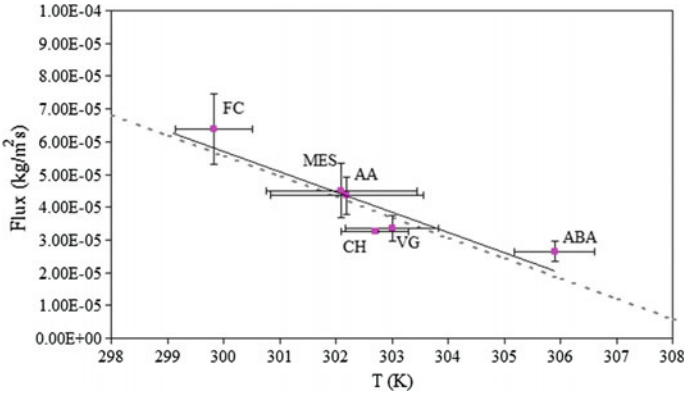

Fig. 2 Correlation of the evaporation flux from leaf surface versus cooling, capitals indicate different treatments (see Ludwig [12] for more)

Considering porous materials, some authors confirmed that can be found a linear dependence between the cooling due to vapotranspiration and the flux rate [1]. Temperature variations on leaves surface are dramatically dependent on the plant moisture level (health, stress, dryness); this level depends on the stomatal conductance. Conductance is also responsible of gas exchange and plays a fundamental role in photosynthetic processes. IRT was successful used to single out the effects of heat that caused partial necrosis on a single plant as well on the whole plantation [11]. Furthermore, a cooling effect has been observed in a research on *Arabidopsis* and tobacco plant, produced by abnormal evaporation from cells before any kind of damage could be detected and monitored [4].

IRT experiments can be divided in two kinds of approaches: passive and active. Dealing with a living being, we should reconsider the definition of active or passive test taking into account these factors: heat production and heat loss inside the biological system in "normal" or non-pathological conditions; very important is also the ability of the system to give a feedback about any external solicitation. Active thermography allows non-destructive measurement of the W_c of leaves related to any changes in heat capacity of tissue. Passive thermography evaluates changes in the evaporation flux Φ [kg m^{-2} s^{-1}]. This approach can localize disease areas remotely but does not give any clue about stress agents such as solar radiation, wind speed, clouds cover, etc. We should consider that the influence of these elements can disguise the effect of more specific natural stresses.

Thermographic analysis has been used for isolation of stomatal mutants by means of screening tests [17] and presymptomatic visualization of the biotic plant stresses in a number of cases [3]. The infection of "*Tobacco Mosaic Virus*" is a well-characterized model due to its hypersensitive response of resistant tobacco plant. Increasing of temperature in the sites due to this infection can be detected by IRT. Data confirmed that this temperature increasing overlapped with the sites of salicylic acid accumulation and it brought to the conclusion that the local temperature is affected by stomatal closure caused by the accumulation of compounds signature of the resistance during pre-necrotic phase [4]. This study showed that thermal detection of pre-necrotic symptoms in tobacco as well as in *Arabidopsis* is possible. These results led some researchers to suppose that any phenomenon characterized by cell death in a plant would be detectable by IRT in the early presymptomatic stage. Another example can be found in thermal anomalies of *Cercospora* leaf characterized by the development of dark circular necrotic stains of sugar beet due to a necrotrophic fungal infection [20].

The capability of passive resistance in vegetables inevitably has consequences on plant metabolism and physiology. The effects on vapotranspiration and photosynthesis were revealed also by imaging of chlorophyll fluorescence and IRT technique. Reactions of metabolism depend on interactions between plant and pathogens [5]. Thermal imaging through both proximal and remote sensing has been proved to be useful for evaluation of biotic stresses as well as for irrigation scheduling. In environments characterized by severe water restriction IRT has been used for genetic screening of stomata efficiency in series of selected crops [10]. In fact, in arid environments and drought conditions, "The combined use of irrigation

procedures and survey technologies can improve the plant water use efficiency" (ibidem). The efficiency is defined as the ratio between the crop biomass and the amount of water consumed by the crop (i.e., irrigation, rainfall, plant, and soil vapotranspiration). In this field it is evident the importance of studying the effect of anti-transpiration and water-repellent compounds applied spraying the foliage in order to reduce water loss [19].

2 Thermal Imaging on Plant: The Energy Balance Approach

Thermal imaging represents nowadays a mature technology useful to study the energy balance at surface level of both leaf and human skin. In plants, the latent heat lost during evaporation is the most important mean for thermoregulation, more than conduction convection and irradiation. When the energy transfer connected to mass transfer (i.e., sap or blood) is negligible, thermal imaging can be the only method to map and evaluate vapotranspiration rates without any sampling.

Vapotranspiration control involves two types of compounds: film-forming and stomatal closing, both acting to increase plant resistance to vapor loss and improve the crop *water-use efficiency* as defined above. It was stated that, "The antitranspirant activity of chitosan (see CHT in Fig. 2) in bean plants is a natural, nontoxic and low cost compound obtained from crustacean, insect and fungal chitin deacetylation, the second most abundant biopolymer after cellulose" [12].

The issues concerning temperature measurements by IRT and the variables linked to wind velocity or environment temperature have been extensively studied because of their role in the physics of vapotranspitration. The main finding is that thermal imaging can easily measure temperature differences of some fractions of degrees caused by differences of 10^{-1} bar in hydric potential. We also warn that the on field observation of plantations is strongly affected by sudden changes in solar radiation produced by clouds.

Leaf vapotranspiration (i.e., the loss of water vapor) can be evaluated by a non-invasive temperature measurement technique. In fact, this evaporation has a heavy influence in the energetic exchange processes and determines the leaf temperature at the thermodynamic equilibrium with the surrounding microclimate. The main advantage of IRT applied to vegetables monitoring is the possibility to employ it in huge crops. The best and yet valuable model for energy balance, applied to plant physiology, was established by Nobel in 80s [18].

Considering at the equilibrium all environmental physical variables such as relative humidity, air temperature, wind velocity, and irradiation, temperature measurement gives the exchanged energy between the local environment and the leaf itself.

Any living being regulating the amount of water vapor lost during vapotranspiration can improve its thermoregulation mechanism, thanks to the high value of

the heat of vaporization (2.25×10^6 J kg^{-1}). When used to compensate for any external stress, we can consider $\Delta Q_{\text{tot}} = 0$ and as a consequence the leaf reaches an equilibrium temperature T_α. All the different amounts of energy exchanged are added to zero at this equilibrium condition as described in Eq. 1:

$$Q_{\text{R}} + Q_{\text{C}} + Q_{\text{T}} + Q_{\text{W}} = 0 \tag{1}$$

where Q_{R} represents both outgoing and incoming radiations, Q_{C} is the heat transfer by convection, Q_{T} represents the energy exchanged by mass transfer, and finally Q_{W} is the heat of vaporization. For more details, we can write Eq. (1) as Eq. (2) with proper physical expressions for each term.

$$\alpha\varepsilon_{\text{env}}\sigma T_{\text{env}}^4 - \varepsilon\sigma T^4 - h(T - T_{\text{air}}) + c_p\Phi_w(T_{\text{air}} - T) - \lambda\Phi_{\text{v}} = 0, \tag{2}$$

where

α is the spectral absorbance,
ε_{env} is the effective emissivity of environment,
ε is the emissivity of the leaf,
σ 5.67×10^{-8} [W m^{-2} K^{-4}], Stefan–Boltzmann constant,
Φ_{v} is the evaporation flux from the leaf stomata,
Φ_{w} is the liquid water flux to the leaf surface,
λ 2.26×10^6 [J kg^{-1}], heat of vaporization of water,
T is leaf temperature,
T_{env} is the environmental temperature,
h is the coefficient of free convection,
c_{p} is the specific heat at constant pressure of the leaf.

Energy balance expression in (2) for a leaf can be connected to their stomata conductance by gas diffusion Fick's law:

$$\Phi^* = -D\frac{\partial C}{\partial x}. \tag{3}$$

Here, the evaporation rate [Φ^*] is not expressed in grams but in moles [m^{-2} s^{-1}], depending on the molar concentration C [mol m^{-3}] while D represents the diffusion coefficient [m^2 s^{-1}].

In this way, a thermal camera can be considered as the best tool to measure stomata conductance without any contact with foliar surface. When the balance equation (2) is in the equilibrium condition, the solution gives the temperature T_α with the following expression by measuring this equilibrium temperature, we can obtain the flux rate,

$$\Phi_{\text{v}} = \frac{\alpha\varepsilon_{\text{env}}\sigma T_{\text{env}}^4 - \varepsilon\sigma T^4 - h(T_\alpha - T_{\text{air}}) + c_{\text{p}}\Phi_{\text{w}}(T_{\text{air}} - T_\alpha)}{\lambda} \tag{4}$$

In normal water supply conditions, the water lost through evaporation corresponds, mostly, to the water provided by roots to the plant. This is due to the simple fact that the capillary rising speed is higher than the vapor diffusion through stomata. Finally, note that the energy associated with the mass of water moved by the capillary system is about two orders of magnitude smaller than the one needed for the evaporation of the same quantity. In fact, the heat required for the evaporation of a single gram of distilled water is about 2 kJ while 20 J is the energy transferred within the capillary system by this mass with a ΔT of 5 °C between roots and leave surface.

So we have $\Phi_v = \Phi_w$ and then:

$$\Phi = \frac{\alpha \varepsilon_{env} \sigma T_{env}^4 - \varepsilon \sigma T^4 - h(T_\alpha - T_{air})}{\lambda - c_p(T_{air} - T_\alpha)} \tag{5}$$

This expression that gives the evaporation rate depending on T_α (i.e., the equilibrium temperature) has been experimentally verified by the author through direct thermographic survey and simultaneous measurements of the evaporation flux using a digital scale (Fig. 2).

It is interesting to note that tests under controlled conditions showed the same direct correlation also on porous building materials like plaster, stone, and brick [16]. In this work considerations can be found about the parameters of Eq. (5) and about their dependency on specimen geometry and other environmental variables.

3 From Plant to Human Body

Some analogies can be found between leaves and the human skin. In spite of some similarities the skin could be also defined a sort of insulating interface between an inner core and the external environment. In particular IRT can be useful to detect and visually represent heat dissipation through the skin during thermoregulation processes [6, 14].

From a thermophysical point of view, human skin is a thin layer of tissues with different values of thermal conductance. This layer separates the parts of the body where exoenergetic processes take place and the colder external environment. Human body tends to remain in steady condition of temperature, to achieve this condition it balances metabolic heat production and heat losses to the surrounding environment in many ways: convection, infrared irradiation, vapotranspiration, and conduction (this last component is usually negligible). The fundamental role played by infrared radiation from human skin has been confirmed since 30s and it has been very well described as a blackbody-like radiator. Inner temperature is maintained within a narrow range and its regulation is essential for normal performances during everyday life considering normal metabolism of healthy subjects or particular conditions as agonistic or intense activity. Quantitatively, vapotranspiration is the

most important mechanism operating on thermoregulation. Theoretically, the evaporation from the skin of just 1 g of water decreases the temperature of one degree in up to 500 g of human tissue.

Industrial application of thermal imaging, as non destructive method, is targeted to detection of possible defects hidden under external surface. Anomalies under the surface cause abnormal thermal conduction toward the inner parts and are easily recognizable by the presence of layers with different thermal properties (i.e., "defects"). On the other hand, in medical applications, many pathologies can reveal themselves through abnormal thermal patterns on the skin. Diagnostics can visually represent this thermal pattern and eventually compare it with the one taken in healthy areas or when possible in corresponding contralateral part. More specifically, in healthy subjects thermal imaging can be used to highlight possible asymmetries in left/right parts of the body caused by a different muscular development. The thermal image in Fig. 3 depicts a typical asymmetrical distribution of temperature of a human back affected by scoliosis. The subject (male 32 y. o.) faced a long term period of exercise (20 year) to prevent damages of a severe scoliosis.

Thermal imaging is also an effective tool to study the follow-up of muscular or skeleton trauma even in absence of skin injuries. Figure 4 shows a strong difference in temperature between the right and left knees of a young volleyball player with a *Ligamenta cruciata genus (LCA)* injury three months after the accident.

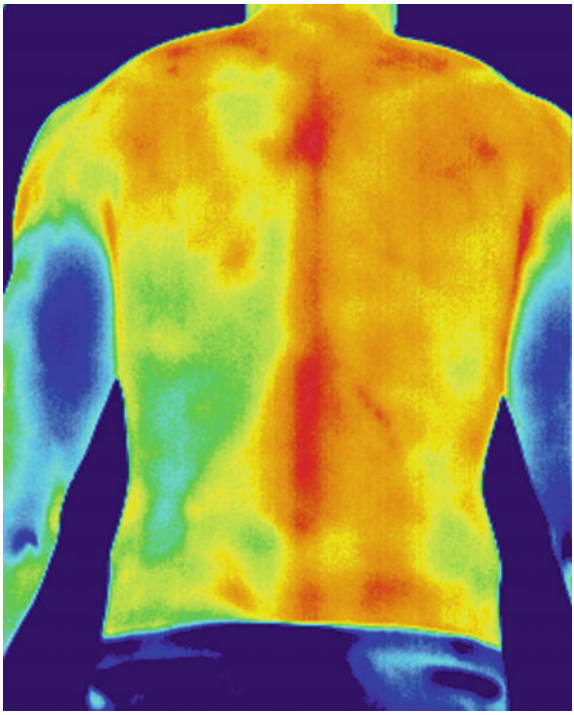

Fig. 3 Thermographic evidence of controlateral thermal anomalies in a trained male subject (34 y. o.) with scoliosis, left part of the mid-back shows a wide colder area

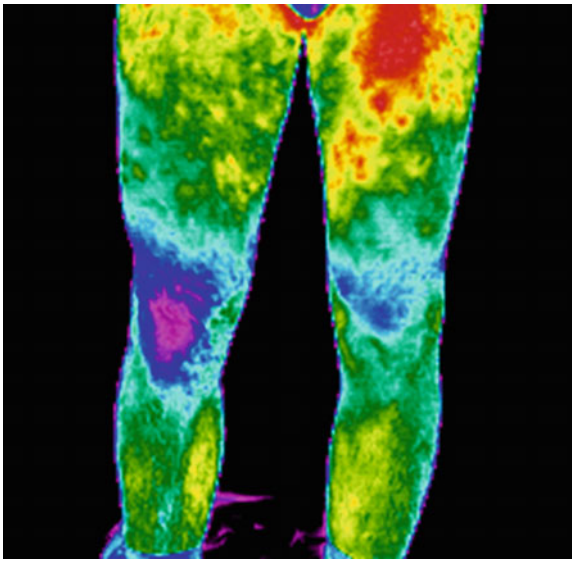

Fig. 4 Thermographic evidence of trauma in right knee (*on left*) on a volley player male subject (23 y. o.) after one month from LCA fracture

Nowadays one of the most important problem in post-processing infrared shots of moving subjects, (i.e., veterinary or sport science) is the need of algorithms for automatic target recognition [13]. The best method suggested by authors is based on the selection of classes of pixels (hottest/coldest/between thresholds) and the extraction of their statistic distribution in a sequence of thermal images. A peculiar method, gathered from this approach, was successfully applied to the study of calves and thighs on trained athletes [7, 15]. It is expected that the introduction of this pixel recognition technique will lead to a paradigm change in thermal image analysis for diagnostic purposes.

4 Thermoregulation Study by IRT

Blood circulation is the main and faster mechanism of heat transfer inside human body, more specifically from the inner core to peripheral areas. A well established relationship between heat of blackbody radiation from the cutaneous surface and the underlying blood flow, is given by the Pennes bioheat equation.

$$Q_{\mathrm{m}} = C_{\mathrm{b}} W_{\mathrm{b}} (T_{\mathrm{a}} - T) - \nabla^2 T, \tag{6}$$

where for a given tissue we have: volumetric metabolic rate (Q_{m}), specific heat capacity (C_{b}) and the mass flow rate of blood per unit volume (W_{b}). T_{a} represents the arterial temperature and T is the variable temperature of the tissue. Starting from the expression above, some researchers developed numerical models used to predict

cutaneous temperature considering metabolic heat production and, inversely, to estimate organs temperature measuring surface temperature of the body. Cooling processes are often effective to improve experimental procedures and defining thermography as a precise diagnostic tool.

Thermal images in Fig. 5 show another late follow-up after a tendinous injury. The left hand of a 20 y. o. free climber with a third- finger tendon injury is shown after a ten-minute immersion in cold water (10 °C). The first shot has been recorded after 10 s while the second 1 min later. In the second image, the injured finger appears, stimulated by cold water, as the one with the lowest thermal recovery, probably due to calcification which reduce the peripheral circulation inside the finger.

During physical exercise, in the body, heat is generated by metabolism and by muscular work [9], this heat is then diffused from the core toward the skin by blood flow through vessels. This occurs especially in limbs and head, where the surface/volume ratio gets the best efficiency for heat dissipation. The possibility to locate interested areas and study this process on the skin surface can provide important details on the different thermoregulation mechanisms.

Thermal pattern of the venous system, even if colder than the arterial one, can be easily revealed because these vessels are, in healthy subjects, not covered by thick layers of fat. Figure 6 shows an example of this pattern in rest condition and Fig. 7 after an hard work (squat exercise) involving the femoral quadriceps of a subject.

Cutaneous temperature is determined by two main factors: convective heating produced by blood flow from deeper blood vessels and cooling by sweat evaporation. Thermography is an efficient tool to monitor thermoregulation processes during sport training sessions or in presence of physical external stimulations (cooling by air or water). In normal subjects, after proper and localized (atriovestibular) stimulation, temperatures of arms, hands, feet, neck and some head

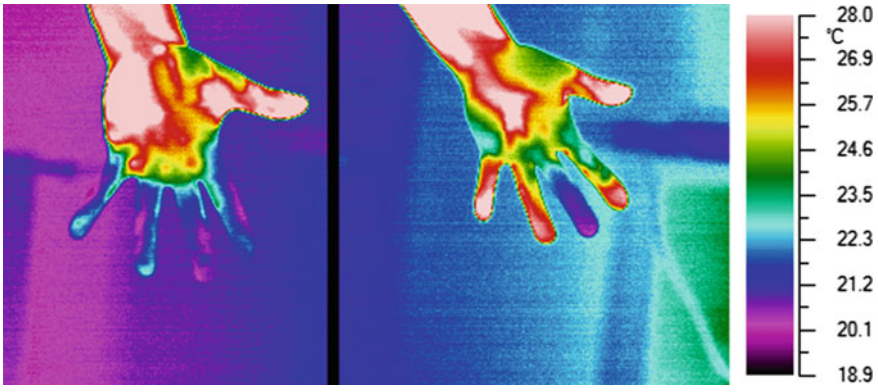

Fig. 5 IR images of the left hand of a free climber subject with former finger tendon injury (male, 19 y. o.), after immersion in cold water. First image after 10 s and second after 1 min. The injured finger can be clearly visualized when circulation recovers the original temperature on the healthy fingers

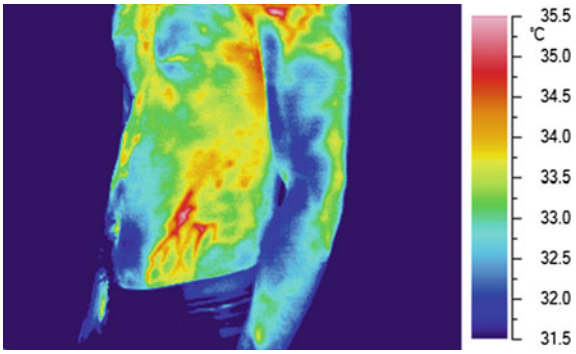

Fig. 6 Thermographic evidence of subcutaneous venous circulation in a male healthy subject (27 y. o.)

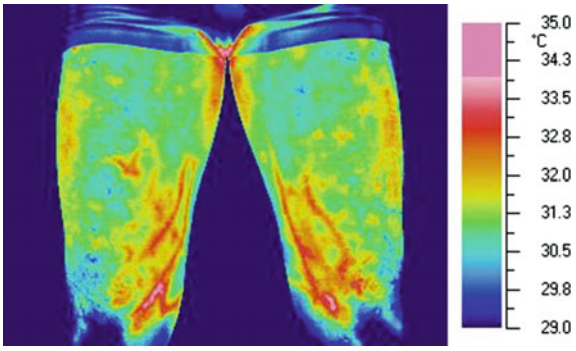

Fig. 7 Thermographic evidence of subcutaneous venous circulation in a male well-trained subject (23 y. o.) during squat exercise (see Formenti [7] for more)

regions, increases also in rest conditions, showing the activation of this thermoregulation mechanism. Vainer in his monograph on skin perspiration and vapotranspiration [21] used a medium-IR camera to study sweating mechanism. Other researchers found an asymmetry in sweat gland but also noted a cold temperature area surrounding secretory ducts.

Studies on sweating rate and thermoregulatory mechanisms involved two different approaches: cold stress and blood flow modulation [2]. In the first method, a more classical approach, a cold stress condition was applied placing the left hand on a cold metal surface with a thermal camera monitoring temperature of both hands. In the second method blood pressure was artificially modified (or "modulated"), in the range of systolic and diastolic values, using a proper constriction applied on arms. After an initial stationary state lasting 85 s, the temperature of the stimulated hand drop-down while an unexpected increase of temperature was observed on the non-stimulated hand. Also this result has been explained as a thermoregulatory mechanism which answers symmetrically to the external stimulus in order to keep the core temperature constant.

We also point out that only few researches deal with problems connected to sweat evaporation from skin surface giving to this field of applied studies chances to be exploited both in medicine and in sport sciences.

5 Conclusions

Water transformation process operated by evaporation can be considered as one of the most important causes of thermal disequilibrium in both living and non-living objects (i.e., porous materials). Vapotranspiration fluxes taking place on surfaces of many kinds of materials has been proved to be quantitatively defined measuring surface temperature of the object being studied. This value, at the equilibrium conditions among all terms of heat exchange occurring through the surface, shows to be strongly dependent on the vapor flux rate.

Correlations between temperature and evaporation rate have been confirmed on different type of materials such as leaves, plaster, brick and human skin, proving the strong correlation between temperature and evaporation rate, both in a thin system such as leaf, porous building, materials and human skin.

Technical Note The thermal images shown in this chapter were shot by an AVIO TVS700 camera equipped with a microbolometer uncooled detector (320 × 240 pixels, thermal resolution 0.07 °C at room temperature, emissivity 0.97).

References

1. Bajons, P., Klinger, G., Schlosser, V.: Determination of stomatal conductance by means of infrared thermography. Infrared Phys. Technol. **46**, 429–439 (2005)
2. Bouzida, A., Bendada, X.P., Maldague, L.J.: Visualization of body thermoregulation by infrared imaging. J. Therm. Biol. **34**, 120–126 (2009)
3. Boccara, M., Boue, C., Garmier, M., De Paepe, R., Boccara, A.C.: Infra-red thermography revealed a role for mitochondria in pre-symptomatic cooling during harpin-induced hypersensitive response. Plant J. **28**, 663–670 (2001)
4. Chaerle, L., De Boever, F., Van Der Straeten, D.: Infrared detection of early biotic and wound stress in plants. Thermol. Int. **12**, 100–106 (2002)
5. Chaerle, L., Hagenbeek, D., De Bruyne, E., Valcke, R., Van Der Straeten, D.: Thermal and chlorophyll-fluorescence imaging distinguish plant-pathogen, interactions at an early stage. Plant Cell Physiol. **45**, 887–896 (2004)
6. Formenti, D., Ludwig, N., Gargano, M., Gondola, M., Dellerma, N., Caumo, A., Alberti, G.: Thermal imaging of exercise-associated skin temperature changes in trained and untrained female subjects. Ann. Biomed. Eng. (2013). doi:10.1007/s10439-012-0718-x
7. Formenti, D., Ludwig, N., Trecroci, A., Gargano, M., Michielon, G., Caumo, A., Alberti, G.: Dynamics of thermographic skin temperature response during squat exercise at two different speeds. J. Therm. Biol. **59**, 58–63 (2016)
8. Jones, H.G.: Use of thermography for quantitative studies of spatial and temporal variation of stomatal conductance over leaf surfaces. Plant Cell Environ. **22**, 1043–1055 (1999)
9. Jones, B.F.: A reappraisal of the use of infrared thermal image analysis in medicine. IEEE Trans. Med. Imaging **17**, 1019–1027 (1998)
10. Hellebrand, H.J., Beuche, H., Linke, M.: Thermal imaging. A promising high-tec method in agriculture and horticulture. In: Blahovec, J., Kutílek, M. (eds.) Physical Methods in Agriculture—Approach to Precision and Quality, pp. 411–427. Kluwer Academic/Plenum Publishers, New York (2002)

11. Leinonen, I., Jones, H.G.: Combining thermal and visible imagery for estimating canopy temperature and identifying plant stress. J. Exp. Bot. **55**, 1423–1431 (2004)
12. Ludwig, N., Cabrini, R., Faoro, F., Gargano, M., Gomarasca, S., Iriti, M., Picchi, V., Soave, C.: Reduction of evaporative flux in bean leaves due to chitosan treatment assessed by infrared thermography. Infrared Phys. Technol. **53**, 65–70 (2010)
13. Ludwig, N., Gargano, M., Luzi, F., Carenzi, C., Verga, M.: Technical note: applicability of infrared thermography as a non invasive measurements of stress in rabbit. World Rabbit Sci. **15**(4) (2007)
14. Ludwig, N.G., Gargano, M., Formenti, D., Bruno, D., Ongaro, L., Alberti, G.: Breathing training characterization by thermal imaging: a case study. Acta Bioeng. Biomech. 41–47 (2012)
15. Ludwig, N., Formenti, D., Gargano, M., Alberti, G.: Skin temperature evaluation by infrared thermography: comparison of image analysis methods. Infrared Phys. Technol. **62**, 1–6 (2014)
16. Milazzo, M., Ludwig, N., Redaelli, V.: Evaluation of evaporation flux in building materials by infrared thermography. In: 6th International Conference on Quantitative Infrared Thermography (2002)
17. Mustilli, A.C., Merlot, S., Vavasseur, A., Fenzi, F., Giraudat, J.: Arabidopsis OST1 protein kinase mediates the regulation of stomatal aperture by abscisic acid and acts upstream of reactive oxygen species production. Plant Cell **14**, 3089–3099 (2002)
18. Nobel, P.S.: Biophysical plant physiology and ecology. WH Freeman and Company, San Francisco, pp. 608–612 (1983)
19. Pereira, L.S., Oweis, T., Zairi, A.: Irrigation management under water scarcity. Agric. Water Manag. **57**, 175–206 (2002)
20. Skaracis, G.N., et al.: Breeding for Cercospora resistance in sugarbeet. Cercospora beticola Sacc. Biol. Agron. Influ. Control Meas. Sugar Beet, pp. 177–195 (2000)
21. Vainer, B.G.: FPA-based infrared thermography as applied to the study of cutaneous perspiration and stimulated vascular response in humans. Phys. Med. Biol. **50**, R63–R94 (2005)

Change in Local Temperature of Venous Blood and Venous Vessel Walls as a Basis for Imaging Superficial Veins During Infrared Phlebography Using Temperature-Induced Tissue Contrasting

Aleksandr L. Urakov, Anton A. Kasatkin and Natalia A. Urakova

Abstract A possibility of fast, safe, and efficient imaging of superficial veins with a thermal imager is demonstrated in experiments with pigs, in studies with healthy adult volunteers, and in clinical observations of adult patients when providing vital medical care in emergency situations. The research describes the original techniques for infrared veins imaging enabling the authors to lay the basis for infrared venography. In order to image superficial veins, we suggest infrared monitoring of local temperature dynamics in the selected part of the body surface under the conditions of artificial multidirectional changes in temperature of veins and/or surrounding tissues. The chapter describes techniques for infrared imaging of the superficial veins in limbs and breast, and provides infrared thermograms of a hand, a forearm, a shoulder, a foot, and a breast, thus showing the prospects of superficial veins imaging using infrared phlebography and temperature-based "displaying." It explains the essence of temperature-based veins "displaying," developed by authors and called "temperature contrasting." It describes the techniques for artificial changes in local venous temperature by changing the temperature of venous blood and/or artificial plasma extender, or by artificial cooling of the tissues surrounding the vein. It also shows the advantages of infrared phlebography over other radiology methods to address urgent and repeated imaging of superficial veins in critical situations to optimize intravascular access for sampling venous blood, its subsequent laboratory testing, and intravenous injections of medications.

Keywords Radiology · Thermal imaging diagnostics · Superficial veins · Temperature contrasting drugs

A.L. Urakov (✉) · A.A. Kasatkin · N.A. Urakova
Institute of Mechanics of Ural Branch of RAS, Izhevsk, Russia
e-mail: urakoval@live.ru

E.Y.K. Ng and M. Etehadtavakol (eds.), *Application of Infrared to Biomedical Sciences*, Series in BioEngineering,
DOI 10.1007/978-981-10-3147-2_24

1 Introduction

Qualitative and quantitative parameters of blood and heart function, as well as venous and arterial parameters, still play a key role in medical diagnostics. However, human veins are more accessible to examinations than arteries, and the total number of veins as well as venous blood volume are more than 2 times greater than the arteries number and arterial blood volume. This automatically increases the possibility of using veins and venous blood in medical diagnostics as compared to arterial blood, heart, and arteries. However, in critical situations, veins may collapse and may be lost in soft tissues. In this regard, due to poor vein visualization, emergency medicine often lacks the possibility of using veins and venous blood in patients for diagnostic and treatment purposes. In particular, the problem of fast, safe, and efficient imaging of superficial veins for intravascular access for sampling venous blood, its subsequent laboratory testing, and injections of intravenous drug solutions has not been solved yet.

The following radiology methods are generally used for vein imaging:

- Examination of skin and mucous membranes color by sight in the visible spectrum;
- Ultrasound examination of soft tissue acoustic properties; and
- X-ray examination of all tissue radial properties.

Each of these methods has its own advantages and disadvantages, but none of them completely satisfies the experts because of low efficiency in case of vein selection by sight, or because of low safety, in case of X-ray imaging. In particular, X-ray vein imaging requires radiopaque agents that were first proposed about 100 years ago [1] and still pose a threat to the health and life of patients [2].

In recent years, a new radiology method has been applied for superficial tissues imaging, called infrared thermography [3–7]. This imaging technique is based on the analysis of the infrared rays emitted by the tissues [8]. Devices that form tissues image in the infrared radiation spectrum are called thermal imaging cameras. The fundamental difference between these devices and other radiology diagnostic devices is that thermal imaging cameras allow you to obtain a color image of the selected exposed body area in the rainbow color palette, based on the local surface temperature. Identifying the area with color that is different from the color of neighboring areas in the thermal image of the body surface suggests that there is a colder or hotter “segment,” i.e., tissue area at this site, or directly under it [9–11].

2 Results

Considering the facts mentioned above, in 2009 we put forward the hypothesis about the possibility of imaging superficial veins without the use of conventional radiology diagnostics methods. To prove it right, we improved the technique for studying the local temperature of the body surface with infrared thermography by artificially contrasting veins temperature and the temperature of surrounding tissues. At first, we developed the technique for infrared phlebography for imaging superficial veins in limbs. This technique is called "A.A. Kasatkin method for infrared imaging of superficial veins in limbs" [12]. This infrared phlebography technique involves traditional laying the patient in "the right position," preparing the surface to be examined for radiology scanning, mechanical compression of the tissues located proximal to the examination area until the blood flow stops, placing the distal part of the limb (a hand) into the water heated to +42 °C until steady local thermal hyperemia is achieved, exposing the surface to be examined and applying an ice pack until steady cold hyperemia is achieved, removing a limb out of water, removing the ice pack, and restoration of blood flow while monitoring the local surface temperature with a thermal camera in the infrared radiation spectrum. At the same time, in order to produce high-quality images we proposed to produce infrared phlebogram at the moment of achieving maximum vein temperature contrast (Figs. 1 and 2).

Later, in 2010, we demonstrated the possibility of imaging veins by infrared phlebography in veins with local inflammation (phlebitis), resulted from irritation of the inner surface of the vein wall caused by intravascular catheter. Initially, this possibility was demonstrated in experiments with pigs [13–15]. Then we showed the possibility of imaging the inflamed area of superficial vein by infrared phlebography in clinic [14] (Fig. 3).

After that, we expanded the scope of application of infrared thermography under artificial tissue temperature contrasting to diagnose their structure [16]. By expanding the diagnostic applications of thermal imaging camera we were able to show the possibility of infrared imaging of cheek structure under heating from the

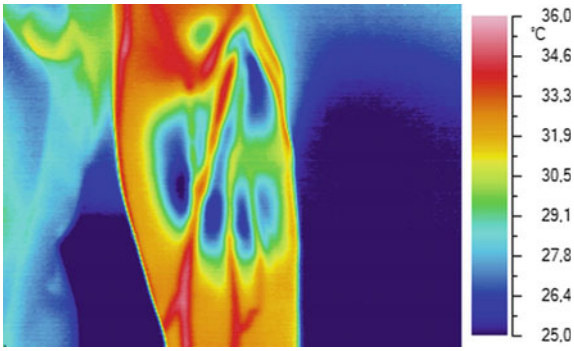

Fig. 1 Infrared phlebogram of the inner surface of the left forearm in a healthy adult volunteer, 23 y.o., produced at the moment of achieving maximum vein temperature contrast, according to the patent RU 2389429

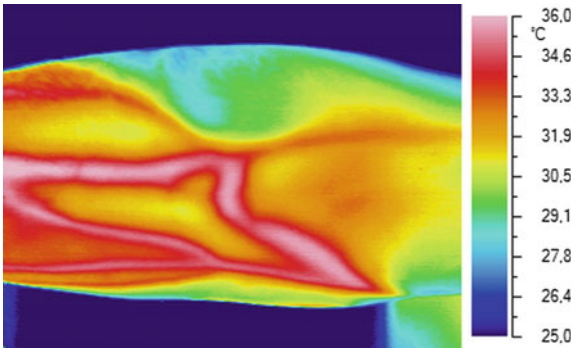

Fig. 2 Infrared phlebogram of the inner surface of the right forearm in a healthy adult volunteer I., 33 y.o., produced at the moment of achieving maximum vein temperature contrast, according to the patent RU 2389429

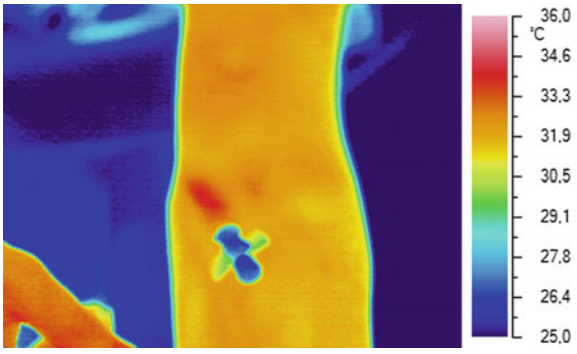

Fig. 3 Infrared image of the left forearm of patient P., 32 y.o., produced 1 h after vein catheterization (*arrow marks* the local hyperthermia of skin in projection of intravascular tip of catheter)

side of oral cavity by placing in it drinking water heated to +42 °C. It was shown that if local temperature change under these conditions is imaged by infrared monitoring as uniform, it indicates the homogeneity of cheek structure. If there is local hypo- or hyperthermia area, we should specify its shape, size, and location as it indicates the area in a cheek with low or high thermal conductivity, respectively.

Later we developed a technique for infrared imaging of hand tissue structures under one-sided heating of the opposite hand surface. This innovative method involves exposing the selected hand, squeezing the arm above the wrist until arterial pulse in periphery disappears, dipping the hand in water at a temperature of +25 to +26 °C for 3–10 s, removing the hand from the water, and then placing its selected side on a flat surface of a thermal source made from a high thermal conductivity material at a temperature of +42 °C. Then we fix the limb in a position enabling infrared imaging of the opposite surface with a thermal imager and continuously monitor the dynamics of local surface temperature under ischemia. The images of the examined surface are performed in red-purple color palette depending on the local temperature, ranging from +26 to +37 °C, respectively. If an area of abnormal local hypo- or hyperthermia is detected in the hand, we specify its shape, size, and location, analyze the data, and provide opinion on the object shape, size, and location in the hand and, respectively, on its low or high thermal conductivity and

heat production. If the area of abnormal hypo- or hyperthermia is not detected, the procedure is repeated, but no earlier than after 5 min, changing the sequence of using the hand surfaces [17].

At present, it is found that the efficiency of superficial veins imaging by infrared phlebography may be enhanced by preheating or precooling venous blood [18]. The matter is that when using thermal imaging camera, the temperature-based vein displaying is better when the liquid flowing inside veins is warmed or cooled (blood and/or plasma-expander solution) (Figs. 4, 5 and 6).

The infrared phlebogram of the hand shown above demonstrates that dipping the hand into the icy water for a short period of time cools the vein blood flowing back to the forearm from the cold hand. In its turn, it cools the forearm veins and the skin over them, providing cold-induced displaying of the superficial veins on the thermal camera screen in accordance with local hypothermia areas locations, shapes, and sizes.

At the same time, we proposed to use artificial temperature contrasting of breast tissue to image its structure using infrared thermography for screening tumors and imaging superficial veins. For infrared phlebography using temperature-induced tissue contrasting, we proposed to conduct infrared monitoring during and after

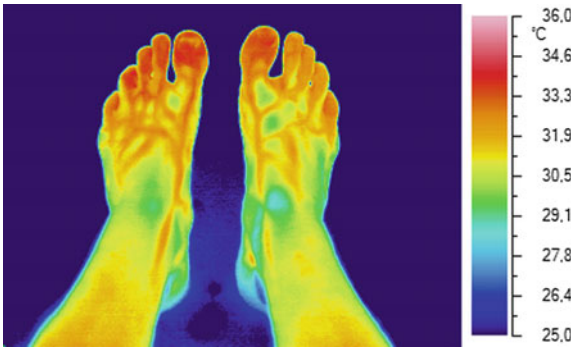

Fig. 4 Infrared phlebogram of both feet of volunteer I., 40 y.o., in 5 min after the beginning of blowing their surface with air flow at a temperature of +25 °C by domestic fan

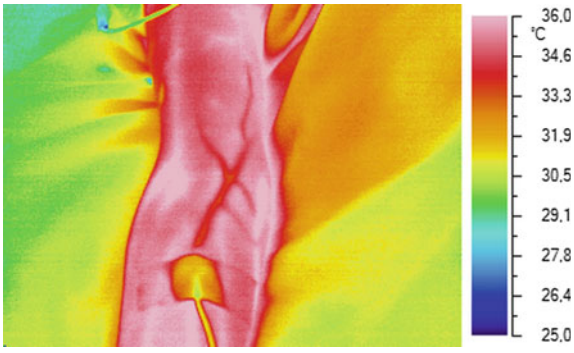

Fig. 5 Infrared phlebogram of the inner surface of the right hand with intravenous catheter inserted in the elbow of patient P., 54 y.o., 3 min after the beginning of intravenous infusion of 0.9% sodium chloride solution at a rate of 4 ml/min at 30 °C

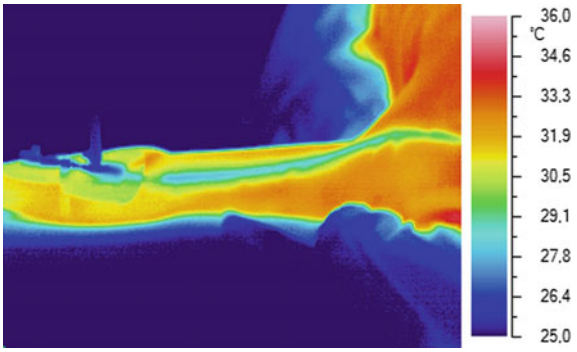

Fig. 6 The image of the left shoulder surface of the patient B., 49 y.o., with intravenous catheter connected with the infusion system immediately after bolus injection of 20 ml of 0.9% sodium chloride solution in the vein at a temperature of +25 °C

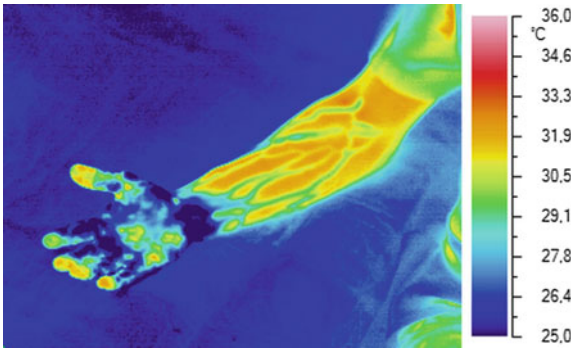

Fig. 7 The image of the right hand of an adult healthy volunteer K., 41 y.o., in 3 min after removing the hand from icy water, where hand was placed for 2 min

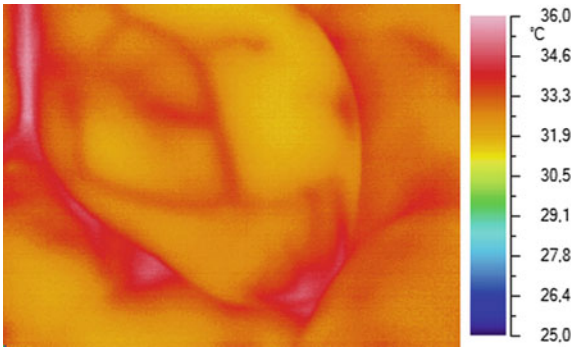

Fig. 8 The image of the left breast in healthy woman, 23 y.o, with "C" breast size, 5 min after beginning of blowing the breast with air from SCARLETT SC-1073 drier at a temperature of 28 °C

blowing the breast surface with ambient temperature air flow from a drier which creates a uniform flow of cooling air.

Infrared phlebograms of breast in a woman (Fig. 7) and foot in a man (Fig. 8) show the possibility of imaging superficial veins under blowing the surface with ambient temperature air flow from a drier and a fan.

It is shown that moderate blowing of the breast with air flow of ambient temperature in summer provides especially clear imaging of superficial veins in women with "C" breast size or more. However, regardless of this we also found that blowing women breast with air flow of ambient temperature provides rapid screening of breast tumors. Here, to make a conclusion the following should be taken into consideration: if thermal camera breast image is homogeneous in terms of color, it implies that it is homogeneous in terms of its local temperature. Therefore, breast image homogeneity in terms of color and temperature indicates the homogeneity of breast structure. Also, if local hypo- or hyperthermia area is detected, it is recommended to specify its shape, size, and location, and after that make a conclusion about the presence of neoplasms of corresponding shape, size, and localization [19].

3 Conclusion

The illustrations shown above prove the possibility of infrared imaging of superficial veins in different anatomical body areas in the conditions of artificial local change in their temperature. The matter is that nominally homogeneous artificial thermal intervention causes uneven change in the temperature of selected body part in alive humans due to penetrating blood vessels with heat-transfer liquid flowing through them. In this case, it is a network of superficial veins with heat-transfer liquid that is the closest to the body surface and plays the role of a superficial radiator that resists the homogeneous surface temperature change in the most effective way. Therefore, the body surface in the area of such projected natural radiator changes its temperature differently than the neighboring areas without them. This principle of inhomogeneity of local tissue temperature is proposed to use for improving the efficiency of infrared imaging of veins as compared to using radiopaque agents in vessel X-ray imaging. That is why this method of displaying invisible vessels was called temperature-based tissue contrasting. In its turn, the technique for imaging veins using temperature-based contrasting may be referred as "infrared phlebography."

References

1. Berberich, J., Hirsh, S.: Roentgenography of blood vessels. Klin Wochenschr **2**, 2226–2228 (1923)
2. McCullough, P.A.: Contrast-induced acute kidney injury. J. Am. Coll. Cardiol. **51**(15), 1419–1428 (2008)
3. Mercer, J.B., Ring, E.F.G.: Fever screening and infrared thermal imaging: concerns and guidelines. Thermol. Int. **19**(3), 67–99 (2009)
4. Ammer, K.: Temperature gradients in Raynaud's phenomenon. Comparison by gender, age class and finger involvement. Thermol. Int. **20**(3), 100–109 (2010)

5. Urakov, A.L., Kasatkin, A.A., Urakova, N.A., et al.: Infrared thermographic investigation of fingers and palms during and after application of cuff occlusion test in patients with hemorrhagic shock. Thermol. Int. **24**(1), 5–10 (2014)
6. Faust, O., Acharya, U.R., Ng, E.Y.K., et al.: Application of infrared thermography in computer aided diagnosis. Infrared Phys. Technol. **66**, 160–175 (2014)
7. Urakov, A., Urakova, N., Kasatkin, A.: Thermal imaging improves the accuracy hemorrhagic shock diagnostics: the concept and practical recommendation. LAP LAMBERT Academic Publishing (2016)
8. Ng, E.Y.K., Acharya, R.U.: Remote-sensing infrared thermography. IEEE Eng. Med. Biol. Mag. **28**, 76–83 (2009)
9. Acharya, U.R., Ng, E.Y.K., Tan, J.H., et al.: Thermography based breast cancer detection using texture feautures and support vector machine. J. Med. Syst. **36**(3), 1503–1510 (2012)
10. Kasatkin, A.A.: Effect of drugs temperature on infrared spectrum of human tissue. Thermol. Int. **23**(2), 72 (2013)
11. Kasatkin, A.A., Urakov, A.L., Lukoyanov, I.A.: Nonsteroidal anti-inflammatory drugs causing local inflammation of tissue at the site of injection. J. Pharmacol. Pharmacother. **7**, 26–28 (2016)
12. Urakov, A.L., Urakova, N.A., Urakova, T.V., et al.: Method of subcutaneous veins imaging in infrared radiation spectrum range according to A.A. Kasatkin. RU Patent 2,389,429 20 May 2010 (2010)
13. Urakov, A.L., Rudnov, V.A., Viter, V.I., et al.: Method for monitoring irritant effect of intravascular catheters. RU Patent 2,405,585 10 December 2010 (2010)
14. Urakov, A.L., Urakova, N.A., Khafiz'janova, R.K., et al.: Method of extremity vein catheterization. RU Patent 2,428,220 10 September 2011 (2011)
15. Kasatkin, A.A., Reshetnikov, A.P.: Assessing the irritating effect of intravenous catheters by infrared thermography. Thermol. Int. **24**(2), 64–65 (2014)
16. Urakov, A.L., Urakova, T.V., Urakova, N.A., et al.: Method of infra-red diagnostics of cheek structure. RU Patent 2,544,291 20 March 2015 (2015)
17. Urakov, A.L., Urakova, T.V., Reshetnikov, A.P., et al.: Method for infrared visualisation of foreign matters in hand. RU Patent 2,557,687 27 July 2015 (2015)
18. Urakov, A.L.: The change of physical-chemical factors of the local interaction with the human body as the basis for the creation of materials with new properties. Epitőanyag—JSBCM **67** (1):2–6 (2015)
19. Urakov, A.L., Urakova, T.V., Urakova, N.A., et al. (2015) Method for infrared screening of breast growths. RU Patent 2,561,302, 27 August 2015

Intraoperative Thermal and Laser Speckle Contrast Imaging Assessment of Bowel Perfusion in Two Cases of Colorectal Resection Surgery

Costanzo Di Maria, Paul J. Hainsworth and John Allen

Abstract The Microvascular Diagnostics Service at Freeman Hospital, Newcastle upon Tyne, holds a comprehensive range of optical and thermal technologies utilised to study the microcirculation both for clinical and research purposes. In the recent years, collaboration has been formed with the colorectal surgical service to look at the feasibility and clinical value of intraoperatively assessing bowel perfusion using microvascular imaging technologies. Anastomotic failure is the most serious complication following colorectal resection that can lead to re-operation, permanent stoma, and even death. The current practice of assessing blood perfusion at the anastomosis bowel ends by direct inspection of bowel pulsatility, bleeding, and tissue coloration has been demonstrated to lack predictive accuracy. The medical community is striving to improve the outcome of colorectal resections and a key aspect in achieving this goal will be the development of more objective techniques to intraoperatively assess and quantify the bowel perfusion. We believe that microvascular imaging technology could play a key role in this respect. In this chapter, we describe two case studies which show the feasibility of performing thermal and laser speckle contrast imaging measurements intraoperatively for assessing bowel perfusion during colorectal resection surgery. This experience could pave the way to a number of other applications for these technologies in the surgical arena.

Keywords Anastomosis · Colorectal resection · Laser speckle contrast imaging · Microvascular imaging · Thermal imaging

C. Di Maria (✉) · J. Allen
Microvascular Diagnostics Service, Northern Medical Physics and Clinical Engineering, The Newcastle upon Tyne Hospitals NHS Foundation Trust, Newcastle upon Tyne, UK
e-mail: Costanzo.Di-Maria@newcastle.ac.uk; costanzo.dimaria@nuth.nhs.uk

P.J. Hainsworth
Colorectal Surgical Service, The Newcastle upon Tyne Hospitals NHS Foundation Trust, Newcastle upon Tyne, UK

C. Di Maria · P.J. Hainsworth · J. Allen
Institute of Cellular Medicine, Medical School, Newcastle University, Newcastle upon Tyne, UK

E.Y.K. Ng and M. Etehadtavakol (eds.), *Application of Infrared to Biomedical Sciences*, Series in BioEngineering,
DOI 10.1007/978-981-10-3147-2_25

1 Research Context

1.1 The Microvascular Diagnostics Service

The Microvascular Diagnostics Service at Freeman Hospital, Newcastle upon Tyne, holds a comprehensive range of optical and thermal technologies utilised to study the physical structure and functioning of the human microcirculation. These microvascular optical techniques include tissue oxygenation, spectroscopy, laser Doppler flowmetry and imaging, capillaroscopy, and thermography [1].

Our clinical test portfolio covers many applications, including assessment of patients with suspected connective tissue disease and Raynaud's phenomenon, inflammation and sweating, and also capabilities for specialist limb studies (i.e., amputation level assessment, muscle compartment perfusion and venous physiology), burn wound depth classification and neurovascular function assessment.

The measurement service greatly benefits from a state-of-the-art temperature- and humidity-controlled facility, which enables standardisation and consistency of environment conditions across patients. The room temperature can be efficiently shifted between cold (<15 °C) and hot (>30 °C) for whole body thermal and physiology studies. Most studies are performed in a normothermic environment (23 °C and 45% relative humidity). Studies intended for assessing tissue inflammation are usually performed at cold room temperature (18 °C), which helps contrast between normal tissues and inflamed areas.

Research and development work includes the assessment of microvascular endothelial function [2], autonomic function in chronic fatigue syndrome (myalgic encephalomyelitis) [3], renal fistula viability [4], thermoregulation in restless legs syndrome [5], and inflammation in thyroid eye disease using thermal imaging [6]. Further work includes the evaluation and validation of various clinical applications for photoplethysmography [7–9], fluorescence spectroscopy in scleroderma [10], and thermal imaging to aid targeted Botox treatment planning in Frey syndrome [11]. In the recent years, we have started collaborating with the colorectal surgical service to determine the feasibility and clinical value of intraoperatively assessing bowel perfusion using microvascular imaging technologies. This experience could pave the way to a number of other uses for these technologies in the surgical arena.

1.2 The Colorectal Surgical Service

The Newcastle upon Tyne Hospitals NHS Foundation Trust is the North-East of England's tertiary referral service for a number of surgical disciplines including multiple organ transplantation, soft tissue sarcomas, intestinal failure, colorectal liver resection, services for early rectal cancer and locally advanced/recurrent rectal cancer and transanal endoscopic microsurgery. The Newcastle Surgical Training

Centre provides laboratory based advanced training courses for laparoscopic colorectal surgery.

The hospital sees approximately 280 new colorectal cancers per annum. The majority of cancer and benign bowel resections are performed using minimally invasive techniques and the hospital currently has two da Vinci robots which are used for colorectal resections. National statistics show the hospital to have among the lowest mortality rates for colorectal cancer resections in the country. Members of the team have been responsible for heading up the national programme for enhanced recovery in colorectal surgery.

Departmental research interests include development of enhanced recovery, perioperative fluid balance and nutrition, collaboration with several national trials including early rectal cancer studies. There is a programme looking at several aspects of anastomotic integrity, including development and assessment of various techniques for measuring intraoperative anastomotic blood flow, aiming to reduce complication rates after colorectal surgery.

2 Introduction

Colorectal resection is the surgical removal of a portion of large bowel, and sometimes small bowel, for either malignant or benign disease. The two remaining ends of bowel are joined together creating an *anastomosis* (Fig. 1). Surgery is often performed laparoscopically (*key hole* or *minimal access* surgery).

This operative procedure includes a *preparation* or *mobilisation stage* (which is performed with the bowel inside the abdominal cavity) and a *resection stage* (which may be completed after the affected bowel has been exteriorised out of the abdominal cavity). During the preparation stage, the portion of bowel that is going to be resected is completely devascularised. When the bowel is exteriorised, the portion to be resected is usually visible along with a portion of healthy bowel that will be used to form the anastomosis. The portion that has been devascularised no

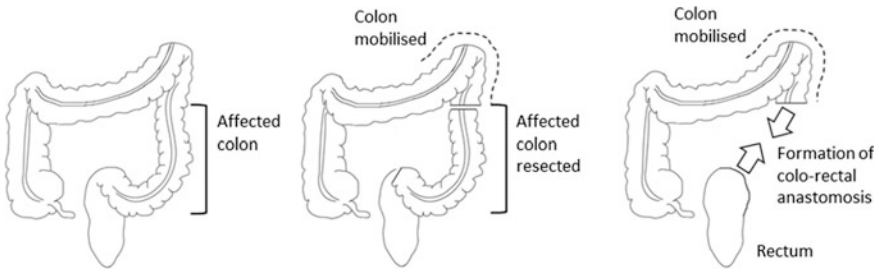

Fig. 1 During colorectal resection surgery, a section of bowel affected by either malignant or benign condition (*left*) is resected (*centre*). The two remaining ends of bowel are then joined together forming an anastomosis (*right*)

longer has direct blood perfusion; the healthy portion still does. The success of the operation depends on healing of the anastomosis, which in turn is recognised to rely on good blood perfusion of the bowel ends at the anastomosis [12]. Currently, bowel blood perfusion is evaluated intra-operatively only by direct inspection of the bowel pulsatility, bleeding, and tissue colouration. However, these measures have been demonstrated to lack predictive accuracy [13] and improvements to this practice are being advocated by the medical community [14].

Microvascular imaging techniques such as thermal imaging (TI) [15] and laser speckle contrast imaging (LSCI) [16] could play an important role in this clinical setting, and ultimately offer a more objective assessment tool. Thermal imaging cameras capture the infrared radiation spontaneously emitted by the human body. The intensity of this radiation is then converted into temperature scale and colour coded to create a temperature map of the area being imaged known as *thermogram*. The tissue temperature can be regarded as a surrogate measure of blood perfusion [17], with higher temperatures being related to higher perfusion. The research into possible medical applications for thermal imaging has been growing into the recent years and many examples are now available in the literature [17, 18]. Laser speckle contrast imaging utilises a coherent infrared beam shone onto the tissue (skin, or internal tissues). The reflected light creates a speckle pattern and statistical techniques are then utilised to quantify the variability of this pattern at different regions within the image over time, with higher variability corresponding to higher blood flow [19].

In this chapter, we present the feasibility of utilising microvascular imaging techniques intraoperatively to identify and objectively quantify the differences in blood perfusion between healthy and devascularised intestine.

3 Methods

3.1 Instrumentation

Thermal imaging was performed using a FLIR A40 thermal camera (Fig. 2, left), which has a spectral range from 7.5 to 13 μm, thermal sensitivity of 0.08 °C at 30 °C, and accuracy of ±2% [20]. Laser speckle contrast imaging was performed using a Moor Instruments FLPI-2 scanner system (Fig. 2, right), which utilises a laser beam at 785 nm wavelength and a cell size for spatial image processing of 5 × 5 pixels; other technical characteristics include acquisition rate up to 25 frames per second and camera resolution of 580 × 752 pixels with a maximum scan size of 15 cm × 20 cm [21].

Before undertaking any measurements in the operating theatre, a technical feasibility stage was performed that included risk assessment, review of electrical safety and infection control guidelines, and pre-clinical measurement. The *risk assessment* was carried out to determine the overall potential risk to patients, staff,

Fig. 2 The FLIR A40 thermal camera (*left*); and the Moor Instruments FLPI-2 scanner system (*right*)

Table 1 Correspondence between risk score and action required to reduce the risk [22]

Risk score	Risk level	Action required
1–3	Low	Minimal
4–6	Medium	Some
8–12	High	Action
15–16	Very high	Urgent
20–25	Extreme	Avoid

The risk score is derived from a matrix that considers the likelihood for a given risk to happen and the severity of the consequences if that risk does happen. Not all combinations are possible and that is the reason why some ranges are not covered in this table. The required action goes from *minimal* (or no cation) up to *avoid* (the risk of the procedure is so high that it is best avoiding it)

and equipment associated with this measurement procedure [22]. The overall risk score was found to be 3 out of 25, which corresponds to low risk (Table 1). The *review* of The Newcastle upon Tyne Hospitals NHS Foundation Trust guidelines on Electrical Safety [23] and Infection Control [24] informed on the most appropriate and clinically safe way to set up our measurement equipment. Electrical Safety measures required setting up a system with cameras and laptops connected to an isolator transformer, and only the latter plugged into the wall socket of the operating theatre room. Infection Control measures required sterilisation of all equipment before entering and leaving the operating theatre using sterile wipes and spray cleaning products. The *pre-clinical measurement* assessments were carried out to evaluate the influence of surgical lights and circulating air currents on the measurements of both cameras, and this was found to be negligible.

The thermal camera was mounted on a tripod and positioned at about 40 cm from the patient with an angle of 60° from the horizontal line. The LSCI camera was mounted on a bespoke boom that positioned the camera perpendicularly over the patient at a distance of 25 cm (accurately determined using the built-in aiming laser functionality). Both cameras were powered up for at least 30 min before

performing any measurements [25]. The skin emissivity parameter for the thermal camera was set to 0.98 [26]. For the laser speckle system, exposure time was set to 20 ms and the time filter to 25 frames.

3.2 Microvascular Imaging

Microvascular imaging measurements were carried out soon after exposure of the bowel (Fig. 3). Close liaison with the surgeon helped determine the most appropriate time for carrying out the measurement. The measurements lasted less than 10 min and this was in order to meet clinical constraint to minimise possible additional risk to the patient due to lengthening of the operation. A maximum window of 10 min was considered to be an appropriate length of time in the context of operations that may last several hours.

3.3 Image Analysis

The thermal images were visualised and analysed offline using FLIR ThermaCAM Research Pro 2.8 software. Temperature was colour-coded with a "rainbow" colour scale [26], across the range 18–36 °C. Two regions of interests (RoIs) were drawn by an expert scientist (CDM), one for the healthy portion of the bowel and one for the portion of bowel that had been devascularised. The temperature of each portion of bowel was calculated as the mean temperature of the pixels within the respective RoI and this was used as a surrogate measure of blood perfusion.

Fig. 3 CDM in the operating theatre performing imaging of the exposed bowel during a case of colorectal resection using thermal imaging (*left*) and laser speckle contrast imaging (*right*)

The laser speckle contrast images were visualised and analysed using Moor Instruments FLPI Review V4.0 software. Flux was colour-coded with a "256 colour palette 1" scale, across the range 100–500 AFU (Arbitrary Flux Units). Similarly to what done with the thermal images, two RoIs were drawn by an expert scientist (CDM), one for the healthy portion of the bowel and one for the portion of bowel that had been devascularised. The flux for each portion of bowel was calculated as the mean flux of the pixels within the respective RoI and this was used as an indirect measure of blood perfusion.

4 Case Study 1

This patient was a 72-year-old man undergoing laparoscopic right hemicolectomy for benign disease. Preoperative fitness assessment revealed the presence of *severe systemic disease* (American Society of Anesthesiologists ASA grade III). Key vital signs—which could influence microvascular measurements—at the time of imaging were as follows: systolic blood pressure 133 mmHg, diastolic blood pressure 70 mmHg, heart rate 65 bpm, peripheral oxygen saturation (SpO_2) 97%, and fraction of inspired oxygen (FiO_2) 0.21.

On thermal imaging, the mean temperature was 28.3 °C for the healthy portion of bowel, and 26.6 °C for the devascularised bowel. On laser speckle contrast imaging, the mean flux was 340 AFU for the healthy portion of bowel, and 67 AFU for the devascularised bowel. Example thermal and laser speckle contrast images are shown in Fig. 4.

5 Case Study 2

This patient was a 54-year-old man undergoing laparoscopic ileocolic resection for benign disease. Pre-operative fitness assessment demonstrated *severe systemic disease* (American Society of Anesthesiologists ASA grade III). Key vital signs—which can influence microvascular measurements—at the time of imaging were as follows: systolic blood pressure 152 mmHg, diastolic blood pressure 78 mmHg, heart rate 104 bpm, peripheral oxygen saturation (SpO_2) 97%, and fraction of inspired oxygen (FiO_2) 0.60.

On thermal imaging, the mean temperature was 30.0 °C for the healthy portion of bowel, and 28.1 °C for the devascularised bowel. On laser speckle contrast imaging, the mean flux was 380 AFU for the healthy portion of bowel, and 162 AFU for the devascularised bowel. Example thermal and laser speckle contrast images are shown in Fig. 5.

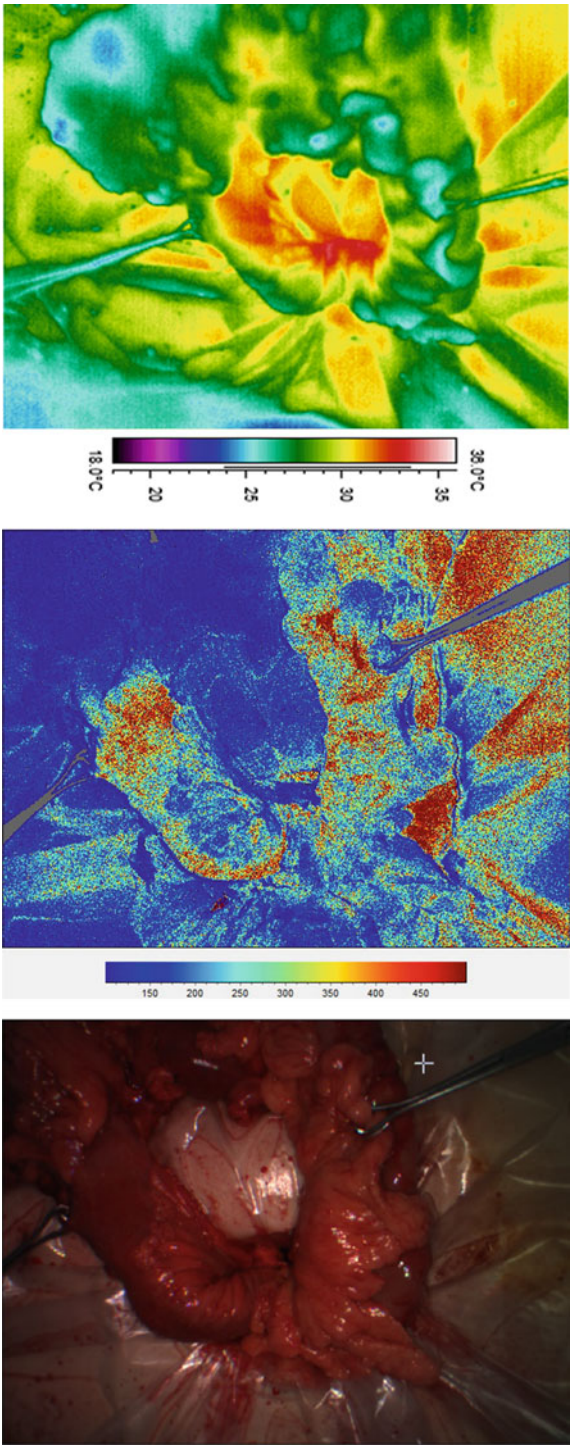

Fig. 4 Example thermal image (*top*) and laser speckle contrast image (*centre*) from patient in case study 1. For reference, the visible light image is also shown (*bottom*). Tissue holding forceps are positioned at the points where bowel was going to be divided. The portion of bowel above the forceps in the picture was going to be removed and had already been devascularised; therefore, it was no longer normally perfused at the time when microvascular images were taken. The portion of bowel below the forceps level was going to be preserved and it was still vascularised and perfused at the time of imaging. The thermal image scale is given in degree Celsius. The laser speckle contrast image scale is given in arbitrary flux units (AFU)

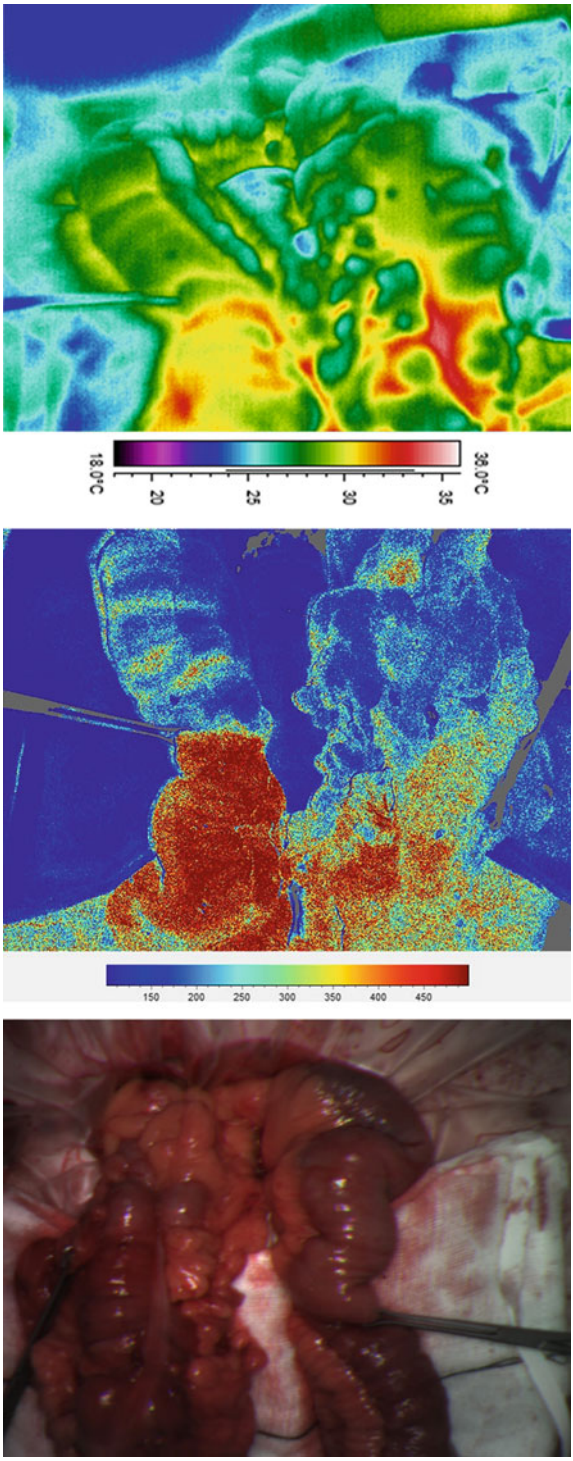

Fig. 5 Example thermal image (*top*) and laser speckle contrast image (*centre*) from patient in case study 2. For reference, the visible light image is also shown (*bottom*). Tissue holding forceps are positioned at the point where the bowel was going to be divided. The portion of bowel above the forceps in the picture was going to be removed and had been devascularised; therefore, it was no longer normally perfused at the time when microvascular images were taken. The portion of bowel below the forceps was going to be preserved and it was still vascularised and perfused at the time of imaging. The thermal image scale is given in degree Celsius. The laser speckle contrast image scale is given in arbitrary flux units (AFU)

6 Discussion and Conclusion

Anastomotic failure is the most serious complication following colorectal resection that happens in up to 19% of cases [27] and can lead to re-operation, permanent stoma, and even death. The current practice to assess the quality of blood perfusion at the bowel ends before creating the anastomosis by direct inspection of bowel pulsatility, bleeding, and tissue coloration has been demonstrated to lack predictive accuracy [13]. The medical community is striving to improve the outcome of colorectal resections [14] and a key aspect in achieving this goal will be the development of more objective techniques to intraoperatively assess and quantify the bowel perfusion. In this chapter, we have described our experience in setting up a system using microvascular imaging technology and have demonstrated the feasibility of performing such measurements intraoperatively. It was possible to obtain high-quality images in a very short length of time and providing objective quantification of blood perfusion.

Thermal imaging allows for rapid and non-contact intraoperative evaluation of bowel blood perfusion during colorectal resection surgery. An electrical system needs to be set up appropriately and a sterilisation procedure carefully followed to meet Electrical Safety and Infection Control requirements [23, 24]. Using a modern handheld and battery-powered camera could simplify these procedures. Measurements can be performed in less than 10 min, which is a clinically acceptable length of time in the context of surgical operations that may last several hours. Tissue temperature measurements can be regarded as a surrogate measure of blood flow [17], with higher temperatures mirroring higher blood flow. For the patient in case study 1, the devascularised bowel was found to be 1.7 °C colder than the healthy bowel; for the patient in case study 2, the devascularised bowel was found to be 1.9 °C colder than the healthy bowel (Table 2). These findings are consistent with the fact that the devascularised portion of bowel did not have direct blood supply at the time of imaging.

Laser speckle contrast imaging measurements can also be performed in less than 10 min, and it is a non-contact technology as well. Similar measures need to be implemented in order to meet Electrical Safety and Infection Control [23, 24]. LSCI

Table 2 Summary of the temperature and flux characteristics in the two portions of bowel for the two case studies. TI thermal imaging; LSCI laser speckle contrast imaging

	Case study 1	Case study 2
TI temperature (°C)		
Normal bowel (*a*)	28.3	30.0
Devascularised bowel (*b*)	26.6	28.1
Difference ($a - b$)	+1.7	+1.9
LSCI flux (AFU)		
Normal bowel (*c*)	340	380
Devascularised bowel (*d*)	67	162
Ratio ($c \div d$)	5.1	2.3

AFU arbitrary flux units

technology gives an indirect measure of blood flow known as flux. For the patient in case study 1, the flux in the devascularised bowel was found to be five times lower than in the healthy bowel; for the patient in case study 2, the flux in the devascularised bowel was found to be half the value of the healthy bowel (Table 2). These findings are consistent with the fact that the devascularised portion of the bowel did not have direct blood supply at the time of imaging.

In conclusion, both TI and LSCI were able to reliably detect the expected differences between the two portions of bowel in both case studies. The differences found with LSCI were larger in value than those found with TI and this is possibly due to the fact that the two techniques inherently measure different physiological phenomena. LSCI is a more direct measure of blood flow and so, when this is (almost) completely inhibited, the flux as measured by LSCI very quickly reduces. TI measures tissue temperature (as surrogate of blood flow) and it takes some time for this temperature to drop significantly after inhibition of the blood flow. As a consequence, LSCI could potentially be able to detect differences in blood perfusion between patients with finer resolution. The space resolution offered by LSCI is also finer than what possible with TI (Figs. 4 and 5). However, LSCI is more sensitive to movement artefacts and statistical noise [28]. This experience of performing intraoperative microvascular measurements was extremely valuable and could pave the way also to a number of other applications for these technologies in the surgical arena.

References

1. Allen, J., Howell, K.: Microvascular imaging: techniques and opportunities for clinical physiological measurements. Physiol. Meas. **35**, R91–R141 (2014)
2. McKay, N., Griffiths, B., Di Maria, C., Hedley, S., Murray, A., Allen, J.: Novel photoplethysmography cardiovascular assessments in patients with Raynaud's phenomenon and systemic sclerosis: a pilot study. Rheumatology **53**, 1855–1863 (2014)
3. Allen, J., Murray, A., Di Maria, C., Newton, J.: Chronic fatigue syndrome and impaired peripheral pulse characteristics on orthostasis—a new potential diagnostic biomarker. Physiol. Meas. **33**, 231–241 (2012)
4. Allen, J., Oates, C., Chishti, A., Ahmed, I., Talbot, D., Murray, A.: Thermography and colour duplex ultrasound assessments of arterio-venous fistula function in renal patients. Physiol. Meas. **27**, 51–60 (2006)
5. Anderson, K., Di Maria, C., Allen, J.: Novel assessment of microvascular changes in idiopathic restless legs syndrome (Willis-Ekbom disease). J. Sleep Res. **22**, 315–321 (2013)
6. Di Maria, C., Allen, J., Dickinson, J., Neoh, C., Perros, P.: Novel thermal imaging analysis technique for detecting inflammation in thyroid eye disease. J. Clin. Endocr. Metab. **99**, 4600–4606 (2014)
7. Allen, J.: Photoplethysmography and its application in clinical physiological measurement. Physiol. Meas. **28**, R1–R39 (2007)
8. Allen, J., Overbeck, K., Nath, A., Murray, A., Stansby, G.: A prospective comparison of bilateral photoplethysmography versus the ankle-brachial pressure index for detecting and quantifying lower limb peripheral arterial disease. J. Vasc. Surg. **47**, 794–802 (2008)

9. Mizeva, I., Di Maria, C., Frick, P., Podtaev, S., Allen, J.: Quantifying the correlation between photoplethysmography and laser Doppler flowmetry microvascular low-frequency oscillations. J. Biomed. Opt. **20**, 037007 (2015)
10. Allen, J., Di Maria, C., Murray, A., Ottewell, L., Griffiths, B.: Utility of combined fluorescence spectroscopy and tissue oxygen saturation measurements in systemic sclerosis: a pilot study. In: 65th Meeting of the British microcirculation society. Abstract in: Microcirculation, vol. 22, pp. 542–676 (2015)
11. Green, R., Endersby, S., Allen, J., Adams, J.: Role of medical thermography in treatment of Frey's syndrome with botulinium toxin. A short communication. Br. J. Oral Maxillofac. Surg. **52**, 92 (2014)
12. Urbanavičius, L., Pattyn, P., Van de Putte, D., Venskutonis, D.: How to assess intestinal viability during surgery: a review of techniques. World J. Gastrointest. Surg. **3**, 59 (2011)
13. Karliczek, A., Harlaar, N.J., Zeebregts, C.J., Wiggers, T., Baas, P.C., van Dam, G.M.: Surgeons lack predictive accuracy for anastomotic leakage in gastrointestinal surgery. Int. J. Colorectal. Dis. **24**, 569–576 (2009)
14. The Association of Coloproctology of Great Britain and Ireland (ACPGBI).: Guidelines for the management of colorectal cancer. ACPGBI, London (2007)
15. Ring, E.F.J., Ammer, K.: Infrared thermal imaging in medicine. Physiol. Meas. **33**, R33–R46 (2012)
16. Briers, J.D.: Laser Doppler, speckle and related techniques for blood perfusion mapping and imaging. Physiol. Meas. **22**, R35–R66 (2001)
17. Ring, F., Jung, A., Žuber, J. (eds.): Infrared imaging: A Casebook in Clinical Medicine. IoP Publishing (2015)
18. Ammer, K., Ring, F. (eds.): The thermal Image in Medicine and Biology. Uhlen-Verlag, Wien (1995)
19. Boas, D., Dunn, A.: Laser speckle contrast imaging in biomedical optics. J. Biomed. Opt. **15**, 011109 (2010)
20. Thermovision A40 M technical specifications. FLIR Systems Inc. (2005). www.flir.com
21. moorFLPI-2 technical benefits. Moor Instruments Ltd., issue 2. www.moor.co.uk
22. The Newcastle upon Tyne Hospitals NHS Foundation Trust.: Risk register—policy for management and use. Internal policy
23. The Newcastle upon Tyne Hospitals NHS Foundation Trust.: Electrical safety policy. Internal policy
24. The Newcastle upon Tyne Hospitals NHS Foundation Trust.: Decontamination of healthcare equipment following patient use and prior to service or repair. Internal policy
25. Richards, R.E., Allen, J., Howell, K.J., Smith, R.E.: Evaluation of three thermal imaging cameras for skin temperature measurement using a blackbody reference source and a spatial resolution test object. Thermol. Int. **13**, 17–23 (2013)
26. British Standards Institution. BS EN 80601-part 2-59: 2009. Medical Electrical Equipment. Particular requirements for the basic safety and essential performance of screening thermographs for human febrile temperature screening. BSI, London (2010)
27. Matthiessen, P., Hallböö, O., Rutegard, J., Simert, G., Sjödal, R.: Defunctioning stoma reduces symptomatic anastomotic leakage after low anterior resection of the rectum for cancer: a randomized multicenter trial. Ann. Surg. **246**, 207–214 (2007)
28. Briers, D., Duncan, D., Hirst, E., Kirkpatrick, S., Larsson, M., Steenbergen, W., Stromberg, T., Thompson, O.: Laser speckle contrast imaging: theoretical and practical limitations. J. Biomed. Opt. **18**, 066018 (2013)

Author Biographies

Costanzo Di Maria (MIET) is a Research Scientist with the Northern Medical Physics and Clinical Engineering directorate at Freeman Hospital, Newcastle upon Tyne, United Kingdom. He is also a Research Associate with the Faculty of Medical Sciences, Newcastle University. His intense research activity within the microvascular service focuses on signal processing, image analysis, data and statistical analysis for the development of novel clinical diagnostic tools, especially utilising optical technologies for the study of microcirculation. He also works in other areas including uterine electromyography, non-invasive foetal electrocardiogram, and clinical engineering. Costanzo is a Full Member of the Institution of Engineering and Technology, an Ordinary Member of the European Association of Thermology, and an Associate Member of the Institute of Engineering and Physics in Medicine.

Newcastle University: http://www.ncl.ac.uk/icm/people/profile/costanzo.di-maria
Research Gate: http://www.researchgate.net/profile/Costanzo_Di_Maria

Paul J. Hainsworth (MB, BS, MD, FRCS) is Foundation Colorectal Surgeon at Freeman Hospital, Newcastle upon Tyne, United Kingdom. He is also Honorary Clinical Lecturer at the Faculty of Medical Sciences, Newcastle University. Paul has got major interest in minimally invasive surgery for colorectal cancer and inflammatory bowel disease, including robotics and transanal microsurgery. He has published in the fields of technical surgery, cancer genetics and inflammatory bowel disease.

John Allen (Ph.D., ASIS FRPS) is Lead Clinical Scientist for Microvascular Diagnostics based in the Northern Medical Physics and Clinical Engineering directorate at the Freeman Hospital. He is the founder of this Newcastle measurement facility and leads service development and associated R&D. John is also an Honorary Clinical Senior Lecturer in the Faculty of Medical Sciences at Newcastle University. His Ph.D. was awarded in 2002 on photoplethysmography and cardiovascular assessments. He has published and presented many papers on various clinical vascular optical measurements and has secured team awards at national level for medical technology and service innovations. He is also a Chartered Engineer and Scientist, a Fellow of the Royal Photographic Society (ASIS FRPS), and a member of the Editorial Board for the journal Physiological Measurement.

Newcastle University: http://www.ncl.ac.uk/icm/people/profile/john.allen
Research Gate: https://www.researchgate.net/profile/John_Allen9

An Approach for Thyroid Nodule Analysis Using Thermographic Images

J.R. González, É.O. Rodrigues, C.P. Damião, C.A.P. Fontes, A.C. Silva, A.C. Paiva, H. Li, C. Du and A. Conci

Abstract Thyroid cancer is said to be the second most common type of cancer in female individuals and the third in males by 2030, according to projections. In general, detecting cancer in its early stages improves the chance of survival of the individual. Thermography is a diagnostic tool that has been increasingly used to detect cancer and abnormalities, including that of thyroid. Various methods to segment and detect hot regions in thermograms and, consequently, to detect suspicious tissues present in these images have been proposed. It is well known that medical diagnosis yields a great deal of information. Thus, physicians have to comprehensively analyse and evaluate this information in a short period of time, which is infeasible in most cases. In this work, we perform a general review of thermography, focusing on the thyroid analysis. We propose protocols for image acquisiton and an autonomous registration for thyroid images. We also perform analyses of the image data, which include feature extraction, image processing, and

J.R. González · É.O. Rodrigues (✉) · A. Conci
Computer Science Department, Universidade Federal Fluminense,
Av. Milton Tavares de Souzas, s/n—Boa Viagem, Niterói, RJ 24210-330, Brazil
e-mail: erickr@id.uff.br

J.R. González
e-mail: jgonzalez@ic.uff.br

A. Conci
e-mail: aconci@ic.uff.br

C.P. Damião · C.A.P. Fontes
Radiology Department, Hospital Universitário Antônio Pedro (HUAP),
Av. Marquês do Paraná, 303, Niterói, RJ, Brazil
e-mail: charbeldamiao@yahoo.com.br

C.A.P. Fontes
e-mail: cfontes@id.uff.br

A.C. Silva · A.C. Paiva
Applied Computation Group NCA-UFMA, Universidade Federal do Maranhão,
Av. dos Portugueses, São Luís, 1966, MA, Brazil
e-mail: ari@dee.ufma.br

E.Y.K. Ng and M. Etehadtavakol (eds.), *Application of Infrared to Biomedical Sciences*, Series in BioEngineering,
DOI 10.1007/978-981-10-3147-2_26

a possible approach for classification of healthy or unhealthy patients. In summary, this work presents a pilot project for detection of tumors in our university hospital, which is part of an effort to support preventive medical actions in our endocrinology department. Under some future adjustments, this project will be submitted for approval by the ethics and research committee of Hospital Universitário Antonio Pedro at Universidade Federal Fluminense (HUAP-UFF) and to the Brazilian Ministry of Health Ethical committee under the name: Evaluation of the importance of thermography to aid diagnosis of thyroid nodules of patients in HUAP-UFF (in Portuguese: Avaliação da importância da termografia no auxílio à investigação diagnóstica de nódulos tireoidianos em pacientes acompanhados no HUAP-UFF).

Keywords Thyroid cancer · Neck nodule · Thermography · Image registration · Classification · Threshold · Sobel · Image analysis

1 Introduction

Equipment used in medical investigation usually rely on local changes in body parameters like density, sound propagation, electromagnetic resonance, etc. Healthy and diseased areas of the human body can be analysed and compared when using these equipment. In general, features extracted from both healthy and diseased areas are usually processed and ultimately compared to infer a diagnosis. These features can be anything that stems from the information encapsulated by these images. However, when primary features such as the physical information are compared directly, it yields low recognition rates [1]. In contrast, more robust features are usually more valuable, e.g., features that extract information from an area of the image instead of a single point, since areas are analysed as a whole.

The temperature distribution on the human skin can be captured with a proper camera, resulting in a thermal image (Fig. 1). These images represent temperature patterns of the body, which are highly symmetric with respect to the vertical axis of

A.C. Paiva
e-mail: paiva@deinf.ufma.br

H. Li
School of Mathematical Sciences, Shandong Normal University,
88 East Wenhua Road, Jinan, Shandong 250014, People's Republic of China
e-mail: lihl@sdnu.edu.cn

C. Du
School of Mathematical Sciences, University of Jinan, 336 West Road
of Nan Xinzhuang, Jinan, Shandong 250022, People's Republic of China
e-mail: sms_duchb@ujn.edu.cn

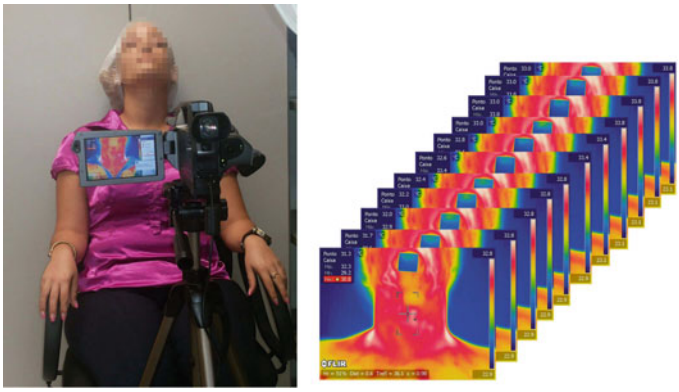

(a) Thermography acquisition. (b) Infrared image sequencing.

Fig. 1 Thermographic imaging

the sagittal plane. Variations of this infrared map on serial imaging (images taken over time) can also evidence a sign of abnormality. Thermography detects temperature modifications in tissues that appear before or during many diseases, including cancer. Besides, it also detects physiologic or functional changes, but it does not have the ability to pinpoint the internal location of the problem. However, the Pennes equation [2] can be used to describe the contributions of the internal body elements to the skin thermal distribution. In such equation, the heat transfer problem is written in a simplified form. However, the thermal conductivity of tissues, their density, the specific heat of the blood, blood perfusion rate, metabolic heat generation rate, core temperature of the body, arterial blood temperature, environment and local temperature of each tissue must be known a priori.

Artificial intelligent methods can also be used to predict and find abnormalities in images. In this case, a reasonable number of exams with proven diagnosis, i.e., ground truth, is usually required. These labelled exams are used by a classification algorithm as source of information for finding patterns. The found patterns are used to classify patients whose diagnoses are unknown. In order to be consistent in this process, the same acquisition protocol, conditions and computer processing techniques should be respected for every patient.

The methodology to capture the images can either consider a (1) dynamic acquisition protocol [1], where several images are acquired as a time series, or a (2) static protocol, where one single image is acquired [3]. In the dynamic protocol, the area to be examined is cooled by an air stream before the examination, which changes the patient body temperature. Meanwhile, a series of images are acquired while their body return to the thermal equilibrium with the environment (Fig. 1b shows a time series).

During the acquisition process, the patients breathe (inhale and exhale) performing some small movements. These movements change the coordinates of points of their body in relation to a previously acquired image. Figure 2 shows the exact movement of keypoints over the time series acquisition. Figure 2a shows a common point located at the patient chin, and Fig. 2b shows a common point located at the patient's neck. Errors can be propagated to the subsequent computational analyses if these errors are not corrected. Therefore, approaches to relate these points should be one of the first steps in the computational analysis of these thermograms.

It is possible to correct these differences using a process named image registration [4], which is more extensively addressed in the next section. Registrations are based on global or local transformations and are fundamental in time series acquisition [5]. Image registration usually matches the maximum number of common points in the images using various types of transformations respecting rigid bodies (translation and rotation) or nonrigid bodies (transformations that do not preserve the distances between two points) [6].

The use of very generic or incorrect transformations increases the overall processing time and may not even produce adequate registered images. To achieve an efficient registration, the movements that the patients perform must be carefully analysed. A function that is sufficient to correct the performed movements must be known a priori to improve the processing time. For instance, there is no need to apply a complex warping or perspective transformation if a simple translation is enough, which is also far less complex.

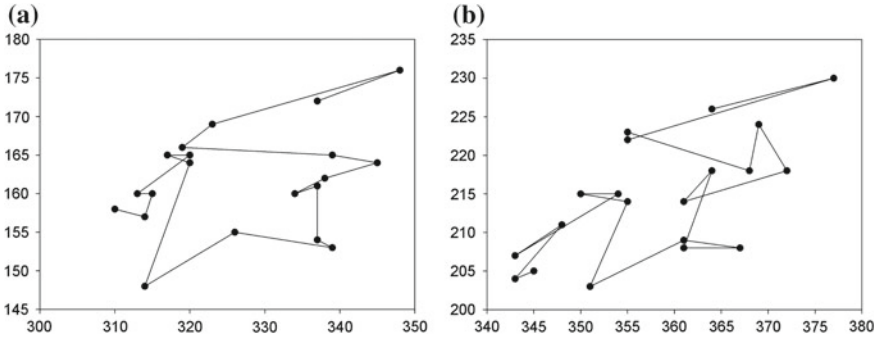

Fig. 2 Displacement of common keypoints over the time series acquisition

2 Literature Review

Thermographic cameras are built with sensors that capture infrared (IR) rays. The camera sensor is able to perceive radiation at temperatures above absolute zero. All objects that have temperatures above this value (i.e., 0 K or −273 °C) emit infrared radiation. The measured infrared radiation emitted by one point of the skin can be converted directly to a temperature value that represents this point.

Some diseases trigger physiological and biological processes that interfere with the human temperature distribution. Nitric oxide, for instance, which is produced by cancer cells, interferes with the normal neuronal control of blood vessel flows, causing a local vasodilation in the early stages of cancerous growth, and also enhancing the angiogenesis in later stages. Increased blood flows can raise the temperature of the related area. Deep lesions seem also to have the ability to induce changes in the skin temperature. Cancerous metabolic processes also seem to contribute to the detectable heat increase.

Among other approaches, IR thermography can detect a disease or abnormality by identifying temperature differences on the symmetric areas being compared. Physiological changes and the development of neoangiogenesis are often associated to these asymmetric temperatures distributions. Asymmetry between symmetric areas is one of the most important indicators that can be quantified. Locating areas within the region of interest (ROI) that contain a high degree of blood perfusion or vessels is also of great importance. Thermogram interpretation is based, in most occasions, on exaggerate vascularisation, hot spots and on asymmetries between the said symmetric areas.

The next sections of this work present a small survey on infrared imaging for thyroidal screening and addresses related works in the light of their applications in computer vision and medicine. Consequently, the ideas in the following two sections are organized according to the standard flowchart of pattern recognition systems. The entire process is composed by: (1) image acquisition protocols, (2) storage, (3) Region of Interest (ROI) and registration, (4) segmentation methods, (5) feature extraction, (6) classification or diagnosis.

2.1 Acquisition Protocol

A protocol for thermal imaging can be categorized as static or dynamic, based on the behaviour of the body in relation to heat transfer. In the static acquisition, the body of the patient is thermally stabilized with the environment. On the other hand, static acquisition relies on the thermal equilibrium of the patient with the environment. Dynamic acquisition is applied to monitor the recovery of the skin temperature after an induced thermal stress (e.g., heating or cooling) or chemical stress (e.g., vasoconstrictions or vasodilations).

The type of acquisition can also be categorized according to the repetition as single, sequential or accompanied capture. In single acquisitions, an image of the patient is captured in an instant of time. This type of acquisition is suitable to identify cold and hot spots and for measuring the asymmetries on skin temperature. In the sequential mode, however, a series of images are acquired sequentially. Finally, in the accompanied mode, the acquired images are separated by a substantial time interval (usually 3 or 6 months) in order to follow the progress of some disease and also to detect it early (i.e., to detect changes in the patterns early).

The influence of the room temperature, as well as the stabilization time of the body in relation to this temperature was investigated by Usuki et al. [7]. In dynamic acquisitions with cold stress protocols, the expected pattern is a balance between heat conduction from tissues and deeper vessels, and heat loss by radiation and air convection at the surface. Beyond the image acquisition, some important aspects should be regarded as well, such as date of examination and patient's age, as well as use of drugs or hormonal therapy.

An alternative acquisition protocol was evaluated by Agostini et al. [8]. The proposed protocol aims to observe the influence of blood perfusion and skin temperature fluctuation. The authors acquire a sequence of consecutive thermal images with rate ranging from 50 to 200 frames/s. Thereafter, they use the frequency domain of the small temperature fluctuation in the studied area, rather than considering the classical static skin temperature. Kapoor et al. [9] recommend their patients to stop smoking for 2 hours before the test, to avoid alcohol and caffeine, and to not apply lotions on the acquisition area. Ng et al. [3] do also orient patients to abstain from any physical activities for 20 min before the exam, in order to reduce the body metabolism and stabilize the body temperature.

2.2 Registration

Image registration is a mapping of points that relate two images where one is usually called reference or fixed image and the other is usually called sensible or moving image. Registration is an optimization problem where the goal is to maximize the correspondence of points from the reference image to the ones in the sensible image using transformations [10]. Figure 3 shows an overall example of a registration.

A desirable registration or transformation T is achieved when the statement $T(SensibleImage) \cong ReferenceImage$ is true. The symbol $\cong$ represents an approximation and is subjective. The comparison depends on the similarity measure chosen to compare the reference and transformed images. After the transformation, the image is converted from the function domain to a raster. That is, rasterization is the defined as the process of discretizing and painting pixels from the function domain to a grid (e.g., an image, screen, etc). Interpolations are required for doing so. The entire registration process is shown in Fig. 4.

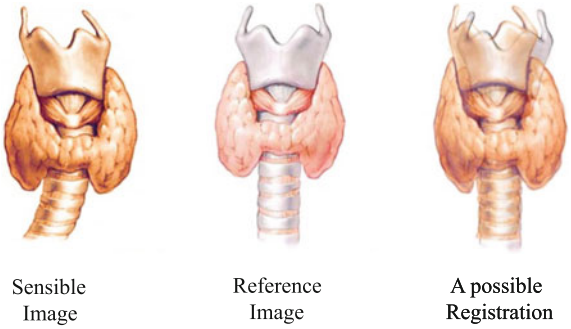

Fig. 3 A registration result

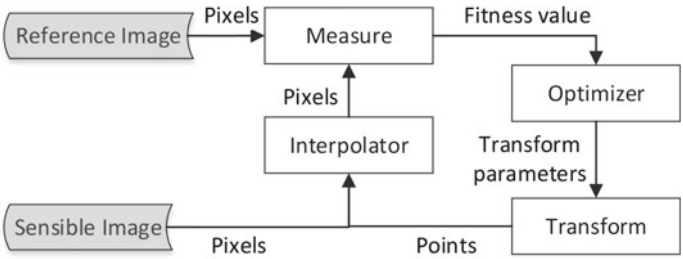

Fig. 4 A registration process

Patients may undergo various magnetic resonance (MR), computed tomography (CT), single proton emission computed tomography (SPECT), and other imaging techniques for general or anatomical reference of a single organ. Therefore, physicians' analyses are benefited from registrations of images from any combination of modalities (including just a single modality). For instance, in radiotherapy treatments, both CT and MR can be used. CT is needed to compute the radiation dose accurately, while MR is usually better for delineating tumor tissues [11].

According to Maintz et al. [11], registrations are divided in three main categories: (1) the intrinsic, (2) the extrinsic and (3) nonimage based. In intrinsic registrations, the corresponding methods are based only on image-related content. The intrinsic registration can be based on the alignment of segmented binary structures or on a limited set of identified salient points (landmarks or keypoints).

In extrinsic registrations, artificial objects are attached to the patient, which are designed to be well visible and accurately detectable in all of the pertinent modalities. Therefore, the registration is comparatively fast and easy, which can virtually always be automated. Furthermore, since its parameters can be often computed explicitly, this kind of registration usually does not demand complex optimization algorithms.

Alternatively, registrations can also be nonimage based. If the imaging coordinate systems of the two scanners involved are calibrated to each other, then registrations can be performed automatically. In this case, scanners are usually required to be brought into the same physical location. Furthermore, it is also required to assume that the patient performs no movements between acquisitions.

Rigid transformations stand for a group of transformations where the distances between every pair of points are preserved [12, 13]. Therefore, rigid transformations comprise operations like translations and reflections, rotations, or combinations of these operations (some authors do not consider reflection as a rigid transformation). Affine transformations regard functions between affine spaces. These transformations preserve straight lines, points, as well as planes [14]. Operations such as scaling, translation, homogeneous and inhomogeneous dilations, reflections, shear mapping rotations and aggregations of these operations are defined as affine. The different types of transformations are depicted in Fig. 5. The overall range of transformations can either be (1) local, i.e., applied with regards to a certain region or (2) global, i.e., applied to the whole image.

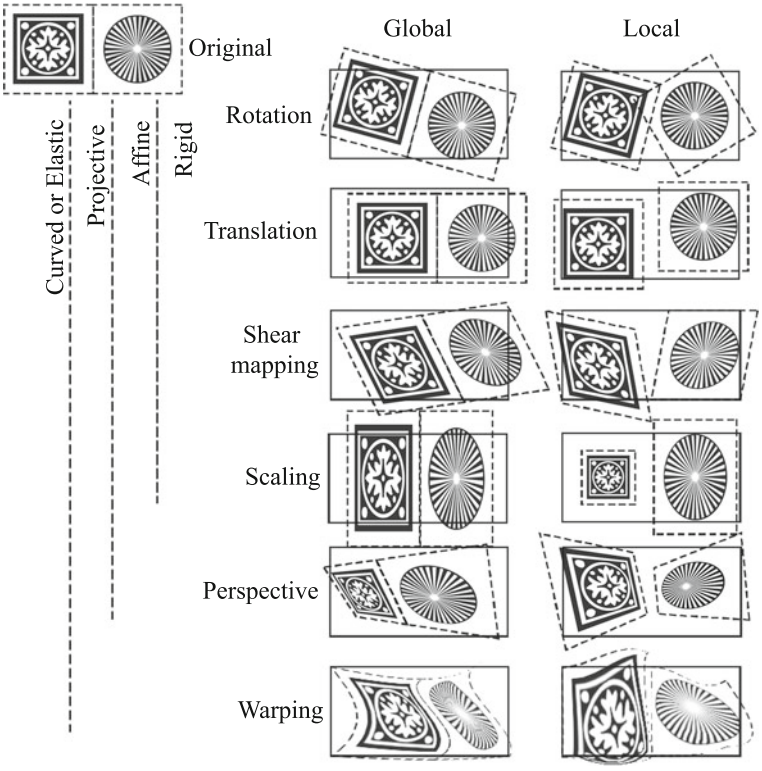

Fig. 5 Possible types of transformations performed in registrations

In this work, we just consider rigid transformations, which in $\mathbb{R}^2$ are usually expressed as a linear matrix multiplication with homogeneous coordinates as shown in Eq. 1.

$$\begin{bmatrix} x' \\ y' \\ l \end{bmatrix} = \begin{bmatrix} \cos\theta & sen\,\theta & t_x \\ sen\,\theta & \cos\theta & t_y \\ 0 & 0 & 1 \end{bmatrix} \begin{bmatrix} x \\ y \\ l \end{bmatrix}, \tag{1}$$

where (x', y') represents the transformed coordinates and (x, y) the coordinates before the transformation. θ represents the angle of rotation and t_x as well as t_y the translation on the respective axes x and y.

Common points of the reference and sensible images can be placed manually or autonomously to compose a landmark or keypoint registration approach. If this is the case, there must be a good precision in order to select the correct pixel in each image. However, it is difficult to manually place points when the number of required points is huge. For this case, some techniques can be used to autonomously detect points in the images such as the Scale-Invariant Feature Transform (SIFT) [15], Affine Scale-Invariant Feature Transform (ASIFT) [16], Speed Up Robust Features (SURF) [17], Harris Corner Detector (HARRIS) [18], etc. However, the disadvantage of these methods is that they often provide point correspondences that are not real. Besides, the amount of points can be huge, which may require some heuristic to discard and consequently reduce the number of points.

2.3 Thyroid-Related Review

The thyroid is a neuroendocrine gland located at the human neck, next to the thyroid cartilage and over the trachea. The function of the gland is to regulate the metabolism of the body, produce proteins and to regulate the body sensibility with regards to other hormones. Some diseases are associated to the malfunction of the thyroid gland, which are usually related to iodine deficiency, such as goiter, hypothyroidism, thyroiditis, and random nodules that may be cancerous.

Thyroid nodules are a common clinical problem, and thyroid cancer is becoming more prevalent. According to the data provided by the American Thyroid Association in 2015 [19], papillary cancer can be the third most common type of cancer in women in 2019. In 2030, it can be the second most common in women and the third in men. Among the main types of cancer there are (1) the well-differentiated ones (papillary, follicular and the ones caused by Hurthle cells), (2) the medullar, and (3) the anaplastic.

In [20], the author observed that thyroid glands produce a very characteristic thermal pattern, which is of easy recognition. However, under hypoactivity, this pattern is not visible. Besides, this work reinforces that it is possible to discriminate benign nodules from malignant ones, according to the temperature pattern. It has

also been observed that cancerous cells raise the temperature on neighboring regions. It also states that the more superficial the lesion, the higher is the temperature on the skin.

Clark et al. developed a prospective study using echography, ultrasound, and thermography on the preoperative evaluation of thyroid nodules [21]. Their objective was improving the accuracy on the differentiation between benign and malignant thyroid nodules, and determining the reliability of echography and thermography on distinguishing between solid and cystic thyroid nodules. The patients were in the supine position with the neck hyperextended. Sixty-one patients were analysed by clinical examination. By the combined use of echography and thermography, the authors were able to distinguish accurately between cystic and solid thyroid nodules.

In [22], D'Arbo et al. studied the usefulness of thermography in the selection of thyroid nodules for surgery. 124 thyroid nodules from 110 patients with ages in the range of 2–77 years old were studied. A hundred of these thyroid nodules were mapped as cold and the rest as hot. Sixteen cold nodules and two hot nodules were diagnosed as malignant. Each test took 15 minutes. Three different techniques were evaluated: heat index (related to a mean temperature of the region where the nodule was palpated), curve or thermal profile (established in respect to a middle point of the region) and, differences of the isotherms (related with the points of the higher temperature in the region compared to a near healthy area).

A design of a prototype device is proposed by Helmy and collaborators in [23]. It is an economical non-invasive system that detects and displays the relative skin temperature variations present in human patients suffering from thyroid disorders. In [24], the authors developed and described a model for thyroid glands, and simulated them using finite element analysis. This model was developed in order to determine the necessary resolutions for thermal sensors that are used to obtain the thermal images of patients' necks. In 2008, an improvement of this prototype was proposed [25]. The authors also present a finite-element analysis of a hot thyroid nodule. This analysis was used to investigate the temperature distribution.

In 2015, a successful computer model utilizing ANSIS software was proposed [26]. This simulation model incorporates three heat transfer coefficients: conduction, convection, and radiation. While the conduction component was a major contributor to the simulation model, the other two coefficients have improved the accuracy and precision of the model. This study also compares simulation data with the applied model generated from IR probe sensors. These data were analysed and processed to produce a thermal image of the thyroid gland. The acquired data were then compared with an Iodine uptake scan of the same patients.

In [27, 28], Gavriloaia et al. explain the details of a system used for acquiring infrared images of necks for thyroid nodules analysis. In these works, the Penne's equation and its applications were analysed. In [27], a few infrared images are explored with the aim of finding infrared signatures that can be descriptors of the thyroid tumors. The authors found that the contour of cancerous nodules is irregular and asymmetric. Using the ABCDE investigation method (based on features as

Asymmetry, Border, Color, Diameter, and Evolution of the contour), 89.3% of the investigated patients with thyroid cancer were correctly recognized.

In [29], the authors apply fractal theory to quantify the irregularity in size and shape of thermal signatures of tumors. The self-similarity and lacunarity features were employed. In [30], an improved method for IR image filtering is proposed. This study is aimed at developing a numerical scheme that significantly reduces the computing time required for thermal image denoizing with edge preservation. This filter allows physicians to assess, faster than using other anisotropic diffusion filters, the contour shape, and to locate the outbreaks in ROIs. Another filtering is used in [31] to improve the quality of the information in thermographic images. In this case, the empirical mode decomposition was used, and it was proved that one or at most two intrinsic mode functions (IMFs) are enough for minimizing the noise effect.

The authors in [31] use thermography with other imaging modalities to diagnose thyroid problems. This work also evidences that female individuals are more susceptible to thyroid diseases than male and that hyperthyroidism is more common than hypothyroidism. The works [32, 33] employ an Otsu thresholding technique to separate the thyroid ROI from the rest of the images. In this work, we propose a novel registration and methodology to extract the ROI.

3 Proposed Approach

The images evaluated in this work (a single patient is shown in Fig. 6) were obtained using the FLIR ThermaCam S45 under the approval of the Ethical committee of Universidade Federal Fluminense, Brazil. The thermograms were acquired at the university hospital. All images were taken from patients and volunteers. These images were corrected for relative humidity and temperature of the room and were acquired after requesting patients to wait for 10 min in order to stabilize their metabolism. Four patients are analysed in this work (two healthy and two with pathological diagnosis or an abnormality in the thyroids). The blue square on the patient chin that can be seen in Fig. 6 is a physical marker that was placed at this region to help with the registration and recognition processes.

1. Protocol

With regards to the acquisition, we have used the dynamic acquisition protocol. However, it is slightly in regards to previous work due to the fact that it has a stopping condition for the thermal stress. Initially, the patient must be sitting down in order to minimize the possible displacements that he or she may perform. When the mean temperature of the skin decreases to 29 °C, the thermal stress is ceased and the sequential acquisition is started. One image is captured at every 15 s over 5 min, which produces the sequence of images shown in Fig. 6. The distance from the camera to the patient is 0.5 m, as shown in Fig. 1. The relative humidity of air and room temperature is recorded and inserted as parameters in the camera.

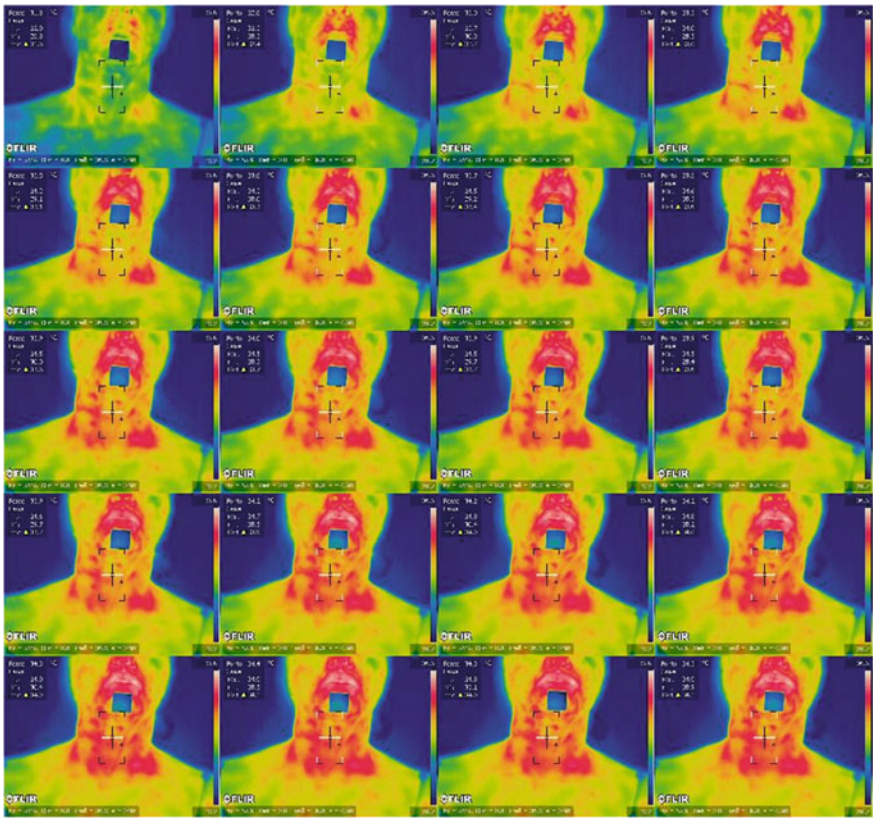

Fig. 6 Sequence of 20 thermal images from an examination

2. Recommendations to Patients

At least 2 h before the examination the patient should avoid: alcohol, caffeine, physical exercises, nicotine and should not apply any cream, oil or deodorant.

3. Room Conditions

Room temperature is maintained between 22 and 25 °C, no windows, no openings, no air flow directed to the patient, and only fluorescent bulbs.

4. Preparation of the patient.

Inside the examination room, the patient is asked to remove earrings, necklaces or any other accessory that can be seen in the thermal image, central temperature is checked by a thermometer and hair stuck with a burrow. The patient must be in the room 20 min before starting the examination and should be sitting with his head tilted slightly back and looking up during acquisition.

3.1 *Preprocessing—Movements During Acquisition*

An important step in the processing of thermograms in the dynamic acquisition is registration. Figure 7 shows super-positions of two images of a single patient that moved during the acquisition (the first and the last one acquired in a sequence of 20 images). As it can be seen, the movements performed by the patients misalign the image content. By analyzing these movements, we can transform one of the images to resemble the other as much as possible. It can be done automatically or manually, and that usually involve transformations and similarity measures to compare the images, as previously addressed. As a remark, the green border of Fig. 7 precedes the red border.

Figure 8 compares the subsequent superposition of acquired images pairwise. It can be noted that the movements are not as severe as in Fig. 7. However, even slightly movements can impact on further processings. The extent of the movement does also vary depending on the patient.

The majority of the movements performed by patients can be described as follows:

1. Full-body Modification

Includes lateral movements to the left or right (Fig. 9a), movements to the top or bottom (Fig. 9b), or combinations of both movements. These tilts can be corrected with a rigid transformation: translation and rotation.

2. Local Modifications

These modifications include movements related to perspective and distortion, such as tilts of the head to the back or front. Figure 10 shows these tilts that disrupt the border of the head without altering the border of the shoulders so much. In these images, the chin of the patient was in a different position regarding the two acquisitions (red and green). These movements and distortions can be corrected with elastic (e.g., perspective, warping, etc.) transformations, which are more complex and more expensive (computational power-wise) than the rigid ones.

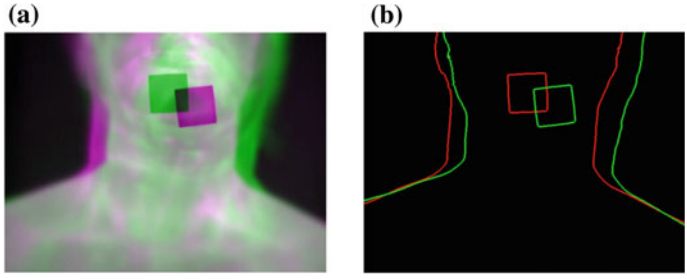

Fig. 7 Movements of a patient during the image acquisition

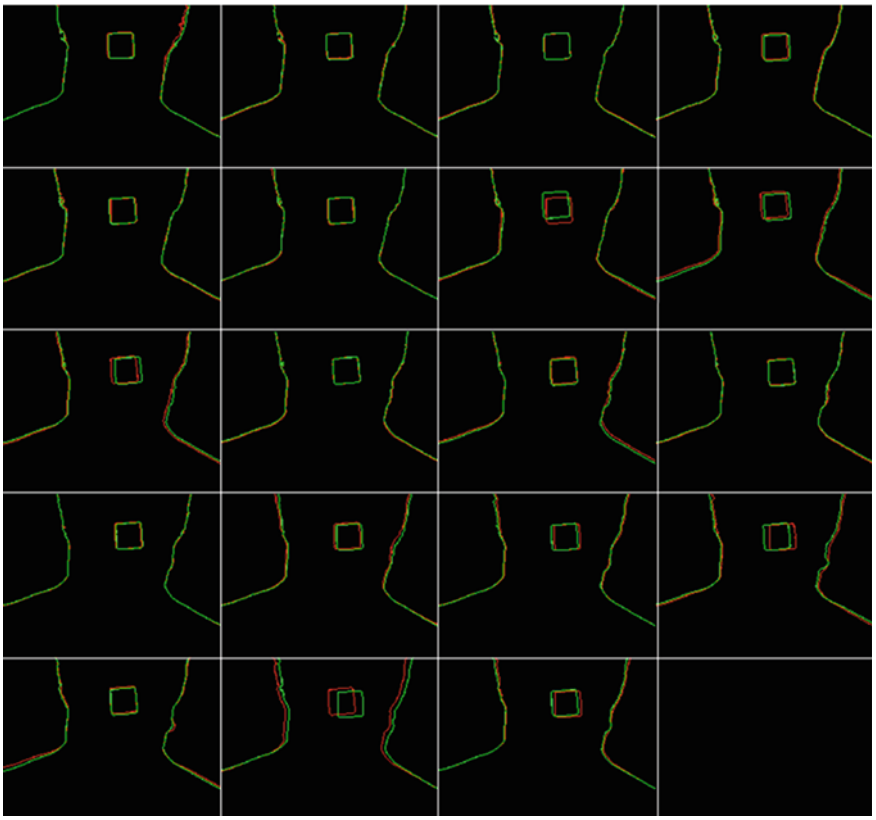

Fig. 8 Subsequent movements on a time series acquisition

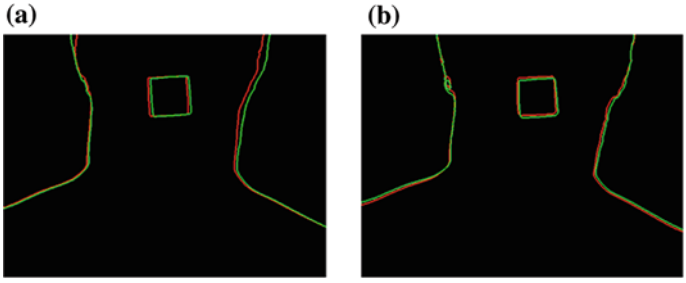

Fig. 9 Slightly movements during the image acquisition

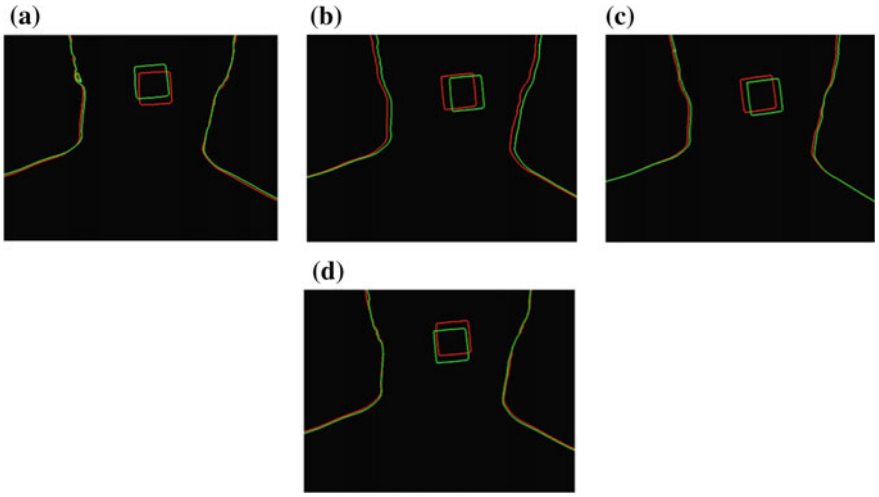

Fig. 10 Complex movements during the image acquisition

3.2 Proposed Registration

As previously discussed, registrations can be oriented by user intervention, where the user selects common points from both images. The advantage of such semi-manual registrations is that they are usually very accurate. However, at the same time they are time consuming and due to that fact it is not practical in several occasions. If some landmarks or keypoints are chosen on the subsequent images such as in Fig. 11, we can use this information to align the images by simply matching the points. Then, we would have something like Fig. 12.

It can be seen in Fig. 12 that the sequence of images is more aligned than in Fig. 8, since we have performed a semi-manual registration. It can also be noted that errors are present still. That is partially because we employed simple operations like translation and rotations only, and also due to the fact that the whole image was registered at once.

3.2.1 Autonomous Registration

Besides this semi-manual registration, we propose a possible autonomous registration for the thyroid thermographic images. At first, we apply a filter based on the Sobel operator, which was presented in a previous work [34] and is available at [35]. The filter is a modification of the classical Sobel filter, it is simple and considers kernels of variable sizes.

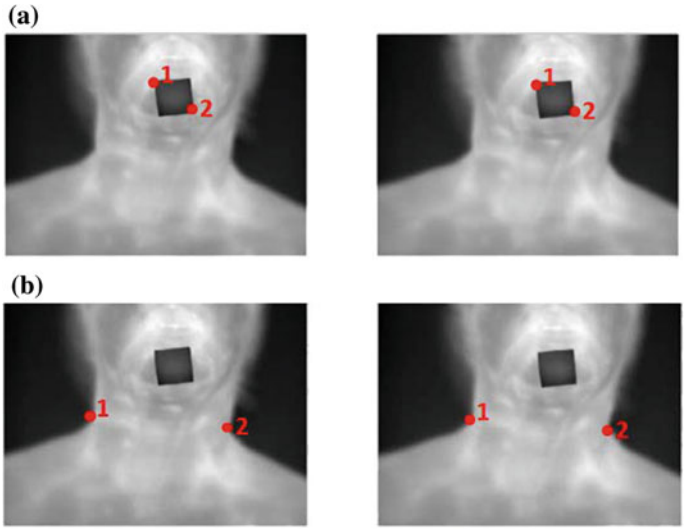

Fig. 11 An example of landmark or keypoint selection

The Shadow and Light Sobel filters are defined by Eqs. 2 and 4, respectively, where P represents the image and $P_{i,j}$ a value of a pixel at line i and column j, t represents a threshold for the edge to be painted, and d a distance parameter (in classical Sobel operators d would be close to 1), and $\wedge$ represents the boolean *and* operation.

$$\mathrm{SS}(P,d,t,i,j) = \begin{cases} 1, & \text{if } (s_1 \wedge s_2) \\ 0, & \text{otherwise} \end{cases} \tag{2}$$

where,

$$\begin{aligned} s_1 &= P_{i-d,j} - P_{i,j} > t \wedge P_{i+d,j} - P_{i,j} > t, \\ s_2 &= P_{i,j-d} - P_{i,j} > t \wedge P_{i,j+d} - P_{i,j} > t \end{aligned} \tag{3}$$

and

$$\mathrm{LS}(P,d,t,i,j) = \begin{cases} 1, & \text{if } (l_1 \wedge l_2) \\ 0, & \text{otherwise} \end{cases} \tag{4}$$

where,

$$\begin{aligned} l_1 &= P_{i,j} - P_{i-d,j} > t \wedge P_{i,j} - P_{i+d,j} > t, \\ l_2 &= P_{i,j} - P_{i,j-d} > t \wedge P_{i,j} - P_{i,j+d} > t \end{aligned} \tag{5}$$

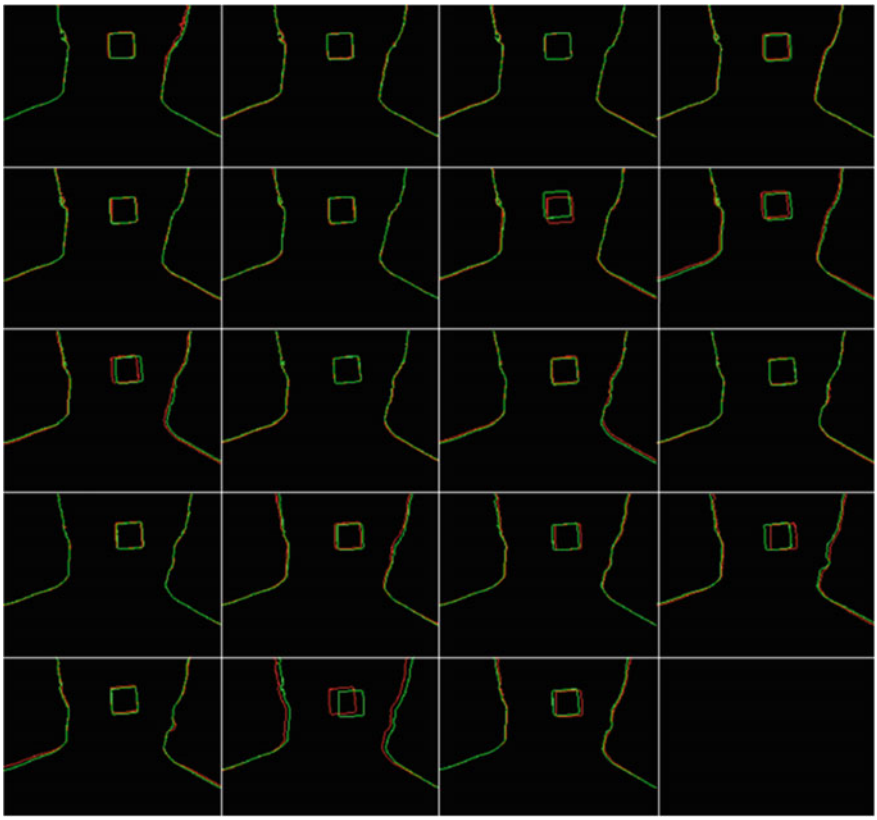

Fig. 12 Registered subsequent images

The main difference between the variables $s_{1..2}$ and $l_{1..2}$ is the orientation of the computation, which captures either light or shadow valleys in each occasion. The parameters used in the proposed process were $t = -40$, and we have performed it only for the shadow and on the x-axis since it provided better results. That is, the LS function was disregarded as well as s_1. Thus, the function in Eq. 6 was applied to the images.

$$\mathrm{SS}(P,d,t,i,j) = \begin{cases} 1, & \text{if } (P_{i-d,j} - P_{i,j} > t \wedge P_{i+d,j} - P_{i,j} > t) \\ 0, & \text{otherwise} \end{cases} \tag{6}$$

Figure 13 shows the results of this filter applied to Fig. 13a. It can be noted that the lateral parts of the neck are clearly segmented and all the remaining stuff in the image is removed. From that image (Fig. 13b), it is very easy to cut off a rectangular shape of the area containing these lines, which would be our ROI.

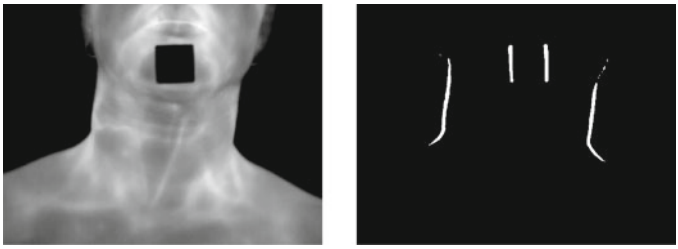

(a) Input image of a random patient.

(b) Image a after applying the filter.

Fig. 13 Our Sobel-like filter

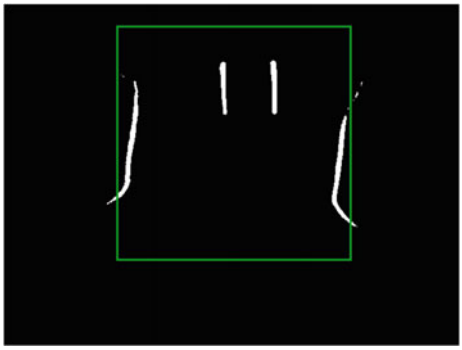

Fig. 14 Autonomously detecting the ROI

Given a rectangle of fixed width and height (we have used 330 for width and 310 for height), a few candidate positions can be evaluated, and the one that contains the highest amount of white pixels would be the chosen ROI. Figure 14 shows an outcome of this described processing. The width or height of the rectangle can be reduced in order to produce different results.

It is clear by Fig. 14 that the two lines on the center of the image (which correspond to the physical marker) influence the position of the green rectangle. Therefore, the rectangle is forced upwards due to this residual "noise."

One would argue that we can erase these two central residuals by using the same heuristic described to find the ROI. And in fact we can. If we reduce the size of the rectangle and apply the same idea, we would find the central residuals. After that, we could just erase them completely from the image. Figure 15 shows the same idea when the size of the rectangle is reduced to 110×110.

After locating the residual noise we remove them. If the same heuristic is performed again, starting from bottom to top with regards to the y-axis, then we have the result shown in Fig. 16.

After extracting the ROI, we can use the different extracted ROIs to perform the registration. There are essentially two paths to follow. The ROI can be extracted before the registration or after the registration. In both ways, the described

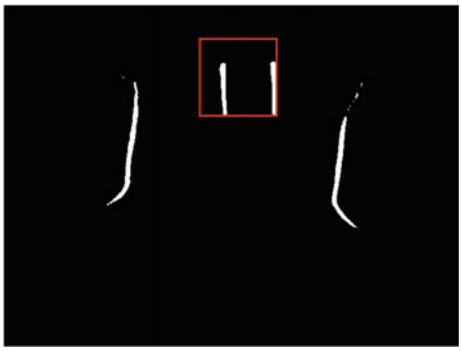

Fig. 15 Removing the residuals

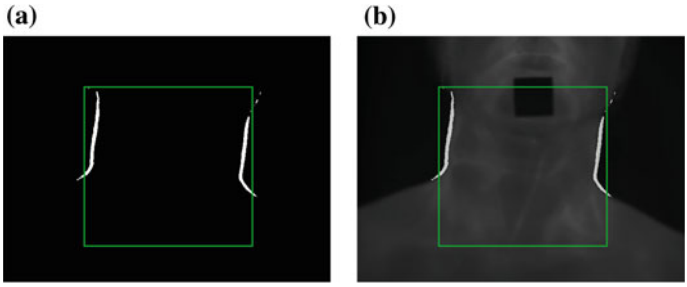

Fig. 16 Final autonomous recognition of the ROI

methodology using the Sobel derived filter would not change and would still be valid. However, there are some strengths and weaknesses on both of the approaches, which are discussed below.

1. ROI before Registration

In this case, just the neck region is considered for registration. The positive side of this is that the registration would probably be more accurate, since we would disregard the information of the shoulders and other structures. For instance, we have observed that some patients perform movements with their heads while their shoulders stand still. If the head is moved, so is the neck. In that way, if the shoulders are regarded in the registration, then they would influence the final registration result. And since the shoulders are already aligned, the registration would not change the image significantly.

The disadvantage of this approach is that the comparison of the images would have to be done regarding the intensity values of the ROIs, which is slightly slower to compute than to consider a few keypoints of both images. However, it is still very fast, lasting only a few milliseconds for a pairwise comparison. As a remark, the intensity values can also vary considerably from one image to another, so that a

proper similarity measure should be employed. A simple similarity measure such as the mean difference would probably achieve a bad performance. The Chamfer distance [34] would probably be more accurate.

2. ROI after Registration

In this case, it is easier to find common landmarks or keypoints between the images, since the shoulders and other structures are still present in the image. However, it would introduce the errors of the shoulders and other structures into the registration, which should be for the neck only in the first place.

Furthermore, no information is disregarded before the registration, so that it can be used for any further processing if required, even to help with the diagnosis, as opposed to the previous paradigm.

3.3 *Feature Analysis and Classification*

We have also noticed that it is possible to locate the nodule of sick patients with a simple threshold operation (which was confirmed by a specialist on the available images). However, we are not sure if this is true for a wider group of diseased patients although it seems so. A threshold operation takes the image as input and changes the pixel or temperature value to white if it is higher or equal than a threshold value or changes it to black if it is lower. The threshold value was set to 209, so, values higher or equal than 209 become white and values lower than that become black.

Given the thresholded images in Fig. 17, it is already possible to extract some valuable information from them. Three features directly based on the area segmented by the threshold operation along with a symmetrical feature were analysed. The features based on the segmented area are computed on the basis of all the pixels within the segmented hot region.

The features based just on the thresholded area are (1) the mean intensity, (2) the standard deviation of these intensities and (3) the maximal intensity or temperature. The fourth feature quantifies the level of symmetry of each ROI in each image, with respect to the vertical axis, and is based on the idea that if two pixels belong to the same symmetric zone then their intensities should be the similar. Thus, the absolute difference between these values should be minimal.

We analyse the intensity values of all the pixels of the ROI in the following manner: let m and n be the height and width of the ROI, $n/2$ be half of the ROI rectangle width (due to the vertical symmetry axis) then, for each pixel (i,j) of the left part of the ROI, we look for the most similar intensity value in the neighborhood (3×3) of the pixel $(i, n-j)$, which is located at the right part of the ROI. Similarly, for each pixel on the right side, a similar intensity is searched for in the

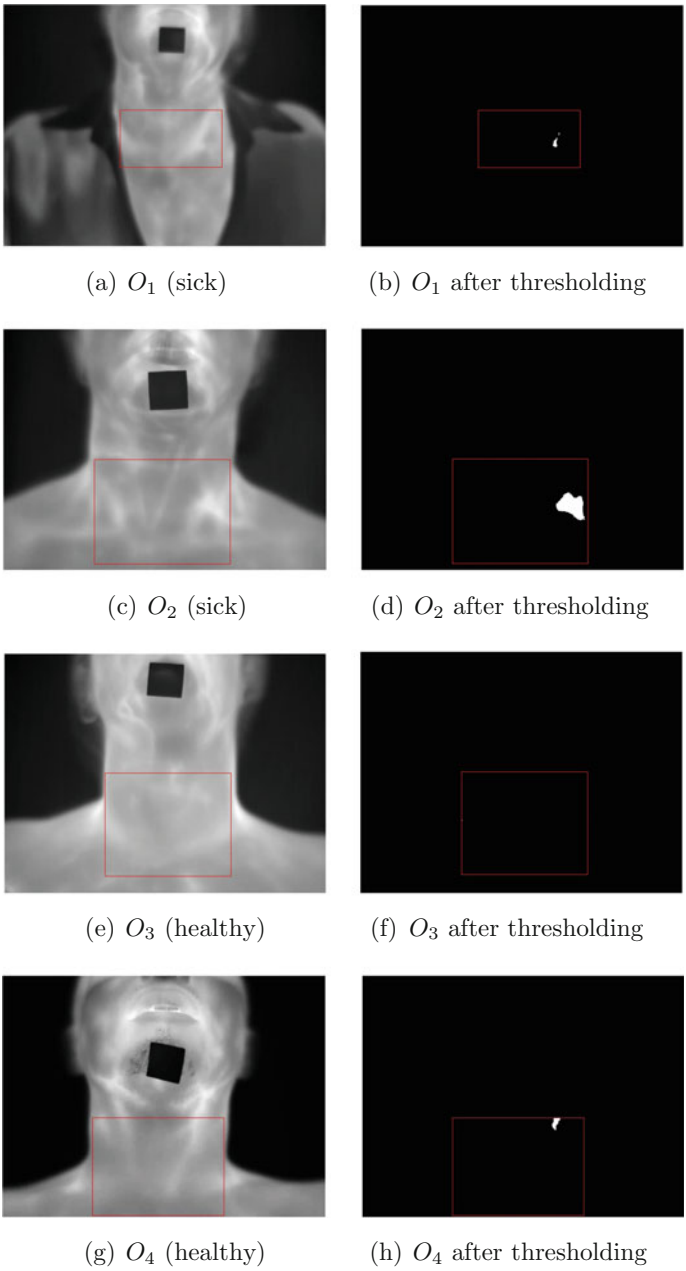

(a) O_1 (sick) (b) O_1 after thresholding

(c) O_2 (sick) (d) O_2 after thresholding

(e) O_3 (healthy) (f) O_3 after thresholding

(g) O_4 (healthy) (h) O_4 after thresholding

Fig. 17 Temperature analysis

left part in the same fashion. The asymmetry level is given by Eq. 7, which stands for the average sum of the absolute values of the intensity difference of each pixel and its most similar one. The difference between each pair of pixels is normalized regarding the highest intensity value (in this case, 255).

$$\mathrm{Asy}(I) = \frac{1}{mn}\left(\sum_{i=1}^{m}\sum_{j=1}^{\frac{n}{2}}\frac{\min_{p,q=-1:1}|I(i,j)-I(i+p,n-j+q)|}{255} + \sum_{i=1}^{m}\sum_{j=\frac{n}{2}+1}^{n}\frac{\min_{p,q=-1:1}|I(i,j)-I(i+p,n-(n-j)+q)|}{255}\right) \tag{7}$$

We have employed the *k*-Nearest Neighbor (*k*-NN) algorithm to perform a classification using the extracted features, where the Euclidean distance was regarded and k was equal to 1. As previously mentioned, two patients contain nodules (O_1 and O_2) while the other two do not (O_3 and O_4). Table 1 shows the Euclidean distances of patient O_1 in relation to all the others. It can be observed that patient O_1 is tightly related to patient O_2, which makes sense, because both of these patients are sick.

Each patient has four feature values. For each patient, we take their four feature values and compute their distance in regards to all the feature values of the remaining patients. For instance, the distance from the standard deviation of O_1 is calculated in relation to the standard deviation of O_2, O_3 and O_4. That calculation is performed for each feature (normalized mean intensity, standard deviation, normalized maximum temperature and asymmetry). For each pair of patients we have a total of four distance values, which represent the four features.

Thus, the lesser the distance value between patients O_k and O_l, the closer patient O_k is in relation to patient O_l and vice-versa. Therefore, in Table 1, the minimal distances of the four features are all related to O_2, which indicates that O_1 is tightly related to O_2. In Table 2, three features indicate that O_3 is related to O_4, so that we assume that its class is the same class as of O_4, which is healthy. For the patient O_2, two of its features indicate similarity with O_1, while the remaining two were closer to O_3. Three features indicate that O_4 can be classified as healthy.

Table 1 Euclidean distance of patient 1 (O_1) in relation to the remaining

Feature	O_2	O_3	O_4
Normalized mean intensity	**0.172**	0.8216	0.414
Standard deviation	**14.648**	28.826	37.26
Normalized maximum temperature	**0.157**	0.833	0.315
Asymmetry	**0.053**	0.063	0.070

Bold values indicate the nearest value, or the smallest difference between the features of patient O_1 and the remaining

Table 2 Euclidean distance of patient 1 (O_3) in relation to the remaining

Feature	O_1	O_2	O_4
Normalized mean intensity	0.821	0.848	**0.811**
Standard *d*eviation	28.826	20.963	**15.977**
Normalized maximum temperature	**0.833**	0.898	0.971
Asymmetry	0.063	0.014	**0.006**

Bold values indicate the nearest value, or the smallest difference between the features of patient O_3 and the remaining

4 Conclusion

This chapter reports a small scale preliminary study that evaluates the feasibility with regards to time, cost, and effect of the use of infrared imaging as a tool in the detection and analysis of thyroid nodules. We perform an overall analysis of thermographic images, focusing on thyroid thermographic acquisition, processing and classification, which is a new field of study. We discuss the data and different approaches with regards to a computer science background, in order to extract, make sense of the information captured by these images, and eventually predict or provide automatic diagnoses.

An autonomous ROI identification for the thyroid images is proposed, which is based on very simple fundamentals of computer vision. We have discussed different approaches with regards to the registration and ROI extraction of these images, highlighting the advantages and disadvantages of each one. More specifically, we discuss whether it is better to extract the ROI before the registration rather than after.

Furthermore, we have also performed an extraction and analysis of four features from the ROI of the patients using a classification algorithm (*k*-NN). In our analysis, we found some evidence that these features may be sufficient to predict whether a patient is sick or not.

Future work involve improving the described methodologies and analysing the reported evidences with regards to a large scale of data. Since there is still a lack of thermographic thyroid images with abnormalities in our repository, we were forced to work with the currently available images. Still, we expect that the evidence found in this work applies to the general case.

Acknowledgments The authors would like to thank to CAPES, CNPq (Project: N0. 201542/2015-2 PQ—CA: EM), FAPERJ and FAPEMA, Brazilian agencies, for partially funding this work. This research has also been partially supported by projects INCT-MACC and SiADE.

References

1. Silva, L.F.A, Santos, A.S.M.D., Bravo, R.S., Silva, A.C., Muchaluat-Saade, D.C., Conci, A.: Hybrid analysis for indicating patients with breast cancer using temperature time series. Comput. Methods Programs Biomed. **130**, 142–153 (2016)

2. Pennes, H.: Analysis of tissue and arterial blood temperatures in the resting human forearm. J. Appl. Physiol. **1**, 93–122 (1948)
3. Ng, E., Kee, E.: Integrative computer-aided diagnostic with breast thermogram. J. Mech. Med. Biol. **7**, 1–10 (2007)
4. Brown, L.G.: A survey of image registration techniques. ACM Comput. Surv. **24**, 325–376 (1992). doi:10.1145/146370.146374
5. Lima, S.S.: Registro de imagens térmicas da mama adquiridas dinamicamente, D. Sc. Thesis, Universidade Federal Fluminense—RJ/Brazil (2015)
6. Espejo, V.M.A.: Registro de imÃ¡genes mediante transformaciones lineales por trozos, ACM Computing Surveys
7. Usuki, H., Ishimura, K., Hagiike, M., Okano, K., Izuishi, K., Karasawa, Y., Goda, F., Maeta, H.: Thermographic examination for carcinoma. Biomed. Thermol. **24**, 1–7 (2002)
8. Agostini, V., Delsanto, S., Knaflitz, M., Molinari, F.: Noise estimation in infrared image sequences: a tool for the quantitative evaluation of the effectiveness of registration algorithms. IEEE Trans. Biomed. Eng. **55**, 1917–1920 (2008)
9. Kapoor, P., Prasad, S.V.A.V.: Image processing for early diagnosis of breast cancer using infrared images. In: 2nd International Conference on Computer and Automation Engineering, vol. 13, pp. 564–566 (2010)
10. Suen, S., Lam, E., Wong, K.: Photographic stitching with optimized object and color matching based on image derivatives. Opt. Express **15**, 7689–7696 (2007)
11. Maintz, J.B.A., Viergever, M.A.: A survey of medical image registration. Med. Image Anal. **2**, 1–36 (1998)
12. McCarthy, J.M.: Introduction to Theoretical Kinematics. MIT Press (1990) (ISBN 0262132524)
13. Galarza, R., Irene, A., Seade, J.: Introduction to Classical Geometries. Birkhauser (2007)
14. Gabrani, M., Tretiak, O.J.: Elastic transformations. Signals Syst. Comput. **1**, 501–505 (1996)
15. Lowe, D.G.: Distinctive image features from scale-invariant keypoints. Int. J. Comput. Vision **60**, 91–110 (2004)
16. Yu, G., Morel, J.M.: ASIFT: An algorithm for fully affine invariant comparison. IPOL J. Image Process. On Line. http://dx.doi.org/10.5201/ipol.2011.my-asift
17. Bay, H., Ess, A., Tuytelaars, T., Gool, L.V.: Speeded-up robust features (SURF). Comput. Vis. Image Underst. **110**, 346–359 (2008)
18. Harris, C., Stephens, M.: A combined corner and edge detector. Alvey vision Conf. **15**, 147–151 (1988)
19. Haugen, B.R., Alexander, E.K., Bible, E.K., Doherty, G.M., Mandel, S.J., Nikiforov, Y.E., Pacini, F., Randolph, G.W., Sawka, A.M., Schlumberger, M., Schuff, K.G., Sherman, S.I., Sosa, J.A., Steward, D.L., Tuttle, M., Wartofsky, L.: 2015 American Thyroid Association Management Guidelines for adult patients with thyroid nodules and differentiated thyroid cancer
20. Samuels, B.I.: Thermography: a valuable tool in the detection of thyroid disease. Radiology **102**, 59–62 (1972). doi:10.1148/102.1.59
21. Coggs, G.C., Clark, O.H., Greenspan, F.S., Goldman, L.: Evaluation of solitary cold thyroid nodules by echography and thermography. Ultrasound Med. **2**, 265–266 (1976)
22. D'Arbo, M.L., Andrade, J., Cherri, J., Moriya, T., Piccinato, C., Okano, N., Llorach-Velludo, M.A., Iazigi, N.: Papel da termografia na seleção de nódulos tireoidianos de indicação cirúrgica, Arquivo Brasileiro de Endocrinologia e Metabolismo 32
23. Helmy, A.W., Holdmann, M., Rizklla, M.E., Salama, P.: A novel approach for a non-invasive diagnostic technique for thyroid glands using thermographic system. In: Proceedings of Circuits and Systems, vol. 3, pp. 1094–1097 (2000a)
24. Helmy, A.W., Rizkalla, M., Holdmann, M., Salama, P.: Finite element analysis for simulating a hot thyroid nodule. In: Proceedings of Circuits and Systems, vol. 3, pp. 1064–1067 (2000b)
25. Helmy, A., Holdmann, M., Rizkalla, M.: Application of thermography for non-invasive diagnosis of thyroid gland disease. IEEE Trans. Biomed. Eng. **55**, 1168–1175 (2008)

26. Rizkalla, J., Tilbury, W., Helmy, A., Suryadevara, V.K., Rizkalla, M.: Computer simulation/practical models for human thyroid thermographic imaging. J. Biomed. Sci. Eng. **8**, 246–256 (2015)
27. Gavriloaia, G., Ghemigian, A.M., Gavriloaia, M.R.: Infrared signature analysis of the thyroid tumors. In: European Conferences on Biomedical Optics, vol. 7371. http://hdl.handle.net/10.1117/12.831756
28. Gavriloaia, G., Hurduc, A., Ghimigean, A.M., Fumarel, R.: Spatial-temperature high resolution map for early cancer diagnosis. In: Proceedings of Multimodal Biomedical Imaging IV, vol. 7171. http://hdl.handle.net/10.1117/12.809185
29. Gavriloaia, G., Gavriloaia, M.R., Sofron, E., Ghemigian, A.M.: Using fractal analyze of thermal signatures for thyroid disease evaluation. In: Proceedings of SPIE, Advanced Topics in Optoelectronics, Microelectronics, and Nanotechnologies, vol. 782110. http://hdl.handle.net/10.1117/12.882294
30. Gavriloia, B.M., Vizireanu, C.R., Fratu, O., Mara, C., Vizireanu, D.N., Preda, R., Gavriloaia, G.: Thermal image filtering by bi-dimensional empirical mode decomposition. In: Advanced Topics in Optoelectronics, Microelectronics, and Nanotechnologies, vol. 9258. http://hdl.handle.net/10.1117/12.2070375
31. Aweda, M.A., Adeyomoye, A.O., Abe, G.A.: Thermographic analysis of thyroid diseases at the Lagos university teaching hospital, Nigeria. Adv. Appl. Sci. Res. **3,** 2027–2032 (2012). http://hdl.handle.net/10.1117/12.2070375
32. Santiagu, V.: Diagnosis of hypo and hyperthyroid using MLPN network. Int. J. Innov. Res. Sci. Eng. Technol. **3**, 14314–14323 (2014)
33. Mahajan, P., Madhe, S.: Hypo and hyperthyroid disorder detection from thermal images using Bayesian Classifier. In: Advances in Communication and Computing Technologies (ICACACT), pp. 1–4 (2014)
34. Rodrigues, E.O., Porcino, T.M., Conci, A., Silva, A.: A simple approach for biometrics: Finger-Knuckle prints recognition based on a Sobel filter and similarity measures. In: International Conference on Systems, Signals and Image Processing (IWSSIP), pp. 1–4 (2016)
35. Rodrigues, E.O.: Uacari Image Library (2016). https://github.com/Oyatsumi/Uacari

Modeling Thermal Infrared Imaging Data for Differential Diagnosis

Enas Ismail and Arcangelo Merla

Abstract Nowadays, thermal infrared imaging (IRI) is thought to be a fascinating and promising complementary imaging tool regarding typical gold-standard medical imaging for differential diagnosis. This chapter presents the commonly used approaches for modeling thermal infrared data for differential diagnosis purposes. Two main modeling approaches were proposed, i.e., (i) qualitative modeling approach based on using statistical and machine learning techniques, (ii) quantitative modeling approach based on performing mathematical/analytical modeling of the thermoregulatory processes by using three main approaches: (i) empirically using automatic control theory, (ii) non-empirically using bioheat equations and (iii) semi-empirically using both bioheat equations and automatic control theory. Also, three main modeling approaches based on control system theory were presented, i.e., (i-a) time domain analysis of the thermoregulatory system's characteristics through a direct estimation of the closed loop dynamic response parameters of a prototype second-order system, (i-b) a direct identification of thermoregulatory system as a second-order system plus delay time (SOPDT) from a closed-loop step response, and (i-c) a state-space representation of the thermoregulatory system as a first-order differential equation from the experimental IR temperature curves. Moreover, this chapter summarizes the advantages and disadvantages of each modeling approach highlighting its assumptions and approximations. By implementing the proposed modeling approaches, thermal infrared imaging has been demonstrated to be able to (i) identify significant averaged and asymmetric temperature parameters that could be used for disease classification, (ii) provide a direct

E. Ismail (✉)
Department of Biomedical Engineering, Faculty of Engineering,
Minia University, Minia, Egypt
e-mail: enas.ismail@mu.edu.eg

A. Merla
Department of Neuroscience, Imaging and Clinical Sciences,
University "G. d'Annunzio", Via dei Vestini, 31, 66013 Chieti, Italy

A. Merla
ITAB-Institute of Advanced Biomedical Technologies,
Via dei Vestini, 32, 66013 Chieti, Italy

E.Y.K. Ng and M. Etehadtavakol (eds.), *Application of Infrared to Biomedical Sciences*, Series in BioEngineering,
DOI 10.1007/978-981-10-3147-2_27

functional IR indicators of the thermoregulatory malfunctions/alternations indirectly assess the severity of functional perturbation of the autonomic sympathetic and parasympathetic physiological activations in the presence of a disease, (iii) compute physiological information, such as localized blood flow, cardiac pulse, and breath rate, and (iv) identify skin's thermal parameters, location of heat source (particularly the vessels), depth of heat source used for defining the location and geometrical shape of the affected-area, mostly required for tumor detection, and (v) provide a clear description of the underlying alterations in the main thermoregulatory functions as for example, environmental heat exchange process, vasoconstriction and/or vasodilation, and sweating actions. The authors consider this chapter as a good material that provides a great insight about the utility of thermal infrared imaging for medical diagnostic purposes.

Keywords Control system · Finite element analysis · Modeling · Thermal infrared (IR) · Cutaneous temperature · Medical diagnosis · Statistics

1 Introduction

While for differential diagnosis, clinicians have still using the typical gold-standard medical imaging techniques, these days thermal infrared imaging (IRI) is thought to be a fascinating and promising complementary imaging tool regarding these typical gold-standard medical imaging [1, 2]. IRI, in fact, is a 'contactless,' 'non-obstructive,' and 'non-radiating' imaging method for examining physiological capabilities and pathologies associated with the body's thermal homeostatic actions expressed through the skin thermoregulation [1, 3, 4]. It screens cutaneous temperature of the human body by detecting naturally emitted infrared radiation from the skin surface that can be directly related to the temperature distribution of a defined body region [5, 6]. Medical application of IRI goes back to early 60's [7, 8]. The medical utility of IRI is based on the physiological fact that the thermal abnormalities, associated with the disease's local or systematic effect on the skin thermoregulatory actions, may accompany with IR-detectable changes in natural skin temperature [9]. Over the past 40 years, IRI has been used in various medical applications, ranging from oncology, dentology, pain, surgery and vascular, respiratory, dermatology, and other disorders, with a great awareness for whether or not IRI should be considered as a valid diagnostic tool [7–10]. In order to study such hypothesis several IR imaging methods were explored for differential diagnosis purposes [9]. Through Classic/Static (i.e., at resting conditions) thermographic imaging method, differential diagnosis is usually performed by analyzing the temperature distribution over the considered skin region represented by only one captured image/frame [3]. This conventional IR imaging method can identify significant changes of skin thermal distributions between two hemisoma or even with respect to an average extrapolated from a control group [6, 11]. But, general absence of certainty has arisen among clinicians regarding the clinical use of these

approaches due to contradictory results and the lack of informative concerning hemodynamic alterations and the underlying thermoregulatory malfunctions which may accompany the presence of a disease [3, 6, 12]. Meanwhile, yet for different purposes, innovative progressions yielded another generation of computerized infrared cameras portrayed by a high spatial resolution and temperature affectability while minimizing the acquisition time [6]. The accurate recording of the cutaneous temperatures' dynamics now permits functional infrared imaging (fIRI) studies of cutaneous thermoregulation [6]. The dynamics of thermoregulatory system could be further understood by analyzing its response to a controlled thermal challenge which effects local thermoregulation [3], like exercising during cold exposure [13, 14] or mechanical isometric exercising [15–17]. Examples of medical IR data acquired during both static and dynamic IR imaging methods are illustrated in Figs. 1, 2 and 3. Others IR imaging methods, such as multispectral, multimodal, and sensor fusion were explored for further medical applications (please read [18] for further information). Most of these medical IR imaging methods were designed in order to collect a significant and effective IR data that allows both qualitative and quantitative evaluation of the cutaneous temperature changes in both basal conditions and in response to diagnostic challenges. Regarding the demands of clinicians, physicians, or even IR researchers, using IR data for differential diagnosis came with four main hypotheses that the evaluation of the cutaneous IR temperature changes could (i) identify significant averaged and asymmetric temperature parameters that could be used for detecting the medical disorders based on correlations between observable IR image characteristics and human physiology without worrying about the physical mechanism that connects them, (ii) provide direct functional IR indicators of the thermoregulatory malfunctions/alternations

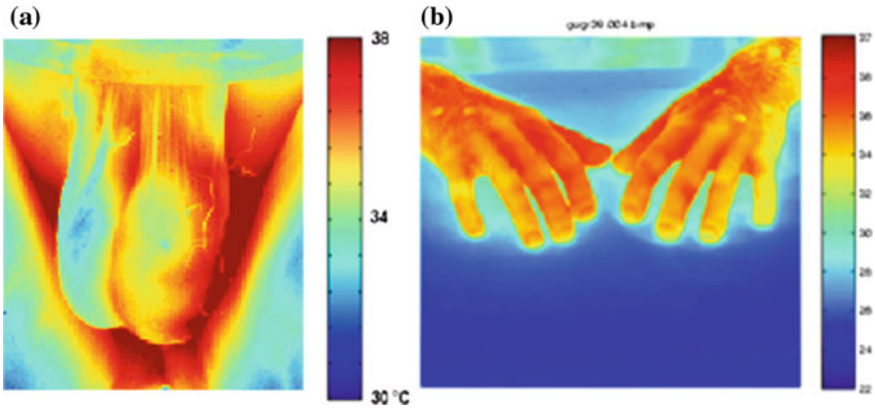

Fig. 1 Examples of the static IR data collected in the thermal infrared imaging laboratory-ITAB. Thermograms showing abnormalities in conjunction with various medical problems: **a** scrotal IR image shows the higher temperature values at the hemi scrota in the presence of grade III varicocele disorder and **b** IR image shows the higher temperature values at affected fingers with the Raynaud' phenomenon disorder

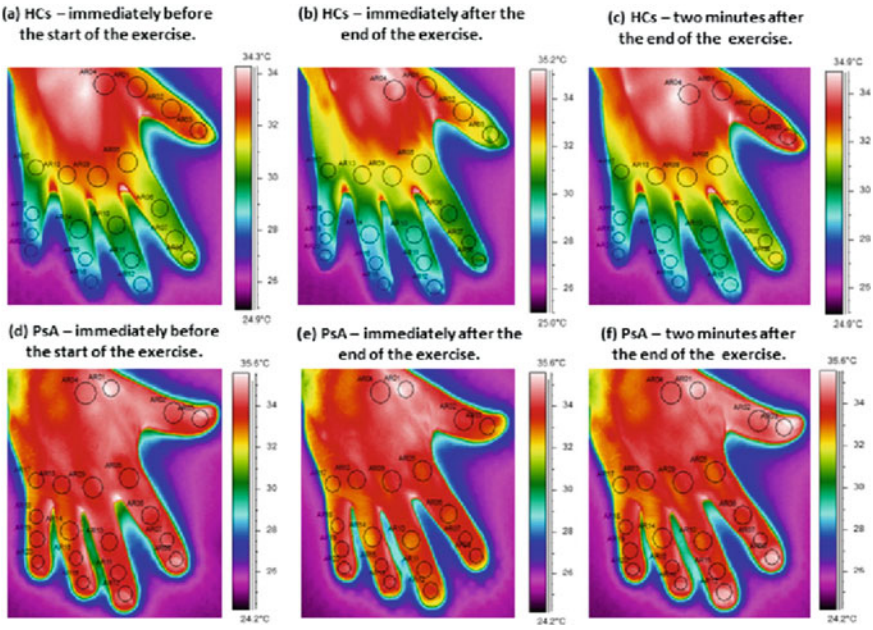

Fig. 2 An example of thermal maps during three different recoding times: for **a**–**c** randomly selected healthy control (HCs) subject, and **d**–**f** randomly selected psoriatic arthritis (PsA) patient [16]

indirectly assessing the severity of functional perturbation of the autonomic sympathetic and parasympathetic physiological activations in the presence of a disease; thus giving an intend to indirectly evaluate the disease activity and help its primary differential diagnosis, (iii) to compute physiological information, as for example localized blood flow, cardiac pulse, and breath rate; thus allowing a noninvasive and noncontact monitoring of the physiological state of the subject and identify skin's thermal parameters, location of heat source (particularly the vessels), depth of heat source used for defining the location, and geometrical shape of the affected-area, mostly required for tumor detection, and (iv) provide a clear description of the underlying alterations in the main thermoregulatory functions as for example, environmental heat exchange process, vasoconstriction and/or vasodilation, and sweating actions. [9, 13–15, 19–21]. In order to study such hypotheses, understanding the significance of false-color (typically, gray levels) representation in a thermal IR image is an important requirement. In fact, changes in gray-level thermogram will follow changes in the emitted surface radiance and the corresponding cutaneous temperature of a given body region [9]. For using medical thermograms in differential diagnosis, two main modeling approaches were explored, (i) Qualitative modeling approach based on using statistical and machine learning techniques, (ii) Quantitative modeling approach based on performing mathematical/analytical modeling of the thermoregulatory processes by using three

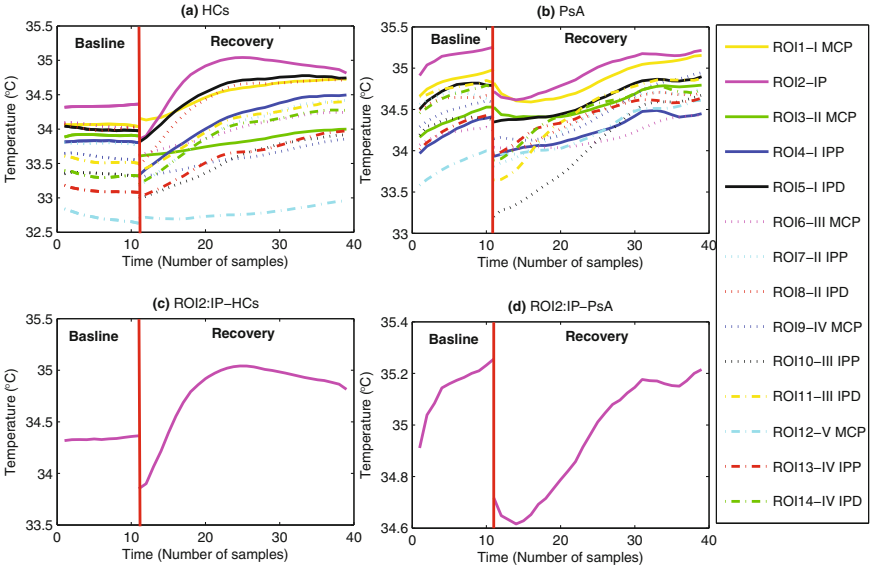

Fig. 3 Temperature versus time curves obtained from thermal imaging data during baseline, i.e., before performing the isometric exercise and 1.6 min after the isometric exercise separated by a *red vertical line* (subjects were required to press every 2 s, and for a total of 2 min, the dynamometer handle, at the 20% of previously assessed maximal individual strength). Measured from: **a** 14 ROIs for healthy HCs subject, **b** 14 ROIs for psoriatic arthritis (PsA) subject, **c** the randomly chosen representative ROI 2 for HCs subject, and **d** the randomly chosen representative ROI 2 curve for PsA [16]

main approaches: (ii-a) empirically using automatic control theory, (ii-b) non-empirically using bioheat equations and (ii-c) semi-empirically using both bioheat equations and automatic control theory. Also, three main modeling approaches based on control system theory were presented, i.e., (a) time domain analysis of the thermoregulatory system's characteristics through a direct estimation of the closed-loop dynamic response parameters of a prototype second-order system, (b) a direct identification of thermoregulatory system as a second-order system plus delay time (SOPDT) from a closed-loop step response, and (c) a state-space representation of the thermoregulatory system as a first-order differential equation from the experimental IR temperature curves. Figure 4 presents a quick summary of the main procedures required for each of the considered modeling approaches in a flowchart version. This chapter is mainly aimed at presenting these modeling approaches and their applications in using medical IR data for differential diagnosis. The remaining of chapter consists of four sections, one section for each modeling approach. In each section, we will present the methodology of the presented modeling approach, review the most recently performed studies for its application

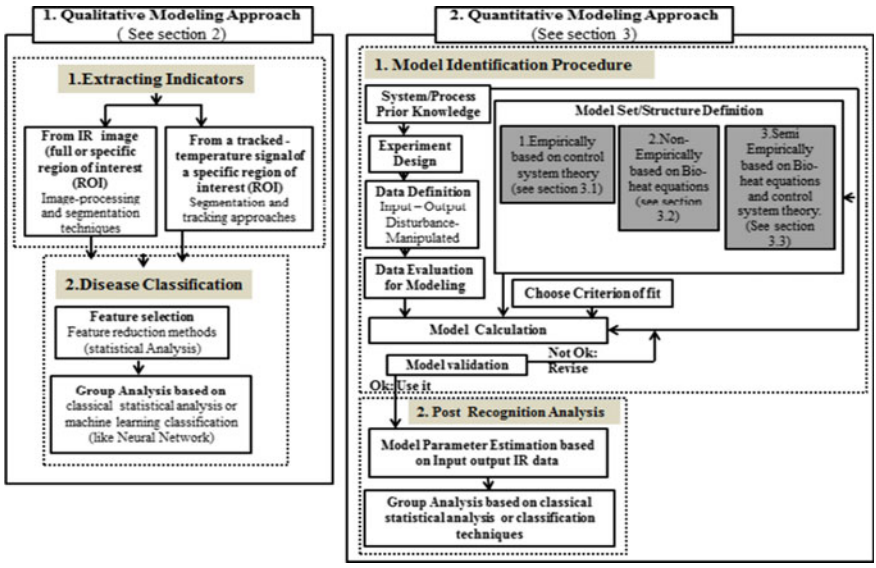

Fig. 4 A quick summary of the main procedures required for each of the considered modeling approaches in a flowchart version

in differential diagnosis and discuss its disadvantages and limitations. Finally, we end up the chapter with a summary and conclusion section.

2 Qualitative Modeling of the Skin Thermoregulatory System Using Statistical and Machine Learning Techniques

IR detection of medical disorders using this approach is mainly based on the correlations between observable characteristics of the medical IR thermograms and human physiology without taking into consideration the physical mechanism that connects them [9]. In fact, this approach relies on extracting significant indicators that could qualitatively evaluate the cutaneous temperature changes in both basal conditions and in response to diagnostic challenges with the main hypothesis that such indicators could provide differential parameters/features for medical diagnostic purposes with a high success rate [1, 9]. Generally, this approach consists of two main processes, i.e., extracting features from the medical IR thermogram, and subsequent classification of the thermogram into healthy and non-healthy classes based on the extracted features [9]. A brief illustration of the involved processes of this approach has been shown in Fig. 4. This section illustrates the brief description of each process as follows:

I. First, regarding the demands of clinicians, physicians, or even the IR researchers and before extracting the indicators from the medical IR thermograms, it is important to decide whether to extract the indicators from the IR image, full image or a segmented region of it, or from a tracked-temperature signal of the segmented regions of interest (ROIs). In fact, some IR studies were based on extracting indicators from the full IR image or a segmented region of interest (ROI) . Such approach usually needs performing several image-processing techniques and some sort of segmentation processes [9]. While other IR studies were based on extracting indicators from the tracked-temperature signal of the segmented regions of interest (ROIs). In such approach, the automatic identification of ROIs necessitates the use of some sort of segmentation and tracking methods [9, 22]. A complete and exhaustive review of the commonly-used data preprocessing techniques for this modeling approach like image-processing, segmentation, and tracking processes cannot be allocated within this chapter (more detailed description and references can be found in [9, 22]).
II. Second, to perform a differential diagnosis of a medical disorder with a high success rate, extracting features as indicators of abnormalities in medical thermograms is critically important process. In fact, abnormalities in medical thermograms usually exist due to the underlying physiological/pathological condition that causes alteration in the thermoregulation of the human body [23]. These conditions are often manifested as abnormal vascular and focal patterns, high-/low-temperature regions, asymmetries in temperature distribution, abnormal contours, etc. [23, 24]. Table 1 illustrates some of the mostly extracted features for using medical IR thermograms in medical diagnosis purposes.
III. Finally, for using medical IR data for differential diagnosis, several studies have been made with a main hypothesis of checking whether or not IR data could detect a medical disorder. Some of these studies stopped at qualitative testing of this hypothesis by using classical statistical evaluation methods as for example Student-T test, inter-class correlation, and nonparametric statistical tests [25, 26]. While other studies did not stop at the statistical evaluation of this hypothesis, but also demonstrated the significant findings with calculating the true-prediction ratios of both healthy and non-healthy groups using the machine learning algorithms as for example Support Vector Machine (SVM) , Decision Tree (DT), Fuzzy Sugeno, *k*-Nearest Neighbor, Probabilistic Neural Network (PNN), Self Organizing Map (SOM), Artificial Neural Network (ANN) , Data resampling and performance evaluation, Receiver Operating Characteristic (ROC) (see [27] for further information about the detailed procedure of the proposed methods).

Medical applications of the proposed modeling approach

With this qualitative modeling approach, thermal IRI technique has been evident to be a potentially and promising imaging tool that could be utilized as a reciprocal technique as a part of relationship with typical medical imaging for the assessment

Table 1 Mostly extracted features from the IR thermograms for medical diagnosis purposes

Feature group	Detailed-features	Applications
Vascular/focal pattern	– Hyperthermic feature (hot spot) – Hypothermic feature (cold spot) – Atypical complexity feature	– Breast cancer [79, 80] – Vascular disorders [81]
Abnormal physical contour	Confined heat along an abnormal physical contour (edge sign)	Breast cancer [82]
Statistical features	– First-order features extracted from histogram (including mean, standard deviation, median, maximum, minimum, skewness, kurtosis, entropy, area, and heat content) – Second-order features extracted from gray-level co-occurrence matrices	Breast cancer [83]
Thermal features	Maximum temperature Minimum temperature Average temperature Heat distribution index	– SARSsevere acute respiratory syndrome (SARS) analysis [84] – Headache [85]. – Vascular disorders (Raynuad' phenomenon [28], varicocele [29]) – Arthritis disorders [2, 86] – Diabetic disorder [27, 87]
Presence/absence of any response to a controlled challenge procedure	Extract any of the previous features from the measured IR temperature data during both after and before periods of applying diagnostic challenge and compare them	Arthritis disorders [2, 17]
Asymmetry-based features	Compare contralateral regions of interest by evaluating the difference of any of the previous features	– Breast cancer [88–90] – All malignant tumor cases [91] – Clinical settings regarding the human posture [92]

A detailed review could be found in [2, 9, 27]

of several medical disorders such as Raynaud' phenomenon, varicocele, thoracic outlet syndrome, knee injuries, psoriasis arthritis, diabetes, fever, breast cancer, skin cancer, eye, pain and inflammation [1, 2, 25–27]. In fact, this modeling approach has been proposed disease classification based on a statistical analysis of some descriptive parameters of the cutaneous temperature curves during both basal and in response to diagnostic challenges [6, 17, 28–33]. However, such statistical descriptive parameters may not provide a clear explanation of the complex mechanism accompanying thermoregulatory malfunctions or alterations associated with the presence of a medical disorder [13–15, 19, 20].

3 Quantitative Modeling of the Skin Thermoregulatory System Based on Mathematical Modeling Approaches

Based on the experimental cutaneous temperature data, in both basal conditions and in response to diagnostic challenges, this approach has been used to establish a mathematical thermoregulatory model with 'quantitative' and 'dynamic' parameters. Such dynamic parameters were hypothetically suggested to (i) provide a direct functional IR indicators of the thermoregulatory malfunctions/alternations indirectly assess the severity of functional perturbation of the autonomic sympathetic and parasympathetic physiological activations in the presence of a disease [13–15, 19, 20], (ii) to compute physiological information, such as localized blood flow, cardiac pulse, and breath rate [34–36], and (iii) identify skin's thermal parameters, location of heat source (particularly the vessels), depth of heat source used for defining the location and geometrical shape of the affected area, mostly required for tumor detection (see [9] for a review of most performed IR studies), and (iv) provide a clear description of the underlying alterations in the main thermoregulatory functions as for example, environmental heat exchange process, vasoconstriction and/or vasodilation, and sweating actions. In order to test these hypotheses, mathematical models of the thermoregulatory processes were established. In fact, this modeling approach contains two main steps: (i) the thermoregulatory model identification procedure based on the IR input–output experimental data and (ii) the post recognition analysis performed on the estimated model dynamic parameters, as follows (see Fig. 4 for a quick summary of these main steps):

i. **The first step is to collect a prior knowledge** about the local skin thermoregulatory system of interest that is going to be represented in the model. So as to make such definitions, it is essential that the reason for making the model be characterized as obviously as could be expected under the circumstances. With this modeling approach, the main target of thermoregulatory modeling is to find dynamic parameters/characteristics of the Skin temperature curves that could investigate the thermoregulatory malfunctions or alterations and indirectly inferring the sympathetic and parasympathetic autonomic (brain regulatory of thermoregulation) alterations in the presence of a disease. Such parameters could be used to differentially diagnose a medical disorder in the medical; thus increasing the thermal infrared imaging potentialities as a diagnostic tool in medical applications [13–15, 19, 20].
ii. **The second step is to collect data during an identification experiment** specifically designed with the objective of making the recorded data maximally informative. The thermoregulatory system is defined by considering the skin temperature $y(t)$ as its output, room temperature as its external input and a basal skin temperature as its steady state reference signal. The input/output temperature time curves can be recorded by thermal IR imaging either in the basal healthy state or in any medical pathological conditions [17, 37, 38].

iii. **The third step is to define the input and output variables in the model** and which input variables are disturbance and whether inputs that could be manipulated. The input/reference value is represented by the basal skin temperature that can be considered steady prior to the performed challenge either diagnostic test, while the output is the skin temperature after the end of the challenge. The disturbance is the environmental temperature changes [13–15, 19, 20].

iv. **The fourth step is to evaluate/check the measured data** for acquiring additional data that could simplify the modeling procedure. For example, if the visual inspection of the system input elucidates that it is constant with time, then the model input could be modeled with a step unit signal. Also, it is important to check whether there is a statistical relationship between the model input and output in order to consume the modeling efforts when there is no input–output relationship. To accomplish this task, qualitative modeling approaches like classical statistical analysis or machine learning classification are usually implemented [39].

v. **The fifth step is to select the model structure and level of model complexity**. Mathematical skin thermoregulatory model was usually achieved by one of three different modeling approaches, i.e., (i) empirical (black-box) modeling approach by employing the automatic control system theory for studying the global picture of thermoregulatory functioning through three main approaches, i.e., (i.a) time domain analysis of the thermoregulatory system's characteristics through a direct estimation of the closed loop dynamic response parameters of a prototype second-order system, (i.b) a direct identification of thermoregulatory system as a second-order system plus delay time (SOPDT) from a closed-loop step response, and (i.c) a state-space representation of the thermoregulatory system as a first-order differential equation from the experimental IR temperature curves, (ii) nonempirical (white-box) modeling approach by establishing the bioheat equations for representing the heat transfer processes within skin tissues, and (iii) semi-empirical (gray-box) modeling approach by establishing the bioheat equations and also employing the control system theory. Such approaches will be presented in the next subsections.

vi. **The sixth step is to estimate the unknown model parameters** through performing a parameter estimation task using a system identification criterion such as linear or nonlinear regression approach and an optimization technique such as nonlinear least square methods [40, 41].

vii. **The seventh step is to evaluate the model accuracy (known as validation process)** using the input–output data based on statistical consideration. It is desirable to use new data (if available) as well as the old data were used to develop the model. If the model does not provide a satisfactory fit, return to the second step and try a different model. If possible, the model should be tested with new data (that is known as, validation data); if the model predictions agree with these data, the model is said to be validated.

The post recognition analysis based on the estimated model dynamic parameters

i. **The first step is to estimate the model parameters** for each IR temperature input/output curves measured for each subject for each considered group (for example healthy subjects versus patients), so as to set up the estimations of the descriptors for the statistical analysis or classification among the considered groups.
ii. **The second and final step is to group analysis based on the classical statistical analysis or the classification algorithms**. This step is important to check whether the considered model dynamic parameters could statistically differentiate among the considered groups and consequently could elucidate the difference in the thermoregulatory control actions, assessing the presence disease.

If this modeling approach will succeed, such a research might reinforce the possibilities and advantages of using thermal infrared imaging in medicine [9, 13–15, 19, 20, 34, 35]. This section in fact will briefly present the utility of each of these three quantitative modeling approaches for using IR data in differential diagnosis.

3.1 Empirical (Black-Box) Modeling of the Skin Thermoregulatory System-Based Control System Theory

The thermoregulatory process of homeostasis can be modeled as control system [42]. A control system model permits one to depict the dynamical behavior of thermal regulation with a specific end goal to evaluate its behavior under different experimental conditions [43].

Indeed, the overall control system has been represented as a 'black box,' whose overall structure can be investigated by analyzing the input–output time-responses. Such assumption came as a result of the skin thermoregulatory complex mechanisms [44]. The general structure and the order of the thermoregulatory control system usually identified with the empirical modeling approaches as a result of a general lack of information about the internal system variables.

3.1.1 Time Domain Analysis of the Thermoregulatory System Characteristics Through a Direct Estimation of the Closed-Loop Dynamic Response Parameters of a Prototype Second-Order System

In automatic control system theory, the dynamic performance of a linear, time-invariant system lower than the third-order system could be evaluated by the standard performance criteria/parameters characterizing the system dynamic response to canonical inputs (like the step input) in the time domain [45]. On the

other hand, in some IR medical applications the visual inspection of the temperature recovery curves suggested considering the system as a second-order time-invariant feedback system with an exponential critically damped decay [46]. Therefore, by employing the control theory, analyzing the time domain characteristics of the dynamic responses extracted from the IR recovery curves could provide a better understanding of the functional and morphological thermoregulatory alterations associated with the disease [19, 20], also providing a powerful discrimination between the healthy controls and patient groups. In this approach, the time domain analysis of the thermoregulatory behavior based on the step dynamic characteristics of a prototype second-order system were performed considering two main assumptions: (i) considering the superficial basal temperature measured prior to the performed a challenge to be steady (i.e., with no change with time as the step signal) and averaging its values over time to provide the thermoregulatory input signal/ reference value, (ii) the visual inspection of the system's thermal recovery, i.e., superficial skin temperature signal after the end of the applied challenge should exhibit an exponential critically damped decay [46] and with any overdamped, or under damped decay with small overshoot curves could be assumed to be critically damped. The detailed description of the proposed modeling approach is illustrated as follows:

i. The standard closed-loop transfer function of the second-order control system, with the real and imaginary parts of its roots S_1, S_2 (poles) are defined in Eqs. 1–4, respectively, with ζ is the damping ratio, ω_n is natural damping frequency, and ω is the oscillating frequency [45].

$$H(s) = \frac{w_n^2}{s^2 + 2\varsigma w_n s + w_n^2} \tag{1}$$

$$s_1, s_2 = -\varsigma w_n \pm j w_n \sqrt{1 - \varsigma^2} = -\sigma \pm j w \tag{2}$$

$$\sigma = \varsigma w_n \tag{3}$$

$$w = w_n \sqrt{1 - \varsigma^2} \tag{4}$$

ii. The time domain analysis of dynamic response of a system involves the evaluation of its transient response, defined as the part of the time response that goes to zero as time becomes very large, and the steady-state response, is simply defined as the part of the total response that remains after the transient has died out [45]. Table 2 presents the time domain dynamic transient and steady sate parameters used with this approach.
iii. The evaluation of the system transient response is important in order to infer the system dynamic behavior related to the deviation between the output response and the input or the desired response, before the steady state is

Table 2 The transient and steady state characteristics of a control system in terms of the unit-step response

Parameter	Name	Calculation description
t_d (transient)	Delay time	The delay time is calculated as the time required for the step response to reach 50% of its final value (i.e., recovery point after 20 min)
t_r (transient)	Rise time	The rise time is calculated as the time required for the step response to rise from 10 to 90% of its final value (i.e., recovery point after 20 min)
S_1, S_2 (transient)	Closed-loop poles	For critically damped system, with zero oscillating frequency ω (by applying $\zeta = 1$ from Eq. 4) is assumed to be equals and at $\sigma = -\omega_n$ in the left half of s-plane [45]. $S_1, S_2 = \frac{-1.8}{t_r}$
e_{ss} (steady state)	Steady-state error	The steady-state error of a system response is defined as the discrepancy between the output and the reference input when the steady state ($t \to \infty$) is reached. e_{ss} = reference input (baseline constant temperature value) − (final value, i.e., final recovery point after 20 min)

reached. While the evaluation of the system is also very important, because it indicates where the system output ends up when the time becomes large [45]. In fact, the delay time (t_d) is used to estimate the delaying behavior shown between the end of the exercise to recovery signal and the rise time (t_r) is used to study the recovery speed performance, the closed loop poles location on the s-plane is used to reflect the speed and stability performance of the controlled system, and the steady state error e_{ss} the steady state performance of the thermoregulatory system [13, 14].

iv. Since this approach assumes knowing the model structure and order of the thermoregulatory system, i.e., standard second-order system, the model identification procedures will be canceled for this thermoregulatory modeling approach. In fact, with this thermoregulatory modeling approach, the standard time domain characteristics, i.e., t_d, t_r, S_1, S_2, $e_{ss,}$ and $T_{b,}$ will be directly and graphically calculated from the thermal IR recovery curves as illustrated in Fig. 5.

v. By employing control system theory, changes in the skin temperature represented by IR curves may be related to the skin thermoregulatory malfunctioning level, that could be evaluated by the actual values of a given set of defined standard characteristics/parameters. Therefore, direct estimation of these characteristic parameters could give quick insight of the dynamics in the rewarming IR recovery curve after an applied challenge or test, and hence classification of the altered rewarming curves from those of healthy/normal subjects will be more easy and sufficient.

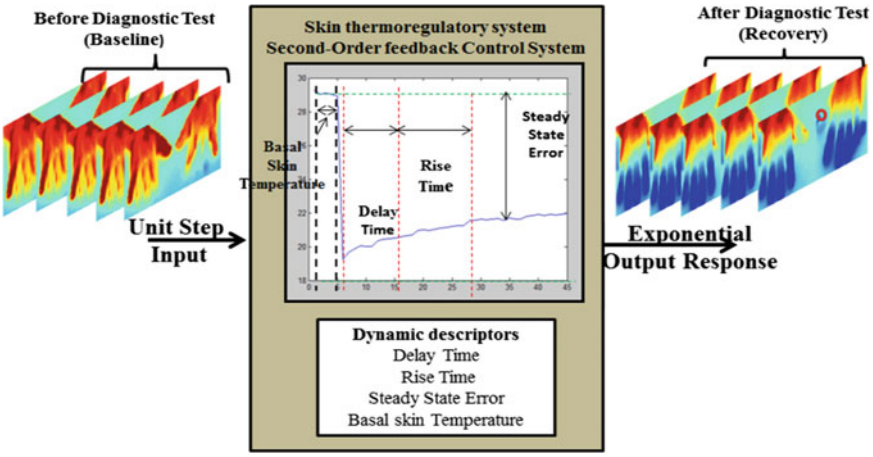

Fig. 5 Direct estimation of the closed loop dynamic response parameters of a prototype second-order system based on time domain analysis of the IR input/output curves for Raynaud' phenomenon patient, measured from the region of interest indicated by the *red circle*

Table 3 A summary of some IR studies that used the quantitative modeling approach "a direct estimation of the closed loop dynamic response parameters of a prototype second-order system based on time domain analysis" for differential diagnosis

Reference	Extracted dynamic parameter	Medical disorder
[28–31, 33, 93]	Time constant, lag time, time constant, integral curves of temperature	Varicocele, Raynaud's phenomenon (RP)
[6]	Rise time named as "tau time"	Vein thrombosis, muscular lesions, and Raynaud's phenomenon
[13]	Delay time, rise time, closed-loop poles, steady-state error, and basal skin temperature	Raynaud's phenomenon
[14]	Delay time, rise time, closed-loop poles, steady-state error, and basal skin temperature	Varicocele (VR)

Medical applications of the proposed modeling approach

Several IR studies have been using such quantitative modeling approach for differential diagnosis of several medical disorders like Raynaud's phenomenon (RP) and Varicocele (VR); emphasizing the promising ability of thermal infrared imaging as a diagnostic tool in the differential diagnosis of the considered medical disorders. Table 3 presents a quick review of these studies. However, it ought to be brought up that this technique is restrictly applicable to systems lower than the third order [45]. Hence, the researcher should have a great insight about the system order and its standard canonical input when using such modeling approach [13, 14].

3.1.2 A Direct Identification of Thermoregulatory System as a Second-Order System Plus Delay Time (SOPDT) from a Closed-Loop Step Response

In some IR applications, like the differential diagnosis of Psoriasis Arthritis (PsA) disease [15], visual inspection of thermal IR recovery curves does not allow studying the thermoregulatory systems' behavioral dynamics based on the direct estimation of the step dynamic characteristics of a prototype second order system. That is because, the altered recovery IR curves exhibit a dynamic response known for a non-minimum-phase system which is different from the standard step dynamic response second-order system in which it has an initial undershoot (Fig. 6) [47].

In these cases, time domain system identification methods based on step dynamic response analysis, known in literature, as classical step response identification techniques, could be used to identify the thermoregulatory system's transfer function based on its closed step dynamic response analysis through employing control system theory [48, 49]. The detailed description of the modeling approach is illustrated as follows [19, 20]:

(i) Based on control system theory, this modeling approach approximated the thermoregulatory system with a second-order transfer function with a time delay (SOPTD) and suggested that its dynamic parameters could be estimated from its negative feedback closed-loop formulation [19, 20].

(ii) This approach is mainly based on considering two main assumptions: (i) the skin thermoregulatory system does not immediately respond after the end of the applied challenge, (ii) visual inspection of the temperature recovery curves suggests considering the thermoregulatory system as a second-order time-invariant feedback system with an exponential critically damped decay with and without an initial undershoot [40, 46], (iii) within this approach the thermoregulatory system was modeled through a feedback control system contains two hierarchical control organizations: a higher supervisor unit and

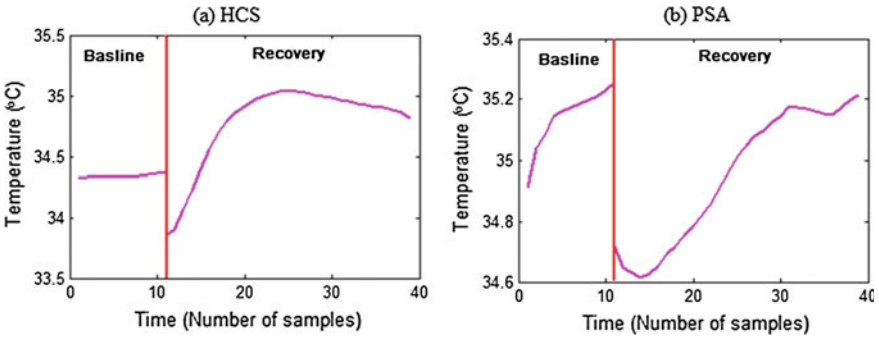

Fig. 6 Different dynamic responses of thermal IR recovery curves for: **a** a healthy control subject (HCS) shows standard dynamics of a standard second-order system, and **b** PSA patient shows a dynamic response with an initial undershoot

a lower feedback executor, driven by the supervisor as shown in Fig. 7. These two hierarchical control units were proposed to model both peripheral/local, and central/systematic thermoregulatory effectors in response to the applied challenge/test. In fact, the supervisor sets the reference signal based on of the basal (i.e., pre-stress) temperature and the onset time. The overall performance of the thermoregulatory actions bases on both the supervisor and the executor activities. Besides the contribution of the thermoregulatory effector mechanisms, the skin temperature (i.e., system output) is also influenced by the environmental thermal exchange with the considered skin tissue. This thermal exchange depends on the temperature difference which constitutes the external input to the thermoregulatory system.

(iii) In particular, the lower feedback unit consists of a controller and a plant block in sequence (Fig. 7), both considered to be time-invariant systems simulated by first-order transfer functions. The theory provides the differential equation to model the plant output $y(t)$ (i.e., the skin temperature) in the time domain:

$$\dot{y}(t) = -a \cdot y(t) + b \cdot u(t) \tag{5}$$

where u is the plant input, and a and b are constant coefficients.

(iv) The diagnostic stress stimulation directly affects the system output, decreasing the skin temperature. The post-stress temperature $y(0)$ (i.e., the temperature measured immediately after the cessation of the diagnostic stress) constitutes the initial condition for the response of the control system. The plant input $u(t)$ is then achieving by summing of the feedback controller output $m(t)$ and the additional external input d:

$$u(t) = m(t) + d \tag{6}$$

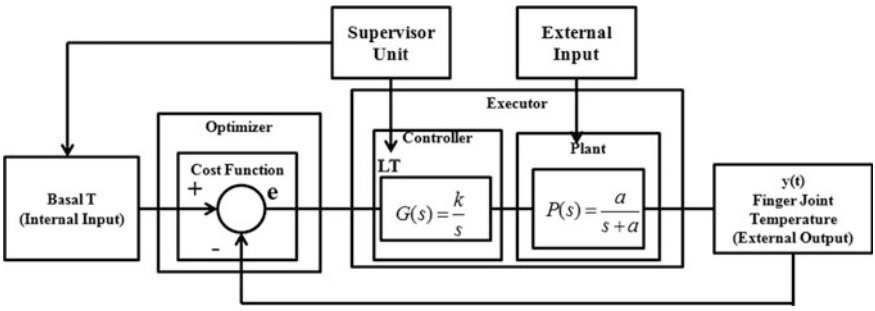

Fig. 7 The overall architecture of the thermoregulatory system. Adapted from [19, 20]

Input d represents the environmental passive heat exchange. Therefore, it depends on room temperature and $y(t)$. Hence, input d can be considered as the non-manipulated effect of environmental conditions on the skin temperature.

(v) The feedback controller produces the signal $m(t)$ stimulated by the output error $e(t)$ signal (i.e., difference between the system output and the reference signal r),

$$e(t) = r - y(t) \tag{7}$$

The feedback controller works to minimize the output error to zero by acting on the plant by the signal $m(t)$.

(vi) Common approaches for modeling homeostatic processes are based on a feedback controller system of an integral type, which annuls stepwise variation of the error signal [50]. The integral controller's behavior could be described by the following time domain differential equation,

$$\dot{m}(t) = k \cdot \dot{e}(t) \tag{8}$$

where k is integral controller constant and h is the proportional controller constant.

(vii) The supervisor unit stimulates this controller by logic signals (on/off transition). When the supervisor logical output is "on," the feedback will activate the controller in order to recover the temperature to its reference settings. On the other hand, when the supervisor logical output is "off" (during the lag time LT), the controller will be deactivated to restore the reference temperature settings, while the external input d is independent of this switching logic. In fact, this plant system could be better represented in the Laplace domain. The Laplace transform (L-transform) of Eq. 5 is given by

$$Y(s) = \frac{1}{(s+a)} \cdot Y(0) + \frac{b}{(s+a)} \cdot U(s) \tag{9}$$

where s is the Laplace variable, and $Y(s)$ and $U(s)$ are the output and input L-transforms, respectively. The ratio between plant output and input defines the plant transfer function $P(s)$, which is computed assuming null $y(0)$ [48]:

$$P(s) = \frac{Y(s)}{U(s)} = \frac{b}{(s+a)} \tag{10}$$

where b is the coefficient of the plant gain and $s = -a$ is its pole, that is, the negative reciprocal of the plant time constant. The plant was as assumed to be unitary gain process with ($b = a$) [19]. According to Eq. 10, the transfer function of the controller $G(s)$ could be represented by

$$G(s) = \frac{k}{s} \tag{11}$$

where k is the integral controller gain.

(viii) When considering the effect of external disturbance input (d) and that the skin thermoregulatory system is not instantaneous the general overall transfer function of the model will depend on the lag time parameter as follows. The overall model works in open loop for $t <$ LT:

$$Y(s) = P(s) \cdot d \tag{12}$$

and in closed loop for $t >$ LT:

$$Y(s) = \frac{G(s) \cdot P(s)}{1 + G(s) \cdot P(s)} \cdot r + \frac{P(s)}{1 + G(s) \cdot P(s)} \cdot d \tag{13}$$

where Y(s), r, and d are the output, reference input, and the disturbance inputs, respectively.

(ix) As the purpose of applying control theory is to offer a model which can fit the sample data well, which means making the error between the calculated system output y^* and the actual/experimental system output y^e as small as possible, the closer those two quantities are, the better fitting impact will be. Therefore, function f can be taken as the fitness function [48].

$$f(x) = \sum_{i}^{\mathrm{NE}} \left(y_i^* - y_i^e\right)^2 \tag{14}$$

where y_i^e is the vector of the experimental finger rewarming curves' data points, y_i^* is the vector of the estimated model's raw data. The raw data are defined from $i = 1$ to number of data points NE, and x is the vector of the model parameters, i.e., a, k, d, and LT. Where a is the plant's open-loop pole location (the inverse of time constant), k is the integral controller gain, d is the disturbance gain, and LT is the system lag time [19].

(x) Broadly speaking, the set of parameters (i.e., a, k, d, and LT) could provide an insight about the dynamics and thermoregulatory activity levels for both healthy and patient states. In fact, the inverse/reciprocal of the plant time constant (a) figures the response speed of the thermal process to external and internal stimuli. The integral controller constant (k) was assumed to describe the active and systemic vasodilation action in maintaining and restoring the reference basal temperature conditions [19], since it figures the control action and could evaluate the feedback control system ability to achieve the steady state. The disturbance input (d) represents the environmental passive heat exchange

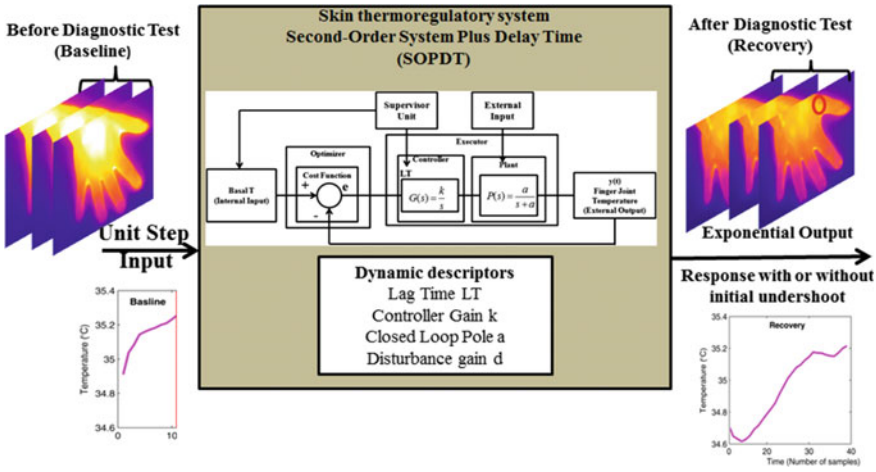

Fig. 8 Direct identification of a second-order system plus delay time (SOPDT) from a closed-loop step response measured by the IR input/output curves for Psoriasis arthritis patient, measured from the region of interest indicated by the *red circle*

and depends on $y(t)$ and the room temperature. LT refers to the time required for the internal thermoregulatory rewarming process to activate after the end of the isometric exercise. The thermal variations during this time are mostly due to the environmental passive heat exchange. After the end of LT, rewarming process starts to activate the controller restoring action to the reference basal conditions T. Figure 8 summarizes the proposed modeling approach.

Medical applications of the proposed modeling approach

Indeed, this modeling approach has been used by Mariotti and colleagues to simulate various thermal responses due to functional, pathological, and morphological alterations in the skin thermoregulation system associated with vascular diseases like Raynaud's Phenomenon (RP) and varicocele (vr) [19, 20]. They demonstrated that this approach cannot predict the dynamics of the IR curves with an initial undershoot, i.e., non-minimum phase response [47]. However, Ismail and colleagues used this modeling approach for the differential diagnosis of psoriasis arthritis demonstrating the ability of this modeling approach to model the dynamics of the IR curves with an initial undershoot, i.e., non-minimum phase response [15].

Finally, the investigated relations between the model parameters and the local thermoregulatory actions like active rewarming remains hypothetical and speculative, given the system complexity and the need for a better understanding of the investigated relation between the model parameters to the actual physiological alterations.

3.1.3 A State-Space Representation of the Thermoregulatory System as a First-Order Differential Equation from the Experimental IR Temperature Curves

Because of the nonlinear nature of thermal regulation, this problem is better suited to state-space model, an alternative form of control system representation [51]. In fact, such models occur naturally in mathematical models of metabolism and signaling pathways. Moreover, the state-space form accommodates nonlinear dynamical biological and physiological features [43]. Moreover, in some IR applications, like the Differential Diagnosis of diabetic peripheral neuropathy (DPN) visual inspection of thermal IR recovery curves suggest using a first-order differential equation for representing the thermoregulatory system [43]. The detailed description of the proposed model is illustrated as follows:

I. Assuming that the amount of heat exchange between blood and tissue varies with time, the regulation parameter r_b written in Eq. 15 should be a function of time. And for human blood, the change of density and thermal capacity (ρc) can be neglected for this temperature range; thus, one must consider the effects of blood perfusion, (t). Equation 15 becomes parametric; therefore, allowing one to substitute the regulation parameter (t) for r.

$$r_b = \frac{(\rho c)_b}{V \rho c} w_b \tag{15}$$

II. Empirically from the experimental thermal IR curves, one can observe that the substantial, essentially exponential, initial thermal recovery rate occurs, thus indicating a negative form of the exponent. One form of $r(t)$ is given by

$$r(t) = k(1 - Q e^{-st}) \tag{16}$$

From Pennes' thermal model [43], Eq. 2 may be written as

$$\frac{dT(t)}{dt} = -k(1 - Q e^{-st})(T(t) - T_A) \tag{17}$$

And has a solution of

$$T_1(t) = T_A + (T_0 - T_A) e^{-k\left(t + \frac{Q}{s}(e^{-st} - 1)\right)} \tag{18}$$

where

T_0	Is the initial value of the output temperature, i.e., recovery temperature
T_A	Is the input temperature, assumed to be the basal blood temperature from [43]
K	Is a constant and a function of the material, the tissue in this application, with the inverse time dimension (s^{-1})
Q	Is the intensity of regulation (*dimensionless*)
s	Is the speed of regulation (s^{-1})

Hence, from the experimental temperature input–output curves, the parameters of interest, i.e., Q, s, and k could be estimated and analyzed providing a quantitative evaluation of the thermoregulatory malfunctions associated with the presence of the disease. In fact, $|Q| \approx 0$ indicates absence of the thermoregulation which corresponds to the Newton's Law of Cooling [52]. Also, larger values of s mean faster thermoregulation, whereas $s \approx 0$ corresponds to the absence of regulation [43].

Medical applications of the proposed modeling approach

This model has been applied for the differential diagnosis of diabetic peripheral neuropathy (DPN) [12, 43, 53]. However, it should be point out that such model is very simple given the elevated complexity of the system and the need for a better understanding of the investigated relations between the model parameters and the actual physiological alterations.

3.2 Nonempirical (White-Box) Modeling of the Skin Thermoregulatory System Based on Bioheat Equations

While IRI shows promise to be a contact-less and effective imaging modality for disease primary assessment [2, 9, 21, 27], it is still hindered by: (i) ignoring subtle interior pathophysiological factors like metabolic heat generation, and localized blood flow, (ii) its poor sensitivity to deeper or smaller disease locations [9, 54]. Such parameters are crucial for investigating the linkage between the thermal distribution over skin surface and internal human pathophysiology that is usually desired in noninvasive thermal diagnostics [9]. Hence, to address this problem, a mathematical model is essential for an overall understanding of the system response and the role of different thermophysical and geometrical properties [55]. To this goal, this white-box modeling approach, also well-known in literature as "inverse problem" has been proposed [9]. This approach has been used for the identification of skin's thermal parameters, location of heat source (particularly the vessels), depth of heat source, etc., and also to compute physiological information, such as localized blood flow, cardiac pulse, and breath rate [9, 34–36, 55–61]. This

modeling approach includes two main steps, i.e. (i) forward thermal modeling problem, i.e., (i.e., finding the simulated skin temperature distribution for given thermal properties with considering various assumptions: some of the parameters are given fixed values from averages over many subjects and other parameters are estimated), and (ii) inverse thermal modeling problem (i.e., finding the unknown thermal or thermophysical properties using the measured skin temperature distribution given by IR camera thermogram). A detail description of the main included procedure will be presented as follows:

I. **The first step, i.e., solving the forward thermal modeling problem** involves the use of the bioheat transfer equation/model to account the heat exchange processes in the body/or even studied area, geometric model to simulate the geometry and the anatomical structure of the skin tissue, including the blood vessels, etc., with considering various assumptions: Some parameters are calculated by averaging their values over many subjects and other parameters are estimated [9].

(a) Adopting a mathematical model for the heat transfer processes between tissue and blood, possibly a variation of Pennes' bioheat transfer model [62]. Using the general Pennes bioheat equation (model of blood perfusion), the amount of heat transferred to the surface from the heat source and the surrounding blood flow can be quantified as

$$C\rho\frac{\partial T}{\partial t} = k\nabla^2 T + C_{\mathrm{b}}\omega_{\mathrm{b}}(T_{\mathrm{a}} - T) + q_{\mathrm{m}} = 0 \tag{19}$$

where

C	Is the specific heat of tissue (J/Kg/°C)
ρ	Is the tissue density (Kg/m^3)
k	Is the thermal conductivity (W/m/°C)
q_{m}	Is volumetric metabolic heat generation rate at the tissue (W/m^3)
C_{b}	Is the specific heat capacity of the blood (J/Kg/°C)
ω_{b}	Is the mass blood flow rate (measured in units per volume of tissue) (Kg/m^3/s)
T	Is the unknown tissue temperature(°C)
T_{b}	Is the arterial temperature (°C)

In a steady state, we have $\frac{\partial T}{\partial t} = 0$ and Eq. 19 takes the following form:

$$k\nabla^2 T + C_{\mathrm{b}}\omega_{\mathrm{b}}(T_{\mathrm{a}} - T) + q_{\mathrm{m}} = 0 \tag{20}$$

The equation left-hand side represents the rate at which thermal energy enters or leaves the unit volume per unit time by conduction, perfusion, and metabolism, respectively. This equation is applicable with the assumptions that (i) all heat

transfer between the tissue and the blood occurs in the capillaries, (ii) there are no large arteries or veins crossing the region of interest, and (iii) the region is sufficiently large to make heat transfer to adjacent tissue areas negligible [61].

Other studies assumed that the heat produced by the body from metabolic processes is transported to the skin level via convection and conduction and is lost to the environment through radiation, evaporation, and air flow convection. The heat loss was modeled as

$$q_s = q_{rad} + q_{con} + q_{ev} \tag{21}$$

where

q_s	Is the total heat loss from the skin surface Under the environmental conditions $(W\,m^{-2})$
q_{rad}	Is the radiative heat loss $(W\,m^{-2})$
q_{con}	Is the convective heat loss $(W\,m^{-2})$
q_{ev}	Is the evaporative heat loss by air $(W\,m^{-2})$

Then the Pennes bioheat model was extended to include the three different mechanisms of heat dissipation to the environment:

$$C\rho\frac{\partial T}{\partial t} = k\nabla^2 T + C_b\omega_b(T_a - T) + q_m - q_s - q_{rad} - q_{con} - q_{ev} = 0 \tag{22}$$

In this model, the blood is assumed to maintain its own temperature Ta until it reaches thermal equilibrium with the skin tissue.

(b) Adapting a geometric model is necessary to simulate the geometry (i.e., depth and size) and the anatomical structure of the skin tissue, including the blood vessels, etc. The model could be sketched as shown respectively in Fig. 9. Figure 10 shows examples of the skin tissue structures considered in literature. The geometric model is considered to be a partial differential equation (PDE) with boundary conditions that attempt to describe bioheat transfer of vascular structure of the considered skin tissue geometry, where the vessels are assumed to be volumetric heat sources for the surrounding layers of tissue structure. Each tissue layer is assumed to be isotropic with respect to tissue specific heat, density, metabolic heat rate, and thermal conductivity. The geometry and the anatomy of vascular skin structure (i.e., the skin, the fat, the muscle, and the core), its thermal properties, the general energy balance between the skin, the tissue, and the environment, as well as the location and the shape of the skin were all taken into consideration in the development of the PDE model to achieve a realistic description of the bioheat transfer processes [56, 63]. Equation 22 then, for this geometric model, according to the geometrical model (Fig. 9c) may be written as

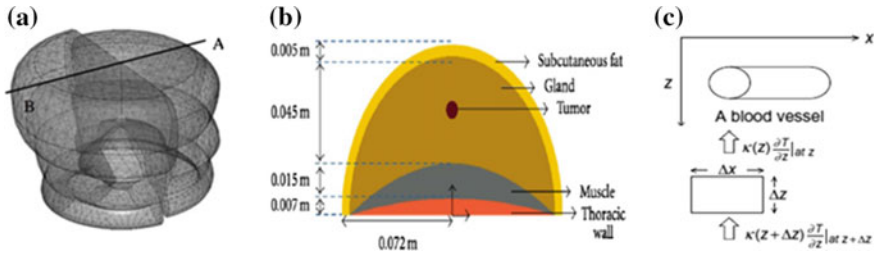

Fig. 9 Examples of sketched geometrical models for representing **a** malignant lesion according to [55], **b** breast tumor according to [77], and **c** blood vessel according to [56]

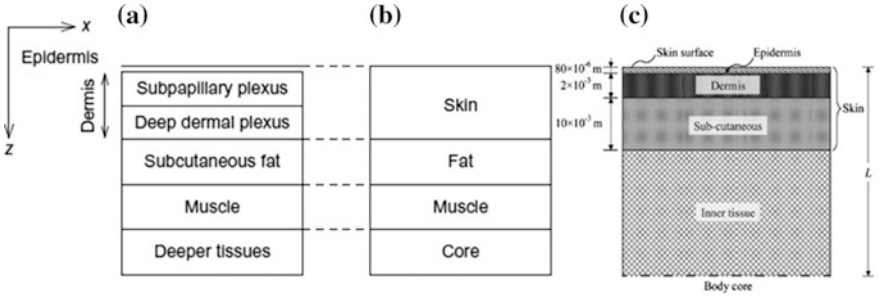

Fig. 10 Examples of vascular skin structures **a** according to [61], **b** according to [56], and **c** according to [78]

$$\rho C\frac{\partial T}{\partial t}-\frac{\partial}{\partial x}\left(k(z)\frac{\partial T}{\partial x}\right)-\frac{\partial}{\partial z}\left(k(z)\frac{\partial T}{\partial z}\right)=q_{\mathrm{b}}(x,t)+q_{\mathrm{m}}(x,z) \tag{23}$$

where: x and z respectively are the parallel axis and the perpendicular axis to toward the inner tissues in the defined coordinate system of the skin surface.

II. **Second step** is solving the inverse thermal modeling problem, i.e., finding the thermal properties for a given thermogram. It involves the use of the solving and simulation method for the bioheat equations and the use of an optimization algorithm as follows:

(a) After totally defining the geometric model and its bioheat equations with their boundary and initial conditions, direct parametric simulation and numerical simulation approaches have been used to calculate the estimated skin temperature distribution [61]. The commonly used numerical methods are the boundary element method (BEM), the finite difference method (FDM) [57, 64], the finite element method (FEM) [54, 65], the Monte Carlo method (MC) [59], and the sensitivity analysis [55]. A simple example of the included methodology, for as example FEM, we can rewrite the algebraic thermal FE equations as $KT = P$ for solving for the unknown temperature vector T.

K is the thermal characteristic matrix of the considered body region; it incorporates the contributions of k and ω in all finite elements of the considered body region, whereas vector P represents the thermal loads, incorporating the effect of q [54].

(b) Optimization algorithm is used to estimate any geometrical parameter (depth, width, and size) or thermophysical parameters like blood perfusion rate, ω_b, by minimizing a fitness function involving the temperature profiles obtained from clinical data captured by a thermal camera across the exposed skin region to those obtained by the bioheat model simulation.

(c) The fitness function links the data from the observed thermographic temperature profile to the estimated temperature profile for a given set of estimated parameters. Several Optimization techniques have been used like pattern search [57], and Levenberg–Marquardt algorithm [54].

Medical applications of the proposed modeling approach

Several medical IR studies have implemented the proposed white-box modeling approach to calculate some medical indicators based on the estimated geometrical or thermophysical parameters (Table 4 summarizes some of these studies). However, this approach has been shown to be (i) complicated because the geometry and properties of biological bodies vary drastically, increasing the complexity of the bioheat transfer solution [59] and (ii) increasing the cpu processing time required for calculating the temperature values at all mesh nodes in order to solve the bioheat transfer equation over the entire region [9].

3.3 Semi-empirical (Gray-Box) Modeling of the Skin Thermoregulatory System Based on Bioheat Equations and Control System Theory

When using IR imaging for differential diagnosis of some medical disorders especially psychological ones like autism, clinicians do not only focus on the disease classification but usually they have a great awareness for finding dynamic parameters that could provide a clear description of the underlying alterations in the main thermoregulatory functions as for example, environmental heat exchange process, vasoconstriction and/or vasodilation, and sweating actions. Such efforts came with a main hypothesis that such dynamic parameters could provide an important insight about the autonomic malfunctions associated with the presence of the studied disorder and consequently provide important keys of the disease therapeutic procedure. Due to the high complexity of the skin thermoregulatory system, intuition considered in the previously presented quantitative modeling approaches, is often not adequate as a basis for that purpose. In fact, empirically simulating the thermoregulatory system as a negative feedback loop may lead hypothetical and speculative linking between the model parameters and the local thermoregulatory

Table 4 Summary of some IR studies that used the white-box modeling approach for medical diagnostic purposes

Study	Estimated parameters	Medical disorder
[54]	Calculate the tumor-induced thermal contrast (TITC) from the estimated tissue thermal properties	Breast cancer
[55]	Calculate properties of the subsurface structures with the estimated temperature distribution	Benign or malignant lesions
[57]	Estimate the location and size of the embedded tumor	Breast cancer
[60]	Calculate subject's blood flow rate	Stress onset detection
[66]	Calculate the doubling time of tumor volume from the estimated values of the metabolic heat production of a tumor	Breast cancer
[66]	Calculate the burn depth from the estimated change in burn temperature	Burn tissues

actions like active rewarming and passive heat exchange [14, 20]. On the other hand, the white-box modeling of thermoregulatory system through bioheat equations came only with a main focus of modeling the heat exchange processes, the geometry and the anatomy of the skin tissue structure without considering the hemostatic controlling actions, i.e., thermoregulation system associated with these thermal processes [9, 36, 54, 55, 57, 59, 66–68]. Hence, as a contrasting option to utilizing these modeling approaches, one can create a semi-empirical model considering the real thermoregulatory activities. Indeed, Kakuta et al. [69, 70] has semi-empirically simulating the heat transfer processes within the human body and their thermoregulatory actions through numerically calculating bioheat transfer equations in combination with a control system theory. However, such model was only applied with a main target of eliminating the influence of thermal environment when evaluating of skin IR temperature distribution measured during several thermal environmental conditions without focusing on studying the changes in the thermoregulatory actions [69, 70]. In fact, since 1940, various trials have been performed trying to elucidate parts of this issue (a bulk of reviews and books are mentioned in [71]). The first detailed representation for the thermoregulation model was the one proposed by Stolwijk and Hardy [72], that approximates the human thermoregulatory mechanism could be model with a negative feedback closed loop with two main systems, i.e., the controlling active system and the controlled passive system. The active system predicts the thermoregulatory effector mechanisms, such as shivering, vasomotion, and sweating. The passive system predicts the physical heat transfer mechanisms through dividing the human body into three segments/cylinders, i.e., head, trunk, and extremities, with two anatomical layers (i.e., skin and core) each, which simulate the body heat transfer phenomena occurring inside the body and at its surface.

Until this decade, Stolwijk's model was the basis for many other thermoregulation models that were aimed at predicting the mean core and skin temperature, dynamic heat exchange, sweating rate, metabolic rate with the main application scopes of human thermal comfort [73], and work load analysis [74]. In fact, most of

these models were mainly based on contact-sensors for collecting the measured temperature data without using the main advantage of IR imaging, i.e., the contact-less measuring ability. Moreover, to the best of our knowledge, none of these models were aimed at investigating the thermoregulatory alterations due to the transient change of the human emotional state; such application that is critical important in the field of affective computing. Hence, as one of the first attempts to achieve this goal, on the basis of Stolwijk model adapted by Konz et al. [75], through one of our most interesting research activities, we propose to semi-empirically develop a mathematical thermoregulatory model using the measured facial skin IR temperature data during the transient change of the human emotional state [that work is under publication].

Given the large number of different available human thermoregulatory models, the selection of Stolwijk model comes with the following reasons: (i) it is a lumped parametric model with influential parameters that could describe the overall thermal response of the human thermoregulatory effector mechanisms to varying inner and outer stimuli, and (ii) it is capable of predicting the spatial skin temperature distribution of the human face, for example, the forehead's skin temperature [76].

Implementing such a model for simulating the thermoregulatory alterations in response to the change in the human emotional state using the facial IR temperature data, comes with considering the following assumptions:

(i) **Approximating the inputs and outputs of the facial thermoregulatory system** considering that (a) the only observable output is the facial skin temperature measured during the subject exposure to the emotional stimuli, (b) the basal facial cutaneous temperature (i.e., before the exposure to the emotional stimuli) is assumed to be the system's reference signal with a constant value calculating by averaging its time-curve values, and head core temperature that is considered to be constant and equals to 36.6 °C [72], (c) the regulated system can be subjected to a outer disturbance environmental heat exchange and inner physiological disturbance due to the change in the human emotional state.

(ii) **Approximating the manipulated variables in the model**:

- Since, the facial IR data is collected for healthy subjects, the passive part of the model, i.e., head' heat capacitance equations will be considered constant for all subjects; resulting that the overall performance of the facial thermoregulatory system will depend only on the activity of the regulating actions of the active system, i.e., vasomotor and sweating actions. Besides the contribution of regulatory actions, facial skin temperature (i.e., system output) is also influenced by the thermal exchange between the facial skin and the surrounding environmental conditions. This heat exchange depends on the change in temperature which constitutes the external input to the thermoregulatory system.
- Approximating the active system: Since the subject is not going to shiver during the exposure to the emotional stimuli, the active system will only

be limited to simulate the alterations in the vasomotor and sweating actions, considering the change in the metabolic activity is zero.

(iii) **Approximating the passive system**:

- Since the main target is to model the skin thermoregulatory system regulating the skin temperature of the human face, the bioheat equations of the Stolwijk passive system could be minimized to only contain those equations that simulate the head cylinder with the core and shell layers. These equations will be used to simulate the heat interactions from the brain center into the facial skin.
- The passive system represents the facial heat capacitance will be approximated with the central blood pool representing the blood circulation and one cylinder with two layers, i.e., the head core and the head skin. The head skin will be assumed to be the facial skin.

Facial skin thermoregulatory model during emotional stimuli

Figure 11 illustrates the overall architecture of the facial skin thermoregulatory system, adapted from the previously proposed model by Stolwijk and Hardy [72] and validated by Konz et al. [72, 75]. The model contains two main parts, i.e., the active system and passive system. The facial thermoregulatory system contains two main components: passive system simulating the head' heat capacitance and the active system simulating the facial skin thermoregulatory actions, i.e., vasomotor actions and the sweating actions.

The passive system: (Facial skin physical passive mechanisms) is modeled with considering the head as a cylinder with two layers, i.e., head core and head skin (assumed to be facial skin). A central blood compartment is used to transport blood from a central blood pool, or the heart, to each head tissue layer. Heat flows between the head core and facial skin by conduction and both layers exchange heat by convection with the central blood compartment. The environmental heat exchanges with the facial skin layer through radiation, evaporation, conduction, and convection.

For each head tissue, heat energy balance considers heat storage effects, conductive heat transfer with adjacent tissue layers, convective heat transfer due to the blood flow and basal metabolic heat generation. All skin energy balance equations include heat losses due to convection, radiation, and the evaporation of the moisture at the body surface.

The results of this derivation were presented in the form of 3 bioheat differential equations by which the change in the facial skin temperature could be evaluated.

(i) The differential bioheat equation for the head core is given by

$$C_{\mathrm{C}} \cdot \frac{\mathrm{d}T_C}{\mathrm{d}t} = \propto_{\mathrm{C}} \rho c \times 48(T_{\mathrm{CB}} - T_{\mathrm{C}}) + M_{0\mathrm{C}} - K_{\mathrm{CS}}(T_{\mathrm{C}} - T_{\mathrm{S}}) - \mathrm{Ev}_{\mathrm{R}} - \mathrm{Ev} \quad (24)$$

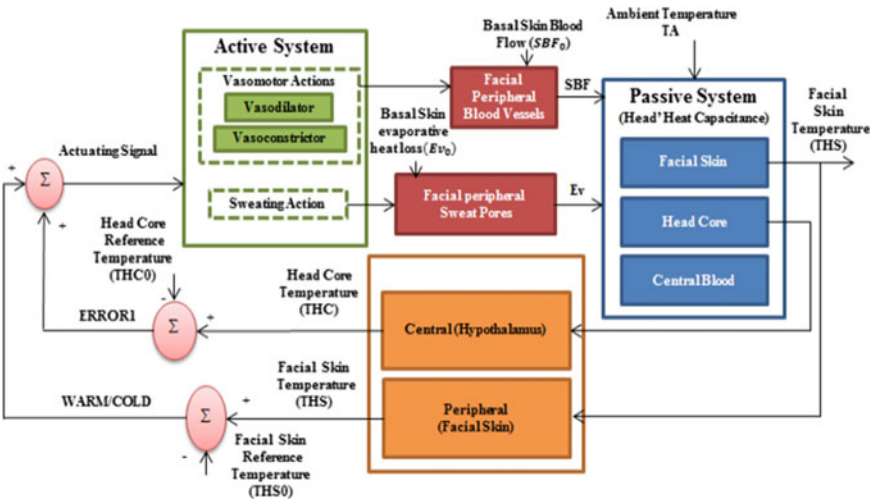

Fig. 11 Overall architecture of the facial skin thermoregulatory system

where

C_C	= the head core thermal capacitance: 3.94 kcal/°C
T_C	= temperature of the head core
T	= time (hours) (/60/60 s; in order to convert an time unit from hour to second)
α_C	= dimensionless fraction accounting for effect of countercurrent heat exchange
Pc	= product of density and specific heat of blood: 0.92 kcal/°C
48.0	= 1/h blood flow to the core of the head; (/60/60 s)
T_{CB}	= temperature of central blood compartment
0.04 ΔM	= fraction, in kcal/h of total shivering metabolism assigned to (muscles) core of the head
K_{CS}	= thermal conductance between core and skin of head: 2.63 kcal/h/°C; (/60/60 s)
M_{0C}	= basal metabolic heat production assigned to core of head: 12.42 kcal/h; (/60/60 s)
T_S	= temperature of head skin, approximated to be the temperature of the facial region of interest
Ev_R	= respiratory heat loss assigned to core of head: 4.5 kcal/h (/60/60 s)

(ii) The differential bioheat equation for the facial skin is given by

$$C_S \cdot \frac{dT_S}{dt} = K_{CS}(T_C - T_S) + M_{0S} - 0.09Ev_{0S} - 0.09E_v + \alpha_S \rho c \times 0.138SBF(T_{CB} - T_S) - A_{HS} \cdot H_0(T_S - T_A) \quad (25)$$

where

C_S	= the head skin thermal capacitance: 0.27 kcal/°C
M_{0S}	= basal metabolic rate of the skin of the head: 0.12 kcal/h (/60/60 s)
0.09 Ev_0	= assigned fraction of insensible evaporative heat loss: 0.8 kcal/h (/60/60 s)
0.09 eV	= assigned fraction of thermal evaporative heat loss, in kcal/h; (/60/60 s)
α_S	= factor for countercurrent heat exchange
0.138 SBF	= assigned fraction of total skin blood flow, in l/h; (/60/60 s)
$A_S \cdot H_0$	= product of area of the skin of the head, and environmental heat transfer coefficient: 0.165 × 6.0 kcal/h/°C (/60/60 s)

(iii) The differential bioheat equation for the central blood compartment, that is approximated to only simulate the fractional blood transport to the head core and head skin tissues, is given by

$$C_{CB} \cdot \frac{dT_{CB}}{dt} = -\alpha_C \rho c \times 51.3(T_{CB} - T_C) - \alpha_{HS} \rho c \times 0.138 SBF \times (T_{CB} - T_S) \quad (26)$$

where

C_{CB}	= the central blood thermal capacitance: 1.12 kcal/°C

The active system: uses temperature of each of these 3 elements as input to modify sweat rate on the skin, blood flow rate in the skin layer. The controlling procedure contains four steps as follows:

In the first step for the controller, the temperature error, T(N), and set temperature (or neutral temperature), TSET(N), is calculated for each component (N), N could be head core (C) or facial skin (S) component. Table 5 illustrates the approximated values for the set/reference temperatures.

$$ERROR_N = T_N - TEST_N \quad (27)$$

The second step is to check whether the sign of **the skin error** is positive or negative, that is, whether the element is warm or cold. If $ERROR_S$ is positive, it is redefined as $WARM_S$; if negative it is redefined as $COLD_S$. Since the measured

Table 5 Reference inputs for the facial skin thermoregulatory model

Set point	Value	Reference
Head core temperature (T_c)	36.6 °C	[72]
Head skin temperature (T_s)	The basal facial cutaneous temperature (i.e., before the exposure to the emotional stimuli) with a constant value calculating by averaging its time-domain curve values	Our research under submission

temperature will be at a region of interest from the face not the whole face, so we present SKINR factor that is simulating the relative weight of skin inside the selected facial region of interest (see Table 5 for knowing its approximated value).

$$\mathrm{WARMS} = \mathrm{SKINR} \times \mathrm{WARM_S} \tag{28.a}$$

$$\mathrm{COLDS} = \mathrm{SKINR} \times \mathrm{COLD_S} \tag{28.b}$$

The third step figures the controller orders to the body to: sweat on the skin layer (SWEAT) and modify skin blood flow due to vessels vasodilation (DILAT) or constriction (STRIC). Each command is the result of a signal from the deviation from the set temperature values at the head core, i.e., $\mathrm{ERROR_1}$, and at the facial skin (WARMS-COLDS) as shown in Eqs. 29a–c. Table 3 reports the definition and the approximated values of the used parameters.

$$\mathrm{SWEAT} = \mathrm{CSW} \times \mathrm{ERROR_1} + \mathrm{SSW} \times (\mathrm{WARMS} - \mathrm{COLDS}) \tag{29a}$$

$$\mathrm{DILAT} = \mathrm{CDIL} \times \mathrm{ERROR_1} + \mathrm{SDIL} \times (\mathrm{WARMS} - \mathrm{COLDS}) \tag{29b}$$

$$\mathrm{STRIC} = -\mathrm{CCON} \times \mathrm{ERROR_1} - \mathrm{SCON} \times (\mathrm{WARMS} - \mathrm{COLDS}) \tag{29c}$$

The fourth step is to take an action based on the received order. (i) Evaporation for the skin (Ev) (as shown in Fig. 11), is basal (diffusion), $\mathrm{Ev_0}$ plus sweat for cooling. (ii) The skin blood flow (SBF) (as shown in Fig. 11) contains the basal skin blood flow ($\mathrm{BFB_S}$) plus the modification from (DILAT) and (STRIC). Table 6 reports the definition and the approximated values of the used parameters in Eqs. 30a, b.

$$\mathrm{Ev} = \mathrm{Ev_{0s}} + \mathrm{SKINS} \times 2 \times \mathrm{ERROR_S}/4 \tag{30a}$$

$$\mathrm{SBF} = \mathrm{BFB_S} + \mathrm{SKINV} \times \mathrm{DILAT}/(1 + \mathrm{SKINC} \times \mathrm{STRIC}) \tag{30b}$$

In summary, starting with the previously illustrated step identification procedures (illustrated in Sect. 3.1), the facial skin thermoregulatory system could be evaluated by implementing the semi-empirical model defined by the set of

Table 6 Symbols used in the facial thermoregulatory model

Symbol	Definition	Value	Reference
α	= countercurrent heat exchange factor	1	[72]
SKINR	= the relative weight of skin inside the selected facial region of interest	0.21/10	[75]
CSW	= head core sweating-command coefficient (hypothalamus)	372	[75]
SSW	= skin sweating-command coefficient (assume skin adds to hypothalamus)	33.7	[75]
CDIL	= head core vasodilation-command coefficient (hypothalamus)	130	[75]
SDIL	= skin vasodilation-command coefficient (assume skin adds to hypothalamus)	10	[75]
CCON	= head core vasoconstriction-command coefficient (hypothalamus)	10.8	[75]
SCON	= skin coefficient-vasoconstriction command (assume skin adds to hypothalamus)	10.8	[75]
EV_{0s}	Basal evaporative heat loss (kcal/60/60 s)	0.81	[75]
BFB_S	Basal skin blood flow (l/60/60 s)	3.63	[75]

Table 7 The dynamic parameters defined in the facial skin thermoregulatory model

Parameter	Definition	Reference
H_0	Proportion to the environmental heat transfer	[72]
SKINV	Proportion to vasodilation of the facial skin blood vessels	[75]
SKINC	Proportion to vasoconstriction the facial skin blood vessels	[75]
SKINS	Proportion to sweating action at the facial skin layer	[75]

Eqs. 24–30a, b with a set of dynamic parameters, i.e., H_0, SKINV, SKINC, and SKINV (defined in Table 7), characterizing, respectively, the thermoregulatory passive heat exchange with the environment and the thermoregulatory vasomotor, vasoconstriction and vasodilation and sweating active effector mechanisms that are mainly controlled with the facial autonomic activity. Such dynamic parameters will be estimated from the facial thermal IR recovery curves by solving the identification fitness function (defined in Eq. 14) using the nonlinear least square optimization technique [40, 41].

As a result from our research efforts, the proposed model was validated to predict the dynamical response exhibited by the facial IR temperature signal measured during all the elicited emotional states and transitions; providing with that, for the first time, a great evidence that the Stolwijk model could be used to predict the facial skin temperature during emotional stimuli. The statistical significant difference provided with the estimated values of the model parameters among the studied groups of the emotional states and transitions elucidated that the proposed model could quantitatively investigate the "transient" and "subtile" change in the facial thermoregulatory passive and effector mechanisms, i.e., passive heat

exchange with the environment, the vasomotor actions (vasoconstriction and vasodilation) and sweating actions mediated with the ultradian rhythm and indirectly infer the transient changes in the facial autonomic sympathetic and parasympathetic activities during the transient change in the human emotional state.

Medical applications of the proposed modeling approach
This approach is used for investigating the facial thermoregulatory alterations in response the transient change of the subject's emotional state; emphasizing the promising ability of thermal infrared imaging as a contact-less emotion recognition tool for affective computing applications. Moreover, such modeling approach could flexibly applicable for IR differential diagnosis of several medical disorders like fever, studying thermal comfort, and predicting other emotional and psychological state of the human like autism and aging cases. However, it should be point out that the researcher should take care when considering any approximation or assumption in order to save the realistic perspective of the approach.

4 Summary and Conclusion

This chapter presents the commonly used approaches for modeling thermal infrared data for differential diagnosis purposes. In summary, two main modeling approaches were proposed, (i) Qualitative modeling approach based on using statistical and machine learning techniques, (ii) Quantitative modeling approach based on performing mathematical/analytical modeling of the thermoregulatory processes by using three main approaches: (i) empirically using automatic control theory, (ii) non-empirically using bioheat equations and (iii) semi-empirically using both bioheat equations and automatic control theory. Also, three main modeling approaches based on control system theory were presented, i.e., (i-a) time domain analysis of the thermoregulatory system's characteristics through a direct estimation of the closed-loop dynamic response parameters of a prototype second-order system, (i-b) a direct identification of thermoregulatory system as a second order system plus delay time (SOPDT) from a closed loop step response, and (i-c) state-space representation of the thermoregulatory system as a first-order differential equation from the experimental IR temperature curves. Table 8 summarizes the advantages and disadvantages of each modeling approach. Such summarized information could be a guide for the IR researcher in selecting the appropriate modeling approach regarding his research scope and interest. However, it should be pointed out that it is important to take care when considering the assumptions and approximations in order to choose the appropriate modeling approach because (i) increasing the considered assumptions and approximations may lead to hypothetical and speculative linking between the model parameters and with the local thermoregulatory actions like active rewarming and passive heat exchange, and (ii) increasing the model complexity may require high cpu processing timing and high research efforts for achieving the better explanation and description of

Table 8 A summary of advantages and disadvantages of the proposed modeling approaches

Item	Modeling approach						
	Statistics	Machine learning	Time domain characteristics of second-order system	SOPDT	State-space representation of first-order system	Bioheat transfer model	Bioheat transfer model + control system
Type of the descriptive parameters	Qualitative with statistical parameters	Qualitative with statistical parameters	Quantitative with hypothetical dynamic parameters	Quantitative with hypothetical dynamic parameters	Quantitative with hypothetical dynamic parameters	Quantitative with real thermal parameters	Quantitative with real thermal parameters and real dynamic parameters
Advantages	Statistical significance between healthy and non-healthy groups	True-prediction ratios of healthy and non-healthy groups	Abroad understanding of the complex mechanism underlying thermoregulatory malfunctions associated with the presence of a medical disorder			Compute parameters physiological (localized blood flow), thermal (metabolic heat production), and geometrical (location, depth and size)	Compute real parameters of the elevated control actions (vascular actions, sweating, shivering) associated with disease
Limitations	Presence of visual discrimination between the IR data of the healthy and non-healthy groups for time-consuming		Applicable only for systems lower than the third order	The measured IR recovery temperature curves should exposed exponential decay		Feasibility of the bioheat solving conditions, as for example, the studied tissue could be assumed to be volumetric and isotropic, and the superposition conditions	

interrelation between model parameters and the actual physiological alterations associated with the presence of a medical disorder. In summary, with the proposed modeling approaches, thermal infrared imaging has been demonstrated to be able to (i) identify significant averaged and asymmetric temperature parameters that could be used for disease classification, (ii) provide a direct functional IR indicators of the thermoregulatory malfunctions/alternations indirectly assess the severity of functional perturbation of the autonomic sympathetic and parasympathetic physiological activations in the presence of a disease, (iii) to compute physiological information, such as localized blood flow, cardiac pulse, and breath rate, and (iv) identify skin's thermal parameters, location of heat source (particularly the vessels), depth of heat source used for defining the location and geometrical shape of the affected area, mostly required for tumor detection, and (v) provide a clear description of the underlying alterations in the main thermoregulatory functions as for example, environmental heat exchange process, vasoconstriction and/or vasodilation, and sweating actions. Hence implementing such modeling approaches highly increase the potential ability of thermal infrared imaging to be a fascinating and promising complementary imaging tool to the gold-standard medical imaging methods for differential diagnosis.

References

1. Szentkuti, A., Kavanagh, H.S., Grazio, S.: Infrared thermography and image analysis for biomedical use. Periodicum Biologorum **113**(4), 385–392 (2011)
2. Calin, M.A., Mologhianu, G., Savastru, R., Calin, M.R., Brailescu, C.M.: A review of the effectiveness of thermal infrared imaging in the diagnosis and monitoring of knee diseases. Infrared Phys. Technol. **69**, 19–25 (2015)
3. Anbar, M., D'Arcy, S.: Localized regulatory frequencies of human skin temperature derived from the analysis of series of infrared images. In: Proceedings of the Fourth Annual IEEE Symposium on Computer-Based Medical Systems, pp. 184–191 (1991)
4. Hildebrandt, C., Raschner, C., Ammer, K.: An overview of recent application of medical infrared thermography in sports medicine in Austria. Sensors (Basel) **10**(5), 4700–4715 (2010)
5. Ring, E.F., Ammer, K.: Infrared thermal imaging in medicine. Physiol. Meas. **33**, 33–46 (2012)
6. Merla, A., Di Donato, L., Luzio, S.D., Romani, G.L.: Quantifying the relevance and stage of disease with the Tau image technique: a complementary diagnostic imaging technique based on infrared functional imaging. IEEE Eng. Med. Biol. Mag. **21**, 6 (2002)
7. Ring, E.F., Ammer, K.: The Technique of Infrared Imaging in Medicine, Thermology International, vol. 10(1), pp. 7–14
8. Merla, A.: Functional infrared imaging: new approaches and applications of thermal imaging to medicine and neuro-psychology. In: 6th International Infrared Conference InfraR&D, Hannover Fair, Hannover, Germany
9. Izhar, L.I., Petrou, M.: Thermal Imaging in Medicine, Advances in Imaging and Electron Physics, vol. 171, ISSN 1076-5670. doi:10.1016/B978-0-12-394297-5.00002-7
10. Lahiri, B.B., Bagavathiappan, S., Jayakumar, T., Philip, J.: Medical applications of infrared thermography. Infrared Phys. Technol. **55**, 221–235 (2012)

11. Montoro, J.C., Anbar, M.: New modes of data handling in computerized thermography. In: Harris, G., Walker, C. (eds.) Proceedings of the Annual International Conference of the IEEE Engineering in Medicine and Biology Society, vol. 10, pp. 845–847. New Orleans (1988)
12. Iven, G., Chekh, V., Luan, S., Mueen, A., Soliz, P., Xu, W., Burge, M.: Non-contact sensation screening of diabetic foot using low cost infrared sensors. In: IEEE 27th International Symposium on Computer-Based Medical Systems, pp. 479–480 (2014)
13. Ismail, E., Orlando, G., Corradini, M.L., Amerio, P., Romani, G.L., Merla, A.: Differential diagnosis of Raynaud's phenomenon based on modeling of finger thermoregulation. Physiol. Meas. **35**, 703–716 (2014)
14. Ismail, E., Orlando, G., Pompa, P., Gabrielli, D., Di Donato, L., Cardone, D., Merla, A.: Time-domain analysis of scrotal thermoregulatory impairment in varicocele. Front. Physiol. **5**, 342 (2014)
15. Ismail, E., Capo, A., Amerio, P., Merla, A.: Functional-thermoregulatory model for the differential diagnosis of psoriatic arthritis. BioMed. Eng. Online **13**, 162 (2014)
16. Capo, A., Ismail, E., Cardone, D., Celletti, E., Auriemma, M., Sabatini, E., Merla, A., Amerio, P.: Joint functional impairment and thermal alterations in patients with psoriatic arthritis: a thermal imaging study. Microvasc. Res. **102**, 86–91 (2015)
17. Capo, A., Merla, A., Mattei, P., Auriemma, M., Panarese, F., Celletti, E., Abate, M., Romani, G.L., Amerio, P.: Assessment of psoriatic arthritis by means of functional infrared imaging: a pilot study. Clin. Drug. Invest. (2013)
18. Diakides, N.A., Diakides, M., Lupo, J.C., Paul, J.L., Balcerak, R.: Advances in medical infrared imaging. In: Diakides, N.A., Bronzino, J.D. (eds.) Medical Infrared Imaging (Chapter 1). CRC Press, Boca Raton, FL (2008)
19. Mariotti, A., Grossi, G., Amerio, P., Orlando, G., Mattei, P.A., Tulli, A., Romani, G.L., Merla, A.: Finger thermoregulatory model assessing functional impairment in Raynaud's phenomenon. Ann. Biomed. Eng. **37**, 2631–2639 (2009)
20. Mariotti, A., Orlando, G., Corradini, M.L., Pompa, P., Iezzi, R., Cotroneo, A.R., Romani, G. L., Merla, A.: Scrotal thermoregulatory model and assessment of the impairment of scrotal temperature control in varicocele. Ann. Biomed. Eng. **39**, 664–673 (2011)
21. Cardone, D., Pinti, P., Merla, A.: Thermal infrared imaging-based computational psychophysiology for psychometrics. In: Computational Psychophysiology for Psychometrics, Computational and Mathematical Methods in Medicine, pp. 8 pages (2015)
22. Dowdall, J., Pavlidis, I., Tsiamyrtzis, P.: Coalitional tracking. Comput. Vis. Image Underst. **106**, 15 (2007)
23. Herry, C.L., Frize, M.: Digital processing techniques for the assessment of pain with infrared thermal imaging. In: Proceedings of the 24th Annual International Conference of the IEEE Engineering in Medicine and Biology Society, vol. 2, pp. 1157–1158 (2002)
24. Kennedy, D., Lee, T., Seely, D.: A comparative review of thermography as a breast screening technique. Integr. Cancer Ther. **8**(1), 9–16 (2009)
25. Ammer, K.: The sensitivity of infrared imaging for diagnosing Raynaud's phenomenon and for thoracic outlet syndrome is depended on the method of temperature extraction from thermal images. In: 9th International Conference on Quantitative InfraRed Thermography, Krakow, Poland (2008)
26. Hildebrandt, C., Raschner, C., Ammer, K.: An overview of recent application of medical infrared thermography in sports medicine in Austria. Sensors **10**, 4700–4715 (2010). doi:10.3390/s100504700
27. Oliver Faust, O., Acharya, U.R., Ng, Y., Hong, T.J., Yu, W.: Application of infrared thermography in computer aided diagnosis. Infrared Phys. Technol. **66**, 160–175 (2014)
28. Merla, A., Di Donato, L., Di Luzio, S., Farina, G., Pisarri, S., Proietti, M., Salsano, F., Romani, G.L.: Infrared functional imaging applied to Raynaud's phenomenon. IEEE Eng. Med. Biol. Mag. **6**, 73–79 (2002)
29. Merla, A., Di Ledda, A., Di Donato, L., Di Luzio, S., Romani, G.L.: Use of infrared functional imaging to detect impaired thermoregulatory control in men with asymptomatic varicocele. Fertil. Steril. **18**, 199–200 (2002)

30. Foerster, J., Kuerth, A., Niederstrasser, E., Krautwald, E., Pauli, R., Paulat, R., Eweleit, M., Riemekasten, G., Worm, M.: A cold-response index for the assessment of Raynaud's phenomenon. J. Dermatol. Sci. **45**, 8 (2007)
31. Hahn, M., Hahn, C., Jünger, M., Steins, A., Zuder, D., Klyscz, T., Büchtemann, A., Rassner, G., Blazek, V.: Local cold exposure test with a new arterial photoplethysmography sensor in healthy controls and patients with secondary Raynaud's phenomenon. Microvasc. Res. **57**, 12 (1999)
32. Gat, Y., Bachar, G., Zukerman, N., Belenky, Z.A., Gornish, M.: Physical examination may miss the diagnosis of bilateral varicocele: a comparative study of 4 diagnostic modalities. Urol **172**(4), 1414–1417 (2004)
33. Merla, A., Ledda, A., Di Donato, L., Di Luzio, S., Romani, G.L.: Assessment of the effects of varicocelectomy on the thermoregulatory control of the scrotum. Fertil. Steril. **81**, 471–472 (2004)
34. Pavlidis, I., Levine, J., Baukol, P.: Thermal image analysis for anxiety detection. In: Proceedings in International Conference on Image Processing, vol. 2, pp. 315–318. Thessaloniki, Greece (2001)
35. Pavlidis, I., Levine, J.: Thermal image analysis for polygraph testing. IEEE Eng. Med. Biol. Mag. **21**(6), 56–64 (2002)
36. Pavlidis, I.: Continuous physiological monitoring. In: Proceedings of the 25th Annual International Conference of the IEEE EMBS, pp. 1084–1087. Cancun, Mexico (2003)
37. Johnson, J.M., scand, J.: Exercise in a hot environment: the skin circulation. Med. Sci. Sports **20**, 29–39 (2010)
38. Johnson, J.M., Minson, C.T., Kellogg, D.L.: Cutaneous vasodilator and vasoconstrictor mechanisms in temperature regulation. Compr. Physiol. **4**, 33–89 (2014)
39. Duda, R.O., Hart, P.E., Stork, D.G.: Pattern Classification, 2nd edition. Wiley
40. Rollins, D., Hulting, S.: System identification of the human thermoregulatory system using continuous-time block-oriented predictive modelling. Chem. Eng. Sci. **61**, 1516–1527 (2006)
41. Nocedal, J.: Wright, Numerical Optimization, 2nd edition, pp. 248–250. Wiley (2006)
42. Tortura, G.J., Grabowski, S.R.: Principles of Anatomy and Physiology. Wiley, New York (2003)
43. Agurto, C., Chek, V., Edwards, A., Jarry, Z., Barriga, S., Simon, J., Soliz, P.: A thermoregulation model to detect diabetic peripheral neuropathy. In: 2016 IEEE Southwest Symposium on Image Analysis and Interpretation (SSIAI), pp. 13–16 (2016)
44. Heller, H.C., Dennis, A.G.: Arteriovenous anastomoses' function and Raynaud's phenomenon. Angiology **1**, 9 (2012)
45. Golnaraghi, F., Kuo, B.C.: Automatic Control Systems in Italic, 9th edn. Wiley, Hoboken (2010)
46. Rollins, D., Di Bhabdar, N., Hulting, S.: System identification of the human thermoregulatory system using continuous-time block-oriented predictive modelling. Chem. Eng. Sci. **61**, 12 (2006)
47. Yurkevich, V.D.: Predictive PID Control of Non-minimum Phase Systems. Kenny Uren and George van School, Intech (2011)
48. Ljung, L.: System Identification: Theory for the User, p. 809. Prentice-Hall, New Jersey (1999)
49. Seborg, D.E., Edgar, T.F., Mellichamp, D.A., Doyle, F.J.: Process Dynamics and Control, pp. 58–77, 102–123. Delhi Press, Delhi (2000)
50. Waterhouse, J.: Homeostatic control mechanism. Anaesth. Intensive Care **5**, 236–240 (2004)
51. Friedland, B.: Control Systems Design: State Space Methods. Dover, New York (2003)
52. Incropera, F.P., DeWitt, D.P., Bergman, T.L., Lavine, A.S.: Introduction to Heat Transfer, 5th edition. Wiley (2006)
53. Chekh, V., Soliz, P., Barriga, S., McGrew, E., Kanagy, N., Luan, S.: Novel model of thermoregulation based on control theory used to evaluate peripheral microvascular function. Exp. Biol. (2013)

54. Jiang, L., Zhan, W., Loew, M.H.: Modelling thermography of tumorous human breast: from forward problem to inverse problem solving. In: 2010 IEEE International Symposium on Biomedical Imaging: From Nano to Macro, pp. 205–208. Rotterdam, The Netherlands (2010)
55. Cetingul, M.P., Herman, C.: A heat transfer model of skin tissue for the detection of lesion: sensitivity analysis. Phys. Med. Biol. **55**(19), 5933–5951 (2010)
56. Pavlidis, I., Dowdall, J., Sun, N., Puri, C., Fei, J., Garbey, M.: Interacting with human physiology. Comput. Vis. Image Underst. **108**, 150–170 (2007)
57. Agnelli, J.P., Cristina, A.B., Turner, V.: Tumor location and parameters estimation by thermography. Retrieved from http://www.famaf.unc.edu.ar/abarrea/Imagenes/tumordetection-25-03-09.pdf (2010). Accessed June 2010
58. Bagavathiappan, S., Saravanan, T., Philip, J., Jayakumar, T., Raj, B., Karunanithi, R., Jagadeesan, K.: Investigation of peripheral vascular disorders using thermal imaging. Br. J. Diab. Vasc. Dis. **8**(2), 102–104 (2008)
59. Deng, Z.-S., Liu, J.: Mathematical modelling of temperature mapping over skin surface and its implementation in thermal disease diagnostics. Comput. Biol. Med. **34**(6), 495–521 (2004)
60. Mital, M., Scott, E.P.: Thermal detection of embedded tumors using infrared imaging. J. Biomed. Eng. **129**(1), 33–39 (2007)
61. WilsonGarbey, nSB, Spence, V.A.: A tissue heat transfer model for relating dynamic skin temperature changes to physiological parameters. Phys. Med. Biol. **33**(8), 895–912 (1988)
62. Pennes, H.H.: Analysis of tissue and arterial blood temperature in resting human forearms. J. Appl. Physiol. **2**, 93–122 (1948)
63. Garbey, M., Merla, A., Pavlidis, I.: Estimation of blood flow speed and vessel location from thermal video. In: Proceedings of the 2004 IEEE Computer Society Conference on Computer Vision and Pattern Recognition (CVPR'04), vol. 1, pp. 356–363 (2004)
64. Jiang, L., Zhan, W., Loew, M.H.: Toward understanding the complex mechanisms behind breast thermography: an overview for comprehensive numerical study. In: Proceedings of SPIE Medical Imaging: Biomedical Applications in Molecular, Structural, and Functional Imaging, vol. 7965 (2011)
65. Ren, Z.P., Liu, J., Wang, C.C., Jiang, P.X.: Boundary element method bem for solving normal or inverse bio heat transfer problem of biological bodies with complex shape. J. Therm. Sci. **4**, 117–124 (1995)
66. González, F.J.: Non-invasive estimation of the metabolic heat production of breast tumors using digital infrared imaging. Quant. InfraRed Thermogr. J. **8**, 2 (2011). doi:10.3166/qirt.8.139-148
67. Miccio, J., Parikh, S., Marinaro, X., Prasad, A., McClain, S., Singer, A.J., Clark, R.A.: Forward looking infrared imaging predicts ultimate burn depth in a porcine vertical injury progression model. Burns **42**(2), 397–404 (2016). doi:10.1016/j.burns.2015.07.006
68. Fujimasa, I., Chinzei, T., Saito, I.: Converting far infrared image information to other physiological data. IEEE Eng. Med. Biol. Mag. **19**(3), 71–76 (2000)
69. Kakuta, N., Yokoyama, S., Suzuki, T., Saito, T., Mabuchi, K.: Evaluation of infrared images by using a human thermal model. In: 2001 Proceedings of the 23rd Annual EMBS International Conference, 25–28 Oct, Istanbul, Turkey (2001)
70. Kakuta, N., Yokoyama, S., Mabuchi, K.: Human thermal models for evaluating infrared images: comparing infrared images under various thermal environmental conditions through normalization of skin surface temperature. IEEE Eng. Med. Biol. Mag. **21**(6), 65–72 (2002)
71. Werner, J.: Thermoregulatory models: recent research, current applications and future development. Scand. J. Work Environ. Health **15**(1), 34–46 (1989)
72. Stolwijk, J.A., Hardy, J.D.: Temperature regulation in man—a theoretical study. Pflügers Archiv **291**, 129–162 (1966)
73. Foda, E., Almesri, I., Awbi, H.B., Sirén, K.: Models of human thermoregulation and the prediction of local and overall thermal sensations. Build. Environ. **46**, 2023–2032 (2011)
74. El-Samahy, E., Mahfouf, M., Linkens, D.A.: A closed-loop hybrid physiological model relating to subjects under physical stress. Artif. Intell. Med. **38**, 257–274 (2006)

75. Konz, S., Hwang, C., Dhiman, B., Duncan, J., Masud, A.: An experimental validation of mathematical simulation of human thermoregulation. Comput. Biol. Med. **7**, 71–82 (1977)
76. Fiala, D., Lomas, K.J., Stohrer, M.: Computer prediction of human thermoregulatory and temperature responses to a wide range of environmental conditions. Int. J. Biometeorol. **45**, 143–159 (2001)
77. Ng, E.Y.K., Sudharsan, N.M.: An improved three-dimensional direct numerical modelling and thermal analysis of a female breast with tumour. Proc. Inst. Mech. Eng. **215** (2001)
78. Zolfaghari, A., Maerefat, M.: A new simplified thermoregulatory bioheat model for evaluating thermal response of the human body to transient environments. Build. Environ. **45**, 2068–2076 (2010)
79. Zavisek, M.: Breast cancer diagnostics using infrared camera. Retrieved from http://www.feec.vutbr.cz/EEICT/2003/msbornik/01-Electronics/03-PhD/08-scallop.pdf (2011a). Accessed Jan 2011
80. Zavisek, M.: Quantitative thermography in breast cancer detection—a survey of current research. Retrieved in January 2011b from http://www.feec.vutbr.cz/EEICT/2004/sbornik/03-Doktorskeprojekty/01-Elektronika/40-michal.pdf (2011b). Accessed 12 Feb 2012
81. Jayakumar, S.B., Saravanan, T., Philip, J., Tammana, Raj, Karunanithi, B., Panicker, R., Korath, T.M.P., Jagadeesan, K.: Investigation of peripheral vascular disorders using thermal imaging. J. Diab. Vasc. Dis. **8**(2), 102–104 (2008)
82. Kennedy, D., Lee, T., Seely, D.: A comparative review of thermography as a breast screening technique. Integr. Cancer Ther. **8**, 9–16 (2009)
83. Acharya, U.R., Ng, E.Y.K, Tan, J.H., Sree, S.V.: Thermography-based breast cancer detection using texture features and support vector machine. J. Med. Syst., 1–8 (2010). doi:10.1007/s10916-010-9611-z
84. Quek, C., Irawan, W., Ng, E.Y.K.: A novel brain-inspired neural cognitive approach to SARS thermal image analysis. Expert Syst. Appl. **37**(4), 3040–3054 (2010)
85. Marzec, M., Koprowski, R., Wrobel, Z.: Automatic temperature measurement on thermograms for headache diagnosis. Meas. Autom. Control **55**(11), 923–926 (2009)
86. Spalding, S.J., Kwoh, K., Boudreau, R., Enama, J., Lunich, J., Huber, D., Denes, L., Hirsch, R.: Three-dimensional and thermal surface imaging produces reliable measures of joint shape and temperature: a potential tool for quantifying arthritis. Arthritis Res. Ther. **10** (2008). doi:10.1186/ar2360
87. Armstrong, D.G., Lavery, L.A., Wunderlich, R.P., Boulton, A.J.M.: Skin temperatures as a one-time screening tool do not predict future diabetic foot complications. J. Am. Podiatr. Med. Assoc. **93**(6), 443–447 (2003)
88. Koay, J., Herry, C., Frize, M.: Analysis of breast thermography with an artificial neural network. In: Proceedings of the 26th Annual International Conference of the IEEE EMBS, pp. 1159–1162. San Francisco, California (2004)
89. Qi, H., Kuruganti, P.T., Snyder, W.E.: Detecting breast cancer from thermal infrared images by asymmetry analysis. In: Diakides, N.A., Bronzino, J.D. (eds.) Medical Infrared Imaging (Chapter 11). CRC Press, Boca Raton, FL (2008)
90. Tarnawski, W., Schaefer, G., Nakashima, T., Miroslaw, L.: Applications of fuzzy rulebased systems in medical image understanding. In: Pal, S.K., Peters, J.F. (eds.) Rough, Fuzzy Image Analysis: Foundations and Methodologies (Chapter 6). CRC Press, Boca Raton, FL (2010)
91. Wiecek, B., Strzelecki, M., Jakubowska, T., Wysocki, M., Drews-Peszynski, C.: Advanced thermal image processing. In: Diakides, N.A., Bronzino, J.D. (eds.) Medicalinfrared Imaging (Chapter 12). CRC Press, Boca Raton, FL (2008)
92. Merla, A., Romani, G.L.: Functional infrared imaging in medicine: quantitative, diagnostic approach. In: Proceedings of the 28th Annual International Conference of the IEEE, EMBS, vol. 1, pp. 224–227. New York City, USA (2006)
93. Grossi, G., Mariotti, A., Di Donato, L., Amerio, P., Tulli, A., Romani, G.L., Merla, A.: Functional infrared imaging of paroxysmal ischemic events in patients with Raynaud's phenomenon. Int. J. Immunopathol. Pharmacol. **23**(2), 627–632 (2010)

3D Dynamic Thermography System for Biomedical Applications

G. Chernov, V. Chernov and M. Barboza Flores

Abstract 3D thermography systems that combine 3D geometric data and 2D thermography data enable users to have a more accurate representation of the surface temperature distribution and aid in its interpretation. A system for 3D dynamic infrared thermography comprising two units is presented; each unit consists of an off-the-shelf depth camera rigidly mounted to a FLIR thermal camera. The units are fixed on the arms of the device that allow their placement in desired positions near the subject. To generate a single 3D thermogram, the data obtained from the depth cameras is registered with the images from the thermal cameras. The process of generating a 3D thermogram is repeated several times while thermally stimulating the surface of the subject to produce a series of 3D thermograms. The developed system provides a number of advantages in research for biomedical applications, such as the correct temperature measurements on curved surfaces, the possibility to select regions of interest by taking into account the shape of the subject and the possibility to use the 3D data to easily eliminate the background from 2D thermograms.

Keywords Infrared thermography · 3d thermography · Medical thermography

G. Chernov (✉)
Departamento de Física, Doctorado en Nanotecnología,
Universidad de Sonora, Hermosillo, Sonora 83000, Mexico
e-mail: g.chernovch@gmail.com

V. Chernov · M. Barboza Flores
Departamento de Investigación en Física,
Universidad de Sonora, Hermosillo, Sonora 83000, Mexico
e-mail: chernov@cifus.uson.mx

M. Barboza Flores
e-mail: mbarboza@cifus.uson.mx

E.Y.K. Ng and M. Etehadtavakol (eds.), *Application of Infrared to Biomedical Sciences*, Series in BioEngineering,
DOI 10.1007/978-981-10-3147-2_28

1 Introduction

Infrared (IR) thermography, as a method for functional diagnostics, is gaining more and more traction in various resource fields. The literature survey provided by Ammer [1] revealed that 1046 thermography related papers were published in 2015 and 206 of them were assigned to research areas related to medicine and biology. Medical IR thermography is an imaging technique that is fast, noncontact and radiation free, has proven useful for detecting and monitoring thermal abnormalities at the skin surface and has been applied with some success as a natural indicator of illness [2].

In addition to the usual passive method of thermography, dynamic IR thermography has been implemented as a valuable extension of static thermography [3]. Dynamic IR thermography is based on the introduction of external thermal stimulation and the subsequent observation of the thermal recovery process in the area of interest. This provides additional information about the distribution of heat flow and the thermal processes in the area below the surface. In medicine, dynamic IR thermography was proposed, in particular, for the detection of breast cancer [4], for skin burn diagnostics [5], for detecting skin cancer [6] and as a promising alternative to computed tomography angiography for preoperative perforator mapping in breast reconstruction [7].

Standard thermograms obtained using conventional IR cameras are two-dimensional in nature, and because of that possess some limitations. One peculiar property of IR cameras is the effect of surface curvature on the reported temperature, as the angle between the viewing axis and the normal of the studied surface increases, the apparent temperature of the surface decreases [8]. This significantly limits the precision of the measurement for surface temperature on objects of complex shapes, such as different parts of the human body, which limits the applicability of thermography as a tool for medical diagnostics. To overcome the limitations and provide more accurate measurement of surface temperature, Sawicki et al. [9] and Wiecek et al. [10] have proposed to apply multichannel image acquisition with single thermal and two visual cameras. 3D object reconstruction enables the possibility to calculate the normals of the surface and to compensate for the error due to viewing angle dependent emissivity.

As of today, more than thirty 3D thermography systems are described in the literature for application in the automotive and manufacturing industry, thermal inspections of buildings, nondestructive testing and medicine. The systems combine thermographic and the surface geometry data of a tested object. They differ in several aspects such as equipment used, 3D scanning technique, calibration and fusion method and application area. In this work we present a new 3D dynamic infrared thermography system that allows us to generate a series of 3D thermograms while thermally stimulating the surface of human body.

2 3D Thermography Systems, Literature Survey

As mentioned in the introduction, 3D thermography allows for more accurate measurements, when compared to 2D thermography. Below, a concise overview of 3D thermography systems that are or could be used for biomedical imaging applications is presented. The overview is divided into three parts based on the type of 3D scanners used in the proposed systems. The first part describes the systems based on passive scanning techniques; the second and third parts are devoted to systems based on custom and commercial active 3D scanners, respectively. The basic characteristics of the systems together with the short description of tested objects are chronologically summarized in Tables 1, 2 and 3.

2.1 Thermography Systems Based on Passive 3D Scanning Techniques

The straightforward and simple technique to construct a 3D temperature map consists of a thermal stereo system, that is, a pair of thermal cameras [11–14]. 3D coordinates of a number of points in a scene are determined by triangulation of

Table 1 Thermography systems based on passive 3D scanning techniques

Paper	3D scanning technique and equipment	Test object
Aksenov et al. [23]	Stereo range finding (photogrammetry) with two high-resolution color cameras	Knees of an athlete who has a knee inflammation
Ju et al. [24]	Stereo range finding (photogrammetry) with two high-resolution color cameras	A face
Ng and Du [17]	Silhouette-based reconstruction from a set of 2D images taken by a thermal camera	A small car model with a heat source
Prakash et al. [12]	Thermal stereo scanning with two thermal cameras	A cup containing hot water
Prakash et al. [13]	Thermal stereo scanning with two thermal cameras	Heated cylinder with an adjustable heating element
Prakash et al. [14]	Thermal stereo scanning with two thermal cameras	A laptop
Mirabella et al. [16]	Thermal stereo scanning with two digital reflex cameras	Twenty healthy subjects and twenty patients with mixed arteriovenous ulcers
Sella et al. [15]	Thermal stereo scanning (?) provided with dual optical heads setup	Breasts of 1827 healthy and cancerous women
Chen et al. [19]	Silhouette/contours reconstruction from a set of 2D images taken by a thermal camera	A light bulb, a computer case with and a metal container, both with an internal heat source

Table 2 Thermography systems based on active 3D custom scanning techniques[a]

Paper	3D scanning technique and equipment	Test object
Xiao et al. [26]	Structured light scanning with a structured pattern projector and a CCD digital camera	A human forearm with a drop of warm water
Barone et al. [27]	Structured light scanning with a standard multimedia video projector and a monochrome digital camera	A hand and a foot of a diabetic patient
Cheng et al. [30]	Structured light scanning with a structured light binocular profilometer consisting of one LCD projector and two black-and-white cameras and a color CCD camera	An aluminous workpiece, the first author's face, a volunteer with a skin infection on his left leg
Barone et al. [28]	Scanning technique based on a coded structured light approach and a fringe projection method with a standard multimedia video projector and a color digital video camera	Wound bed areas of seven different leg ulcers
Grubišić et al. [21]	Structured light scanning with a digital light processing video projector and a digital firewire camera	None presented
Yang and Chen [29]	Structured light scanning with two color cameras and a liquid crystal display projector	A human face, pork surface in hyperthermia
Sun et al. [31]	Structured light scanning with two visible light cameras and a digital projector	A storage box, a rudder model and a person's outstretched arm
An and Zhang [20]	Static object measurement system based on structured light scanning with a DLP and CMOS camera	A small statue
An and Zhang [20]	Real-time measurement system based on structured light scanning with a high-speed DLP projector, a high-speed CMOS camera and an external timing generator	A hand and a human face

[a]All systems include one IR camera for 2D thermal image acquisition

matching points. When searching for matching points between two thermal images the isotherms of the thermal images can be used. Sella et al. [15] have presented dual-head 3D infrared imaging that should help to providing metabolic signatures from breast lesions. Unfortunately, the authors did not describe neither dual optical heads setup used for thermal image acquisition nor 3D scanning technique. Later, Mirabella et al. [16] have applied passive stereo vision for generation of a 3D model with a thermographic texture. However, as was noted in [13], the thermal stereo method will only work if there is a temperature gradient on the object surface, otherwise there will be no distinctive isotherms to work with.

Table 3 Thermography systems based on commercial active 3D scanners[a]

Paper	3D scanning technique and equipment	Test object
Scala et al. [33]	Structured light scanning with a Microsoft Kinect depth camera	None presented
Rangel et al. [32]	Structured light scanning with a Microsoft Kinect depth camera	An outstretched utility corridor
Moghadam [34]	Structured light scanning with a ASUS Xtion Pro Live RGB-D color and range sensor	A torso with a right shoulder chronic inflammation, lower limbs with a history of injuries, a thigh with sealed wound
Müller and Kroll [38]	Structured light scanning with a depth sensor	A small process furnace
de Souza et al. [39]	Structured light scanning with A 3D Gemini scanner	A head of an asymptomatic volunteer

[a]All systems include one IR camera for 2D thermal image acquisition

Instead of using two thermal cameras, Ng and Du [17] have processed a sequence of 2D thermal infrared images of an object (a small Ferrari car model with a chemical warmer inside it) taken around the model with a 20 degree interval between each image. They then reconstructed the 3D temperature distribution using the rapid octree carving technique [18] to acquire the geometric information from the silhouettes of the object. Similarly, Chen et al. [19] have proposed a 3D infrared imaging system that uses silhouette volume intersection to reconstruct the 3D model of objects in the thermal images.

Because of the limitations of the stereo thermal camera setup, most 3D thermography systems combine a thermal camera with a 3D scanning device or system. Over the past decades, a number of 3D shape scanning techniques have been developed. Depending on the 3D acquisition method, the techniques can be divided into two groups: passive and active [20, 21]. The passive techniques, focus/defocus and stereo vision, do not require active illumination, while the active ones use external light sources. The depth from focus/defocus technique, which is common in photography and microscopy can not be applied to thermal imaging yet [22]. Another passive 3D scanning technique that is frequently used in 3D thermography systems is stereo vision.

Aksenov et al. [23] and Ju et al. [24] have used two high-resolution color cameras to generate differing views of an object. A 3D model of the object can be built by comparing the two images and using stereo photogrammetry. The generation of a 3D thermogram is achieved by mapping the IR picture taken by the infrared camera to the 3D model. Since the thermal camera and the stereo cameras are calibrated together, the mapping phase is quite straightforward.

2.2 Thermography Systems Based on Custom Active 3D Scanning Techniques

Among the active 3D scanning techniques, the structured light system features high quality and reliability for 3D measurement [25]. This technique is compact, simple and most suitable for biomedical applications.

Xiao et al. [26] developed a simple and compact surface profiling system consisting of a double pinhole interferometer, in which an interference fringe pattern is directly projected onto a human body and a CCD camera captures the reflected fringes. A structured light scanning technique that combines phase analysis and a triangulation method was used for the 3D surface reconstruction.

Barone et al. [27] have presented an optical system based on integrating thermal imaging with a 3D vision machine. High quality 3D models containing both geometry and surfaces color information were obtained with a structured light scanner. The point cloud acquisition uses a gray code approach and structured light generated by the projector. The texture acquisition methodology consists in the projection of images corresponding to the decomposition of white light into primary colors. Later, Barone et al. [28] modified the 3D thermography system by adding a color digital video camera that enabled the simultaneous acquisition of 3D geometrical data, color texture and surface temperature information of the anatomical parts. The direct mapping of chromatic and thermal images to the 3D model is performed by a calibration procedure spatially relating the IR detector with respect to the video camera sensor.

The system proposed by Grubišić et al. [21] consists of a thermal camera and a 3D scanner that is in turn composed of a digital light processing video projector and a digital camera. The 3D reconstruction component of the system developed by Yang and Chen [29] is based on the structured light technique and uses two color cameras that reduce the shaded area on the object surface, improve the accuracy of the sensor, and aid in the calibrations of structured light and thermal cameras.

Cheng et al. [30] developed a system that could simultaneously provide a precise 3D true-color photograph and 3D thermogram. A structured light binocular profilometer consists of an LCD projector installed between two black-and-white cameras, which limits shadow effects due to surface occlusions. The obtained range coordinates are mapped to 2D visual and thermal images to create 3D color photograph and 3D thermograph, respectively.

Sun et al. [31] have integrated a thermal camera into a structured light based binocular stereo vision system and realized 3D infrared imaging by fusing the metric information and IR information of the tested object. The registration of the 2D infrared image to the 3D point cloud was accomplished based on trifocal tensor and bilinear interpolation.

An and Zhang [20] have developed a holistic approach to calibrate both structured light system and thermal camera under exactly the same world coordinate system and a computational framework to determine the sub-pixel corresponding

temperature for each 3D point as well as discard those occluded points. They have designed two 3D different thermography systems. The first system, whose 3D scanner consists of a DLP projector and a CMOS camera was designed for static object measurement. The second one that uses a high-speed DLP projector, a high-speed CMOS camera and an external timing generator provides simultaneous acquisition in real time. Testing experiments verified the accuracy of the developed method of mutual calibration and demonstrated that the static and real-time system systems can achieve simultaneous 3D geometric shape and surface temperature measurement with a resolution of 1280 × 1024 points per frame and with a resolution of 768 × 960 pixels per frame at 26 Hz, respectively.

2.3 *Thermography Systems Based on Commercial Active 3D Scanners*

An approach that has been gaining popularity in recent years is the usage of off-the-shelf depth cameras for obtaining the 3D shape directly from the depth map produced by these devices [32, 33]. A depth camera is a device that produces an image in which the value of each pixel is proportional to the distance from the camera to the object at that pixel location. In recent years, a variety of such devices has become available commercially at a relatively low cost, for example the Microsoft Kinect and the SoftKinetic DS325. These devices provide an accurate, but somewhat noisy, depth image that can be used for 3D reconstruction and to produce 3D thermograms with relatively little setup. These systems also have the advantage of having a small, self contained package that aids portability.

Skala et al. [33] were one of the first who developed 4D thermography system through integration of the Microsoft Kinect device and a thermal camera. The Microsoft Kinect consists of a depth camera composed of a near-infrared projector, near-infrared camera, RGB camera and four microphones, all rigidly mounted together. The depth camera and RGB camera track the motion and record reconstructed real-time 3D model of a tested object providing its 3D dynamic scanning. Mutual calibration of the depth, RGB and thermal cameras makes it possible to register the images and create a set of real-time 3D thermograms.

Rangel et al. [32] have presented an approach allowing automatic creation of 3D thermal models by using a Microsoft Kinect depth camera and a thermal camera. The cameras were arranged in a fixed way and their spatial relation was obtained by means of a geometric calibration based on the pinhole camera model.

Moghadam [34] has described a small, portable 3D medical thermography device consisting of a ASUS Xtion Pro Live RGB-D (color and range) sensor (similar in concept to Microsoft Kinect) and a thermal camera rigidly attached in close proximity and mounted on an ergonomic handle. The device is similar to the 3D thermography systems described in [35–37] and gives an operator holding the

device the ability to take several images from multiple viewpoints. The device, in this case, will adaptively combine temperature from multiple viewpoints by taking into account the reliability of each individual measurement [38].

Müller and Kroll [34] have developed a handheld 3D thermography system consisting of a thermal camera and a PrimeSense Carmine 1.09 depth sensor rigidly attached to an acrylic frame to maintain the relative position and orientation of both sensors. During the generation of a 3D thermogram the system is moved around the object and multiple temperature measurements corresponding to the same point on the object's surface are taken. The measured temperatures are averaged with weights depending on the distance to target, emission angle, and observation angle.

de Souza et al. [39] have developed a methodology for combining into a single representation thermographic data measured with a thermal camera and a precise 3D spatial model generated by a 3D commercial scanner. The structure from motion technique was applied to a set of thermal images for finding the correct thermal camera positions and rotations in space and generating an "auxiliary mesh." Then, the methodology was consisted of using the auxiliary mesh as an intermediate stage in order to aid with the projection of infrared images onto a precise 3D scanned surface mesh.

2.4 Brief Overview of 3D Thermography Systems

Tables 1, 2 and 3 briefly describe 23 3D thermography systems designed between 2003 and today that are used or could be used for biomedical imaging applications. All the proposed systems provide the reconstruction of a 3D model from an object under study and its fusion with thermographic data.

All these systems use the 3D model and thermographic data only to provide a visualization of the subject that can be freely rotated in space and viewed from any angle. These systems do not take the geometric information provided by the 3D model to do any kind of additional processing of the thermogram.

Almost all proposed 3D thermography systems ignore the effect of angle of incidence, distance between the device and the subject or other factor and fuse a 3D model with temperatures directly given by a thermal camera. There are only few exceptions.

One attempt to use three dimensional information to create more accurate representations of an object's surface temperature was presented by Sawicki et al. [9]. Their proposed method involved estimating the emission angle to compensate for the error due to viewing angle dependence of the emissivity. Aksenov et al. [23] and Ju et al. [24] took into account the angle and distance between the object and the thermal camera and have proposed to construct so called standardized 3D thermograms. Vidas and Moghadam [36] have proposed a new raycasting method, which implements a multivariable weighting scheme to accurately map temperature and color estimates to the 3D model from multiple views. A similar idea was used

by Müller and Kroll [34], who proposed to take multiple thermal images from various directions and average measured temperatures taking into account relative positioning of a camera and the test surface.

To our knowledge, none of the existing 3D thermography systems used available 3D surface information for the segmentation of obtained thermograms and selection of ROIs.

3 Construction of a 3D Thermogram

To construct a 3D thermogram, information about surface temperature must be combined with information about surface geometry. Surface temperature information can be provided by thermal imaging cameras and surface geometry information by depth cameras, the former captures a temperature map and the latter, a depth map. Additionally, a method to relate the temperature information to the geometry information is required. This chapter presents the basic models and calculations necessary for this.

In computer graphics and image processing the standard way to describe a camera is the pinhole camera model. This model relies on several parameters in order to approximate a real world camera, and these parameters must be obtained via a calibration procedure. In order to register together a temperature map and a depth map, the relative positions and rotations of the cameras, also known as camera pose, are needed, and these can also be obtained via a proper calibration procedure. Once a frame of reference is established and all the camera poses are known, the depth maps must be converted to a set of points from which one or more surfaces of interest can be extracted for visualization and analysis. The surface can then be projected onto the temperature map in order to obtain the temperatures on the surface of the objects under study.

3.1 The Pinhole Camera Model

A camera is a device that generates images, which are two-dimensional representations of the objects that the camera can see in its field of view. Light that is emitted or reflected by an object enters through the camera lens and is collected on the camera sensor to form an image. When working with image processing or computer visualization, an abstraction used to describe this behavior and to represent a camera is the pinhole camera model, this model is used to describe the relationship between the objects in the field of view of the camera and the 2D image produced by the camera. The components of this model are the center of projection of the camera, known as the pinhole, the points or objects in space, known as the scene, and the image plane, onto which the scene is projected.

The camera and the objects that the camera is looking at are located in space and light rays originating from the scene pass through the center of projection and land on a point in the image plane. In order to simplify the calculations, the center of projection, $\mathbf{O} = (0, 0, 0)^{\mathrm{T}}$, is set as the origin of the coordinate system and all the points of the scene are specified relative to this origin, this coordinate system is known as camera space. The distance from the center of projection to the image plane is known as the focal length, f. The image plane is perpendicular to the optical axis of the camera, which describes the viewing direction of the camera and passes through the center of projection. The purpose of the camera model is to describe how a point in space, $\mathbf{P} = (X, Y, Z)^{\mathrm{T}}$, is projected onto the image plane and how to calculate its corresponding image coordinates $(u, v)^{\mathrm{T}}$.

If the image plane is behind the center of projection, as it would be in a pinhole camera setup, then the image will be generated upside down, thus it is more practical to modify the model to one in which the image plane is between the center of projection and the scene, this model is shown in Fig. 1.

Since the model is used to describe real cameras, several things must be taken into account. In practice, f is not enough, because the pixels are not square, so f_x and f_y are introduced to describe the focal lengths along the x and y axis of the image plane. Additionally, an image captured by a digital camera is represented in memory as a 2D array, thus image coordinates often start at the top left corner of the image, and in the case of certain visualization packages like OpenGL, image coordinates start at the bottom left of the image. Thus it is necessary for the model to account for this, an appropriate displacement must be introduced into the model, c_x and c_y are used to specify the coordinates of the center of the image plane. It is

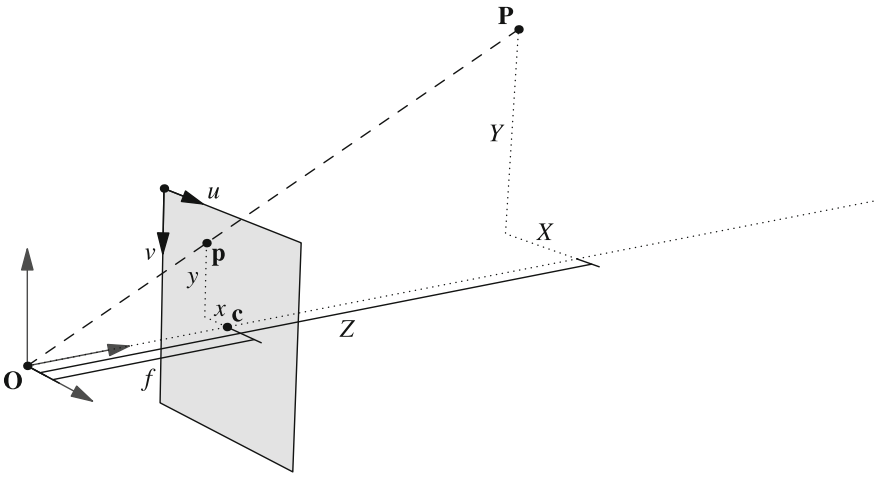

Fig. 1 Camera model: a point **P** is projected onto the image plane, the resulting point **p** is on the intersection of the image plane and the ray connecting the point **P** and the center of projection **O**

possible to approximate these displacements as half the image width and height in pixels, for c_x and c_y respectively, however in practice the sensor is usually misaligned so c_x and c_y need to be obtained during calibration. Furthermore, real cameras use lenses and due to manufacturing defects the sensor is not always totally perpendicular to the optical axis, which introduces radial and tangential distortions, which need to be accounted for.

Thus, using the camera model and by the properties of similar triangles, the image coordinates of the point **P**, u and v are calculated as follows:

$$\begin{aligned} u &= f_x \frac{X}{Z} + c_x \\ v &= f_y \frac{Y}{Z} + c_y \end{aligned} \tag{1}$$

The focal lengths of the camera as well as the coordinates of the center of the image plane are known as the intrinsic camera parameters. These parameters are usually specified as a matrix, K, that is known as the intrinsic camera matrix:

$$K = \begin{bmatrix} f_x & 0 & c_x \\ 0 & f_y & c_y \\ 0 & 0 & 1 \end{bmatrix}$$

To use the intrinsic camera matrix, the calculations in 1 must be written as $\mathbf{p}' = K\mathbf{P}$, which results in a $\mathbf{p}'$ of the form $(x, y, Z)^{\mathrm{T}}$, thus to obtain the final u and v the perspective divide must be performed:

$$\begin{aligned} u &= \frac{x}{Z} \\ v &= \frac{y}{Z} \end{aligned}$$

The model described so far is based on the fact that the points to be projected are specified relative to the camera and that the camera itself is located at the origin, that is, the points are specified in camera space. However, points are usually specified in a frame of reference tied to a different origin, and a camera will have its own position and rotation in this frame of reference, which is also known as world space. Thus, to fully describe a camera, the model needs to be extended to describe the pose of the camera. The pose is composed of a 3×3 rotation matrix R and a 3×1 translation vector $\mathbf{t}$, which together form a transformation matrix $T = [R|\mathbf{t}]$, that is known as the extrinsic camera matrix.

Thus, a camera can be described using an intrinsic matrix K and an extrinsic matrix T. For real cameras, these matrices are estimated using a calibration procedure.

3.2 Calibration and Pose Estimation

Camera calibration refers to the procedure by which the parameters of a real camera are computed. More specifically, calibration consists of intrinsic camera calibration and extrinsic camera calibration, also known as pose estimation. Additionally, camera calibration must account for any image distortion introduced by the camera. Camera calibration is performed using a calibration target. A calibration target consists of an object with features arranged in a known pattern and easily detectable using computer vision algorithms. Commonly used calibration targets include a checkerboard pattern printed on a flat surface or a grid of circles, either holes or printed, on a flat surface. Particular care must be taken when choosing a calibration target for use with thermal and depth cameras. A flat target with a pattern consisting of an asymmetric grid of circular holes of a fixed diameter works well for this purpose [32], holes are visible to both a depth camera and a thermal camera, and thermal contrast could be further enhanced by heating the target. Additionally, such a target is easy to make. Figure 2 shows an example of a target, a rectangular board with an asymmetric grid of circles, used for the calibration of the 3D dynamic thermography system as it appears on a thermal camera and on a depth camera.

Both intrinsic and extrinsic calibration procedures work by detecting a known pattern in a series of images and computing the transformations needed to achieve the position of the pattern in the camera image. The details of the camera calibration algorithms are complicated and beyond the scope of this work, however, a standard software library, OpenCV, implements all the methods required to achieve reliable camera calibration [40].

Intrinsic camera calibration needs to be performed for each camera individually. Certain cameras, like the Creative Senz3D, have intrinsic calibration values available, either provided by their software development kit (SDK) or in the documentation, and these values are generally enough for most applications. However, most cameras need to be calibrated. The intrinsic calibration procedure works with multiple images of the same pattern, taken at slightly different angles (as shown in Fig. 3). The result of the procedure is the set of intrinsic camera parameters, which

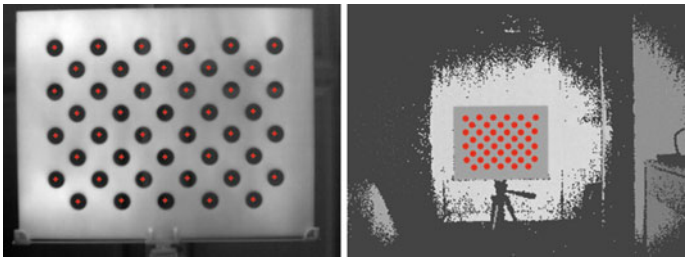

Fig. 2 Calibration target as seen on the thermal image (*left*) and the depth image (*right*). *Red dots* represent the locations of the hole centers in the calibration target as detected automatically by the software

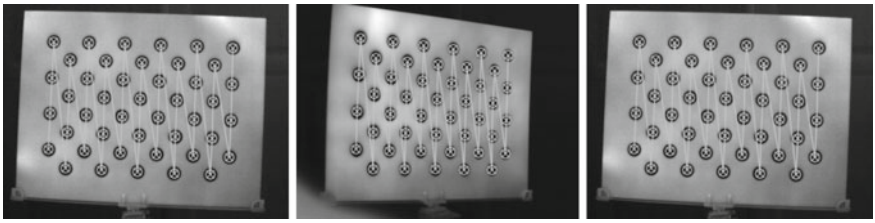

Fig. 3 Example images of the calibration target taken with a FLIR A320 camera used for finding intrinsic parameters of the camera

are stored in the intrinsic camera matrix (K). Additionally a vector of values representing the radial and tangential distortion of the camera is computed, and these values are used to correct the distortion in the image.

Extrinsic camera calibration needs to be performed for each camera in the system at the same time, in order to establish a frame of reference for the positions of all the cameras. The procedure consists of aiming the cameras in the system toward a known pattern, and the result of the procedure is a transformation matrix T for each camera that gives the camera pose in space, with the pattern as the origin of the world coordinate system.

3.3 Transforming a Depth Map to a Point Cloud

A depth camera provides information about the surface it's pointed at in the form of a depth map D. A depth map is an image in which each value $D(u, v)$ is directly proportional to the distance from the camera to the surface visible at location (u, v). In order to be able to work with these values, it is required to transform the depth map into a collection of homogeneous points $\mathbf{p}_w = (x_w, y_w, z_w, 1)^{\mathrm{T}}$ in the world coordinate system. Since the depth map consists of depth values relative to the camera, first the values have to be transformed into points $\mathbf{p}_c = (x_c, y_c, z_c, 1)^{\mathrm{T}}$ in the camera coordinate system, that is, a coordinate system whose origin is the camera center of projection. The transformation from world coordinates to the camera coordinate system is provided by a transformation matrix:

$$T_d = \begin{bmatrix} R_d & \mathbf{t}_d \\ \mathbf{0} & 1 \end{bmatrix} \tag{2}$$

Thus, $\mathbf{p}_w = T_d \mathbf{p}_c$. The transformation matrix T_d corresponds to the six degree of freedom (6DOF) estimated camera pose for the depth camera in world space.

To calculate a point $\mathbf{p}_c$ for each value $D(u, v)$, some information about the depth camera is needed. Different models of depth cameras provide different types of depth maps and some of them require additional work to convert the value $D(u, v)$

to an actual distance measurement. In the case of the Creative Senz3D depth camera, each pixel value corresponds directly to the Cartesian distance z_c in meters from the camera to the surface. Once z_c is known, it is possible to use the pinhole camera model to calculate x_c and y_c, using the intrinsic parameters of the camera (f_x, f_y, c_x and c_y).

Each pixel (u, v) with the value $D(u, v)$ corresponds to a point on the image plane $\mathbf{p}_D = (x_D, y_D, z_D)$, where:

$$\begin{aligned} x_D &= u - c_x \\ y_D &= v - c_y \\ z_D &= f \end{aligned}$$

In practice, since camera pixels are not square, the focal length f is actually two different focal lengths f_x and f_y. Using this information it is possible to calculate the point $\mathbf{p}_c = (x_c, y_c, z_c, 1)^{\mathrm{T}}$ with simple geometry, using the properties of similar triangles and the fact that $z_c = D(u, v)$: (Fig. 4)

$$\begin{aligned} \frac{x_D}{f_x} &= \frac{x_c}{z_c} \\ \frac{y_D}{f_y} &= \frac{y_c}{z_c} \end{aligned}$$

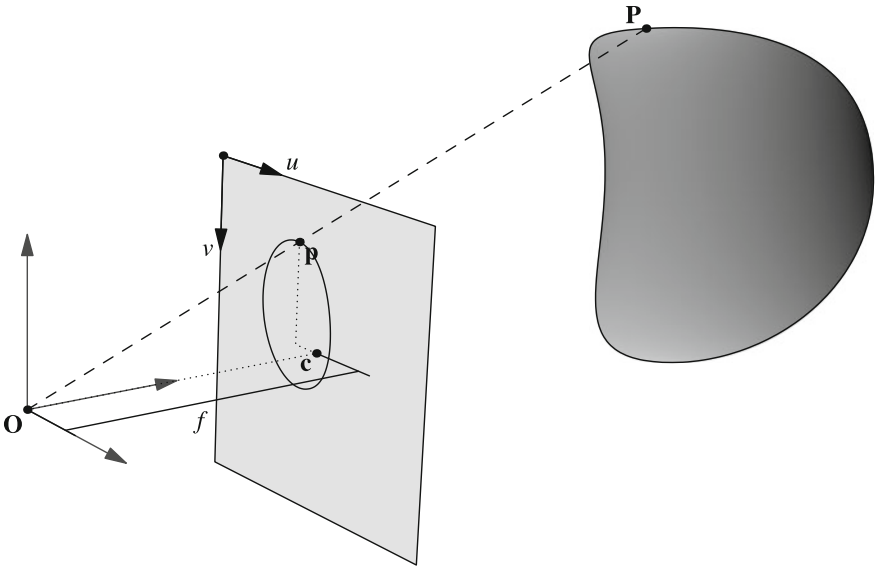

Fig. 4 A point $\mathbf{p}_c$ can be calculated from the value at $D(u, v)$. The point **O** is the center of projection of the depth camera, the point $\mathbf{c} = (c_x, c_y)$ is the center of the imaging sensor, and f is the focal length

It follows that, for each pixel (u, v) with value $D(u, v)$, the Cartesian coordinates of the corresponding point $\mathbf{p}_c = (x_c, y_c, z_c, 1)^{\mathrm{T}}$ are:

$$x_c = D(u, v)\frac{u - c_x}{f_x}$$
$$y_c = D(u, v)\frac{v - c_y}{f_y}$$
$$z_c = D(u, v)$$

Finally, the world coordinates of the point $\mathbf{p}_w$ are calculated by the transformation $\mathbf{p}_w = T_d\mathbf{p}_c$.

In addition to providing a depth map D, the Creative Senz3D camera also provides a corresponding confidence map C, where the value of each pixel $C(u, v)$ represents how confident the device is in the accuracy of the measurement at the pixel (u, v). Thus gives a possibility to discard any pixel with the confidence value below a certain threshold and avoid any unnecessary calculations on that particular pixel.

3.4 Projection

Once the depth map is converted to a set of points in the world coordinate system, the next step is to calculate to which point in the thermal image the point $\mathbf{p}_w$ corresponds to, as this is needed to calculate the temperature of that point. This means that the point $\mathbf{p}_w$ must be projected to a point on the image plane of the thermal camera. During the calibration process, an intrinsic thermal camera matrix K_t and an extrinsic thermal camera matrix T_t are obtained for a thermal camera. Generally, these matrices could be used as-is to project the point $\mathbf{p}_w$, however this presents a problem. Since the thermal camera is located in a different position from the depth cameras used to obtain the point cloud and there can be multiple depth cameras with different views, it is entirely possible that two points correspond to the same coordinate on the thermal image. Thus, a way to determine which point is closer to the camera is needed. Additionally, it is convenient for visualization and to speed up processing to present the intrinsic matrix in a way compatible with existing visualization packages, namely OpenGL. All this can be accomplished by extending the intrinsic camera matrix K_t to a 4×4 projection matrix M_t

$$M_t = \begin{bmatrix} f_x & 0 & -c_x & 0 \\ 0 & f_y & -c_y & 0 \\ 0 & 0 & z_n + z_f & z_n z_f \\ 0 & 0 & -1 & 0 \end{bmatrix}$$

where f_x, f_y, c_x and c_y are the same as in the intrinsic camera matrix K_t and z_n and z_f are the near and far clipping planes, which are constants that can be chosen as is convenient since they do not correspond to any real property of the camera.

The projection matrix M_t maps points from coordinates relative to the camera (camera space) to the coordinates of an image (image space). To transform the points from world space to camera space, another transformation is needed. The 6DOF camera pose in world space is specified by the matrix T_t obtained during camera calibration

$$T_t = \begin{bmatrix} R_t & \mathbf{t}_t \\ \mathbf{0} & 1 \end{bmatrix}$$

where a R_t is the rotation of the camera relative to the world coordinates, $\mathbf{t}_t = (x_t, y_t, z_t)^{\mathrm{T}}$ is the position of the camera in world coordinates.

In camera space, the camera is at origin and aligned with the coordinate system, thus a transformation T_c from world space to camera space, when applied to the camera pose T_t must be equal to I:

$$T_c = T_t^{-1} = \begin{bmatrix} R_t & \mathbf{t}_t \\ \mathbf{0} & 1 \end{bmatrix}^{-1} = \begin{bmatrix} R_t^{\mathrm{T}} & -R_t^{\mathrm{T}}\mathbf{t}_t \\ \mathbf{0} & 1 \end{bmatrix}$$

Thus, to project a point $\mathbf{p}_w$ using the camera parameters to a point $\mathbf{u}_t = (u_t, v_t)^{\mathrm{T}}$ on the image plane of the thermal camera, the following steps are done.

First, the point $\mathbf{p}_w$ is transformed into the camera coordinate space:

$$\mathbf{p}_c = T_c \mathbf{p}_w$$

The point in camera coordinate space must then be projected onto the image plane of the thermal camera:

$$\mathbf{p}_i = M_t \mathbf{p}_c$$

where $\mathbf{p}_i = (x_i, y_i, z_i, w_i)^{\mathrm{T}}$. Finally, a perspective divide must be performed, thus:

$$u_t = \frac{x_i}{w_i}$$
$$v_t = \frac{y_i}{w_i}$$

and the coordinate z_i/w_i can be used to determine the relative depth of the points.

3.5 Surface Reconstruction

After the data from the depth cameras is obtained, cleaned and transformed to a point cloud, there still remains the problem of reconstructing the surface of the subject, including the segmentation of the point cloud into various sets, like the background, the subject and any other object of interest. Additionally, in order to apply temperature correction, the normals of the surface must be calculated.

The first step in reconstructing the surface is to determine which points belong to the subject and which points do not. In this particular case, this can be achieved by means of a simple distance threshold, since the subject is closer to the camera than any background points, thus it can be confidently said that any points farther away from the depth camera than a certain distance do not belong to the subject. While this simple process eliminates most of the background, there may be several outlier points which are closer to the camera than the threshold but still don't belong to the subject. Points like these are removed using the tools provided by the PCL library [41] for removal of statistical outliers.

After the point cloud is cleaned and segmented, the surface of the subject can be calculated from the point cloud data using the moving least squares method for surface reconstruction [42]. This method produces a set of points that is closer to the real surface, as well as the approximate normal of the surface at each point in the set. These point normals can be used to calculate the angle between the image plane of the thermal camera and the normal of the surface, allowing for temperature correction.

3.6 Temperature Correction

An IR camera absorbs photons emitted by heated surfaces and converts their energy into electric signals of the pixels on the focal plane array in the camera. The pixel signals (after self-calibration) are proportional to the radiance reaching the camera, which in the classical case can be modeled as [43]:

$$L(T) = \tau\varepsilon L_{\mathrm{bb}}(T) + \tau(1-\varepsilon)L_{\mathrm{bb}}(T) + (1-\tau)L_{\mathrm{bb}}(T_{\mathrm{at}}), \tag{3}$$

where ε is effective sample emissivity, τ is the effective atmosphere transmission coefficient, T_{at} and T_a are the atmospheric and radiative environment temperatures, respectively, and T is the temperature of the surface area focused in the pixel. $L_{\mathrm{bb}}(T)$ in Eq. 3 presents the effective black body emittance in the spectral range of detector:

$$L_{\mathrm{bb}}(T) = \int_{\lambda_1}^{\lambda_2} Q_{\mathrm{bb}}(\lambda, T)\mathrm{d}\lambda. \tag{4}$$

where

$$Q_{\mathrm{bb}} = \frac{c_1}{\lambda^5[\exp(c_2/\lambda T) - 1]}, \mathrm{W\ m^{-2}} \tag{5}$$

is the spectral radiant exitance for a black body given by Planck's law, $c_1 = 3.743 \times 10^{-16}\mathrm{W\ m^2}$ and $c_2 = 1.439 \times 10^{-2}\mathrm{m\ K}$, the first and second radiant constants; the wavelength and temperature are expressed in meters and Kelvin, respectively, λ_1 and λ_2 are the are lower and upper wavelengths of the spectral range, respectively.

The first term of Eq. 3 describes the radiation coming directly from a target surface, which is supposed to be a gray body (that emits radiation at each wave-length in a constant ratio to that emitted by a black body at the same temperature). The emissivity of human skin is equal to 0.98 ± 0.01 between wavelengths of 2 and 14 μm [44]. Thus, human skin behaves as a gray body in this wavelength region.

Any gray body reflects the IR emitted by the surroundings. The reflection coefficient, ρ of an opaque surface is directly related to the emissivity:

$$\rho = 1 - \varepsilon. \tag{6}$$

Thus, in accordance with Eq. 6, the reflection coefficient of human skin is equal to 0.02 between wavelengths of 2 and 14 mkm. Therefore, if the surrounding surfaces have sufficiently low temperature (during a medical thermography exam, temperatures are usually close to 25 °C) the second term of Eq. 3 is negligible relative to the first one. The third term is the IR emission of air between the target surface and the camera. In biomedical applications, the camera is sufficiently close to the object and the IR emission of air is negligible. In addition, the atmosphere transmission could be considered equal to unity. Therefore, Eq. 3 can be rewritten as

$$L(\lambda_1, \lambda_2, \theta, T) \int_{\lambda_1}^{\lambda_2} \frac{\varepsilon(\lambda, \theta) c_2}{\lambda^5[\exp(c_2/\lambda T) - 1]} \mathrm{d}\lambda. \tag{7}$$

Here the angle θ is the angle between the surface normal and the camera direction vector.

To evaluate integral (7) it is useful to define a lumped filter function, $f(\lambda_1, \lambda_2, \theta, T)$, as [45]

$$\int_{\lambda_1}^{\lambda_2} Q_{\mathrm{bb}}(\lambda, T)\mathrm{d}\lambda = f(\lambda_1, \lambda_2, \theta, T) \int_0^{\infty} Q_{\mathrm{bb}}(\lambda, T)\mathrm{d}\lambda = f(\lambda_1, \lambda_2, \theta, T)\sigma T^4, \tag{8}$$

where σ is the Stephan–Boltzmann constant.

By direct computation, Fuchs and Tanner [45] have shown that in the spectral range between 8 and 13 μm the lumped filter function changes from 0.3 to 0.34 for the temperature changes from 0 to 50 °C and, therefore, may be considered as constant in range of biological temperatures.

In 2D medical thermography it is usually supposed that all parts of a body surface have the same emissivity equal to 0.98 and that the temperature measured by calibrated IR camera corresponds to the real temperature of the body surface. This is true if all parts of a body are oriented perpendicular to the camera direction. For an oblique oriented surface, the emissivity depends on the angle of view and the apparent temperature of the surface of interest will differ from the real temperature.

Watmough et al. [8] were the first who estimated the errors in surface temperature measurements caused by the surface curvature. Their calculations consist of two stages. First, they found the angular dependence of the reflection coefficient and emissivity. Considering the human skin as a dielectric material with the real refractive index $n(\lambda)$, the angular dependence of emissivity was described by the formula:

$$\varepsilon(\lambda,\theta) = 1 - \frac{1}{2}\left(\frac{\beta - \cos\theta}{\beta + \cos\theta}\right)^2 \left[1 + \left(\frac{\beta\cos\theta - \sin^2\theta}{\beta\cos\theta + \sin^2\theta}\right)^2\right] \tag{9}$$

where $\beta = \sqrt{n(\lambda)^2 - \sin^2\theta}$.

The reflection coefficient and refractive index for the normal direction $(\theta = 0)$ are related by well-known Fresnel equation [13, p. 51, Eq. 4.16]:

$$\rho(\lambda,0) = \left[\frac{n(\lambda) - 1}{n(\lambda) - 1}\right]^2. \tag{10}$$

Taking into account Eq. 6 we can relate $n(\lambda)$ to $\varepsilon(\lambda,0)$:

$$n(\lambda) = \frac{2 + 2\sqrt{1 - \varepsilon(\lambda,0)}}{\varepsilon(\lambda,0)} - 1. \tag{11}$$

Substitution of $\varepsilon(\lambda,0) = 0.98$ into Eq. 11 gives $n(\lambda) = 1.329$ for the human skin.

The calculation of the human skin emissivity with Eqs. 9 and 11 shows that $\varepsilon(\lambda,\theta)$ is almost independent of the angle up to $\theta = \pi/4$ but thereafter the emissivity decreases drastically.

To calculate the error caused by the surface curvature, Watmough et al. [8] related the changes in the difference between the apparent temperatures, T_{ap} to corresponding changes of emissivity:

$$\Delta T = T_{\text{ap}}(0) - T_{\text{ap}}(\theta) = \left[1 - \sqrt[n]{\frac{\varepsilon(\lambda,\theta)}{\varepsilon(\lambda,0)}}\right] T_{\text{ap}}(0). \tag{12}$$

with $n = C_2/\lambda T$.

The temperature difference calculated with Eq. 12 depends on λ and is only valid for IR cameras with a narrow bandwidth filter. For IR cameras with a uniform response between λ_1 and λ_2 the apparent temperature can be estimated by using Eqs. 7 and 8. Suppose that a small area with normal angle θ has real temperature T and the emissivity is constant for wavelengths between λ_1 and λ_2. Then, the effective black body emittance can be written as

$$L(\lambda_1, \lambda_2, \theta, T) = \varepsilon(\theta) f(\lambda_1, \lambda_2, T) \sigma T^4. \tag{13}$$

If the IR camera is calibrated with a black body and the emissivity of any surface point of body is supposed to be equal to $\varepsilon(0)$, then apparent temperature, T_{ap} of a point with normal angle θ and the emissivity $\varepsilon(0)$ is defined as a temperature that fits the equation:

$$L(\lambda_1, \lambda_2, \theta, T) = f\left[\lambda_1, \lambda_2, T_{\text{ap}}(\theta)\right] \left[T_{\text{ap}}(\theta)\right]^4. \tag{14}$$

The comparison of Eqs. 13 and 14 gives

$$f(\lambda_1, \lambda_2, T) T^4 = \frac{f\left[\lambda_1, \lambda_2, T_{\text{ap}}(\theta)\right] \left[T_{\text{ap}}(\theta)\right]^4}{\varepsilon(\theta)} \tag{15}$$

If the two points with angles 0 and θ have the same real temperature, their apparent temperatures can be related with Eq. 15

$$\frac{f\left[\lambda_1, \lambda_2, T_{\text{ap}}(0)\right] \left[T_{\text{ap}}(0)\right]^4}{\varepsilon(0)} = \frac{f\left[\lambda_1, \lambda_2, T_{\text{ap}}(\theta)\right] \left[T_{\text{ap}}(\theta)\right]^4}{\varepsilon(\theta)} \tag{16}$$

Computations show that in the spectral range between 7.5 and 13.5 μm (the long-wave atmospheric window) $f(T) = 0.3796 + 9.760 \times 10^{-4}(T - 300) - 8.619 \times 10^{-6}(T - 300)^2$, where T in K. If the difference between $T_{\text{ap}}(0)$ and $T_{\text{ap}}(\theta)$ is less than few degrees, the lumped filter function can be considered as the constant and Eq. 16 is simplified to

$$T_{\text{ap}}(\theta) = \sqrt[4]{\frac{\varepsilon(\theta)}{\varepsilon(0)}} T_{\text{ap}}(0) \tag{17}$$

For IR cameras used for medical applications an emissivity value is usually setting at 0.98 corresponding to the emissivity of human skin. In this case, the apparent temperature $T_{\text{ap}}(0)$ for parts of a body are oriented perpendicular to the

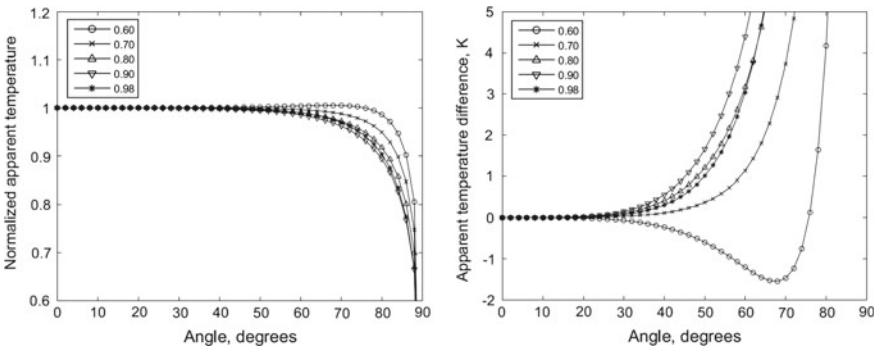

Fig. 5 Decrease in apparent temperature as a function of angle of view for indicated emissivities. *Left* the apparent temperature is normalized on those for the normal direction ($\theta = 0$). *Right* the difference $\Delta T = T_{\mathrm{ap}}(0) - T_{\mathrm{ap}}(\theta)$ calculated for $T_{\mathrm{ap}}(0)$ = 300 K

camera direction will coincide with real temperature T_r. The errors in surface temperature measurements caused by the surface curvature can be found from Eq. 17, in which $T_{\mathrm{ap}}(0)$ is replaced with T_r:

$$\Delta T = T_r - T_{\mathrm{ap}}(\theta) = \left[1 - \sqrt[4]{\frac{\varepsilon(\lambda,\theta)}{\varepsilon(\lambda,0)}}\right] T_r. \tag{18}$$

The derived equation is similar to those obtained by Watmough et al. [8] (Eq. 12). The only difference is the exponent of the root, which is equal to four for cameras with bandpass filters and depends on temperature and wavelength for narrow bandwidth filters.

The effect of the surface curvature on measured temperature for a number of emissivities calculated with Eqs. 17 and 18 is presented in Fig. 5. The left panel shows the relative apparent temperature respect to the temperature of normally oriented surface. For emissivities higher than 0.65 the apparent temperature monotonically increases as the angle θ increases. For lower emissivities the non-monotonous behavior is observed due to the non-monotonous dependence of emissivity on the angle between the surface normal and the camera direction. The right panel shows the difference $\Delta T = T_{\mathrm{ap}}(0) - T_{\mathrm{ap}}(\theta)$ calculated for $T_{\mathrm{ap}}(0)$ = 300 K.

4 3D Dynamic Thermography System

In this section a system for taking and analyzing 3D dynamic thermograms is presented. The system consists of structural elements and sliding and rotating joints that allow the placement of cameras and sensors in space around the subject, at fixed positions and angles. Two FLIR thermal cameras and two depth sensors were

Fig. 6 Photograph of the 4D thermography system with two camera units mounted on rotating arms around a subject, each camera unit (inset photograph) consists of a FLIR A320 thermal imaging camera and a Creative Senz3D depth sensor

used for the image acquisition and the construction of 3D thermograms. The depth sensors were rigidly mounted to the thermal cameras and their sensors were aligned, forming a single unit as seen in the inset photograph in Fig. 6. Two such units are mounted on the arms of the device and turned to face the subject of the study. Using two sets of cameras ensures that the subject is visible from both sides simultaneously (Fig. 6). The system also includes a computer to run the software used to acquire and process the 3D thermograms.

The choice of depth sensors for this application is of particular importance, since it needs to meet two specific criteria: the acquisition speed must be fast and the sensors must not interfere with each other, since they must operate simultaneously. In particular on the second point, a sensor like the Microsoft Kinect V1 uses structured light with a near-infrared projector and two such sensors operating at the same time would cause interference and return false data. A pair of Creative Senz3D time-of-flight sensors were chosen, due to the fact that their principle of operation is more resistant to interference from another sensor [46].

4.1 Data Acquisition and Processing

The software of the 3D thermography system is responsible for the camera calibration, data acquisition, processing and the construction of dynamic 3D thermograms.

Calibration is performed individually for each camera to obtain their intrinsic matrices, and then for all the cameras in the system together to obtain the camera poses in a unified world coordinate system. The calibration setup is shown in Fig. 7. The calibration target used is a rectangular piece of 5 mm foamboard on which an asymmetrical grid of circles has been cut with a laser cutter.

During the data acquisition phase, the raw thermal and depth images are downloaded from the connected sensors. The raw data is often noisy and may have missing values, which means that the data must be filtered to remove as much noise as possible and compensate for any missing data. Once the quality of the incoming data is ensured, the next phase of the process consists of the transformation of the distance information obtained from the depth sensors into a point cloud in 3D space and the generation of a surface based on this point cloud, as well as the projection of the thermal images onto this surface to obtain a 3D thermogram. To perform this step, it is essential to know the physical parameters, such as focal lengths and distortion coefficients, of the cameras used and their locations in space relative to each other, all of which were obtained during the camera calibration.

In order to build a 3D thermogram at a particular instant in time, and image must be taken by each of the four cameras and transferred to a computer where the 3D thermogram can be assembled. It is important to ensure that the four images are taken as close as possible in time in order to provide adequate synchronization between depth and thermal images. The FLIR A320 cameras used stream their images over the network in an RTSP stream. Each thermal image consists of an array of 16-bit wide unsigned integers that linearly correspond to the apparent temperature of the target object as seen by the camera. The Creative Senz3D cameras connect via standard USB 2.0 and the data is obtained using an SDK provided by SoftKinetic for their DepthSense cameras. The Senz3D cameras

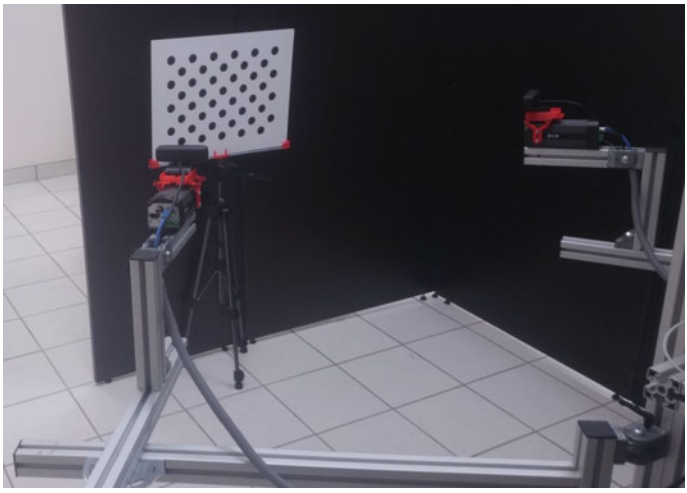

Fig. 7 Calibration setup used to find the intrinsic and extrinsic parameters of the camera system

provide a stream of depth images. Each depth image consists of an array of floating point numbers that correspond to the distance in meters to the object in that position. The thermal images provided by the FLIR A320 cameras do not require processing to remove the noise, however, they must be corrected for distortion. On the other hand, depth images provided by modern time-of-flight sensors are somewhat noisy and require some cleanup. The noise is reduced by taking multiple depth images in succession and averaging them, and then applying a bilateral filter to the result [47]. This treatment improves the quality of the depth image and makes it more useful for surface reconstruction. Figure 8 presents an example visualization of a 3D thermogram obtained by the software.

In addition to visualizing a 3D thermogram from all angles, the presence of geometric data allows new ways to analyze a traditional thermogram. One problem with a traditional two-dimensional thermal image is that due to low thermal contrast it can be difficult to segment the image into various regions of interest and to separate the background from the subject of study. Background segmentation is achieved by projecting only the points of the subject onto a thermal image, and only those parts of the image that fall under the projected points can be considered as part of the subject, and the rest as part of the background. Figure 9 presents an example of this process applied to a thermal image of a mannequin with poor thermal contrast.

Once the subject is found on the thermal image by means of background segmentation, the correct temperature of the pixels that correspond to the subject can be calculated by taking into account the surface curvature. Each point of the subject that was projected onto the thermogram has an associated normal in world coordinates, which is be used to calculate the angle between the surface normal and the camera direction vector of said point. Based on the position of the subject points on the thermogram, the angle is calculated for each pixel of the thermogram that

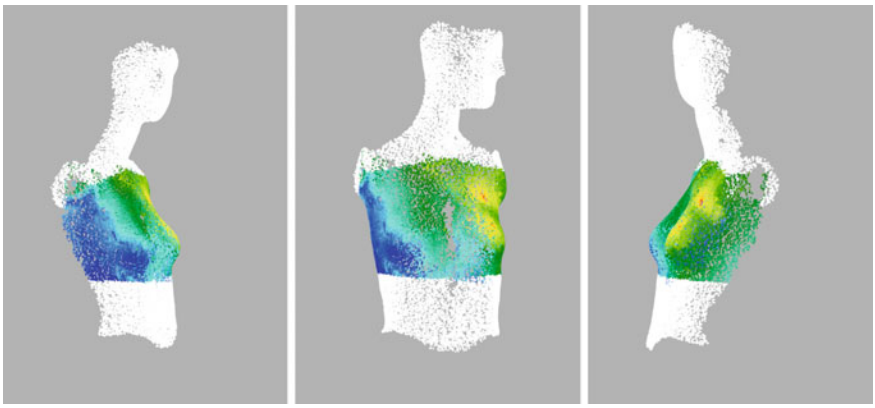

Fig. 8 Example of a 3D thermogram taken with the system, showing the reconstruction of the subject from different angles. Points that are white are not visible by the thermal cameras and thus have no temperature assigned to them

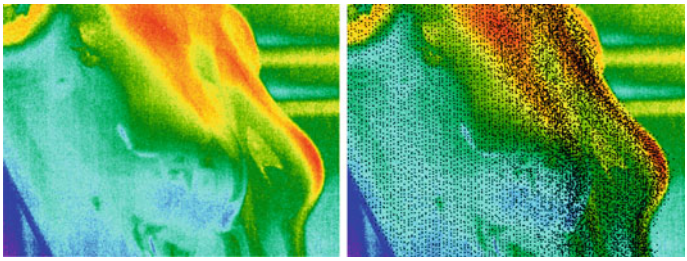

Fig. 9 Segmentation of the background and the subject on a thermogram of a mannequin, the *black points* correspond to the extracted and projected subject

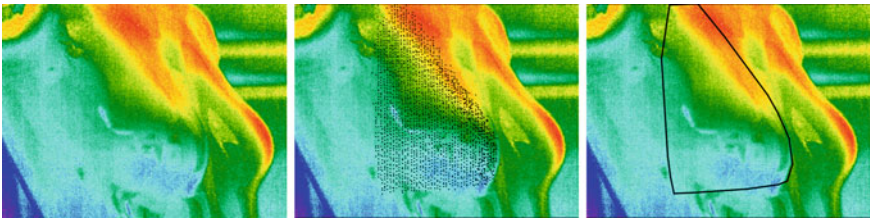

Fig. 10 Steps taken for the selection of the ROI of a breast thermogram

belongs to the subject, and this angle is be used to apply the temperature correction using Eq. 18 to produce the correct temperature.

To extract areas of interest from the thermogram, a similar process to the one used for background segmentation. Before projecting the points onto the thermal image, the region of interest is segmented from the subject point cloud, which can be achieved either by an operator or through simple heuristics. The key advantage of this method is that a region of interest will often be clearly visible on the surface, when it is not identifiable on the 3D thermogram. Figure 10 shows an example of this process applied to the selection of the breast on a thermal image of a mannequin with poor thermal contrast.

5 Future Work

A mannequin presents a simple object to work with, however when applying the techniques presented in this work to a live human being, several problems arise. A mannequin is an unmoving target, this means that several frames of a depth map can be collected and averaged in order to help eliminate noise. On the other hand, a human subject will find it difficult to sit still for an extended amount of time and will invariably shift and move, thus the time available for collecting data is smaller, which results in noisier 3D data. Additionally, commercial depth sensors produce

relatively low resolution images, and any 3D models produced from these images will be coarse and inaccurate, particularly for smaller body parts like feet and hands. This problem can be solved by using the depth sensor to perform a high quality 3D scan using the fusion of multiple depth images taken at different angles around the object, however this would require the subject to remain still for the duration of the scan and since it takes a relatively long time, 10 to 20 min, it is unsuitable for dynamic thermography. A possible approach is to combine a high quality 3D scan and register it with dynamic 3D thermograms obtained on the fly using the techniques presented in this work to produce high quality dynamic 3D thermograms.

Another direction for the future of this work is the presentation of 3D thermograms and their analysis in a way that is useful to a medical specialist performing the study. The traditional way to present 3D data is with a software visualization that allows the user to rotate and position a virtual camera at any point around the studied object, however, this is not very useful and does not present any new information. Studies need to be conducted to determine what kind of information is useful to medical practitioners working with the thermograms and what is the best way to present it.

6 Conclusion

The presence of 3D data about the surface under study has a lot of utility in research for biomedical applications. A big advantage of 3D data is the availability of information about the curvature and shape of the object, in particular, since the temperature shown by a thermal camera depends on the difference between the surface normal and the camera direction, having the surface normal means that it is possible to calculate the correct surface temperature at a given point on the surface, taking into account its curvature. Another advantage is the possibility to use the information about the shape of the subject to select a region of interest for further study taking into account the anatomy of the subject. Finally, it is possible to use the 3D data to simply eliminate the background from a 2D thermogram. While the presence of 3D data carries many advantages, working with more data carries additional costs and trade-offs. The major complication in working with 3D data as opposed to simple 2D images is that the required computing power grows exponentially. Additionally, due to the fact that depth images are noisy, there has to be a trade-off between accuracy and acquisition time, the more accurate one wants the 3D representation to be, the more depth images are needed to calculate said surface.

Acknowledgements Authors gratefully acknowledge the financial support from CONACyT (Mexico) under grant 213208, from Convocatoria “Proyectos de desarrollo cientifco para atender problem as nacionales, 2013” and under grant 222496, from Convocatoria “Programa de Estímulos a la Innovación, 2015.” We also wish to thank C. Dávila Peralta and R. Rodriquez Carvajal for active participation in part of these projects.

References

1. Ammer, K.: Thermography 2015—a computer-assisted literature survey. Thermol. Int. **26**(1), 5–42 (2016)
2. Lahiri, B., Bagavathiappan, S., Jayakumar, T., Philip, J.: Medical applications of infrared thermography: a review. Infrared Phys. Technol. **55**(4), 221–235 (2012)
3. Kaczmarek, M., Nowakowski, A.: Active IR-thermal imaging in medicine. J. Nondestr. Eval. **35**(1), 1–16 (2016)
4. Saniei, E., Setayeshi, S., Akbari, M.E., Navid, M.: A vascular network matching in dynamic thermography for breast cancer detection. Quant. InfraRed Thermogr. J. **12**(1), 24–36 (2015)
5. Renkielska, A., Kaczmarek, M., Nowakowski, A., Grudziński, J., Czapiewski, P., Krajewski, A., Grobelny, I.: Active dynamic infrared thermal imaging in burn depth evaluation. J. Burn Care Res., 1 (2014). doi:10.1097/BCR.0000000000000059
6. Godoy, S.E., Ramirez, D.A., Myers, S.A., von Winckel, G., Krishna, S., Berwick, M., Padilla, R.S., Sen, P., Krishna, S.: Dynamic infrared imaging for skin cancer screening. Infrared Phys. Technol. **70**, 147–152 (2015)
7. Weum, S., Mercer, J.B., de Weerd, L.: Evaluation of dynamic infrared thermography as an alternative to CT angiography for perforator mapping in breast reconstruction: a clinical study. BMC Med. Imag. **16**, 43 (2016)
8. Watmough, D.J., Fowler, P.W., Oliver, R.: The thermal scanning of a curved isothermal surface: implications for clinical thermography. Phys. Med. Biol. **15**(1), 1 (1970)
9. Sawicki, P., Stein, R., Wiecek, B.: Directional emissivity correction by photogrammetric 3D object reconstruction. Quant. InfraRed Thermogr. **1998-052**, 327–332 (1998). http://qirt.org/archives/qirt1998/papers/052.pdf
10. Wiecek, B., Zwolenik, S., Jung, A., Zuber, J.: Advanced thermal, visual and radiological image processing for clinical diagnostics. In: Proceedings of the First Joint Engineering in Medicine and Biology, 1999. 21st Annual Conference and the 1999 Annual Fall Meeting of the Biomedical Engineering Society BMES/EMBS Conference, vol. 2, p. 1108 (1999)
11. Hilsenstein, V.: Surface reconstruction of water waves using thermographic stereo imaging. In: Image and Vision Computing New Zealand, vol. 2. Citeseer (2005)
12. Prakash, S., Lee, P.Y., Caelli, T.: 3D mapping of surface temperature using thermal stereo. In: 2006 9th International Conference on Control, Automation, Robotics and Vision (2006). doi:10.1109/icarcv.2006.345342
13. Prakash, S., Lee, P.Y., Caelli, T., Raupach, T.: Robust Thermal Camera Calibration and 3D Mapping of Object Surface Temperatures, p. 62050J (2006). doi:10.1117/12.668459
14. Prakash, S., Lee, P.Y., Robles-Kelly, A.: Stereo techniques for 3D mapping of object surface temperatures. Quant. InfraRed Thermogr. J. **4**(1), 63–84 (2007)
15. Sella, T., Sklair-Levy, M., Cohen, M., Rozin, M., Shapiro-Feinberg, M., Allweis, T., Libson, E., Izhaky, D.: A novel functional infrared imaging system coupled with multiparametric computerised analysis for risk assessment of breast cancer. Eur. Radiol. **23**(5), 1191–1198 (2013). doi:10.1007/s00330-012-2724-7
16. Mirabella, C., Bellandi, S., Graziani, G., Tolomei, L., Manetti, L., Fortuna, D.: Hemodynamic 3D infrared thermal stereoscopic imaging (TSI) investigation in chronic vascular leg ulcers: a feasibility study. Wounds Compendium Clin. Res. Pract. **23**(9), 276–284 (2011)
17. Ng, H.Y.M., Du, R.: Acquisition of 3D surface temperature distribution of a car body. In: 2005 IEEE International Conference on Information Acquisition, pp. 16–20. IEEE (2005). doi:10.1109/ICIA.2005.1635046
18. Szeliski, R.: Rapid Octree Construction from Image Sequences. CVGIP: Image Underst. **58** (1), 23–32 (1993)
19. Chen, C.Y., Yeh, C.H., Chang, B.R., Pan, J.M.: 3D reconstruction from IR thermal images and reprojective evaluations. In: Mathematical Problems in Engineering, pp. 1–8 (2015)
20. An, Y., Zhang, S.: High-resolution, real-time simultaneous 3D surface geometry and temperature measurement. Opt. Expr. **24**(13), 14552 (2016)

21. Grubišić, I.: Medical 3D thermography system. Periodicum Biologorum **113**(4), 401–406 (2011)
22. Soldan, S.: On extended depth of field to improve the quality of automated thermographic measurements in unknown environments. Quant. InfraRed Thermogr. J. **9**(2), 135–150 (2012)
23. Aksenov, P., Clark, I., Grant, D., Inman, A., Vartikovski, L., Nebel, J.C.: 3D thermography for quantification of heat generation resulting from inflammation. In: 3D Modelling Symposium. Citeseer (2003)
24. Ju, X., Nebel, J.C., Siebert, J.P.: 3D thermography imaging standardization technique for inflammation diagnosis. In: Photonics Asia 2004, pp. 266–273. International Society for Optics and Photonics (2005)
25. Chen, S., Li, Y.F., Wang, W., Zhang, J.: Active Sensor Planning for Multiview Vision Tasks, vol. 1. Springer (2008)
26. Xiao, H., Zhang, Y., Wang, A.: Multispectral three-dimensional digital infrared thermal imaging. Opt. Eng. **42**(4), 906–911 (2003)
27. Barone, S., Paoli, A., Razionale, A.V.: A biomedical application combining visible and thermal 3D imaging. In: XVIII Congreso internactional de Ingenieria Grafica, Barcelona, pp. 1–9 (2006)
28. Barone, S., Paoli, A., Razionale, A.V.: Assessment of chronic wounds by three-dimensional optical imaging based on integrating geometrical, chromatic, and thermal data. Proc. Inst. Mech. Eng. **225**(2), 181–193 (2011)
29. Yang, R., Chen, Y.: Design of a 3D infrared imaging system using structured light. IEEE Trans. Instrum. Meas. **60**(2), 608–617 (2011)
30. Cheng, V.S., Bai, J., Chen, Y.: A high-resolution three-dimensional far-infrared thermal and true-color imaging system for medical applications. Med. Eng. Phys. **31**(9), 1173–1181 (2009)
31. Sun, J., Ma, H., Zeng, D.: Three-dimensional infrared imaging method based on binocular stereo vision. Opt. Eng. **54**(10), 103, 111 (2015)
32. Rangel, J., Soldan, S., Kroll, A.: 3D thermal imaging: fusion of thermography and depth cameras. In: International Conference on Quantitative InfraRed Thermography (2014)
33. Skala, K., Lipić, T., Sović, I., Gjenero, L., Grubišić, I.: 4D thermal imaging system for medical applications. Periodicum Biologorum **113**(4), 407–416 (2011)
34. Müller, A.O., Kroll, A.: On the temperature assignment problem and the use of confidence textures in the creation of 3D thermograms. In: 2015 9th International Conference on Sensing Technology (ICST), pp. 223–228 (2015)
35. Vidas, S., Moghadam, P.: Heatwave: a handheld 3D thermography system for energy auditing. Energy Build. **66**, 445–460 (2013)
36. Vidas, S., Moghadam, P., Bosse, M.: 3D thermal mapping of building interiors using an RGB-D and thermal camera. In: 2013 IEEE International Conference on Robotics and Automation (ICRA), pp. 2311–2318 (2013)
37. Vidas, S., Moghadam, P., Sridharan, S.: Real-time mobile 3D temperature mapping. IEEE Sens. J. **15**(2), 1145–1152 (2015)
38. Moghadam, P., Vidas, S.: Heatwave: The Next Generation of Thermography Devices, pp. 91050F (2014). doi:10.1117/12.2053950
39. de Souza, M.A., Krefer, A.G., Borba, G.B., Centeno, T.M., Gamba, H.R.: Combining 3D models with 2D infrared images for medical applications. In: 2015 37th Annual International Conference of the IEEE Engineering in Medicine and Biology Society (EMBC), pp. 2395–2398. IEEE (2015)
40. Wang, Y., Li, Y., Zheng, J.: A camera calibration technique based on opencv. In: 2010 3rd International Conference on Information Sciences and Interaction Sciences (ICIS), pp. 403–406. IEEE (2010)
41. Rusu, R.B., Cousins, S.: 3D is here: point cloud library (PCL). In: 2011 IEEE International Conference on Robotics and Automation (ICRA), pp. 1–4. IEEE (2011)
42. Berger, M., Tagliasacchi, A., Seversky, L., Alliez, P., Levine, J., Sharf, A., Silva, C.: State of the art in surface reconstruction from point clouds. Eurogr. Star Rep. **1**, 161–185 (2014)

43. Horny, N.: FPA camera standardisation. Infrared Phys. Technol. **44**(2), 109–119 (2003)
44. Jones, B.F.: A reappraisal of the use of infrared thermal image analysis in medicine. IEEE Trans. Med. Imag. **17**(6), 1019–1027 (1998)
45. Fuchs, M., Tanner, C.B.: Infrared thermometry of vegetation. Agron. J. **58**(6), 597–601 (1966)
46. Li, L.: Time-of-flight camera—an introduction. Technical white paper, May (2014)
47. Paris, S., Kornprobst, P., Tumblin, J., Durand, F.: A gentle introduction to bilateral filtering and its applications. In: ACM SIGGRAPH 2007 Courses, p. 1. ACM (2007)

Index

E.Y.K. Ng and M. Etehadtavakol (eds.), *Application of Infrared to Biomedical Sciences*, Series in BioEngineering,
DOI 10.1007/978-981-10-3147-2